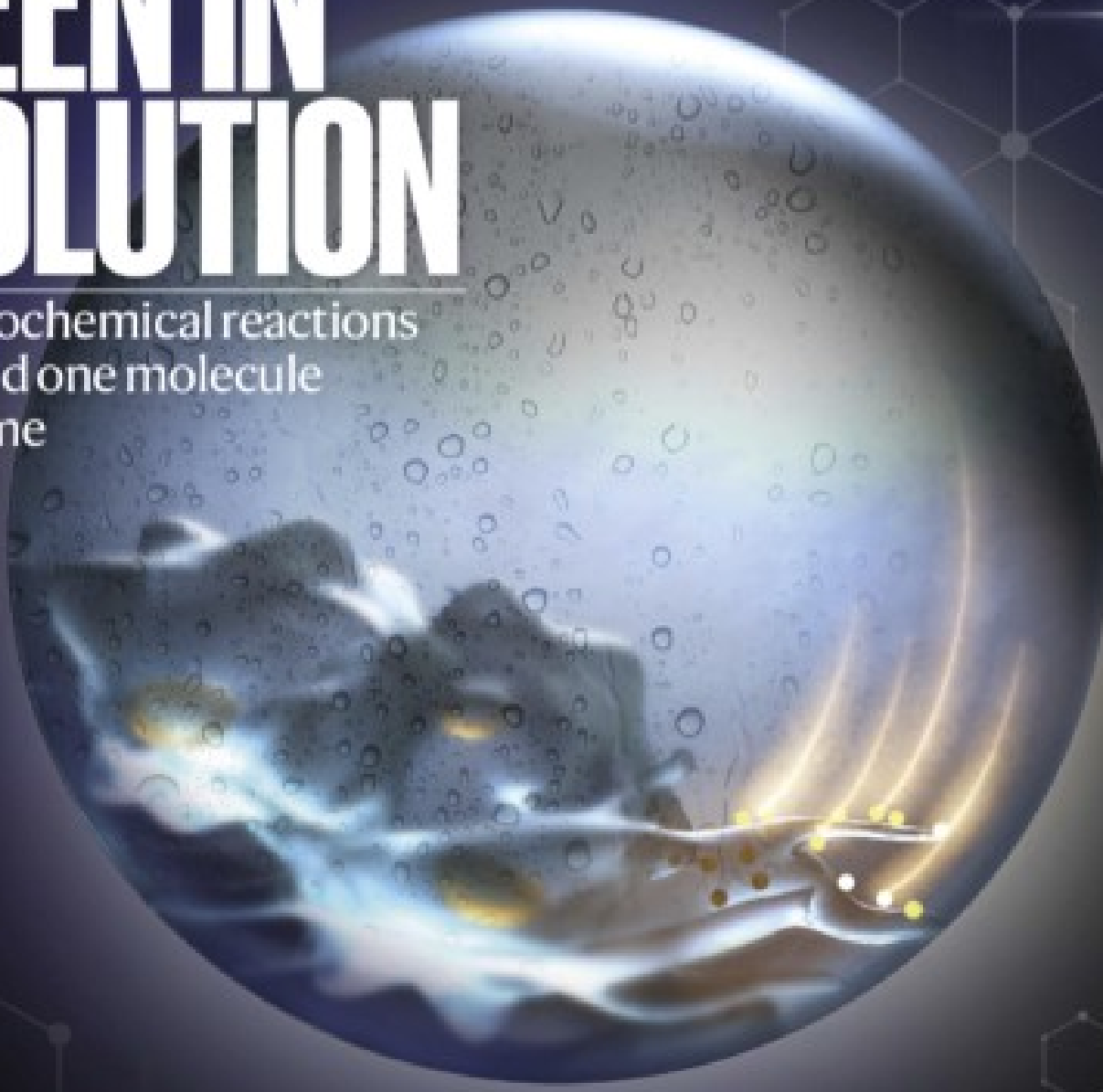


nature

SEEN IN SOLUTION

Electrochemical reactions
imaged one molecule
at a time



Coronavirus
Are plans for vaccine
booster jabs really
necessary?

Orphaned by COVID
Lessons from HIV
can help children
weather adversity

Nematode nemesis
Unwanted proteins
cause problems for
ageing worms

Vol 595 No. 7892

Nature.2021.08.14

[Sat, 14 Aug 2021]

- [This Week](#)
- [News in Focus](#)
- [Books & Arts](#)
- [Opinion](#)
- [Work](#)
- [Research](#)
- [Amendments & Corrections](#)

| [Next section](#) | [Main menu](#) |

Donation

| [Next section](#) | [Main menu](#) |

This Week

- **[The world must cooperate to avoid a catastrophic space collision](#)** [11 August 2021]
Editorial • Governments and companies urgently need to share data on the mounting volume of satellites and debris orbiting Earth.
- **[Talking to science deniers and sceptics is not hopeless](#)** [05 August 2021]
World View • Fears of backfire effects are overblown, and advice to listen and interact still stands.
- **[Squirrels do parkour](#)** [05 August 2021]
Research Highlight • Squirrels show off multiple landing styles as they speed through the canopy.
- **[Volcano that built an island paradise is attuned to the sea](#)** [02 August 2021]
Research Highlight • Eruptions of Santorini volcano, which created the Greek island of the same name, are linked to drops in sea level.
- **[An absorbing tale: poison dart frogs might have a ‘toxin sponge’](#)** [05 August 2021]
Research Highlight • Experiments suggest that the frogs use internal proteins to soak up their own toxins.
- **[‘Robber’ experiment tests generosity — with sobering results](#)** [02 August 2021]
Research Highlight • People who give freely to a single individual get selfish in a crowd.
- **[How old is Machu Picchu? The dead whisper a hint](#)** [03 August 2021]
Research Highlight • Analysis of human bones suggests that historical records about the iconic site in Peru are inaccurate.
- **[How the daddy-long-legs gets long legs](#)** [05 August 2021]
Research Highlight • A single genetic toolkit gives rise to the spider-lookalike’s slender gams and to the grasping legs of related animals.
- **[Wildfire smoke creates brighter clouds — and weather changes](#)** [03 August 2021]

Research Highlight • Data from research flights through smoke plumes show that tiny particulates affect cloud droplet formation.

| [Next section](#) | [Main menu](#) | [Previous section](#) |

- EDITORIAL
- 11 August 2021

The world must cooperate to avoid a catastrophic space collision

Governments and companies urgently need to share data on the mounting volume of satellites and debris orbiting Earth.





•

[Download PDF](#)



Space junk such as broken spacecraft and inactive satellites (illustration) adds to mounting congestion in Earth's orbit. Credit: European Space Agency/SPL

There's an awful lot of stuff orbiting Earth, with more arriving all the time. More than 29,000 satellites, pieces of rockets and other bits of debris large enough to track from the ground are circling the planet. Smaller items number in the millions. The Californian company SpaceX alone has launched some 1,700 satellites over the past 2 years as part of its Starlink network, which provides broadband Internet, with thousands more planned. Other companies are also planning such megaconstellations, and more and more nations are launching or plan to launch satellites.

This growing congestion is drastically increasing the risk of collisions in space. At the European Space Agency's operations centre in Darmstadt, Germany, which controls key research spacecraft, hundreds of e-mail alerts arrive each day warning of potential space smash-ups. And, in May, NASA engineers spotted a 5-millimetre-wide hole in one of the International Space

Station's robotic arms, created by a collision with an unknown piece of space junk.

These close calls highlight not only the need to be more thoughtful about what we put into space, but also that it's well past time the global space community developed a sustainable framework for managing space traffic. Such a move would benefit both the scientists who rely on observations from orbit and humanity as a whole, because satellites are crucial for modern communication and navigation.



[Astronomers push for global debate on giant satellite swarms](#)

History offers some lessons about how to operate safely in newly crowded domains. During the early twentieth century, aviation boomed and pilots ran into congestion in the skies. Air-traffic controllers ultimately developed a system of coordinating between cities and across borders, sharing information about aeroplanes' locations so that pilots could avoid crashing into one another.

But there are no traffic cops in space, nor international borders with clearly delineated areas of responsibility. To avoid further damage, it's crucial that satellite operators have an accurate and up-to-date list of where objects are in space. At present, the main global catalogue of space objects is published at Space-Track.org by the US Space Command, a branch of the military. The

catalogue is the most widely used public listing available, but it lacks some satellites that countries — including the United States, China and Russia — have not acknowledged publicly. In part because of this lack of transparency, other nations also track space objects, and some private companies maintain commercially available catalogues.

Rather than this patchwork of incomplete sources, what the world needs is a unified system of space traffic management. Through this, spacefaring nations and companies could agree to share more of their tracking data and cooperate to make space safer. This might require the creation of a new global regime, such as an international convention, through which rules and technical standards could be organized. One analogy is the International Telecommunication Union, the United Nations agency that coordinates global telecommunications issues such as who can transmit in which parts of the radio spectrum.

It won't be easy to create such a system for space traffic. For it to succeed, questions of safety (such as avoiding smashing up a satellite) will need to be disentangled from questions of security (such as whether that satellite is spying on another nation) so that countries can be assured that participating in such an effort would not compromise national security. Countries could, for instance, share information about the location of a satellite without sharing details of its capabilities or purpose for being in space.



How satellite ‘megaconstellations’ will photobomb astronomy images

One near-term move that would help would be for the United States to complete a planned shift of responsibility for the Space-Track.org catalogue from the military to the civilian Department of Commerce. Because this catalogue has historically been the most widely used around the world, shifting it to a civilian agency could start to defuse geopolitical tensions and so improve global efforts to manage space debris. It might one day feed into a global space-traffic agreement between nations; even the nascent space superpower China would have a big incentive to participate, despite rivalries with the United States. The transition was called for in a 2018 US presidential directive that recognizes that companies are taking over from national governments as the dominant players in space, but it has yet to occur, in part because Congress has not allocated the necessary funds.

On 25 August, the UN Committee on the Peaceful Uses of Outer Space will meet to discuss a range of topics related to international cooperation in space. The UN is the right forum through which spacefaring nations can work together to establish norms for responsible space behaviour, and that should include how the world can track objects to make space safer. It should continue recent work it has been doing emphasizing space as a secure and sustainable environment, which at least brings countries such as the United States and China into the same conversation.

Basic research has a role, too: innovations such as techniques to track and display the locations of orbiting objects in real time, and artificial intelligence to help automate debris-avoidance manoeuvres, could bolster any global effort to monitor and regulate space.

If governments and companies around the world do not take urgent action to work together to make space safer, they will one day face a catastrophic collision that knocks out one or more satellites key to their safety, economic well-being or both. Space is a global commons and a global resource. A global organization responsible for — and capable of — managing the flow of space traffic is long overdue.

doi: <https://doi.org/10.1038/d41586-021-02167-5>

Related Articles

-  [How satellite ‘megaconstellations’ will photobomb astronomy images](#)
-  [Astronomers push for global debate on giant satellite swarms](#)
- [The challenge of satellite megaconstellations](#)

Subjects

- [Space physics](#)
- [Government](#)
- [Politics](#)

nature careers

[Jobs](#) >

- [Technology and Knowledge Transfer Officer / Commercialization](#)

University of Luxembourg
Luxembourg, Luxembourg
- [Technology and Knowledge Transfer Officer / Social Sciences, Humanities](#)

University of Luxembourg

Luxembourg, Luxembourg

- [Postdoctoral Research Assistant \(m/f/div\) in modelling and data science](#)

Max Planck Institute for the Science of Human History

Jena, Germany

- [Postdoc researcher in de novo design of transmembrane beta-barrels for nanopore sensing applications](#)

Flanders Institute for Biotechnology (VIB)

Brussels, Belgium

Nature Briefing

An essential round-up of science news, opinion and analysis, delivered to your inbox every weekday.

[Download PDF](#)

Related Articles



- [How satellite ‘megaconstellations’ will photobomb astronomy images](#)



- [Astronomers push for global debate on giant satellite swarms](#)
- [The challenge of satellite megaconstellations](#)

Subjects

- [Space physics](#)
- [Government](#)
- [Politics](#)

This article was downloaded by **calibre** from <https://www.nature.com/articles/d41586-021-02167-5>

| [Section menu](#) | [Main menu](#) |

- WORLD VIEW
- 05 August 2021

Talking to science deniers and sceptics is not hopeless



Fears of backfire effects are overblown, and advice to listen and interact still stands.

- [Lee McIntyre](#) 0

1. [Lee McIntyre](#)

1. Lee McIntyre is a research fellow at the Center for Philosophy and History of Science at Boston University, Massachusetts, and author of the forthcoming book *How to Talk to a Science Denier: Conversations With Flat Earthers, Climate Deniers, and Others Who Defy Reason* (MIT Press, 2021).

[View author publications](#)

You can also search for this author in [PubMed](#) [Google Scholar](#)

-



•

[Download PDF](#)

I was at the March for Science in Boston, Massachusetts, on 22 April 2017, as were many scientists. About 70,000 of us descended on the Boston Common, a famous park in the city. We were there to stand up for facts and truth.

Where are the crowds of scientists now? Since then, harms from science denial have only increased: global suffering has grown owing to inaction on climate change, and COVID-19 infections have risen along with the scourge of vaccine scepticism.

I've been out there — I talked to flat-earthers at a convention in Denver, Colorado, and went to rural Pennsylvania to talk to coal miners about climate change — and I've asked my scientist friends to come with me. No dice.

"Those people just aren't worth talking to," they'll say. "I wouldn't make a difference anyway."

That's wrong, both factually and morally. Those people can and do change their minds, although it requires someone to put in the time to overcome distrust.



You can't fight feelings with facts: start with a chat

To be sure, many experts have launched themselves against misinformation, enduring abuse on social media and even threats to their safety. But when scientists turn down my invitations, it's not because of fear. Most often, their excuses are grounded in the 'backfire effect', an irreproducible 2010 finding that people sometimes embrace misconceptions more strongly when faced with corrective information, implying that pushing back against falsehoods is counterproductive. Even the researchers whose results were exaggerated to popularize this idea do not embrace it any more, and argue that the true challenge is learning how best to target corrective information

([B. Nyhan Proc. Natl Acad. Sci. USA 118, e1912440117; 2021](#)). (Public-engagement-101 advice to ‘build trust and listen’ is still paramount.)

Meanwhile, evidence is growing that rebuttals can be effective. Science deniers — whether on vaccines, evolution or climate — all draw on the same flawed reasoning techniques: cherry-picking evidence, relying on conspiracy theories and fake experts, engaging in illogical reasoning and insisting that science must be perfect. A landmark 2019 study ([P. Schmid & C. Betsch Nature Hum. Behav. 3, 931–939; 2019](#)) showed that critiquing flawed techniques can mitigate disinformation. (Admittedly, this study did not examine whether this works in person or with hard-core deniers.)

So how does ‘technique rebuttal’ work in practice? Here’s my experience. When I attended the Flat Earth International Conference in 2018, I chose to say nothing on the first day, although it was hard to keep my mouth shut when I heard that Antarctica is a wall of ice that keeps the sea from flowing off Earth. By the second day, I was glad I’d waited. I knew if I’d offered evidence, they’d say that space was fake and scientists were liars.



[Pseudoscience and COVID-19 — we’ve had enough already](#)

Although I didn’t convince any flat-earthers on the spot, I did learn how to get them to listen. I let them speak, then followed up with questions once the dialogue was rolling. Instead of refuting arguments, I asked, “What

evidence might change your mind?” If they said they needed ‘proof’, I asked why existing evidence was insufficient. If they shared a conspiracy theory, I asked why they trusted the evidence for it. By doing that — and not monologuing the facts — I was able to let them wonder why they couldn’t answer my questions.

It is an axiom of science communication that you cannot convince a science denier with facts alone; most science deniers don’t have a deficit of information, but a deficit of trust. And trust has to be built, with patience, respect, empathy and interpersonal connections. Because I spent the first day listening, even committed deniers were interested in what I had to say.

Arnaud Gagneur, a researcher and physician at the University of Sherbrooke in Canada, and his colleagues conducted more than 1,000 20-minute interviews in which they listened to new parents’ concerns about vaccinations and answered their questions. Those parents’ children were 9% more likely to receive all the vaccines on the schedule than were those of uninterviewed parents whose babies were delivered in the same maternity ward ([T. Lemaitre et al. Hum. Vaccin. Immunother. 15, 732–739; 2019](#)). One mother told him: “It’s the first time that I’ve had a discussion like this, and I feel respected, and I trust you.”



[Coronavirus misinformation, and how scientists can help to fight it](#)

So what should scientists do? Even non-experts can use technique rebuttal. A geologist can engage a neighbour who is vaccine hesitant. A protein biologist can coach an aunt or uncle who wants ‘more evidence’ that climate change is real. (‘Content rebuttal’ can also be effective, but requires expertise.) Instead of shifting to more comfortable conversations, engage in respectful exchange. If you spend more time asking questions than offering explanations, people will be more likely to heed the explanations that you do offer.

Where should you do this? Wherever science deniers can be found. Speak up in line at the pharmacy. Volunteer to speak at your kids’ school. Or, if you’re ambitious, join me at the upcoming flat-earth convention. I already have a physicist friend coming along.

Those who want to make a difference can learn how to do so. Resources are available through the Alan Alda Center for Communicating Science in Stony Brook, New York, and the University of Cincinnati’s Center for Public Engagement with Science in Ohio. It isn’t as comfortable as cheering with fellow marchers, but it can be more effective.

Nature **596**, 165 (2021)

doi: <https://doi.org/10.1038/d41586-021-02152-y>

Competing Interests

The author declares no competing interests.

Related Articles

-  [**You can't fight feelings with facts: start with a chat**](#)



- [Pseudoscience and COVID-19 — we've had enough already](#)



- [Coronavirus misinformation, and how scientists can help to fight it](#)

Subjects

- [Communication](#)
- [Society](#)

nature careers

[Jobs](#) >

- [Technology and Knowledge Transfer Officer / Commercialization](#)

University of Luxembourg

Luxembourg, Luxembourg

- [Technology and Knowledge Transfer Officer / Social Sciences, Humanities](#)

University of Luxembourg

Luxembourg, Luxembourg

- [Postdoctoral Research Assistant \(m/f/div\) in modelling and data science](#)

Max Planck Institute for the Science of Human History

Jena, Germany

- [Postdoc researcher in de novo design of transmembrane beta-barrels for nanopore sensing applications](#)

Flanders Institute for Biotechnology (VIB)

Brussels, Belgium

Nature Briefing

An essential round-up of science news, opinion and analysis, delivered to your inbox every weekday.

[Download PDF](#)

Related Articles



- [You can't fight feelings with facts: start with a chat](#)



- [Pseudoscience and COVID-19 — we've had enough already](#)



- [Coronavirus misinformation, and how scientists can help to fight it](#)

Subjects

- [Communication](#)
- [Society](#)

This article was downloaded by **calibre** from <https://www.nature.com/articles/d41586-021-02152-y>.

| [Section menu](#) | [Main menu](#) |



A fox squirrel displays its genius for adjusting its leaps on the fly. Credit:
Nate Hunt, UC Berkeley

Animal behaviour

05 August 2021

Squirrels do parkour

Squirrels show off multiple landing styles as they speed through the canopy.





•

The acrobatic rodents called fox squirrels learn to leap from branch to branch with a mix of careful calculation and ‘parkour’, according to experiments that had them bounding through a simulated forest.

Nathaniel Hunt at the University of Nebraska Omaha and his colleagues provided free-ranging fox squirrels (*Sciurus niger*) with faux branches, each near a landing pad baited with peanuts. The researchers varied the branches’ flexibility and the distance between the branch and the pad. Then, they watched as the squirrels adjusted their leaps.

Analysis of more than 100 trials recorded by high-speed cameras showed that choosing a launch location is a trade-off: the further out on a bendy limb

a squirrel goes, the shorter the leap to the next branch, but the bouncier the launch pad. Landing requires instant adjustments if the take-off branch is bendier than expected.

The researchers were surprised to see the squirrels bouncing off a vertical support with a “parkour leaping maneuver”, named after a form of urban gymnastics popular among humans. Although the parkour moves look fun, the actual goal is probably to modify horizontal velocity before landing.

[Science \(2021\)](#)

- [Animal behaviour](#)

This article was downloaded by **calibre** from <https://www.nature.com/articles/d41586-021-02153-x>

| [Section menu](#) | [Main menu](#) |



A village on the Greek island of Santorini overlooks a flooded volcanic caldera. The volcano's eruptions over the past 360,000 years have been tied to falls in sea level. Credit: DC Premiumstock/Alamy

Volcanology

02 August 2021

Volcano that built an island paradise is attuned to the sea

Eruptions of Santorini volcano, which created the Greek island of the same name, are linked to drops in sea level.





•

The volcano that created the island of Santorini, a popular tourist destination in Greece, tends to erupt when the sea level drops substantially, according to data from the past 360,000 years.

The global sea level falls during planetary cold spells, when ice sheets freeze, and rises again when the ice melts, pouring back into the oceans. This pattern can affect the timing of eruptions by island volcanoes.

Chris Satow at Oxford Brookes University, UK, and his colleagues compared the history of Santorini's eruptions over the past 360,000 years with records of sea-level height during that period. Almost every time sea level dropped by 40 metres below today's level, molten rock began squirting

upwards inside the volcano. When sea level dropped by another 30 or 40 metres, that molten rock usually made it to the surface, causing an eruption.

Drops in sea level reduce the weight pressing down on the volcano. This alters stress levels in the rocks, which fracture and provide paths for molten rock to rise towards the surface. Similar changes in stress could affect many other island and coastal volcanoes around the world, influencing their eruptions.

[Nature Geosci. \(2021\)](#)

- [Volcanology](#)

This article was downloaded by **calibre** from <https://www.nature.com/articles/d41586-021-02121-5>

| [Section menu](#) | [Main menu](#) |



It's not clear what makes golden poison frogs impervious to the toxin in their tissues — a toxin so potent that just 100 micrograms can kill a human.
Credit: David and Micha Sheldon/Alamy

Physiology

05 August 2021

An absorbing tale: poison dart frogs might have a ‘toxin sponge’

Experiments suggest that the frogs use internal proteins to soak up their own toxins.





•

Poison dart frogs lace their bodies with deadly toxins to deter hungry predators. But how do toxic animals avoid poisoning themselves? The answer might lie with ‘toxin sponges’.

The lethal molecule batrachotoxin is found not only in many species of poison dart frog but also in several toxic birds. Batrachotoxin kills by disabling proteins embedded in nerve-cell membranes that control neural activity. Scientists have long theorized that batrachotoxin-laden animals have evolved mutant membrane proteins to which batrachotoxin cannot bind.

But an analysis by Daniel Minor at the University of California, San Francisco, and his colleagues found no such mutations in batrachotoxin-wielding animals such as the golden poison frog (*Phyllobates terribilis*). The researchers also showed that captive-raised golden poison frogs have batrachotoxin-sensitive membrane proteins but do not succumb to the toxin's effects.

The researchers propose that the animals sequester the compound with 'toxin sponge' proteins. No such protein has been identified for batrachotoxin. But the team showed that a sponge protein found in the American bullfrog (*Rana catesbeiana*) soaks up a batrachotoxin-like toxin — and can shield the membrane proteins of poison frogs from that toxin's effects.

J. Gen. Physiol. (2021)

- [Physiology](#)

This article was downloaded by **calibre** from <https://www.nature.com/articles/d41586-021-02104-6>

| [Section menu](#) | [Main menu](#) |



A passer-by gives money in Hong Kong. Such generosity to a single person can coexist with a willingness to take advantage of groups of people, a new experiment shows. Credit: Ed Jones/AFP/Getty

Human behaviour

02 August 2021

‘Robber’ experiment tests generosity — with sobering results

People who give freely to a single individual get selfish in a crowd.





•

A research game called Big Robber might help to explain why a banker would steal money from clients but buy a warm meal for a homeless person: individuals tend to be selfish in their dealings with large groups of people, although they can be generous to just one other person.

Carlos Alós-Ferrer at the University of Zurich in Switzerland and his colleagues asked 640 people to play 3 types of game in which each participant decides how much of a small sum of money to transfer to another participant. The researchers found that most participants gave some money away.

The authors also devised the Big Robber game: a ‘robber’ decides whether to steal up to half of the earnings of 16 other participants. More than 80% of 320 robbers took at least one-third of the money, and 56% took as much as they could — half of it, about €100 (US\$118). Only 2% of individuals refused to rob.

The findings suggest that, if given the opportunity, people will harm a large group in exchange for a high reward, but the same individuals can be compassionate one-on-one.

[Nature Hum. Behav. \(2021\)](#)

- [Human behaviour](#)

This article was downloaded by **calibre** from <https://www.nature.com/articles/d41586-021-02120-6>

| [Section menu](#) | [Main menu](#) |



Carbon dating has pushed back the construction date of Machu Picchu, one of the grandest physical remnants of the Inca empire. Credit: Bérenger Zyla/Getty

Archaeology

03 August 2021

How old is Machu Picchu? The dead whisper a hint

Analysis of human bones suggests that historical records about the iconic site in Peru are inaccurate.





•

The ancient palace complex called Machu Picchu, located high in the Peruvian Andes, is decades older than thought, according to data from skeletons buried at the site.

Machu Picchu was built as a royal retreat for the ninth ruler of the Incas, Pachacuti. Most estimates of its age are based on historical records of the date he rose to power, suggesting a construction date of around 1450. But the records, which were mostly written by Spaniards during the colonial period, are often contradictory and inaccurate.

Richard Burger at Yale University in New Haven, Connecticut, and his colleagues collected samples of bone and teeth from 26 people who were

probably courtiers assigned to care for the Inca elite. Their remains were unearthed from the site in the 1910s.

Using carbon dating, a method of determining the age of organic samples, the team found that Machu Picchu was probably occupied between 1420 and 1530. The authors say their discovery demands that researchers revisit other assumptions about the Inca empire that are based on colonial records.

[Antiquity \(2021\)](#)

- [Archaeology](#)

This article was downloaded by **calibre** from <https://www.nature.com/articles/d41586-021-02126-0>

| [Section menu](#) | [Main menu](#) |



A daddy-long-legs of the species *Phalangium opilio*. Despite its spider-like appearance, it is a member of a grouping called harvestmen. Credit: Caitlin M. Baker

Genomics

05 August 2021

How the daddy-long-legs gets long legs

A single genetic toolkit gives rise to the spider-lookalike's slender gams and to the grasping legs of related animals.





•

The first sequenced genome of a daddy-long-legs has revealed the genetic tricks that these creatures use to make their lengthy, grasping legs.

Most of these leggy invertebrates are not spiders but belong instead to a group called harvestmen (order *Opiliones*). Guilherme Gainett at the University of Wisconsin-Madison, Vanessa González at the National Museum of Natural History in Washington DC and their colleagues sequenced the genome of the long-legged harvestman *Phalangium opilio* and found that the creature has a single cluster of Hox genes, a type of master gene that influences the body plan of all animals.

By disabling the activity of *P. opilio*'s Hox genes, the team revealed that several work together to produce its characteristic legs. Disabling a gene in an important growth pathway shared with other arthropods — a vast invertebrate group that includes harvestmen — led to hatchlings with legs that are shorter and less flexible than those of ordinary hatchlings.

The authors' analysis suggests that daddy-long-legs, insects and other arthropods all have a set of genes that independently gave rise to bendable, grasping legs in each group.

[Proc. R. Soc. B Biol. Sci. \(2021\)](#)

- [Genomics](#)

This article was downloaded by **calibre** from <https://www.nature.com/articles/d41586-021-02127-z>

| [Section menu](#) | [Main menu](#) |



Firefighters battle the Mendocino Complex Fire in California in 2018. Data from this and other blazes suggest that wildfire smoke could brighten clouds.
Credit: Noah Berger/AFP/Getty

Atmospheric science

03 August 2021

Wildfire smoke creates brighter clouds — and weather changes

Data from research flights through smoke plumes show that tiny particulates affect cloud droplet formation.





•

Smoke from wildfires in the western United States causes water molecules in the atmosphere to form large numbers of small droplets inside clouds, brightening the clouds and potentially affecting local weather and climate.

Smoke particles can serve as seeds around which water condenses. Scientists have measured smoke's cloud-seeding effect above many regions, such as the Amazon, while the landscape burned.

In North America, wildfires are charring broader swathes than in previous years, owing to climate change. Cynthia Twohy at NorthWest Research Associates in Bellevue, Washington, and her colleagues flew a research

aircraft through clouds and smoke plumes, gathering data on the size and distribution of particles of smoke and other substances.

Compared with clouds in smoke-free skies, clouds in smoky skies formed roughly 5 times as many droplets — sometimes more than 3,000 droplets per cubic centimetre. In smoky skies, the droplets were also much smaller, about half the size of those in clear skies.

As clouds gain more and smaller droplets, they reflect more sunlight, which means they become brighter and produce less rain.

Correction: An earlier version of this article misstated the name of the fire shown in the accompanying photograph.

[Geophys. Res. Lett. \(2021\)](#)

- [Atmospheric science](#)

This article was downloaded by **calibre** from <https://www.nature.com/articles/d41586-021-02105-5>

News in Focus

- **[Deer infections, vaccination nudges and predicting ‘breakthrough’ COVID cases](#)** [11 August 2021]
News Round-Up • The latest science news, in brief.
- **[IPCC climate report: Earth is warmer than it’s been in 125,000 years](#)** [09 August 2021]
News • Landmark assessment says that greenhouse gases are unequivocally driving extreme weather — but that nations can still prevent the worst impacts.
- **[Flawed ivermectin preprint highlights challenges of COVID drug studies](#)** [02 August 2021]
News • The study’s withdrawal from a preprint platform deals a blow to the anti-parasite drug’s chances as a COVID treatment, researchers say.
- **[After Trump, US researchers urge Biden to block political meddling in science](#)** [04 August 2021]
News • White House science office is expected to deliver a review of US scientific-integrity policies next month.
- **[Surprise dip in UK COVID cases baffles researchers](#)** [03 August 2021]
News • Daily recorded infections have more than halved since mid-July. Few researchers anticipated such a sharp decline, and they are now struggling to interpret it.
- **[More women than ever are starting careers in science](#)** [05 August 2021]
News • But a study of the publications of millions of researchers also suggests that women are less likely to continue their academic careers than their male counterparts.
- **[COVID vaccine boosters: the most important questions](#)** [05 August 2021]
News Feature • Concerns over waning immunity and SARS-CoV-2 variants have convinced some countries to deploy extra vaccine doses — but it’s not clear to scientists whether most people need them.

- NEWS ROUND-UP
- 11 August 2021

Deer infections, vaccination nudges and predicting ‘breakthrough’ COVID cases

The latest science news, in brief.





•

[Download PDF](#)



A white-tailed deer fawn. Deer in the north-eastern United States show evidence of exposure to SARS-CoV-2. Credit: John Cancalosi/Nature Picture Library

Coronavirus rife in common US deer

One-third of white-tailed deer (*Odocoileus virginianus*) in the northeastern United States have antibodies against SARS-CoV-2 — a sign that they have been infected with the virus.

The findings, reported in a preprint on 29 July ([J. C. Chandler et al. preprint at bioRxiv https://doi.org/gmc8t6; 2021](https://doi.org/gmc8t6)), represent the first detection of widespread exposure to the virus in a population of wild animals.

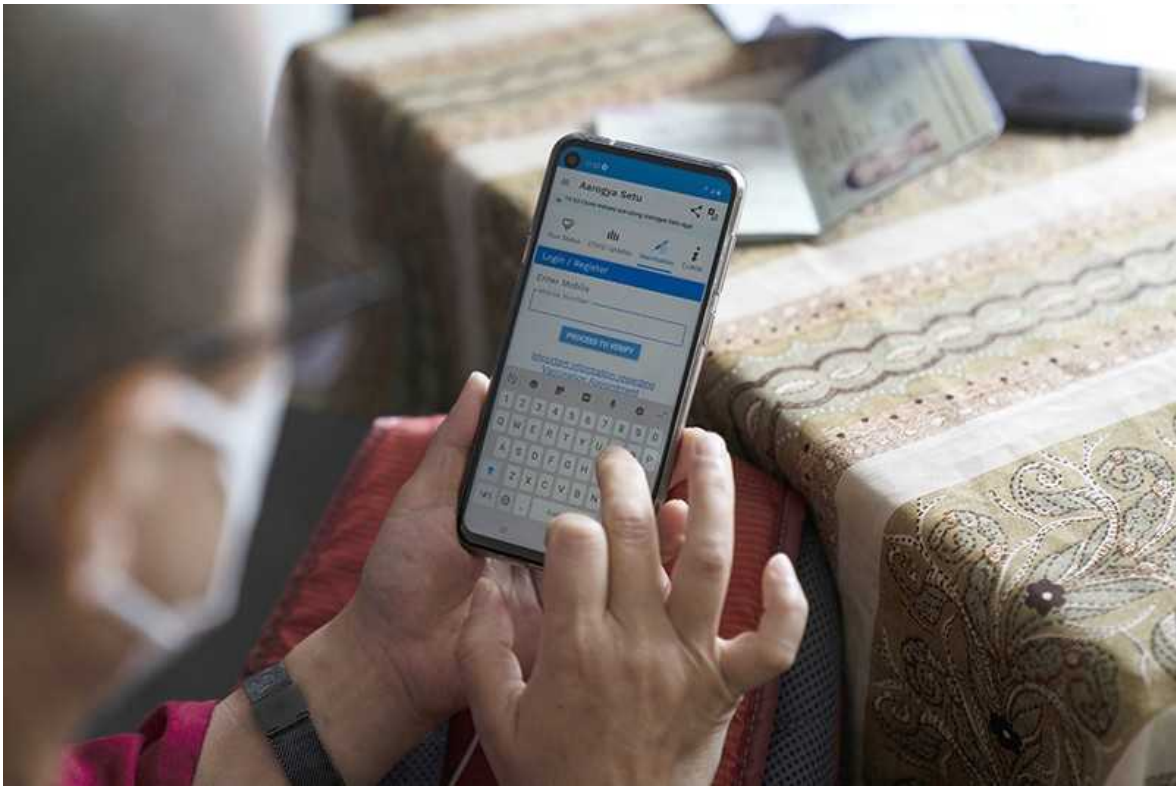
There are concerns about the emergence of new animal ‘reservoirs’ — animal populations that harbour SARS-CoV-2. Previous laboratory experiments have shown that white-tailed deer can become infected with the coronavirus and transmit it to other deer. In the wild, the animals live in herds, which could make it easier for the virus to spread.

Scientists at the US Department of Agriculture in Fort Collins, Colorado, and Ames, Iowa, tested 385 deer blood samples collected as part of regular wildlife surveillance between January and March 2021 in Michigan, Pennsylvania, Illinois and New York state. They found that a striking [40% of the samples contained SARS-CoV-2 antibodies](#), which are produced in response to infection. None of the surveyed deer showed signs of illness.

The testing of archived samples also turned up antibodies in three samples from early 2020, when SARS-CoV-2 was beginning to circulate in the United States. All told, one-third of the 2020 and 2021 samples had antibodies for the virus.

It is not clear how the deer were exposed. It could have been through contact with people, other animals or even contaminated wastewater.

Researchers say that the rapid exposure of a large number of animals to the virus is concerning, but that more studies are needed to assess whether the deer can infect each other — and other species — in the wild. “It’s an intriguing observation but still needs to be interpreted with caution,” says Aaron Irving, an infectious-diseases researcher at Zhejiang University in Haining, China.



Even a brief mobile-phone reminder that COVID-19 vaccinations are available can increase vaccination rates. Credit: Sumit Dayal/Bloomberg via Getty

Text nudge can increase COVID vaccinations

A short text message reminding people to book a COVID-19 jab can boost vaccination rates by several percentage points, according to a study of more than 90,000 people in California.

A reminder sent one day after individuals became eligible for the jab boosted appointments and vaccination rates by 6 percentage points and roughly 3.6 percentage points, respectively, compared with rates in a separate group that did not receive the reminder (H. Dai et al. *Nature* <https://doi.org/gqtk>; 2021). A second reminder to those who still hadn't booked a vaccination appointment a week later boosted appointments and jabs by another 1.7 and 1.1 percentage points, respectively.

The researchers tested reminder texts consisting of two different wordings, which were sent to members of a large health-care system. Some people received a ‘basic’ reminder telling them that they could get the vaccine. Others received an ‘ownership’ reminder telling them that a vaccine had “just been made available” to them, with instructions on how to “claim” their dose.

The ownership reminder was more effective: when sent one day after people became eligible for the vaccine, it raised the recipients’ vaccination rates by about 4.1 percentage points, compared with a 3-percentage-point increase for the ‘basic’ reminder.

These small gains, if applied to a large population, could speed up vaccinations for millions of people, the authors say.



A worker at Sheba Medical Center in Israel prepares a dose of the Pfizer–BioNTech COVID-19 vaccine. Breakthrough cases among the centre’s vaccinated health-care workers were rare in the first months of 2021. Credit: Jack Guez/AFP via Getty

Blood marker predicts breakthrough COVID cases

People fully vaccinated against COVID-19 are less likely to become infected with the coronavirus if they have relatively high levels of virus-blocking antibodies, according to a study of more than 10,000 health-care workers who received the Pfizer–BioNTech jab ([M. Bergwerk *et al.* *N. Engl. J. Med.* \[https://doi.org/gmc77b; 2021\]\(https://doi.org/gmc77b\)](https://doi.org/gmc77b)).

The analysis adds to a growing body of evidence that a person's levels of 'neutralizing' antibodies, which block SARS-CoV-2 from infecting cells, [predict whether that person will become infected](#).

A robust predictive marker could help regulators to approve new vaccines without requiring large clinical trials. It could also help them to assess the need for booster shots to guard against emerging viral variants. The study "is an important step in further validating the use of neutralization titre", says Miles Davenport, an immunologist at the University of New South Wales in Sydney, Australia.

But the analysis does have drawbacks. It is based on a small number of cases among young and healthy adults, limiting its application. It also doesn't suggest a particular level of antibodies that is associated with protection.

Nature **596**, 169 (2021)

doi: <https://doi.org/10.1038/d41586-021-02168-4>

Subjects

- [SARS-CoV-2](#)
- [Health care](#)
- [Vaccines](#)

Jobs >

- [Technology and Knowledge Transfer Officer / Commercialization](#)

University of Luxembourg

Luxembourg, Luxembourg

- [Technology and Knowledge Transfer Officer / Social Sciences, Humanities](#)

University of Luxembourg

Luxembourg, Luxembourg

- [Postdoctoral Research Assistant \(m/f/div\) in modelling and data science](#)

Max Planck Institute for the Science of Human History

Jena, Germany

- [Postdoc researcher in de novo design of transmembrane beta-barrels for nanopore sensing applications](#)

Flanders Institute for Biotechnology (VIB)

Brussels, Belgium

Nature Briefing

An essential round-up of science news, opinion and analysis, delivered to your inbox every weekday.

[Download PDF](#)

Subjects

- [SARS-CoV-2](#)
 - [Health care](#)
 - [Vaccines](#)
-

This article was downloaded by **calibre** from <https://www.nature.com/articles/d41586-021-02168-4>

| [Section menu](#) | [Main menu](#) |

- NEWS
- 09 August 2021

IPCC climate report: Earth is warmer than it's been in 125,000 years

Landmark assessment says that greenhouse gases are unequivocally driving extreme weather — but that nations can still prevent the worst impacts.

- [Jeff Tollefson](#)
 1. Jeff Tollefson
[View author publications](#)

You can also search for this author in [PubMed](#) [Google Scholar](#)





•

[Download PDF](#)



As temperatures rise in the future, extreme weather events — such as California's persistent drought — will become more severe. Credit: Robyn Beck/AFP/Getty

Modern society's continued dependence on fossil fuels is warming the world at a pace that is unprecedented in the past 2,000 years — and its effects are already apparent as record droughts, wildfires and floods devastate communities worldwide — according to a [landmark report from the United Nations on the state of climate science](#). The assessment from the UN's Intergovernmental Panel on Climate Change (IPCC) says things are poised to get worse if greenhouse-gas emissions continue, and makes it clear that the future of the planet depends, in large part, on the choices that humanity makes today.

“The evidence is everywhere: if we don’t act, the situation is going to get really bad,” says Xuebin Zhang, a climatologist at Environment Canada in Toronto, Ontario, and a coordinating lead author on the report, released on 9 August.



Diagnosing Earth: the science behind the IPCC's upcoming climate report

Compiled by more than 200 scientists over the course of several years and approved by 195 governments during a virtual meeting last week, the report is the first in a trio assessing the state of climate change and efforts to mitigate it and adapt to it. The document — part of the IPCC's sixth climate assessment since 1990 — arrives less than three months before the next major global climate summit in Glasgow, UK. There, governments will have the opportunity to make pledges to reverse course and decrease their emissions.

If global emissions hit net zero by around 2050 — a target that many countries have committed to over the past year — then the world can achieve the goal laid out in the 2015 Paris accord and limit global warming to 1.5 °C above pre-industrial levels over the course of the twenty-first century, says Valérie Masson-Delmotte, a climatologist at the Laboratory of Climate and Environmental Sciences in Gif-sur-Yvette, France, and co-chair of the physical-science working group that produced the current report. “The climate we experience in the future depends on our decisions now,” she says.

Hotting up

Earth's global surface temperature has increased by around 1.1 °C compared with the average in 1850–1900 — a level that hasn't been witnessed since 125,000 years ago, before the most recent ice age. This is just one of the blunt facts appearing in a summary released with the IPCC report that is intended for policymakers.

The overall assessment underscores efforts to pin down how much more temperatures will rise if atmospheric emissions continue, and provides climate scientists' [most confident projections yet](#) for the twenty-first century. One key metric that researchers use to make their projections is 'climate sensitivity', a measure of how much long-term warming would be expected on Earth from a doubling of atmospheric carbon dioxide concentrations compared with pre-industrial levels. Although the IPCC's best estimate remains at 3 °C, the report reduces the uncertainty in that figure, narrowing the probable range to 2.5–4 °C, using evidence such as modern and ancient climate records. This compares with 1.5–4.5 °C, the wider range for sensitivity reported in the IPCC's last climate assessment, released in 2013.



[The hard truths of climate change — by the numbers](#)

This narrowing of climate sensitivity bolsters scientists' confidence in their projections for what will happen on Earth in a number of different scenarios. In a moderate emissions scenario that features little change from today's global-development patterns, for instance, average global temperatures will rise by 2.1–3.5 °C, according to the IPCC report. This is well above the 1.5–

2 °C limit laid out as a goal by the nations that signed the 2015 Paris climate agreement. Even in a scenario in which governments aggressively cut their greenhouse-gas emissions, the report projects that global temperatures are likely to surpass the 1.5 °C threshold in the coming years, before dropping back below it towards the end of the century.

“Is it still possible to limit global warming to 1.5 °C? The answer is yes,” says Maisa Rojas, a coordinating lead author on the report and director of the University of Chile’s Center for Climate and Resilience Research in Santiago. “But unless there are immediate, rapid and large-scale reductions of all greenhouse gases, limiting global warming to 1.5 °C will be beyond reach.”

Extreme impacts

The report lists a dizzying array of impacts that climate change has had on Earth — and that are already evident from pole to pole. The coverage of sea ice in the Arctic during the late summer has been lower over the past decade than it has been in at least 1,000 years. The ongoing global retreat of glaciers is unparalleled in at least 2,000 years. And oceans are heating up at a pace not seen since the end of the most recent ice age, 11,000 years ago.

Beyond these sobering measurements, the IPCC report emphasizes some of the most significant scientific advances in understanding the regional effects of climate change, including where extreme heat, precipitation and drought have hit hardest. Extreme drought, for instance, has affected various regions around the globe, with particularly widespread impacts in the Mediterranean region and in southwest Africa.



Can the world's most influential climate report carry on?

As temperatures rise in the future, says Zhang, extreme weather events will become increasingly severe. Over land, an extreme temperature event that occurred once every 50 years in centuries past will probably occur every 3–4 years if Earth reaches 2 °C above pre-industrial temperatures, according to the report. The world should also expect more compound events, such as heatwaves and long-term droughts occurring simultaneously.

“We are not going to be hit just by one thing, we are going to be hit by multiple things at the same time,” says Zhang.

Irreversible changes

Global warming’s impact on bodies such as glaciers, ice sheets and oceans, which adjust slowly to rising temperatures, will continue to be felt for centuries or even millennia, according to the report. Sea levels around the world are projected to rise by 2–3 metres over the next 2,000 years, even if temperatures are held in check at 1.5 °C of warming, and up to 6 metres with 2 °C of warming, which would alter entire coastlines currently inhabited by hundreds of millions of people.

The report warns that some of the most severe impacts of climate warming — such as ice-sheet collapse, massive forest loss or an abrupt change in

ocean circulation — cannot be ruled out, particularly in scenarios in which high emissions and significant warming occur towards the end of the century. But it notes that the biggest uncertainty in all climate-change projections is how humans will act.



[IPCC says limiting global warming to 1.5 °C will require drastic action](#)

Although the IPCC has been warning about the perils of global warming for three decades, governments have yet to take the kind of action necessary to transition to clean-energy sources and halt greenhouse-gas emissions. But perhaps things are about to change, says Zhang, if only because people all over the world are starting to see the impacts of climate change around them.

“Climate change is happening, and people actually feel it,” says Zhang. “The report just provides scientific validation to the general public that, yes, what you feel is actually true.”

But the IPCC report also states something even more important: many of the most dire effects of climate change can still be avoided if aggressive action is taken now. Every degree of warming matters, says Rojas. “That is a very powerful idea,” she says. “The future is in our hands.”

doi: <https://doi.org/10.1038/d41586-021-02179-1>

Related Articles

-  [Diagnosing Earth: the science behind the IPCC's upcoming climate report](#)
-  [IPCC says limiting global warming to 1.5 °C will require drastic action](#)
-  [Arctic sea ice hits second-lowest level on record](#)
-  [Can the world's most influential climate report carry on?](#)
-  [The hard truths of climate change — by the numbers](#)

Subjects

- [Policy](#)
- [Climate sciences](#)
- [Climate change](#)

- [Technology and Knowledge Transfer Officer / Commercialization](#)

University of Luxembourg

Luxembourg, Luxembourg

- [Technology and Knowledge Transfer Officer / Social Sciences, Humanities](#)

University of Luxembourg

Luxembourg, Luxembourg

- [Postdoctoral Research Assistant \(m/f/div\) in modelling and data science](#)

Max Planck Institute for the Science of Human History

Jena, Germany

- [Postdoc researcher in de novo design of transmembrane beta-barrels for nanopore sensing applications](#)

Flanders Institute for Biotechnology (VIB)

Brussels, Belgium

Nature Briefing

An essential round-up of science news, opinion and analysis, delivered to your inbox every weekday.

[Download PDF](#)

Related Articles



- [Diagnosing Earth: the science behind the IPCC's upcoming climate report](#)



- [IPCC says limiting global warming to 1.5 °C will require drastic action](#)



- [Arctic sea ice hits second-lowest level on record](#)



- [Can the world's most influential climate report carry on?](#)



- [The hard truths of climate change — by the numbers](#)

Subjects

- [Policy](#)
- [Climate sciences](#)
- [Climate change](#)

This article was downloaded by **calibre** from <https://www.nature.com/articles/d41586-021-02179-1>

| [Section menu](#) | [Main menu](#) |

- NEWS
- 02 August 2021

Flawed ivermectin preprint highlights challenges of COVID drug studies

The study's withdrawal from a preprint platform deals a blow to the anti-parasite drug's chances as a COVID treatment, researchers say.

- [Sara Reardon](#)

1. Sara Reardon
[View author publications](#)

You can also search for this author in [PubMed](#) [Google Scholar](#)





•

[Download PDF](#)



People in Bolivia and other countries have been purchasing the anti-parasite drug ivermectin throughout the pandemic as protection against COVID-19. Credit: Rodrigo Urzagasti/Reuters/Alamy

Throughout the pandemic, the anti-parasite drug ivermectin has attracted much attention, [particularly in Latin America](#), as a potential way to treat COVID-19. But scientists say that recent, shocking revelations of widespread flaws in the data of a preprint study reporting that the medication greatly reduces COVID-19 deaths dampens ivermectin's promise — and highlights the challenges of investigating drug efficacy during a pandemic.

"I was shocked, as everyone in the scientific community probably were," says Eduardo López-Medina, a paediatrician at the Centre for the Study of Paediatric Infections in Cali, Colombia, who was not involved with the study and who has investigated whether ivermectin can improve COVID-19 symptoms. "It was one of the first papers that led everyone to get into the idea ivermectin worked" in a clinical-trial setting, he adds.



[Latin America's embrace of an unproven COVID treatment is hindering drug trials](#)

The paper summarized the results of a clinical trial seeming to show that ivermectin can reduce COVID-19 death rates by more than 90%¹ — among the largest studies of the drug’s ability to treat COVID-19 to date. But on 14 July, after [internet sleuths raised concerns](#) about plagiarism and data manipulation, the preprint server Research Square withdrew the paper because of “ethical concerns”.

Ahmed Elgazzar at Benha University in Egypt, who is one of the authors on the paper, told *Nature* he was not given a chance to defend his work before it was removed.

Early in the pandemic, scientists showed that ivermectin could inhibit the coronavirus SARS-CoV-2 in cells in laboratory studies². But data on ivermectin’s efficacy against COVID-19 in people are still scarce, and study conclusions conflict greatly, making the withdrawal of a major trial particularly noteworthy.

Although the World Health Organization advises against taking ivermectin as a COVID-19 treatment outside clinical trials, the over-the-counter drug has become popular in some regions of the world. Some view it as a stopgap until vaccines become available in their areas, even though it has not yet

been proven effective; scientists worry that it will also be seen as an alternative to vaccines, which are highly effective.

Ripple effects

The paper's irregularities came to light when Jack Lawrence, a master's student at the University of London, was reading it for a class assignment and noticed that some phrases were identical to those in other published work. When he contacted researchers who specialize in detecting fraud in scientific publications, the group found other causes for concern, including dozens of patient records that seemed to be duplicates, inconsistencies between the raw data and the information in the paper, patients whose records indicate they died before the study's start date, and numbers that seemed to be too consistent to have occurred by chance.



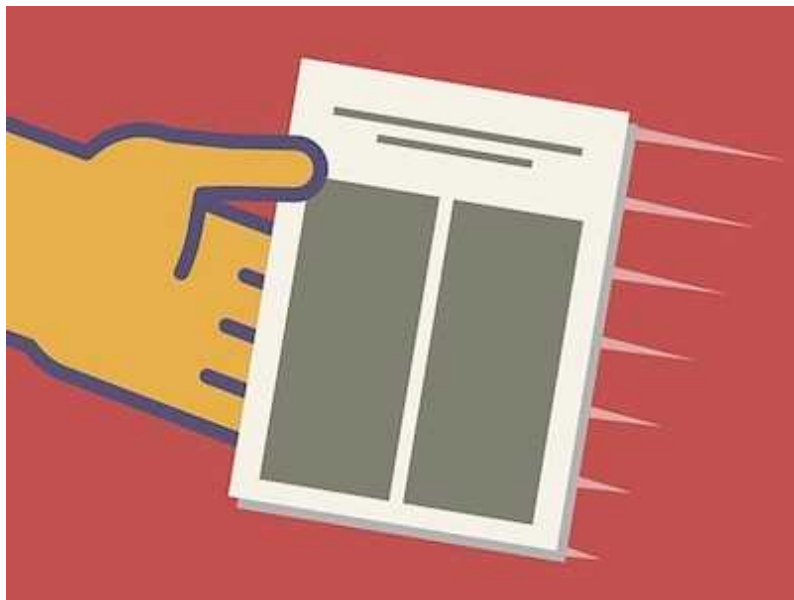
[High-profile coronavirus retractions raise concerns about data oversight](#)

In an editorial note, Research Square said that it has launched a formal investigation into the concerns raised by Lawrence and his colleagues. [According to the Egyptian newspaper Al-Shorouk](#), Egypt's minister of higher education and scientific research is also examining the allegations.

The paper was “withdrawn from the Research Square platform without informing or asking me”, Elgazzar wrote in an e-mail to *Nature*. He defended the paper, and said of the plagiarism allegations that “often phrases or sentences are commonly used and referenced” when researchers read one another’s papers.

Although dozens of ivermectin clinical trials have been launched over the past year³, the Elgazzar paper was notable for announcing one of the first positive results, as well as for its size — it included 400 people with symptoms of COVID-19 — and the magnitude of the drug’s effect. Few therapies can claim such an impressive reduction in death rates. “It was a significant difference, and that stood out,” says Andrew Hill, who studies repurposed drugs at the University of Liverpool, UK. “It should have raised red flags even then.”

Lawrence agrees. “I was absolutely shocked that no one had uncovered it,” he says.



[How swamped preprint servers are blocking bad coronavirus research](#)

Before its withdrawal, the paper was viewed more than 150,000 times, cited more than 30 times and included in a number of meta-analyses that collect trial findings into a single, statistically weighted result. In one recent meta-analysis in the *American Journal of Therapeutics* that found ivermectin

greatly reduced COVID-19 deaths⁴, the Elgazzar paper accounted for 15.5% of the effect.

One of the authors of the meta-analysis, statistician Andrew Bryant at Newcastle University, UK, says that his team corresponded with Elgazzar before publishing the work to clarify some data. “We had no reason to doubt the integrity of [Professor] Elgazzar,” he said in an e-mail. He added that in a pandemic setting, no one can reanalyse all of the raw data from patient records when writing a review. Bryant went on to say that his group will revise the conclusion if investigations find the study to be unreliable. However, even if the study is removed, the meta-analysis would still show that ivermectin causes a major reduction in deaths from COVID-19, he says.

Reliable data needed

The paper’s withdrawal is not the first scandal to dog studies of ivermectin and COVID-19. Hill thinks many of the other ivermectin trial papers that he has scanned are likely to be flawed or statistically biased. Many rely on small sample sizes or were not randomized or well controlled, he says. And in 2020, an observational study of the drug [was withdrawn after scientists](#) raised concerns about it and a few other papers using data by the company Surgisphere that investigated a range of repurposed drugs against COVID-19. “We’ve seen a pattern of people releasing information that’s not reliable,” says Hill. “It’s hard enough to do work on COVID and treatment without people distorting databases.”

Carlos Chaccour, a global-health researcher at the Barcelona Institute for Global Health in Spain, says it has been difficult to conduct rigorous studies on ivermectin. That’s partly because funders and academics in wealthy countries haven’t supported them, and, he suspects, have often dismissed trials of ivermectin because most of them have been done in lower-income countries. Furthermore, says Rodrigo Zoni, a cardiologist at the Corrientes Cardiology Institute in Argentina, it is difficult to recruit participants because many people — particularly in Latin America — are already taking the widely available drug in an attempt to prevent COVID-19.

How a torrent of COVID science changed research publishing — in seven charts

Adding to the difficulty are conspiracy theories holding that ivermectin has been proven to work and that drug companies are depriving the public of a cheap cure. Chaccour says he has been called ‘genocidal’ for doing research on the drug rather than just endorsing it.

Although the jury is still out on ivermectin, many say the retraction speaks to the difficulty of assessing research during a pandemic. “I personally have lost all faith in the results of [ivermectin] trials published to date,” says Gideon Meyerowitz-Katz, an epidemiologist at the University of Wollongong in Australia who helped Lawrence to analyse the Elgazzar paper. It’s not yet possible to assess whether ivermectin works against COVID-19 because the data currently available are not of sufficiently high quality, he says, adding that he is reading other ivermectin papers in his spare time, looking for signs of fraud or other problems.

Chaccour and others studying ivermectin say that proof of whether the drug is effective against COVID-19 rests on a handful of large, ongoing studies, including a trial in Brazil with more than 3,500 participants. By the end of 2021, says Zoni, around 33,000 people will have participated in some kind of ivermectin trial.

“I think it is our duty to exhaust all potential benefits,” says Chaccour, especially given that most countries still do not have widespread access to vaccines. “Ultimately if you do a trial and it fails, fine, but at least we tried.”

Nature **596**, 173-174 (2021)

doi: <https://doi.org/10.1038/d41586-021-02081-w>

References

1. 1.

Elgazzar, A. *et al.* Preprint at Research Square
<https://doi.org/10.21203/rs.3.rs-100956/v3> (2020).

2. 2.

Caly, L., Druce, J. D., Catton, M. G., Jans, D. A. & Wagstaff, K. M. *Antiviral Res.* **178**, 104787 (2020).

[PubMed](#) [Article](#) [Google Scholar](#)

3. 3.

Popp, M. *et al. Cochrane Data. System. Rev.* <https://doi.org/10.1002/14651858.CD015017.pub2> (2021).

[Article](#) [Google Scholar](#)

4. 4.

Bryant, A. *et al. Am. J. Ther.* **28**, e434–e460 (2021).

[PubMed](#) [Article](#) [Google Scholar](#)

[Download references](#)

Related Articles



- [Latin America's embrace of an unproven COVID treatment is hindering drug trials](#)



- [High-profile coronavirus retractions raise concerns about data oversight](#)



- [How swamped preprint servers are blocking bad coronavirus research](#)
- [How a torrent of COVID science changed research publishing — in seven charts](#)

Subjects

- [Research data](#)
- [SARS-CoV-2](#)
- [Public health](#)
- [Publishing](#)

nature careers

[Jobs](#) >

- [Technology and Knowledge Transfer Officer / Commercialization](#)

University of Luxembourg

Luxembourg, Luxembourg

- [Technology and Knowledge Transfer Officer / Social Sciences, Humanities](#)

University of Luxembourg

Luxembourg, Luxembourg

- [Postdoctoral Research Assistant \(m/f/div\) in modelling and data science](#)

Max Planck Institute for the Science of Human History

Jena, Germany

- [Postdoc researcher in de novo design of transmembrane beta-barrels for nanopore sensing applications](#)

Flanders Institute for Biotechnology (VIB)

Brussels, Belgium

Nature Briefing

An essential round-up of science news, opinion and analysis, delivered to your inbox every weekday.

[Download PDF](#)

Related Articles



- [Latin America's embrace of an unproven COVID treatment is hindering drug trials](#)



- [High-profile coronavirus retractions raise concerns about data oversight](#)



- [How swamped preprint servers are blocking bad coronavirus research](#)

- [**How a torrent of COVID science changed research publishing — in seven charts**](#)

Subjects

- [Research data](#)
- [SARS-CoV-2](#)
- [Public health](#)
- [Publishing](#)

This article was downloaded by **calibre** from <https://www.nature.com/articles/d41586-021-02081-w>

| [Section menu](#) | [Main menu](#) |

- NEWS
- 04 August 2021

After Trump, US researchers urge Biden to block political meddling in science

White House science office is expected to deliver a review of US scientific-integrity policies next month.

- [Nidhi Subbaraman](#)

1. Nidhi Subbaraman
[View author publications](#)

You can also search for this author in [PubMed](#) [Google Scholar](#)





•

[Download PDF](#)



Researchers have called for safeguarding US science and scientific evidence against political interference. Credit: Stefani Reynolds/Bloomberg via Getty

US researchers and science groups appealed to President Joe Biden's administration last week to protect government science from political interference and to empower federal scientists to speak to the media and public. They made this request during public listening sessions hosted by the White House Office of Science and Technology Policy (OSTP) — the first such sessions held since the science office kicked off a massive project to bolster scientific integrity in the federal government.



Four ways Trump has meddled in pandemic science — and why it matters

After four years in which former president Donald Trump's administration sidelined science and scientists in government decisions, researchers were hopeful that Biden would safeguard independent scientific work and communication. In January, he made moves in this direction when he instructed the OSTP to review rules at all US agencies, with the goal of ensuring policies that “ban improper political interference in the conduct of scientific research” are in place. The OSTP convened a task force in May, comprised of nearly 50 representatives from several US agencies, to tackle the issue. The group has so far met in closed-door sessions and with scientific-integrity experts.

“This level of engagement has not really happened before in the federal government around the issue of scientific integrity,” says Alondra Nelson, OSTP’s deputy director for science and society, who co-chairs the task force.

The current effort expands on a push to protect scientific integrity that former president Barack Obama began a decade ago. Policies at US science agencies were the focus of that OSTP-led drive, Nelson tells *Nature*, but Biden’s project further aims to guide the use of evidence at all government agencies.

Speaking up

During the three public listening sessions last week, attendees urged government agencies to be transparent about how science is used in policy and regulation, and recommended that scientists be enabled to pursue their work without political interference — and be free to speak about it.

Andrew Rosenberg, director of the Center for Science and Democracy at the Union of Concerned Scientists, said that government scientists must be encouraged to speak directly to the public and media, including through social media. Critics have complained that it has become harder over the years to gain access to government scientists for information and insight, and that it became even more difficult when Trump took office. In its first days, the Trump administration [issued restrictions](#) on agency employees speaking about their work. And during the COVID-19 pandemic, top public-health officials, including infectious-disease chief Anthony Fauci, were [restricted from addressing the public](#). “Agencies should not be scared of scientists speaking up,” Rosenberg said.

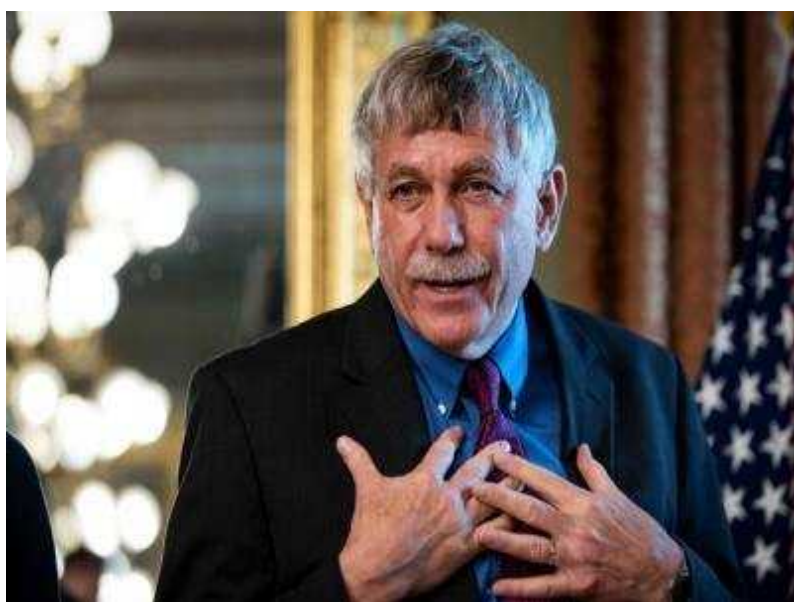


Alondra Nelson is the OSTP's deputy director for science and society. Credit: Alex Wong/Getty

Since Trump was elected in 2016, the non-profit Climate Science Legal Defense Fund (CSLDF) and the Sabin Center for Climate Change Law at Columbia Law School, both in New York City, have tracked anti-science actions by the US government, including state-level decisions and actions by individual members of Congress. That tally [has now grown to](#) nearly 500 entries.

Augusta Wilson, a staff attorney at CSLDF, said at one of the sessions that close to half of those cases involved censorship of scientific information. In her remarks, she asked that the OSTP “call on agencies to adopt strong, explicit protections against censorship and other interference with scientists’ ability to communicate about their work”.

The CSLDF and the Sabin Center are among groups that have created guidelines for keeping science free of political interference and ensuring that scientific evidence carries weight. Among such suggestions are integrity-policy training for agency employees and designating government offices and leaders to settle disputes; some have suggested that Congress should pass legislation that requires agencies to shore up their rules.



First science adviser in US president's cabinet talks COVID, spying and more

Tom Sinks, who worked at the US Centers for Disease Control and Prevention and the US Environmental Protection Agency (EPA) for decades, told *Nature* there needs to be a ‘firewall’ established between scientific evidence and political leaders at agencies. “Creating a firewall that enables science to be science and politics to be politics — this is where scientific integrity plays a big role,” he said.

During one of the sessions, he suggested that to construct such a barrier, each agency should establish a senior scientist, who is not a political appointee, as the ultimate approver of scientific products such as publications. Sinks himself is no stranger to scientific-integrity conflicts. Before he resigned in 2020 as director of the EPA’s Office of the Science Advisor, he [wrote a rebuke](#) of the agency’s own ‘secret science’ rule, championed by then-administrator Scott Pruitt, a Trump appointee. Touted as a move towards transparency, the proposed rule would have prevented the EPA from using studies that rely on non-public data as a basis for regulations. But critics [argued this would cut out foundational health data](#) about the harms of environmental pollutants — and would ultimately weaken the regulatory agency’s power to curb polluters. The Biden EPA is currently reconsidering the rule.

The next steps

The new effort “reaffirms and builds on” Obama’s scientific-integrity work, according to President Biden’s January memo instructing the OSTP to take up this issue.



How Trump damaged science — and why it could take decades to recover

Obama had pledged to “restore science to its rightful place” during his inauguration, and his OSTP director, John Holdren, [detailed a series of actions](#) that agencies should take to protect the independence of scientists. This came after previous president George W. Bush and his administration [blocked stem-cell science](#) and [downplayed climate research](#).

Sinks says the ‘Holdren memo’ protected some EPA science during the Trump years, allowing scientific reports to pass that might have otherwise faltered. But he hopes the Biden effort will go further.

A 2019 [review by the US Government Accountability Office](#) concluded that the Obama-era memorandum was unevenly embraced across agencies and recommended further actions to strengthen the integrity of federal research.

The public comments collected at the listening sessions and received in writing will inform the Biden OSTP’s deliberations. “This is an issue that the public really cares about and is engaged in,” says Nelson.

The OSTP task force is due to deliver a review of existing agency-integrity policies in September.

Nature **596**, 174–175 (2021)

doi: <https://doi.org/10.1038/d41586-021-02132-2>

Related Articles

-  [How Trump damaged science — and why it could take decades to recover](#)
-  ['Inspired choice': Biden appoints sociologist Alondra Nelson to top science post](#)
-  [Four ways Trump has meddled in pandemic science — and why it matters](#)
-  [First science adviser in US president's cabinet talks COVID, spying and more](#)
-  [US EPA science advisers question 'secret science' rule on data transparency](#)

Subjects

- [Government](#)
- [Scientific community](#)

- [Politics](#)
- [Policy](#)

nature careers

[Jobs](#) >

- [Technology and Knowledge Transfer Officer / Commercialization](#)

University of Luxembourg

Luxembourg, Luxembourg

- [Technology and Knowledge Transfer Officer / Social Sciences, Humanities](#)

University of Luxembourg

Luxembourg, Luxembourg

- [Postdoctoral Research Assistant \(m/f/div\) in modelling and data science](#)

Max Planck Institute for the Science of Human History

Jena, Germany

- [Postdoc researcher in de novo design of transmembrane beta-barrels for nanopore sensing applications](#)

Flanders Institute for Biotechnology (VIB)

Brussels, Belgium

Nature Briefing

An essential round-up of science news, opinion and analysis, delivered to your inbox every weekday.

[Download PDF](#)

Related Articles



- [How Trump damaged science — and why it could take decades to recover](#)



- ['Inspired choice': Biden appoints sociologist Alondra Nelson to top science post](#)



- [Four ways Trump has meddled in pandemic science — and why it matters](#)



- [First science adviser in US president's cabinet talks COVID, spying and more](#)



- [US EPA science advisers question 'secret science' rule on data transparency](#)

Subjects

- [Government](#)
 - [Scientific community](#)
 - [Politics](#)
 - [Policy](#)
-

This article was downloaded by **calibre** from <https://www.nature.com/articles/d41586-021-02132-2>

| [Section menu](#) | [Main menu](#) |

- NEWS
- 03 August 2021

Surprise dip in UK COVID cases baffles researchers

Daily recorded infections have more than halved since mid-July. Few researchers anticipated such a sharp decline, and they are now struggling to interpret it.

- [Philip Ball](#)
 1. Philip Ball
[View author publications](#)

You can also search for this author in [PubMed](#) [Google Scholar](#)





•

[Download PDF](#)



A temporary COVID-19 testing centre in England.Credit: Oli Scarff/AFP/Getty

Scientists are scratching their heads over the precipitous decline in daily COVID-19 infections in the United Kingdom following their rapid rise earlier in the year. Officially recorded new cases more than halved in just 2 weeks: from a high of 54,674 on 17 July to 22,287 on 2 August.

“Nobody really knows what’s going on,” says epidemiologist John Edmunds at the London School of Hygiene & Tropical Medicine (LSHTM). In particular, it’s not clear whether this sudden trend indicates that the peak of the third wave has passed, or whether it is a blip caused by complex social factors.



Why England's COVID 'freedom day' alarms researchers

The spread of the more-infectious Delta variant of SARS-CoV-2 in the United Kingdom seemed, despite the country's successful vaccination roll-out, to be creating a dangerous crisis. Exponential growth in infections since June led to predictions of as many as 100,000 new cases being reported daily, and fears that the National Health Service (NHS) could be overwhelmed by hospitalizations. In such a climate, [many scientists felt](#) that the government's full relaxation of mitigating restrictions in England, such as mask wearing and the closure of nightclubs and other venues, on 19 July was reckless.

It is still too early to know what effect the relaxation will have, given that the data on new cases and hospitalizations have a lag of around two weeks. Few public-health experts, however, anticipated the recent sharp drop — and they are struggling to interpret it.

Not herd immunity

One thing it doesn't mean, says Edmunds, is that the United Kingdom has built up enough population immunity through vaccination and natural infection to stop the virus spreading. "The drop in cases is unprecedented to some extent, in that it seemed to occur everywhere," he says — something that has previously been seen only after lockdowns. "But herd immunity would come in different places at different times."

Despite around 70% of the UK adult population now being fully vaccinated against COVID-19, there is still a large pool of susceptible people. The highest proportion of infections is occurring in people aged 16–24, most of whom are either unvaccinated or have not yet received both jabs, although there are also ‘breakthrough’ infections among the fully vaccinated and those who have previously recovered from the disease.



[COVID vaccines slash viral spread – but Delta is an unknown](#)

Some random fluctuations in infection rates are inevitable, says epidemiological modeller Graham Medley, also at the LSHTM. “This is exactly the situation faced by, say, climate change — apparent signals appear in the data, and the question is at what point does it become reasonable to infer about something underlying?”

The decline in cases over many days seems to imply a specific underlying cause. But that cause might be a combination of many things, says Edmunds.

First, the drop might appear more pronounced because of a spike in infections in England in mid-July, caused by the delayed Euro 2020 football tournament, which led many people to congregate in pubs, bars and private homes, as well as stadiums. That, Edmunds says, is consistent with the higher infection rate among males at this time.

Subsequently, many people in the United Kingdom were alerted by NHS contact-tracing apps that they had recently been in close proximity to someone who tested positive. This spate of alerts, dubbed the ‘pingdemic’, has caused disruption to work and services throughout the country as many people were forced to self-isolate. But, says Edmunds, it might have done its job in slowing the spread of the virus.

Schools effect

Another major reason for the decline could be the end of the school term. Many schools in England closed around 23 July — which is too recent for an effect to show in the COVID-19 data. But a school-related decline in cases could already be apparent because some finished a week or so earlier, many older students were already off school after their exams, and around 20% of pupils were self-isolating at this time. “The contacts of school-age kids have dropped quite dramatically over the past several weeks,” says Edmunds.

If so, this reflects how big a driver of UK infections schools and young people now are — which has implications for the government’s recent decision not to vaccinate most under-18s.

There could be other factors at play too, says Christina Pagel, a specialist in health-care data analysis at University College London. Recent warm weather has led to a preference for outdoor socializing, for example, which could reduce transmission.



[Is one vaccine dose enough if you've had COVID? What the science says](#)

It is also possible that the drop in recorded cases could be the result of fewer people getting tested for COVID-19, rather than a genuine fall in infections. Paget says that people might be reluctant to take a test if they have only mild symptoms, perhaps because they cannot afford to self-isolate or do not want to jeopardize holiday plans.

Clinical immunologist Alex Richter at the University of Birmingham, UK, says that there might be reduced testing because of the end of school term and because of general social fatigue, but she warns that this is hard to quantify at this point. The number of test results being reported has fallen, but so has the proportion of tests that are positive.

Hospitalizations in England have also started to decline gradually — there were 645 admissions on 1 August, compared with 836 on 25 July. However, Paget cautions that there is some indication that infections might now be creeping up again. More data in the coming days and weeks, for example from the UK Office of National Statistics and Imperial College London's Real-time Assessment of Community Transmission (REACT) programme — which conducts regular home testing of more than 100,000 people — could shed some light on what is really happening.

Looking ahead

It has yet to be seen how the easing of restrictions will change public behaviour, and thus infections. This, says Edmunds, is really key to how the UK pandemic will play out over the coming months. “We can’t predict human behaviour very well at all,” he says. “None of us had the Euros [football matches] in our models for example, but it’s looking increasingly likely that that really did have an effect.”

He suggests that England might look to Scotland for what to expect in the coming weeks. Scotland’s school holidays and its Euro 2020 COVID-19 peak both came a few weeks ago — and cases have stayed low since. However, researchers agree that the return of school pupils, university students and office workers in September, as well as the possibility that protection from the first round of vaccines will wane, is likely to fuel another rise. “I think the summer will be a bit of a firebreak, but that the pandemic will slowly grow again and things will escalate in the autumn,” says Richter. It is by no means all over yet.

Nature **596**, 175-176 (2021)

doi: <https://doi.org/10.1038/d41586-021-02125-1>

Related Articles

-  [Why England's COVID 'freedom day' alarms researchers](#)
-  [COVID vaccines slash viral spread – but Delta is an unknown](#)



- [COVID and schools: the evidence for reopening safely](#)



- [Is one vaccine dose enough if you've had COVID? What the science says](#)



- [Six months of COVID vaccines: what 1.7 billion doses have taught scientists](#)

Subjects

- [Epidemiology](#)
- [Infection](#)
- [SARS-CoV-2](#)

nature careers

[Jobs](#) >

- [Technology and Knowledge Transfer Officer / Commercialization](#)

University of Luxembourg

Luxembourg, Luxembourg

- [Technology and Knowledge Transfer Officer / Social Sciences, Humanities](#)

University of Luxembourg

Luxembourg, Luxembourg

- [Postdoctoral Research Assistant \(m/f/div\) in modelling and data science](#)

Max Planck Institute for the Science of Human History

Jena, Germany

- [Postdoc researcher in de novo design of transmembrane beta-barrels for nanopore sensing applications](#)

Flanders Institute for Biotechnology (VIB)

Brussels, Belgium

Nature Briefing

An essential round-up of science news, opinion and analysis, delivered to your inbox every weekday.

[Download PDF](#)

Related Articles



- [Why England's COVID 'freedom day' alarms researchers](#)



- [COVID vaccines slash viral spread – but Delta is an unknown](#)

-  [COVID and schools: the evidence for reopening safely](#)
-  [Is one vaccine dose enough if you've had COVID? What the science says](#)
-  [Six months of COVID vaccines: what 1.7 billion doses have taught scientists](#)

Subjects

- [Epidemiology](#)
- [Infection](#)
- [SARS-CoV-2](#)

This article was downloaded by **calibre** from <https://www.nature.com/articles/d41586-021-02125-1>

- NEWS
- 05 August 2021

More women than ever are starting careers in science

But a study of the publications of millions of researchers also suggests that women are less likely to continue their academic careers than their male counterparts.

- [Katharine Sanderson](#) ⁰
 1. Katharine Sanderson
 1. Katharine Sanderson is a freelance journalist based in Cornwall, UK.

[View author publications](#)

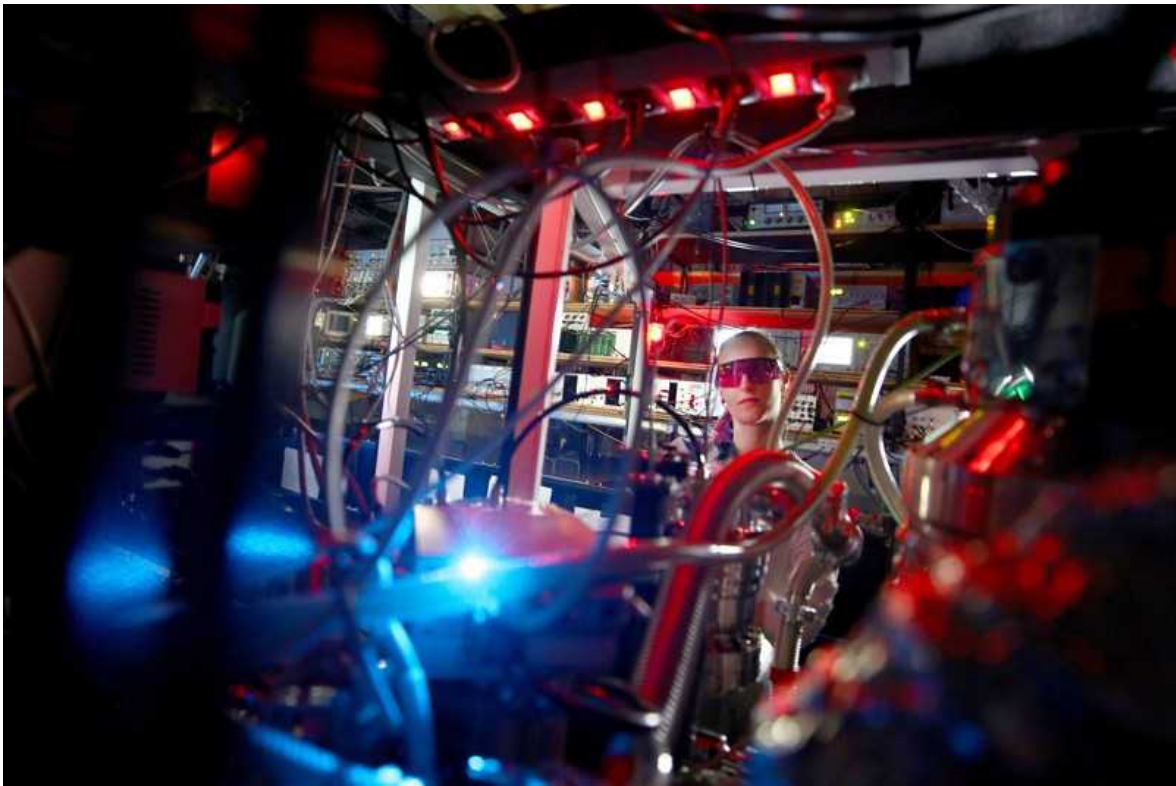
You can also search for this author in [PubMed](#) [Google Scholar](#)





•

[Download PDF](#)



Quantum physicist Lisa Ringena makes adjustments to the Atom Trap Trace Analysis system at the Kirchhoff Institute for Physics in Heidelberg, Germany. Credit: Lisi Niesner/Reuters

Women are more likely to start a research career now than they were 20 years ago, reveals a longitudinal study of the publishing records of millions of researchers around the world. But they are less likely to continue their academic careers than are their male contemporaries, and in general publish fewer papers.

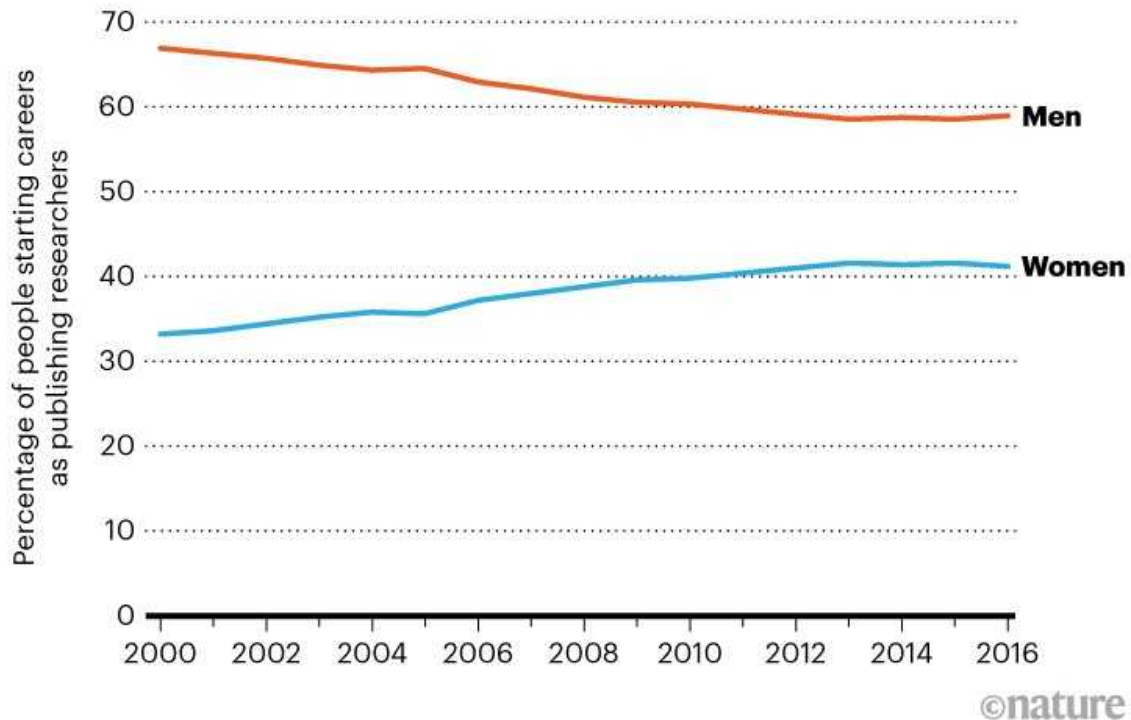
Ludo Waltman, a quantitative scientist at Leiden University in the Netherlands, and his colleagues took a deep dive into the huge Scopus citation and abstract database, hosted by Elsevier. They looked at the publication careers of some six million researchers globally who had authored at least three papers between 1996 and 2018. The team posted its findings on the preprint server arXiv.org¹.

The authors found that the proportion of women starting a career in science rose over time. In 2000, 33% of researchers starting their publishing career were women; that grew to 40% in recent years (see ‘Gender gap’). Waltman

says that although the results are not surprising, it's important that we now have concrete statistics confirming the trend for many countries and scientific disciplines.

GENDER GAP

The proportion of scientists starting their publishing careers who are women increased by nearly one-fifth between 2000 and 2016.



Source: Ref. 1

In the physical sciences, mathematics and engineering, male authors still made up a much higher proportion of authors than did women, even in more recent years (see 'Differences by discipline').

Career progression

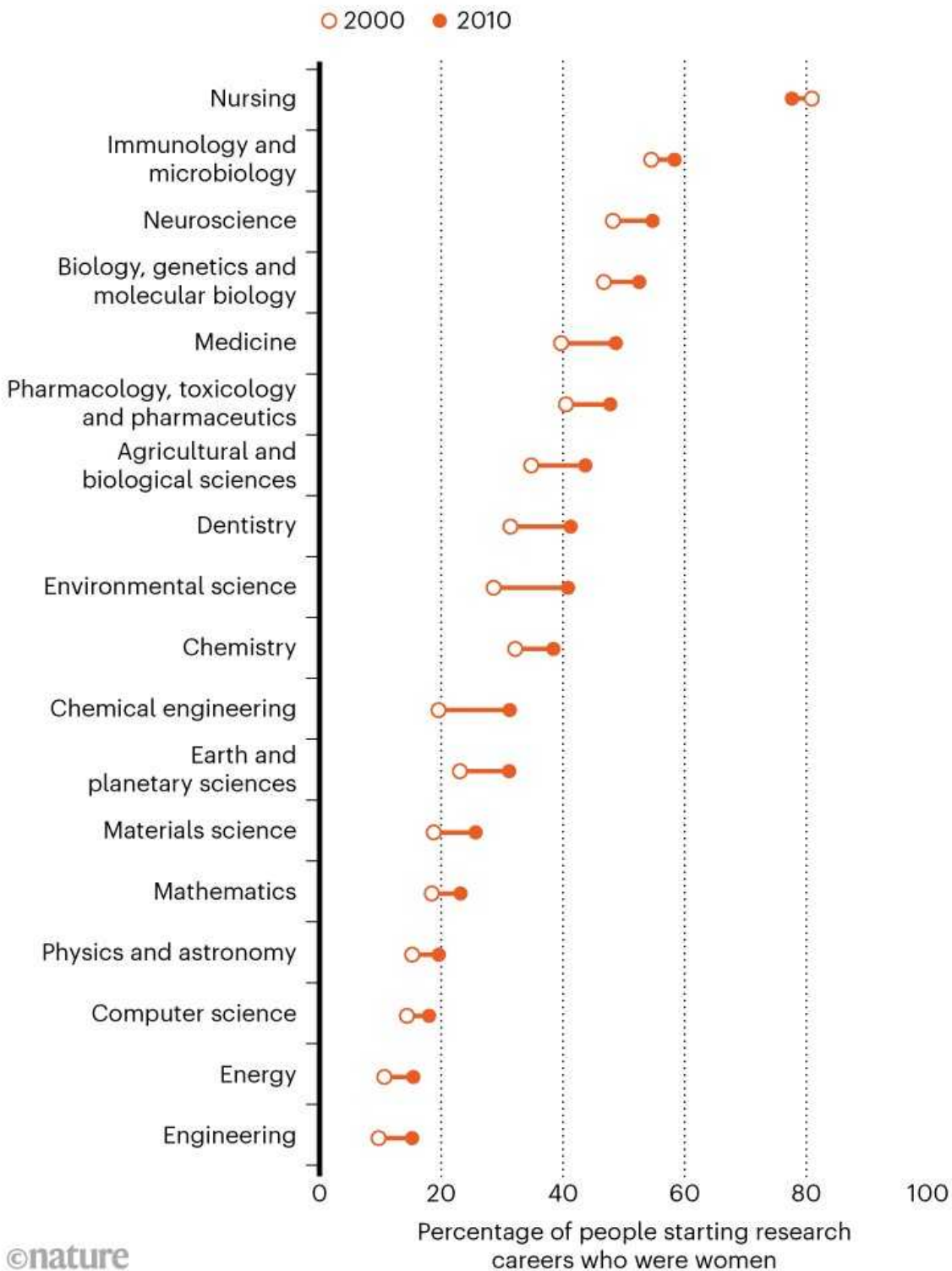
Waltman and his team took their work further by tracking the researchers' publication records to see whether they continued authoring scientific papers — a proxy for continuing a career in science. They discovered that women

were less likely to continue publishing papers than were men, whatever year they began their careers.

But Waltman says his team was surprised — given that there is a well-known problem of fewer women than men progressing to senior roles in science — that women were only slightly less likely to continue to publish papers than were men. They found that 54% of women who started publishing in 2000 had dropped out 15 years later, as opposed to 52% of men.

DIFFERENCES BY DISCIPLINE

The proportion of women starting research careers varies widely between disciplines, but has increased in nearly all fields between 2000 and 2010.



Source: Ref. 1

Nevertheless, “while the length of the scientific careers of men and women is quite similar, there are important differences between men and women in the way in which their scientific careers develop”, he says. In general, men seemed to progress to senior roles — roughly judged by appearing as the last author on a paper — more quickly. On average, they also published 15–20% more papers than did women over the time span of the data, though there is wide variation across different fields.

One important limitation of the study was that it excluded data from India and China — which together account for around one-third of the world’s population — because the authors’ algorithms struggled to assign gender unambiguously to names from these nations. It also did not account for non-binary authors.

Positive picture

Flaminio Squazzoni, a sociologist at the University of Milan in Italy, agrees that the lack of data from India and China is a big gap. “It is probable that if we would have data on these two countries, the perspective on women academics could be slightly worse,” Squazzoni predicts.



The women who cracked science's glass ceiling

Nevertheless, “it’s an honest study” and the Scopus database is a rich source of information, says Squazzoni. His own team published work this year showing that there is little gender bias in peer-review processes². That, combined with this latest study, suggests that investments in gender-diversity schemes in science could be paying off, he says.

Waltman says that although the overall picture looks positive for more women entering science, it’s important to remember that the increase is an average over many countries and scientific disciplines, and that there is huge variation within the numbers. He is also keen to point out that scientific careers are about more than publication numbers. “The bibliometric lens through which many studies, including our own, look at diversity in science is a very narrow one,” he says.

Nature **596**, 177 (2021)

doi: <https://doi.org/10.1038/d41586-021-02147-9>

References

1. 1.

Boekhout, H., van der Weijden, I. & Waltman, L. Preprint at <https://arxiv.org/abs/2106.12624> (2021).

2. 2.

Squazzoni, F. *et al.* *Sci. Adv.* **7**, eabd0299 (2021).

[PubMed](#) [Article](#) [Google Scholar](#)

[Download references](#)

Related Articles

-  [The women who cracked science's glass ceiling](#)
-  [Women from some under-represented minorities are given too few talks at world's largest Earth-science conference](#)
-  [Three extraordinary women run the gauntlet of science — a documentary](#)

Subjects

- [Peer review](#)
- [Careers](#)
- [Publishing](#)

nature careers

[Jobs](#) >

- [Technology and Knowledge Transfer Officer / Commercialization](#)

University of Luxembourg

Luxembourg, Luxembourg

- [Technology and Knowledge Transfer Officer / Social Sciences, Humanities](#)

University of Luxembourg

Luxembourg, Luxembourg

- [Postdoctoral Research Assistant \(m/f/div\) in modelling and data science](#)

Max Planck Institute for the Science of Human History

Jena, Germany

- [Postdoc researcher in de novo design of transmembrane beta-barrels for nanopore sensing applications](#)

Flanders Institute for Biotechnology (VIB)

Brussels, Belgium

Nature Briefing

An essential round-up of science news, opinion and analysis, delivered to your inbox every weekday.

[Download PDF](#)

Related Articles

-  [The women who cracked science's glass ceiling](#)



- [Women from some under-represented minorities are given too few talks at world's largest Earth-science conference](#)



- [Three extraordinary women run the gauntlet of science — a documentary](#)

Subjects

- [Peer review](#)
- [Careers](#)
- [Publishing](#)

This article was downloaded by **calibre** from <https://www.nature.com/articles/d41586-021-02147-9>

| [Section menu](#) | [Main menu](#) |

- NEWS FEATURE
- 05 August 2021

COVID vaccine boosters: the most important questions

Concerns over waning immunity and SARS-CoV-2 variants have convinced some countries to deploy extra vaccine doses — but it's not clear to scientists whether most people need them.

- [Ewen Callaway](#)
 1. Ewen Callaway
[View author publications](#)

You can also search for this author in [PubMed](#) [Google Scholar](#)





•



Britain is one of several countries looking to administer booster shots for COVID-19 in the coming months; some have already started. Credit: Henry Nicholls/Reuters/Alamy

[Download PDF](#)

To boost or not to boost? That is the question facing countries fortunate enough to have vaccinated much of their adult population. In the face of soaring infection numbers caused by the highly contagious Delta variant of

SARS-CoV-2, and hints that immunity triggered by COVID-19 vaccines might fade over time, some countries are considering whether to give further doses to those who have been fully vaccinated. Germany and Israel have announced plans for booster-shot programmes, and a growing list of countries including the United Arab Emirates, China and Russia have already started administering extra doses.

But scientists say that the case for COVID-19 vaccine boosters at this point is weak. They might not be necessary for most people, and could [divert much-needed doses away from others](#). On 4 August, the World Health Organization called for a moratorium on boosters until at least the end of September. “Wasting resources on boosters for those who are already protected against severe disease does not really make too much sense,” says Laith Jamal Abu-Raddad, an infectious-disease epidemiologist at Weill Cornell Medicine—Qatar in Doha. “Down the line, probably, we would need to think of it. But really, we don’t have strong arguments for it right now.”



[COVID boosters for wealthy nations spark outrage](#)

The data on whether and when boosters might be needed are trickling in. But it’s likely that key gaps will remain for some time. As a result, people might start getting boosters that have no real benefit. Meanwhile, not enough is known about groups that might really need extra doses, such as older people

and those with compromised immune systems. And, as the Delta variant surges in many countries, health authorities might not have the luxury of waiting around for definitive answers. “It’s a difficult call and it will almost certainly have to be made on incomplete evidence,” says Robert Aldridge, an infectious-disease epidemiologist at University College London.

Here, *Nature* looks at what scientists know — and what they wish they knew — about COVID-19 vaccine boosters.

Do boosters actually work?

Vaccination produces an initial surge in the number of immune cells churning out antibodies and other molecules, which then slowly drops. This leaves behind a small pool of long-lasting ‘memory’ B and T cells that patrol the body for future infections by that pathogen.



A health worker administers vaccines door-to-door in a rural area of Jerusalen, Colombia. Credit: Guillermo Legaria/Getty

A booster does several things to these cells, says Ali Ellebedy, a B-cell immunologist at Washington University in St. Louis, Missouri. It causes antibody-making B cells to multiply, elevating the levels of antibodies against the pathogen once more. In time, their numbers will dwindle again, but the pool of memory B cells left behind will be larger than before, leading to a faster, stronger response to subsequent exposures. Boosters also promote a process called affinity maturation, in which ‘engaged’ B cells — those that have been triggered by the vaccine — travel to the lymph nodes. Here, they gain mutations, making the antibodies they produce bind to pathogens more strongly, potentially enhancing their potency.

Numbers of memory B cells and antibody levels will eventually plateau with repeated boosting (or reinfection), but it is unlikely that such levels have been reached in people who have had the recommended regimen of COVID-19 vaccine or a previous infection, says Ellebedy. A booster shot should elicit stronger immune responses, says Rafi Ahmed, an immunologist at Emory University in Atlanta, Georgia. “It will boost.”



Can COVID vaccines stop transmission? Scientists race to find answers

The few trials to have tested extra doses support this. Third doses of vaccines developed by Moderna, Pfizer–BioNTech, Oxford–AstraZeneca and Sinovac prompted a spike in levels of infection-blocking ‘neutralizing’ antibodies, when administered several months after the second dose. An

ongoing UK trial will test various combinations of boosters, including using a different vaccine from the original inoculations. Preliminary studies of these ‘mix and match’ strategies suggest that they could lead to more robust immune responses, characterized by high levels of both antibodies and T cells, which kill infected cells and support other antiviral responses^{1,2,3}.

These trials also suggest that common vaccine-related side effects, such as headache and fever, aren’t very different from those seen with earlier immunizations. “I would take a third dose at some point,” Ahmed says. “I don’t see a downside.”

Is immunity from vaccines waning?

Scientists typically look at antibody levels, or titres, as a proxy for how well a vaccine has worked. These usually spike along with the surge in short-lived B cells and then fall as the cells dwindle. Memory B cells and bone-marrow plasma cells continue to churn out antibodies, but at reduced levels, for decades. That’s expected. “There isn’t a vaccine where you don’t see a drop over time in antibody titres and T-cell titres,” says Ahmed. “There is always a drop.”

Early indications suggest that antibody levels triggered by most COVID-19 vaccines are falling, too⁴. What scientists don’t know is whether these drops reflect a decline in protection against the virus. Teams around the world are racing to determine what level of neutralizing antibodies or another immune marker is most closely associated with a vaccine’s effectiveness. They’re seeking what’s known as a correlate of protection.

“What that magic number is, is something that we have a hint of — but not a firm handle on,” says Kanta Subbarao, a virologist at the Peter Doherty Institute for Infection and Immunity in Melbourne, Australia. Knowing this threshold would allow researchers to determine more precisely whether and when a booster becomes necessary — such as in response to waning immunity or to the emergence of new variants that evade antibody recognition. “Without having that properly defined correlate, it’s hard to say if we really need a booster,” says Ellebedy.



An employee runs a machine filling vials with COVID-19 vaccine at the Serum Institute of India in Pune. Credit: Rafiq Maqbool/AP/Shutterstock

Are vaccinations given months ago still preventing infections?

In the absence of a reliable correlate of protection, researchers are looking for signs of waning immunity in real-world data from countries that have advanced vaccination programmes. Are people who were vaccinated early on getting infected at higher rates than those who were vaccinated more recently? Drawing clear conclusions from such data is fraught, says Dvir Aran, a biomedical data scientist at Technion — Israel Institute of Technology in Haifa.

Last month, the Ministry of Health in Israel, a country that has one of the world's highest vaccination rates, released raw data on vaccinations and infections from December 2020 to July 2021. The ministry estimated that vaccine protection against both infection and disease had dropped [from](#)

above 90% in the early months of its programme to around 40% by late June — a decline that could be due to the effects of the Delta variant.

To look more closely for evidence of waning protection, scientists at Kahn Sagol Maccabi in Tel Aviv — the research arm of Israeli health-maintenance organization Maccabi Healthcare Services — analysed health records from more than 1.3 million people who were vaccinated between January and April 2021. Those vaccinated in January and February were 53% more likely to test positive for SARS-CoV-2 during those four months, compared with people vaccinated in March and April. The differences were even starker among the earliest and latest vaccinated⁵.



Six months of COVID vaccines: what 1.7 billion doses have taught scientists

But reduced protection isn't the only explanation for this observation, says Aran. Data were stratified by age groups, and younger individuals who were vaccinated early on tended to be health-care workers, who are at a higher risk of infection than the younger people vaccinated later. Early-vaccinated individuals also tended to be wealthier than people who got vaccinated later in Israel, and might have taken COVID-19 tests at a higher rate because of worries over the virus or an eagerness to travel internationally. That could introduce biases into the data, says Aran.

Another way to weigh the evidence in support of boosters is efficacy trials — the double-blinded, placebo-controlled, randomized studies used to earn

vaccine authorization by health authorities. On 28 July, researchers at Pfizer–BioNTech, who have pushed strongly for third doses, published data on the preprint server medRxiv showing that the vaccine's efficacy against symptomatic disease had slipped from 96% to 84% after 6 months⁶. Before that, an April press release from Moderna put its vaccine's efficacy at “greater than 90%” after half a year, compared to its original efficacy figure of 94%.

These trials are meant to minimize confounding variables that dog real-world studies. But once vaccines became publicly available, Pfizer and other vaccine-makers unblinded the studies, allowing participants to learn whether they had received a vaccine or a placebo. “All the participants heard the news about the 95% protection and those that received the vaccine would clearly feel more safe and will take more risks,” says Aran, who thinks this behaviour change — and not waning protection — could explain the apparent drop in the efficacy of the Pfizer–BioNTech vaccine. Representatives from Pfizer had no comment on this hypothesis.

What about protection from serious illness with COVID-19?

It is clear from the trial data that protection against severe disease remains high. Pfizer–BioNTech and Moderna reported percentage efficacy estimates in the high 90s against severe COVID-19, after 6 months. Real-world data from Israel, the United Kingdom and elsewhere suggest that vaccines are hugely effective at [keeping people out of hospital — even when the Delta variant is the cause.](#)

COVID-19 vaccines were largely developed with this goal in mind, researchers point out. “It should be enough,” says Ellebedy. But what’s unclear is whether relatively mild infections among vaccinated individuals being observed now are a harbinger of further loss of protection, says Aldridge. “Is that an early warning sign? That’s what we don’t know.”

Natalie Dean, a biostatistician at Emory University, says that discussions around boosters need to look at their incremental value to improving

protection against various outcomes, [from stopping transmission](#) to preventing symptomatic infections and severe disease.



[COVID vaccines slash viral spread – but Delta is an unknown](#)

In this context, many scientists see offering extra doses in the coming months as a poor use of resources, on both global and national levels. “A small dent in the efficacy against infection does not justify, in my view, someone like me getting a booster when someone else has not even had one dose,” says Abu-Raddad. Dean agrees: “We just don’t have clear evidence of enough of a loss of efficacy to change our focus or distract from the main goal, which is trying to get as many people first doses” as possible.

The lack of evidence around boosters also means that scientists do not have a clear picture of who would benefit most. A large proportion of organ-transplant recipients on immunosuppressive drugs do not generate high levels of antibodies after two doses of a COVID-19 vaccine, for instance. One study⁷ found that only about half of them produced detectable levels. There is evidence that a third dose can elevate those titres, but for many people, they remain below levels seen in other vaccinated groups⁷. Unfortunately, without a correlate of protection, it’s not clear what level is adequate for transplant recipients or older people, whose immune systems tend to be less robust than those of younger individuals, or how to achieve such a level, says Ellebedy. If these groups don’t mount protective immune

responses after two doses, he says, “that’s when booster immunization is not going to be a luxury”.

Aldridge’s team is tracking the vaccine responses of thousands of people in the United Kingdom, while collecting information about immunosuppressive drug regimens, blood cancers and other health factors that could compromise immunity. He hopes his team’s study can inform the deployment of boosters.

What else could change the calculation on boosters?

The surge in cases caused by the Delta variant have caused some countries to look more closely at boosters, says Subbarao. “I think everybody is really quite sobered by what’s happening with the Delta variant.”

Countries that have relied heavily on inactivated-virus vaccines, which seem to be less effective at preventing symptomatic infections than viral vector and messenger RNA vaccines, have been among the first to deploy boosters. The United Arab Emirates is giving people who received Sinopharm’s inactivated-virus vaccine a booster with the Pfizer–BioNTech vaccine, and China plans to use domestically produced mRNA and protein-based vaccines as boosters for its inactivated-virus vaccine.



What it will take to vaccinate the world against COVID-19

There is anecdotal evidence of large outbreaks in some countries that deployed both inactivated-virus vaccines and other vaccine types, such as the Seychelles and Chile. But Subbarao says it's not yet clear whether such breakthrough infections are more likely in people who received the inactivated-virus vaccines than in those given other vaccines, or whether they lead to more severe disease. For countries that have decided to offer third doses to people who received inactivated-virus vaccines, she adds, "I haven't seen the data that's prompting those decisions."

Despite the lack of evidence in favour of offering boosters now, Aran expects policymakers to err on the side of caution and begin offering boosters to at-risk groups in the coming weeks. "The risk is low, the advantage is high," he says. After initially spurning the idea of third doses for most people, the US government is now considering them, according to news reports. And on 29 July, Israel announced plans to give people aged over 60 a third dose of the Pfizer–BioNTech vaccine. The United Kingdom has drawn up tentative plans to offer vaccines to those over 50, as well as other high-risk groups, from September.

"It's a gamble," says Aran. "Is it based on enough evidence? I think not."

Nature **596**, 178-180 (2021)

doi: <https://doi.org/10.1038/d41586-021-02158-6>

References

1. 1.

Hillus, D. *et al.* Preprint at medRxiv
<https://doi.org/10.1101/2021.05.19.21257334> (2021).

2. 2.

Schmidt, T. *et al.* Preprint at medRxiv
<https://doi.org/10.1101/2021.06.13.21258859> (2021).

3. 3.

Borobia, A. M. *et al.* Preprint at SSRN
<https://doi.org/10.2139/ssrn.3854768> (2021).

4. 4.

Shrotri, M. *et al.* *Lancet* **398**, 385–387 (2021).

[PubMed](#) [Article](#) [Google Scholar](#)

5. 5.

Mizrahi, B. *et al.* Preprint at medRxiv
<https://doi.org/10.1101/2021.07.29.21261317> (2021).

6. 6.

Thomas, S. J. *et al.* Preprint at medRxiv
<https://doi.org/10.1101/2021.07.28.21261159> (2021).

7. 7.

Kamar, N. *et al.* *N. Engl. J. Med.*
<https://doi.org/10.1056/NEJMc2108861> (2021).

[Download references](#)

Related Articles

-  [**COVID boosters for wealthy nations spark outrage**](#)



- [COVID vaccines slash viral spread – but Delta is an unknown](#)



- [Can COVID vaccines stop transmission? Scientists race to find answers](#)



- [Six months of COVID vaccines: what 1.7 billion doses have taught scientists](#)



- [What it will take to vaccinate the world against COVID-19](#)

Subjects

- [SARS-CoV-2](#)
- [Vaccines](#)
- [Immunology](#)

nature careers

[Jobs](#) >

- [Technology and Knowledge Transfer Officer / Commercialization](#)

University of Luxembourg

Luxembourg, Luxembourg

- [Technology and Knowledge Transfer Officer / Social Sciences, Humanities](#)

University of Luxembourg

Luxembourg, Luxembourg

- [Postdoctoral Research Assistant \(m/f/div\) in modelling and data science](#)

Max Planck Institute for the Science of Human History

Jena, Germany

- [Postdoc researcher in de novo design of transmembrane beta-barrels for nanopore sensing applications](#)

Flanders Institute for Biotechnology (VIB)

Brussels, Belgium

Nature Briefing

An essential round-up of science news, opinion and analysis, delivered to your inbox every weekday.

[Download PDF](#)

Related Articles



- [COVID boosters for wealthy nations spark outrage](#)



- [COVID vaccines slash viral spread – but Delta is an unknown](#)



- [Can COVID vaccines stop transmission? Scientists race to find answers](#)



- [Six months of COVID vaccines: what 1.7 billion doses have taught scientists](#)



- [What it will take to vaccinate the world against COVID-19](#)

Subjects

- [SARS-CoV-2](#)
- [Vaccines](#)
- [Immunology](#)

This article was downloaded by **calibre** from <https://www.nature.com/articles/d41586-021-02158-6>

Books & Arts

- **[Think outside the brain box](#)** [10 August 2021]
Book Review • Can our bodies, tools and surroundings take more of the cognitive load?
 - **[Pain in the brain, climate racism, and quantum cusp: Books in brief](#)** [27 July 2021]
Book Review • Andrew Robinson reviews five of the week's best science picks.
-

- BOOK REVIEW
- 10 August 2021

Think outside the brain box

Can our bodies, tools and surroundings take more of the cognitive load?

- [Alison Abbott](#) 0

1. [Alison Abbott](#)

1. Alison Abbott is a science writer based in Munich, Germany.

[View author publications](#)

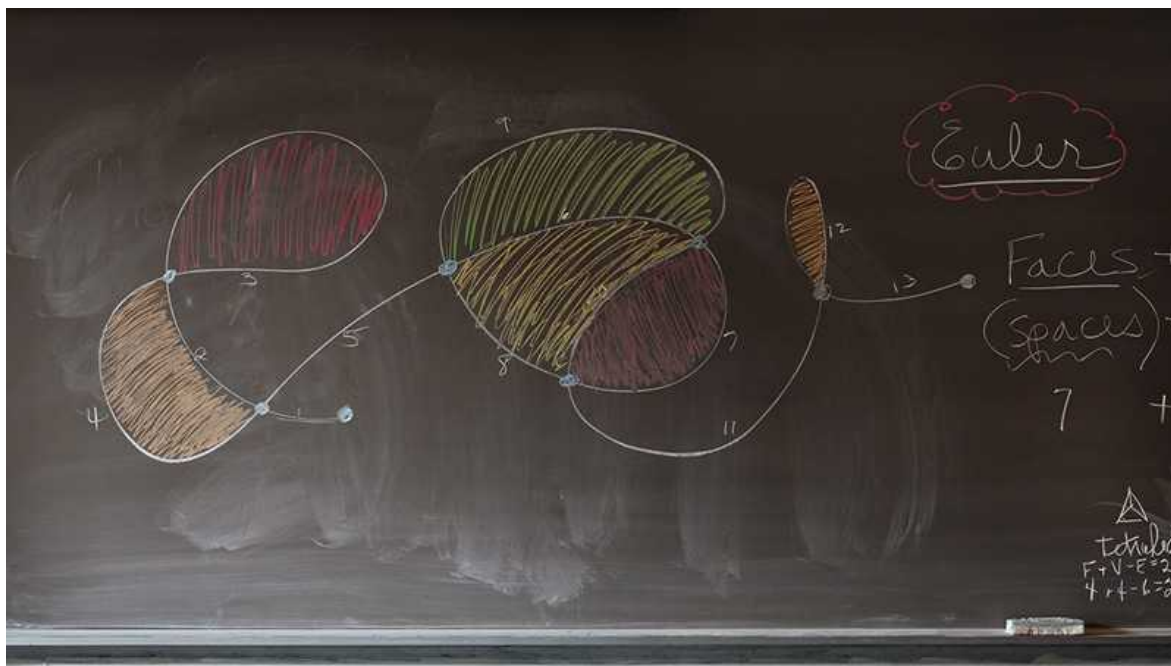
You can also search for this author in [PubMed](#) [Google Scholar](#)





•

[Download PDF](#)



Some mathematicians find chalk and board so essential for thinking that their tools are celebrated in a 2021 book, *Do Not Erase*. Credit: Jessica Wynne

The Extended Mind: The Power of Thinking Outside the Brain *Annie Murphy Paul* Houghton Mifflin Harcourt (2021)

The disembodied brain in a vat is an amusing trope of science fiction. Without a vat, the brain needs a body to generate the nutrients to maintain itself and to furnish information about its environment. Sight, hearing, touch, taste, smell and proprioception help us to navigate, and find food or reproductive partners. Science fiction assumes that, with those basic needs taken care of by the vat, the brain can devote its full energies to developing genius intelligence.

Not so, argues science writer Annie Murphy Paul. Her book *The Extended Mind* lays out arguments that the body — and the world more generally — is part of being smart. The human brain is a structure with serious limits: in memory, in attention, in handling abstract concepts. But it can extend its thinking apparatus beyond its skull-bound membranes. Given that the modern world is ever more centred on non-intuitive ideas and abstractions,

we need all the help that mind extension can offer. Society fails to recognize this, is Paul's claim.



From spoons to semiconductors — we are what we make

We can, for example, offload information from our heads to Post-it notes, phones, computers, friends, colleagues or our gesturing hands. Or we can transform ideas into concrete objects by building models — from blocks, bricks or bits. With the information thus externalized, we can contemplate and manipulate it from a distance — without paying the high cognitive price of having to hold it in the front of our minds while doing so. Relieved, the brain has more resources for understanding or problem-solving. Perhaps that's why Leonardo da Vinci drew and crafted, or nineteenth-century chemist John Dalton built atomic models out of balls and sticks. There's many a mathematician who still uses chalk and board like a plug-in hard drive.

I don't completely buy the premise that today's society quashes or undervalues 'extensions'. Collaboration is ubiquitous from schools to CERN's high-energy physics experiments. Or perhaps the issue is that digital extensions are greatly privileged over physical ones: too much Slack, not enough pacing (like Charles Darwin along his "thinking path"). But the framing of the brain-body complex as a borderless thinking apparatus is

interesting, bringing together a wide range of research, from education and business practice to psychology and cognitive neuroscience.

Hacks and hands

Paul explores the many tricks that can foster people's ability to recall, focus and analyse. One is the venerable memory palace, in which items to be remembered are associated with a particular spot. Ancient Greek and Roman orators used this 'method of loci' to mentally attach points to be remembered in their speeches to, for example, the windows of a building, or the shop fronts in a street.

The method has been validated in scientific studies. It exploits the brain's built-in navigational system, and cognitive neuroscientists have shown that memory champions — and London taxi drivers — activate brain regions associated with spatial memory and navigation to a greater degree than average.



A grasp on human thinking

The simple act of gesturing while speaking can also drop what Paul describes as "mental hooks" into, say, a lecture to be learnt, to help reel in that piece of information when at the podium. Movements, even the fidgety

ones that a standing desk can engender, might help concentration. Pity the students required to sit still at their desks, she writes.

The book delves into the issue of how our surroundings affect how we think. Why, for example, does being in nature reduce the stress that erodes our cognitive powers, and why is natural light important in a workplace? Humans have, after all, evolved to function optimally in an outdoor environment. Paul lobbies for biophilic architecture that builds in generous windows and greenery. She lauds the design of the Salk Institute for Biological Studies in San Diego, California: a modern take on the medieval monastery, with spaces for meeting and talking, and others for solitary contemplation. These, she says, serve researchers' dual need to think through difficult concepts without distraction, and to engage in fruitful discussions.

The latter exploits the mind extension of “thinking with our relationships”. The catalogue of studies on this phenomenon looks at the various ways in which social interaction — with peers, with experts and through teaching, arguing or group training — can help learning or analysis. Tapping into the hive mind, she argues, can spread the cognitive load.



[Science in hand: how art and craft can boost reproducibility](#)

So much research is covered at speed that it's not always clear what's robust and what's flimsy. Given that psychology has known reproducibility problems, these distinctions are important. The book contains more than 70 pages of notes for those who want to follow up on some of the many studies mentioned. But somehow, the whole is less than the sum of the parts.

The 'how to' element, so beloved of publishers, seems rather one-size-fits-all. To live a more intelligent life, Paul recommends gesturing freely, enacting abstract academic concepts with our bodies (perhaps the annual [Dance Your Ph.D. contest](#) is on to something?), learning in groups, and many other activities that could help only in particular circumstances. She does not consider important issues of personality that would affect the value of many such measures. Would an introvert gain as much from group learning as an extrovert? Would an uncoordinated person take as much as a graceful one from physical action? Such questions are not addressed.

Still, many of the messages are indisputable. Evolution has built our brains to respond to signals that constantly monitor our environment and our bodies. Society should indeed give more thought to its environment. Individuals should heed what their bodies are telling them. But let's not exaggerate: it's the brain, and not the body, that does the actual thinking.

Nature **596**, 181-182 (2021)

doi: <https://doi.org/10.1038/d41586-021-02169-3>

Competing Interests

The author declares no competing interests.

Related Articles

- [Medicine: Discovery through doing](#)

-  [A grasp on human thinking](#)
-  [Science in hand: how art and craft can boost reproducibility](#)
-  [From spoons to semiconductors — we are what we make](#)

Subjects

- [Neuroscience](#)
- [Psychology](#)

nature careers

[Jobs](#) >

- [Technology and Knowledge Transfer Officer / Commercialization](#)

University of Luxembourg

Luxembourg, Luxembourg

- [Technology and Knowledge Transfer Officer / Social Sciences, Humanities](#)

University of Luxembourg

Luxembourg, Luxembourg

- [Postdoctoral Research Assistant \(m/f/div\) in modelling and data science](#)

Max Planck Institute for the Science of Human History

Jena, Germany

- [Postdoc researcher in de novo design of transmembrane beta-barrels for nanopore sensing applications](#)

Flanders Institute for Biotechnology (VIB)

Brussels, Belgium

Nature Briefing

An essential round-up of science news, opinion and analysis, delivered to your inbox every weekday.

[Download PDF](#)

Related Articles



- [Medicine: Discovery through doing](#)



- [A grasp on human thinking](#)



- [Science in hand: how art and craft can boost reproducibility](#)



- [From spoons to semiconductors — we are what we make](#)

Subjects

- [Neuroscience](#)
- [Psychology](#)

This article was downloaded by **calibre** from <https://www.nature.com/articles/d41586-021-02169-3>

| [Section menu](#) | [Main menu](#) |

- BOOK REVIEW
- 27 July 2021

Pain in the brain, climate racism, and quantum cusp: Books in brief

Andrew Robinson reviews five of the week's best science picks.

- [Andrew Robinson](#) 0
1. [Andrew Robinson](#)
 - 1. Andrew Robinson's many books include *Lost Languages: The Enigma of the World's Undeciphered Scripts* and *Einstein on the Run: How Britain Saved the World's Greatest Scientist*. He is based in London.

[View author publications](#)

You can also search for this author in [PubMed](#) [Google Scholar](#)





•

[Download PDF](#)

'An enthralling read'

Dr Rachel Clarke

Monty Lyman

Shortlisted for the Royal Society
Science Book Prize

The **Painful Truth**

The new science of why we hurt
and how we can heal



The Painful Truth

Monty Lyman *Penguin* (2021)

Why is pain, a universal experience, so poorly understood by both doctors and patients, asks clinician-researcher Monty Lyman. He relieved his irritable bowel syndrome through self-hypnosis, including visualizing his bowels changing from “rocky rapids to the languid Oxfordshire Thames”. But hypnotherapy went unmentioned at his medical school — probably owing to an outdated view that pain arises only from injury to the body. Lyman’s compelling mix of science and anecdote shows that persistent pain is “messy, complex and human”.

JEREMY WILLIAMS

Climate Change*

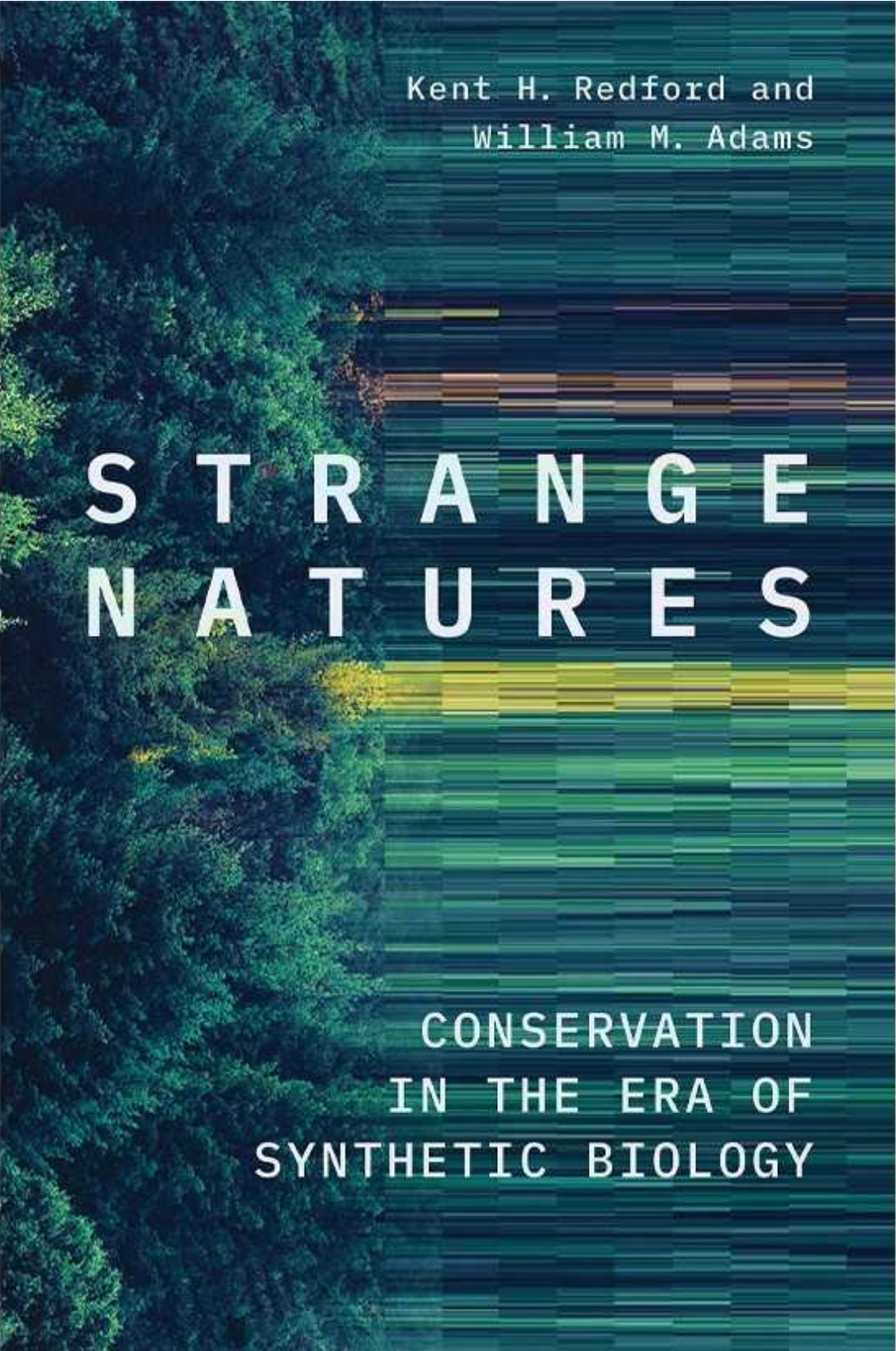
*Is Racist
**Race, Privilege and the
Struggle for Climate Justice**

Foreword by DR SHOLA MOS-SHOGBAMIMU,
author of *This Is Why I Resist*

Climate Change Is Racist

Jeremy Williams *Icon* (2021)

In a 2020 survey about the global impacts of climate change, conducted in the United Kingdom, 31% of respondents thought white people were hardest hit by droughts, floods, storms, food insecurity and air pollution. This gets “the injustice completely backwards”, says environmental and social justice campaigner Jeremy Williams. He argues that the countries most responsible for emissions are disproportionately white; those most vulnerable to its effects are mostly people of colour. Climate change, he writes, is “structurally racist”.



Kent H. Redford and
William M. Adams

STRANGE NATURES

CONSERVATION
IN THE ERA OF
SYNTHETIC BIOLOGY

Strange Natures

Kent H. Redford & William M. Adams *Yale Univ. Press* (2021)

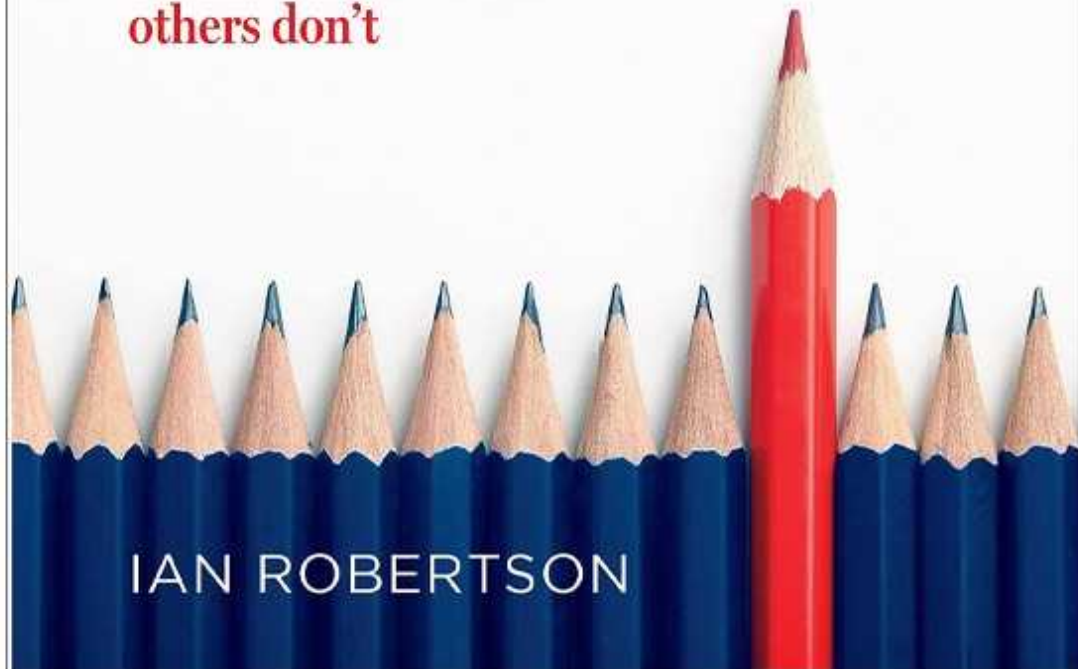
Lakenheath Fen is a nature reserve for birds, consisting of water bodies, reed beds and wet grazing marshes. It was dug from former farmland in 1995: “a mix of naturalness and artificiality”. The birds arrived on their own, but what if they, too, were to be artificially moulded? “Conservation faces a huge challenge in the rise of genome editing and of biotechnology,” observe Kent Redford and William Adams in their thoughtful study. They think these controversial techniques might help species survive in an increasingly unnatural world.

'Interesting and important.'
Steven Pinker

'Revelatory and practical . . .
important for everyone
but crucial for women.'
Mary Robinson

How Confidence --- Works

The new science of self-belief,
why some people learn it and
others don't



IAN ROBERTSON

How Confidence Works

Ian Robertson *Bantam* (2021)

Confidence is a “bridge to the future”, writes neuroscientist and clinical psychologist Ian Robertson: a capacity to visualize something non-existent and then to realize it. It can be strengthened, he notes. His appealing book ranges from neuroscience to politics, including over-confident male leadership in the United States, Brazil, Russia and the United Kingdom, contrasted with female leadership in Taiwan, Germany, Finland, Denmark, Iceland and New Zealand — in relation to COVID-19 death rates.



QUANTUM COMPUTING

The Transformative Technology
of the Qubit Revolution

BRIAN CLEGG

Quantum Computing

Brian Clegg *Icon* (2021)

With Google, IBM and others pumping in money, quantum computing is “at a cusp”, says Brian Clegg. In 1981, physicist Richard Feynman speculated about ‘quantum bits’ operating on the superposed states of quantum particles, rather than binary bits of 0 or 1. Work began around 2000; after two decades of development of algorithms and experimental rigs, will the qubit finally become a “significant force”? Clegg thinks so, probably through quantum computers at specialist locations — like telescopes in modern astronomy.

Nature **596**, 182 (2021)

doi: <https://doi.org/10.1038/d41586-021-02063-y>

Competing Interests

The author declares no competing interest.

Subjects

- [Arts](#)
- [Culture](#)

nature careers

[Jobs](#) >

- [Technology and Knowledge Transfer Officer / Commercialization](#)

University of Luxembourg

Luxembourg, Luxembourg

- [Technology and Knowledge Transfer Officer / Social Sciences, Humanities](#)

University of Luxembourg

Luxembourg, Luxembourg

- [**Postdoctoral Research Assistant \(m/f/div\) in modelling and data science**](#)

Max Planck Institute for the Science of Human History

Jena, Germany

- [**Postdoc researcher in de novo design of transmembrane beta-barrels for nanopore sensing applications**](#)

Flanders Institute for Biotechnology (VIB)

Brussels, Belgium

Nature Briefing

An essential round-up of science news, opinion and analysis, delivered to your inbox every weekday.

[Download PDF](#)

Subjects

- [Arts](#)
- [Culture](#)

This article was downloaded by **calibre** from <https://www.nature.com/articles/d41586-021-02063-y>.

Opinion

- [**Steven Weinberg \(1933–2021\)**](#) [06 August 2021]
Obituary • Theoretical physicist whose electroweak theory won the Nobel prize.
- [**Use HIV's lessons to help children orphaned by COVID-19**](#)
[09 August 2021]
Comment • Young people who have lost parents to the pandemic need urgent support and long-term study to avert the cascade of adversity that can follow. Decades of research into the HIV epidemic provide a solid foundation.
- [**Call to update US re-entry rules for international researchers**](#) [09 August 2021]
Correspondence •
- [**What costs half a year's pay for African scholars? Open access**](#) [10 August 2021]
Correspondence •
- [**After malaria: which parasitic disease will China eliminate next?**](#) [10 August 2021]
Correspondence •
- [**Iran: drought must top new government's agenda**](#) [10 August 2021]
Correspondence •

- OBITUARY
- 06 August 2021

Steven Weinberg (1933–2021)

Theoretical physicist whose electroweak theory won the Nobel prize.

- [Frank Wilczek](#) 9

1. [Frank Wilczek](#)

1. Frank Wilczek is Herman Feshbach Professor of Physics at the Massachusetts Institute of Technology and founding director of the Tsung-Dao Lee Institute in Shanghai, China. He has been an admiring friend of, and an occasional competitor with, Steven Weinberg throughout his adult life.

[View author publications](#)

You can also search for this author in [PubMed](#) [Google Scholar](#)





•

[Download PDF](#)



Credit: CERN/Science Photo Library

Steven Weinberg brought the fundamental understanding of nature to new levels of power and completeness. He played a central part in formulating and establishing theoretical physics' two standard models — the standard model of fundamental interactions and the standard model of cosmology. His greatest achievement was to propose the unified theory of electromagnetism and weak interactions, which is still in use. This won him the Nobel Prize in Physics in 1979, shared with his school classmate Sheldon Lee Glashow, and with Abdus Salam.

His 1967 *Physical Review Letters* paper, ‘[A Model of Leptons](#)’, combined disparate ideas about gauge symmetry, symmetry breaking and the classification of particles into an elegant whole. Given the state of knowledge at the time, the breakthrough still calls to mind Einstein’s description of Niels Bohr’s atomic model: “the highest form of musicality in the sphere of thought”.

Amazingly, given its scope and ambition, nothing in the paper needs essential revision today. But it was incomplete in two important ways. First, Weinberg conjectured, but could not prove, that his theory was ‘renormalizable’, in that incorporating quantum fluctuations would not lead to ill-defined mathematical expressions. That problem was solved for quantum electrodynamics — the theory of photons and their interactions — in the 1950s. It was even harder to crack in Weinberg’s unified theory, and its solution brought in new ideas.

Second, it really was just a theory of leptons — electrons, muons and their neutrinos. It left out the world of strongly interacting hadrons, including protons, neutrons and most of the vast zoo of particles observed in high-energy accelerators. Remarkably, however, quantum chromodynamics — the modern theory of strong interactions, based on quarks and gluons — combines harmoniously with Weinberg’s model. The same is true for general relativity, Einstein’s theory of gravity.



Ideal witness: a physicist takes on the world

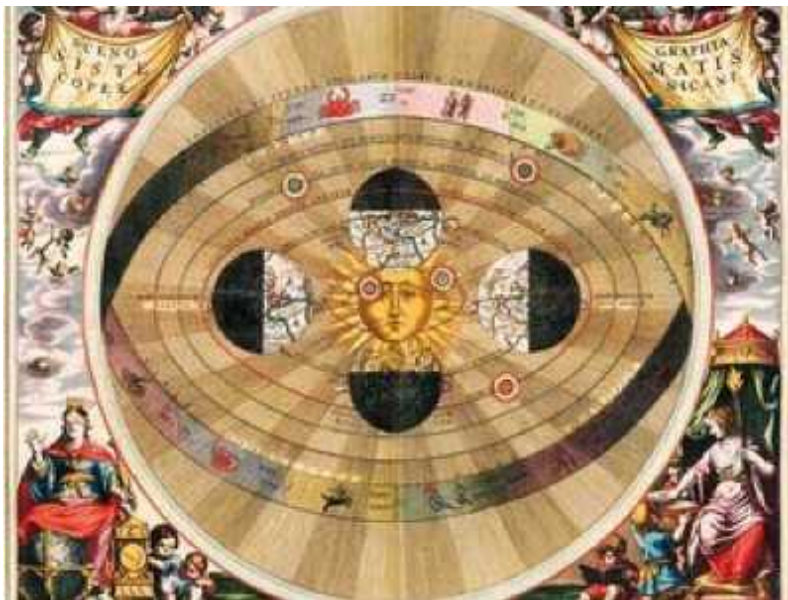
Weinberg had a leading role in orchestrating this powerful consolidation of fundamental physics, in particular by calculating its experimental consequences. The discovery, in the 1980s, of the W and Z bosons, which had precisely the masses and other properties predicted by his model, was its crowning success.

The other major strand in Weinberg's work was physical cosmology. When his landmark book *Gravitation and Cosmology* first appeared in 1972, high-energy particle physics and cosmology were regarded as distinct subjects, with different cultures and communities. After Weinberg knocked down the barriers, a new generation prospered in the border zone. A central message of the book was that the Big Bang should be considered as a unique, gigantic experiment in high-energy physics. He made his case by showing how hypotheses about neutrino properties could be tested through cosmological observations. His popular book on the topic, *The First Three Minutes* (1977), found a large audience.

Weinberg was born in New York City to Jewish immigrant parents. He credited his father with encouraging his interest in science. He graduated in 1950 from the Bronx High School of Science, the city's flagship for educating young scientists. Leon Cooper and Melvin Schwartz were near-contemporaries, as well as Glashow, to name just those who went on to get Nobel prizes in physics. It is hard to resist the implication that it is probably good science policy to welcome immigrants and bring bright children together.

After undergraduate studies at Cornell University in Ithaca, New York, Weinberg spent a year at Nordita (the Nordic Institute for Theoretical Physics) in Copenhagen, working on quantum field theory with Gunnar Källén, whom he often mentioned as a strong influence. He completed his PhD at Princeton University, New Jersey, with Sam Treiman advising on his thesis about how the strong interaction complicates the interpretation of weak-interaction observations. He went on to positions at Columbia University, New York; the University of Berkeley, California; the Massachusetts Institute of Technology in Cambridge; and, in 1973, to Harvard University in Cambridge, where he was Higgins Professor of

Physics. In 1982, he moved to the University of Texas at Austin, where he remained, teaching until earlier this year.



Unshadowed lens on the past

Scientists, no less than composers, have styles. Einstein and Richard Feynman were rebellious, most comfortable when they were ‘thinking different’. Weinberg was not like that. His approach was scholarly. Most obviously, he was keenly interested in the history of physics in the West, about which he wrote several deeply researched and unashamedly ‘Whiggish’ books, most recently *To Explain the World* (2015).

He paid close attention to other people’s work. I remember several rather terrifying phone calls during which he quizzed me about details of mathematical derivations in my or others’ papers.

He would not let go of obscurities that caught his attention. Several of his most important investigations were sparked when he perceived gaps or unexplored consequences. His work on electroweak interactions grew out of wrestling with the confused literature of its component ideas. If Einstein and Feynman call to mind Beethoven, Weinberg calls to mind Bach.

Later in his career, Weinberg extended the ideas he had pioneered in new directions. He made suggestions about unified field theory, the nature of

dark matter and the possibility of a multiverse. These ideas, attractive but as yet unproven, continue to inspire research.

Weinberg sometimes expressed strong views against religion, such as this: “Anything that we scientists can do to weaken the hold of religion should be done and may in the end be our greatest contribution to civilization.” His, more usual, jovial appreciation of the human comedy was exemplified by the way that, given the chance, he would sneak off from stiff parties to play games with the children.

Nature **596**, 183 (2021)

doi: <https://doi.org/10.1038/d41586-021-02170-w>

Competing Interests

The author declares no competing interests.

Related Articles

-  [Unshadowed lens on the past](#)
-  [Ideal witness: a physicist takes on the world](#)
-  [Abdus Salam \(1926–96\)](#)
-  [Four golden lessons](#)

Subjects

- [History](#)
- [Cosmology](#)
- [Physics](#)

nature careers

[Jobs](#) >

- [Technology and Knowledge Transfer Officer / Commercialization](#)

University of Luxembourg

Luxembourg, Luxembourg

- [Technology and Knowledge Transfer Officer / Social Sciences, Humanities](#)

University of Luxembourg

Luxembourg, Luxembourg

- [Postdoctoral Research Assistant \(m/f/div\) in modelling and data science](#)

Max Planck Institute for the Science of Human History

Jena, Germany

- [Postdoc researcher in de novo design of transmembrane beta-barrels for nanopore sensing applications](#)

Flanders Institute for Biotechnology (VIB)

Brussels, Belgium

Nature Briefing

An essential round-up of science news, opinion and analysis, delivered to your inbox every weekday.

[Download PDF](#)

Related Articles



- [Unshadowed lens on the past](#)



- [Ideal witness: a physicist takes on the world](#)



- [Abdus Salam \(1926–96\)](#)



- [Four golden lessons](#)

Subjects

- [History](#)
- [Cosmology](#)
- [Physics](#)

| [Section menu](#) | [Main menu](#) |

- COMMENT
- 09 August 2021

Use HIV's lessons to help children orphaned by COVID-19

Young people who have lost parents to the pandemic need urgent support and long-term study to avert the cascade of adversity that can follow. Decades of research into the HIV epidemic provide a solid foundation.

- [Rachel Kidman](#) 0

1. [Rachel Kidman](#)

1. Rachel Kidman is core faculty in the Program in Public Health and associate professor in the Department of Family, Population and Preventive Medicine at Stony Brook University, Stony Brook, New York, USA.

[View author publications](#)

You can also search for this author in [PubMed](#) [Google Scholar](#)





•

[Download PDF](#)



Three siblings from Pattapur in eastern India are among the thousands of children who have lost their parents to COVID-19 in the country. Credit: Rebecca Conway/NYT/Redux/eyevine

I have spent my career studying how the HIV epidemic affects children. One profound way is through the death of one or both parents — the United Nations definition of an orphan. As of 2020, about 15 million children and adolescents, mostly in sub-Saharan Africa, had lost one or both parents to HIV/AIDS. These youngsters face immense challenges. Through decades of research, the field is slowly learning how to help them lead healthy lives and succeed in school.

I never thought that my expertise on pandemics and mass child bereavement would be relevant to the United States. And then the COVID-19 pandemic hit. As I saw the daily death counts grow, I worried about the children being left behind. There were some anecdotal stories published, but no rigorous estimates that captured the true scale of this crisis for children. So, my colleagues and I set out to answer the question: how many young people are losing parents to the pandemic?

It was an ever-increasing target. With every draft of our paper, we had to revise the count. We ran the last model just before publication; our estimate

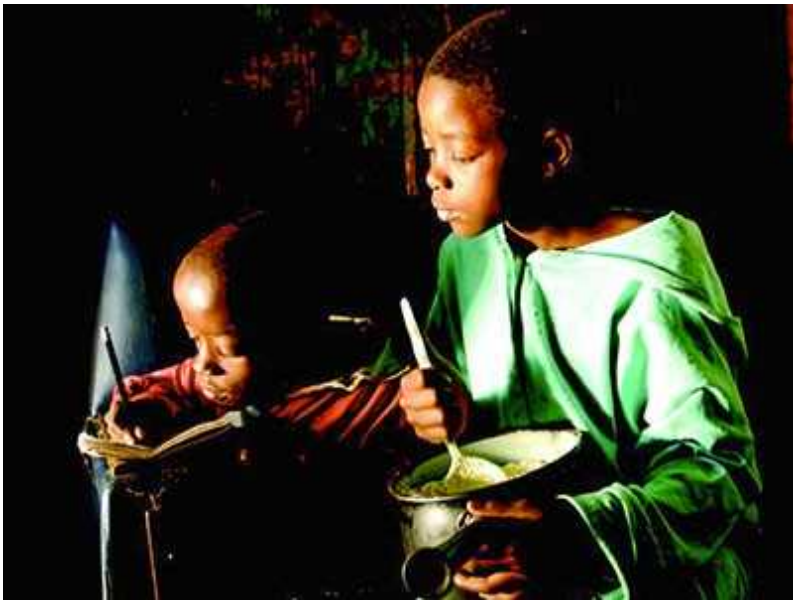
was that, between February 2020 and February 2021, about 40,000 children had been orphaned as a result of the pandemic, just in the United States¹. To put this another way: for every 13 or so US COVID-19 deaths, a child loses a parent.

A second research group, led by epidemiologist Susan Hillis at the US Centers for Disease Control and Prevention in Atlanta, Georgia, published its global orphanhood estimates last month². The team focused on 21 countries where the bulk of infections were reported in 2020–21. They estimate that, already, more than one million children globally have lost a parent to COVID-19.

These numbers vastly undercount the current orphan crisis: COVID-19 deaths in 2021 have already surpassed those in 2020 and are still growing. These children need urgent support and long-term study.

Childhood adversity

From my own work and that of many others globally, we know that children who lose a parent can experience a cascade of negative consequences³. In one study, for example, we found that children in sub-Saharan Africa who lost both parents were 50% more likely to experience sexual abuse than were non-orphaned children⁴. Many children develop depression, anxiety and post-traumatic stress disorder in the wake of a parent’s death⁵. If unaddressed, these disorders can persist for years, and might worsen as orphaned adolescents reach young adulthood⁶. Orphans are also more likely to drop out of school and to become stuck in a cycle of poverty⁷. One study found that their risk of suicide was twice that of peers who hadn’t experienced a parent’s death; the risk remained elevated for 25 years following such a death⁸.



Children of the AIDS pandemic

The death of a parent can be understood in the larger framework of adverse childhood experiences. There is a rich and compelling literature demonstrating the ways that distressing and traumatic events are embodied through chronic stress responses. These affect biological, behavioural and social processes throughout a person's life⁹.

It is a sad fact that millions of children have experienced adversity in the context of the COVID-19 pandemic, and will continue to do so. We are seeing a rise in child abuse, family violence and food insecurity, to give just a few examples¹⁰.

The death of a parent is distinct, however, both in its severity and because it often increases the frequency of other adversities. The cumulative burden matters: there is a clear link between the number of adverse childhood experiences and the likelihood of negative outcomes^{9,11}.

Support children

The good news is that most children are resilient. With the right combination of services and resources, orphaned children can be healthy, happy and do well in school. Researchers can critically appraise the evidence from both

high- and low-resource contexts, including those most affected by the HIV epidemic, and adapt these lessons to the relevant sociopolitical context.

The research on child bereavement support is sparse, but there are brief evidence-based interventions that could be adapted and scaled up³. In our study¹, we found that three-quarters of those orphaned by COVID-19 in the United States were adolescents, so working through school counsellors could be a feasible way to reach a large population with trauma-informed care.



An infant whose parents died of ebolavirus is cared for by an Ebola survivor in Beni, Democratic Republic of the Congo.Credit: Zohra Bensemra/Reuters/Alamy

Individualistic societies lean towards supporting children with counselling, and this might be necessary for many. But research from the HIV response shows that supporting the family is also crucial: carer and household factors

are key determinants of child outcomes¹². A promising strategy is to deliver ‘cash plus care’¹³. This approach aims to strengthen the family’s economic capacity and deliver complementary interventions to improve the quality of care, such as by enhancing parenting skills^{14,15}.

Globally, interventions that provide cash benefits have been shown to improve orphans’ health and psychological and educational outcomes¹⁶. In Tanzania, for example, orphans who were randomly selected to receive cash transfers demonstrated a 22 percentage point increase in primary-school completion; the programme similarly benefited other children living in poverty¹⁷. A Kenyan study showed that government cash transfers reduced anxiety and trauma symptoms among orphans¹⁸.

In the United States, new federal policies, such as the temporary expansion of the child tax credit, will raise some families out of dire poverty. Social security is selectively available to children who lose parents, and has been shown to improve their education and lifetime earnings¹⁹. However, less than half (45%) of all orphaned children take up this support¹⁹. We need initiatives that proactively identify eligible children and that help families to navigate the application process. Many others are left out because their parents earned too little, immigrated too recently or were homemakers. Hence the need for policies that ensure universal economic support for families in poverty.



Should children get COVID vaccines? What the science says

Studies of adversity show that a stable, supportive carer is often a key determinant of resilience in children^{20,21}. With a parent's death, a child loses one of the most important adults in their life. The surviving parent (or other carer) carries a huge burden: helping the child to cope with loss while navigating their own grief, legal matters and often a full-time job. Expanding access to bereavement leave would help. In the United States, bereavement is not yet covered by the Family and Medical Leave Act.

Another evidence-based initiative that could be made more widely available is positive parenting programmes. These have been shown to help carers form a strong, nurturing relationship with a child who has experienced adversity, including recent bereavement²¹. A new initiative, COVID-19 Playful Parenting, brings together evidence-based and open-access resources that are geared towards improving child–carer bonds, reducing stress and violence, and talking about COVID-19 (www.covid19parenting.com). None directly addresses bereavement, yet.

All of these recommendations are inclusive. Investing in school counsellors, families' financial stability and parenting programmes will benefit a large range of vulnerable children and families who are struggling through the COVID-19 pandemic — not just orphans.

Research gaps

Much has changed during the pandemic; we can't just draw on past research to inform our response. Early interventions are crucial to reducing trauma and promoting future health⁹. The scientific community must step up to help tailor current actions, and work to fill the following research gaps.

Collect data on how the pandemic changes orphans' needs. Children orphaned by AIDS had worse mental-health outcomes than did children orphaned by other causes, possibly because of the stigma and isolation of losing a parent to the disease⁶. Data should be collected to determine whether children orphaned by COVID-19 experience similarly disproportionate impacts.

One difference might be baseline stress: the pandemic has reduced social connectedness, closed schools and created economic insecurity. Another issue is re-traumatization. About 10% of children develop prolonged traumatic grief under normal circumstances^{[22](#)}. Today, everyone, everywhere is talking about COVID-19, providing constant reminders and triggers for grief.



A carer swims with a baby orphaned by HIV in Eswatini, which in 2019 had the highest prevalence of the virus in the world. Credit: Colin McPherson/Corbis/Getty

Identify services and resources that best reduce harmful effects. The rich global literature on childhood adversity and bereavement provides a sense of which types of support might help children who have lost a parent. In some nations, there has been action towards many programmes that could help, such as a temporary expansion of the child tax credit and renewed interest in

family leave. This is an opportunity to evaluate what is working for vulnerable children and families, and to push for science-based policy.

Observational studies, particularly those using causal analyses, can quickly evaluate existing programmes to identify those that work. Randomized controlled trials (RCTs) can rigorously test single, new initiatives. For instance, RCTs focused on orphans have shown the effectiveness of trauma-informed therapy in Zambia²³, economic empowerment in Uganda²⁴ and a family bereavement programme to enhance resilience in the United States²⁵.

Research disparities. Our research¹ found that Black children are more likely than white children in the United States to experience parental death: Black children make up 14% of the US population, but comprise 20% of children orphaned by COVID-19. This mirrors long-standing trends: before the pandemic, one study estimated that Black children were two to three times as likely as white children to lose a parent, contributing to disadvantage throughout life²⁶. Black children are also 59% less likely to receive survivor benefits through social security; those whose parents were born outside the United States are even less likely to benefit¹⁹. Generating this type of evidence is the first step in advocating for a more equitable response.



[COVID-19 vaccines: how to ensure Africa has access](#)

Create a longitudinal cohort. We need research infrastructure that can capture data on how orphaned children are doing now, and that can follow them into the future. A longitudinal cohort is a flexible tool for identifying emerging challenges (through epidemiological surveillance), quickly assessing the potential of interventions (through observational data and pilot studies) and testing programme options rigorously (through RCTs that differentiate effects by ethnicity, age, gender and disability status).

Longitudinal cohorts, such as the Orphan Resilience Study in South Africa⁶, [helped to ground the HIV response in science](#).

Rapidly fund new research. To fill the gaps described, the field requires a funding mechanism that is nimble enough to respond to new crises, and that values immediate, real-world benefits. Although there are some pockets of money for rapid study, many depend on being able to bend existing projects to new aims. Moreover, funding is largely targeted at scientific novelty and innovation — not necessarily on immediate value for society.

We have been at this crossroads before. In the 2014 Ebola outbreak in West Africa, an estimated 9,600 children under 15 were orphaned²⁷ while living in fear of a fast-spreading pathogen and under extreme social isolation because of lockdowns. Little systematic research was conducted on these children — a missed opportunity to learn and innovate. This time, to help children orphaned by COVID-19 and by the next emergent pandemic, we need to base our response on data collected during the crisis. And we need funding mechanisms that can match this pace.

Act now

Integrating research and programmes to assist children orphaned by COVID-19 would be a huge undertaking, but it is not without precedent. There is a fund to meet the mental-health and educational needs of the 3,000 US children who lost parents in the terrorist attacks of 11 September 2001, for example (see www.ttof.org). As part of the global HIV response, the US government created the President's Emergency Plan for AIDS Relief (PEPFAR). Ten percent of its US\$5.4-billion bilateral-aid budget is dedicated to programmes for orphans and vulnerable children globally (see go.nature.com/3f8jgrd).

PEPFAR was launched in 2003 amid a global AIDS emergency. Governments, scientists and communities knew they had to take swift action to support orphans, but there was no evidence base to guide efforts¹². In the two decades since, robust research has helped the field to evolve and deliver more-effective programming.

It's time to build on those lessons to support children who have been orphaned by COVID-19.

Nature **596**, 185–188 (2021)

doi: <https://doi.org/10.1038/d41586-021-02155-9>

References

1. 1.

Kidman, R., Margolis, R., Smith-Greenaway, E. & Verdery, A. M. *JAMA Pediatr.* **175**, 745–746 (2021).

[PubMed](#) [Article](#) [Google Scholar](#)

2. 2.

Hillis, S. D. *et al. Lancet* **398**, 391–402 (2021).

[PubMed](#) [Article](#) [Google Scholar](#)

3. 3.

Bergman, A.-S., Axberg, U. & Hanson, E. *BMC Palliat. Care* **16**, 39 (2017).

[PubMed](#) [Article](#) [Google Scholar](#)

4. 4.

Kidman, R. & Palermo, T. *Child Abuse Negl.* **51**, 172–180 (2016).

[PubMed](#) [Article](#) [Google Scholar](#)

5. 5.

Chi, P. & Li, X. *AIDS Behav.* **17**, 2554–2574 (2013).

[PubMed](#) [Article](#) [Google Scholar](#)

6. 6.

Cluver, L. D., Orkin, M., Gardner, F. & Boyes, M. E. *J. Child Psychol. Psychiatry* **53**, 363–370 (2012).

[PubMed](#) [Article](#) [Google Scholar](#)

7. 7.

Case, A., Paxson, C. & Ableidinger, J. *Demography* **41**, 483–508 (2004).

[PubMed](#) [Article](#) [Google Scholar](#)

8. 8.

Guldin, M.-B. *et al. JAMA Psychiatry* **72**, 1227–1234 (2015).

[PubMed](#) [Article](#) [Google Scholar](#)

9. 9.

Shonkoff, J. P., Boyce, W. T. & McEwen, B. S. *JAMA* **301**, 2252–2259 (2009).

[PubMed](#) [Article](#) [Google Scholar](#)

10. 10.

UNICEF. *Averting a Lost COVID Generation: A Six-Point Plan to Respond, Recover and Reimagine a Post-Pandemic World for Every Child* (UNICEF, 2020).

[Google Scholar](#)

11. 11.

Kidman, R., Piccolo, L. R. & Kohler, H.-P. *Am. J. Prev. Med.* **58**, 285–293 (2020).

[PubMed](#) [Article](#) [Google Scholar](#)

12. 12.

Nyberg, B. J. *et al.* *JAIDS J. Acquir. Immune Defic. Syndr.* **60**, S127–S135 (2012).

[PubMed](#) [Article](#) [Google Scholar](#)

13. 13.

Laumann, L. *Cash Plus Care 2.0: Leveraging USG OVC And Dreams Programs To Improve Use Of Cash Transfers For Children's Well-Being* (USAID, 2019).

[Google Scholar](#)

14. 14.

Roelen, K. *Policy in Focus* **15**, 20–21 (2018).

[Google Scholar](#)

15. 15.

Sherr, L., Macedo, A., Tomlinson, M., Skeen, S. & Cluver, L. D. *BMC Pediatr.* **17**, 123 (2017).

[PubMed](#) [Article](#) [Google Scholar](#)

16. 16.

Thomas, T., Tan, M., Ahmed, Y. & Grigorenko, E. L. *Ann. Behav. Med.* **54**, 853–866 (2020).

[PubMed](#) [Article](#) [Google Scholar](#)

17. 17.

Evans, D. K., Gale, C. & Kosec, K. *The Educational Impacts of Cash Transfers for Children with Multiple Indicators of Vulnerability* (Center for Global Development, 2021).

[Google Scholar](#)

18. 18.

Shangani, S. *et al.* *PLoS ONE* **12**, e0178076 (2017).

[PubMed](#) [Article](#) [Google Scholar](#)

19. 19.

Weaver, D. A. *Popul. Rev.* **58**, 23–60 (2019).

[Google Scholar](#)

20. 20.

Bethell, C., Jones, J., Gombojav, N., Linkenbach, J. & Sege, R. *JAMA Pediatr.* **173**, e193007 (2019).

[PubMed](#) [Article](#) [Google Scholar](#)

21. 21.

Sandler, I., Ingram, A., Wolchik, S., Tein, J.-Y. & Winslow, E. *Child Dev. Perspect.* **9**, 164–171 (2015).

[PubMed](#) [Article](#) [Google Scholar](#)

22. 22.

Melhem, N. M., Porta, G., Shamseddeen, W., Walker Payne, M. & Brent, D. A. *Arch. Gen. Psychiatry* **68**, 911–919 (2011).

[PubMed](#) [Article](#) [Google Scholar](#)

23. 23.

Ventevogel, P. & Spiegel, P. *JAMA* **314**, 511–512 (2015).

[PubMed](#) [Article](#) [Google Scholar](#)

24. 24.

Ssewamala, F. M., Han, C.-K. & Neilands, T. B. *Soc. Sci. Med.* **69**, 191–198 (2009).

[PubMed](#) [Article](#) [Google Scholar](#)

25. 25.

Sandler, I. N., Wolchik, S. A., Ayers, T. S., Tein, J.-Y. & Luecken, L. *Fam. Sci.* <https://doi.org/10.1080/19424620.2013.821763> (2013).

[Article](#) [Google Scholar](#)

26. 26.

Umberson, D. *et al. Proc. Natl Acad. Sci. USA* **114**, 915–920 (2017).

[PubMed](#) [Article](#) [Google Scholar](#)

27. 27.

Evans, D. K. & Popova, A. *Lancet* **385**, 945–946 (2015).

[PubMed](#) [Article](#) [Google Scholar](#)

[Download references](#)

Competing Interests

The author declares no competing interests.

Related Articles



- [Children of the AIDS pandemic](#)



- [Should children get COVID vaccines? What the science says](#)



- [Long COVID and kids: scientists race to find answers](#)



- [COVID-19 vaccines: how to ensure Africa has access](#)

Subjects

- [SARS-CoV-2](#)
- [Society](#)
- [Policy](#)

nature careers

[Jobs](#) >

- [**Technology and Knowledge Transfer Officer / Commercialization**](#)

University of Luxembourg

Luxembourg, Luxembourg

- [**Technology and Knowledge Transfer Officer / Social Sciences, Humanities**](#)

University of Luxembourg

Luxembourg, Luxembourg

- [**Postdoctoral Research Assistant \(m/f/div\) in modelling and data science**](#)

Max Planck Institute for the Science of Human History

Jena, Germany

- [**Postdoc researcher in de novo design of transmembrane beta-barrels for nanopore sensing applications**](#)

Flanders Institute for Biotechnology (VIB)

Brussels, Belgium

Nature Briefing

An essential round-up of science news, opinion and analysis, delivered to your inbox every weekday.

[Download PDF](#)

Related Articles



- [Children of the AIDS pandemic](#)



- [Should children get COVID vaccines? What the science says](#)



- [Long COVID and kids: scientists race to find answers](#)



- [COVID-19 vaccines: how to ensure Africa has access](#)

Subjects

- [SARS-CoV-2](#)
- [Society](#)
- [Policy](#)

This article was downloaded by **calibre** from <https://www.nature.com/articles/d41586-021-02155-9>

- CORRESPONDENCE
- 09 August 2021

Call to update US re-entry rules for international researchers

- [Alice Braga](#) ORCID: <http://orcid.org/0000-0003-3273-9742>⁰,
- [Valerio Francioni](#) ORCID: <http://orcid.org/0000-0002-2130-5204>¹,
- [Valeria Barra](#) ORCID: <http://orcid.org/0000-0003-1129-2056>²,
- [Carmen Falcone](#) ORCID: <http://orcid.org/0000-0001-9892-1171>³ &
- [Gabrielle String](#) ORCID: <http://orcid.org/0000-0002-0266-923X>⁴

1. [Alice Braga](#)

1. Tufts University, Boston, Massachusetts, USA.

[View author publications](#)

You can also search for this author in [PubMed](#) [Google Scholar](#)

2. Valerio Francioni

1. Massachusetts Institute of Technology, Cambridge, Massachusetts, USA.

[View author publications](#)

You can also search for this author in [PubMed](#) [Google Scholar](#)

3. Valeria Barra

1. California Institute of Technology, Pasadena, California, USA.

[View author publications](#)

You can also search for this author in [PubMed](#) [Google Scholar](#)

4. Carmen Falcone

1. Shriners Hospital for Children, Sacramento, California, USA.

[View author publications](#)

You can also search for this author in [PubMed](#) [Google Scholar](#)

5. Gabrielle String

1. Tufts University, Medford, Massachusetts, USA.

[View author publications](#)

You can also search for this author in [PubMed](#) [Google Scholar](#)





•

[Download PDF](#)

As organizers of an open letter (see go.nature.com/2viu3ei) to the US government, signed by more than 1,000 scientists, we are calling for an urgent update to the COVID-19 travel restrictions affecting international researchers holding US visas. These scientists cannot re-enter the United States from any of more than 30 countries, including most of Europe (see go.nature.com/3fwu2jp).

Since July, many areas affected by the US travel ban have had higher vaccination rates and lower infection rates than the United States. By

contrast, some high-risk countries, such as Mexico, Russia and Turkey, are on the US government's approved list. And despite the ban, the Delta SARS-CoV-2 variant now comprises 92% of new US COVID-19 cases.

The restrictions are discriminatory: re-entry is unconditional for US citizens and for most with student visas. US government policies have prevented most international scholars from visiting their home country for almost 18 months. Their mental health and careers, as well as the output of US research institutions, have been adversely affected.

As US-based researchers, we firmly believe that the inconsistencies behind these policies undermine the scientific community and efforts to protect public health. In our view, policies should instead be based on individual travel-risk assessments.

Nature **596**, 189 (2021)

doi: <https://doi.org/10.1038/d41586-021-02172-8>

Competing Interests

The authors declare no competing interests.

Related Articles

- [See more letters to the editor](#)

Subjects

- [Policy](#)
- [Public health](#)
- [SARS-CoV-2](#)
- [Government](#)

Jobs >

- **Technology and Knowledge Transfer Officer / Commercialization**

University of Luxembourg

Luxembourg, Luxembourg

- **Technology and Knowledge Transfer Officer / Social Sciences, Humanities**

University of Luxembourg

Luxembourg, Luxembourg

- **Postdoctoral Research Assistant (m/f/div) in modelling and data science**

Max Planck Institute for the Science of Human History

Jena, Germany

- **Postdoc researcher in de novo design of transmembrane beta-barrels for nanopore sensing applications**

Flanders Institute for Biotechnology (VIB)

Brussels, Belgium

Nature Briefing

An essential round-up of science news, opinion and analysis, delivered to your inbox every weekday.

[Download PDF](#)

Related Articles

- [See more letters to the editor](#)

Subjects

- [Policy](#)
- [Public health](#)
- [SARS-CoV-2](#)
- [Government](#)

This article was downloaded by **calibre** from <https://www.nature.com/articles/d41586-021-02172-8>

| [Section menu](#) | [Main menu](#) |

- CORRESPONDENCE
- 10 August 2021

What costs half a year's pay for African scholars? Open access

- [Addisu Mekonnen](#) ORCID: <http://orcid.org/0000-0001-8403-1071>⁰,
- [Colleen Downs](#) ORCID: <http://orcid.org/0000-0001-8334-1510>¹,
- [Edu O. Effiom](#)²,
- [Onja Razafindratsima](#) ORCID: <http://orcid.org/0000-0003-1655-6647>³,
- [Nils Chr. Stenseth](#) ORCID: <http://orcid.org/0000-0002-1591-5399>⁴ &
- [Colin A. Chapman](#) ORCID: <http://orcid.org/0000-0002-8827-8140>⁵

1. [Addisu Mekonnen](#)

1. Bahir Dar University, Bahir Dar, Ethiopia.

[View author publications](#)

You can also search for this author in [PubMed](#) [Google Scholar](#)

2. Colleen Downs

1. University of KwaZulu-Natal, Pietermaritzburg, South Africa.

[View author publications](#)

You can also search for this author in [PubMed](#) [Google Scholar](#)

3. Edu O. Effiom

1. Cross River State Forestry Commission, Calabar, Nigeria.

[View author publications](#)

You can also search for this author in [PubMed](#) [Google Scholar](#)

4. Onja Razafindratsima

1. University of California, Berkeley, Berkeley, USA.

[View author publications](#)

You can also search for this author in [PubMed](#) [Google Scholar](#)

5. Nils Chr. Stenseth

1. University of Oslo, Oslo, Norway.

[View author publications](#)

You can also search for this author in [PubMed](#) [Google Scholar](#)

6. Colin A. Chapman

1. Wilson Center, Washington DC, USA.

[View author publications](#)

You can also search for this author in [PubMed](#) [Google Scholar](#)





•

[Download PDF](#)

Open access to the scholarly literature is crucial for African academics but, without urgent action, the move from paywall to pay-to-publish wall will continue to disenfranchise researchers.

In an unpublished study, we looked at the 40 journals with the highest impact factors in our field (ecology), and found that the average article-processing charge was US\$3,150. Three-quarters of these journals do not offer waivers for scientists from low-income nations. The waiver process is complicated and opaque, and often seems to be based on special pleading.

African governments and universities rarely, if ever, fund article-processing fees. Most African scientists cannot afford to pay these fees themselves. Average monthly salaries are, for example, \$531 in Madagascar and \$365 in Ethiopia. In Uganda, the cost of publishing two articles could cover a year's tuition and field expenses for a master's student. In Nigeria, the fees for one paper could cover the costs of three master's students.

We applaud the efforts of funders and publishers who are promoting the accessibility of research and creating a more equitable process. To grapple with the challenges Africa faces, building research capacity depends on scientists being able to publish in — as well as read — journals.

Nature **596**, 189 (2021)

doi: <https://doi.org/10.1038/d41586-021-02173-7>

Competing Interests

The authors declare no competing interests.

Related Articles

- [See more letters to the editor](#)

Subjects

- [Publishing](#)
- [Research management](#)
- [Policy](#)

nature careers

[Jobs](#) >

- [Technology and Knowledge Transfer Officer / Commercialization](#)

University of Luxembourg

Luxembourg, Luxembourg

- [**Technology and Knowledge Transfer Officer / Social Sciences, Humanities**](#)

University of Luxembourg

Luxembourg, Luxembourg

- [**Postdoctoral Research Assistant \(m/f/div\) in modelling and data science**](#)

Max Planck Institute for the Science of Human History

Jena, Germany

- [**Postdoc researcher in de novo design of transmembrane beta-barrels for nanopore sensing applications**](#)

Flanders Institute for Biotechnology (VIB)

Brussels, Belgium

Nature Briefing

An essential round-up of science news, opinion and analysis, delivered to your inbox every weekday.

[Download PDF](#)

Related Articles

- [**See more letters to the editor**](#)

Subjects

- [Publishing](#)
 - [Research management](#)
 - [Policy](#)
-

This article was downloaded by **calibre** from <https://www.nature.com/articles/d41586-021-02173-7>

| [Section menu](#) | [Main menu](#) |

- CORRESPONDENCE
- 10 August 2021

After malaria: which parasitic disease will China eliminate next?

- [Men-Bao Qian](#)⁰,
- [Shi-Zhu Li](#)¹ &
- [Xiao-Nong Zhou](#)²

1. Men-Bao Qian

1. National Institute of Parasitic Diseases, Chinese Center for Disease Control and Prevention, Shanghai, China.

[View author publications](#)

You can also search for this author in [PubMed](#) [Google Scholar](#)

2. Shi-Zhu Li

1. Chinese Center for Tropical Diseases Research, Shanghai, China.

[View author publications](#)

You can also search for this author in [PubMed](#) [Google Scholar](#)

3. [Xiao-Nong Zhou](#)

1. Shanghai Jiao Tong University, Shanghai, China.

[View author publications](#)

You can also search for this author in [PubMed](#) [Google Scholar](#)





•

[Download PDF](#)

China was certified as malaria-free by the World Health Organization (WHO) in June. This triumph was part of a 70-year drive by the Chinese government to eliminate the country's parasitic diseases — including schistosomiasis, leishmaniasis, lymphatic filariasis and hookworm. Which are left?

Lymphatic filariasis was the first success, announced by the WHO in 2007 ([Y. Fang and Y. Zhang *Infect. Dis. Poverty* 8, 66; 2019](#)). Continuing control efforts have meant that only around 200 leishmaniasis cases have been

reported annually since 2017 ([M. B. Qian et al. *Infect. Dis. Poverty* **8**, 86; 2019](#)). By 2018, hookworm infections — due primarily to poor sanitation — affected less than 1% of the population ([H. Zhu et al. *China CDC Wkly* **2**, 34–38; 2020](#)).

Schistosomiasis, down from 11.6 million in a population of 0.55 billion in the 1950s, is targeted for elimination within the next decade.

Nature **596**, 189 (2021)

doi: <https://doi.org/10.1038/d41586-021-02188-0>

Competing Interests

The authors declare no competing interests.

Related Articles

- [See more letters to the editor](#)

Subjects

- [Diseases](#)
- [Public health](#)

nature careers

[Jobs](#) >

- [Technology and Knowledge Transfer Officer / Commercialization](#)

University of Luxembourg

Luxembourg, Luxembourg

- [Technology and Knowledge Transfer Officer / Social Sciences, Humanities](#)

University of Luxembourg

Luxembourg, Luxembourg

- [Postdoctoral Research Assistant \(m/f/div\) in modelling and data science](#)

Max Planck Institute for the Science of Human History

Jena, Germany

- [Postdoc researcher in de novo design of transmembrane beta-barrels for nanopore sensing applications](#)

Flanders Institute for Biotechnology (VIB)

Brussels, Belgium

Nature Briefing

An essential round-up of science news, opinion and analysis, delivered to your inbox every weekday.

[Download PDF](#)

Related Articles

- [See more letters to the editor](#)

Subjects

- [Diseases](#)

- Public health

This article was downloaded by **calibre** from <https://www.nature.com/articles/d41586-021-02188-0>

| [Section menu](#) | [Main menu](#) |

- CORRESPONDENCE
- 10 August 2021

Iran: drought must top new government's agenda

- [Jamshid Parchizadeh](#) ⁰ &
- [Jerrold L. Belant](#) ¹

1. [Jamshid Parchizadeh](#)

1. Global Wildlife Conservation Center, State University of New York College of Environmental Science and Forestry, Syracuse, New York, USA.

[View author publications](#)

You can also search for this author in [PubMed](#) [Google Scholar](#)

2. Jerrold L. Belant

1. Global Wildlife Conservation Center, State University of New York College of Environmental Science and Forestry, Syracuse, New York, USA.

[View author publications](#)

You can also search for this author in [PubMed](#) [Google Scholar](#)





•

[Download PDF](#)

We urge Iran's incoming government to give priority to resolving the country's worst drought in 50 years (see go.nature.com/2wkwyqn). In our view, the government needs to consult with international as well as domestic water experts to prevent the imposition of flawed agendas. It should also revise earlier policies that have contributed to the crisis.

Outgoing president Hassan Rouhani blamed the drought on a 52% reduction in rainfall since last year. However, unregulated aquifer depletion

and mismanagement of water resources by the authorities (see, for example, go.nature.com/3cce7or) have contributed.

The drought and its associated dust haze is also severely affecting ecosystems in and around Iran (see go.nature.com/3jhauvc and <http://pana.ir/news/1178597>).

Nature **596**, 189 (2021)

doi: <https://doi.org/10.1038/d41586-021-02189-z>

Competing Interests

The authors declare no competing interests.

Related Articles

- [See more letters to the editor](#)

Subjects

- [Water resources](#)
- [Climate sciences](#)
- [Ecology](#)
- [Politics](#)

nature careers

[Jobs](#) >

- [Technology and Knowledge Transfer Officer / Commercialization](#)

University of Luxembourg

Luxembourg, Luxembourg

- [Technology and Knowledge Transfer Officer / Social Sciences, Humanities](#)

University of Luxembourg

Luxembourg, Luxembourg

- [Postdoctoral Research Assistant \(m/f/div\) in modelling and data science](#)

Max Planck Institute for the Science of Human History

Jena, Germany

- [Postdoc researcher in de novo design of transmembrane beta-barrels for nanopore sensing applications](#)

Flanders Institute for Biotechnology (VIB)

Brussels, Belgium

Nature Briefing

An essential round-up of science news, opinion and analysis, delivered to your inbox every weekday.

[Download PDF](#)

Related Articles

- [See more letters to the editor](#)

Subjects

- [Water resources](#)

- [Climate sciences](#)
 - [Ecology](#)
 - [Politics](#)
-

This article was downloaded by **calibre** from <https://www.nature.com/articles/d41586-021-02189-z>

| [Section menu](#) | [Main menu](#) |

Work

- **UK academics seethe over universities' cost-cutting moves**

[09 August 2021]

Career News • A survey of faculty and staff members uncovers anger and fear over job cuts and other measures following the pandemic.

- **Power plants: making electricity from flowers and fruits**

[09 August 2021]

Where I Work • Chemist María Fernanda Cerdá uses natural dyes from Uruguay's indigenous flora to build solar cells.

- CAREER NEWS
- 09 August 2021

UK academics seethe over universities' cost-cutting moves

A survey of faculty and staff members uncovers anger and fear over job cuts and other measures following the pandemic.

- [Natasha Gilbert](#) 0

1. Natasha Gilbert

1. Natasha Gilbert is a freelance writer in Washington DC.

[View author publications](#)

You can also search for this author in [PubMed](#) [Google Scholar](#)





•

[Download PDF](#)



Empty gestures: UK academics say universities could do more to protect posts during the pandemic. Credit: Getty

Faculty members, postdoctoral researchers and PhD students at UK universities are enraged by moves to cut jobs, and are accusing institutions of adopting ‘autocratic’ decision-making practices under cover of the COVID-19 pandemic, finds a survey of academics around the nation.

The survey, which had 1,099 respondents, was conducted between June and August 2020 by higher-education researcher Richard Watermeyer, at the University of Bristol, and his colleagues. Half the respondents held the rank of lecturer or above, 14% were PhD students and another 14% were postdocs. Two-thirds of respondents were from ‘research-intensive’ universities; two-thirds identified as female and 61% were on permanent or open-ended contracts. The survey results were published last month ([R. Watermeyer et al. Br. J. Sociol. Educ. <https://doi.org/gk7hrb>; 2021](#)).



Nature special: Young scientists

Respondents describe widespread concern over what they say is a small number of university administrators making decisions on employment and the future direction of institutions, often without consulting faculty or staff members. They also complain of major increases in teaching workloads without extra compensation or recognition. Many of these changes especially affect junior researchers, including postdocs, the survey finds. “There seems to be a real sense among the academic community in the UK that universities are using the pandemic as an opportunity to push through certain cost-cutting agendas,” says Watermeyer, adding that junior researchers felt exploited.

In open-ended responses to the survey, one PhD student wrote, “money will be prioritised before people be they staff or students”, adding that universities “will work the academics who survive the jobs cuts into the ground to achieve financial gain”.

But UK universities say that the pandemic has forced them to tighten their belts. Raj Jethwa, chief executive of the Universities and Colleges Employers Association, based in London, says its 172 member institutions are acting honourably as they struggle to deal with great financial pressure. “While the pandemic has put severe strain on the finances of institutions, their fundamental mission has not changed,” he says. “Higher-education

institutions have worked hard to minimize the impact of the pandemic upon jobs, workload and health and well-being.”

‘Gold Command’

Seventy per cent of respondents say that pandemic-related cuts have created job insecurity and a culture of fear among staff, with university leaders becoming more autocratic as a result. Some respondents say that they fear shifts towards “undemocratic governance” will undermine academic independence. “My university’s executives leapt on the opportunity to call themselves ‘Gold Command’ and state that consultation on anything would no longer be possible,” an associate professor wrote.



[Researchers' career insecurity needs attention and reform now, says international coalition](#)

David Harvie, a researcher in finance and political economy at the University of Leicester, is among faculty and staff members there who have been made redundant since the start of the pandemic; his last day in post was 11 August. Of these, around two-thirds held teaching and research positions, says Harvie, who manages communications for the Leicester branch of University and College Union (UCU). The union represents 120,000 employees at universities and other institutions across the United Kingdom.

Harvie says that he was forced to take redundancy and that, in his opinion, the university's efforts to consult with faculty and staff members over its workforce-restructuring plans were a "sham". In June, the UCU highlighted 200 job losses at the university over a 15-month period, with a further 26 posts still at risk. Harvie also alleges that the university tried to silence critical voices, including scholars who have spoken out against it.

Nishan Canagarajah, the university's president and vice-chancellor, told *Nature* that the changes taking place there are "not a knee-jerk reaction" to the pandemic. Rather, he says, the moves are part of the university's long-term plans. "Our strategic plan will focus investment in areas aligned to our research strengths including support for staff from early-career PhDs right through to professors," he says.

Academics' concerns about UK university leadership were simmering even before the pandemic. One survey carried out in 2017 and published in January 2020 ([M. Erickson et al. Stud. High. Educ. https://doi.org/ggk7j6; 2020](https://doi.org/ggk7j6)) found that almost nine out of ten academic faculty and staff members gave a thumbs-down to their institution's senior-management team. The 5,888 respondents cited a lack of accountability, poor leadership and an over-reliance on performance metrics, among other issues.

Duty of care

Watermeyer's survey exposes widespread feelings of distrust and distress at what respondents call universities' lack of care for academics' health and well-being. "The crisis has highlighted how much staff well-being is readily sacrificed and ignored," wrote an assistant professor in a response. Another respondent described their role as a "dumping ground for student problems", adding: "I am tired, fed up and fearful. I have been having suicidal thoughts. This is all I know — I feel helpless."



Richard Watermeyer.Credit: Richard Watermeyer

Patricia Murray, a cell biologist at the University of Liverpool, says that faculty and staff members there were blindsided in January, when the university announced 47 proposed compulsory redundancies in health and life sciences. She says that university management doesn't appreciate the effect of job cuts on people's health. "Every week we are sent a meaningless

well-being letter, but there has been no mention of the serious adverse impact on the health of those targeted for redundancy.”

The university’s actions have caused a huge amount of stress for early-career researchers, with management abandoning their duty of care to staff, says Murray. The compulsory redundancies have caused PhD students and postdocs at Liverpool to rethink their hopes for a UK academic career, she adds.

A University of Liverpool spokesperson says that the downsizing plan had been in the works for a year and a half. “The university does not make proposals of redundancies lightly and the project to restructure the faculty of health and life sciences has been carefully considered over 18 months,” the spokesperson says. “This project was being worked on pre-COVID-19.”

Watermeyer thinks that the job-insecurity practices that UK academics are now struggling with can be traced to a shift among universities, starting in the late 1990s, to behave more like businesses concerned with their bottom line than as institutions serving the public good.

Global problems

The developments at UK universities are not unique. The pandemic has also tightened budgets at US universities, and postdocs and other early-career researchers are among those hit hardest, says Thomas Kimbis, head of the US National Postdoctoral Association, based in Rockville, Maryland. “Postdocs remain a vulnerable class of workers,” he says.

Peter Hurley, a higher-education policy researcher at Victoria University in Melbourne, Australia, says that the country’s universities are struggling to keep afloat after losing tuition fees and other revenue from international students. He says that there is a lot of uncertainty in Australia’s academic job market, with an estimated 17,000 positions already lost. “I don’t think it is a good time for early-career researchers and those looking to become postdocs in Australia,” he says.

Watermeyer says that to stay afloat, universities worldwide must change their business model to become less reliant on student tuition revenue.

Governments will need to invest more in universities, he adds. Otherwise, he says, “the situation found in the pandemic may only worsen”.

Nature **596**, 307-308 (2021)

doi: <https://doi.org/10.1038/d41586-021-02163-9>

Related Articles

-  [Researchers' career insecurity needs attention and reform now, says international coalition](#)
-  [Uncertain prospects for postdoctoral researchers](#)
-  [Job losses and falling salaries batter US academia](#)
-  [Nature special: Young scientists](#)

Subjects

- [Careers](#)
- [Institutions](#)
- [Policy](#)

- [Technology and Knowledge Transfer Officer / Commercialization](#)

University of Luxembourg

Luxembourg, Luxembourg

- [Technology and Knowledge Transfer Officer / Social Sciences, Humanities](#)

University of Luxembourg

Luxembourg, Luxembourg

- [Postdoctoral Research Assistant \(m/f/div\) in modelling and data science](#)

Max Planck Institute for the Science of Human History

Jena, Germany

- [Postdoc researcher in de novo design of transmembrane beta-barrels for nanopore sensing applications](#)

Flanders Institute for Biotechnology (VIB)

Brussels, Belgium

Nature Briefing

An essential round-up of science news, opinion and analysis, delivered to your inbox every weekday.

[Download PDF](#)

Related Articles

-  [Researchers' career insecurity needs attention and reform now, says international coalition](#)
-  [Uncertain prospects for postdoctoral researchers](#)
-  [Job losses and falling salaries batter US academia](#)
-  [Nature special: Young scientists](#)

Subjects

- [Careers](#)
- [Institutions](#)
- [Policy](#)

This article was downloaded by **calibre** from <https://www.nature.com/articles/d41586-021-02163-9>

- WHERE I WORK
- 09 August 2021

Power plants: making electricity from flowers and fruits

Chemist María Fernanda Cerdá uses natural dyes from Uruguay's indigenous flora to build solar cells.

- [Linda Nordling](#) ⁰
 1. Linda Nordling
 1. Linda Nordling is a freelance writer in Cape Town, South Africa.

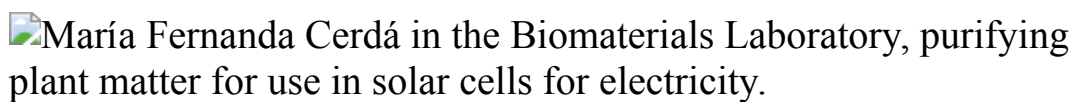
[View author publications](#)

You can also search for this author in [PubMed](#) [Google Scholar](#)





•



María Fernanda Cerdá is a chemist at the University of the Republic in Montevideo. Credit: Pablo Albarenga for *Nature*

[Download PDF](#)

I build solar cells using natural dyes that I find in fruit and flowers. Plant pigments called anthocyanins absorb light and turn it into energy to fuel photosynthesis, and I harness that power to generate electricity. The technology to convert plant dyes into electricity was developed in

Switzerland, but I'm applying it to plants that are indigenous to my home country, Uruguay, including its national flower, the ceibo (*Erythrina cristagalli*).

In this picture, I'm purifying a ceibo extract. Once I remove the bright-red dyes, I measure their efficiency in converting sunlight to energy. For that, I use a solar simulator, which mimics the Sun's rays. Here, the simulator is the grey box with a little black box on the side. The wooden stand, which my husband made by hand, enables me to raise the instrument to control the amount of radiation reaching my sample.

I've worked at the University of the Republic in Montevideo for 30 years, first on synthesizing radioactive materials for use in medicine, then as an electrochemist. Some say that natural dyes aren't stable enough to use in solar cells, but I built a prototype panel in 2019 that I tested for two years at Uruguay's Artigas Base in Antarctica. It never stopped working, not even in winter when there is very little light.

Photovoltaic devices produce less than 1% of the energy of my country. But I hope that my work will prepare us for the future.

My country is very small and has very few scientists, and nobody else does what I do. My field, photoelectric engineering, is populated mainly by men. I'm a woman and a chemist. As a result, I've felt stuck in my career. But my three daughters are growing up differently: they are going to reach further.

Funding is scarce, and without it I cannot pay salaries. That's why I still work in the laboratory at the age of 54. But I don't complain: I love lab work. That's my corner, in the picture, and everyone in my group knows that and respects it.

Nature **596**, 310 (2021)

doi: <https://doi.org/10.1038/d41586-021-02171-9>

Related Articles



- [Too intelligent for the life sciences in Brazil: how two female researchers fought back](#)



- [Better together: collaborative spaces can inspire scientists of all ages](#)



- [Technology transfer: Career-boosting computing skills for girls in Argentina](#)

Subjects

- [Careers](#)
- [Chemistry](#)
- [Energy](#)

nature careers

[Jobs](#) >

- [Technology and Knowledge Transfer Officer / Commercialization](#)

University of Luxembourg

Luxembourg, Luxembourg

- [Technology and Knowledge Transfer Officer / Social Sciences, Humanities](#)

University of Luxembourg

Luxembourg, Luxembourg

- [Postdoctoral Research Assistant \(m/f/div\) in modelling and data science](#)

Max Planck Institute for the Science of Human History

Jena, Germany

- [Postdoc researcher in de novo design of transmembrane beta-barrels for nanopore sensing applications](#)

Flanders Institute for Biotechnology (VIB)

Brussels, Belgium

Nature Briefing

An essential round-up of science news, opinion and analysis, delivered to your inbox every weekday.

[Download PDF](#)

Related Articles



- [Too intelligent for the life sciences in Brazil: how two female researchers fought back](#)



- [Better together: collaborative spaces can inspire scientists of all ages](#)



- [Technology transfer: Career-boosting computing skills for girls in Argentina](#)

Subjects

- [Careers](#)
- [Chemistry](#)
- [Energy](#)

This article was downloaded by **calibre** from <https://www.nature.com/articles/d41586-021-02171-9>

| [Section menu](#) | [Main menu](#) |

Research

- **[Protein pile-up plays havoc in ageing nematode worms](#)** [28 July 2021]

News & Views • An analysis in ageing nematode worms reveals reductions in the tagging of certain proteins for clearance. This can lead to the accumulation of unnecessary proteins, in turn impairing cellular and tissue function.

- **[How the amino acid leucine activates the key cell-growth regulator mTOR](#)** [21 July 2021]

News & Views • Cells can tailor their growth to current conditions by sensing nutrients. The protein complex mTORC1 enables cell growth to be coordinated with the level of certain amino acids, and how it senses the amino acid leucine has now become clearer.

- **[A microscopy technique that images single reaction events in total darkness](#)** [11 August 2021]

News & Views • Single photons emitted from individual electrochemically excited molecules in solution can now be detected. The technique can be used to image cells at nanometre resolution, without using an external light source.

- **[Chain-mail fabric stiffens under confining pressure](#)** [11 August 2021]

News & Views • The mechanical properties of chain mail have been revisited. The findings reveal that, under confining pressure, chain-mail-inspired materials can switch from pliable to stiff structures that have outstanding load-bearing capacities.

- **[Deep continental roots and cratons](#)** [11 August 2021]

Review Article • Cratons are the oldest parts of the Earth's continents; this Review concludes that the production of widespread, thick and strong lithosphere via the process of orogenic thickening was fundamental to the eventual emergence of extensive continental landmasses.

- **[Exploring tissue architecture using spatial transcriptomics](#)** [11 August 2021]

Review Article • This review describes the state of spatial transcriptomics technologies and analysis tools that are being used to generate biological insights in diverse areas of biology.

- **[Demonstration of reduced neoclassical energy transport in Wendelstein 7-X](#)** [11 August 2021]

Article • Previously documented record values of the fusion triple product in the stellarator Wendelstein 7-X are shown to be evidence for reduced neoclassical energy transport in this optimized device.

- **Evidence for an atomic chiral superfluid with topological excitations** [11 August 2021]
Article • A globally chiral atomic superfluid is induced by time-reversal symmetry breaking in an optical lattice and exhibits global angular momentum, which is expected to lead to topological excitations and the demonstration of a topological superfluid.
- **Actively variable-spectrum optoelectronics with black phosphorus** [11 August 2021]
Article • High-performance optoelectronic devices that operate in the infrared regime at room temperature exhibit wide-range, active and reversible tunability of the operating wavelengths with black phosphorus.
- **Structured fabrics with tunable mechanical properties** [11 August 2021]
Article • A structured fabric constructed of linked hollow polyhedral particles (resembling chain mail) can be simply and reversibly tuned between flexible and rigid states; when it is compressed, its linked particles become jammed.
- **Direct imaging of single-molecule electrochemical reactions in solution** [11 August 2021]
Article • Optical imaging of single-molecule electrochemical reactions in aqueous solution enables super-resolution electrochemiluminescence microscopy, which can be used to monitor the adhesion dynamics of live cells with high spatiotemporal resolution.
- **Photoinduced copper-catalysed asymmetric amidation via ligand cooperativity** [28 June 2021]
Article • In the presence of three ligands and light, two distinct copper catalysts combine to produce enantioenriched secondary amides from racemic alkyl electrophiles and primary amide nucleophiles.
- **Connectomes across development reveal principles of brain maturation** [04 August 2021]
Article • Serial-section electron microscopy is used to reconstruct the full brain connectome of eight individual *Caenorhabditis elegans* at various stages of development, providing insight into the principles underlying brain maturation.
- **Microbes exploit death-induced nutrient release by gut epithelial cells** [04 August 2021]
Article • Intestinal microorganisms exploit nutrients released by apoptotic gut epithelial cells for growth.
- **Immunogenicity of Ad26.COV2.S vaccine against SARS-CoV-2 variants in humans** [09 June 2021]

Article • Analysis of the immunogenicity of the Ad26.COV2.S vaccine against the B1.351 and P.1 SARS-CoV-2 variants of concern shows reduced neutralization antibody titres, but comparable T cell responses and antibody-dependent effector functions.

- **BNT162b2-elicited neutralization of B.1.617 and other SARS-CoV-2 variants** [10 June 2021]

Article • Samples of serum from individuals immunized with the BNT162b2 vaccine show neutralization activity against engineered SARS-CoV-2s bearing the spike mutations from B.1.617 and other variants.

- **Reduced sensitivity of SARS-CoV-2 variant Delta to antibody neutralization** [08 July 2021]

Article • The SARS-CoV-2 Delta variant partially evades neutralization by several monoclonal antibodies and by sera from individuals who have had COVID-19, but two doses of anti-COVID-19 vaccines still generate a strong neutralizing response.

- **SAR1B senses leucine levels to regulate mTORC1 signalling** [21 July 2021]

Article • SAR1B, which is conserved between mammals and nematodes, is a leucine sensor that is involved in regulating mTORC1 signalling and potentially has a role in the development of lung cancer.

- **Rewiring of the ubiquitinated proteome determines ageing in *C. elegans*** [28 July 2021]

Article • Global loss of targeted protein degradation with age results in harmful accumulation of specific proteins in worms.

- **Regulated control of gene therapies by drug-induced splicing** [28 July 2021]

Article • A switch system is developed to control the expression of therapeutic genes, involving the administration of a small-molecule drug to induce splicing-mediated control of mRNA translation.

- **Structural insights into how Prp5 proofreads the pre-mRNA branch site** [04 August 2021]

Article • The cryo-electron microscopy structure of a newly identified, early spliceosomal complex reveals the mechanism by which the RNA helicase Prp5 enhances the fidelity of the excision of introns from precursor mRNAs.

- **Structural basis of ketamine action on human NMDA receptors** [28 July 2021]

Article • Structures of ketamine bound to human NMDA receptors show how ketamine inhibits receptor activity.

- **Phantom epistasis between unlinked loci** [11 August 2021]

Matters Arising •

| [Next section](#) | [Main menu](#) | [Previous section](#) |

- NEWS AND VIEWS
- 28 July 2021

Protein pile-up plays havoc in ageing nematode worms

An analysis in ageing nematode worms reveals reductions in the tagging of certain proteins for clearance. This can lead to the accumulation of unnecessary proteins, in turn impairing cellular and tissue function.

- [Bart P. Braeckman](#) 0

1. [Bart P. Braeckman](#)

1. Bart P. Braeckman is in the Department of Biology, Ghent University, Ghent B-9000, Belgium.

[View author publications](#)

You can also search for this author in [PubMed](#) [Google Scholar](#)





•

[Download PDF](#)

Unwanted, damaged or misfolded proteins inside cells are tagged with a chain of ubiquitin molecules. This tagging serves as a signal for destruction by the 26S proteasome, a complex of enzymes that breaks proteins down for clearance¹ (Fig. 1a). [Writing in Nature](#), Koyuncu *et al.*² show that, in the ageing nematode worm *Caenorhabditis elegans*, some proteins escape the clean-up by the ubiquitin–proteosomal system, and that reducing the accumulation of such proteins can extend lifespan.

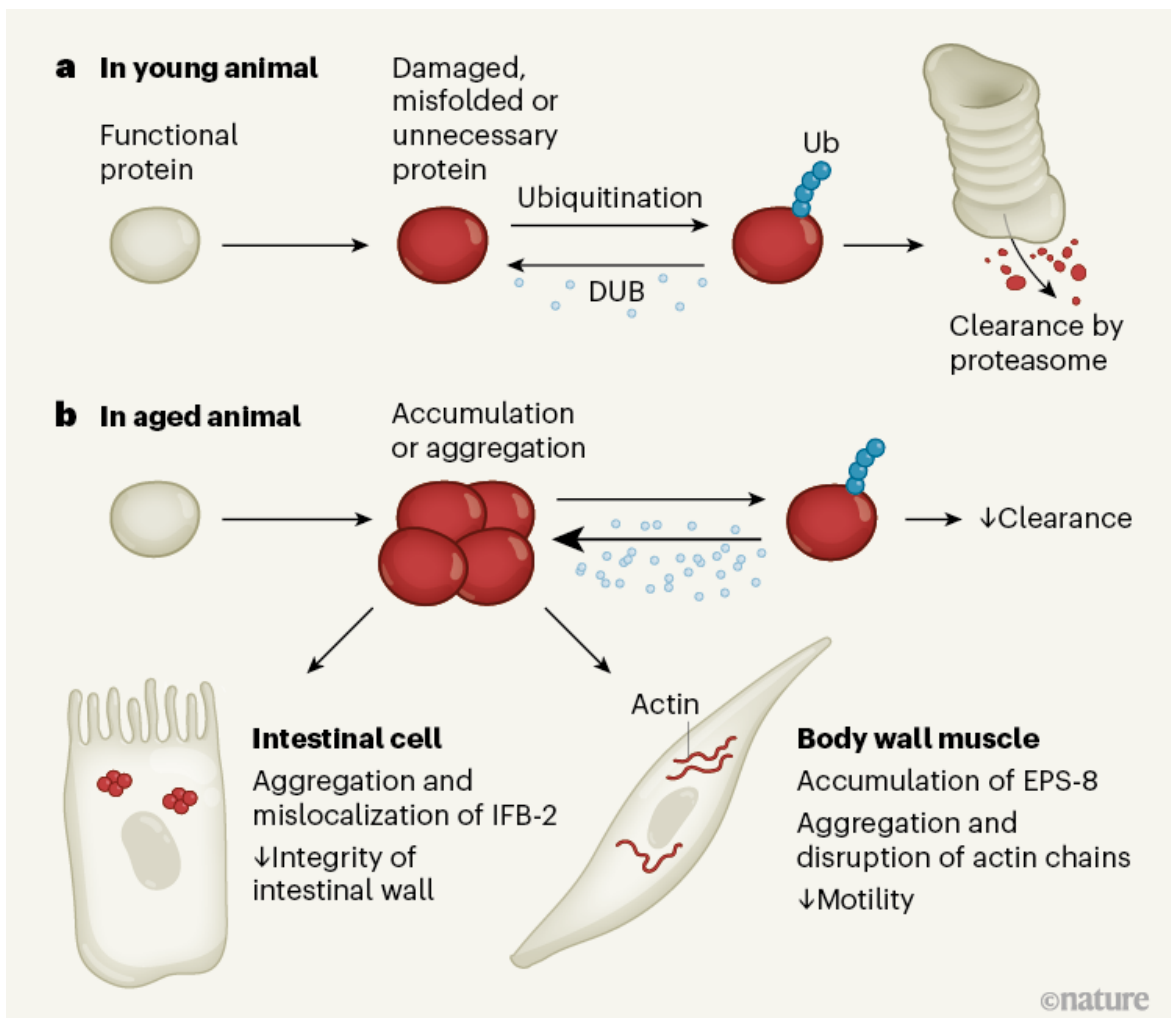
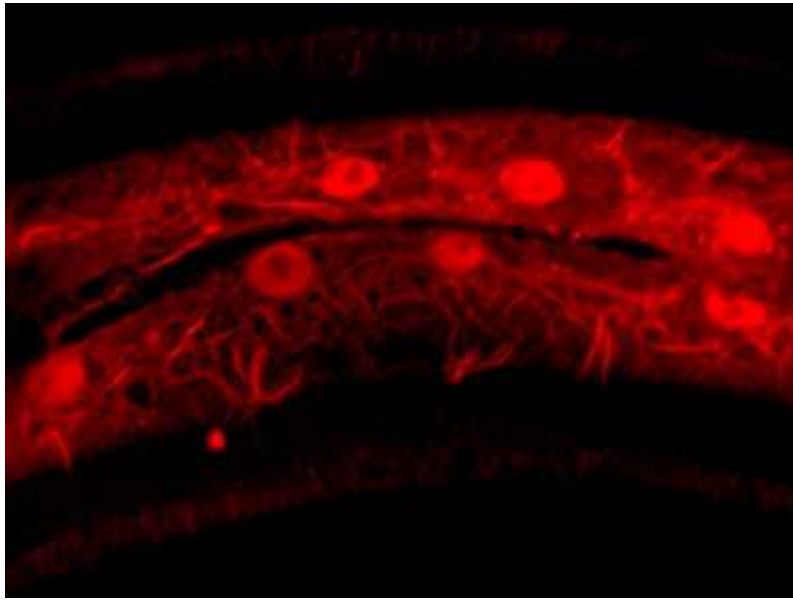


Figure 1 | Dysfunction of protein clearance in old worms leads to decline of tissue function. **a**, Unwanted proteins are reversibly tagged with ubiquitin molecules (Ub), which signal that the protein is ready for clearance by the proteasome, a complex of proteins that breaks down proteins. Ubiquitin molecules are removed by deubiquitinase (DUB) enzymes. **b**, Koyuncu *et al.*² assessed ubiquitination in *Caenorhabditis elegans* worms as the worms aged. Ubiquitination of most proteins decreased with age, in part owing to increased activity of DUB enzymes. Some proteins that are normally targets of the proteasome accumulated with age, and the lifespan of *C. elegans* was extended when expression of these proteins was decreased during adulthood (not shown). Such proteins include IFB-2 and EPS-8. With ageing, IFB-2 aggregation resulted in a loss of intestinal integrity, and reduction of EPS-8 ubiquitination led to disruption of the actin proteins that

make up the cell ‘skeleton’ in the muscles of the body wall and a reduction in the worm’s motility.

Koyuncu *et al.* measured the levels of different proteins in the cells of worms at different ages using mass spectrometry. Ubiquitinated proteins were quantified by purifying them using antibodies that could recognize signs of previous ubiquitination on fragments of the proteins digested by the enzyme trypsin. Old worms showed a general reduction in ubiquitination compared with their younger counterparts. Lifespan can be extended in worms by specific dietary manipulations³, or by genetic modifications that reduce intracellular signalling along the insulin/IGF-1-like pathway⁴. The authors found that, in worms that were long-lived — owing to dietary restriction or reduced insulin/IGF-1 signalling — ubiquitination either did not change substantially with ageing or was increased, hinting at a link between protein ubiquitination and longevity.



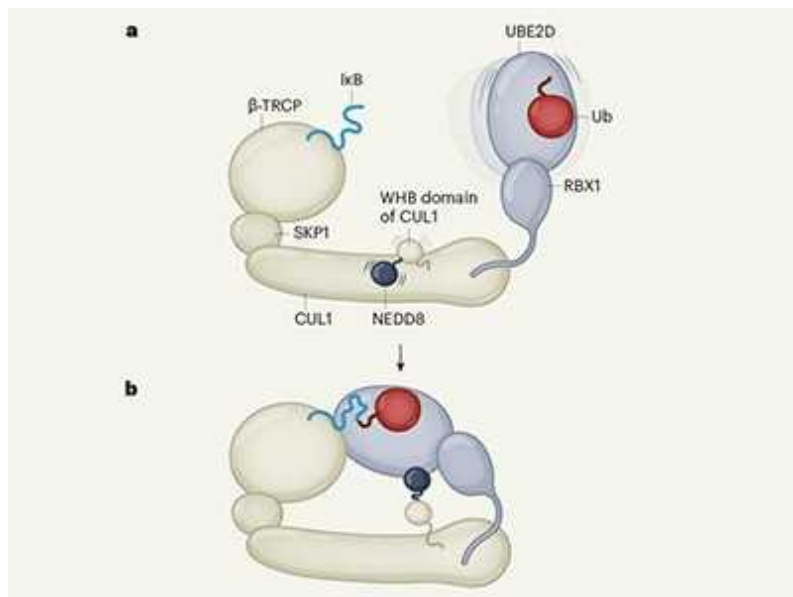
[Read the paper: Rewiring of the ubiquitinated proteome determines ageing in *C. elegans*](#)

The authors determined that the reduction in protein ubiquitination with age is not caused by dwindling expression of ubiquitin or changes in the rate of ubiquitin turnover. Rather, it is probably caused by the increased activity of deubiquitinases (DUBs) — enzymes that detach ubiquitin from proteins. In line with this idea, treating old worms with the broad-spectrum DUB-

inhibiting drug PR-619 increased ubiquitination to a level similar to that seen in young worms.

Although there seems to be no straightforward correlation between protein abundance and the level of ubiquitination, the authors found that a considerable fraction of proteins that were less ubiquitinated accumulated in the old worms. The cellular accumulation of such proteins might be responsible for age-related decline in cell function (Fig. 1b). Six of these proteins also accumulated in young worms that were genetically engineered to have proteasomal dysfunction, and the proteins were ubiquitinated in a way that identifies them as genuine proteasomal targets. The authors found that artificially reduced expression (knockdown) of the genes encoding these proteins in adult worms prevented accumulation of the proteins and, in half of these cases, extended the worms' lifespan. Knockdown of the genes *iβ-2* and *eps-8* had the strongest effect, and so these two genes deserved closer scrutiny.

The *iβ-2* gene encodes a protein component of a network of fibres that contribute to the structural 'skeleton' of intestinal cells, and that are necessary for the function and integrity of these cells. In aged worms, Koyuncu *et al.* observed IFB-2 protein aggregates throughout the intestinal cell. Knockdown of *iβ-2* during adulthood prevented this aggregation and the age-related decline in intestinal integrity (Fig. 1b), which was assessed by measuring bacterial invasion of the intestine in later life.



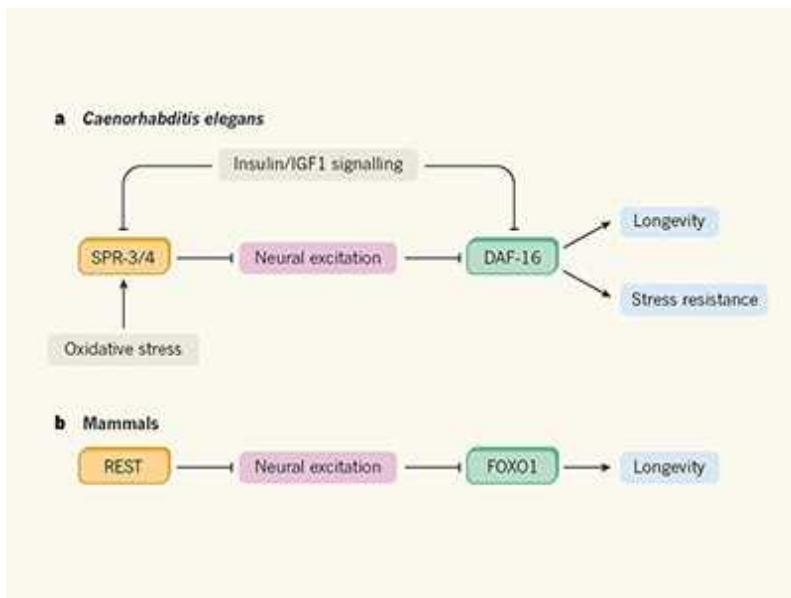
Transfer of ubiquitin protein caught in the act

The *eps-8* gene is an activator of the RAC intracellular signalling pathway, and EPS-8 protein and RAC signalling affect the dynamics of actin — a structural protein of the cell skeleton. Knockdown of *eps-8* in adult worms prevented the destabilization of actin networks in muscles of the body wall and the concomitant decrease in motility in old worms (Fig. 1b). When *eps-8* expression was reduced specifically in the muscles or neuronal cells of adult worms, the worms lived longer than normal. Concordantly, knockdown in adulthood of *mig-2*, one of the three *C. elegans* genes that encode RAC-like proteins, also extended lifespan.

In summary, Koyuncu *et al.* successfully link the age-related decrease in ubiquitination and subsequent increase in the abundance of two proteins, IFB-2 and EPS-8, to the loss of intestinal and muscular integrity — both problems well known to be associated with age in *C. elegans*^{5,6}. A key feature of this study is that it bridges the gap between molecular changes that occur with ageing and their effects on tissue function and lifespan in the worm.

This work opens up several new research opportunities, yet also leaves open intriguing questions. One such question concerns the potential for leveraging these findings to explore ways of extending lifespan. Koyuncu *et al.* showed that knocking down individual genes that express proteins that tend to accumulate and aggregate with age can extend lifespan by a maximum of 21%. Given that these genes probably act independently in different tissues, reducing the expression of a combination of different genes in different tissues might result in a much stronger effect on longevity. This strategy should not necessarily be limited to the targets identified in this study.

Treatment of old worms with the DUB inhibitor PR-619 generally returned ubiquitination in old worms to levels seen in younger worms, possibly by preventing or delaying age-related accumulation of protein aggregates in multiple tissues simultaneously. However, given its broad activity, PR-619 might also interfere with crucial deubiquitination and therefore disturb cellular homeostasis in a way that is not compatible with longevity.



Moderation of neural excitation promotes longevity

Another remaining pertinent question is, what causes the increase in DUB activity in old animals? The culprit could be sustained insulin/IGF-1 activity in the worms, because the authors found that its reduction was sufficient to prevent upregulation of all age-dysregulated DUBs. Moreover, insulin/IGF-1 activity has been proposed to promote senescence and age-related tissue deterioration in *C. elegans*, thus causing older individuals to die, while increasing fitness of the species at the colony level⁷. Hence, the increase in DUB activity with age might be one of the mechanisms by which the insulin/IGF-1 signalling pathway controls lifespan.

The increased ubiquitination of proteins in aged worms with reduced insulin/IGF-1 signalling compared with wild-type aged worms is consistent with previous work showing that, in the mutant worms, deubiquitination is actively repressed and proteasome activity is increased⁸. Previous work also showed that the longevity of these animals is, in part, supported by an increase in ubiquitination⁹.

From a broader perspective, Koyuncu and co-workers' findings elegantly support the antagonistic-pleiotropy hypothesis¹⁰ — an evolutionary explanation for why ageing is adaptive and therefore occurs. This hypothesis posits that genes that are beneficial for development or reproduction, but are

detrimental later in life, will be selected for during evolution. The study identifies two excellent examples of such genes — *iβ-2* and *eps-8*.

A final and major question is whether or not the age-associated deubiquitination that triggers late-life protein accumulation and aggregation in worms is also seen in more-complex animals. In rats, protein ubiquitination seems to increase, rather than decrease, with age^{11–13}, suggesting that the dynamics of ubiquitination in worms are different from those in mammals. The distinctive ubiquitination pattern observed in *C. elegans* might relate to its peculiar ‘boom-and-bust’ life history that favours both a programmed early collapse of the regulation of protein levels¹⁴ and ageing⁷. However, it is still possible that proteins for which proteasomal clearance is dysregulated with ageing have an important role in the development of age-related mammalian disorders that involve protein aggregation, such as Parkinson’s disease and Alzheimer’s disease¹⁵. Therefore, understanding how the ubiquitination dynamics for different proteins change in different species with ageing could provide insight into potential strategies for treating such disorders.

Nature **596**, 191–192 (2021)

doi: <https://doi.org/10.1038/d41586-021-02009-4>

References

1. 1.

Komander, D. *Biochem. Soc. Trans.* **37**, 937–953 (2009).

[PubMed](#) [Article](#) [Google Scholar](#)

2. 2.

Koyuncu, S. *et al.* *Nature* **596**, 285–290 (2021).

[Article](#) [Google Scholar](#)

3. 3.

Greer, E. L. & Brunet, A. *Aging Cell* **8**, 113–127 (2009).

[PubMed](#) [Article](#) [Google Scholar](#)

4. 4.

Murphy, C. T. & Hu, P. J. in *WormBook* (eds the *C. elegans* Research Community) available at <https://doi.org/10.1895/wormbook.1.164.1> (WormBook, 2013).

[Google Scholar](#)

5. 5.

McGee, M. D. *et al.* *Aging Cell* **10**, 699–710 (2011).

[PubMed](#) [Article](#) [Google Scholar](#)

6. 6.

Herndon, L. A. *et al.* *Nature* **419**, 808–814 (2002).

[PubMed](#) [Article](#) [Google Scholar](#)

7. 7.

Lohr, J. N., Galimov, E. R. & Gems, D. *Ageing Res. Rev.* **50**, 58–71 (2019).

[PubMed](#) [Article](#) [Google Scholar](#)

8. 8.

Matilainen, O., Arpalahti, L., Rantanen, V., Hautaniemi, S. & Holmberg, C. I. *Cell Rep.* **3**, 1980–1995 (2013).

[PubMed](#) [Article](#) [Google Scholar](#)

9. 9.

Ghazi, A., Henis-Korenblit, S. & Kenyon, C. *Proc. Natl Acad. Sci. USA* **104**, 5947–5952 (2007).

[PubMed](#) [Article](#) [Google Scholar](#)

10. 10.

Williams, G. C. *Evolution* **11**, 398–411 (1957).

[Article](#) [Google Scholar](#)

11. 11.

Li, F. *et al. Mech. Ageing Dev.* **129**, 515–521 (2008).

[PubMed](#) [Article](#) [Google Scholar](#)

12. 12.

Zhang, L., Li, F., Dimayuga, E., Craddock, J. & Keller, J. N. *FEBS Lett.* **581**, 5543–5547 (2007).

[PubMed](#) [Article](#) [Google Scholar](#)

13. 13.

Altun, M. *et al. J. Biol. Chem.* **285**, 39597–39608 (2010).

[PubMed](#) [Article](#) [Google Scholar](#)

14. 14.

Ben-Zvi, A., Miller, E. A. & Morimoto, R. *Proc. Natl Acad. Sci. USA* **106**, 14914–14919 (2009).

[PubMed](#) [Article](#) [Google Scholar](#)

15. 15.

Lim, K.-H., Joo, J.-Y. & Baek, K.-H. *Aging Res. Rev.* **61**, 101088 (2020).

[Article](#) [Google Scholar](#)

[Download references](#)

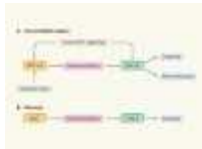
Competing Interests

The author declares no competing interests.

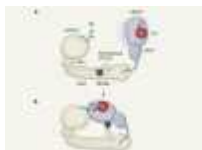
Related Articles



- [Read the paper: Rewiring of the ubiquitinated proteome determines ageing in C. elegans](#)



- [Moderation of neural excitation promotes longevity](#)



- [Transfer of ubiquitin protein caught in the act](#)

- [See all News & Views](#)

Subjects

- [Ageing](#)
- [Proteomics](#)

- [Technology and Knowledge Transfer Officer / Commercialization](#)

University of Luxembourg

Luxembourg, Luxembourg

- [Technology and Knowledge Transfer Officer / Social Sciences, Humanities](#)

University of Luxembourg

Luxembourg, Luxembourg

- [Postdoctoral Research Assistant \(m/f/div\) in modelling and data science](#)

Max Planck Institute for the Science of Human History

Jena, Germany

- [Postdoc researcher in de novo design of transmembrane beta-barrels for nanopore sensing applications](#)

Flanders Institute for Biotechnology (VIB)

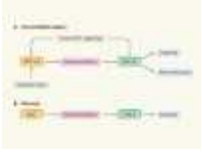
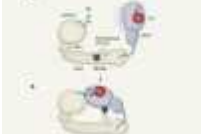
Brussels, Belgium

Nature Briefing

An essential round-up of science news, opinion and analysis, delivered to your inbox every weekday.

[Download PDF](#)

Related Articles

-  [Read the paper: Rewiring of the ubiquitinated proteome determines ageing in *C. elegans*](#)
-  [Moderation of neural excitation promotes longevity](#)
-  [Transfer of ubiquitin protein caught in the act](#)
- [See all News & Views](#)

Subjects

- [Ageing](#)
- [Proteomics](#)

This article was downloaded by **calibre** from <https://www.nature.com/articles/d41586-021-02009-4>

- NEWS AND VIEWS
- 21 July 2021

How the amino acid leucine activates the key cell-growth regulator mTOR

Cells can tailor their growth to current conditions by sensing nutrients. The protein complex mTORC1 enables cell growth to be coordinated with the level of certain amino acids, and how it senses the amino acid leucine has now become clearer.

- [Tibor Vellai](#) 0
1. [Tibor Vellai](#)
 1. Tibor Vellai is in the Department of Genetics, Eötvös Loránd University, Budapest H-1117, Hungary.

[View author publications](#)

You can also search for this author in [PubMed](#) [Google Scholar](#)

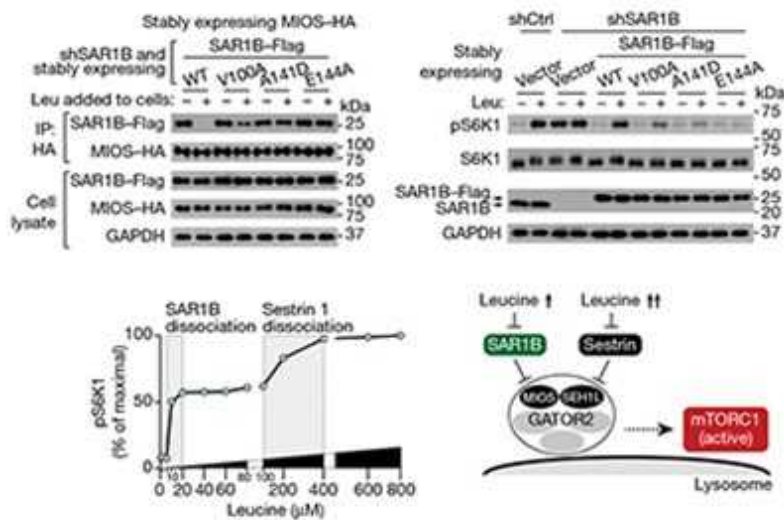




•

[Download PDF](#)

The protein mTOR is a type of enzyme called a kinase, and it functions in two distinct complexes, termed mTORC1 and mTORC2. mTORC1 boosts cell growth and proliferation in response to nutrient availability and hormone-dependent signals that promote cell division. [Writing in Nature](#), Chen *et al.*¹ provide insights into how mTORC1 is regulated by a specific amino acid — leucine.



[Read the paper: SAR1B senses leucine levels to regulate mTORC1 signalling](#)

mTORC1 carries out its role by regulating certain anabolic (synthetic) and catabolic (degradative) processes. These involve protein synthesis; production of the protein-synthesis machinery in the form of ribosomes; lipid synthesis; and autophagy, a degradation process mediated by organelles called lysosomes². mTORC1 deficiency has been implicated in various human disorders, including cancer, neurodegeneration, metabolic diseases and muscle atrophy, as well as being linked to changes involved in the ageing process³. Yet despite its major physiological and clinical significance, how mTORC1 signalling is influenced by upstream regulatory factors is not fully understood.

The amino acid leucine is a potent stimulator of mTORC1: it blocks the inhibitory effect of the protein sestrin 2 on the GATOR2 complex that activates mTORC1⁴. Such regulation links the cellular nutrient status — the level of intracellular amino acids — to the control of cell growth (Fig. 1).

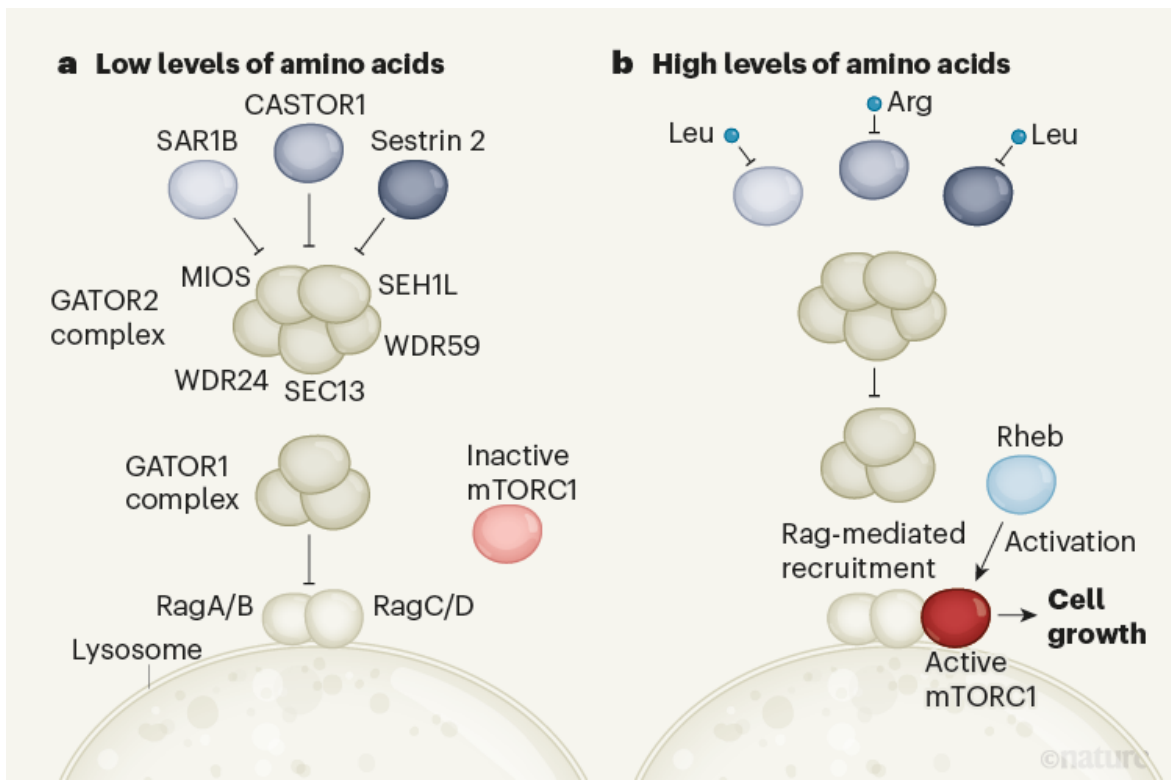
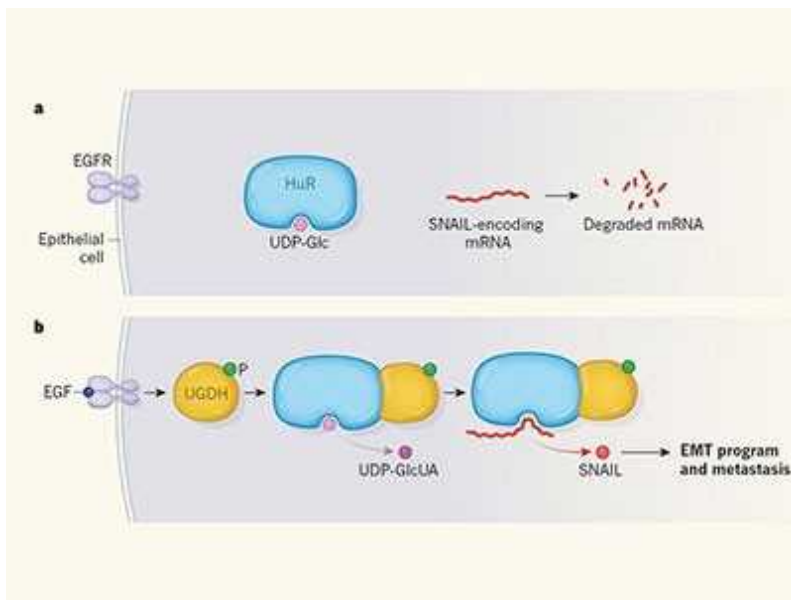


Figure 1 | A mechanism to activate the mTORC1 complex that depends on the level of specific amino acids. The complex mTORC1 regulates cell growth, and its activity is modulated by the intracellular availability of amino acids. Chen *et al.*¹ report their discovery that the protein SAR1B functions in this pathway. **a**, If amino-acid levels are low, SAR1B and two other proteins, CASTOR1 and sestrin 2, inhibit the protein complex GATOR2 (which consists of the proteins MIOS, SEH1L, WDR24, SEC13 and WDR59). SAR1B inhibits MIOS and sestrin 2 inhibits SEH1L. The complex GATOR1 (subunits not named here) inhibits the enzymes RagA, RagB, RagC and RagD, and the inactive mTORC1 complex fails to be recruited to an organelle called the lysosome. **b**, High levels of the amino acid leucine (Leu) inhibit SAR1B and sestrin 2, and high levels of arginine (Arg) inhibit CASTOR1. As a result, GATOR2 is able to inhibit GATOR1. The Rag enzymes, which are no longer inhibited, then recruit mTORC1 to the lysosome, and mTORC1 is activated by the protein Rheb (which can sense aspects of cellular function such as energy levels). This pathway can thereby integrate information about the cell to initiate growth when conditions are suitable.

Chen and colleagues show that leucine is also sensed by another regulatory factor in mammalian cells, the protein SAR1B, which is a type of enzyme called a small GTPase. The authors report that reduced expression of the *SAR1B* gene makes cells insensitive to leucine scarcity and activates the mTORC1 pathway. Similarly to the way in which sestrin 2 functions, SAR1B interacts physically with GATOR2 when leucine is removed, affecting GATOR2's function. However, the authors show that SAR1B binds to a different GATOR2 subunit (the protein MIOS) from sestrin 2 (which binds to the SEH1L protein). When leucine levels in the cell are sufficiently high, the amino acid binds to SAR1B, causing a conformational change in the protein, which then dissociates from GATOR2. The liberated GATOR2 inhibits another protein complex, GATOR1, which leads four Rag GTPase enzymes⁵ (RagA, RagB, RagC and RagD) to recruit mTORC1 to the surface of the lysosome, where the enzyme Rheb GTPase activates mTOR (Fig. 1). Thus, the inhibitory function of GATOR1 on Rag GTPases is SAR1B-dependent. Loss of SAR1B function enables mTORC1 to localize to lysosomes, even under conditions of leucine starvation.

The authors found that SAR1B and sestrin 2 detect leucine by recognizing different parts of the amino acid's structure. They report that SAR1B recognizes the amino group and side chain of leucine, whereas it was known⁶ that sestrin 2 identifies leucine's amino and carboxyl groups. These two leucine sensors bind to the amino acid with different affinities: SAR1B has a higher binding affinity than does sestrin 2. These features permit mTORC1 activation to occur over two steps by sequentially prompting the dissociation of SAR1B and sestrin 2 from GATOR2 at different intracellular leucine concentrations. Furthermore, the relative levels of SAR1B and sestrin 2 in a cell can vary in different tissues. At the subcellular level, some SAR1B localizes to lysosomes, and leucine stimulates its dissociation from both GATOR2 and lysosomes. Together, the authors' evidence indicates that SAR1B is a previously unknown leucine sensor that regulates mTORC1 activity through modulation of GATOR2.



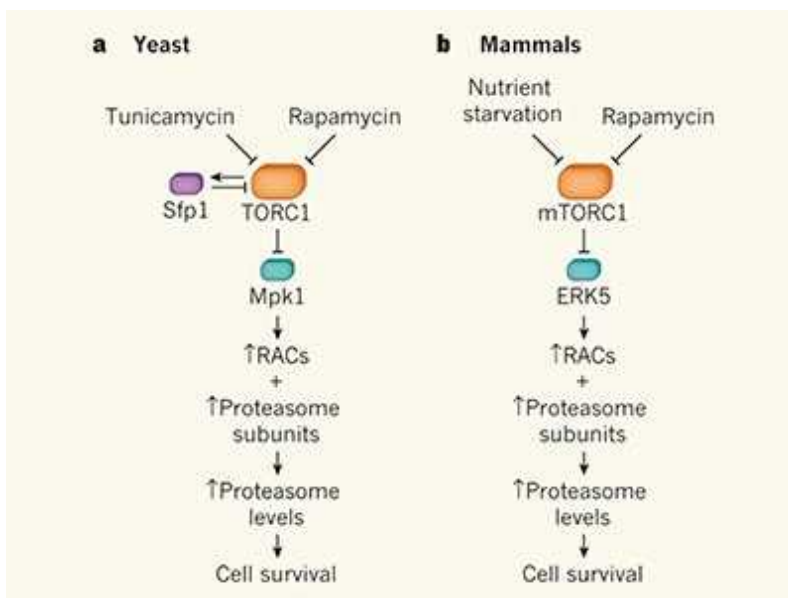
Metabolic signal curbs cancer-cell migration

The authors report that inhibition of SAR-1 protein, the counterpart of human SAR1B in the nematode worm *Caenorhabditis elegans*, also renders the worm version of mTORC1, called *Ce*TORC1, insensitive to nutrient starvation in a GATOR2-dependent manner. When a human *SARI B* gene is introduced into nematodes defective in SAR-1 production, *Ce*TORC1 sensitivity to nutrient restriction is restored. And, consistent with *Ce*TORC1's function in ageing⁷, SAR-1 affects the lifespan of *C. elegans* under prolonged starvation. These results suggest that SAR1B's role in the control of mTORC1 is evolutionarily conserved.

Consistent with the association between mTORC1 hyperactivity and cancer², Chen *et al.* report that the *SARI B* gene is frequently deleted in lung tumours called squamous cell carcinoma and adenocarcinoma. The authors also find that treatment of cultured SAR1B-deficient human cells with the mTORC1 inhibitor rapamycin significantly suppresses proliferation. Finally, eliminating SAR1B activity promotes tumour growth in mice given transplants of human tumour cells. These findings suggest that SAR1B might serve as a potent target for antitumour therapy.

Arginine was previously shown^{8,9} to be another essential amino acid that activates the mTORC1 pathway (Fig. 1). This amino acid is sensed by the CASTOR1 protein, which also interacts directly with GATOR2^{8,9}. Loss of

CASTOR1 function or arginine abundance also leads to mTORC1 activation.



The TORC1 pathway to protein destruction

Why do these two amino acids, leucine and arginine, seem to have a specific role in controlling mTORC1 signalling, given that they are sensed^{4,9} by different GATOR2 modulators? An organism's genetic code has redundancy because different nucleotide triplets (codons) can specify the same amino acid. Methionine and tryptophan are each encoded by a single codon, whereas all the other amino acids are specified by multiple codons. It is intriguing that leucine and arginine are two of the three amino acids that are determined by the highest number of codons — six in total. The relative frequency of a given amino acid in protein is affected by the number of codons that can code for it (see go.nature.com/36xqd31)

Thus, it is possible that a system has evolved in which the amino acids that are used most frequently in proteins also function as signalling factors that determine the activity of the major orchestrator of cell growth, mTORC1. Indeed, the third amino acid that is specified by six codons is serine, and there is evidence that this amino acid is also involved in mTORC1 control¹⁰. The intracellular level of methionine, one of the amino acids that occurs less frequently in proteins, is sensed by the SAMTOR protein, which induces GATOR1 to repress mTORC1 signalling¹¹.

Together, these data trace out a model in which the regulatory factors modulating mTORC1 activity can sense the intracellular level of specific amino acids that limit the rate of protein synthesis. Using this strategy, there would be no need for the intracellular concentration of every amino acid to be monitored in a cell; instead, only those used the most and the least frequently in protein synthesis would need to be tracked. That would enable the evolution and operation of a relatively simple, robust and economical regulatory network for maintaining a balance between protein synthesis and degradation.

Nature **596**, 192–194 (2021)

doi: <https://doi.org/10.1038/d41586-021-01943-7>

References

1. 1.

Chen, J. *et al.* *Nature* **596**, 281–284 (2021).

[Article](#) [Google Scholar](#)

2. 2.

Saxton, R. A. & Sabatini, D. M. *Cell* **168**, 960–976 (2017).

[PubMed](#) [Article](#) [Google Scholar](#)

3. 3.

Liu, G. Y. & Sabatini, D. M. *Nature Rev. Mol. Cell Biol.* **21**, 183–203 (2020).

[PubMed](#) [Article](#) [Google Scholar](#)

4. 4.

Wolfson, R. L. *et al.* *Science* **351**, 43–48 (2016).

[PubMed](#) [Article](#) [Google Scholar](#)

5. 5.

Bar-Peled, L. *et al.* *Science* **340**, 1100–1106 (2013).

[PubMed](#) [Article](#) [Google Scholar](#)

6. 6.

Saxton, R. A. *et al.* *Science* **351**, 53–58 (2016).

[PubMed](#) [Article](#) [Google Scholar](#)

7. 7.

Vellai, T. *et al.* *Nature* **426**, 620 (2003).

[PubMed](#) [Article](#) [Google Scholar](#)

8. 8.

Saxton, R. A., Chantranupong, L., Knockenhauer, K. E., Schwartz, T. U. & Sabatini, D. M. *Nature* **536**, 229–233 (2016).

[PubMed](#) [Article](#) [Google Scholar](#)

9. 9.

Chantranupong, L. *et al.* *Cell* **165**, 153–164 (2016).

[PubMed](#) [Article](#) [Google Scholar](#)

10. 10.

Maddock, O. D. K. *et al.* *Nature* **493**, 542–546 (2013).

[PubMed](#) [Article](#) [Google Scholar](#)

11. 11.

Gu, X. *et al.* *Science* **358**, 813–818 (2017).

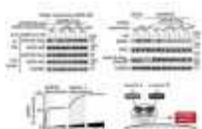
[PubMed](#) [Article](#) [Google Scholar](#)

[Download references](#)

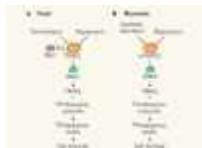
Competing Interests

The author declares no competing interests.

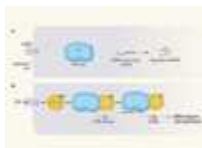
Related Articles



- [Read the paper: SAR1B senses leucine levels to regulate mTORC1 signalling](#)



- [The TORC1 pathway to protein destruction](#)



- [Metabolic signal curbs cancer-cell migration](#)

- [See all News & Views](#)

Subjects

- [Cell biology](#)
- [Metabolism](#)
- [Cancer](#)

nature careers

Jobs >

- [Technology and Knowledge Transfer Officer / Commercialization](#)

University of Luxembourg

Luxembourg, Luxembourg

- [Technology and Knowledge Transfer Officer / Social Sciences, Humanities](#)

University of Luxembourg

Luxembourg, Luxembourg

- [Postdoctoral Research Assistant \(m/f/div\) in modelling and data science](#)

Max Planck Institute for the Science of Human History

Jena, Germany

- [Postdoc researcher in de novo design of transmembrane beta-barrels for nanopore sensing applications](#)

Flanders Institute for Biotechnology (VIB)

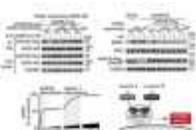
Brussels, Belgium

Nature Briefing

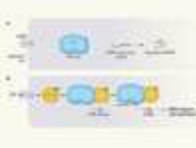
An essential round-up of science news, opinion and analysis, delivered to your inbox every weekday.

[Download PDF](#)

Related Articles

- 
• [Read the paper: SAR1B senses leucine levels to regulate mTORC1 signalling](#)

- 
• [The TORC1 pathway to protein destruction](#)

- 
• [Metabolic signal curbs cancer-cell migration](#)

- [See all News & Views](#)

Subjects

- [Cell biology](#)
- [Metabolism](#)
- [Cancer](#)

This article was downloaded by **calibre** from <https://www.nature.com/articles/d41586-021-01943-7>

- NEWS AND VIEWS
- 11 August 2021

A microscopy technique that images single reaction events in total darkness

Single photons emitted from individual electrochemically excited molecules in solution can now be detected. The technique can be used to image cells at nanometre resolution, without using an external light source.

- [Frédéric Kanoufi](#) ⁰ &
- [Neso Sojic](#) ¹

1. [Frédéric Kanoufi](#)

1. Frédéric Kanoufi is at the University of Paris, ITODYS, CNRS, 75006 Paris, France.

[View author publications](#)

You can also search for this author in [PubMed](#) [Google Scholar](#)

2. [Neso Sojic](#)

1. Neso Sojic is at the University of Bordeaux, CNRS, Bordeaux INP, ISM, UMR 5255, 33607 Pessac, France.

[View author publications](#)

You can also search for this author in [PubMed](#) [Google Scholar](#)



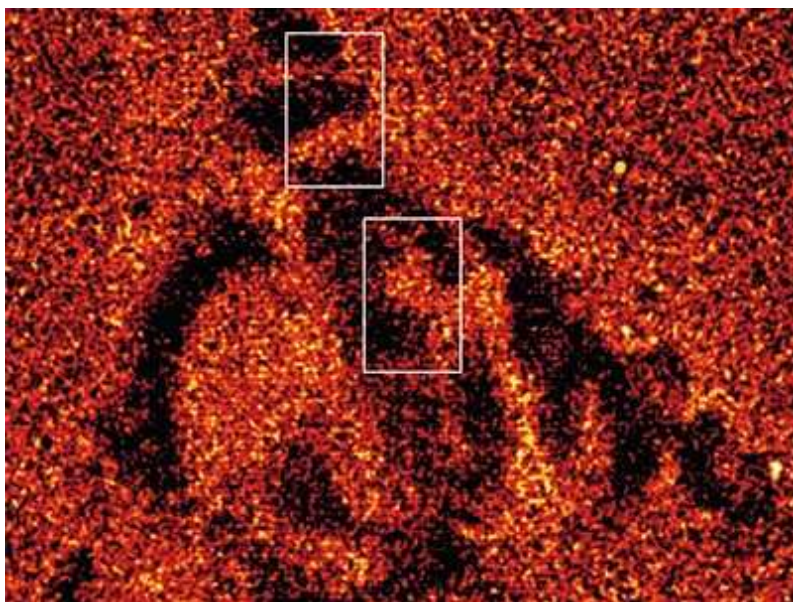


•

[Download PDF](#)

If you want to admire the Milky Way in all its splendour, you should choose a moonless (and possibly romantic) night, away from urban light pollution. Exactly the same principle applies in microscopy, at the other end of the observational size scale: it is much easier to observe faint objects in complete darkness. In [a paper in *Nature*](#), Dong *et al.*¹ report their use of this simple but powerful idea in a direct optical method for imaging single photons generated by individual chemical-reaction events in solution. The authors' method is conceptually different from the fluorescence-based approaches used in conventional single-molecule microscopy, because the

excitation process that leads to photon emission is controlled by electrochemistry and chemical reactivity, and does not require irradiation with light. The authors demonstrate that their imaging method can be used for super-resolution microscopy of living cells.

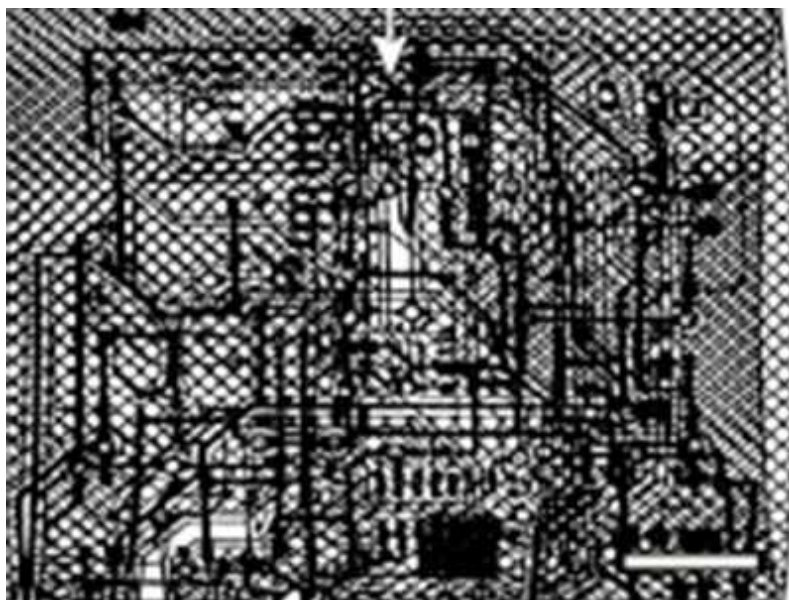


[Read the paper: Direct imaging of single-molecule electrochemical reactions in solution](#)

Chemical reactions typically involve the collisions of individual molecules in solution. However, because measurements of reactions usually record the average parameters of ensembles of these molecular events, the characteristics of individual events are usually obscured, and the precise location and time of each reacting molecule in the solution is unknown. This issue can be partly overcome by restricting the volume of the solution, or by separating events in space and/or time, allowing each one to be detected alone. For example, high-throughput single-molecule measurements have been developed in ultrasmall containers, to detect individual biomolecules². Extraordinary achievements in single-molecule studies have also have been reported using scanning tunnelling microscopy³, nano-electrochemistry⁴ and an optical technique called super-resolution localization microscopy (which achieves a resolution higher than the diffraction limit — a fundamental restriction that usually limits the resolution of optical imaging techniques)⁵.

After decades of development, methods in which samples are irradiated with light have arguably become the most useful means of ‘seeing’ individual molecules — the 2014 Nobel Prize in Chemistry was awarded for discoveries in this field (see go.nature.com/3zs4aph). Biologists, physicists and chemists quickly adopted these revolutionary microscopy techniques, all of which use clever arrangements of light and dark — similar to the chiaroscuro technique in art. However, because these methods require the use of short, high-power laser pulses, their performance is often limited by background scattered light and photobleaching (the extinguishing of fluorescence as a result of the continuous excitation of fluorescent molecules by light). In biological applications, samples can also be damaged by the intense laser pulses, or produce their own fluorescence, obscuring the image of the fluorescent molecule of interest.

Some organisms can produce light *in situ* using biochemical reactions, rather than relying on external light sources — such bioluminescence illuminates the darkest regions of the oceans, for example. Dong and colleagues’ approach to single-molecule imaging takes a similar tack: the authors detect photons emitted by a dye molecule that has been excited using an electrochemically triggered phenomenon called electrochemiluminescence (ECL)^{6,7}. Because this phenomenon does not require any optical excitation, the experiments can be performed in complete darkness.



[Glowing nanocrystals enable 3D X-ray imaging](#)

Analytical methods based on ECL are powerful and have been widely adopted, because the use of an electrochemical trigger, rather than light, allows an ultrasensitive readout of the optical signal. This has been especially useful in clinical diagnostics⁸: about two billion ECL-based immunoassays are run worldwide each year⁹. In the past decade, ECL has also been adapted for use in imaging¹⁰.

In principle, the near-zero background optical noise of ECL-based methods should enable them to reach the ultimate analytical limit: the detection of a single molecule. But although single-molecule detection is now common in fluorescence-based imaging techniques, methods for detecting single ECL events have been almost completely lacking. Just one approach was known, in which single photons are detected from individual ECL reactions under stringently controlled experimental conditions, but without any spatial resolution¹¹. Many authors have reported ECL imaging of single nano- or micrometre-scale objects (see refs 12 and 13, for example), but not of single molecules.

Dong *et al.* have addressed this challenge by developing a method that images the positions of single photons emitted by individual excited dye molecules in ECL events, which are triggered near the surface of an electrode. The authors use a dilute solution of the dye to ensure that these molecules are spatially separated, a strategy used in many single-molecule measurements. However, the isolation of individual ECL events in space and time also arises from careful control of the reactivity of both the dye and the other reagent that takes part in each event (Fig. 1). Light emission occurs when a dye molecule reacts with a radical that is generated by the electrode. The extremely short lifetime of the radical ensures that it is present only at very high dilution, near the electrode surface. The diluted dye molecules therefore encounter the diluted radicals so rarely that each millisecond-duration snapshot of the experiment captures only one reaction, and thus only one photon.

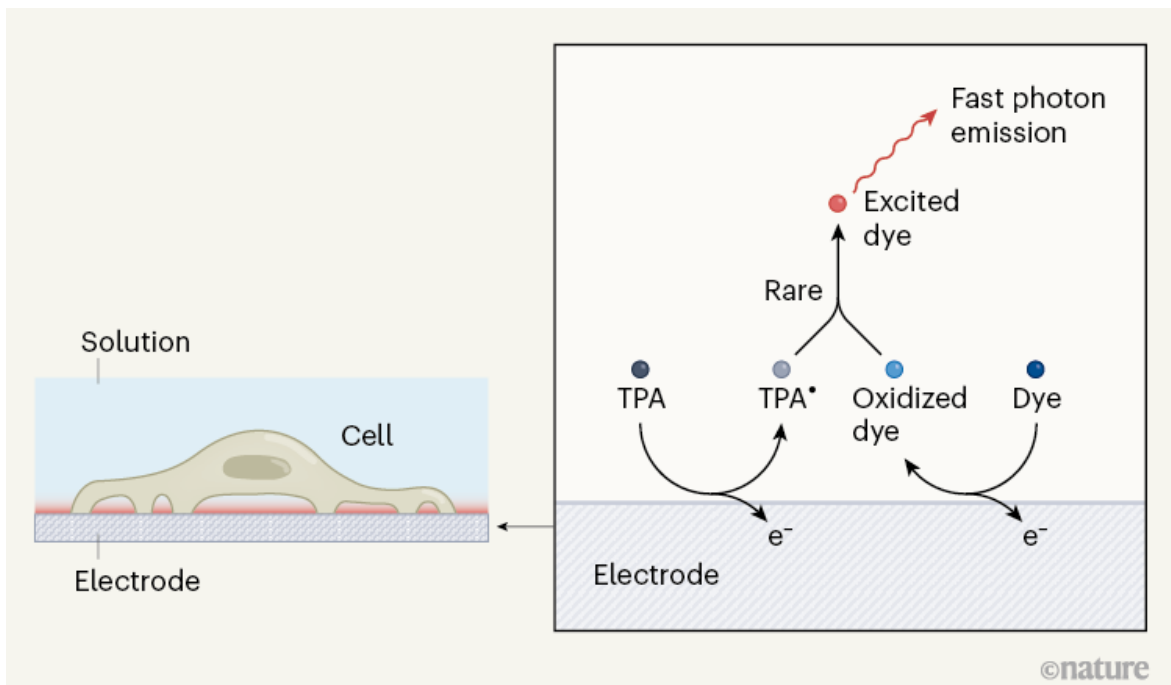


Figure 1 | A microscopy technique involving single-molecule imaging of electrochemical reactions. Dong *et al.*¹ have produced images of cells attached to the surface of electrodes using a phenomenon called electrochemiluminescence. The electrode is immersed in a solution of dye molecules (a ruthenium complex) and a co-reactant (tripropylamine, TPA). TPA is oxidized (loses an electron, e^-) at an electrode, and produces a radical (TPA^\bullet). The radicals have an extremely short lifetime, and are therefore found only at very high dilution in a thin region above the electrode surface. The radicals thus encounter dye molecules only rarely. If dye molecules are oxidized at the electrode and encounter a radical, the dye enters its excited state. The excited dye molecules almost instantaneously emit a photon, revealing the location and time of the reaction event. By imaging photons over time, an image of the electrode surface is produced. Photons are not produced at regions where the cell is attached, thus creating a negative image of the cell.

By analysing multiple experiments, the authors convincingly show that the statistical distribution of the number of photons detected per exposure follows Poisson statistics at different exposure times and at different dye concentrations — thus demonstrating that the collisions of dye molecules with the electrode occur randomly. Furthermore, by analysing the

relationship between the dye concentration and the time interval between detected events, the authors show that the rate of the process is controlled by the diffusion of the dye to the electrode surface, rather than by its adsorption at the electrode; by contrast, adsorption controls the rate of many single-molecule fluorescence studies.

The authors' findings open the way to a new concept in imaging: a chemistry-based approach to super-resolution microscopy. By imaging the photon emissions at the surface of a nanoelectrode over time, Dong *et al.* were able to visualize the surface with a spatial resolution down to 22 nanometres. They extended this approach to image cells attached to an electrode: the adhesive regions of the cells hinder the diffusion of ECL reactants to the electrode surface, blocking photon emission and thereby producing a negative image of those regions¹⁴ (Fig. 1). The resulting images were remarkably sharp (Fig. 2), and correlated with images produced using super-resolution fluorescence microscopy, validating the effectiveness of the approach. Notably, the ECL technique does not require labels to be attached to the cells.

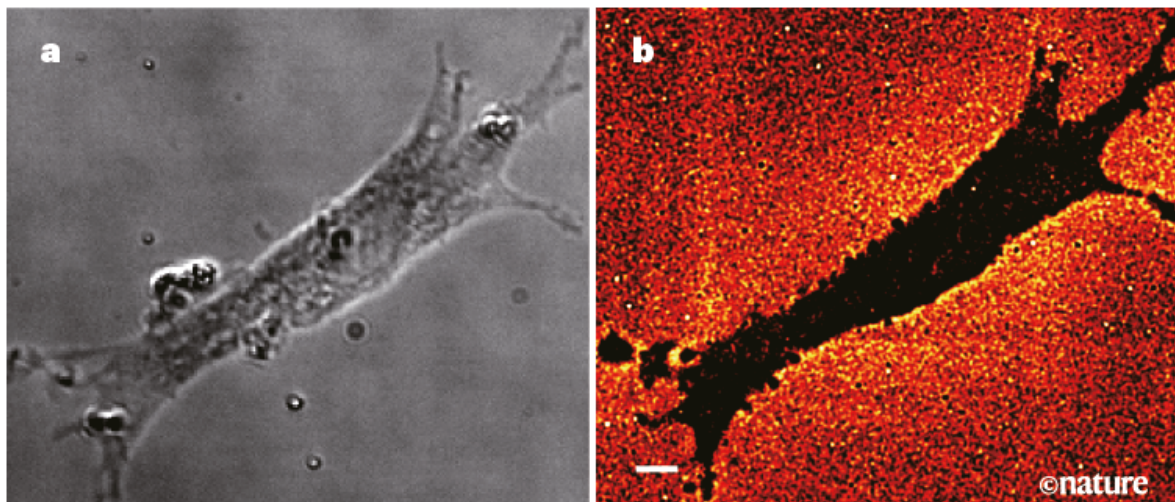


Figure 2 | Cell imaging using ECL-based microscopy. **a**, An image of a cell obtained using an optical microscopy technique. **b**, A negative image of the same cell produced using Dong and colleagues' microscopy technique¹. The image combines 15,000 frames, each with an exposure time of 10 milliseconds. Scale bar, 5 micrometres. (Images from Supplementary Information Fig. 27 of ref. 1.)

Although single photons are imaged, these are emitted by only a fraction of the excited dye molecules produced in solution; the excited molecules, in turn, are produced using just a small fraction of the electron flow through the electrode. In other words, it is not possible to correlate every electron transferred to the electrode from the reagents during an ECL reaction unequivocally to a detected photon. The detection and localization of single-electron events therefore remains a challenging objective in electrochemistry.

The long-term goal is to develop Dong and colleagues' method further, foster its adoption by diverse scientific communities, and design an ECL-based single-photon microscope suitable for commercialization. Moreover, the reported approach opens up exciting opportunities for the investigation of individual electrochemical reactions, or of any reaction involving electron transfer. It could also lead to the development of new strategies for bioassays and cell imaging, complementing well-established fluorescence-based single-molecule microscopy techniques.

Nature **596**, 194–195 (2021)

doi: <https://doi.org/10.1038/d41586-021-02098-1>

References

1. 1.

Dong, J. L. *et al.* *Nature* **596**, 244–249 (2021).

[Article](#) [Google Scholar](#)

2. 2.

Cohen, L. & Walt, D. R. *Annu. Rev. Anal. Chem.* **10**, 345–363 (2017).

[Article](#) [Google Scholar](#)

3. 3.

Cocker, T. L., Peller, D., Yu, P., Repp, J. & Huber, R. *Nature* **539**, 263–267 (2016).

[PubMed](#) [Article](#) [Google Scholar](#)

4. 4.

Fan, F.-R. F. & Bard, A. J. *Science* **267**, 871–874 (1995).

[PubMed](#) [Article](#) [Google Scholar](#)

5. 5.

Hell, S. W. *Science* **316**, 1153–1158 (2007).

[PubMed](#) [Article](#) [Google Scholar](#)

6. 6.

Bard, A. J. (ed.) *Electrogenerated Chemiluminescence* (Dekker, 2004).

[Google Scholar](#)

7. 7.

Liu, Z., Qi, W. & Xu, G. *Chem. Soc. Rev.* **44**, 3117–3142 (2015).

[PubMed](#) [Article](#) [Google Scholar](#)

8. 8.

Zanut, A. *et al.* *Nature Commun.* **11**, 2668 (2020).

[PubMed](#) [Article](#) [Google Scholar](#)

9. 9.

Cao, Z., Shu, Y., Qin, H., Su, B. & Peng, X. *ACS Cent. Sci.* **6**, 1129–1137 (2020).

[PubMed](#) [Article](#) [Google Scholar](#)

10. 10.

Ding, H., Guo, W. & Su, B. *Angew. Chem. Int. Edn* **59**, 449–456 (2020).

[Article](#) [Google Scholar](#)

11. 11.

Collinson, M. M. & Wightman, R. M. *Science* **268**, 1883–1885 (1995).

[PubMed](#) [Article](#) [Google Scholar](#)

12. 12.

Zhu, M.-J. *et al.* *Angew. Chem. Int. Edn* **57**, 4010–4014 (2018).

[Article](#) [Google Scholar](#)

13. 13.

Zhang, J., Jin, R., Jiang, D. & Chen, H.-Y. *J. Am. Chem. Soc.* **141**, 10294–10299 (2019).

[PubMed](#) [Article](#) [Google Scholar](#)

14. 14.

Ding, H. *et al.* *Angew. Chem. Int. Edn* **60**, 11769–11773 (2021).

[Article](#) [Google Scholar](#)

[Download references](#)

Competing Interests

The authors declare no competing interests.

Related Articles

-  • [Read the paper: Direct imaging of single-molecule electrochemical reactions in solution](#)
-  • [Glowing nanocrystals enable 3D X-ray imaging](#)
-  • [A close-up view of coupled molecules](#)
- [See all News & Views](#)

Subjects

- [Physical chemistry](#)
- [Chemistry](#)
- [Microscopy](#)
- [Imaging](#)

nature careers

[Jobs](#) >

- [Technology and Knowledge Transfer Officer / Commercialization](#)

University of Luxembourg

Luxembourg, Luxembourg

- [Technology and Knowledge Transfer Officer / Social Sciences, Humanities](#)

University of Luxembourg

Luxembourg, Luxembourg

- [Postdoctoral Research Assistant \(m/f/div\) in modelling and data science](#)

Max Planck Institute for the Science of Human History

Jena, Germany

- [Postdoc researcher in de novo design of transmembrane beta-barrels for nanopore sensing applications](#)

Flanders Institute for Biotechnology (VIB)

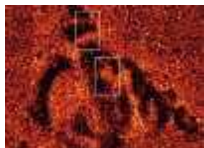
Brussels, Belgium

Nature Briefing

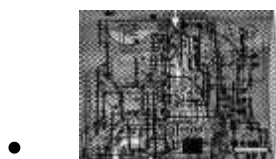
An essential round-up of science news, opinion and analysis, delivered to your inbox every weekday.

[Download PDF](#)

Related Articles



- [Read the paper: Direct imaging of single-molecule electrochemical reactions in solution](#)



- [Glowing nanocrystals enable 3D X-ray imaging](#)



- [A close-up view of coupled molecules](#)
- [See all News & Views](#)

Subjects

- [Physical chemistry](#)
- [Chemistry](#)
- [Microscopy](#)
- [Imaging](#)

This article was downloaded by **calibre** from <https://www.nature.com/articles/d41586-021-02098-1>

- NEWS AND VIEWS
- 11 August 2021

Chain-mail fabric stiffens under confining pressure

The mechanical properties of chain mail have been revisited. The findings reveal that, under confining pressure, chain-mail-inspired materials can switch from pliable to stiff structures that have outstanding load-bearing capacities.

- [Laurent Orgéas](#) [ORCID: http://orcid.org/0000-0003-1668-688X](http://orcid.org/0000-0003-1668-688X)⁰

1. [Laurent Orgéas](#)

1. Laurent Orgéas is in the 3SR Lab, Université Grenoble Alpes, CNRS, Grenoble INP, 38000 Grenoble, France.

[View author publications](#)

You can also search for this author in [PubMed](#) [Google Scholar](#)





•

[Download PDF](#)

Writing in Nature, Wang *et al.*¹ report fabrics that consist of layers of interlocked, 3D particles — a high-tech version of the chain-mail armour used by medieval knights. Under confining pressure, these materials undergo a phase transition known as a jamming transition. This profoundly alters their mechanical properties, transforming them from floppy textiles into rigid shells. These remarkable fabrics could be useful for applications in medicine and engineering.



[Read the paper: Structured fabrics with tunable mechanical properties](#)

There is growing demand for materials that have properties optimized for a particular application, combinations of useful properties or even extraordinary properties not found in nature. The standard approach to achieving these goals is to modulate and refine the chemistry and nanostructure of materials, but this strategy sometimes has limits. A complementary approach² is to design ‘architected’ materials, which have tailored topology and morphology at the mesoscale (which typically ranges from a few micrometres to a few millimetres), and can contain composite substructures. Related systems include: cellular materials^{3,4}, such as foams and honeycomb structures; materials made from entangled fibres⁵ or interlocked subunits⁶; and materials whose mesoscale structures are active (they change behaviour in response to a stimulus) or programmable^{7–9}.

Architected materials have attracted increasing interest over the past two decades, fuelled by advances in processes that can be used to manufacture mesoscale structures and, more recently, by the use of artificial intelligence (AI) and machine learning for materials design¹⁰. However, mesostructured materials are not new: paper and textiles are mesostructured, for instance.

Another historical example is chain-mail armour, which consists of interlocked metal rings. Chain mail was designed to have a high tensile

strength and to protect the wearer from blows from weapons, but also to be pliable, so that it would drape and properly fit the human body. In fact, all material systems composed of discrete components, including chain mail and granular materials, exhibit a jamming transition¹¹ under load that switches them from soft to stiff mechanics. But unlike granular systems, the jamming transition in chain mail can occur on bending or under tensile loading, because of the non-convex shape and interlocking of its structural elements.

Wang *et al.* have revisited the mechanics of chain mail, focusing on the jamming transition. They show that the tensile and bending properties of a chain-mail-inspired fabric can be radically and reversibly altered using confining pressure as a driving force. The authors used 3D printing to fabricate chain mail from a polymer, in which each link is a hollow, 3D particle constructed from connecting struts (Fig. 1a). When the authors put the material into a flexible, sealed plastic bag and pumped out the air, the resulting confining pressure was large enough to trigger the chain mail's jamming transition — increasing the confining pressure from 0 to 93 kilopascals could increase the chain mail's stiffness by a factor of about 25 (Fig. 1b).

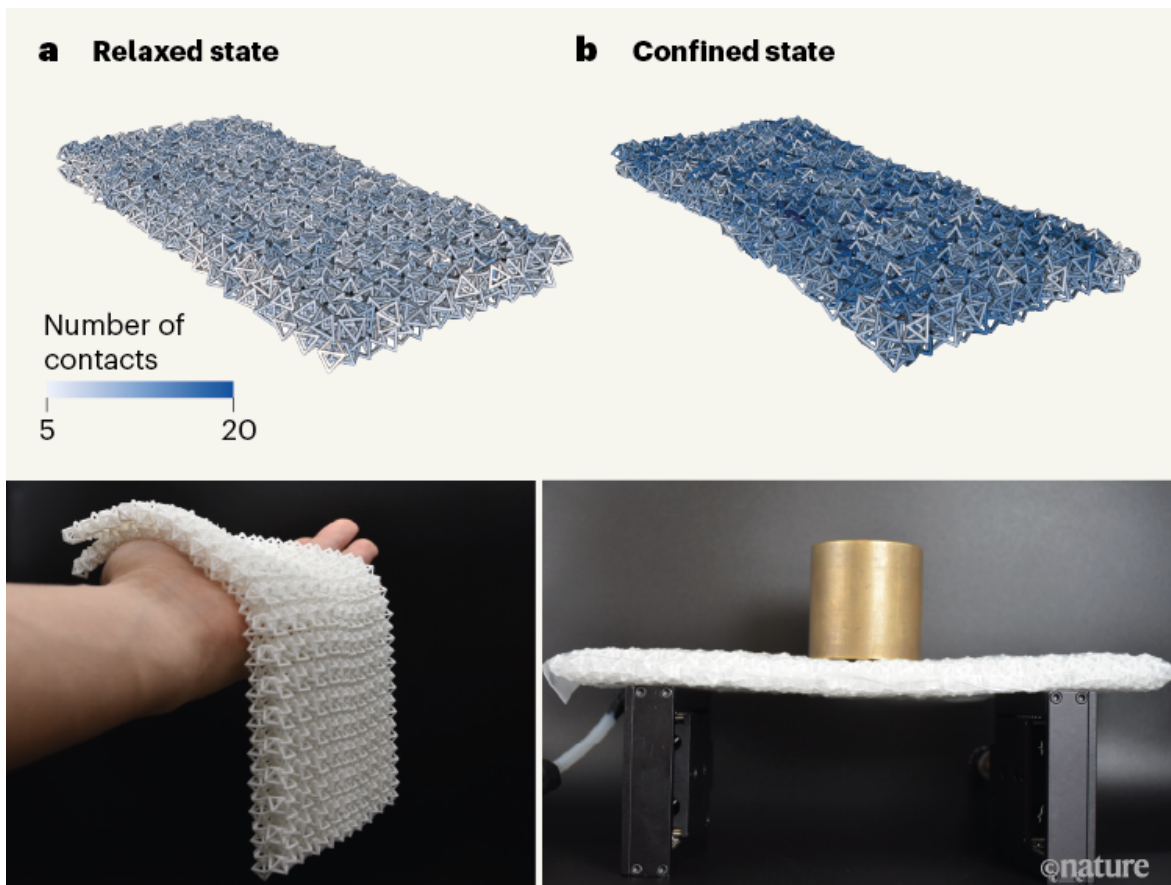
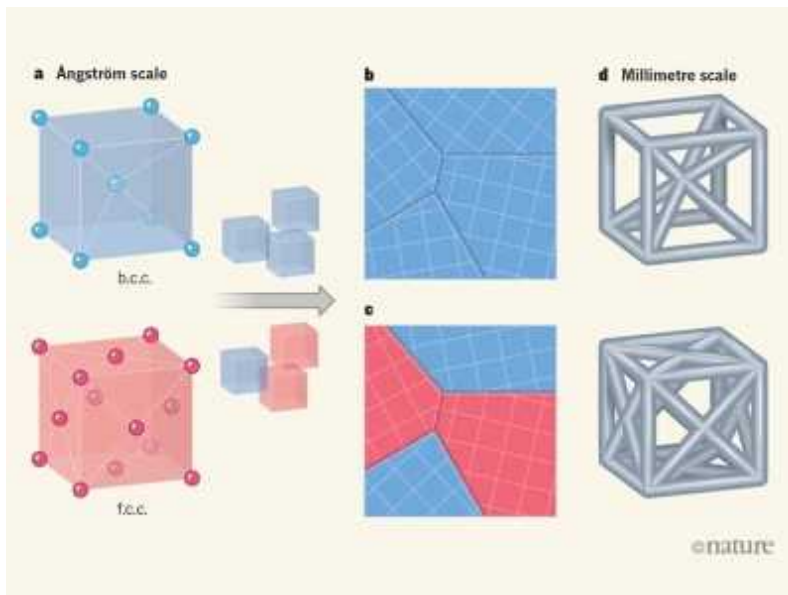


Figure 1 | Increased contacts between particles alter the mechanical properties of a chain-mail fabric under confining pressure. Wang *et al.*¹ prepared a fabric that consists of layers of interlocked, 3D particles, inspired by chain mail. **a**, At low confining pressures (including ambient pressure), the particles in the fabric make relatively few contacts with each other, and the material is pliable. The number of contacts shown in the graphic are produced by a confining pressure of 2 kilopascals. **b**, At higher confining pressures (93 kPa in the graphic), the particles make a greater number of contacts with each other. The material becomes much stiffer and capable of bearing heavy loads, such as the 1.5-kilogram mass shown. Adapted from Figs 1 and 3 of ref. 1.

To understand the underlying mesoscale deformation mechanisms, Wang *et al.* carried out numerical simulations of various chain-mail architectures under tension or bending, at various confining pressures. The simulations showed that the experimentally observed stiffening is accompanied by a small reduction (less than 5%) in the volume of the chain mail, which results

in an increase in the number of contacts between the links in different chains (Fig. 1). Wang *et al.* show that contacts induced by the non-convex shape of the links and by link-interlocking have a central role in determining the efficiency of the jamming transition under tension and bending.

Astonishingly, the authors also found that the increase of a chain mail's apparent bending modulus (which measures the stiffness of a material on bending) scales as a power law of the average number of contacts per chain-mail link, regardless of the simulated architecture.



Atomic-scale hardening mechanisms apply on larger scales in ‘architected’ materials

Wang and colleagues' chain mail presents intriguing opportunities for applications, taking advantage of the fact that these pliable, lightweight, porous materials can easily be turned into rigid shells. A chain mail could conceivably be draped into multiple configurations before being jammed into a chosen static shape that has load-bearing capabilities, such as an exoskeleton for biomedical, sport or military applications. Chain mails could also be useful in civil or mechanical engineering as deployable structures (objects that can change shape in a way that greatly alters their size — for example, to create a temporary shelter or bridge).

There are some limitations to the current findings, which present stimulating challenges for future work. For instance, Wang *et al.* carried out experiments

in which they measured how much a sample of the material flexes in response to an applied bending force at various confining pressures. They observed a linear relationship between force and flexure — that is, elastic behaviour — for small forces, and focused mainly on this elasticity in their analysis. But a non-linear relationship was observed for large forces, which became more pronounced at higher confining pressures. The mesoscale mechanisms responsible for this non-linear behaviour should be analysed further.

Moreover, there are numerous architectures of chain-mail links that could now be tested to explore their effect on the mechanical properties of chain mail. The use of AI algorithms¹⁰ might be an attractive approach to optimize the geometry of the links for targeted combinations of flexibility, jamming behaviour and load-bearing capabilities. It would also be interesting to switch from the conventional polymer used by Wang *et al.* to active materials, such as nanostructured thermoelastic polymers⁷ or shape-memory alloys^{5,9}. The use of such materials might allow the stiffness of the chains in a chain mail to be tuned at different positions. Finally, it should be noted that the reported chain mails are essentially 2D structures; the mechanical properties of 3D versions of these materials now deserve investigation.

Nature **596**, 196–197 (2021)

doi: <https://doi.org/10.1038/d41586-021-02116-2>

References

1. 1.

Wang, Y., Li, L., Hofmann, D., Andrade, J. E. & Daraio, C. *Nature* **596**, 238–243 (2021).

[Article](#) [Google Scholar](#)

2. 2.

Ashby, M. F. *Scripta Mater.* **68**, 4–7 (2013).

[Article](#) [Google Scholar](#)

3. 3.

Bertoldi, K., Vitelli, V., Christensen, J. & van Hecke, M. *Nature Rev. Mater.* **2**, 17066 (2017).

[Article](#) [Google Scholar](#)

4. 4.

Lakes, R. *Science* **235**, 1038–1040 (1987).

[PubMed](#) [Article](#) [Google Scholar](#)

5. 5.

Rodney, D., Gadot, B., Riu Martinez, O., Rolland du Boscoat, S. & Orgéas, L. *Nature Mater.* **15**, 72–77 (2016).

[PubMed](#) [Article](#) [Google Scholar](#)

6. 6.

Dyskin, A. V., Estrin, Y., Kanel-Belov, A. J. & Pasternak, E. *Scripta Mater.* **44**, 2689–2694 (2001).

[Article](#) [Google Scholar](#)

7. 7.

Haines, C. S. *et al.* *Science* **343**, 868–872 (2014).

[PubMed](#) [Article](#) [Google Scholar](#)

8. 8.

Gladman, A. S., Matsumoto, E. A., Nuzzo, R. G., Mahadevan, L. & Lewis, J. A. *Nature Mater.* **15**, 413–418 (2016).

[PubMed](#) [Article](#) [Google Scholar](#)

9. 9.

Gadot, B. *et al.* *Acta Mater.* **93**, 311–323 (2015).

[Article](#) [Google Scholar](#)

10. 10.

Mao, Y., He, Q. & Zhao, X. *Sci. Adv.* **6**, eaaz4169 (2020).

[PubMed](#) [Article](#) [Google Scholar](#)

11. 11.

Liu, A. J. & Nagel, S. R. *Nature* **396**, 21–22 (1998).

[Article](#) [Google Scholar](#)

[Download references](#)

Competing Interests

The author declares no competing interests.

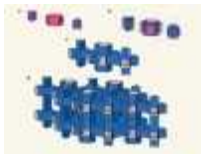
Related Articles



- [Read the paper: Structured fabrics with tunable mechanical properties](#)



- [Atomic-scale hardening mechanisms apply on larger scales in ‘architected’ materials](#)



- [Algorithm for architectural origami](#)
- [See all News & Views](#)

Subjects

- [Materials science](#)
- [Engineering](#)

nature careers

[Jobs](#) >

- [Technology and Knowledge Transfer Officer / Commercialization](#)

University of Luxembourg

Luxembourg, Luxembourg

- [Technology and Knowledge Transfer Officer / Social Sciences, Humanities](#)

University of Luxembourg

Luxembourg, Luxembourg

- [Postdoctoral Research Assistant \(m/f/div\) in modelling and data science](#)

Max Planck Institute for the Science of Human History

Jena, Germany

- [Postdoc researcher in de novo design of transmembrane beta-barrels for nanopore sensing applications](#)

Flanders Institute for Biotechnology (VIB)

Brussels, Belgium

Nature Briefing

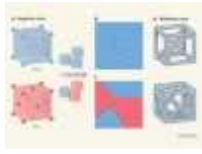
An essential round-up of science news, opinion and analysis, delivered to your inbox every weekday.

[Download PDF](#)

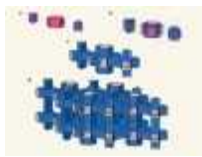
Related Articles



- [Read the paper: Structured fabrics with tunable mechanical properties](#)



- [Atomic-scale hardening mechanisms apply on larger scales in ‘architected’ materials](#)



- [Algorithm for architectural origami](#)
- [See all News & Views](#)

Subjects

- [Materials science](#)
 - [Engineering](#)
-

This article was downloaded by **calibre** from <https://www.nature.com/articles/d41586-021-02116-2>

| [Section menu](#) | [Main menu](#) |

- Review Article
- [Published: 11 August 2021](#)

Deep continental roots and cratons

- [D. Graham Pearson](#) [ORCID: orcid.org/0000-0001-5974-4192¹](#),
- [James M. Scott](#) [ORCID: orcid.org/0000-0001-5185-6261²](#),
- [Jingao Liu](#) [ORCID: orcid.org/0000-0002-8800-5898³](#),
- [Andrew Schaeffer⁴](#),
- [Lawrence Hongliang Wang⁵](#),
- [Jeroen van Hunen](#) [ORCID: orcid.org/0000-0002-3050-6753⁶](#),
- [Kristoffer Szilas](#) [ORCID: orcid.org/0000-0002-5541-306X⁷](#),
- [Thomas Chacko¹](#) &
- [Peter B. Kelemen⁸](#)

[Nature](#) volume **596**, pages 199–210 (2021) [Cite this article](#)

- 1245 Accesses
- 16 Altmetric
- [Metrics details](#)

Subjects

- [Geochemistry](#)
- [Geodynamics](#)
- [Precambrian geology](#)

Abstract

The formation and preservation of cratons—the oldest parts of the continents, comprising over 60 per cent of the continental landmass—

remains an enduring problem. Key to craton development is how and when the thick strong mantle roots that underlie these regions formed and evolved. Peridotite melting residues forming cratonic lithospheric roots mostly originated via relatively low-pressure melting and were subsequently transported to greater depth by thickening produced by lateral accretion and compression. The longest-lived cratons were assembled during Mesoarchean and Palaeoproterozoic times, creating the stable mantle roots 150 to 250 kilometres thick that are critical to preserving Earth's early continents and central to defining the cratons, although we extend the definition of cratons to include extensive regions of long-stable Mesoproterozoic crust also underpinned by thick lithospheric roots. The production of widespread thick and strong lithosphere via the process of orogenic thickening, possibly in several cycles, was fundamental to the eventual emergence of extensive continental landmasses—the cratons.

Access options

Subscribe to Journal

Get full journal access for 1 year

\$199.00

only \$3.90 per issue

[Subscribe](#)

All prices are NET prices.

VAT will be added later in the checkout.

Tax calculation will be finalised during checkout.

Rent or Buy article

Get time limited or full article access on ReadCube.

from \$8.99

[Rent or Buy](#)

All prices are NET prices.

Additional access options:

- [Log in](#)
- [Access through your institution](#)
- [Learn about institutional subscriptions](#)

Fig. 1: Defining cratonic regions with seismic imaging of continental mantle lithosphere.

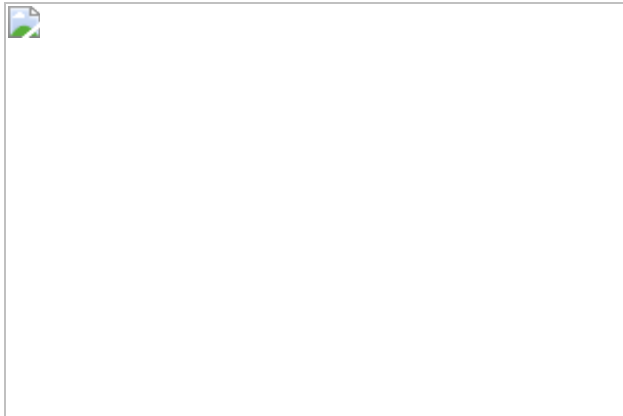
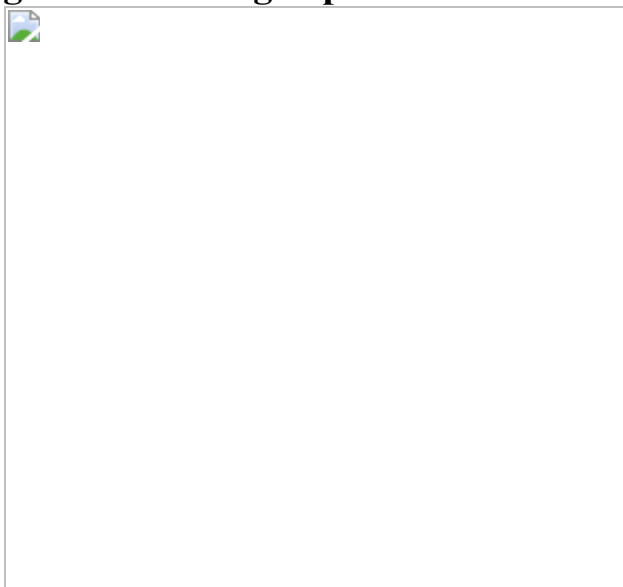
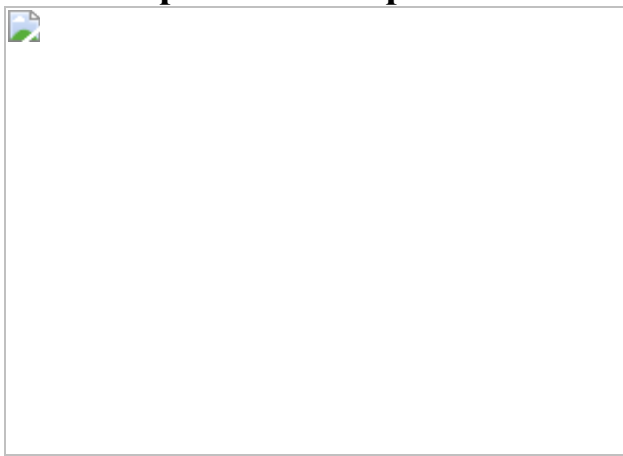


Fig. 2: Estimating depth of melt extraction for lithospheric peridotites.



**Fig. 3: Geodynamic modelling of possible craton formation processes:
lateral compression and plume residue dispersal.**



References

1. 1.

Artemieva, I. M. *The Lithosphere: An Interdisciplinary Approach* 794 (Cambridge Univ. Press, 2011).

2. 2.

Jordan, T. H. Continental tectosphere. *Rev. Geophys.* **13**, 1–12 (1975). **This paper was key to recognizing the fast seismic wave speeds and deep thermal boundary layers beneath parts of the continents, and the need for compositional compensation of the negative thermal buoyancy of the continental lithosphere.**

[ADS](#) [Google Scholar](#)

3. 3.

Eaton, D. W. & Claire Perry, H. K. Ephemeral isopycnicity of cratonic mantle keels. *Nat. Geosci.* **6**, 967–970 (2013).

[ADS](#) [CAS](#) [Google Scholar](#)

4. 4.

Gibson, S. A., Rooks, E. E., Day, J. A., Petrone, C. M. & Leat, P. T. The role of sub-continental mantle as both “sink” and “source” in deep Earth volatile cycles. *Geochim. Cosmochim. Acta* **275**, 140–162 (2020).

[ADS](#) [CAS](#) [Google Scholar](#)

5. 5.

Hoggard, M. A. et al. Global distribution of sediment-hosted metals controlled by craton edge stability. *Nat. Geosci.* **13**, 504–510 (2020).

[ADS](#) [CAS](#) [Google Scholar](#)

6. 6.

Kober, L. *Der Bau der Erde* (Gebrüder Borntraeger, 1921).

7. 7.

Kennedy, W. Q. The structural differentiation of Africa in the Pan-African (± 500 m.y.) tectonic episode. In *Annual Report of the Research Institute of African Geology* 48–49 (Univ. Leeds, 1964). **This paper laid the foundations of recognizing stability as a key part of continental evolution and mineralization, inspiring ref. 8 (Clifford, 1966).**

8. 8.

Clifford, T. N. Tectono-metallogenetic units and metallogenetic provinces of Africa. *Earth Planet. Sci. Lett.* **1**, 421–434 (1966).

[ADS](#) [CAS](#) [Google Scholar](#)

9. 9.

de Wit, M. J. & Hart, R. A. Earth's earliest continental lithosphere, hydrothermal flux and crustal recycling. *Lithos* **30**, 309–335 (1993).

[ADS](#) [Google Scholar](#)

10. 10.

Bleeker, W. Archaean tectonics: a review, with illustrations from the Slave craton. *Geol. Soc. Lond. Spec. Publ.* **199**, 151–181 (2002).

[ADS](#) [Google Scholar](#)

11. 11.

Priyatkina, N., Khudoley, A. K., Collins, W. J., Kuznetsov, N. B. & Huang, H.-Q. Detrital zircon record of Meso- and Neoproterozoic sedimentary basins in northern part of the Siberian Craton: characterizing buried crust of the basement. *Precambr. Res.* **285**, 21–38 (2016).

[ADS](#) [CAS](#) [Google Scholar](#)

12. 12.

Santos, J. O. S. et al. Duration of the trans-Amazonian cycle and its correlation within South America based on U-Pb SHRIMP geochronology of the La Plata craton, Uruguay. *Int. Geol. Rev.* **45**, 27–48 (2003).

[Google Scholar](#)

13. 13.

Carneiro, M. A., Júnior, I. M. D. C. & Teixeira, W. Petrologia, geoquímica e geocronologia dos diques máficos do complexo metamórfico bonfim setentrional (quadrilátero ferrífero) e suas implicações na evolução crustal do craton do São Francisco meridional. *Rev. Brasil. Geocienc.* **28**, 29–44 (1998).

[CAS](#) [Google Scholar](#)

14. 14.

Jordan, T. H. Composition and development of the continental tectosphere. *Nature* **274**, 544–548 (1978). **Furthered the notion of the compositionally induced robustness of continents to convective disruption and proposed a compressional thickening model for the origin of deep continental roots**

[ADS](#) [CAS](#) [Google Scholar](#)

15. 15.

Boyd, F. R. & Gurney, J. J. Diamonds and the African lithosphere. *Science* **232**, 472–477 (1986).

[ADS](#) [CAS](#) [PubMed](#) [PubMed Central](#) [Google Scholar](#)

16. 16.

Pearson, D. G. The age of continental roots. *Lithos* **48**, 171–194 (1999).

[ADS](#) [CAS](#) [Google Scholar](#)

17. 17.

Hawkesworth, C. J., Cawood, P. A., Dhuime, B. & Kemp, T. I. S. Earth's continental lithosphere through time. *Annu. Rev. Earth Planet. Sci.* **45**, 169–198 (2017).

[ADS](#) [CAS](#) [Google Scholar](#)

18. 18.

Sleep, N. H., Ebinger, C. J. & Kendall, J. M. Deflection of mantle plume material by cratonic keels. *Geol. Soc. Lond. Spec. Publ.* **199**, 135–150 (2003).

[Google Scholar](#)

19. 19.

Foley, S. F. Rejuvenation and erosion of the cratonic lithosphere. *Nat. Geosci.* **1**, 503–510 (2008).

[ADS](#) [CAS](#) [Google Scholar](#)

20. 20.

Wang, H., van Hunen, J. & Pearson, D. G. The thinning of subcontinental lithosphere: the roles of plume impact and metasomatic

weakening. *Geochem. Geophys. Geosyst.* **16**, 1156–1171 (2015).

[ADS](#) [Google Scholar](#)

21. 21.

Simons, F. J., Zielhuis, A. & van der Hilst, R. D. The deep structure of the Australian continent from surface wave tomography. *Lithos* **48**, 17–43 (1999). **This paper revealed the widespread presence of very deep mantle roots beneath western Australia, outside of Archean nuclei.**

[ADS](#) [CAS](#) [Google Scholar](#)

22. 22.

James, D. E., Fouch, M. J., VanDecar, J. C., van der Lee, S. & Kaapvaal-Seismic-Group. Tectospheric structure beneath Southern Africa. *Geophys. Res. Lett.* **28**, 2485–2488 (2001).

[ADS](#) [Google Scholar](#)

23. 23.

Schaeffer, A. & Lebedev, S. in *The Earth's Heterogeneous Mantle* 3–46 (Springer, 2015).

24. 24.

Schaeffer, A. J. & Lebedev, S. Imaging the North American continent using waveform inversion of global and USArray data. *Earth Planet. Sci. Lett.* **402**, 26–41 (2014).

[ADS](#) [CAS](#) [Google Scholar](#)

25. 25.

Ortiz, K. et al. Upper mantle P and S wave velocity structure of the Kalahari Craton and surrounding Proterozoic terranes, southern Africa.

Geophys. Res. Lett. **46**, 9509–9518 (2019).

[ADS](#) [Google Scholar](#)

26. 26.

McKenzie, D. & Priestley, K. The influence of lithospheric thickness variations on continental evolution. *Lithos* **102**, 1–11 (2008).

[ADS](#) [CAS](#) [Google Scholar](#)

27. 27.

Artemieva, I. M. Global $1^\circ \times 1^\circ$ thermal model TC1 for the continental lithosphere: implications for lithosphere secular evolution. *Tectonophysics* **416**, 245–277 (2006).

[ADS](#) [Google Scholar](#)

28. 28.

Menzies, M. A., Fan, W.-M. & Zhang, M. Paleozoic and Cenozoic lithoprobes and the loss of >120 km of Archean lithosphere, Sino-Korean craton, China. In *Magmatic Processes and Plate Tectonics* 71–81 (Geological Soc., 1993). **This paper was the first to propose the dramatic lithospheric thinning beneath the eastern North China Craton.**

29. 29.

Carlson, R. W. & Irving, A. J. Depletion and enrichment history of subcontinental lithospheric mantle—an Os, Sr, Nd and Pb isotopic study of ultramafic xenoliths from the Northwestern Wyoming Craton. *Earth Planet. Sci. Lett.* **126**, 457–472 (1994).

[ADS](#) [CAS](#) [Google Scholar](#)

30. 30.

Gao, S., Rudnick, R. L., Carlson, R. W., McDonough, W. F. & Liu, Y. S. Re-Os evidence for replacement of ancient mantle lithosphere beneath the North China craton. *Earth Planet. Sci. Lett.* **198**, 307–322 (2002). **This paper convincingly demonstrates, using peridotite dating, that the ancient deep root of the North China Craton was replaced by shallow young lithosphere.**

[ADS](#) [CAS](#) [Google Scholar](#)

31. 31.

Snyder, D. B., Humphreys, E. & Pearson, D. G. Construction and destruction of some North American cratons. *Tectonophysics* **694**, 464–485 (2017).

[ADS](#) [CAS](#) [Google Scholar](#)

32. 32.

Ringwood, A. E. *Composition and Petrology of the Earth's Upper Mantle* (McGraw-Hill, 1975).

33. 33.

Afonso, J. C. & Schutt, D. L. The effects of polybaric partial melting on density and seismic velocities of mantle restites. *Lithos* **134/135**, 289–303 (2012).

[ADS](#) [Google Scholar](#)

34. 34.

Bernstein, S., Kelemen, P. B. & Brooks, C. K. Highly depleted spinel harzburgite xenoliths in Tertiary dikes from East Greenland. *Earth Planet. Sci. Lett.* **154**, 221–235 (1998).

[ADS](#) [CAS](#) [Google Scholar](#)

35. 35.

Walter, M. J. Melting of garnet peridotite and the origin of komatiite and depleted lithosphere. *J. Petrol.* **39**, 29–60 (1998). **These benchmark melting experiments calibrated much of our understanding of how the composition of mantle melt residues vary with melt fraction.**

[ADS](#) [CAS](#) [Google Scholar](#)

36. 36.

Herzberg, C. Geodynamic information in peridotite petrology. *J. Petrol.* **45**, 2507–2530 (2004).

[ADS](#) [CAS](#) [Google Scholar](#)

37. 37.

Bernstein, S., Kelemen, P. B. & Hanghøj, K. Consistent olivine Mg# in cratonic mantle reflects Archean mantle melting to the exhaustion of orthopyroxene. *Geology* **35**, 459–462 (2007). **This paper used olivine composition to recognize the ultra-depleted harzburgite/dunite nature of cratonic mantle, prior to ubiquitous metasomatism of these protoliths.**

[ADS](#) [CAS](#) [Google Scholar](#)

38. 38.

Afonso, J. C. et al. 3-D multiobservable probabilistic inversion for the compositional and thermal structure of the lithosphere and upper mantle. I: A priori petrological information and geophysical observables. *J. Geophys. Res. Solid Earth* **118**, 2586–2617 (2013).

[ADS](#) [Google Scholar](#)

39. 39.

Baptiste, V. & Tommasi, A. Petrophysical constraints on the seismic properties of the Kaapvaal craton mantle root. *Solid Earth* **5**, 45–63

(2014).

[ADS](#) [Google Scholar](#)

40. 40.

Peslier, A. H., Schönbächler, M., Busemann, H. & Karato, S.-I. Water in the Earth's interior: distribution and origin. *Space Sci. Rev.* **212**, 743–810 (2017).

[ADS](#) [CAS](#) [Google Scholar](#)

41. 41.

Doin, M. P., Fleitout, L. & Christensen, U. Mantle convection and stability of depleted and undepleted continental lithosphere. *J. Geophys. Res. Solid Earth* **102**, 2771–2787 (1997). **This paper and ref. 42 (Lenardic, 1999) are the pioneering dynamical models exploring the factors controlling cratonic mantle root stability.**

[Google Scholar](#)

42. 42.

Lenardic, A. & Moresi, L. N. Some thoughts on the stability of cratonic lithosphere: effects of buoyancy and viscosity. *J. Geophys. Res. Solid Earth* **104** (B6), 12747–12758 (1999).

[Google Scholar](#)

43. 43.

Artemieva, I. M., Thybo, H. & Cherepanova, Y. Isopycnicity of cratonic mantle restricted to kimberlite provinces. *Earth Planet. Sci. Lett.* **505**, 13–19 (2019).

[ADS](#) [CAS](#) [Google Scholar](#)

44. 44.

Snyder, D. B. & Lockhart, G. Does seismically anisotropic subcontinental mantle lithosphere require metasomatic wehrlite-pyroxenite dyke stockworks? *Lithos* **112**, 961–965 (2009).

[ADS](#) [Google Scholar](#)

45. 45.

Smith, D., Griffin, W. L., Ryan, C. G. & Sie, S. H. Trace-element zonation in garnets from The Thumb—heating and melt infiltration below the Colorado Plateau. *Contrib. Mineral. Petrol.* **107**, 60–79 (1991).

[ADS](#) [CAS](#) [Google Scholar](#)

46. 46.

Kopylova, M. G. & Russell, J. K. Chemical stratification of cratonic lithosphere: constraints from the Northern Slave craton, Canada. *Earth Planet. Sci. Lett.* **181**, 71–87 (2000).

[ADS](#) [CAS](#) [Google Scholar](#)

47. 47.

Pearson, D. G. & Wittig, N. in *Treatise on Geochemistry* 2nd edn, 255–292 (Elsevier, 2014).

48. 48.

Hanghoj, K., Kelemen, P., Bernstein, S., Blusztajn, J. & Frei, R. Osmium isotopes in the Wiedemann Fjord mantle xenoliths: a unique record of cratonic mantle formation by melt depletion in the Archaean. *Geochem. Geophys. Geosyst.* **2**, 2000GC000085 (2001).

[Google Scholar](#)

49. 49.

Pearson, D. G., Irvine, G. J. & Carlson, R. W. G., K. M. & Ionov, D. A. The development of lithospheric mantle keels beneath the earliest continents: time constraints using PGE and Re-Os isotope systematics. In *The Early Earth: Physical, Chemical and Biological Development* Vol. 199, 65–90 (Geological Society of London, Special Publication, 2002).

50. 50.

Smith, D. & Boyd, F. R. Compositional zonation in garnets in peridotite xenoliths. *Contrib. Mineral. Petrol.* **112**, 134–147 (1992).

[ADS](#) [CAS](#) [Google Scholar](#)

51. 51.

van Achterbergh, E., Griffin, W. L. & Stiefenhofer, J. Metasomatism in mantle xenoliths from the Letlhakane kimberlites: estimation of element fluxes. *Contrib. Mineral. Petrol.* **141**, 397–414 (2001).

[ADS](#) [Google Scholar](#)

52. 52.

Shimizu, N., Pokhilenko, N. P., Boyd, F. R. & Pearson, D. G. Geochemical characteristics of mantle xenoliths from Udachnaya kimberlite pipe. *Geol. Geof.* **38**, 194–205 (1997).

[CAS](#) [Google Scholar](#)

53. 53.

Simon, N. S. C., Irvine, G. J., Davies, G. R., Pearson, D. G. & Carlson, R. W. The origin of garnet and clinopyroxene in “depleted” Kaapvaal peridotites. *Lithos* **71**, 289–322 (2003).

[ADS](#) [CAS](#) [Google Scholar](#)

54. 54.

Boyd, F. R. et al. Composition of the Siberian cratonic mantle: evidence from Udachnaya peridotite xenoliths. *Contrib. Mineral. Petrol.* **128**, 228–246 (1997).

[ADS](#) [CAS](#) [Google Scholar](#)

55. 55.

Griffin, W. L., O'Reilly, S. Y., Afonso, J. C. & Begg, G. C. The composition and evolution of lithospheric mantle: a re-evaluation and its tectonic implications. *J. Petrol.* **50**, 1185–1204 (2009).

[ADS](#) [CAS](#) [Google Scholar](#)

56. 56.

Aulbach, S. Craton nucleation and formation of thick lithospheric roots. *Lithos* **149**, 16–30 (2012).

[ADS](#) [CAS](#) [Google Scholar](#)

57. 57.

Pearson, D. G. et al. Characteristics and origin of the mantle root beneath the Murowa diamond mine: implications for craton and diamond formation. In *Geoscience and Exploration of the Argyle, Bunder, Diavik and Murowa Diamond Deposits* Vol. 20 (eds Davy, A. T. et al.) Ch. 19, 403–424 (Society of Economic Geologists Special Publication, 2018).

58. 58.

Bernstein, S., Hanghøj, K., Kelemen, P. B. & Brooks, C. K. Ultra-depleted, shallow cratonic mantle beneath West Greenland: dunitic xenoliths from Ubekendt Ejland. *Contrib. Mineral. Petrol.* **152**, 335–347 (2006).

[ADS](#) [CAS](#) [Google Scholar](#)

59. 59.

Wittig, N. et al. Origin of cratonic lithospheric mantle roots: a geochemical study of peridotites from the North Atlantic Craton, West Greenland. *Earth Planet. Sci. Lett.* **274**, 24–33 (2008).

[ADS](#) [CAS](#) [Google Scholar](#)

60. 60.

Boyd, F. R. Compositional distinction between oceanic and cratonic lithosphere. *Earth Planet. Sci. Lett.* **96**, 15–26 (1989). **This paper documented the striking compositional contrast between modern oceanic and cratonic mantle lithosphere and proposed that the latter is comprised of residues from komatiite extraction.**

[ADS](#) [CAS](#) [Google Scholar](#)

61. 61.

Pearson, D. G. et al. Re-Os, Sm-Nd, and Rb-Sr isotope evidence for thick archean lithospheric mantle beneath the Siberian Craton modified by multistage metasomatism. *Geochim. Cosmochim. Acta* **59**, 959–977 (1995).

[ADS](#) [CAS](#) [Google Scholar](#)

62. 62.

Brey, G. P. & Shu, Q. The birth, growth and ageing of the Kaapvaal subcratonic mantle. *Mineral. Petrol.* **112**, 23–41 (2018).

[ADS](#) [CAS](#) [Google Scholar](#)

63. 63.

Canil, D. Mildly incompatible elements in peridotites and the origins of mantle lithosphere. *Lithos* **77**, 375–393 (2004).

[ADS](#) [CAS](#) [Google Scholar](#)

64. 64.

Gibson, S. A., Malarkey, J. & Day, J. A. Melt depletion and enrichment beneath the Western Kaapvaal Craton: evidence from Finsch peridotite xenoliths. *J. Petrol.* **49**, 1817–1852 (2008).

[ADS](#) [CAS](#) [Google Scholar](#)

65. 65.

Helmstaedt, H. H. & Schulze, D. J. Southern African kimberlites and their mantle sample: implications for Archean tectonics and lithosphere evolution. In *Kimberlites and Related Rocks* (eds Ross, J. et al.) Vol. 1, 358–368 (GSA Spec. Publ. 14, Blackwell, 1989).

66. 66.

Herzberg, C. & Rudnick, R. Formation of cratonic lithosphere: an integrated thermal and petrological model. *Lithos* **149**, 4–15 (2012).

[ADS](#) [CAS](#) [Google Scholar](#)

67. 67.

Kelemen, P. B., Hart, S. R. & Bernstein, S. Silica enrichment in the continental upper mantle via melt/rock reaction. *Earth Planet. Sci. Lett.* **164**, 387–406 (1998). **This paper was first to outline a quantitative metasomatic origin for orthopyroxene enrichment in cratonic mantle, using trace elements to document low-pressure melt extraction followed by higher-pressure growth of metamorphic garnet.**

[ADS](#) [CAS](#) [Google Scholar](#)

68. 68.

Lee, C.-T. A., Luffi, P. & Chin, E. J. Building and destroying continental mantle. *Annu. Rev. Earth Planet. Sci.* **39**, 59–90 (2011).

[ADS](#) [CAS](#) [Google Scholar](#)

69. 69.

Lee, C. T. A. in *Archean Geodynamics and Environments* 89–110 (Geophysical Monograph, American Geophysical Union, 2006).

70. 70.

Servali, A. & Korenaga, J. Oceanic origin of continental mantle lithosphere. *Geology* **46**, 1047–1050 (2018).

[ADS](#) [CAS](#) [Google Scholar](#)

71. 71.

Stachel, T., Viljoen, K. S., Brey, G. & Harris, J. W. Metasomatic processes in lherzolitic and harzburgitic domains of diamondiferous lithospheric mantle: REE in garnets from xenoliths and inclusions in diamonds. *Earth Planet. Sci. Lett.* **159**, 1–12 (1998). **This paper used garnet Cr systematics to document high-pressure metamorphic origin of cratonic peridotites from low pressure melt residues.**

[ADS](#) [CAS](#) [Google Scholar](#)

72. 72.

Tainton, K. M. & McKenzie, D. The generation of kimberlites, lamproites, and their source rocks. *J. Petrol.* **35**, 787–817 (1994).

[ADS](#) [CAS](#) [Google Scholar](#)

73. 73.

Parman, S. W., Grove, T. L., Dann, J. C. & De Wit, M. J. A subduction origin for komatiites and cratonic lithospheric mantle. *S. Afr. J. Geol.*

107, 107–118 (2004).

[Google Scholar](#)

74. 74.

Carlson, R. W., Pearson, D. G. & James, D. E. Physical, chemical, and chronological characteristics of continental mantle. *Rev. Geophys.* **43**, <https://doi.org/10.1029/2004RG000156> (2005).

75. 75.

Simon, N. S. C., Carlson, R. W., Pearson, D. G. & Davies, G. R. The origin and evolution of the Kaapvaal cratonic lithospheric mantle. *J. Petrol.* **48**, 589–625 (2007).

[ADS](#) [CAS](#) [Google Scholar](#)

76. 76.

Pearson, D. G. & Wittig, N. Formation of Archaean continental lithosphere and its diamonds: the root of the problem. *J. Geol. Soc. Lond.* **165**, 895–914 (2008).

[Google Scholar](#)

77. 77.

Pearson, D. G., Carlson, R. W., Shirey, S. B., Boyd, F. R. & Nixon, P. H. Stabilization of Archean lithospheric mantle—a Re-Os isotope study of peridotite xenoliths from the Kaapvaal Craton. *Earth Planet. Sci. Lett.* **134**, 341–357 (1995).

[ADS](#) [CAS](#) [Google Scholar](#)

78. 78.

Walter, M. J. Melt extraction and compositional variability in the mantle. In *Treatise on Geochemistry* Vol. 2, Ch. 8, 363–394 (Elsevier,

2003).

79. 79.

Bell, D. R. et al. Silica and volatile-element metasomatism of Archean mantle: a xenolith-scale example from the Kaapvaal Craton. *Contrib. Mineral. Petrol.* **150**, 251–267 (2005).

[ADS](#) [CAS](#) [Google Scholar](#)

80. 80.

Ganne, J. & Feng, X. Primary magmas and mantle temperatures through time. *Geochem. Geophys. Geosyst.* **18**, 872–888 (2017).

[ADS](#) [CAS](#) [Google Scholar](#)

81. 81.

Pearson, D. G. & Wittig, N. The formation and evolution of the subcontinental mantle lithosphere—evidence from mantle xenoliths. In *Treatise of Geochemistry Vol. 3 The Mantle and Core Ch. 3.6*, 255–292 (2014).

82. 82.

Shu, Q. et al. The evolution of the Kaapvaal craton: a multi-isotopic perspective from lithospheric peridotites from Finsch diamond mine. *Precambr. Res.* **331**, 105380 (2019).

[ADS](#) [CAS](#) [Google Scholar](#)

83. 83.

Su, B. & Chen, Y. Making cratonic lithospheric mantle. *J. Geophys. Res. Solid Earth* **123**, 7688–7706 (2018).

[ADS](#) [CAS](#) [Google Scholar](#)

84. 84.

Gibson, S. A. & Mills, S. On the nature and origin of garnet in highly-refractory Archean lithospheric mantle: constraints from garnet exsolved in Kaapvaal craton orthopyroxenes. *Mineral. Mag.* **81**, 781–809 (2017).

[CAS](#) [Google Scholar](#)

85. 85.

Canil, D. & Lee, C. T. A. Were deep cratonic mantle roots hydrated in Archean oceans? *Geology* **37**, 667–670 (2009).

[ADS](#) [CAS](#) [Google Scholar](#)

86. 86.

Schulze, D. J. Calcium anomalies in the mantle and a subducted metaserpentinite origin for diamonds. *Nature* **319**, 483–485 (1986).
Initial exploration of the idea of subducted precursors to deep cratonic roots.

[ADS](#) [CAS](#) [Google Scholar](#)

87. 87.

Perchuk, A. L., Gerya, T. V., Zakharov, V. S. & Griffin, W. L. Building cratonic keels in precambrian plate tectonics. *Nature* **586**, 395–401 (2020).

[ADS](#) [CAS](#) [PubMed](#) [PubMed Central](#) [Google Scholar](#)

88. 88.

Regier, M. et al. An oxygen isotope test for the origin of Archean mantle roots. *Geochem. Persp. Lett.* **9**, 6–10 (2018).

[Google Scholar](#)

89. 89.

Liu, J. et al. Plume-driven retronization of deep continental lithosphere. *Nature* **592**, 732–736 (2021).

[ADS](#) [CAS](#) [PubMed](#) [PubMed Central](#) [Google Scholar](#)

90. 90.

Lee, C.-T. A. & Chin, E. J. Calculating melting temperatures and pressures of peridotite protoliths: implications for the origin of cratonic mantle. *Earth Planet. Sci. Lett.* **403**, 273–286 (2014).

[ADS](#) [CAS](#) [Google Scholar](#)

91. 91.

Scott, J. et al. Continent stabilisation by lateral accretion of subduction zone-processed depleted mantle residues; insights from Zealandia. *Earth Planet. Sci. Lett.* **507**, 175–186 (2019).

[ADS](#) [CAS](#) [Google Scholar](#)

92. 92.

Brandon, A. D., Snow, J. E., Walker, R. J., Morgan, J. W. & Mock, T. D. ^{190}Pt - ^{186}Os and ^{187}Re - ^{187}Os systematics of abyssal peridotites. *Earth Planet. Sci. Lett.* **177**, 319–335 (2000).

[ADS](#) [CAS](#) [Google Scholar](#)

93. 93.

Harvey, J. et al. Ancient melt extraction from the oceanic upper mantle revealed by Re–Os isotopes in abyssal peridotites from the Mid-Atlantic ridge. *Earth Planet. Sci. Lett.* **244**, 606–621 (2006).

[ADS](#) [CAS](#) [Google Scholar](#)

94. 94.

Kramers, J. D. Lead, uranium, strontium, potassium and rubidium in inclusion-bearing diamonds and mantle-derived xenoliths from southern Africa. *Earth Planet. Sci. Lett.* **42**, 58–70 (1979).

[ADS](#) [CAS](#) [Google Scholar](#)

95. 95.

Menzies, M. & Murthy, V. R. Enriched mantle: Nd and Sr isotopes in diopsides from kimberlite nodules. *Nature* **283**, 634–636 (1980).

Along with ref. 94 (Kramers, 1979) and ref. 96 (Richardson, 1984), this is a pioneering study defining the geochemical evidence for the longevity of cratonic roots.

[ADS](#) [CAS](#) [Google Scholar](#)

96. 96.

Richardson, S. H., Gurney, J. J., Erlank, A. J. & Harris, J. W. Origin of diamonds in old enriched mantle. *Nature* **310**, 198–202 (1984).

[ADS](#) [CAS](#) [Google Scholar](#)

97. 97.

Walker, R. J., Carlson, R. W., Shirey, S. B. & Boyd, F. R. Os, Sr, Nd, and Pb isotope systematics of southern African peridotite xenoliths—implications for the chemical evolution of subcontinental mantle. *Geochim. Cosmochim. Acta* **53**, 1583–1595 (1989). **These authors were the first to document melt-depletion ages in cratons using Re-Os isotopes.**

[ADS](#) [CAS](#) [Google Scholar](#)

98. 98.

Carlson, R. W. et al. Re-Os systematics of lithospheric peridotites: Implications for lithosphere formation and preservation. In *The J.B. Dawson Volume, Proceedings of the VIIth International Kimberlite Conference* (eds Gurney, J. J. Gurney, J. L. Pascoe, M. D. & Richardson, S. H.) 99–108 (Red Roof Design, 1999).

99. 99.

Griffin, W. L., Spetsius, Z. V., Pearson, N. J. & O'Reilly, S. Y. In situ Re-Os analysis of sulfide inclusions in kimberlitic olivine: new constraints on depletion events in the Siberian lithospheric mantle. *Geochem. Geophys. Geosyst.* **3**, <https://doi.org/10.1029/2001GC000287> (2002).

100. 100.

Irvine, G. J., Pearson, D. G. & Carlson, R. W. Lithospheric mantle evolution of the Kaapvaal Craton: a Re-Os isotope study of peridotite xenoliths from Lesotho kimberlites. *Geophys. Res. Lett.* **28**, 2505–2508 (2001).

[ADS](#) [CAS](#) [Google Scholar](#)

101. 101.

Rudnick, R. L. & Walker, R. J. Interpreting ages from Re-Os isotopes in peridotites. *Lithos* **112**, 1083–1095 (2009).

[ADS](#) [Google Scholar](#)

102. 102.

Liu, J. et al. Mapping lithospheric boundaries using Os isotopes of mantle xenoliths: an example from the North China Craton. *Geochim. Cosmochim. Acta* **75**, 3881–3902 (2011).

[ADS](#) [CAS](#) [Google Scholar](#)

103. 103.

Luguet, A. & Pearson, G. Dating mantle peridotites using Re-Os isotopes: the complex message from whole rocks, base metal sulfides, and platinum group minerals. *Am. Mineral.* **104**, 165–189 (2019).

[ADS](#) [Google Scholar](#)

104. 104.

Griffin, W. L. et al. The world turns over: Hadean–Archean crust–mantle evolution. *Lithos* **189**, 2–15 (2014).

[ADS](#) [CAS](#) [Google Scholar](#)

105. 105.

Meibom, A. et al. Re-Os isotopic evidence for long-lived heterogeneity and equilibration processes in the Earth’s upper mantle. *Nature* **419**, 705–708 (2002).

[ADS](#) [CAS](#) [PubMed](#) [PubMed Central](#) [Google Scholar](#)

106. 106.

Pearson, D. G., Parman, S. W. & Nowell, G. M. A link between large mantle melting events and continent growth seen in osmium isotopes. *Nature* **449**, 202–205 (2007).

[ADS](#) [CAS](#) [PubMed](#) [PubMed Central](#) [Google Scholar](#)

107. 107.

Bragagni, A. et al. The geological record of base metal sulfides in the cratonic mantle: a microscale $^{187}\text{Os}/^{188}\text{Os}$ study of peridotite xenoliths from Somerset Island, Rae Craton (Canada). *Geochim. Cosmochim. Acta* **216**, 264–285 (2017).

[ADS](#) [CAS](#) [Google Scholar](#)

108. 108.

van Acken, D. et al. Mesoarchean melting and Neoarchean to Paleoproterozoic metasomatism during the formation of the cratonic mantle keel beneath West Greenland. *Geochim. Cosmochim. Acta* **203**, 37–53 (2017).

[ADS](#) [Google Scholar](#)

109. 109.

Wainwright, A. N., Luguet, A., Fonseca, R. O. C. & Pearson, D. G. Investigating metasomatic effects on the ^{187}Os isotopic signature: a case study on micrometric base metal sulphides in metasomatised peridotite from the Letlhakane kimberlite (Botswana). *Lithos* **232**, 35–48 (2015).

[ADS](#) [CAS](#) [Google Scholar](#)

110. 110.

Beall, A. P., Moresi, L. & Cooper, C. M. Formation of cratonic lithosphere during the initiation of plate tectonics. *Geology* **46**, 487–490 (2018).

[ADS](#) [CAS](#) [Google Scholar](#)

111. 111.

Doucet, L. S., Ionov, D. A. & Golovin, A. V. Paleoproterozoic formation age for the Siberian cratonic mantle: Hf and Nd isotope data on refractory peridotite xenoliths from the Udachnaya kimberlite. *Chem. Geol.* **391**, 42–55 (2015).

[ADS](#) [CAS](#) [Google Scholar](#)

112. 112.

Ionov, D. A., Liu, Z., Golovin, A. V., Korsakov, A. V. & Xu, Y. The age and origin of cratonic lithospheric mantle: Archean dunites vs.

Paleoproterozoic harzburgites from the Udachnaya kimberlite, Siberian craton. *Geochim. Cosmochim. Acta* **281**, 67–90 (2020).

[ADS](#) [CAS](#) [Google Scholar](#)

113. 113.

Liu, J. et al. Diamondiferous Paleoproterozoic mantle roots beneath Arctic Canada: a study of mantle xenoliths from Parry Peninsula and Central Victoria Island. *Geochim. Cosmochim. Acta* **239**, 284–311 (2018).

[ADS](#) [CAS](#) [Google Scholar](#)

114. 114.

Czas, J., Pearson, D. G., Stachel, T., Kjarsgaard, B. A. & Read, G. H. A Palaeoproterozoic diamond-bearing lithospheric mantle root beneath the Archean Sask Craton, Canada. *Lithos* **356/357**, 105301 (2020).

[Google Scholar](#)

115. 115.

Luguet, A. et al. An integrated petrological, geochemical and Re-Os isotope study of peridotite xenoliths from the Argyle lamproite, Western Australia and implications for cratonic diamond occurrences. *Lithos* **112**, 1096–1108 (2009).

[ADS](#) [Google Scholar](#)

116. 116.

Wittig, N. et al. Formation of the North Atlantic Craton: timing and mechanisms constrained from Re-Os isotope and PGE data of peridotite xenoliths from SW Greenland. *Chem. Geol.* **276**, 166–187 (2010).

[ADS](#) [CAS](#) [Google Scholar](#)

117. 117.

Griffin, W. L., Graham, S., O'Reilly, S. Y. & Pearson, N. J. Lithosphere evolution beneath the Kaapvaal Craton: Re–Os systematics of sulfides in mantle-derived peridotites. *Chem. Geol.* **208**, 89–118 (2004).

[ADS](#) [CAS](#) [Google Scholar](#)

118. 118.

Schoene, B., de Wit, M. J. & Bowring, S. A. Mesoarchean assembly and stabilization of the eastern Kaapvaal craton: a structural-thermochronological perspective. *Tectonics* **27**, <https://doi.org/10.1029/2008TC002267> (2008).

119. 119.

Eglington, B. Evolution of the Namaqua-Natal Belt, southern Africa—a geochronological and isotope geochemical review. *J. Afr. Earth Sci.* **46**, 93–111 (2006).

[ADS](#) [CAS](#) [Google Scholar](#)

120. 120.

Janney, P. E. et al. Age, composition and thermal characteristics of South African off-craton mantle lithosphere: evidence for a multi-stage history. *J. Petrol.* **51**, 1849–1890 (2010).

[ADS](#) [CAS](#) [Google Scholar](#)

121. 121.

Eglington, B. M. & Armstrong, R. A. The Kaapvaal Craton and adjacent orogens, southern Africa: a geochronological database and overview of the geological development of the craton. *S. Afr. J. Geol.* **107**, 13–32 (2004).

[Google Scholar](#)

122. 122.

Mather, K. A., Pearson, D. G., McKenzie, D., Kjarsgaard, B. A. & Priestley, K. Constraints on the depth and thermal history of cratonic lithosphere from peridotite xenoliths, xenocrysts and seismology. *Lithos* **125**, 729–742 (2011).

[ADS](#) [CAS](#) [Google Scholar](#)

123. 123.

Ionov, D. A., Carlson, R. W., Doucet, L. S., Golovin, A. V. & Oleinikov, O. B. The age and history of the lithospheric mantle of the Siberian craton: Re–Os and PGE study of peridotite xenoliths from the Obnazhennaya kimberlite. *Earth Planet. Sci. Lett.* **428**, 108–119 (2015).

[ADS](#) [CAS](#) [Google Scholar](#)

124. 124.

Pernet-Fisher, J. F. et al. Plume impingement on the Siberian SCLM: evidence from Re–Os isotope systematics. *Lithos* **218–219**, 141–154 (2015).

[ADS](#) [Google Scholar](#)

125. 125.

Liu, J. et al. Age and evolution of the deep continental root beneath the central Rae craton, northern Canada. *Precambr. Res.* **272**, 168–184 (2016).

[ADS](#) [CAS](#) [Google Scholar](#)

126. 126.

Smit, K. V., Pearson, D. G., Stachel, T. & Seller, M. Peridotites from Attawapiskat, Canada: Mesoproterozoic reworking of Palaeoarchaean lithospheric mantle beneath the Northern Superior Superterrane. *J. Petrol.* **55**, 1829–1863 (2014).

[ADS](#) [CAS](#) [Google Scholar](#)

127. 127.

Liu, J., Scott, J. M., Martin, C. E. & Pearson, D. G. The longevity of Archean mantle residues in the convecting upper mantle and their role in young continent formation. *Earth Planet. Sci. Lett.* **424**, 109–118 (2015).

[ADS](#) [CAS](#) [Google Scholar](#)

128. 128.

Kamber, B. S. & Tomlinson, E. L. Petrological, mineralogical and geochemical peculiarities of Archean cratons. *Chem. Geol.* **511**, 123–151 (2019).

[ADS](#) [CAS](#) [Google Scholar](#)

129. 129.

Cawood, P. A. et al. Accretionary orogens through Earth history. *Geol. Soc. Lond. Spec. Publ.* **318**, <https://doi.org/10.1144/SP318.1> (2009).

130. 130.

Herzberg, C., Condie, K. & Korenaga, J. Thermal history of the Earth and its petrological expression. *Earth Planet. Sci. Lett.* **292**, 79–88 (2010).

[ADS](#) [CAS](#) [Google Scholar](#)

131. 131.

Li, X., Kind, R., Yuan, X., Wolbern, I. & Hanka, W. Rejuvenation of the lithosphere by the Hawaiian plume. *Nature* **427**, 827–829 (2004).

[ADS](#) [CAS](#) [PubMed](#) [PubMed Central](#) [Google Scholar](#)

132. 132.

Sand, K. K. et al. The lithospheric mantle below southern West Greenland: a geothermobarometric approach to diamond potential and mantle stratigraphy. *Lithos* **112**, 1155–1166 (2009).

[ADS](#) [Google Scholar](#)

133. 133.

Bernstein, S., Szilas, K. & Kelemen, P. B. Highly depleted cratonic mantle in West Greenland extending into diamond stability field in the Proterozoic. *Lithos* **168–169**, 160–172 (2013).

[ADS](#) [Google Scholar](#)

134. 134.

Hamilton, M. A., Pearson, D. G., Thompson, R. N., Kelley, S. P. & Emeleus, C. H. Rapid eruption of Skye lavas inferred from precise U-Pb and Ar-Ar dating of the Rum and Cuillin plutonic complexes. *Nature* **394**, 260–263 (1998).

[ADS](#) [CAS](#) [Google Scholar](#)

135. 135.

Nixon, P. H. Kimberlites in the south-west Pacific. *Nature* **287**, 718–720 (1980). **The study was the first to recognise thick oceanic lithospheric mantle and deeply derived oceanic magmas.**

[ADS](#) [Google Scholar](#)

136. 136.

Ishikawa, A., Pearson, D. G. & Dale, C. W. Ancient Os isotope signatures from the Ontong Java Plateau lithosphere: tracing lithospheric accretion history. *Earth Planet. Sci. Lett.* **301**, 159–170 (2011).

[ADS](#) [CAS](#) [Google Scholar](#)

137. 137.

Celli, N. L., Lebedev, S., Schaeffer, A. J. & Gaina, C. African cratonic lithosphere carved by mantle plumes. *Nat. Commun.* **11**, 92 (2020).

[ADS](#) [CAS](#) [PubMed](#) [PubMed Central](#) [Google Scholar](#)

138. 138.

Ayalew, D. & Gibson, S. L. Head-to-tail transition of the Afar mantle plume: geochemical evidence from a Miocene bimodal basalt–rhyolite succession in the Ethiopian Large Igneous Province. *Lithos* **112**, 461–476 (2009).

[ADS](#) [CAS](#) [Google Scholar](#)

139. 139.

Capitanio, F. A., Nebel, O. & Cawood, P. A. Thermochemical lithosphere differentiation and the origin of cratonic mantle. *Nature* **588**, 89–94 (2020).

[ADS](#) [CAS](#) [PubMed](#) [PubMed Central](#) [Google Scholar](#)

140. 140.

Moyen, J. F. & van Hunen, J. Short-term episodicity of Archaean plate tectonics. *Geology* **40**, 451–454 (2012).

[ADS](#) [Google Scholar](#)

141. 141.

Wang, H., van Hunen, J. & Pearson, D. G. Making Archean cratonic roots by lateral compression: a two-stage thickening and stabilization model. *Tectonophysics* **746**, 562–571 (2018).

[ADS](#) [Google Scholar](#)

142. 142.

Oxburgh, E. R. & Parmentier, E. M. Thermal processes in the formation of continental lithosphere. *Phil. Trans. R. Soc. Math. Phys. Eng. Sci.* **288**, 415–425 (1978).

[ADS](#) [Google Scholar](#)

143. 143.

Jordan, T. H. Structure and formation of the continental lithosphere. *J. Petrol. Special Lithosphere Issue (Oceanic and Continental Lithosphere; Similarities and Differences)* 11–37 (1988).

144. 144.

McKenzie, D., Jackson, J. & Priestley, K. Thermal structure of oceanic and continental lithosphere. *Earth Planet. Sci. Lett.* **233**, 337–349 (2005).

[ADS](#) [CAS](#) [Google Scholar](#)

145. 145.

McKenzie, D. & Priestley, K. Speculations on the formation of cratons and cratonic basins. *Earth Planet. Sci. Lett.* **435**, 94–104 (2016).

[ADS](#) [Google Scholar](#)

146. 146.

Gray, R. & Pysklywec, R. N. Geodynamic models of mature continental collision: Evolution of an orogen from lithospheric

subduction to continental retreat/delamination. *J. Geophys. Res. Solid Earth* **117**, <https://doi.org/10.1029/2011JB008692> (2012).

147. 147.

Nicolas, A., Boudier, F. & Boullier, M. Mechanisms of flow in naturally and experimentally deformed peridotites. *Am. J. Sci.* **273**, 853–876 (1973). **Key study relating olivine flow in experiments, with real rock structures and seismic anisotropy.**

[ADS](#) [CAS](#) [Google Scholar](#)

148. 148.

Liddell, M. V., Bastow, I. D., Darbyshire, F., Gilligan, A. & Pugh, S. The formation of Laurentia: evidence from shear wave splitting. *Earth Planet. Sci. Lett.* **479**, 170–178 (2017).

[ADS](#) [CAS](#) [Google Scholar](#)

149. 149.

Priestley, K., Ho, T. & McKenzie, D. The formation of continental roots. *Geology* **49**, 190–194 (2020).

[ADS](#) [Google Scholar](#)

150. 150.

Hoffman, P. F. United plates of America, the birth of a craton: Early Proterozoic assembly and growth of Laurentia. *Annu. Rev. Earth Planet. Sci.* **16**, 543–603 (1988).

[ADS](#) [Google Scholar](#)

151. 151.

Percival, J. A. & Pysklywec, R. N. Are Archean lithospheric keels inverted? *Earth Planet. Sci. Lett.* **254**, 393–403 (2007).

[ADS](#) [CAS](#) [Google Scholar](#)

152. 152.

Van Kranendonk, M. J., Smithies, R. H., Hickman, A. H. & Champion, D. C. Secular tectonic evolution of Archean continental crust: interplay between horizontal and vertical processes in the formation of the Pilbara Craton, Australia. *Terra Nova* **19**, 1–38 (2007).

[ADS](#) [Google Scholar](#)

153. 153.

Francheteau, J. et al. High heat flow in southern Tibet. *Nature* **307**, 32–36 (1984).

[Google Scholar](#)

154. 154.

England, P. C. & Thompson, A. B. in *Collisional Tectonics* (eds Coward, M. P. & Reis, A. C.) Vol. 19, 83–94 (The Geological Society of London Special Publication, 1986).

155. 155.

Davis, W. J., Fryer, B. J. & King, J. E. Geochemistry and evolution of Late Archean plutonism and its significance to the tectonic development of the Slave Craton. *Precambr. Res.* **67**, 207–241 (1994).

[ADS](#) [Google Scholar](#)

156. 156.

Peterson, T. D., Scott, J. M. J., LeCheminant, A. N., Jefferson, C. W. & Pehrsson, S. J. The Kivalliq Igneous Suite: anorogenic bimodal magmatism at 1.75 Ga in the western Churchill Province, Canada. *Precambr. Res.* **262**, 101–119 (2015).

[ADS](#) [CAS](#) [Google Scholar](#)

157. 157.

Weller, O. M., Copley, A., Miller, W. G. R., Palin, R. M. & Dyck, B. The relationship between mantle potential temperature and oceanic lithosphere buoyancy. *Earth Planet. Sci. Lett.* **518**, 86–99 (2019).

[ADS](#) [CAS](#) [Google Scholar](#)

158. 158.

Rudnick, R. L. & Fountain, D. M. Nature and composition of the lower continental crust—a lower crustal perspective. *Rev. Geophys.* **33**, 267–309 (1995).

[ADS](#) [Google Scholar](#)

159. 159.

Reimink, J. R., Davies, J. H. F. L. & Ielpi, A. Global zircon analysis records a gradual rise of continental crust throughout the Neoarchean. *Earth Planet. Sci. Lett.* **554**, 116654 (2021).

[CAS](#) [Google Scholar](#)

160. 160.

Stern, T. A. et al. in *Continental Plate Boundary, Tectonics at South Island, New Zealand* (eds O’kaya, D., Stern, T. & Davey, F.) Vol. 175, 207–233 (American Geophysical Union, Geophysical Monograph, 2007).

161. 161.

Crameri, F., Shephard, G. E. & Heron, P. J. The misuse of colour in science communication. *Nat. Commun.* **11**, 5444 (2020).

[ADS](#) [CAS](#) [PubMed](#) [PubMed Central](#) [Google Scholar](#)

162. 162.

Moresi, L.-N. & Solomatov, V. S. Numerical investigation of 2D convection with extremely large viscosity variations. *Phys. Fluids* **7**, 2154–2162 (1995).

[ADS](#) [MATH](#) [Google Scholar](#)

163. 163.

Zhong, S., Zuber, M. T., Moresi, L. & Michael, G. Role of temperature-dependent viscosity and surface plates in spherical shell models of mantle convection. *J. Geophys. Res.* **105**, 11063–11082 (2000).

[ADS](#) [Google Scholar](#)

164. 164.

van Hunen, J., Zhong, S., Shapiro, N. M. & Ritzwoller, M. H. New evidence for dislocation creep from 3-D geodynamic modeling of the Pacific upper mantle structure. *Earth Planet. Sci. Lett.* **238**, 146–155 (2005).

[ADS](#) [Google Scholar](#)

165. 165.

Christensen, U. & Yuen, D. Layered convection induced by phase transitions. *J. Geophys. Res.* **90**, 10291–10300 (1985).

[ADS](#) [Google Scholar](#)

166. 166.

King, S. D. et al. A community benchmark for 2-D Cartesian compressible convection in the Earth's mantle. *Geophys. J.* **180**, 73–87 (2010).

[ADS](#) [Google Scholar](#)

167. 167.

Katz, R. F. A new parameterization of hydrous mantle melting. *Geochem. Geophys. Geosyst.* **4**, <https://doi.org/10.1029/2002GC000433> (2003).

168. 168.

Schutt, D. L. & Lesher, C. E. Effects of melt depletion on the density and seismic velocity of garnet and spinel lherzolite. *J. Geophys. Res.* **111**, B05401 (2006).

[ADS](#) [Google Scholar](#)

169. 169.

Chesley, J. T., Rudnick, R. L. & Lee, C. T. Re-Os systematics of mantle xenoliths from the East African Rift: age, structure, and history of the Tanzanian craton. *Geochim. Cosmochim. Acta* **63**, 1203–1217 (1999).

[ADS](#) [CAS](#) [Google Scholar](#)

170. 170.

Pearson, D. G., Irvine, G. J., Ionov, D. A., Boyd, F. R. & Dreibus, G. E. Re-Os isotope systematics and platinum group element fractionation during mantle melt extraction: a study of massif and xenolith peridotite suites. *Chem. Geol.* **208**, 29–59 (2004).

[ADS](#) [CAS](#) [Google Scholar](#)

171. 171.

Alard, O., Griffin, W. L., Pearson, N. J., Lorand, J.-P. & O'Reilly, S. Y. New insights into the Re–Os systematics of sub-continental

lithospheric mantle from in situ analysis of sulphides. *Earth Planet. Sci. Lett.* **203**, 651–663 (2002).

[ADS](#) [CAS](#) [Google Scholar](#)

172. 172.

Aulbach, S. et al. Mantle formation and evolution, Slave Craton: constraints from HSE abundances and Re–Os isotope systematics of sulfide inclusions in mantle xenocrysts. *Chem. Geol.* **208**, 61–88 (2004).

[ADS](#) [CAS](#) [Google Scholar](#)

173. 173.

Korenaga, J. Urey ratio and the structure and evolution of Earth's mantle. *Rev. Geophys.* **46**, <https://doi.org/10.1029/2007RG000241> (2008).

[Download references](#)

Acknowledgements

D.G.P. is grateful for a Canada Excellence Research Chair, which allowed the development of the data and ideas presented. A University of Otago, William Evans Visiting Fellowship was crucial to completing this manuscript. Modelling performed by L.H.W. was funded by Research Council of Norway (grant 280567). We thank P. Cawood for constructive comments.

Author information

Affiliations

1. Department of Earth and Atmospheric Sciences, University of Alberta, Edmonton, Alberta, Canada

D. Graham Pearson & Thomas Chacko

2. Department of Geology, University of Otago, Dunedin, New Zealand

James M. Scott

3. State Key Laboratory of Geological Processes and Mineral Resources, China University of Geosciences, Beijing, China

Jingao Liu

4. Geological Survey of Canada, Pacific Division, Natural Resources Canada, Sidney, BC, Canada

Andrew Schaeffer

5. Department of Environmental Analyses, Institute of Energy Technology, Oslo, Norway

Lawrence Hongliang Wang

6. Department of Earth Sciences, Durham University, Durham, UK

Jeroen van Hunen

7. Department of Geosciences and Natural Resource Management,
University of Copenhagen, Copenhagen, Denmark

Kristoffer Szilas

8. Lamont-Doherty Earth Observatory, Columbia University, Palisades,
USA

Peter B. Kelemen

Authors

1. D. Graham Pearson

[View author publications](#)

You can also search for this author in [PubMed](#) [Google Scholar](#)

2. James M. Scott

[View author publications](#)

You can also search for this author in [PubMed](#) [Google Scholar](#)

3. Jingao Liu

[View author publications](#)

You can also search for this author in [PubMed](#) [Google Scholar](#)

4. Andrew Schaeffer

[View author publications](#)

You can also search for this author in [PubMed](#) [Google Scholar](#)

5. Lawrence Hongliang Wang

[View author publications](#)

You can also search for this author in [PubMed](#) [Google Scholar](#)

6. Jeroen van Hunen

[View author publications](#)

You can also search for this author in [PubMed](#) [Google Scholar](#)

7. Kristoffer Szilas

[View author publications](#)

You can also search for this author in [PubMed](#) [Google Scholar](#)

8. Thomas Chacko

[View author publications](#)

You can also search for this author in [PubMed](#) [Google Scholar](#)

9. Peter B. Kelemen

[View author publications](#)

You can also search for this author in [PubMed](#) [Google Scholar](#)

Contributions

D.G.P. wrote the manuscript, with major contributions to the various concepts covered by J.M.S., T.C., J.L., A.S., L.H.W., J.v.H., P.B.K. and K.S. J.M.S. drafted the figures. A.S. provided the seismology models, L.H.W. performed the geodynamic models, augmented by J.v.H. J.L. performed the trace element modelling.

Corresponding author

Correspondence to [D. Graham Pearson](#).

Ethics declarations

Competing interests

The authors declare no competing interests.

Additional information

Peer review information *Nature* thanks Peter Cawood, Jolante van Wijk and the other, anonymous, reviewer(s) for their contribution to the peer review of this work.

Publisher's note Springer Nature remains neutral with regard to jurisdictional claims in published maps and institutional affiliations.

Supplementary information

Supplementary Information

This file contains Supplementary Figure 1a & 1b, and Supplementary Location Notes to Box 3a and 3b.

Supplementary Video 1

Video of dynamic model of lateral compression of cratonic mantle showing temperature and degree of melt depletion in the mantle. See “On-line Methods” for model methodology and caption to Figure 3 for further details.

Supplementary Video 2

Video of dynamic model of lateral compression of cratonic mantle showing temperature and viscosity in the mantle. See “On-line Methods” for model methodology and caption to Figure 3 for further details.

Supplementary Video 3

Video of the dynamics of the dispersion of mantle melting residues produced by mantle plumes showing temperature and extent of melt depletion in the mantle. See “On-line Methods” for model methodology and caption to Figure 3 for further details.

Supplementary Video 4

Video of the dynamics of the dispersion of mantle melting residues produced by mantle plumes showing temperature and viscosity in the mantle. See “On-line Methods” for model methodology and caption to Figure 3 for further details.

Rights and permissions

Reprints and Permissions

About this article



Check for
updates

Cite this article

Pearson, D.G., Scott, J.M., Liu, J. *et al.* Deep continental roots and cratons. *Nature* **596**, 199–210 (2021). <https://doi.org/10.1038/s41586-021-03600-5>

Download citation

- Received: 24 July 2020
- Accepted: 30 April 2021
- Published: 11 August 2021
- Issue Date: 12 August 2021

- DOI: <https://doi.org/10.1038/s41586-021-03600-5>

Comments

By submitting a comment you agree to abide by our [Terms](#) and [Community Guidelines](#). If you find something abusive or that does not comply with our terms or guidelines please flag it as inappropriate.

[Access through your institution](#)

[Change institution](#)

[Buy or subscribe](#)

Advertisement

This article was downloaded by **calibre** from <https://www.nature.com/articles/s41586-021-03600-5>

| [Section menu](#) | [Main menu](#) |

- Review Article
- [Published: 11 August 2021](#)

Exploring tissue architecture using spatial transcriptomics

- [Anjali Rao](#) [ORCID: orcid.org/0000-0001-8815-9865](#)^{1,na1},
- [Dalia Barkley](#)^{1,na1},
- [Gustavo S. França](#)¹ &
- [Itai Yanai](#) [ORCID: orcid.org/0000-0002-8438-2741](#)^{1,2}

[Nature](#) volume **596**, pages 211–220 (2021) [Cite this article](#)

- 5110 Accesses
- 163 Altmetric
- [Metrics details](#)

Subjects

- [Computational biology and bioinformatics](#)
- [Gene expression](#)
- [Physiology](#)
- [Transcriptomics](#)

Abstract

Deciphering the principles and mechanisms by which gene activity orchestrates complex cellular arrangements in multicellular organisms has far-reaching implications for research in the life sciences. Recent technological advances in next-generation sequencing- and imaging-based

approaches have established the power of spatial transcriptomics to measure expression levels of all or most genes systematically throughout tissue space, and have been adopted to generate biological insights in neuroscience, development and plant biology as well as to investigate a range of disease contexts, including cancer. Similar to datasets made possible by genomic sequencing and population health surveys, the large-scale atlases generated by this technology lend themselves to exploratory data analysis for hypothesis generation. Here we review spatial transcriptomic technologies and describe the repertoire of operations available for paths of analysis of the resulting data. Spatial transcriptomics can also be deployed for hypothesis testing using experimental designs that compare time points or conditions—including genetic or environmental perturbations. Finally, spatial transcriptomic data are naturally amenable to integration with other data modalities, providing an expandable framework for insight into tissue organization.

Access options

Subscribe to Journal

Get full journal access for 1 year

\$199.00

only \$3.90 per issue

[Subscribe](#)

All prices are NET prices.

VAT will be added later in the checkout.

Tax calculation will be finalised during checkout.

Rent or Buy article

Get time limited or full article access on ReadCube.

from \$8.99

Rent or Buy

All prices are NET prices.

Additional access options:

- [Log in](#)
- [Access through your institution](#)
- [Learn about institutional subscriptions](#)

Fig. 1: The technologies of spatial transcriptomics provide a gene-expression matrix.

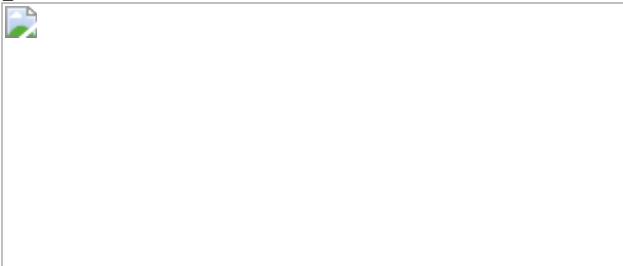


Fig. 2: Exploratory data analysis using spatial transcriptomic datasets.

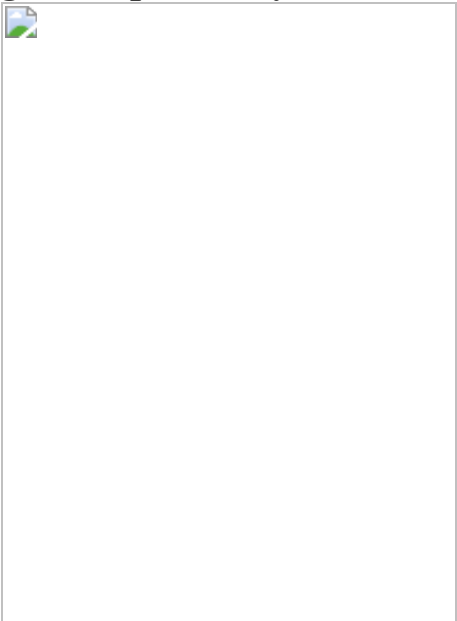
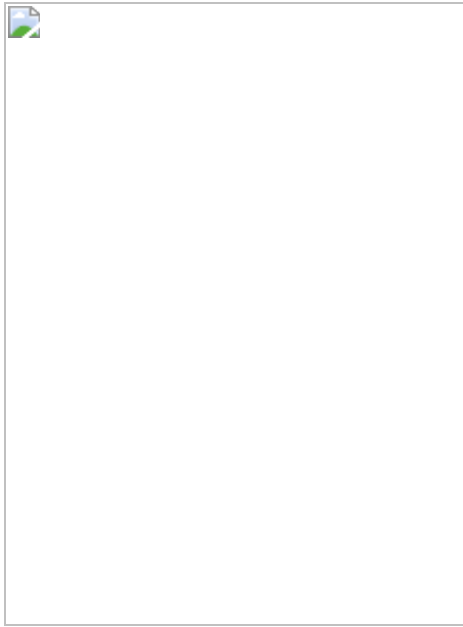


Fig. 3: Hypothesis generation and testing using spatial transcriptomics.



References

1. 1.

Barresi, M. J. F. & Gilbert, S. F. *Developmental Biology* (Sinauer Associates, 2019).

2. 2.

Damjanov, I. & McCue, P. A. *Histopathology: A Color Atlas and Textbook* (Lippincott Williams & Wilkins, 1996).

3. 3.

Safai, B. & Good, R. A. *Immunodermatology* (Springer Science & Business Media, 2013).

4. 4.

Lehmann, R. & Tautz, D. in *Methods in Cell Biology* Vol. 44 (eds Lawrence, S. B. & Fyrberg, E. A.) 575–598 (Academic Press, 1994).

5. 5.

Swanson, P. E. Foundations of immunohistochemistry. A practical review. *Am. J. Clin. Pathol.* **90**, 333–339 (1988).

[CAS](#) [Google Scholar](#)

6. 6.

Mincarelli, L., Lister, A., Lipscombe, J. & Macaulay, I. C. Defining cell identity with single-cell omics. *Proteomics* **18**, e1700312 (2018).

[Google Scholar](#)

7. 7.

Macaulay, I. C., Ponting, C. P. & Voet, T. Single-cell multiomics: multiple measurements from single cells. *Trends Genet.* **33**, 155–168 (2017).

[CAS](#) [PubMed](#) [PubMed Central](#) [Google Scholar](#)

8. 8.

Tanay, A & Regev A. Scaling single-cell genomics from phenomenology to mechanism. *Nature* **541**, 331–338 (2017).

[ADS](#) [CAS](#) [PubMed](#) [PubMed Central](#) [Google Scholar](#)

9. 9.

Xia, B. & Yanai, I. A periodic table of cell types. *Development* **146**, dev169854 (2019).

[CAS](#) [PubMed](#) [PubMed Central](#) [Google Scholar](#)

10. 10.

Stubbington, M. J. T., Rozenblatt-Rosen, O., Regev, A. & Teichmann, S. Single-cell transcriptomics to explore the immune system in health and disease. *Science* **358**, 58–63 (2017).

[ADS](#) [CAS](#) [PubMed](#) [PubMed Central](#) [Google Scholar](#)

11. 11.

Lawson, D. A., Kessenbrock, K., Davis, R. T., Pervolarakis, N. & Werb, Z. Tumour heterogeneity and metastasis at single-cell resolution. *Nat. Cell Biol.* **20**, 1349–1360 (2018).

[CAS](#) [PubMed](#) [PubMed Central](#) [Google Scholar](#)

12. 12.

Papalexis, E. & Satija, R. Single-cell RNA sequencing to explore immune cell heterogeneity. *Nat. Rev. Immunol.* **18**, 35–45 (2018).

[CAS](#) [Google Scholar](#)

13. 13.

Combs, P. A. & Eisen, M. B. Sequencing mRNA from cryo-sliced *Drosophila* embryos to determine genome-wide spatial patterns of gene expression. *PLoS ONE* **8**, e71820 (2013).

[ADS](#) [CAS](#) [PubMed](#) [PubMed Central](#) [Google Scholar](#)

14. 14.

Junker, J. P. et al. Genome-wide RNA tomography in the zebrafish embryo. *Cell* **159**, 662–675 (2014).

[CAS](#) [Google Scholar](#)

15. 15.

Lacraz, G. P. A. et al. Tomo-seq identifies SOX9 as a key regulator of cardiac fibrosis during ischemic injury. *Circulation* **136**, 1396–1409 (2017).

[CAS](#) [Google Scholar](#)

16. 16.

van den Brink, S. C. et al. Single-cell and spatial transcriptomics reveal somitogenesis in gastruloids. *Nature* **582**, 405–409 (2020).

[ADS](#) [Google Scholar](#)

17. 17.

Nichterwitz, S. et al. Laser capture microscopy coupled with Smart-seq2 for precise spatial transcriptomic profiling. *Nat. Commun.* **7**, 12139 (2016).

[ADS](#) [CAS](#) [PubMed](#) [PubMed Central](#) [Google Scholar](#)

18. 18.

Nichterwitz, S., Benitez, J. A., Hoogstraaten, R., Deng, Q. & Hedlund, E. LCM-seq: a method for spatial transcriptomic profiling using laser capture microdissection coupled with PolyA-based RNA sequencing. *Methods Mol. Biol.* **1649**, 95–110 (2018).

[CAS](#) [Google Scholar](#)

19. 19.

Aguila, J. et al. Spatial transcriptomics and in silico random pooling identify novel markers of vulnerable and resistant midbrain dopamine neurons. Preprint at <https://doi.org/10.1101/334417> (2021).

20. 20.

Moor, A. E. et al. Spatial reconstruction of single enterocytes uncovers broad zonation along the intestinal villus axis. *Cell* **175**, 1156–1167.e15 (2018).

[CAS](#) [PubMed](#) [PubMed Central](#) [Google Scholar](#)

21. 21.

Chen, J. et al. Spatial transcriptomic analysis of cryosectioned tissue samples with Geo-seq. *Nat. Protoc.* **12**, 566–580 (2017).

[CAS](#) [PubMed](#) [PubMed Central](#) [Google Scholar](#)

22. 22.

Tirosh, I. et al. Dissecting the multicellular ecosystem of metastatic melanoma by single-cell RNA-seq. *Science* **352**, 189–196 (2016).

[ADS](#) [CAS](#) [PubMed](#) [PubMed Central](#) [Google Scholar](#)

23. 23.

Peng, G. et al. Molecular architecture of lineage allocation and tissue organization in early mouse embryo. *Nature* **572**, 528–532 (2019).

[ADS](#) [CAS](#) [Google Scholar](#)

24. 24.

Geiss, G. K. et al. Direct multiplexed measurement of gene expression with color-coded probe pairs. *Nat. Biotechnol.* **26**, 317–325 (2008).

[CAS](#) [Google Scholar](#)

25. 25.

Halpern, K. B. et al. Paired-cell sequencing enables spatial gene expression mapping of liver endothelial cells. *Nat. Biotechnol.* **36**, 962–970 (2018).

[CAS](#) [PubMed](#) [PubMed Central](#) [Google Scholar](#)

26. 26.

Boisset, J.-C. et al. Mapping the physical network of cellular interactions. *Nat. Methods* **15**, 547–553 (2018).

[CAS](#) [Google Scholar](#)

27. 27.

Giladi, A. et al. Dissecting cellular crosstalk by sequencing physically interacting cells. *Nat. Biotechnol.* **38**, 629–637 (2020).

[CAS](#) [Google Scholar](#)

28. 28.

Manco, R. et al. Clump sequencing exposes the spatial expression programs of intestinal secretory cells. *Nat. Commun.* **12**, 3074 (2021).

[ADS](#) [CAS](#) [PubMed](#) [PubMed Central](#) [Google Scholar](#)

29. 29.

Satija, R., Farrell, J. A., Gennert, D., Schier, A. F. & Regev, A. Spatial reconstruction of single-cell gene expression data. *Nat. Biotechnol.* **33**, 495–502 (2015).

[CAS](#) [PubMed](#) [PubMed Central](#) [Google Scholar](#)

30. 30.

Achim, K. et al. High-throughput spatial mapping of single-cell RNA-seq data to tissue of origin. *Nat. Biotechnol.* **33**, 503–509 (2015).

[CAS](#) [Google Scholar](#)

31. 31.

Pettit, J.-B. et al. Identifying cell types from spatially referenced single-cell expression datasets. *PLOS Comput. Biol.* **10**, e1003824 (2014).

[PubMed](#) [PubMed Central](#) [Google Scholar](#)

32. 32.

Karaïkos, N. et al. The *Drosophila* embryo at single-cell transcriptome resolution. *Science* **358**, 194–199 (2017).

[ADS](#) [CAS](#) [Google Scholar](#)

33. 33.

Cang, Z. & Nie, Q. Inferring spatial and signaling relationships between cells from single cell transcriptomic data. *Nat. Commun.* **11**, 2084 (2020).

[ADS](#) [CAS](#) [PubMed](#) [PubMed Central](#) [Google Scholar](#)

34. 34.

Zhuang, X. Spatially resolved single-cell genomics and transcriptomics by imaging. *Nat. Methods* **18**, 18–22 (2021).

[CAS](#) [Google Scholar](#)

35. 35.

Larsson, L., Frisén, J. & Lundeberg, J. Spatially resolved transcriptomics adds a new dimension to genomics. *Nat. Methods* **18**, 15–18 (2021).

[CAS](#) [Google Scholar](#)

36. 36.

Crosetto, N., Bienko, M. & van Oudenaarden, A. Spatially resolved transcriptomics and beyond. *Nat. Rev. Genet.* **16**, 57–66 (2015).

[CAS](#) [Google Scholar](#)

37. 37.

Moor, A. E. & Itzkovitz, S. Spatial transcriptomics: paving the way for tissue-level systems biology. *Curr. Opin. Biotechnol.* **46**, 126–133 (2017).

[CAS](#) [Google Scholar](#)

38. 38.

Asp, M., Bergenstråhle, J. & Lundeberg, J. Spatially resolved transcriptomes-next generation tools for tissue exploration. *BioEssays* **42**, e1900221 (2020).

[Google Scholar](#)

39. 39.

Waylen, L. N., Nim, H. T., Martelotto, L. G. & Ramialison, M. From whole-mount to single-cell spatial assessment of gene expression in 3D. *Commun. Biol.* **3**, 602 (2020).

[PubMed](#) [PubMed Central](#) [Google Scholar](#)

40. 40.

Teves, J. M. & Won, K. J. Mapping cellular coordinates through advances in spatial transcriptomics technology. *Mol. Cells* **43**, 591–599 (2020).

[CAS](#) [PubMed](#) [PubMed Central](#) [Google Scholar](#)

41. 41.

Ståhl, P. L. et al. Visualization and analysis of gene expression in tissue sections by spatial transcriptomics. *Science* **353**, 78–82 (2016).
This paper was the first to perform array-based spatial transcriptomics, using positional barcodes at a resolution of 200 µm, and demonstrated the approach on the mouse olfactory bulb.

[ADS](#) [Google Scholar](#)

42. 42.

Jemt, A. et al. An automated approach to prepare tissue-derived spatially barcoded RNA-sequencing libraries. *Sci. Rep.* **6**, 37137 (2016).

[ADS](#) [CAS](#) [PubMed](#) [PubMed Central](#) [Google Scholar](#)

43. 43.

Salmén, F. et al. Barcoded solid-phase RNA capture for spatial transcriptomics profiling in mammalian tissue sections. *Nat. Protoc.* **13**, 2501–2534 (2018).

[PubMed](#) [PubMed Central](#) [Google Scholar](#)

44. 44.

Thrane, K., Eriksson, H., Maaskola, J., Hansson, J. & Lundeberg, J. Spatially resolved transcriptomics enables dissection of genetic heterogeneity in stage III cutaneous malignant melanoma. *Cancer Res.* **78**, 5970–5979 (2018).

[CAS](#) [Google Scholar](#)

45. 45.

Baron, M. et al. The stress-like cancer cell state is a consistent component of tumorigenesis. *Cell Syst.* **11**, 536–546.e7 (2020).

[CAS](#) [Google Scholar](#)

46. 46.

Moncada, R. et al. Integrating microarray-based spatial transcriptomics and single-cell RNA-seq reveals tissue architecture in pancreatic ductal adenocarcinomas. *Nat. Biotechnol.* **38**, 333–342 (2020).

[CAS](#) [Google Scholar](#)

47. 47.

Ji, A. L. et al. Multimodal analysis of composition and spatial architecture in human squamous cell carcinoma. *Cell* **182**, 497–514.e22 (2020).

[CAS](#) [PubMed](#) [PubMed Central](#) [Google Scholar](#)

48. 48.

Hildebrandt, F. et al. Spatial transcriptomics to define transcriptional patterns of zonation and structural components in the liver. Preprint at <https://doi.org/10.1101/2021.01.11.426100> (2021).

49. 49.

Spatial Transcriptomics. *10x Genomics*
<https://www.10xgenomics.com/spatial-transcriptomics/> (2021).

50. 50.

Ortiz, C. et al. Molecular atlas of the adult mouse brain. *Sci. Adv.* **6**, eabb3446 (2020).

[ADS](#) [CAS](#) [PubMed](#) [PubMed Central](#) [Google Scholar](#)

51. 51.

Grauel, A. L. et al. TGF β -blockade uncovers stromal plasticity in tumors by revealing the existence of a subset of interferon-licensed fibroblasts. *Nat. Commun.* **11**, 6315 (2020).

[ADS](#) [CAS](#) [PubMed](#) [PubMed Central](#) [Google Scholar](#)

52. 52.

Asp, M. et al. A spatiotemporal organ-wide gene expression and cell atlas of the developing human heart. *Cell* **179**, 1647–1660.e19 (2019).

[CAS](#) [Google Scholar](#)

53. 53.

Rodrigues, S. G. et al. Slide-seq: A scalable technology for measuring genome-wide expression at high spatial resolution. *Science* **363**, 1463–1467 (2019). **This paper describes Slide-seq, an array-based method with 10µm resolution, performed in the cerebellum and hippocampus.**

[ADS](#) [CAS](#) [PubMed](#) [PubMed Central](#) [Google Scholar](#)

54. 54.

Stickels, R. R. et al. Highly sensitive spatial transcriptomics at near-cellular resolution with Slide-seqV2. *Nat. Biotechnol.* **39**, 313–319 (2021).

[CAS](#) [Google Scholar](#)

55. 55.

Vickovic, S. et al. High-definition spatial transcriptomics for *in situ* tissue profiling. *Nat. Methods* **16**, 987–990 (2019).

[CAS](#) [PubMed](#) [PubMed Central](#) [Google Scholar](#)

56. 56.

Liu, Y. et al. High-spatial-resolution multi-omics sequencing via deterministic barcoding in tissue. *Cell* **183**, 1665–1681.e18 (2020).

[CAS](#) [Google Scholar](#)

57. 57.

Chen, A. et al. Large field of view-spatially resolved transcriptomics at nanoscale resolution. Preprint at <https://doi.org/10.1101/2021.01.17.427004> (2021).

58. 58.

Cho, C.-S. et al. Microscopic examination of spatial transcriptome using Seq-scope. *Cell* **184**, 3559–3572.e22 (2021).

[CAS](#) [Google Scholar](#)

59. 59.

Fu, X. et al. Continuous polony gels for tissue mapping with high resolution and RNA capture efficiency. Preprint at <https://doi.org/10.1101/2021.03.17.435795> (2021).

60. 60.

Ke, R. et al. In situ sequencing for RNA analysis in preserved tissue and cells. *Nat. Methods* **10**, 857–860 (2013). **This was the first report of ISS, which was used to map the expression of 31 transcripts using four-base reads in breast cancer.**

[CAS](#) [Google Scholar](#)

61. 61.

Darmanis, S. et al. Single-cell RNA-seq analysis of infiltrating neoplastic cells at the migrating front of human glioblastoma. *Cell Rep.* **21**, 1399–1410 (2017).

[CAS](#) [PubMed](#) [PubMed Central](#) [Google Scholar](#)

62. 62.

Carow, B. et al. Spatial and temporal localization of immune transcripts defines hallmarks and diversity in the tuberculosis granuloma. *Nat. Commun.* **10**, 1823 (2019).

[ADS](#) [PubMed](#) [PubMed Central](#) [Google Scholar](#)

63. 63.

Tiklová, K. et al. Single-cell RNA sequencing reveals midbrain dopamine neuron diversity emerging during mouse brain development. *Nat. Commun.* **10**, 581 (2019).

[ADS](#) [PubMed](#) [PubMed Central](#) [Google Scholar](#)

64. 64.

Wang, X. et al. Three-dimensional intact-tissue sequencing of single-cell transcriptional states. *Science* **361**, eaat5691 (2018).

[PubMed](#) [PubMed Central](#) [Google Scholar](#)

65. 65.

Chen, X., Sun, Y.-C., Church, G. M., Lee, J. H. & Zador, A. M. Efficient in situ barcode sequencing using padlock probe-based BaristaSeq. *Nucleic Acids Res.* **46**, e22 (2018).

[CAS](#) [Google Scholar](#)

66. 66.

Chen, X. et al. High-throughput mapping of long-range neuronal projection using in situ sequencing. *Cell* **179**, 772–786.e19 (2019).

[CAS](#) [PubMed](#) [PubMed Central](#) [Google Scholar](#)

67. 67.

Gyllborg, D. et al. Hybridization-based in situ sequencing (HybISS) for spatially resolved transcriptomics in human and mouse brain tissue. *Nucleic Acids Res.* **48**, e112 (2020).

[CAS](#) [PubMed](#) [PubMed Central](#) [Google Scholar](#)

68. 68.

Fürth, D., Hatini, V. & Lee, J. H. In situ transcriptome accessibility sequencing (INSTA-seq). Preprint at <https://doi.org/10.1101/722819> (2019).

69. 69.

Alon, S. et al. Expansion sequencing: spatially precise in situ transcriptomics in intact biological systems. *Science* **371**, eaax2656 (2021).

[CAS](#) [PubMed](#) [PubMed Central](#) [Google Scholar](#)

70. 70.

Lee, J. H. et al. Highly multiplexed subcellular RNA sequencing in situ. *Science* **343**, 1360–1363 (2014). **This paper introduced an untargeted ISS method, FISSEQ, that generated 30 base reads from 8,102 genes in human primary fibroblasts.**

[ADS](#) [CAS](#) [PubMed](#) [PubMed Central](#) [Google Scholar](#)

71. 71.

Codeluppi, S. et al. Spatial organization of the somatosensory cortex revealed by osmFISH. *Nat. Methods* **15**, 932–935 (2018).

[CAS](#) [Google Scholar](#)

72. 72.

Chen, K. H., Boettiger, A. N., Moffitt, J. R., Wang, S. & Zhuang, X. Spatially resolved, highly multiplexed RNA profiling in single cells. *Science* **348**, aaa6090 (2015).

[PubMed](#) [PubMed Central](#) [Google Scholar](#)

73. 73.

Moffitt, J. R. et al. High-throughput single-cell gene-expression profiling with multiplexed error-robust fluorescence *in situ* hybridization. *Proc. Natl Acad. Sci. USA* **113**, 11046–11051 (2016).

[CAS](#) [PubMed](#) [PubMed Central](#) [Google Scholar](#)

74. 74.

Wang, G., Moffitt, J. R. & Zhuang, X. Multiplexed imaging of high-density libraries of RNAs with MERFISH and expansion microscopy. *Sci. Rep.* **8**, 4847 (2018).

[ADS](#) [PubMed](#) [PubMed Central](#) [Google Scholar](#)

75. 75.

Xia, C., Babcock, H. P., Moffitt, J. R. & Zhuang, X. Multiplexed detection of RNA using MERFISH and branched DNA amplification. *Sci. Rep.* **9**, 7721 (2019).

[ADS](#) [PubMed](#) [PubMed Central](#) [Google Scholar](#)

76. 76.

Moffitt, J. R. et al. Molecular, spatial, and functional single-cell profiling of the hypothalamic preoptic region. *Science* **362**, eaau5324 (2018).

[ADS](#) [PubMed](#) [PubMed Central](#) [Google Scholar](#)

77. 77.

Lubeck, E., Coskun, A. F., Zhiyentayev, T., Ahmad, M. & Cai, L. Single-cell *in situ* RNA profiling by sequential hybridization. *Nat. Methods* **11**, 360–361 (2014).

[CAS](#) [PubMed](#) [PubMed Central](#) [Google Scholar](#)

78. 78.

Shah, S., Lubeck, E., Zhou, W. & Cai, L. In situ transcription profiling of single cells reveals spatial organization of cells in the mouse hippocampus. *Neuron* **92**, 342–357 (2016).

[CAS](#) [PubMed](#) [PubMed Central](#) [Google Scholar](#)

79. 79.

Shah, S. et al. Dynamics and spatial genomics of the nascent transcriptome by intron seqFISH. *Cell* **174**, 363–376.e16 (2018).

[CAS](#) [PubMed](#) [PubMed Central](#) [Google Scholar](#)

80. 80.

Eng, C. L. et al. Transcriptome-scale super-resolved imaging in tissues by RNA seqFISH. *Nature* **568**, 235–239 (2019).

[ADS](#) [CAS](#) [PubMed](#) [PubMed Central](#) [Google Scholar](#)

81. 81.

Najman, L. & Schmitt, M. Watershed of a continuous function. *Signal Processing* **38**, 99–112 (1994).

[Google Scholar](#)

82. 82.

Park, J. et al. Segmentation-free inference of cell types from in situ transcriptomics data. Preprint at <https://doi.org/10.1101/800748> (2020).

83. 83.

Littman, R. et al. JSTA: joint cell segmentation and cell type annotation for spatial transcriptomics. Preprint at <https://doi.org/10.1101/2020.09.18.304147> (2020).

84. 84.

Qian, X. et al. Probabilistic cell typing enables fine mapping of closely related cell types in situ. *Nat. Methods* **17**, 101–106 (2020).

[CAS](#) [Google Scholar](#)

85. 85.

BRAIN Initiative Cell Census Network (BICCN). A multimodal cell census and atlas of the mammalian primary motor cortex. Preprint at <https://doi.org/10.1101/2020.10.19.343129>.

86. 86.

Kebschull, J. M. et al. Cerebellar nuclei evolved by repeatedly duplicating a conserved cell-type set. *Science* **370**, eabd5059 (2020).

[CAS](#) [Google Scholar](#)

87. 87.

Maynard, K. R. et al. Transcriptome-scale spatial gene expression in the human dorsolateral prefrontal cortex. *Nat. Neurosci.* **24**, 425–1436 (2021).

[CAS](#) [PubMed](#) [PubMed Central](#) [Google Scholar](#)

88. 88.

Chen, H. et al. Dissecting mammalian spermatogenesis using spatial transcriptomics. Preprint at <https://doi.org/10.1101/2020.10.17.343335> (2020).

89. 89.

Fawkner-Corbett, D. et al. Spatiotemporal analysis of human intestinal development at single-cell resolution. *Cell* **184**, 810–826.e23 (2021).

[CAS](#) [PubMed](#) [PubMed Central](#) [Google Scholar](#)

90. 90.

Garcia-Alonso, L. et al. Mapping the temporal and spatial dynamics of the human endometrium in vivo and in vitro. Preprint at <https://doi.org/10.1101/2021.01.02.425073> (2021).

91. 91.

Rozenblatt-Rosen, O. et al. The Human Tumor Atlas Network: charting tumor transitions across space and time at single-cell resolution. *Cell* **181**, 236–249 (2020).

[CAS](#) [PubMed](#) [PubMed Central](#) [Google Scholar](#)

92. 92.

Lein, E. S. et al. Genome-wide atlas of gene expression in the adult mouse brain. *Nature* **445**, 168–176 (2007).

[ADS](#) [CAS](#) [Google Scholar](#)

93. 93.

Berglund, E. et al. Spatial maps of prostate cancer transcriptomes reveal an unexplored landscape of heterogeneity. *Nat. Commun.* **9**, 2419 (2018).

[ADS](#) [PubMed](#) [PubMed Central](#) [Google Scholar](#)

94. 94.

Wang, Y., Ma, S. & Ruzzo, W. L. Spatial modeling of prostate cancer metabolic gene expression reveals extensive heterogeneity and selective vulnerabilities. *Sci. Rep.* **10**, 3490 (2020).

[ADS](#) [CAS](#) [PubMed](#) [PubMed Central](#) [Google Scholar](#)

95. 95.

Hwang, W. L. et al. Single-nucleus and spatial transcriptomics of archival pancreatic cancer reveals multi-compartment reprogramming after neoadjuvant treatment.
<https://doi.org/10.1101/2020.08.25.267336> (2020).

96. 96.

Smith, E. A. & Hodges, H. C. The spatial and genomic hierarchy of tumor ecosystems revealed by single-cell technologies. *Trends Cancer* **5**, 411–425 (2019).

[PubMed](#) [PubMed Central](#) [Google Scholar](#)

97. 97.

Navarro, J. F. et al. Spatial transcriptomics reveals genes associated with dysregulated mitochondrial functions and stress signaling in Alzheimer disease. *iScience* **23**, 101556 (2020).

[ADS](#) [CAS](#) [PubMed](#) [PubMed Central](#) [Google Scholar](#)

98. 98.

Chen, W.-T. et al. Spatial transcriptomics and *in situ* sequencing to study Alzheimer's disease. *Cell* **182**, 976–991.e19 (2020).

[CAS](#) [Google Scholar](#)

99. 99.

Maniatis, S. et al. Spatiotemporal dynamics of molecular pathology in amyotrophic lateral sclerosis. *Science* **364**, 89–93 (2019).

[ADS](#) [CAS](#) [Google Scholar](#)

100. 100.

Ma, F. et al. Single cell and spatial transcriptomics defines the cellular architecture of the antimicrobial response network in human leprosy granulomas. <https://doi.org/10.1101/2020.12.01.406819> (2020).

101. 101.

Boyd, D. F. et al. Exuberant fibroblast activity compromises lung function via ADAMTS4. *Nature* **587**, 466–471 (2020).

[ADS](#) [PubMed](#) [PubMed Central](#) [Google Scholar](#)

102. 102.

Janosevic, D. et al. The orchestrated cellular and molecular responses of the kidney to endotoxin define a precise sepsis timeline. *eLife* **10**, e62270 (2021).

[PubMed](#) [PubMed Central](#) [Google Scholar](#)

103. 103.

Carlberg, K. et al. Exploring inflammatory signatures in arthritic joint biopsies with Spatial Transcriptomics. *Sci. Rep.* **9**, 18975 (2019).

[ADS](#) [CAS](#) [PubMed](#) [PubMed Central](#) [Google Scholar](#)

104. 104.

Vickovic, S. et al. Three-dimensional spatial transcriptomics uncovers cell type dynamics in the rheumatoid arthritis synovium. Preprint at <https://doi.org/10.1101/2020.12.10.420463> (2020).

105. 105.

Tukey, J. W. *Exploratory Data Analysis* (1970). **John Tukey established the field of exploratory data analysis as an approach to discover trends prior to testing for any particular model.**

106. 106.

Yanai, I. & Lercher, M. What is the question? *Genome Biol.* **20**, 289 (2019).

[PubMed](#) [PubMed Central](#) [Google Scholar](#)

107. 107.

Yanai, I. & Lercher, M. The data-hypothesis conversation. *Genome Biol.* **22**, 58 (2021).

[PubMed](#) [PubMed Central](#) [Google Scholar](#)

108. 108.

Dries, R. et al. Giotto: a toolbox for integrative analysis and visualization of spatial expression data. *Genome Biol.* **22**, 78 (2021).

[CAS](#) [PubMed](#) [PubMed Central](#) [Google Scholar](#)

109. 109.

Stuart, T. et al. Comprehensive integration of single-cell data. *Cell* **177**, 1888–1902.e21 (2019).

[CAS](#) [PubMed](#) [PubMed Central](#) [Google Scholar](#)

110. 110.

Butler, A., Hoffman, P., Smibert, P., Papalexi, E. & Satija, R. Integrating single-cell transcriptomic data across different conditions, technologies, and species. *Nat. Biotechnol.* **36**, 411–420 (2018).

[CAS](#) [PubMed](#) [PubMed Central](#) [Google Scholar](#)

111. 111.

Bergensträhle, J., Larsson, L. & Lundeberg, J. Seamless integration of image and molecular analysis for spatial transcriptomics workflows. *BMC Genomics* **21**, 482 (2020).

[PubMed](#) [PubMed Central](#) [Google Scholar](#)

112. 112.

Pham, D. et al. stLearn: integrating spatial location, tissue morphology and gene expression to find cell types, cell-cell interactions and spatial trajectories within undissociated tissues. Preprint at <https://doi.org/10.1101/2020.05.31.125658> (2020).

113. 113.

Hafemeister, C. & Satija, R. Normalization and variance stabilization of single-cell RNA-seq data using regularized negative binomial regression. *Genome Biol.* **20**, 296 (2019).

[CAS](#) [PubMed](#) [PubMed Central](#) [Google Scholar](#)

114. 114.

Zhou, B. & Jin, W. Visualization of single cell RNA-seq data using *t*-SNE in R. *Methods Mol. Biol.* **2117**, 159–167 (2020).

[ADS](#) [CAS](#) [Google Scholar](#)

115. 115.

Becht, E. et al. Dimensionality reduction for visualizing single-cell data using UMAP. *Nat. Biotechnol.* **37**, 38–44 (2018).

[Google Scholar](#)

116. 116.

Kiselev, V. Y., Andrews, T. S. & Hemberg, M. Challenges in unsupervised clustering of single-cell RNA-seq data. *Nat. Rev. Genet.* **20**, 273–282 (2019).

[CAS](#) [Google Scholar](#)

117. 117.

Lundmark, A. et al. Gene expression profiling of periodontitis-affected gingival tissue by spatial transcriptomics. *Sci. Rep.* **8**, 9370 (2018).

[ADS](#) [PubMed](#) [PubMed Central](#) [Google Scholar](#)

118. 118.

Giacomello, S. et al. Spatially resolved transcriptome profiling in model plant species. *Nat. Plants* **3**, 17061 (2017).

[CAS](#) [Google Scholar](#)

119. 119.

Lee, D. D. & Seung, H. S. Learning the parts of objects by non-negative matrix factorization. *Nature* **401**, 788–791 (1999).

[ADS](#) [CAS](#) [MATH](#) [Google Scholar](#)

120. 120.

Gao, Y. & Church, G. Improving molecular cancer class discovery through sparse non-negative matrix factorization. *Bioinformatics* **21**, 3970–3975 (2005).

[CAS](#) [Google Scholar](#)

121. 121.

Zhao, E. et al. Spatial transcriptomics at subspot resolution with BayesSpace. *Nat. Biotechnol.* <https://doi.org/10.1038/s41587-021-00935-2> (2021).

122. 122.

Hunter, M. V., Moncada, R., Weiss, J. M., Yanai, I. & White, R. M. Spatial transcriptomics reveals the architecture of the

tumor/microenvironment interface. Preprint at
<https://doi.org/10.1101/2020.11.05.368753> (2021).

123. 123.

Moran, P. A. P. Notes on continuous stochastic phenomena. *Biometrika* **37**, 17–23 (1950).

[MathSciNet](#) [CAS](#) [PubMed](#) [MATH](#) [Google Scholar](#)

124. 124.

Vandenbon, A. & Diez, D. A clustering-independent method for finding differentially expressed genes in single-cell transcriptome data. *Nat. Commun.* **11**, 4318 (2020).

[ADS](#) [CAS](#) [PubMed](#) [PubMed Central](#) [Google Scholar](#)

125. 125.

Edsgård, D., Johnsson, P. & Sandberg, R. Identification of spatial expression trends in single-cell gene expression data. *Nat. Methods* **15**, 339–342 (2018).

[PubMed](#) [PubMed Central](#) [Google Scholar](#)

126. 126.

Illian, J., Penttinen, A., Stoyan, H. & Stoyan, D. *Statistical Analysis and Modelling of Spatial Point Patterns* (John Wiley & Sons, 2008).

127. 127.

Svensson, V., Teichmann, S. A. & Stegle, O. SpatialDE: identification of spatially variable genes. *Nat. Methods* **15**, 343–346 (2018).

[CAS](#) [PubMed](#) [PubMed Central](#) [Google Scholar](#)

128. 128.

Sun, S., Zhu, J. & Zhou, X. Statistical analysis of spatial expression patterns for spatially resolved transcriptomic studies. *Nat. Methods* **17**, 193–200 (2020).

[CAS](#) [PubMed](#) [PubMed Central](#) [Google Scholar](#)

129. 129.

Subramanian, A. et al. Gene set enrichment analysis: a knowledge-based approach for interpreting genome-wide expression profiles. *Proc. Natl Acad. Sci. USA* **102**, 15545–15550 (2005).

[ADS](#) [CAS](#) [PubMed](#) [PubMed Central](#) [Google Scholar](#)

130. 130.

The Gene Ontology Consortium. Gene ontology: tool for the unification of biology. *Nat. Genet.* **25**, 25–29 (2000).

[PubMed](#) [PubMed Central](#) [Google Scholar](#)

131. 131.

Kanehisa, M. & Goto, S. KEGG: Kyoto Encyclopedia of Genes And Genomes. *Nucleic Acids Res.* **28**, 27–30 (2000).

[CAS](#) [PubMed](#) [PubMed Central](#) [Google Scholar](#)

132. 132.

Elosua, M., Nieto, P., Mereu, E., Gut, I. & Heyn, H. SPOTlight: Seeded NMF regression to Deconvolute Spatial Transcriptomics Spots with Single-Cell Transcriptomes.

<https://doi.org/10.1101/2020.06.03.131334>.

133. 133.

Andersson, A. et al. Single-cell and spatial transcriptomics enables probabilistic inference of cell type topography. *Commun. Biol.* **3**, 565

(2020).

[PubMed](#) [PubMed Central](#) [Google Scholar](#)

134. 134.

Kleshchevnikov, V. et al. Comprehensive mapping of tissue cell architecture via integrated single cell and spatial transcriptomics. Preprint at <https://doi.org/10.1101/2020.11.15.378125> (2020).

135. 135.

Cable, D. M. et al. Robust decomposition of cell type mixtures in spatial transcriptomics. *Nat. Biotechnol.* <https://doi.org/10.1038/s41587-021-00830-w> (2021).

136. 136.

Lopez, R. et al. Multi-resolution deconvolution of spatial transcriptomics data reveals continuous patterns of inflammation. Preprint at <https://doi.org/10.1101/2021.05.10.443517> (2021).

137. 137.

Zeira, R., Land, M. & Raphael, B. J. Alignment and integration of spatial transcriptomics data. Preprint at <https://doi.org/10.1101/2021.03.16.435604> (2021).

138. 138.

Su, J. & Song, Q. DSTG: Deconvoluting Spatial Transcriptomics Data through Graph-based artificial intelligence. *Brief Bioinform.* <https://doi.org/10.1093/bib/bbaa414> (2021).

139. 139.

Biancalani, T. et al. Deep learning and alignment of spatially-resolved whole transcriptomes of single cells in the mouse brain with Tangram. Preprint at <https://doi.org/10.1101/2020.08.29.272831> (2020).

140. 140.

Nelson, M. E., Riva, S. G. & Cvejic, A. SMaSH: A scalable, general marker gene identification framework for single-cell RNA sequencing and spatial transcriptomics. Preprint at <https://doi.org/10.1101/2021.04.08.438978> (2021).

141. 141.

Dong, R. & Yuan, G.-C. SpatialDWLS: accurate deconvolution of spatial transcriptomic data. Preprint at <https://doi.org/10.1101/2021.02.02.429429> (2021).

142. 142.

Teng, H., Yuan, Y. & Bar-Joseph, Z. Cell type assignments for spatial transcriptomics data. Preprint at <https://doi.org/10.1101/2021.02.25.432887> (2021).

143. 143.

La Manno, G. et al. RNA velocity of single cells. *Nature* **560**, 494–498 (2018).

[ADS](#) [PubMed](#) [PubMed Central](#) [Google Scholar](#)

144. 144.

Patel, A. P. et al. Single-cell RNA-seq highlights intratumoral heterogeneity in primary glioblastoma. *Science* **344**, 1396–1401 (2014).

[ADS](#) [CAS](#) [PubMed](#) [PubMed Central](#) [Google Scholar](#)

145. 145.

Elyanow, R., Zeira, R., Land, M. & Raphael, B. STARCH: Copy number and clone inference from spatial transcriptomics data. *Phys. Biol.* **18**, 035001 (2021).

[CAS](#) [Google Scholar](#)

146. 146.

Armingol, E., Officer, A., Harismendy, O. & Lewis, N. E. Deciphering cell–cell interactions and communication from gene expression. *Nat. Rev. Genet.* **22**, 71–88 (2021).

[CAS](#) [Google Scholar](#)

147. 147.

Efremova, M., Vento-Tormo, M., Teichmann, S. A. & Vento-Tormo, R. CellPhoneDB: inferring cell-cell communication from combined expression of multi-subunit ligand-receptor complexes. *Nat. Protoc.* **15**, 1484–1506 (2020).

[CAS](#) [PubMed](#) [Google Scholar](#)

148. 148.

Browaeys, R., Saelens, W. & Saeys, Y. NicheNet: modeling intercellular communication by linking ligands to target genes. *Nat. Methods* **17**, 159–162 (2020).

[CAS](#) [Google Scholar](#)

149. 149.

Bergensträhle, L. et al. Super-resolved spatial transcriptomics by deep data fusion. Preprint at <https://doi.org/10.1101/2020.02.28.963413> (2020).

150. 150.

Tan, X., Su, A., Tran, M. & Nguyen, Q. SpaCell: integrating tissue morphology and spatial gene expression to predict disease cells. *Bioinformatics* **36**, 2293–2294 (2020).

[CAS](#) [Google Scholar](#)

151. 151.

Monjo, T., Kido, M., Nagasawa, S., Suzuki, Y. & Kamatani, Y. Efficient prediction of a spatial transcriptomics profile better characterizes breast cancer tissue sections without costly experimentation. Preprint at <https://doi.org/10.1101/2021.04.22.440763> (2021).

152. 152.

Bao, F. et al. Characterizing tissue composition through combined analysis of single-cell morphologies and transcriptional states. Preprint at <https://doi.org/10.1101/2020.09.05.284539> (2021).

153. 153.

He, B. et al. Integrating spatial gene expression and breast tumour morphology via deep learning. *Nat. Biomed. Eng.* **4**, 827–834 (2020).

[CAS](#) [Google Scholar](#)

154. 154.

Levy-Jurgenson, A., Tekpli, X., Kristensen, V. N. & Yakhini, Z. Spatial transcriptomics inferred from pathology whole-slide images links tumor heterogeneity to survival in breast and lung cancer. *Sci. Rep.* **10**, 18802 (2020).

[ADS](#) [CAS](#) [PubMed](#) [PubMed Central](#) [Google Scholar](#)

155. 155.

Takei, Y. et al. Integrated spatial genomics reveals global architecture of single nuclei. *Nature* **590**, 344–350 (2021).

[ADS](#) [CAS](#) [PubMed](#) [PubMed Central](#) [Google Scholar](#)

156. 156.

Deng, Y. et al. Spatial epigenome sequencing at tissue scale and cellular level. Preprint at <https://doi.org/10.1101/2021.03.11.434985> (2021).

157. 157.

Nguyen, H. Q. et al. 3D mapping and accelerated super-resolution imaging of the human genome using *in situ* sequencing. *Nat. Methods* **17**, 822–832 (2020).

[CAS](#) [PubMed](#) [PubMed Central](#) [Google Scholar](#)

158. 158.

Su, J.-H., Zheng, P., Kinrot, S. S., Bintu, B. & Zhuang, X. Genome-scale imaging of the 3D organization and transcriptional activity of chromatin. *Cell* **182**, 1641–1659.e26 (2020).

[CAS](#) [Google Scholar](#)

159. 159.

Payne, A. C. et al. *In situ* genome sequencing resolves DNA sequence and structure in intact biological samples. *Science* **371**, eaay3446 (2021).

[CAS](#) [Google Scholar](#)

160. 160.

Schulz, D. et al. Simultaneous multiplexed imaging of mRNA and proteins with subcellular resolution in breast cancer tissue samples by mass cytometry. *Cell Syst.* **6**, 531 (2018).

[CAS](#) [PubMed](#) [PubMed Central](#) [Google Scholar](#)

161. 161.

Stoeckius, M. et al. Simultaneous epitope and transcriptome measurement in single cells. *Nat. Methods* **14**, 865–868 (2017).

[CAS](#) [PubMed](#) [PubMed Central](#) [Google Scholar](#)

162. 162.

Angelo, M. et al. Multiplexed ion beam imaging of human breast tumors. *Nat. Med.* **20**, 436–442 (2014).

[CAS](#) [PubMed](#) [PubMed Central](#) [Google Scholar](#)

163. 163.

Keren, L. et al. A structured tumor-immune microenvironment in triple negative breast cancer revealed by multiplexed ion beam imaging. *Cell* **174**, 1373–1387.e19 (2018).

[CAS](#) [PubMed](#) [PubMed Central](#) [Google Scholar](#)

164. 164.

Piehowski, P. D. et al. Automated mass spectrometry imaging of over 2000 proteins from tissue sections at 100- μm spatial resolution. *Nat. Commun.* **11**, 8 (2020).

[ADS](#) [CAS](#) [PubMed](#) [PubMed Central](#) [Google Scholar](#)

165. 165.

Lin, J.-R. et al. Highly multiplexed immunofluorescence imaging of human tissues and tumors using t-CyCIF and conventional optical microscopes. *eLife* **7**, e31657 (2018).

[PubMed](#) [PubMed Central](#) [Google Scholar](#)

166. 166.

Goltsev, Y. et al. Deep profiling of mouse splenic architecture with CODEX multiplexed imaging. *Cell* **174**, 968–981.e15 (2018).

[CAS](#) [PubMed](#) [PubMed Central](#) [Google Scholar](#)

167. 167.

Kohman, R. E. & Church, G. M. Fluorescent *in situ* sequencing of DNA barcoded antibodies. Preprint at <https://doi.org/10.1101/2020.04.27.060624> (2020).

168. 168.

Liu, Y., Enninfu, A., Deng, Y. & Fan, R. Spatial transcriptome sequencing of FFPE tissues at cellular level. Preprint at <https://doi.org/10.1101/2020.10.13.338475> (2020).

169. 169.

Nagarajan, M. B., Tentori, A. M., Zhang, W. C., Slack, F. J. & Doyle, P. S. Spatially resolved and multiplexed MicroRNA quantification from tissue using nanoliter well arrays. *Microsyst. Nanoeng.* **6**, 51 (2020).

[ADS](#) [CAS](#) [Google Scholar](#)

170. 170.

Lander, E. S. et al. Initial sequencing and analysis of the human genome. *Nature* **409**, 860–921 (2001).

[ADS](#) [CAS](#) [Google Scholar](#)

171. 171.

Venter, J. C. et al. The sequence of the human genome. *Science* **291**, 1304–1351 (2001).

[ADS](#) [CAS](#) [Google Scholar](#)

172. 172.

Nitzan, M., Karaïkos, N., Friedman, N. & Rajewsky, N. Gene expression cartography. *Nature* **576**, 132–137 (2019).

[ADS](#) [CAS](#) [Google Scholar](#)

173. 173.

Xia, C., Fan, J., Emanuel, G., Hao, J. & Zhuang, X. Spatial transcriptome profiling by MERFISH reveals subcellular RNA compartmentalization and cell cycle-dependent gene expression. *Proc. Natl Acad. Sci. USA* **116**, 19490–19499 (2019).

[CAS](#) [PubMed](#) [PubMed Central](#) [Google Scholar](#)

174. 174.

Friedrich, S. & Sonnhammer, E. L. L. Fusion transcript detection using spatial transcriptomics. *BMC Med. Genomics* **13**, 110 (2020).

[CAS](#) [PubMed](#) [PubMed Central](#) [Google Scholar](#)

175. 175.

Joglekar, A. et al. A spatially resolved brain region- and cell type-specific isoform atlas of the postnatal mouse brain. *Nat. Commun.* **12**, 463 (2021).

[ADS](#) [CAS](#) [PubMed](#) [PubMed Central](#) [Google Scholar](#)

176. 176.

Frieda, K. L. et al. Synthetic recording and in situ readout of lineage information in single cells. *Nature* **541**, 107–111 (2017).

[ADS](#) [CAS](#) [Google Scholar](#)

177. 177.

Rodrigues, S. G. et al. Slide-seq: A scalable technology for measuring genome-wide expression at high spatial resolution. *Science* **363**, 1463–1467 (2019).

[ADS](#) [CAS](#) [PubMed](#) [PubMed Central](#) [Google Scholar](#)

[Download references](#)

Acknowledgements

We thank F. Kuperwaser, A. Pountain, B. Xia and other members of the Yanai laboratory, as well as M. Phillips for critical reading and feedback. We thank the students of the exploratory data analysis course at NYU Langone Health. I.Y. was supported by grants from the NIH (R01AI143290 and R01LM013522) and the Lowenstein Foundation, and D.B. was supported by the National Institutes for Health (F30CA257400).

Author information

Author notes

1. These authors contributed equally: Anjali Rao, Dalia Barkley

Affiliations

1. Institute for Computational Medicine, NYU Langone Health, New York, NY, USA

Anjali Rao, Dalia Barkley, Gustavo S. França & Itai Yanai

2. Department of Biochemistry and Molecular Pharmacology, NYU Langone Health, New York, NY, USA

Itai Yanai

Authors

1. Anjali Rao

[View author publications](#)

You can also search for this author in [PubMed](#) [Google Scholar](#)

2. Dalia Barkley

[View author publications](#)

You can also search for this author in [PubMed](#) [Google Scholar](#)

3. Gustavo S. França

[View author publications](#)

You can also search for this author in [PubMed](#) [Google Scholar](#)

4. Itai Yanai

[View author publications](#)

You can also search for this author in [PubMed](#) [Google Scholar](#)

Contributions

A.R., D.B. and I.Y. collectively wrote the review. A.R., D.B., G.S.F. and I.Y. edited and revised the manuscript and conceptualized the figures, which G.S.F. then designed and created.

Corresponding author

Correspondence to [Itai Yanai](#).

Ethics declarations

Competing interests

The authors declare no competing interests.

Additional information

Peer review information *Nature* thanks Guo-Cheng Yuan and the other, anonymous, reviewer(s) for their contribution to the peer review of this work.

Publisher's note Springer Nature remains neutral with regard to jurisdictional claims in published maps and institutional affiliations.

Rights and permissions

[Reprints and Permissions](#)

About this article



Cite this article

Rao, A., Barkley, D., França, G.S. *et al.* Exploring tissue architecture using spatial transcriptomics. *Nature* **596**, 211–220 (2021).
<https://doi.org/10.1038/s41586-021-03634-9>

[Download citation](#)

- Received: 03 February 2021
- Accepted: 11 May 2021
- Published: 11 August 2021
- Issue Date: 12 August 2021
- DOI: <https://doi.org/10.1038/s41586-021-03634-9>

Comments

By submitting a comment you agree to abide by our [Terms](#) and [Community Guidelines](#). If you find something abusive or that does not comply with our terms or guidelines please flag it as inappropriate.

[Access through your institution](#)

[Change institution](#)

[Buy or subscribe](#)

Advertisement

| [Section menu](#) | [Main menu](#) |

Demonstration of reduced neoclassical energy transport in Wendelstein 7-X

[Download PDF](#)

- Article
- Open Access
- [Published: 11 August 2021](#)

Demonstration of reduced neoclassical energy transport in Wendelstein 7-X

- [C. D. Beidler](#) [ORCID: orcid.org/0000-0002-4395-239X¹](#),
- [H. M. Smith¹](#),
- [A. Alonso](#) [ORCID: orcid.org/0000-0001-6863-8578²](#),
- [T. Andreeva¹](#),
- [J. Baldzuhn¹](#),
- [M. N. A. Beurskens¹](#),
- [M. Borchardt](#) [ORCID: orcid.org/0000-0003-4514-7391¹](#),
- [S. A. Bozhenkov¹](#),
- [K. J. Brunner](#) [ORCID: orcid.org/0000-0002-0974-0457¹](#),
- [H. Damm](#) [ORCID: orcid.org/0000-0001-9423-1608¹](#),
- [M. Drevlak¹](#),
- [O. P. Ford](#) [ORCID: orcid.org/0000-0002-5646-4758¹](#),
- [G. Fuchert¹](#),
- [J. Geiger](#) [ORCID: orcid.org/0000-0003-4268-7480¹](#),
- [P. Helander¹](#),
- [U. Hergenhahn](#) [ORCID: orcid.org/0000-0003-3396-4511^{1 nAffs}](#),
- [M. Hirsch¹](#),
- [U. Höfel](#) [ORCID: orcid.org/0000-0003-0971-5937¹](#),
- [Ye. O. Kazakov](#) [ORCID: orcid.org/0000-0001-6316-5441³](#),
- [R. Kleiber](#) [ORCID: orcid.org/0000-0002-2261-2855¹](#),
- [M. Krychowiak¹](#),
- [S. Kwak¹](#),
- [A. Langenberg](#) [ORCID: orcid.org/0000-0002-2107-5488¹](#),
- [H. P. Laqua¹](#),
- [U. Neuner¹](#),
- [N. A. Pablant⁴](#),

- [E. Pasch¹](#),
- [A. Pavone¹](#),
- [T. S. Pedersen](#) [ORCID: orcid.org/0000-0002-9720-1276¹](#),
- [K. Rahbarnia](#) [ORCID: orcid.org/0000-0002-5550-1801¹](#),
- [J. Schilling](#) [ORCID: orcid.org/0000-0002-6363-6554¹](#),
- [E. R. Scott](#) [ORCID: orcid.org/0000-0002-1389-1151¹](#),
- [T. Stange¹](#),
- [J. Svensson¹](#),
- [H. Thomsen](#) [ORCID: orcid.org/0000-0002-6835-1494¹](#),
- [Y. Turkin](#) [ORCID: orcid.org/0000-0002-6127-9266¹](#),
- [F. Warmer](#) [ORCID: orcid.org/0000-0001-9585-5201¹](#),
- [R. C. Wolf](#) [ORCID: orcid.org/0000-0002-2606-5289¹](#),
- [D. Zhang¹](#) &
- [the W7-X Team](#)

Nature volume **596**, pages 221–226 (2021) [Cite this article](#)

- 1709 Accesses
- 110 Altmetric
- [Metrics details](#)

Subjects

- [Magnetically confined plasmas](#)
- [Plasma physics](#)

Abstract

Research on magnetic confinement of high-temperature plasmas has the ultimate goal of harnessing nuclear fusion for the production of electricity. Although the tokamak¹ is the leading toroidal magnetic-confinement concept, it is not without shortcomings and the fusion community has therefore also pursued alternative concepts such as the stellarator. Unlike axisymmetric tokamaks, stellarators possess a three-dimensional (3D) magnetic field geometry. The availability of this additional dimension opens up an extensive configuration space for computational optimization of both the field geometry itself and the current-carrying coils that produce it. Such an optimization was undertaken in designing Wendelstein 7-X (W7-X)², a large helical-axis advanced stellarator (HELIAS), which began operation in 2015 at Greifswald, Germany. A major drawback of 3D magnetic field geometry, however, is that it introduces a strong

temperature dependence into the stellarator's non-turbulent 'neoclassical' energy transport. Indeed, such energy losses will become prohibitive in high-temperature reactor plasmas unless a strong reduction of the geometrical factor associated with this transport can be achieved; such a reduction was therefore a principal goal of the design of W7-X. In spite of the modest heating power currently available, W7-X has already been able to achieve high-temperature plasma conditions during its 2017 and 2018 experimental campaigns, producing record values of the fusion triple product for such stellarator plasmas^{3,4}. The triple product of plasma density, ion temperature and energy confinement time is used in fusion research as a figure of merit, as it must attain a certain threshold value before net-energy-producing operation of a reactor becomes possible^{1,5}. Here we demonstrate that such record values provide evidence for reduced neoclassical energy transport in W7-X, as the plasma profiles that produced these results could not have been obtained in stellarators lacking a comparably high level of neoclassical optimization.

[Download PDF](#)

Main

In the quest for a viable fusion reactor, consideration of the plasma energy balance shows that—regardless of the confinement concept—a minimum value of the fusion triple product, $nT\tau_E$, must be attained before net-energy-producing operation becomes possible^{1,5}. Here, n is the fuel density, T is its temperature and τ_E is the energy confinement time, defined by the ratio W/P , where W is the stored plasma energy and P is the heating power provided by fusion reactions. The temperature dependence of the fuel's fusion reactivity provides an additional constraint; for deuterium–tritium fusion, this reactivity falls rapidly below a temperature of 10 keV ($\approx 1.2 \times 10^8$ K). High temperatures are thus mandatory in fusion plasmas but must be simultaneously consistent with a tolerable level of energy transport if the required τ_E is to be achieved.

Toroidal magnetic confinement of fully ionized fusion plasmas requires that field lines spiral around the minor axis of the torus poloidally as they encircle the major axis toroidally, tracing out magnetic flux surfaces in the course of numerous transits about the device. For a tokamak these toroidal and poloidal components of \mathbf{B} are provided, respectively, by planar current-carrying coils situated outside the plasma and by a toroidal plasma current induced with a central solenoid. The strength of the magnetic field in a tokamak plasma scales inversely with the distance from the major axis of the torus and $B \equiv |\mathbf{B}|$ thus varies along field lines, being largest on the inboard side of the torus and smallest on the outboard side. For strongly magnetized plasmas, both the total energy and the magnetic moment are constants of the particle motion, so that particles having only a small portion of their velocity vector aligned with the magnetic

field will become trapped in this variation of B , and in axisymmetric tokamaks they perform so-called banana orbits, which are a consequence of the vertical drift caused by the $\mathbf{B} \times \nabla B$ terms in the particles' guiding centre equation of motion^{6,7}. In the absence of collisions, these banana orbits experience no net radial displacement on average over the course of their periodic 'bounce' motion. However, as in the 'classical' case of plasma immersed in a homogeneous magnetic field, Coulomb collisions will cause such particle orbits to undergo a random-walk diffusive process with a repetition rate linearly proportional to the collision frequency, ν . As the 'width' of banana orbits is larger than the particle's gyroradius, the resulting transport will exceed the classical level and the adjective 'neoclassical' is used to signify that the inhomogeneity of B has been accounted for^{8,9}.

High-temperature fusion plasmas are characterized by low collisionality (ν^* , the ratio of collision frequency to banana bounce frequency), which scales as $\nu^* \propto nT^{-2}$. For such plasmas, aside from the large geometrical factor due to tokamak banana orbits⁹, the neoclassical energy flux through the magnetic surface with a minor radius of r will obey $(V' Q_{\text{neo}}) \propto n^{1/2} T^{1/2} B_0^{-2}$, where the left-hand side of this expression is the product of magnetic surface area, V' , and flux-surface-averaged neoclassical energy-flux density, Q_{neo} , and where B_0 is the average magnetic field strength at the major radius of the plasma axis (denoted by R_0). This is noteworthy as these scalings are identical to those of the classical case, and the temperature dependence is therefore benign.

In the majority of tokamak experiments, energy confinement is found to be worse than predicted by neoclassical theory, which is thought to be predominantly due to plasma turbulence. If the turbulence is of gyro-Bohm nature, the energy flux will scale with $T^{5/2}$ (ref. ¹⁰), and as neoclassical and turbulent losses are additive, the former are generally ignored when assessing the overall energy confinement to be expected in a tokamak reactor. The situation is very different in a high-temperature stellarator plasma, however, as will be discussed next.

The need to and means of reducing the stellarator Q_{neo}

Stellarators have the advantage over tokamaks of producing both the toroidal and poloidal components of their magnetic field with current-carrying coils external to the plasma, thereby possessing an inherent steady-state capability that tokamaks lack. Numerous possibilities exist for the placement of coils so as to provide the spiraling of field lines needed for the formation of flux surfaces, the most intuitive of which is the use of continuous helical windings as employed in heliotrons such as the Large Helical Device (LHD)¹¹. Strong plasma shaping, however, is more readily produced with a set of modular coils¹² appropriately twisted into non-planar forms, and it is this concept

that underlies W7-X. In either case, the coil shapes combine both toroidal and poloidal excursions so that the magnetic field they produce cannot be axisymmetric and, indeed, an additional corrugation of B arises, which is commonly referred to as the stellarator's 'helical' ripple. Particles that become trapped in these ripples are said to be localized, as they experience only a small variation of poloidal angle between successive reflection points and this leads to a non-zero time average of their vertical drift over this bounce period, unlike the case of tokamak banana orbits¹³. As a consequence, the collisionless trajectories of localized particles may be able to leave the plasma after numerous reflections, and confinement of such particles will occur only if collisions are frequent enough to limit their radial excursions. Collisions are thus beneficial, and in such a case, typical for electrons in high-temperature stellarator plasmas, the random-walk diffusive transport becomes inversely proportional to the collision frequency and electrons are therefore said to be in the ' $1/v$ regime'. This regime is most remarkable for the very unfavourable temperature dependence of its neoclassical energy flux which scales as $\langle V' \rangle Q_{\text{neo}} \propto \epsilon_{\text{eff}}^{3/2} T^{9/2} R_0^{-1} B_0^{-2}$ (ref. ¹⁴). The quantity ϵ_{eff} is referred to as the effective helical ripple for $1/v$ transport^{15,16} and is a figure of merit devised to allow comparisons of devices that have different magnetic field geometries. As the name implies, ϵ_{eff} will have the same value as the helical-ripple amplitude, ϵ_h , for the limiting case in which this amplitude is a constant over the entire flux surface.

The temperature dependence of this result has long been considered a serious hindrance to the prospects of stellarator reactors, and clearly favours operation at the highest collisionality tolerable. High magnetic field strength and large aspect ratio, R_0/a ($r = a$ denotes the radius of the plasma's last closed flux surface), are also beneficial but imply substantial capital cost for reactor construction as such expenditure scales with the stored magnetic energy of the device. The most 'economical' option offered by the $1/v$ scalings is reduction of the effective helical ripple, which requires appropriate tailoring of the magnetic field so as to diminish the time-averaged radial drifts experienced by localized particles, and this has become a common goal of stellarator optimization since the inception of W7-X¹⁷. This device has five field periods (the integer number of times the magnetic field geometry repeats itself when going around the device once in the toroidal direction) and these periods are oriented such that the coil system appears nearly pentagonal when viewed from above (see Extended Data Fig. 1). The largest values of B are located in the pentagon's 'corners', where the field curvature is particularly strong, but the majority of localized particles are thereby trapped in regions that have small $\mathbf{B} \times \nabla B$, which reduces the associated radial drifts. Making use of this, W7-X was optimized for sufficiently reduced neoclassical energy transport that future HELIAS reactors with plasma

volumes of 1,500 m³ become conceivable, requiring ϵ_{eff} values of a few per cent at most^{[18,19,20](#)}.

In addition to causing $1/v$ transport, localized particles are also responsible for the appearance of a radial electric field, E_r , which must arise in stellarators to establish ambipolarity of the neoclassical particle fluxes (meaning that no net radial current flows in the plasma). This electric field introduces an $\mathbf{E} \times \mathbf{B}$ drift into the particles' equation of motion, which causes localized particles to drift poloidally with a precession frequency $\Omega_E \approx |E_r|/(rB_0)$, thereby placing an additional limit on the radial excursion of orbits. This poloidal precession is more important than collisions for particles that have $\Omega_E > v_{\text{eff}}$, where v_{eff} is the frequency with which collisional removal from the ripple occurs. For fusion plasmas, the collision frequency of electrons will exceed that of the ions by roughly two orders of magnitude and the ions will not be subject to $1/v$ transport but will instead have their orbits constrained by Ω_E , with a value of E_r such that the neoclassical ion particle flux is reduced to the value for electrons. For the interested reader, a more detailed presentation of neoclassical results is provided in Methods, where, in particular, it is demonstrated that strong reduction of electron $1/v$ transport is also of direct benefit for reducing energy fluxes in the ion channel.

Given these ingredients, the recipe for reducing the sum of electron and ion neoclassical energy losses becomes readily apparent. Paramount is a minimization of electron $1/v$ transport, which is best achieved in magnetic fields having small ϵ_{eff} and for plasmas at the highest tolerable collisionality. This strong reduction of the neoclassical electron energy transport is accompanied by a comparable decrease of the electron particle transport and ion neoclassical losses are then beneficially influenced by the ambipolar radial electric field. Reduction of ion transport is thus a knock-on effect relying on the actual realization of this predicted value of E_r . Theoretically, such expectations are justified as particle transport is known to be intrinsically ambipolar for any turbulence satisfying the gyrokinetic orderings^{[21,22](#)}, but experimental verification in W7-X is required for certainty.

In addition to reduced neoclassical transport, W7-X was also optimized for improved magnetohydrodynamic equilibrium and stability, negligible bootstrap current and good confinement of collisionless fast-particle orbits in plasmas with reactor-relevant pressure profiles^{[2](#)}. The W7-X coil set was designed with a great deal of flexibility so as to provide access to a large configuration space, having candidates for which each of these goals is weighted to varying degrees^{[23](#)}. Of particular interest for neoclassical transport studies is the portion of this space that has extremely small values of $\epsilon_{\text{eff}}(\rho = r/a)$, an excellent example of which is the ‘standard’ configuration, which has equal currents in all five different types of non-planar coils. However, this

configuration is expected to have larger bootstrap current and poorer fast-particle confinement than are desirable. Both deficiencies can be addressed by choosing a portion of the configuration space that has a larger variation of B along the magnetic axis. Such a ‘high-mirror’ configuration is achieved by adjusting the current ratios in non-planar coils of the same type so that these ratios are largest at the beginning of each field period (at the corners of the pentagon—see Extended Data Fig. 1) and smallest at its mid-point. The larger mirror term increases the fraction of trapped particles, however, leading to ϵ_{eff} values for the high-mirror configuration that exceed those of the standard configuration by factors of between 2.5 and 3.5, as can be seen by comparison of the radial profiles plotted in Fig. 1. These values are nevertheless small enough to pose no obstacle to reactor operation and, indeed, all HELIAS reactor studies are based on variants of the high-mirror configuration^{19,20}.

Fig. 1: Radial profiles of the effective helical ripple.



Radial profiles of ϵ_{eff} are shown for the W7-X standard (black continuous curve) and high-mirror (black broken curve) configurations as well as for the LHD $R_0 = 3.6$ m (red continuous curve) and $R_0 = 3.75$ m (red broken curve) configurations. In the last of these cases, the ‘missing’ portion of the curve that extends above the plot area increases roughly quadratically with normalized minor radius, $\rho = r/a$, to reach a value of 0.225 at $\rho = 0.93$.

[Full size image](#)

Also shown in Fig. 1 are ϵ_{eff} profiles for two reference configurations of LHD¹¹, a heliotron that has been in operation in Toki, Japan, since 1998. Such a comparison is a natural undertaking as W7-X and LHD are the largest members of the stellarator family currently in existence. These two devices have nearly the same plasma volume, although the aspect ratio of LHD ($R_0/a \approx 6$) is more compact than that of W7-X ($R_0/a \geq 10$). At LHD, vertical field coils can be used to shift the plasma column in the radial direction and configurations are typically differentiated according to the position of their major axis in vacuum; configurations with $R_0 = 3.6$ m and $R_0 = 3.75$ m are depicted here. As is typical for heliotrons, $\epsilon_{\text{eff}}(\rho)$ is reduced by shifting the plasma inwards, whereas the case with the larger major radius is a good approximation to a stellarator field that has $\epsilon_{\text{eff}} \approx \epsilon_h$. Neoclassical transport coefficients for both LHD and W7-X have been calculated and benchmarked within an international collaboration²⁴ and provide a basis for the calculations of neoclassical energy transport presented in the next section.

To visualize the benefit of optimizing the magnetic field geometry for reduced neoclassical transport, collisionless single-particle orbits of ions in W7-X standard and LHD $R_0 = 3.75$ m are also provided here in two videos (see Supplementary Videos 1, 2).

***Q* neo for W7-X discharge 20180918.045**

In many stellarator plasmas, the electron and ion temperatures are too low to cause neoclassical energy losses of a magnitude relevant for the plasma energy balance. As in tokamaks, this is attributed to turbulent transport, and the global energy confinement exhibited by the two concepts is quite comparable for devices of the same volume (see figure 36 of ref. ²⁵). So far, plasma performance in W7-X is commonly limited by turbulence as well, and an experimental assessment of the neoclassical energy confinement in this device therefore requires a plasma scenario for which the turbulent transport is reduced.

In this regard, a substantial transient improvement of the energy confinement has been observed in certain W7-X experiments fuelled with hydrogen pellets^{26,27}; the discharge 20180918.045, performed in the W7-X standard configuration, provides such an example. Time traces of interest for this experiment are provided in Extended Data Fig. 2, showing that a density ramp was initiated at $t = 1.86$ s by injecting a series of twenty-eight frozen hydrogen pellets into the plasma at a frequency of 30 Hz. In the aftermath of pellet fuelling the central density exceeds 10^{20} m⁻³ and the stored energy

measured by a diamagnetic loop reaches a maximum value of $W_{\text{dia}} = 1.02 \text{ MJ}$ with central electron and ion temperatures both in excess of 2.5 keV, although the plasma is heated with only 4.5 MW of electron cyclotron resonance heating (ECRH). Taking fully ionized carbon as the predominant plasma impurity and a core value of the effective charge state equal to the global experimental value, $Z_{\text{eff}} = 1.4$, yields a central triple product of $n^i T^i \tau_E > 5.3 \times 10^{19} \text{ m}^{-3} \text{ keV s}$ (where n^i and T^i indicate the density and temperature of ions, respectively), which is in the typical range of results achieved in W7-X during the high-performance phase of pellet-fuelled discharges^{3,27}. The strong temperature dependence of stellarator neoclassical energy transport immediately raises the question of whether such record triple-product results are also experimental evidence for the reduction of neoclassical energy losses by optimization of the W7-X magnetic field. This discharge is particularly attractive for such an investigation as the 1.02 MJ are maintained for a full energy confinement time of 230 ms, thereby simplifying the plasma energy balance as the $\partial W / \partial t$ term appearing in this equation will be of negligible importance by the end of the high-energy phase. For interested readers, further details of this experiment can be found in Methods.

Calculation of the neoclassical losses requires knowledge of the plasma profiles. These are shown in Fig. 2 for $t = 3.35 \text{ s}$ at the end of the time period in which maximum W_{dia} is reached. The abscissa in these plots, r , is a flux-surface label, often referred to as the effective minor radius. The red data points depict n^e and T^e , the density and temperature of electrons, respectively, obtained from Thomson scattering, and electron temperatures obtained with the electron cyclotron emission (ECE) system are shown in black. Values of T^i determined with charge exchange recombination spectroscopy (CXRS) are given by the blue circles. See [Methods](#) for information concerning these measurements and the error bars associated with them. Profile fits to these experimental data are depicted in Fig. 2 by continuous curves in red for electrons and in blue for ions. The stored energy associated with these profiles is $W = 1.01 \text{ MJ}$, in good agreement with the experimentally measured W_{dia} . To account for the uncertainty in experimental profiles, neoclassical results will also be determined here assuming certain variations of the plasma parameters, but, as will be seen, such sensitivity studies do not lead to fundamentally different conclusions.

Fig. 2: Density and temperature profiles for W7-X discharge 20180918.045 at $t = 3.35 \text{ s}$.



Thomson scattering measurements of n^e and T^e are shown by red data points, ECE results for T^e are plotted in black and CXRS values of T^i are given by blue circles. Error bars depict one standard deviation in the evaluation of the measurements. Fits to the experimental data used in the neoclassical analysis are depicted by the continuous curves with red used for the electron profiles and blue for the ions. The last closed flux surface of the equilibrium is at $r = 0.508$ m.

[Full size image](#)

Before proceeding to the analysis of these experimental results and their interpretation, it should be noted that two tenets underlie this process. First, that quantitative values of the neoclassical fluxes can be accurately determined for specified magnetic equilibria and plasma parameters, and second, that these fluxes represent the minimum value of transport that can be achieved for the given conditions. To substantiate the first of these claims, numerical means of solving the linearized drift kinetic equation and determining neoclassical transport coefficients have been thoroughly benchmarked as part of an international collaboration²⁴. For the second, although there are various examples in the literature of stellarator confinement being consistent with neoclassical theory in the plasma core^{25,28}, there are no published claims of experimental results for which the observed confinement exceeds neoclassical predictions.

The importance of the neoclassical optimization for attaining record fusion-triple-product results in high-temperature stellarator plasmas can be demonstrated by calculating and comparing the neoclassical energy fluxes associated with the density and temperature profiles of Fig. 2 for configurations with different levels of optimization. This comparison is provided in Fig. 3a for the configurations (Fig. 3b)

W7-X standard, (Fig. 3c) W7-X high-mirror, (Fig. 3d) LHD $R_0 = 3.6$ m, and (Fig. 3e) LHD $R_0 = 3.75$ m, and depicts the sum of electron and ion neoclassical energy fluxes, normalized to the heating power $P_{\text{heat}} = 4.5$ MW of discharge 20180918.045, as a function of normalized minor radius. Of primary interest here is to isolate the influence of the magnetic field configuration on the neoclassical results and, to this end, effects of the plasma volume on confinement have been removed by a slight linear upscaling of both LHD configurations so as to have the same plasma volume as W7-X; such scaling leaves the ϵ_{eff} profile and the aspect ratio unchanged. Influence of the magnetic field strength on the results is avoided by setting $B_0 = 2.5$ T in all cases. This comparison demonstrates that the plasma profiles of discharge 20180918.045 in the W7-X standard configuration are only conceivable in magnetic configurations that have a comparably high level of neoclassical optimization. Indeed, the temperatures attained are high enough to imply a peak neoclassical energy flux nearly commensurate with the heating power for the W7-X high-mirror configuration, and for the LHD examples these energy fluxes exceed P_{heat} over a portion of the plasma and are thus physically impossible.

Fig. 3: Comparison of the neoclassical energy fluxes associated with the high-temperature experimental conditions of discharge 20180918.045 at $t = 3.35$ s, for stellarator configurations with different degrees of neoclassical optimization.

 figure3



The plasma profiles used for this comparison are the fits of Fig. 2 and $P_{\text{heat}} = 4.5 \text{ MW}$. **b–e**, Results are plotted for the configurations W7-X standard (**b**), W7-X high-mirror (**c**), LHD $R_0 = 3.6 \text{ m}$ (**d**), and LHD $R_0 = 3.75 \text{ m}$ (**e**). **a**, Radial profiles of the total neoclassical energy fluxes are provided for the four configurations (**b–e**) in a single plot to make direct comparison of the results straightforward. Physically impossible levels of the neoclassical energy fluxes are indicated by the appearance of regions with $(V')^{\prime}((Q)_{{\rm rm}\{n\}}{\rm rm}\{e\}{\rm rm}\{o\})^{\prime}{\rm rm}\{e\}) + (Q)_{{\rm rm}\{n\}}{\rm rm}\{e\}{\rm rm}\{o\})^{\prime}{\rm rm}\{i\}) / (P)_{{\rm rm}\{h\}}{\rm rm}\{e\}{\rm rm}\{a\}{\rm rm}\{t\}) > 1$ (lying above the dotted horizontal line), which shows that the plasma profiles of Fig. 2 would not be attainable in the given configuration. More detailed results for each configuration are provided in the individual plots, where electron fluxes are shown in red, ion fluxes in blue and their sum appears as the black ball-and-chain curve. Also depicted are results for the sum of electron and ion fluxes obtained from a temperature-sensitivity study at constant pressure, that is, by replacing (n^e, T^α) with $(gn^e, g^{-1}T^\alpha)$ and varying g from 0.9 (upper extent of the shaded region) to 1.1 (lower extent).

[Full size image](#)

Further details of the neoclassical results are provided for each individual configuration in the remaining four frames of Fig. 3. In these plots, constituent contributions to the neoclassical energy fluxes made by electrons, $(Q)_{{\rm rm}\{neo\}}^{\prime}$, and ions, $(Q)_{{\rm rm}\{neo\}}^{\prime}{\rm rm}\{i\}$, are shown by the red and blue curves, respectively; their sum is again given by the black ball-and-chain curve. To illustrate the sensitivity of this sum to variations in plasma parameters, results for the total neoclassical energy fluxes are also depicted with (n^e, T^α) replaced by $(gn^e, g^{-1}T^\alpha)$ and varying the scaling factor g in the range $0.9 \leq g \leq 1.1$, where $\alpha = \{e, i\}$ indicates the values for electrons and ions, respectively). As the pressure profile is unaffected by this variation it is possible to perform all calculations using the same equilibrium. The values of collisionality remain sufficiently small in all these cases to ensure that the electron neoclassical fluxes are predominantly due to $1/v$ transport. Given the strong temperature dependence of the losses in this regime, it is apparent that $(Q)_{{\rm rm}\{neo\}}^{\prime}{\rm rm}\{e\}$ will attain its largest value for $g = 0.9$ and then decrease as g increases. The same behaviour is found for $(Q)_{{\rm rm}\{neo\}}^{\prime}{\rm rm}\{i\}$ although the relative reduction is much weaker and can only be accounted for accurately by enforcing the ambipolarity constraint so as to obtain the correct value of the radial electric field. The sum $(Q)_{{\rm rm}\{neo\}}^{\prime}{\rm rm}\{e\} + (Q)_{{\rm rm}\{neo\}}^{\prime}{\rm rm}\{i\}$ is thus a monotonically decreasing function of g over the range of values considered and confirms the theoretical expectations mentioned in the previous section.

As expected qualitatively, the results of Fig. 3 confirm that $(V \wedge \{\prime\})^2 (Q_{\rm n} \wedge Q_{\rm e} \wedge Q_{\rm o})^2 + (Q_{\rm n} \wedge Q_{\rm e} \wedge Q_{\rm i})^2$ is an increasing function of ϵ_{eff} but quantification of this statement is far more difficult. For example, comparing the results of the two W7-X configurations, one finds $(Q_{\rm neo} \wedge Q_{\rm e})^2$ larger in the high-mirror case by a factor of five, which corresponds well with the $(\epsilon_{\text{eff}})^{3/2}$ dependence of $1/v$ transport. However, the total neoclassical energy flux for W7-X high-mirror is increased by a factor only somewhat larger than two, owing to the much smaller increase in $(Q_{\rm neo} \wedge Q_{\rm i})^2$. This example also demonstrates the nonlinearity of the neoclassical fluxes—quantitative accuracy in the determination of these fluxes cannot rely only on comparisons of ϵ_{eff} .

With regard to the higher levels of neoclassical energy transport for the LHD configurations, it should be emphasized that these are provided only to give the reader some idea of how large neoclassical energy fluxes can become at high T^α in stellarator-type devices that were not explicitly optimized to reduce neoclassical transport. Such observations have been accounted for in contemporary designs of heliotron reactors by shifting the plasma column further inwards and also adjusting the pitch modulation of the helical windings so as to obtain a tolerable level of neoclassical transport for the envisaged plasma conditions²⁹.

As explained in the previous section, the structure of B is critical in determining the level of electron neoclassical transport and the reduction of losses in the ion channel relies on the appearance of the radial electric field needed to satisfy the ambipolarity constraint. Experimental profiles of E_r obtained from X-ray imaging crystal spectrometer (XICS) measurements have been published for other examples of pellet-fuelled discharges in W7-X and have been shown to conform with neoclassical predictions³⁰. The same claim can be made for discharge 20180918.045, which has E_r profiles obtained from CXRS in addition to those from XICS (see Extended Data Fig. 3). With this additional information, plasma profiles leading to large values of the triple product in W7-X high-temperature plasmas may be taken as experimental evidence for the reduction of neoclassical losses through an appropriate optimization of the confining magnetic field. In particular, the very small values of $\epsilon_{\text{eff}}(\rho)$, which characterize the W7-X standard configuration, are indispensable for achievement of the high electron and ion temperatures of discharge 20180918.045 with a heating power of only 4.5 MW. As the behaviour of the bootstrap current in W7-X has already been shown to conform with neoclassical expectations³¹, reduction of all neoclassical fluxes and flows in line with the W7-X optimization goals is also substantiated.

Confirming the importance of the W7-X neoclassical optimization for improving plasma performance is only a first step, however, as high-triple-product phases have

been of limited duration in the device so far. It is postulated that—owing to properties of the turbulent transport³²—such performance requires the establishment and sustainment of sufficiently steep density gradients. A similar tendency was also observed in the preceding Wendelstein experiment, W7-AS, where the appearance of ‘optimum confinement’ conditions was always accompanied by such gradients²⁵. These W7-AS discharges were heated using a combination of ECRH and neutral beam injection (NBI), the latter providing the plasma with a strong central particle source, while simultaneously the edge particle source due to recycling neutrals dropped to unusually low levels. Under such conditions, steep density gradients could be maintained throughout the 250-ms heating pulse but, although long in comparison to τ_E , such pulses were insufficient to claim ‘steady-state’ conditions as the sinks due to neutral-particle pumping by plasma-facing components did not saturate during this time. At W7-X, NBI was successfully commissioned during the second portion of the 2017–2018 campaign and will allow future investigations into whether optimum confinement conditions can also be realized in this device during the 10-s duration of NBI pulses. To truly test the steady-state perspectives of the HELIAS concept, the ECRH at W7-X has been designed to provide the plasma with 1,800 s of continuous-wave power and a water-cooled, high-heat-flux divertor is currently being installed in the device to provide the necessary particle and heat exhaust over this period of time. If steep density gradients are indeed the key to improving the confinement of W7-X plasmas, density profile tailoring over such time scales will probably need to rely on the capabilities of a new steady-state pellet injector, which should also go into operation during the next campaign.

Methods

Theoretical details

In high-temperature stellarator plasmas, the radial components of the flux-surface-averaged neoclassical particle and energy flux densities (Γ_{neo} and Q_{neo} , respectively) of particle species α may be expressed as²⁴

$$\begin{aligned}
 & \$\$[\begin{array}{c} \backslash varGamma _{\alpha} = \\ \{ \backslash rm{n} \}^{\alpha} \{ \backslash rm{e} \}^{\alpha} \{ \backslash rm{o} \}^{\alpha} \end{array}] = \\
 & \{ \backslash n \}^{\alpha} \{ \backslash L \}_{11}^{\alpha} \left(\frac{1}{\{ \backslash rm{d} \}^{\alpha}} - \frac{\{ \backslash rm{d} \} r}{\{ \backslash q \}^{\alpha} \{ \backslash E \}_r^{\alpha}} \right) + \\
 & \{ \backslash rm{d} \} \left(\frac{\{ \backslash rm{d} \}^{\alpha} \{ \backslash rm{d} \}^{\alpha} \{ \backslash rm{d} \}^{\alpha}}{\{ \backslash rm{d} \}^{\alpha} \{ \backslash rm{d} \}^{\alpha} \{ \backslash rm{d} \}^{\alpha}} - \frac{\{ \backslash rm{d} \}^{\alpha} \{ \backslash rm{d} \}^{\alpha} \{ \backslash rm{d} \}^{\alpha}}{\{ \backslash rm{d} \}^{\alpha} \{ \backslash rm{d} \}^{\alpha} \{ \backslash rm{d} \}^{\alpha}} \right) \\
 & \$\$ (1)
 \end{aligned}$$

where $n = n(r)$, $T = T(r)$ and q are the density, temperature and charge of the given species, respectively, $E_r = E_r(r)$ is the radial electric field and the δ_{ij} are normalized transport coefficients

$$\begin{aligned} \$\$ \{\delta\}_{12} &= \frac{\{L\}_{12}}{\{L\}_{11}} - \frac{3}{2}, \\ \{\delta\}_{21} &= \frac{\{L\}_{21}}{\{L\}_{11}}, \\ \{\delta\}_{22} &= \frac{\{L\}_{22}}{\{L\}_{11}} - \frac{3\{L\}_{21}}{2\{L\}_{11}}, \end{aligned} \quad \$\$$$

comprising appropriate combinations of elements of the neoclassical transport matrix

$$\begin{aligned} \$\$ \{L\}_{ij} &= \frac{2}{\sqrt{\pi}} \underbrace{\int_0^{\infty} \overline{\sin^2(\theta)} \int_0^\pi \{h\}_i \{h\}_j \{e\}^2 (-K) D(K) \, d\theta \, d\phi}_{\{rm{d}\} K \sqrt{K} \{h\}_i \{h\}_j \{e\}^2 (-K) D(K) \{rm{with}\} \{h\}_1 = 1}, \\ \{h\}_2 &= K \end{aligned} \quad \$\$$$

where $K \equiv \kappa/T = mv^2/(2T)$ is the normalized kinetic energy and D is the so-called mono-energetic radial transport coefficient. The terminology ‘radial’ is used here to denote quantities that are oriented perpendicularly to flux surfaces so that the radial coordinate r should be understood as a flux-surface label.

To understand how the neoclassical energy transport scales with various plasma and configuration parameters, it is sufficient to consider a simple heuristic description of random-walk diffusion processes having $D \propto \mathcal{F}(\Delta r)^2 v_{\text{eff}}$ where \mathcal{F} is the fraction of particles participating in the process, Δr is the characteristic step size of such particles and v_{eff} is the frequency with which a step is taken. For the cases of interest here, the transport is due to the pitch-angle scattering portion of the linearized collision operator, allowing one to express the ‘effective’ step frequency as $v_{\text{eff}} = v/\mathcal{F}^2$ where v is the 90° -deflection frequency and the \mathcal{F}^{-2} enhancement accounts for the fact that scattering through the portion of phase space comprising \mathcal{F} occurs more often than scattering through 90° . The heuristic expression for the transport coefficient then simplifies to $D \propto (\Delta r)^2 v/\mathcal{F}$ leaving only Δr and \mathcal{F} to be determined.

The variation of \mathbf{B} along field lines in toroidal devices causes a $\mathbf{B} \times \nabla B$ drift of guiding centre particle trajectories in this field, having a characteristic velocity $v_d = \kappa/(|q|R_0 B_0)$ (refs. 6,7). For particles localized in a stellarator’s helical ripple, this drift will lead to a displacement from the flux surface by an amount $\Delta r = \min(v_d/v_{\text{eff}}, v_d/\Omega_E)$, depending on whether the effective collision frequency, v_{eff} , or the $\mathbf{E} \times \mathbf{B}$ precessional frequency, $\Omega_E = |E_r|/(rB_0)$, is larger for the given particle. The first of these cases is typical for electrons in a high-temperature stellarator plasma and will be considered in the remainder of this paragraph. For the simplest of stellarator magnetic fields having a constant helical-ripple amplitude over the entire flux surface, $\epsilon_h = \epsilon_h(r)$, the fraction of localized particles scales as $\mathcal{F} \propto$

$\{\{\epsilon\}\}_{\rm h}\}^{1/2})$) and the heuristic expression for the radial transport coefficient then yields $\propto \{\epsilon\}_{\rm h}\}^{3/2}$. Substituting this result into the formula for the L_{ij} and taking the collision frequency proportional to nv^{-3} , one recovers the scaling $\propto (L_{ij})^{3/2}T^{7/2}n^{-1}(R_0B_0)^{-2}$. This result can be generalized to arbitrary stellarator fields if one replaces ϵ_h with the appropriate value of ϵ_{eff} , which explains why this latter quantity is given the name ‘effective helical ripple for $1/v$ transport’. To derive the scalings of the neoclassical energy flux in the $1/v$ regime, one approximates $V \propto rR_0$ and the inverse gradient scale lengths appearing in the braces of equation (1) as a^{-1} to obtain $\propto (V')^{3/2}Q_n^{3/2}T^{9/2}R_0^{-1}B_0^{-2}$.

For a fusion plasma having equal species temperatures the collision frequency of electrons will exceed that of the ions by roughly two orders of magnitude. Consequently, for localized ions the characteristic radial step size of the diffusive random-walk process will be $\Delta r \propto v_d/\Omega_E$ and \mathcal{F} will combine the fractions of phase space in which particle orbits change their trapping states due to either collisions or drifts. For the stellarator field with $\epsilon_h = \epsilon_h(r)$, the former case is characterized by a ‘collisional boundary layer’ of width¹³ $\propto (\epsilon_h)^{1/2}(\nu/\Omega_E)^{1/2} = (\nu/\Omega_E)^{1/2}$ whereas the latter is signified by \mathcal{F}_{tr} , the fraction of ‘transition’ orbits³³, which is a largely geometric factor reflecting the topology of the local maxima of B . Substitution of these quantities into the heuristic expression for the transport coefficient then yields for the ions $\propto (v_d/\varOmega_E)^2\nu^{1/2}(\sqrt{\nu}/\varOmega_E + (\mathcal{F}_t/\mathcal{F}_{\text{tr}}))^{-1}$ which is more commonly found in the literature as two separate results for the limiting cases in which one of the terms within the parentheses is far larger than its counterpart, the so-called \sqrt{v} regime with $\propto v_d^2\nu/\varOmega_E^{3/2}$ and the ‘ v regime’ with $\propto v_d^2\nu/\mathcal{F}_{\text{tr}}$. Using \mathcal{A} to signify those parameters in v/Ω_E that are not of direct relevance to plasma-parameter scalings, the neoclassical ion energy losses are then seen to obey

$$\begin{aligned} & \propto V' Q_n^{3/2} T^{9/2} R_0^{-1} B_0^{-2} \\ & \propto \frac{n^{1/2}}{(E_r T^{3/2})^{1/2} (R_0 B_0)^{1/2}} \left(\frac{\mathcal{F}_t}{\mathcal{F}_{\text{tr}}} + \frac{\mathcal{F}_t}{\mathcal{F}_{\text{tr}}} \right)^{-1} \end{aligned}$$

Although this expression is conveniently compact, it leaves the complicated dependence of E_r on plasma and device parameters unspecified. This will be addressed next for the case of most relevance to the reduction of neoclassical transport in W7-X.

Unlike the axisymmetric tokamak, neoclassical particle fluxes are not intrinsically ambipolar in a stellarator, and thus a theoretical means of determining the E_r profile is provided by enforcing the ambipolarity constraint. In a pure hydrogen plasma (using $\alpha = e$ to denote electrons and $\alpha = i$ for ions) for which $n^e = n^i = n$ and for which $q^e = -e$ and $q^i = e$, where e is the elementary charge, equating $\langle \{ \{ \rm neo \} \} \rangle^{\{ \{ \rm e \} \}}$ and $\langle \{ \{ \rm Gamma \} \} \rangle^{\{ \{ \rm neo \} \}^{\{ \{ \rm i \} \}}}$ will yield

$$\begin{aligned} \$\$ \frac{e \{ E \}_r \{ T \}^{\{ \alpha \}}}{\frac{1}{n} \left(\frac{\{ \rm d \}_n \{ \rm d \}_r + \{ L \}_{11}^{\{ \rm i \}}}{\{ \rm d \}_r - \{ L \}_{11}^{\{ \rm e \}}} \right)^{\{ \alpha \}} \frac{\{ \rm d \}_r + \{ L \}_{11}^{\{ \rm i \}}}{\{ \rm d \}_r - \{ L \}_{11}^{\{ \rm e \}}} \right)} = & \frac{\{ T \}^{\{ \{ \rm e \} \}} \{ T \}^{\{ \{ \rm i \} \}}}{\{ T \}^{\{ \{ \rm e \} \}} \{ T \}^{\{ \{ \rm i \} \}} + \{ L \}_{11}^{\{ \{ \rm i \} \}} \{ T \}^{\{ \{ \rm e \} \}} + \{ L \}_{11}^{\{ \{ \rm e \} \}} \{ T \}^{\{ \{ \rm i \} \}}} \\ & \left(\frac{\{ \rm d \}_n \{ \rm d \}_r + \{ L \}_{11}^{\{ \rm i \}}}{\{ \rm d \}_r - \{ L \}_{11}^{\{ \rm e \}}} \right)^{\{ \alpha \}} \frac{1}{\{ \rm d \}_r - \{ L \}_{11}^{\{ \rm e \}}} \frac{\{ \rm d \}_r + \{ L \}_{11}^{\{ \rm i \}}}{\{ \rm d \}_r - \{ L \}_{11}^{\{ \rm e \}}} \frac{\{ \rm d \}_r + \{ L \}_{11}^{\{ \rm i \}}}{\{ \rm d \}_r - \{ L \}_{11}^{\{ \rm e \}}} \frac{\{ \rm d \}_r + \{ L \}_{11}^{\{ \rm i \}}}{\{ \rm d \}_r - \{ L \}_{11}^{\{ \rm e \}}} \frac{\{ \rm d \}_r + \{ L \}_{11}^{\{ \rm i \}}}{\{ \rm d \}_r - \{ L \}_{11}^{\{ \rm e \}}} \end{aligned} . \$\$$$

Substituting this result back into the neoclassical expressions, one obtains for the particle flux density

$$\begin{aligned} \$\$ \langle \{ \{ \rm Gamma \} \} \rangle^{\{ \{ \rm neo \} \}^{\{ \alpha \}}} = & - \frac{n \{ T \}^{\{ \{ \rm e \} \}} + \{ T \}^{\{ \{ \rm i \} \}} \{ L \}_{11}^{\{ \{ \rm e \} \}} \{ L \}_{11}^{\{ \{ \rm i \} \}}}{\{ L \}_{11}^{\{ \{ \rm e \} \}} \{ T \}^{\{ \{ \rm i \} \}} + \{ L \}_{11}^{\{ \{ \rm i \} \}} \{ T \}^{\{ \{ \rm e \} \}}} \\ & \left(\frac{1}{n} \frac{\{ \rm d \}_n \{ \rm d \}_r + \{ L \}_{11}^{\{ \rm i \}}}{\{ \rm d \}_r - \{ L \}_{11}^{\{ \rm e \}}} \right)^{\{ \alpha \}} \left(\frac{\{ \rm d \}_r + \{ L \}_{11}^{\{ \rm i \}}}{\{ \rm d \}_r - \{ L \}_{11}^{\{ \rm e \}}} \right)^{\{ \alpha \}} \left(\frac{\{ \rm d \}_r + \{ L \}_{11}^{\{ \rm i \}}}{\{ \rm d \}_r - \{ L \}_{11}^{\{ \rm e \}}} \right)^{\{ \alpha \}} \left(\frac{\{ \rm d \}_r + \{ L \}_{11}^{\{ \rm i \}}}{\{ \rm d \}_r - \{ L \}_{11}^{\{ \rm e \}}} \right)^{\{ \alpha \}} \end{aligned} . \$\$$$

and for the energy flux densities

$$\begin{aligned} \$\$ \begin{array}{l} \{ c \} \{ Q \}_{\{ \{ \rm neo \} \}^{\{ \alpha \}}} = - \frac{n \{ L \}_{11}^{\{ \{ \rm e \} \}} \{ T \}^{\{ \{ \rm i \} \}} \{ L \}_{11}^{\{ \{ \rm e \} \}} \{ T \}^{\{ \{ \rm i \} \}}}{\{ L \}_{11}^{\{ \{ \rm e \} \}} \{ T \}^{\{ \{ \rm i \} \}} + \{ L \}_{11}^{\{ \{ \rm i \} \}} \{ T \}^{\{ \{ \rm e \} \}}} \left(\frac{\{ L \}_{11}^{\{ \{ \rm e \} \}} \{ T \}^{\{ \{ \rm i \} \}}}{\{ L \}_{11}^{\{ \{ \rm e \} \}} + \{ L \}_{11}^{\{ \{ \rm i \} \}}} \right)^{\{ \alpha \}} \left(\frac{\{ \rm d \}_{21}^{\{ \{ \rm alpha \} \}}}{\{ \rm d \}_{21}^{\{ \{ \rm alpha \} \}} + \{ \rm d \}_{22}^{\{ \{ \rm alpha \} \}}} \right)^{\{ \alpha \}} \\ \frac{\{ \rm d \}_{21}^{\{ \{ \rm alpha \} \}}}{\{ \rm d \}_{21}^{\{ \{ \rm alpha \} \}} + \{ \rm d \}_{22}^{\{ \{ \rm alpha \} \}}} \left(\frac{\{ \rm d \}_{21}^{\{ \{ \rm alpha \} \}}}{\{ \rm d \}_{21}^{\{ \{ \rm alpha \} \}} + \{ \rm d \}_{22}^{\{ \{ \rm alpha \} \}}} \right)^{\{ \alpha \}} \left(\frac{\{ \rm d \}_{21}^{\{ \{ \rm alpha \} \}}}{\{ \rm d \}_{21}^{\{ \{ \rm alpha \} \}} + \{ \rm d \}_{22}^{\{ \{ \rm alpha \} \}}} \right)^{\{ \alpha \}} \left(\frac{\{ \rm d \}_{21}^{\{ \{ \rm alpha \} \}}}{\{ \rm d \}_{21}^{\{ \{ \rm alpha \} \}} + \{ \rm d \}_{22}^{\{ \{ \rm alpha \} \}}} \right)^{\{ \alpha \}} \left(\frac{\{ \rm d \}_{21}^{\{ \{ \rm alpha \} \}}}{\{ \rm d \}_{21}^{\{ \{ \rm alpha \} \}} + \{ \rm d \}_{22}^{\{ \{ \rm alpha \} \}}} \right)^{\{ \alpha \}} \end{array} . \$\$$$

where the species indices are chosen to be $[\alpha, \beta] = [e, i]$ or $[i, e]$ as appropriate. However, one should recall that the $\langle\{L\}_{ij}\rangle$ are dependent on E_r , so that profitable use of these equations requires that special circumstances hold. One such example is the fusion-relevant case that has $T^e = T^i = T$ for which the radial electric field equation becomes

and will yield $E_r \propto T$ for the limiting case in which electron 1/v transport has been sufficiently reduced to satisfy $\langle L_{11}^{\{1\}} \rangle / \langle L_{11}^{\{e\}} \rangle \ll 1$. In the same limit, the particle flux density is well approximated by

```
 $$\left( \frac{2}{n} \frac{\alpha}{\delta_1^2} + \frac{\delta_2^2}{\delta_1^2} \right) \frac{1}{T} \frac{d}{dT} \right), $$

```

making it evident that electrons are the rate-controlling species. Additionally, one notices that the factor outside the braces in $\langle\{Q\}_{\rm neo}\rangle^{\alpha}$ simplifies to $nT_{\rm L}^{11}\langle\{e\}\rangle$ and that the largest normalized transport coefficients associated with the temperature gradients are $\langle\{\delta_{12}\}^{22}\rangle\langle\{e\}\rangle + \langle\{\delta_{12}\}^{12}\rangle\langle\{i\}\rangle\langle\{\delta_{21}\}^{21}\rangle\langle\{e\}\rangle$ for electrons and $\langle(\{\delta_{12}\}^{22}\rangle\langle\{i\}\rangle - \langle\{\delta_{12}\}^{12}\rangle\langle\{i\}\rangle)\langle\{\delta_{21}\}^{21}\rangle\langle\{i\}\rangle\rangle / \langle\{L\}_{\rm L}^{11}\rangle\langle\{i\}\rangle / \langle\{L\}_{\rm L}^{11}\rangle\langle\{e\}\rangle$ for ions. At first glance, the largeness of $\langle\{L\}_{\rm L}^{11}\rangle\langle\{i\}\rangle / \langle\{L\}_{\rm L}^{11}\rangle\langle\{e\}\rangle$ might lead one to expect a considerable difference in the size of these two terms, but the strong temperature dependence of $1/v$ transport makes the $\langle\{\delta_{ij}\}^{ij}\rangle\langle\{e\}\rangle$ considerably larger than their $\langle\{\delta_{ij}\}^{ij}\rangle\langle\{i\}\rangle$ counterparts. Indeed, under the assumption of ‘pure’ regimes, the L_{ij} may be expressed in terms of the so-called gamma function, and one finds $\langle\{\delta_{12}\}^{12}\rangle\langle\{e\}\rangle = 7/2$, $\langle\{\delta_{21}\}^{21}\rangle\langle\{e\}\rangle = 5$ and $\langle\{\delta_{12}\}^{22}\rangle\langle\{e\}\rangle = 45/2$ whereas $(1/2) \leq \langle\{\delta_{12}\}^{12}\rangle\langle\{i\}\rangle \leq 5/4$, $(2) \leq \langle\{\delta_{21}\}^{21}\rangle\langle\{i\}\rangle \leq 11/4$ and $(3) \leq \langle\{\delta_{12}\}^{22}\rangle\langle\{i\}\rangle \leq 99/16$ where the smaller values hold in the v regime and the larger for the \sqrt{v} regime³⁴. When these limits apply one obtains $(25) \leq \langle\{\delta_{12}\}^{22}\rangle\langle\{e\}\rangle + \langle\{\delta_{12}\}^{12}\rangle\langle\{i\}\rangle\langle\{\delta_{21}\}^{21}\rangle\langle\{e\}\rangle \leq 115/4$ and $(2) \leq \langle\{\delta_{12}\}^{22}\rangle\langle\{i\}\rangle - \langle\{\delta_{12}\}^{12}\rangle\langle\{i\}\rangle\langle\{\delta_{21}\}^{21}\rangle\langle\{i\}\rangle \leq 11/4$ so that the δ_{ij} combination of relevance for electrons is an order of magnitude larger than its counterpart for ions. The neoclassical energy

transport of electrons and ions will thus be of similar magnitudes and the strong reduction of $\langle L \rangle_{11}^{\rm rm{e}}$ is clearly seen to be of benefit to both species.

Details concerning the calculation of neoclassical energy fluxes

For the magnetic configurations considered in this work all equilibria have been determined with the Variational Moments Equilibrium Code (VMEC)³⁵ and subsequently expressing the results in terms of Boozer flux coordinates³⁶. This provides all information concerning the magnetic field needed as input by the Drift Kinetic Equation Solver (DKES)³⁷, which is used to prepare a dataset of mono-energetic transport coefficients covering the entire range of v^* and E_r values relevant for determining the L_{ij} given any combination of density and temperature producing the pressure profile of the VMEC equilibrium. The radial electric field profile is determined self-consistently by using numerical root-finding techniques to determine solutions to the nonlinear ambipolarity constraint.

For the W7-X calculations, equilibria for the pressure profile of discharge 20180918.045 at $t = 3.35$ s have been used, whereas the LHD results presented here have been obtained for vacuum equilibria. The LHD equilibria thus ignore the outward shift of the plasma column due to non-zero plasma pressure—the so-called Shafranov shift³⁸—which leads to an increase of the neoclassical energy losses^{39,40}. This deleterious effect can be counteracted to an extent by using the vertical field coils to shift the plasma axis back to its vacuum position, but a deformation in the shape of flux surfaces remains, which serves to degrade the neoclassical confinement. The neoclassical energy losses calculated here for LHD are thus ‘best case’ results. By contrast, the W7-X optimization had the explicit goal of using finite-plasma-pressure effects to its benefit; for the high-mirror configuration, ϵ_{eff} decreases monotonically as the pressure increases, whereas for the standard configuration, small-to-modest pressure has little influence on this quantity.

The results plotted in Fig. 3 also allow a rough assessment of the reactor prospects for these four configurations with regard to their neoclassical energy confinement. For a deuterium-tritium plasma meant to produce a power of 3 gigawatts thermal (GWth) and that has 600 MW of α -particle heating, it is necessary to increase the temperatures of discharge 20180918.045 by a factor of six and the density by a factor of three, assuming that reactor-sized versions of W7-X and LHD have their dimensions increased by a factor of four and their magnetic field strength doubled. Scaling up the configurations leaves ϵ_{eff} unchanged so that the electron $1/v$ energy fluxes will increase according to $\langle T \rangle^{9/2} \langle R \rangle_0^{-1} \langle B \rangle_0^{-2}$, and thus by a factor of roughly 200. Scaling the maximum electron energy fluxes of Fig. 3 by this factor, one obtains 75 MW for W7-X standard, 340 MW for W7-X high-mirror, 640 MW for

LHD $R_0 = 3.6$ m and 1,320 MW for LHD $R_0 = 3.75$ m. For stellarator reactor plasmas, ion neoclassical energy fluxes are at least as large as those of the electrons but even the somewhat extreme assumption of $\langle Q \rangle_{\rm neo}^{\rm i} = 2 \langle Q \rangle_{\rm neo}^{\rm e}$ would make the total neoclassical energy fluxes only a fraction of the α -particle heating for W7-X standard. At first glance, the reactor prospects of W7-X high-mirror appear questionable, but one must realize that this back-of-the-envelope estimate ignores changes to the configuration due to increased plasma pressure. In the current example, the normalized plasma pressure, $\beta \propto nTB^{-2}$, is increased by a factor of 4.5 and, when this is accounted for, ϵ_{eff} in the high-mirror configuration is reduced by enough that $\langle Q \rangle_{\rm e}$ would drop by a factor of two. For the LHD cases it is necessary to choose different scaling factors; the $R_0 = 3.6$ m case becomes viable with a factor five larger size and the somewhat reduced temperature that this allows. (This assumes that the vertical field coils of the heliotron are used to compensate the Shafranov shift as the neoclassical transport in such a high-pressure equilibrium would otherwise become intolerable).

It should also be pointed out that the optimization of W7-X was undertaken roughly thirty years ago and that great improvements in the projected fast-particle confinement of HELIAS have been made in the intervening years. Such improvements have simultaneously reduced the ϵ_{eff} values from the per cent level of W7-X to the per mille level in new reactor candidates, thereby decreasing neoclassical energy transport for prospective fusion plasmas to very small levels. This development, coupled with the predominance of turbulent transport in the W7-X experiment, have focused recent theoretical and numerical efforts on the further optimization of the HELIAS concept to also contend with this transport channel. Such efforts are still in their infancy, however, and it is not yet possible to foresee what combination of optimized magnetic field and plasma conditions will best reduce turbulent transport and what influence such a combination will have on the other HELIAS optimization goals.

Background and experimental details

Since its inception, W7-X has been conceived as a means of demonstrating the attractive properties that advanced stellarators offer as prospective fusion reactors. Ultimately, this envisions not only the achievement of high-triple-product plasma operation but the ability to maintain such operation over time scales far in excess of those characterizing all physical processes of the plasma and the plasma-facing components. To enable such ‘steady-state’ scenarios, electron cyclotron resonance heating (ECRH) of W7-X plasmas is available using ten gyrotrons, each of which is capable of providing continuous-wave power over a time interval of 1,800 s (ref. [41](#)). The gyrotron frequency of 140 GHz is resonant at the second harmonic for a magnetic field strength of $B = 2.5$ T with cutoff densities of $n_c = 1.2 \times 10^{20} \text{ m}^{-3}$ for waves with extraordinary-mode (X2) polarization and $2n_c$ for ordinary-mode (O2) polarization. At these densities and for W7-X plasma volumes of nearly 30 m^3 the collisional transfer of energy from electrons to ions should be excellent, so that $T^i \approx T^e$ can be expected in spite of lacking a direct means of heating the ions. Such operational conditions also mimic qualitatively those of a reactor where the heating power of fusion α -particles goes chiefly to electrons, which subsequently heat deuterium and tritium ions by collisional energy exchange.

With regard to plasma-facing components, steady-state operation of W7-X will only become possible after the installation of a water-cooled, high-heat-flux (HHF) divertor capable of providing the necessary particle and power exhaust throughout the course of such experiments. The installation of this divertor with all its intricate plumbing requirements was started at the end of 2018, with completion scheduled for the end of 2021. The experimental results considered here were obtained in the latter portion of 2018, during the second half of a campaign in which initial experience with divertor operation in W7-X was acquired through the use of an uncooled test divertor unit (TDU) having the same geometry that its HHF successor will have. Pellet fuelling was already observed to improve plasma performance during the first portion of this TDU campaign [3,26](#) and such results motivated further investigations once wall conditioning had been

greatly improved following ‘boronization’ of the device, early in the second half of the TDU campaign. On many occasions, considerable increases of the plasma diamagnetic energy, W_{dia} , were measured in the aftermath of pellet fuelling and the discharge 20180918.045 is used here to illustrate such results.

Time traces for this discharge are plotted in Extended Data Fig. 2.

Following a short start-up phase in X-mode to achieve plasma breakdown, the ECRH power (first plot in the figure) is launched exclusively with O-mode polarization so as to avoid large amounts of reflected power should pellet fuelling lead transiently to densities above the X2 cutoff. Also shown by the dotted curve is the radiated power measured with bolometer arrays; this power originates in roughly equal portions from the confined plasma and from the region outside the last closed flux surface, which includes the large magnetic islands that are the basis of the W7-X divertor concept.

Initially, the line-integrated electron density, $\int d\ell n^e$, is held at a value of roughly $3 \times 10^{19} \text{ m}^2$, which is too low to promote effective collisional energy transfer from electrons to ions (where the $d\ell$ appearing in the integrand is the differential length along the line of sight). Consequently, the 3.2 MW of ECRH used during this phase produces plasmas that have $T^e \gg T^i$ centrally as the core temperature measurements from Thomson scattering and the X-ray imaging crystal spectrometer (XICS) diagnostics show (third plot in the figure). A density ramp is initiated 1.86 s into the discharge by injecting a series of 28 frozen hydrogen pellets into the plasma at a frequency of 30 Hz using a so-called blower gun⁴². Although the fuelling efficiency of the first few pellets is poor, noticeable improvement occurs thereafter²⁶ and increments in the line-integrated density caused by individual pellets become clearly discernible with $\int d\ell n^e$ slightly exceeding $12 \times 10^{19} \text{ m}^{-2}$ when the series ends at $t = 2.8$ s. At this time point, the ECRH power is increased to 4.5 MW to maintain T^e at values sufficient for good O2 absorption. This is further aided at W7-X by a multi-pass launch scheme which uses specially prepared reflecting surfaces to redirect unabsorbed ECRH power back into the plasma. With this scheme, ray-tracing simulations predict that more than 95% of the launched ECRH power will be deposited in the plasma during the high-performance phase of discharge 20180918.045, a value that has been confirmed by the analysis of

stray-radiation measurements from the experiment taken with ‘sniffer’ probes.

The pellets obviously provide the plasma with a particle source but their thermalization also introduces a considerable energy sink into the electron energy balance particularly as the thermalization process also strongly heats the ions for the given initial conditions⁴³. In response, T^e falls and the central electron temperature has dropped below 2 keV—nearly to the level of central T^i —when the increase in ECRH power occurs. To this time point, pellet fuelling has been accompanied by a rise in the diamagnetic energy from $W_{\text{dia}} = 0.40 \text{ MJ}$ at $t = 1.8 \text{ s}$ to $W_{\text{dia}} = 0.68 \text{ MJ}$ at $t = 1.8 \text{ s}$. With the larger heating power, the time rate of change of W_{dia} then increases considerably and the diamagnetic energy attains its maximum value of 1.02 MJ after another 400 ms. In the absence of pellet fuelling, the line-integrated density decreases throughout this time, making it evident that a temperature increase must also have taken place and, indeed, the central values exceed 2.5 keV for both electrons and ions. Thus, an experimental situation has arisen that has high density and high temperatures simultaneously, a situation ideal for testing the efficacy of the W7-X optimization regarding reduction of the neoclassical transport. The discharge shown here is particularly attractive for such an investigation as the 1.02 MJ are maintained for 230 ms which corresponds to one energy confinement time given the 4.5 MW of ECRH used to heat the plasma. This simplifies considerations of the energy balance as the $\partial W / \partial t$ term appearing in this equation will be of negligible importance by the end of the high-energy phase.

ECRH power deposition was not highly localized for discharge 20180918.045, as the electron cyclotron waves were launched with ordinary-mode polarization. Nevertheless, the great majority of the heating power is deposited within $\rho < 0.4$ at the time point of the analysis. At this radius, and in the neighbouring vicinity at least out to $\rho = 0.55$, the sum of electron and ion neoclassical energy fluxes exceeds 25% of the heating power and is thus of relevance when considering the energy balance. A larger share of this balance remains unaccounted for, however, even after deducting the observed energy losses due to radiation. This shortfall indicates that turbulent transport must still be of importance for explaining

the experimental results, especially in the plasma periphery where low temperatures lead to negligible neoclassical energy transport. In spite of the level of turbulent transport needed to fully explain this discharge, the high temperatures achieved are nevertheless responsible for an experimentally relevant neoclassical energy flux, even though the W7-X standard configuration has extremely small values of the effective helical ripple. Assuming such temperatures had been achieved in configurations without a comparably high level of neoclassical optimization quickly leads to the physically impossible result of neoclassical energy fluxes exceeding the heating power, as is demonstrated in the comparison of Fig. 3.

Diagnostics

The plasma energy has been measured with a diamagnetic loop, located in the (toroidal) symmetry plane of one of the five field periods⁴⁴. It encircles the plasma and is equipped with four compensation coils, which are also located inside the vacuum vessel and directly attached to the diamagnetic loop itself. These do not encircle the plasma and can therefore be used to compensate measurements of the main loop for errors due to eddy currents in the adjacent vacuum vessel as well as fluctuations of externally driven currents in the main superconducting magnetic field coils.

The line-integrated electron density was determined by a single-channel dispersion interferometer employing a CO₂ laser measuring at a fundamental wavelength of 10.6 μm (ref. ⁴⁵). The probing beam passes through the plasma twice by making use of a corner cube reflector; the single-pass path length through the plasma is roughly 1.3 m. The statistical error for $\int d\ell n^e$ is generally given as 10¹⁸ m⁻² and there was an additional systematic error $\leq 4 \times 10^{18}$ m⁻² during the portion of the experimental campaign during which discharge 20180918.045 was performed.

The Thomson scattering system at W7-X employs three YAG lasers to provide full profiles of electron density and temperature at a rate of 30 Hz. Scattered light is collected by two in-vessel optical systems and routed to polychromators outside the torus hall via optical fibres. Forty-two spatial channels are available, each employing five interference filters to provide spectral resolution^{46,47}. Spectral calibration is done ex vessel by

withdrawing the optical systems and illuminating a diffuse-reflecting screen with a supercontinuum light source⁴⁶. Absolute calibration for density measurements was obtained by performing anti-Stokes rotational Raman scattering in nitrogen. Bayesian analysis is used to determine the most probable electron temperature and density for each Thomson scattering volume, as well as their uncertainties and cross-correlation. Error bars in Fig. 2 depict the width of the 95% confidence interval divided by four, which corresponds to the one-standard-deviation interval of a normal distribution; see ref. ⁴⁷ for full details.

Electron cyclotron emission is used at W7-X to determine the electron temperature using a 32-channel heterodyne radiometer probing X2 emission⁴⁸. The T^e data plotted in Fig. 2 give ECE values of the electron temperature averaged over a centred 20-ms time window, with the error bars depicting the standard deviation of these values and also accounting for systematic calibration uncertainties, largely due to the unknown thermal drifts of the radiometer sensitivity. An optimized line-of-sight is realized across the 3D plasma shape by means of an in vessel Gauss telescope. The radiometer channels are calibrated relative to each other and absolute calibration is carried out using a second ‘identical’ Gauss telescope outside the torus that views a hot-cold light source⁴⁹. For the results presented here, the absolute calibration has been scaled up by a factor of 1.58 to account for the relative mismatch with Thomson data on the day of the experiment. Direct interpretation of the radiometer signals as a local temperature measurement would require that ideal blackbody conditions be fulfilled in the plasma, whereas in reality, non-thermal ‘hot’ components of the electron distribution function appear in the spectrum as well. A further complication arises in semi-transparent plasmas owing to a degradation of spatial resolution. The T^e profile is therefore inferred by applying Bayesian analysis with forward modelling of the radiation transport in the plasma; for full details, see ref. ⁵⁰.

The CXRS diagnostic at W7-X makes use of a high-étendue spectrometer to provide measurements of T^i at 51 spatial locations as well as E_r at 25 of these. Given the prevalence of carbon in the device’s plasma-facing components, this element is always present as an impurity in W7-X plasmas

and the visible charge exchange line C^{VI} at 529.07 nm provides the strongest possible signal. Active charge exchange measurements are enabled by using short ‘blips’ of neutral beam injection (NBI) for diagnostic purposes and subtracting the passive spectrum observed before and after the NBI from this data. A complete description may be found in ref. [51](#).

The XICS diagnostic is based on spectroscopic analysis of emission from highly charged argon impurities that are seeded into the plasma in trace amounts for diagnostic purposes [52](#). The XICS system records a 1D image of line-integrated spectra, from which the ion temperature is found by measuring the Doppler-broadened width of the emission lines. The local plasma parameters are found by using a tomographic inversion based on a known VMEC equilibrium [53](#). Detailed descriptions of the XICS diagnostic on W7-X can be found in ref. [54](#) although improvements in the diagnostic analysis have since been implemented, including compensation for spherical aberrations and the sub-pixel distribution of photons on the detector. At the time point analysed for this discharge, the XICS values of T^i exceed those of CXRS by 150 to 200 eV and indicate $T^i > T^e$ for $r > 0.2$ m despite the fact that no direct heating of the ions occurs using ECRH. This is at odds with energy balance considerations, however, which argue for $T^i \approx T^e$ outside the region of power deposition. These expectations are better fulfilled by the CXRS data and, given the strong dependence of the neoclassical losses on temperature, it has therefore been decided to err on the side of caution by using only the CXRS values of T^i for the profile fits used in the calculations of neoclassical fluxes. The time evolution of the T^i profile measured by CXRS has also been confirmed through the measurements of the XICS system.

Plasma radiation is measured by two bolometer cameras—each with arrays of detectors that have a 5 μm blackened gold-foil absorber—installed in one of the mid-field-period toroidal-symmetry planes of W7-X, and with spatial resolution of between 3 and 4 cm (ref. [55](#)). Line-integrated signals from 65 channels are used to obtain radiation intensity distributions by tomographic reconstruction with ‘relative gradient smoothing’ as regularization functional (to be published). Flux-surface-averaged radial

emissivity profiles are then derived by averaging these 2D-emissivity distributions in the poloidal direction. The total radiated power loss is a linear interpolation of radiation from the observation volume to that of the entire plasma volume. Toroidal variations of the radiation strength are not considered, an assumption supported by the results of edge modelling.

Data availability

The data depicted in the plots of this paper and other findings of this study are available from the corresponding author upon reasonable request.

References

1. 1.

Wesson, J. *Tokamaks* 2nd edn (Oxford Univ. Press, 1997).

2. 2.

Grieger, G. et al. Modular stellarator reactors and plans for Wendelstein 7-X. *Fusion Technol.* **21**, 1767–1778 (1992).

[CAS](#) [Google Scholar](#)

3. 3.

Pedersen, T. S. et al. First results from divertor operation in Wendelstein 7-X. *Plasma Phys. Contr. Fusion* **61**, 014035 (2019).

[ADS](#) [CAS](#) [Google Scholar](#)

4. 4.

Wolf, R. C. et al. Performance of Wendelstein 7-X stellarator plasmas during the first divertor operation phase. *Phys. Plasmas* **26**, 082504 (2019).

[ADS](#) [Google Scholar](#)

5. 5.

Lawson, J. D. Some criteria for a power producing thermonuclear reactor. *Proc. Phys. Soc. B* **70**, 6–10 (1957).

[ADS](#) [Google Scholar](#)

6. 6.

Alfvén, H. On the motion of a charged particle in a magnetic field. *Ark. Mat. Astr. Fys.* **27A**, 1–20 (1940).

[MathSciNet](#) [MATH](#) [Google Scholar](#)

7. 7.

Northrop, T. G. The guiding center approximation to charged particle motion. *Ann. Phys.* **15**, 79–101 (1961).

[ADS](#) [MATH](#) [Google Scholar](#)

8. 8.

Galeev, A. A. & Sagdeev, R. Z. Transport phenomena in a collisionless plasma in a toroidal magnetic system. *Sov. Phys. JETP* **26**, 233–240 (1968).

[ADS](#) [Google Scholar](#)

9. 9.

Hinton, F. L. & Hazeltine, R. D. Theory of plasma transport in toroidal confinement systems. *Rev. Mod. Phys.* **48**, 239–308 (1976).

[ADS](#) [MathSciNet](#) [CAS](#) [Google Scholar](#)

10. 10.

Connor, J. W. Invariance principles and plasma confinement. *Plasma Phys. Contr. Fusion* **30**, 619–650 (1988).

[ADS](#) [CAS](#) [Google Scholar](#)

11. 11.

Iiyoshi, A., Fujiwara, M., Motojima, O., Ohyabu, N. & Yamazaki, K. Design study for the Large Helical Device. *Fusion Technol.* **17**, 169–187 (1990).

[CAS](#) [Google Scholar](#)

12. 12.

Wobig, H. & Rehker, S. A stellarator coil system without helical windings. In *Proc. 7th Symp. Fusion Technology* 345–357 (1972).

13. 13.

Galeev, A. A., Sagdeev, R. Z., Furth, H. P. & Rosenbluth, M. N. Plasma diffusion in a toroidal stellarator. *Phys. Rev. Lett.* **22**, 511–514 (1969).

[ADS](#) [Google Scholar](#)

14. 14.

Ho, D. D. M. & Kulsrud, R. M. Neoclassical transport in stellarators. *Phys. Fluids* **30**, 442–461 (1987).

[ADS](#) [CAS](#) [MATH](#) [Google Scholar](#)

15. 15.

Dommaschk, W., Lotz, W. & Nührenberg, J. Monte-Carlo simulations of neoclassical transport in stellarators. *Nucl. Fusion* **24**, 794–799 (1984).

[CAS](#) [Google Scholar](#)

16. 16.

Beidler, C. D. & Hitchon, W. N. G. Ripple transport in helical-axis advanced stellarators: a comparison with classical stellarator/torsatrons. *Plasma Phys. Contr. Fusion* **36**, 317–353 (1994).

[ADS](#) [CAS](#) [Google Scholar](#)

17. 17.

Beidler, C. D. et al. Physics and engineering design for Wendelstein 7-X. *Fusion Technol.* **17**, 148–168 (1990).

[CAS](#) [Google Scholar](#)

18. 18.

Painter, S. L. & Lyon, J. F. Transport analysis of stellarator reactors. *Nucl. Fusion* **31**, 2271–2290 (1991).

[CAS](#) [Google Scholar](#)

19. 19.

Beidler, C. D. et al. The Helias reactor. In *16th Int. Conf Fusion Energy* Vol. 3, 407–418 (International Atomic Energy Agency, 1996).

20. 20.

Beidler, C. D. et al. The Helias reactor HSR4/18. *Nucl. Fusion* **41**, 1759–1766 (2001).

[ADS](#) [CAS](#) [Google Scholar](#)

21. 21.

Sugama, H., Okamoto, M., Horton, W. & Wakatani, M. Transport processes and entropy production in toroidal plasmas with gyrokinetic electromagnetic turbulence. *Phys. Plasmas* **3**, 2379–2394 (1996).

[ADS](#) [MathSciNet](#) [CAS](#) [Google Scholar](#)

22. 22.

Helander, P. Theory of plasma confinement in non-axisymmetric magnetic fields. *Rep. Prog. Phys.* **77**, 087001 (2014); corrigendum **81**, 099501 (2018).

[ADS](#) [PubMed](#) [PubMed Central](#) [Google Scholar](#)

23. 23.

Geiger, J. et al. Physics in the magnetic configuration space of W7-X. *Plasma Phys. Contr. Fusion* **57**, 014004 (2015).

[ADS](#) [CAS](#) [Google Scholar](#)

24. 24.

Beidler, C. D. et al. Benchmarking of the mono-energetic transport coefficients — results from the International Collaboration on Neoclassical Transport in Stellarators (ICNTS). *Nucl. Fusion* **51**, 076001 (2011).

[ADS](#) [Google Scholar](#)

25. 25.

Hirsch, M. et al. Major results from the stellarator W7-AS. *Plasma Phys. Contr. Fusion* **50**, 053001 (2008).

[ADS](#) [Google Scholar](#)

26. 26.

Baldzuhn, J. et al. Pellet fueling experiments in Wendelstein 7-X. *Plasma Phys. Contr. Fusion* **61**, 095012 (2019).

[ADS](#) [CAS](#) [Google Scholar](#)

27. 27.

Bozhenkov, S. A. et al. High-performance plasmas after pellet injections in Wendelstein 7-X. *Nucl. Fusion* **60**, 066011 (2020).

[ADS](#) [CAS](#) [Google Scholar](#)

28. 28.

Dinklage, A. et al. Inter-machine validation study of neoclassical transport modelling in medium- to high-density stellarator-heliotron plasmas. *Nucl. Fusion* **53**, 063022 (2013).

[ADS](#) [CAS](#) [Google Scholar](#)

29. 29.

Goto, T. et al. Conceptual design of a compact helical fusion reactor FFHR-c1 for the early demonstration of year-long electric power generation. *Nucl. Fusion* **59**, 076030 (2019).

[ADS](#) [CAS](#) [Google Scholar](#)

30. 30.

Pablant, N. A. et al. Investigation of the neoclassical ambipolar electric field in ion-root plasmas on W7-X. *Nucl. Fusion* **60**, 036021 (2020).

[ADS](#) [CAS](#) [Google Scholar](#)

31. 31.

Dinklage, A. et al. Magnetic configuration effects on the Wendelstein 7-X stellarator. *Nat. Phys.* **14**, 855–860 (2018); correction **14**, 867

(2018).

[CAS](#) [Google Scholar](#)

32. 32.

Alcusón, J. A. et al. Suppression of electrostatic micro-instabilities in maximum- J stellarators. *Plasma Phys. Contr. Fusion* **62**, 035005 (2020).

[ADS](#) [Google Scholar](#)

33. 33.

Mynick, H. E. Effect of collisionless detrapping on non-axisymmetric transport in a stellarator with radial electric field. *Phys. Fluids* **26**, 2609–2615 (1983).

[ADS](#) [CAS](#) [MATH](#) [Google Scholar](#)

34. 34.

Maaßberg, H., Beidler, C. D. & Simmet, E. E. Density control problems in large stellarators with neoclassical transport. *Plasma Phys. Contr. Fusion* **41**, 1135–1153 (1999).

[ADS](#) [Google Scholar](#)

35. 35.

Hirshman, S. P., van Rij, W. I. & Merkel, P. Three-dimensional free boundary calculations using a spectral Green's function method. *Comput. Phys. Commun.* **43**, 143–155 (1986).

[ADS](#) [MathSciNet](#) [CAS](#) [Google Scholar](#)

36. 36.

Boozer, A. H. Guiding center drift equations. *Phys. Fluids* **23**, 904–908 (1980).

[ADS](#) [MathSciNet](#) [MATH](#) [Google Scholar](#)

37. 37.

van Rij, W. I. & Hirshman, S. P. Variational bounds for transport coefficients in three-dimensional toroidal plasmas. *Phys. Fluids B* **1**, 563–569 (1989).

[ADS](#) [Google Scholar](#)

38. 38.

Shafranov, V. D. Equilibrium of a toroidal pinch in a magnetic field. *Sov. At. Energy* **13**, 1149–1158 (1963).

[Google Scholar](#)

39. 39.

Mynick, H. E. The effect of finite β on stellarator transport. *Phys. Fluids* **28**, 1139–1147 (1985).

[ADS](#) [MATH](#) [Google Scholar](#)

40. 40.

Wakasa, A., Murakami, S. & Oikawa, S. Study of neoclassical transport in LHD plasmas by applying the DCOM/NNW neoclassical transport database. *Plasma Fusion Res.* **3**, S1030 (2008).

[ADS](#) [Google Scholar](#)

41. 41.

Erckmann, V. et al. Electron cyclotron heating for W7-X: physics and technology. *Fus. Sci. Technol.* **52**, 291–312 (2007).

[CAS](#) [Google Scholar](#)

42. 42.

Dibon, M. et al. Blower gun pellet injection system for W7-X. *Fusion Eng. Des.* **98-99**, 1759–1762 (2015).

[CAS](#) [Google Scholar](#)

43. 43.

Aleynikov, P., Breizman, B. N., Helander, P. & Turkin, Y. Plasma ion heating by cryogenic pellet injection. *J. Plasma Phys.* **85**, 905850105 (2019).

[CAS](#) [Google Scholar](#)

44. 44.

Rahbarnia, K. et al. Diamagnetic energy measurement during the first operational phase at the Wendelstein 7-X stellarator. *Nucl. Fusion* **58**, 096010 (2018).

[ADS](#) [Google Scholar](#)

45. 45.

Brunner, K. J. et al. Real-time dispersion interferometry for density feedback in fusion devices. *J. Instrum.* **13**, P09002 (2018).

46. 46.

Pasch, E. et al. The Thomson scattering system at Wendelstein 7-X. *Rev. Sci. Instrum.* **87**, 11E729 (2016).

[CAS](#) [Google Scholar](#)

47. 47.

Bozhenkov, S. A. et al. The Thomson scattering diagnostic at Wendelstein 7-X and its performance in the first operation phase. *JINST* **12**, P10004 (2017).

[ADS](#) [Google Scholar](#)

48. 48.

Hirsch, M. et al. ECE diagnostic for the initial operation of Wendelstein 7-X. In *20th Joint Workshop on Electron Cyclotron Emission and Electron Cyclotron Resonance Heating (EC20)* (eds Oosterbeek, J. et al.) 03007 (2019).

49. 49.

Höfel, U. et al. Bayesian modeling of microwave radiometer calibration on the example of the Wendelstein 7-X electron cyclotron emission diagnostic. *Rev. Sci. Instrum.* **90**, 043502 (2019).

[ADS](#) [Google Scholar](#)

50. 50.

Höfel, U. *Bayesian Analysis of Electron Cyclotron Emission Measurements at Wendelstein 7-X*. PhD thesis, Technische Universität Berlin (2020); <https://doi.org/10.14279/depositonce-9621>.

51. 51.

Ford, O. P. et al. Charge exchange recombination spectroscopy at Wendelstein 7-X. *Rev. Sci. Instrum.* **91**, 023507 (2020).

[ADS](#) [CAS](#) [PubMed](#) [PubMed Central](#) [Google Scholar](#)

52. 52.

Bitter, M. et al. Objectives and layout of a high-resolution X-ray imaging crystal spectrometer for the Large Helical Device. *Rev. Sci. Instrum.* **81**, 10E328 (2010).

[CAS](#) [PubMed](#) [PubMed Central](#) [Google Scholar](#)

53. 53.

Pablant, N. A. et al. Tomographic inversion techniques incorporating physical constraints for line integrated spectroscopy in stellarators and tokamaks. *Rev. Sci. Instrum.* **85**, 11E424 (2014).

[CAS](#) [PubMed](#) [PubMed Central](#) [Google Scholar](#)

54. 54.

Langenberg, A. et al. Prospects of X-ray imaging spectrometers for impurity transport: recent results from the stellarator Wendelstein 7-X. *Rev. Sci. Instrum.* **89**, 10G101 (2018).

[CAS](#) [PubMed](#) [PubMed Central](#) [Google Scholar](#)

55. 55.

Zhang, D. et al. First observation of a stable highly dissipative divertor plasma regime on the Wendelstein 7-X stellarator. *Phys. Rev. Lett.* **123**, 025002 (2019).

[ADS](#) [CAS](#) [PubMed](#) [PubMed Central](#) [Google Scholar](#)

[Download references](#)

Acknowledgements

This work has been carried out within the framework of the EUROfusion Consortium and has received funding from the Euratom research and training programme 2014–2018 and 2019–2020 under grant agreement no. 633053. The views and opinions expressed herein do not necessarily reflect those of the European Commission.

Funding

Open access funding provided by Max Planck Society.

Author information

Author notes

1. U. Hergenhahn

Present address: Fritz-Haber-Institut der Max-Planck-Gesellschaft,
Berlin, Germany

Affiliations

1. Max-Planck-Institut für Plasmaphysik, Greifswald, Germany

C. D. Beidler, H. M. Smith, T. Andreeva, J. Baldzuhn, M. N. A. Beurskens, M. Borchardt, S. A. Bozhenkov, K. J. Brunner, H. Damm, M. Drevlak, O. P. Ford, G. Fuchert, J. Geiger, P. Helander, U. Hergenhahn, M. Hirsch, U. Höfel, R. Kleiber, M. Krychowiak, S. Kwak, A. Langenberg, H. P. Laqua, U. Neuner, E. Pasch, A. Pavone, T. S. Pedersen, K. Rahbarnia, J. Schilling, E. R. Scott, T. Stange, J. Svensson, H. Thomsen, Y. Turkin, F. Warmer, R. C. Wolf, D. Zhang, I. Abramovic, S. Äkäslompolo, J. Alcusón, P. Aleynikov, K. Aleynikova, A. Ali, J. P. Bähner, M. Banduch, A. Benndorf, C. Biedermann, M. Blatzheim, T. Bluhm, D. Böckenhoff, L.-G. Böttger, H.-S. Bosch, R. Brakel, C. Brandt, T. Bräuer, H. Braune, K.-J. Brunner, R. Burhenn, R. Bussiahn, B. Buttenschön, V. Bykov, A. Carls, N. Chaudhary, M. Cole, M. Czerwinski, S. Degenkolbe, C. P. Dhard, A. Dinklage, P. Drewelow, G. Ehrke, M. Endler, J. Fellinger, Y. Feng, B. Geiger, D. Gradic, M. Grahl, H. Grote, O. Grulke, P. Hacker, D. Hartmann, D. Hathiramani, B. Hein, P. Helander, S. Henneberg, U. Hergenhahn, A. Hölting, Z. Huang, M. Jakubowski, H. Jenzsich, J.-P. Kallmeyer, U. Kamionka, C. Killer, T. Klinger, J. Knauer, A. Könies, R. König, P. Kornejew, J.-P. Koschinsky, R. Krampitz, J. Krom, G. Kühner, P. A. Kurz, H. Laqua, R. Laube, C. Li, J.-F. Lobsien, J. Loizu Cisquella, A. Lorenz, H. Maaßberg, S. Marsen, M. Marushchenko, P. McNeely, A. Mishchenko, B. Missal, A.

Mollen, T. Mönnich, D. Moseev, M. Nagel, D. Naujoks, H. Niemann, T. Nishizawa, C. Nührenberg, J. Nührenberg, J. W. Oosterbeek, M. Otte, N. Panadero, T. S. Pedersen, V. Perseo, D. Pilopp, S. Pingel, G. Plunk, A. Puig Sitjes, F. Purps, F. Reimold, J. Riemann, K. Risse, D. Rondeshagen, P. Rong, L. Rudischhauser, K. Rummel, T. Rummel, A. Runov, N. Rust, J. Schacht, F. Schauer, G. Schlisio, M. Schneider, W. Schneider, P. Scholz, M. Schröder, T. Schröder, R. Schroeder, B. Shanahan, P. Sinha, C. Slaby, A. Spring, U. Stridde, H. Trimino Mora, I. Vakulchyk, S. Valet, P. van Eeten, H. Viebke, R. Vilbrandt, A. von Stechow, A. Vorköper, F. Wagner, Z. Wang, L. Wegener, T. Wegner, G. Weir, J. Wendorf, U. Wenzel, A. Werner, F. Wilde, T. Windisch, M. Winkler, A. Winter, R. C. Wolf, P. Xanthopoulos, M. Zanini, J. Zhu & A. Zocco

2. Laboratorio Nacional de Fusion, CIEMAT, Madrid, Spain

A. Alonso, A. Alonso, E. Ascasibar, E. Blanco, I. Calvo, A. Cappa, F. Castejon, A. de la Pena, H. Esteban, T. Estrada, J. Fontdecaba, J. García Regaña, C. Guerard, J. Hernandez Sanchez, C. Hidalgo, D. Loesser, K. McCarthy, L. Pacios Rodriguez, N. Panadero Alvarez, M. Sanchez, B. van Milligen, J.-L. Velasco & H. Zhang

3. Laboratory for Plasma Physics (LPP), École royale militaire/Koninklijke Militaire School (ERM/KMS), Brussels, Belgium

Ye. O. Kazakov, F. Durodie, A. Goriaev, J. Ongena, B. Schweer, M. Vergote, M. Vervier & T. Wauters

4. Princeton Plasma Physics Laboratory, Princeton, NJ, USA

N. A. Pablant, D. Gates, B. Israeli, S. Langish, S. Lazerson, D. Mikkelsen, J. Mittelstaedt, H. Neilson, A. Reiman, M. Sibilia & M. Zarnstorff

5. Wigner Research Centre for Physics, Budapest, Hungary

G. Anda, G. Cseh, T. Ilkei, G. Kocsis, G. Náfrádi, S. Récsei, V. Szabó, T. Szabolics, T. Szepesi, Z. Szökefalvi-Nagy, S. Tulipán, L. Vanó & S. Zoletnik

6. Massachusetts Institute of Technology, Cambridge, MA, USA

S. G. Baek, S. Ballinger, E. Edlund, M. Porkolab, J. Terry & A. White

7. Max Planck Institute for Plasma Physics, Garching, Germany

M. Balden, B. Böswirth, J. Boscaro, M. Dibon, S. Elgeti, H. Frerichs, H. Greuner, B. Heinemann, P. Junghanns, P. Lang, M. Mayer, B. Mendelevitch, R. Neu, R. Nocentini, S. Obermayer, G. Orozco, P. Pölöskei, R. Riedl, V. Rohde, R. Stadler, J. Tretter, A. J. van Vuuren & M. Zilker

8. University of Wisconsin Madison, Madison, WI, USA

T. Barbui, F. Effenberg, E. Flom, J. Green, T. Kremeyer, O. Schmitz, L. Stephey & V. Winters

9. Institute for Energy and Climate Research – Plasma Physics, Research Center Jülich, Jülich, Germany

W. Behr, W. Biel, V. Borsuk, S. Brezinsek, J. Cai, A. Charl, J. Coenen, G. Czymek, T. Dittmar, P. Drews, A. Freund, Y. Gao, X. Han, M. Henkel, K. P. Hollfeld, D. Höschen, M. Hubeny, M. Jia, A. Kirschner, M. Knaup, A. Knieps, A. Krämer-Flecken, M. Lennartz, C. Li, Y. Li, Y. Liang, C. Linsmeier, S. Liu, O. Marchuk, P. Mertens, O. Neubauer, D. Nicolai, G. Offermanns, J. Ölmanns, M. Rack, D. Reiter, G. Satheeswaran, F. Schluck, H. Schmitz, S. Sereda, J. Thomas, B. Unterberg, E. Wang, N. Wang & Y. Wei

10. The Australian National University, Canberra, Australian Capital Territory, Australia

B. Blackwell, J. H. Matthew & A. Wright

11. Technical University of Denmark, Kongens Lyngby, Denmark

L.-G. Böttger, O. Grulke, S. K. Nielsen, M. Salewski, M. Stejner & A. Tancetti

12. Eindhoven University of Technology, Eindhoven, Netherlands

H. Brand, J. Howard, S. Paqay, J. Proll & M. Zuin

13. University of Cagliari, Cagliari, Italy

B. Cannas & F. Pisano

14. Consorzio RFX, Padova, Italy

L. Carraro & N. Vianello

15. Instituto de Plasmas e Fusao Nuclear, Lisbon, Portugal

B. Carvalho

16. CEA Cadarache, Saint-Paul-lez-Durance, France

D. Chauvin, A. da Silva, H. Fernandes, B. Goncalves, A. Grosman, M. Houry, V. Moncada, T. Ngo, S. Renard & J. M. Travere

17. Ioffe Physical-Technical Institute of the Russian Academy of Sciences, St Petersburg, Russian Federation

F. Chernyshev

18. Oak Ridge National Laboratory, Oak Ridge, TN, USA

M. Cianciosa, M. J. Cole, J. H. Harris, J. Lore, A. Lumsdaine & D. A. Spong

19. University of Salerno, Fisciano, Italy

R. Citarella & V. Giannella

20. ENEA Centro Ricerche Frascati, Frascati, Italy

G. Claps & F. Cordella

21. Institute of Plasma Physics and Laser Microfusion, Warsaw, Poland

A. Czarnecka, W. Figacz, T. Fornal, A. Galkowski, M. Gruca, S. Jablonski, J. Kacmarczyk, N. Krawczyk, M. Kubkowska, G. Pelka & L. Ryc

22. University of Szczecin, Szczecin, Poland

K. Czerski & M. Slezak

23. University of Milano-Bicocca, Milan, Italy

A. da Molin

24. Auburn University, Auburn, AL, USA

D. Ennis, D. Maurer, J. Schmitt & P. Traverso

25. Karlsruhe Institute of Technology, Eggenstein-Leopoldshafen, Germany

W. H. Fietz, G. Gantenbein, M. Huber, H. Hunger, S. Illy, J. Jelonnek, T. Kobarg, R. Lang, W. Leonhardt, M. Losert, A. Meier, D. Mellein, D. Papenfuß, A. Samartsev, T. Scherer, A. Schlaich, W. Spiess, M. Thumm, S. Wadle & J. Weggen

26. National Institute for Fusion Science, Toki, Japan

T. Funaba, X. Huang, K. Ida, H. Kasahara, N. Kenmochi, S. Masuzaki, T. Morisaki, K. Ogawa, B. Peterson, S. Ryosuke, R. Sakamoto, S. Satake, C. Suzuki, N. Tamura, H. Tsuchiya, T. Tsujimura, H. Yamada, I. Yamada, R. Yasuhara & M. Yokoyama

27. Universidad Carlos III de Madrid, Madrid, Spain

A. Gogoleva & L. Vela

28. Greifswald University, Greifswald, Germany

P. Helander, T. Klinger & T. S. Pedersen

29. Institute for Surface Process Engineering and Plasma Technology,
University of Stuttgart, Stuttgart, Germany

T. Jesche, W. Kasperek, M. Krämer, C. Lechte, B. Plaum, F.
Remppel, H. Röhlinger, B. Roth, K.-H. Schlüter, S. Wolf & A. Zeitler

30. Austrian Academy of Science, Vienna, Austria

F. Köchl & R. Schrittwieser

31. Institute for Nuclear Research, Kiev, Ukraine

Y. Kolesnichenko & V. Lutsenko

32. Technical University of Berlin, Berlin, Germany

F. Köster & R. C. Wolf

33. University of Opole, Opole, Poland

I. Ksiazek & E. Pawelec

34. Aalto University, Espoo, Finland

T. Kurki-Suonio & S. Sipliä

35. University of Maryland, College Park, MA, USA

M. Landreman

36. Physikalisch Technische Bundesanstalt (PTB), Braunschweig,
Germany

A. Lücke, H. Schumacher & B. Wiegel

37. Kyoto University, Kyoto, Japan

T. Mizuuchi, S. Murakami & F. Sano

38. Istituto di Fisica del Plasma “Piero Caldirola”, Milan, Italy

M.-E. Puiatti & M. Romé

39. Culham Centre for Fusion Energy, Abingdon, UK

S. Schmuck

40. Los Alamos National Laboratory, Los Alamos, NM, USA

G. Wurden

Authors

1. C. D. Beidler

[View author publications](#)

You can also search for this author in [PubMed](#) [Google Scholar](#)

2. H. M. Smith

[View author publications](#)

You can also search for this author in [PubMed](#) [Google Scholar](#)

3. A. Alonso

[View author publications](#)

You can also search for this author in [PubMed](#) [Google Scholar](#)

4. T. Andreeva

[View author publications](#)

You can also search for this author in [PubMed](#) [Google Scholar](#)

5. J. Baldzuhn

[View author publications](#)

You can also search for this author in [PubMed](#) [Google Scholar](#)

6. M. N. A. Beurskens

[View author publications](#)

You can also search for this author in [PubMed](#) [Google Scholar](#)

7. M. Borchardt

[View author publications](#)

You can also search for this author in [PubMed](#) [Google Scholar](#)

8. S. A. Bozhenkov

[View author publications](#)

You can also search for this author in [PubMed](#) [Google Scholar](#)

9. K. J. Brunner

[View author publications](#)

You can also search for this author in [PubMed](#) [Google Scholar](#)

10. H. Damm

[View author publications](#)

You can also search for this author in [PubMed](#) [Google Scholar](#)

11. M. Drevlak

[View author publications](#)

You can also search for this author in [PubMed](#) [Google Scholar](#)

12. O. P. Ford

[View author publications](#)

You can also search for this author in [PubMed](#) [Google Scholar](#)

13. G. Fuchert

[View author publications](#)

You can also search for this author in [PubMed](#) [Google Scholar](#)

14. J. Geiger

[View author publications](#)

You can also search for this author in [PubMed](#) [Google Scholar](#)

15. P. Helander

[View author publications](#)

You can also search for this author in [PubMed](#) [Google Scholar](#)

16. U. Hergenhahn

[View author publications](#)

You can also search for this author in [PubMed](#) [Google Scholar](#)

17. M. Hirsch

[View author publications](#)

You can also search for this author in [PubMed](#) [Google Scholar](#)

18. U. Höfel

[View author publications](#)

You can also search for this author in [PubMed](#) [Google Scholar](#)

19. Ye. O. Kazakov

[View author publications](#)

You can also search for this author in [PubMed](#) [Google Scholar](#)

20. R. Kleiber

[View author publications](#)

You can also search for this author in [PubMed](#) [Google Scholar](#)

21. M. Krychowiak

[View author publications](#)

You can also search for this author in [PubMed](#) [Google Scholar](#)

22. S. Kwak

[View author publications](#)

You can also search for this author in [PubMed](#) [Google Scholar](#)

23. A. Langenberg

[View author publications](#)

You can also search for this author in [PubMed](#) [Google Scholar](#)

24. H. P. Laqua

[View author publications](#)

You can also search for this author in [PubMed](#) [Google Scholar](#)

25. U. Neuner

[View author publications](#)

You can also search for this author in [PubMed](#) [Google Scholar](#)

26. N. A. Pablot

[View author publications](#)

You can also search for this author in [PubMed](#) [Google Scholar](#)

27. E. Pasch

[View author publications](#)

You can also search for this author in [PubMed](#) [Google Scholar](#)

28. A. Pavone

[View author publications](#)

You can also search for this author in [PubMed](#) [Google Scholar](#)

29. T. S. Pedersen

[View author publications](#)

You can also search for this author in [PubMed](#) [Google Scholar](#)

30. K. Rahbarnia

[View author publications](#)

You can also search for this author in [PubMed](#) [Google Scholar](#)

31. J. Schilling

[View author publications](#)

You can also search for this author in [PubMed](#) [Google Scholar](#)

32. E. R. Scott

[View author publications](#)

You can also search for this author in [PubMed](#) [Google Scholar](#)

33. T. Stange

[View author publications](#)

You can also search for this author in [PubMed](#) [Google Scholar](#)

34. J. Svensson

[View author publications](#)

You can also search for this author in [PubMed](#) [Google Scholar](#)

35. H. Thomsen

[View author publications](#)

You can also search for this author in [PubMed](#) [Google Scholar](#)

36. Y. Turkin

[View author publications](#)

You can also search for this author in [PubMed](#) [Google Scholar](#)

37. F. Warmer

[View author publications](#)

You can also search for this author in [PubMed](#) [Google Scholar](#)

38. R. C. Wolf

[View author publications](#)

You can also search for this author in [PubMed](#) [Google Scholar](#)

39. D. Zhang

[View author publications](#)

You can also search for this author in [PubMed](#) [Google Scholar](#)

Consortia

the W7-X Team

- , I. Abramovic
- , S. Äkäslompolo
- , J. Alcusón
- , P. Aleynikov
- , K. Aleynikova
- , A. Ali
- , A. Alonso
- , G. Anda
- , T. Andreeva
- , E. Ascasibar
- , J. P. Bähner
- , S. G. Baek
- , M. Balden
- , J. Baldzuhn
- , M. Banduch
- , T. Barbui
- , W. Behr
- , C. D. Beidler
- , A. Benndorf
- , M. N. A. Beurskens
- , C. Biedermann
- , W. Biel
- , B. Blackwell
- , E. Blanco
- , M. Blatzheim
- , S. Ballinger
- , T. Bluhm
- , D. Böckenhoff
- , B. Böswirth
- , L.-G. Böttger
- , M. Borchardt
- , V. Borsuk
- , J. Boscary
- , H.-S. Bosch

- , S. A. Bozhenkov
- , R. Brakel
- , H. Brand
- , C. Brandt
- , T. Bräuer
- , H. Braune
- , S. Brezinsek
- , K.-J. Brunner
- , R. Burhenn
- , R. Bussiahn
- , B. Buttenschön
- , V. Bykov
- , J. Cai
- , I. Calvo
- , B. Cannas
- , A. Cappa
- , A. Carls
- , L. Carraro
- , B. Carvalho
- , F. Castejon
- , A. Charl
- , N. Chaudhary
- , D. Chauvin
- , F. Chernyshev
- , M. Cianciosa
- , R. Citarella
- , G. Claps
- , J. Coenen
- , M. Cole
- , M. J. Cole
- , F. Cordella
- , G. Cseh
- , A. Czarnecka
- , K. Czerski
- , M. Czerwinski
- , G. Czymek
- , A. da Molin

- , A. da Silva
- , H. Damm
- , A. de la Pena
- , S. Degenkolbe
- , C. P. Dhard
- , M. Dibon
- , A. Dinklage
- , T. Dittmar
- , M. Drevlak
- , P. Drewelow
- , P. Drews
- , F. Durodie
- , E. Edlund
- , F. Effenberg
- , G. Ehrke
- , S. Elgeti
- , M. Endler
- , D. Ennis
- , H. Esteban
- , T. Estrada
- , J. Fellinger
- , Y. Feng
- , E. Flom
- , H. Fernandes
- , W. H. Fietz
- , W. Figacz
- , J. Fontdecaba
- , O. P. Ford
- , T. Fornal
- , H. Frerichs
- , A. Freund
- , G. Fuchert
- , T. Funaba
- , A. Galkowski
- , G. Ganzenbein
- , Y. Gao
- , J. García Regaña

- , D. Gates
- , B. Geiger
- , J. Geiger
- , V. Giannella
- , A. Gogoleva
- , B. Goncalves
- , A. Goriaev
- , D. Gradic
- , M. Grahl
- , J. Green
- , H. Greuner
- , A. Grosman
- , H. Grote
- , M. Gruca
- , O. Grulke
- , C. Guerard
- , P. Hacker
- , X. Han
- , J. H. Harris
- , D. Hartmann
- , D. Hathiramani
- , B. Hein
- , B. Heinemann
- , P. Helander
- , S. Henneberg
- , M. Henkel
- , U. Hergenhahn
- , J. Hernandez Sanchez
- , C. Hidalgo
- , M. Hirsch
- , K. P. Hollfeld
- , U. Höfel
- , A. Hölting
- , D. Höschen
- , M. Houry
- , J. Howard
- , X. Huang

- , Z. Huang
- , M. Hubeny
- , M. Huber
- , H. Hunger
- , K. Ida
- , T. Ilkei
- , S. Illy
- , B. Israeli
- , S. Jablonski
- , M. Jakubowski
- , J. Jelonnek
- , H. Jenzsch
- , T. Jesche
- , M. Jia
- , P. Junghanns
- , J. Kacmarczyk
- , J.-P. Kallmeyer
- , U. Kamionka
- , H. Kasahara
- , W. Kasperek
- , Ye. O. Kazakov
- , N. Kenmochi
- , C. Killer
- , A. Kirschner
- , R. Kleiber
- , T. Klinger
- , J. Knauer
- , M. Knaup
- , A. Knieps
- , T. Kobarg
- , G. Kocsis
- , F. Köchl
- , Y. Kolesnichenko
- , A. Könies
- , R. König
- , P. Kornejew
- , J.-P. Koschinsky

- , F. Köster
- , M. Krämer
- , R. Krampitz
- , A. Krämer-Flecken
- , N. Krawczyk
- , T. Kremeyer
- , J. Krom
- , M. Krychowiak
- , I. Ksiazek
- , M. Kubkowska
- , G. Kühner
- , T. Kurki-Suonio
- , P. A. Kurz
- , S. Kwak
- , M. Landreman
- , P. Lang
- , R. Lang
- , A. Langenberg
- , S. Langish
- , H. Laqua
- , H. P. Laqua
- , R. Laube
- , S. Lazerson
- , C. Lechte
- , M. Lennartz
- , W. Leonhardt
- , C. Li
- , C. Li
- , Y. Li
- , Y. Liang
- , C. Linsmeier
- , S. Liu
- , J.-F. Lobsien
- , D. Loesser
- , J. Loizu Cisquella
- , J. Lore
- , A. Lorenz

- , M. Losert
- , A. Lücke
- , A. Lumsdaine
- , V. Lutsenko
- , H. Maaßberg
- , O. Marchuk
- , J. H. Matthew
- , S. Marsen
- , M. Marushchenko
- , S. Masuzaki
- , D. Maurer
- , M. Mayer
- , K. McCarthy
- , P. McNeely
- , A. Meier
- , D. Mellein
- , B. Mendelevitch
- , P. Mertens
- , D. Mikkelsen
- , A. Mishchenko
- , B. Missal
- , J. Mittelstaedt
- , T. Mizuuchi
- , A. Mollen
- , V. Moncada
- , T. Mönnich
- , T. Morisaki
- , D. Moseev
- , S. Murakami
- , G. Náfrádi
- , M. Nagel
- , D. Naujoks
- , H. Neilson
- , R. Neu
- , O. Neubauer
- , U. Neuner
- , T. Ngo

- , D. Nicolai
- , S. K. Nielsen
- , H. Niemann
- , T. Nishizawa
- , R. Nocentini
- , C. Nührenberg
- , J. Nührenberg
- , S. Obermayer
- , G. Offermanns
- , K. Ogawa
- , J. Ölmanns
- , J. Ongena
- , J. W. Oosterbeek
- , G. Orozco
- , M. Otte
- , N. A. Pablant
- , L. Pacios Rodriguez
- , N. Panadero
- , N. Panadero Alvarez
- , D. Papenfuß
- , S. Paqay
- , E. Pasch
- , A. Pavone
- , E. Pawelec
- , T. S. Pedersen
- , G. Pelka
- , V. Perseo
- , B. Peterson
- , D. Pilopp
- , S. Pingel
- , F. Pisano
- , B. Plaum
- , G. Plunk
- , P. Pölöskei
- , M. Porkolab
- , J. Proll
- , M.-E. Puiatti

- , A. Puig Sitjes
- , F. Purps
- , M. Rack
- , K. Rahbarnia
- , S. Récsei
- , A. Reiman
- , F. Reimold
- , D. Reiter
- , F. Remppel
- , S. Renard
- , R. Riedl
- , J. Riemann
- , K. Risse
- , V. Rohde
- , H. Röhlinger
- , M. Romé
- , D. Rondeshagen
- , P. Rong
- , B. Roth
- , L. Rudischhauser
- , K. Rummel
- , T. Rummel
- , A. Runov
- , N. Rust
- , L. Ryc
- , S. Ryosuke
- , R. Sakamoto
- , M. Salewski
- , A. Samartsev
- , M. Sanchez
- , F. Sano
- , S. Satake
- , J. Schacht
- , G. Satheeswaran
- , F. Schauer
- , T. Scherer
- , J. Schilling

- , A. Schlaich
- , G. Schlisio
- , F. Schluck
- , K.-H. Schlüter
- , J. Schmitt
- , H. Schmitz
- , O. Schmitz
- , S. Schmuck
- , M. Schneider
- , W. Schneider
- , P. Scholz
- , R. Schrittwieser
- , M. Schröder
- , T. Schröder
- , R. Schroeder
- , H. Schumacher
- , B. Schweer
- , E. R. Scott
- , S. Sereda
- , B. Shanahan
- , M. Sibilia
- , P. Sinha
- , S. Sipliä
- , C. Slaby
- , M. Slezcka
- , H. M. Smith
- , W. Spiess
- , D. A. Spong
- , A. Spring
- , R. Stadler
- , T. Stange
- , M. Stejner
- , L. Stephey
- , U. Stridde
- , C. Suzuki
- , J. Svensson
- , V. Szabó

- , T. Szabolics
- , T. Szepesi
- , Z. Szökefalvi-Nagy
- , N. Tamura
- , A. Tancetti
- , J. Terry
- , J. Thomas
- , H. Thomsen
- , M. Thumm
- , J. M. Travere
- , P. Traverso
- , J. Tretter
- , H. Trimino Mora
- , H. Tsuchiya
- , T. Tsujimura
- , S. Tulipán
- , Y. Turkin
- , B. Unterberg
- , I. Vakulchyk
- , S. Valet
- , L. Vanó
- , P. van Eeten
- , B. van Milligen
- , A. J. van Vuuren
- , L. Vela
- , J.-L. Velasco
- , M. Vergote
- , M. Vervier
- , N. Vianello
- , H. Viebke
- , R. Vilbrandt
- , A. von Stechow
- , A. Vorköper
- , S. Wadle
- , F. Wagner
- , E. Wang
- , N. Wang

- , Z. Wang
- , F. Warmer
- , T. Wauters
- , L. Wegener
- , J. Weggen
- , T. Wegner
- , Y. Wei
- , G. Weir
- , J. Wendorf
- , U. Wenzel
- , A. Werner
- , A. White
- , B. Wiegel
- , F. Wilde
- , T. Windisch
- , M. Winkler
- , A. Winter
- , V. Winters
- , S. Wolf
- , R. C. Wolf
- , A. Wright
- , G. Wurden
- , P. Xanthopoulos
- , H. Yamada
- , I. Yamada
- , R. Yasuhara
- , M. Yokoyama
- , M. Zanini
- , M. Zarnstorff
- , A. Zeitler
- , D. Zhang
- , H. Zhang
- , J. Zhu
- , M. Zilker
- , A. Zocco
- , S. Zoletnik
- & M. Zuin

Contributions

J.B., S.A.B., Ye.O.K. and H.P.L. planned and coordinated the experiment described here. T.S. provided the ECRH power and its deposition profile. K.J.B. calculated the unabsorbed ECRH power using sniffer probe data. S.A.B., H.D., G.F., E.P. and E.R.S. supplied Thomson data. K.J.B. provided interferometer data. M.H. and U. Höfel supplied ECE data. A.L. and N.A.P. supplied XICS data. O.P.F. supplied CXRS data. U. Hergenhahn, M.K., S.K., A.P. and J. Svensson provided experimental data for the effective charge state or helped in analysis of this data. T.A., U.N., K.R., J. Schilling and H.T. supplied measurements of the diamagnetic energy. D.Z. provided results for the radiated power. A.A., O.P.F., N.A.P. and A.L. provided experimental profiles of E_r . M.N.A.B., U. Höfel, A.L., N.A.P. and F.W. performed data analysis. J.B. provided data concerning the pellet series. J.G. carried out VMEC calculations. H.M.S. created the DKES datasets and performed the calculations of neoclassical fluxes. Y.T. determined the profiles of effective helical ripple. C.D.B. created the figures (except for Extended Data Fig. 1) and is the principal author of this paper with contributions to the body of the text from P.H., T.S.P. and R.C.W. and with text concerning the diagnostics from K.J.B., M.H., N.A.P., K.R. and D.Z. M.D. provided the depiction of the W7-X non-planar coils. Particle orbit videos were prepared by M.B. and R.K. All authors provided feedback and contributed to improving the paper.

Corresponding author

Correspondence to [C. D. Beidler](#).

Ethics declarations

Competing interests

The authors declare no competing interests.

Additional information

Peer review information *Nature* thanks Dennis Whyte and the other, anonymous, reviewer(s) for their contribution to the peer review of this work. Peer reviewer reports are available.

Publisher's note Springer Nature remains neutral with regard to jurisdictional claims in published maps and institutional affiliations.

Extended data figures and tables

[Extended Data Fig. 1 Non-planar coil system of W7-X, viewed from above.](#)

The complete set of superconducting coils also includes 20 planar coils, four in each field period, which are used to change the rotational transform and/or shift the plasma column; these are not shown as they remain current-free for the configurations considered here.

[Extended Data Fig. 2 Time traces for W7-X discharge 20180918.045.](#)

In the top frame, the launched ECRH power is shown, as well as the radiated power measured by bolometers (dotted curve). The second frame plots the line-integrated density measured by an interferometer. The third frame depicts ‘core’ electron (red) and ion (blue) temperatures from Thomson scattering and XICS measurements, respectively. The diamagnetic energy trace during this discharge is given in the bottom frame. A series of 28 pellets is injected into the plasma at a frequency of 30 Hz during the time phase indicated in grey. W_{dia} values exceeding 1.02 MJ are recorded during the phase indicated in yellow.

[Extended Data Fig. 3 Profiles of the radial electric field as a function of the normalized plasma radius.](#)

Experimental results from CXRS (blue) and XICS (red) measurements are compared to the theoretical expectations from the ambipolarity constraint (black) for the plasma profiles of Fig. 2. Error bars depict one standard

deviation in the evaluation of the measurements. The XICS analysis is described in ref. [30](#); documentation of the methodology used to evaluate the CXRS measurements is in preparation.

Supplementary information

Supplementary Information

This file contains detailed notes regarding Supplementary Videos 1 and 2.

Video 1

Localized ion trajectory in the W7-X standard configuration – see Supplementary Information document for detailed description.

Video 2

Localized ion trajectory in the LHD configuration having a major radius of 3.75 m - see Supplementary Information document for detailed description.

Rights and permissions

Open Access This article is licensed under a Creative Commons Attribution 4.0 International License, which permits use, sharing, adaptation, distribution and reproduction in any medium or format, as long as you give appropriate credit to the original author(s) and the source, provide a link to the Creative Commons license, and indicate if changes were made. The images or other third party material in this article are included in the article's Creative Commons license, unless indicated otherwise in a credit line to the material. If material is not included in the article's Creative Commons license and your intended use is not permitted by statutory regulation or exceeds the permitted use, you will need to obtain permission directly from the copyright holder. To view a copy of this license, visit <http://creativecommons.org/licenses/by/4.0/>.

Reprints and Permissions

About this article



Cite this article

Beidler, C.D., Smith, H.M., Alonso, A. *et al.* Demonstration of reduced neoclassical energy transport in Wendelstein 7-X. *Nature* **596**, 221–226 (2021). <https://doi.org/10.1038/s41586-021-03687-w>

Download citation

- Received: 30 April 2020
- Accepted: 02 June 2021
- Published: 11 August 2021
- Issue Date: 12 August 2021
- DOI: <https://doi.org/10.1038/s41586-021-03687-w>

Comments

By submitting a comment you agree to abide by our [Terms](#) and [Community Guidelines](#). If you find something abusive or that does not comply with our terms or guidelines please flag it as inappropriate.

Download PDF

Advertisement

| [Section menu](#) | [Main menu](#) |

Evidence for an atomic chiral superfluid with topological excitations

[Download PDF](#)

- Article
- Open Access
- [Published: 11 August 2021](#)

Evidence for an atomic chiral superfluid with topological excitations

- [Xiao-Qiong Wang^{1,2}](#) ✉ [ORCID: orcid.org/0000-0002-9941-518X⁶](#),
- [Guang-Quan Luo^{1,2}](#) ✉ [ORCID: orcid.org/0000-0002-9941-518X⁶](#),
- [Jin-Yu Liu^{1,2}](#),
- [W. Vincent Liu](#) ^{2,3,4,5},
- [Andreas Hemmerich](#) [ORCID: orcid.org/0000-0002-9941-518X⁶](#) &
- [Zhi-Fang Xu](#) [ORCID: orcid.org/0000-0003-3280-7493^{1,2}](#)

[Nature](#) volume **596**, pages 227–231 (2021) [Cite this article](#)

- 3277 Accesses
- 1 Altmetric
- [Metrics details](#)

Subjects

- [Bose–Einstein condensates](#)
- [Quantum simulation](#)
- [Ultracold gases](#)

Abstract

Topological superfluidity is an important concept in electronic materials as well as ultracold atomic gases¹. However, although progress has been made by hybridizing superconductors with topological substrates, the search for a material—natural or artificial—that intrinsically exhibits topological superfluidity has been ongoing since the discovery of the superfluid ³He-A phase². Here we report evidence for a globally

chiral atomic superfluid, induced by interaction-driven time-reversal symmetry breaking in the second Bloch band of an optical lattice with hexagonal boron nitride geometry. This realizes a long-lived Bose–Einstein condensate of ^{87}Rb atoms beyond present limits to orbitally featureless scenarios in the lowest Bloch band. Time-of-flight and band mapping measurements reveal that the local phases and orbital rotations of atoms are spontaneously ordered into a vortex array, showing evidence of the emergence of global angular momentum across the entire lattice. A phenomenological effective model is used to capture the dynamics of Bogoliubov quasi-particle excitations above the ground state, which are shown to exhibit a topological band structure. The observed bosonic phase is expected to exhibit phenomena that are conceptually distinct from, but related to, the quantum anomalous Hall effect^{3,4,5,6,7} in electronic condensed matter.

[Download PDF](#)

Main

Quantum simulation involves the use of a comparably simple and precisely controlled synthetic quantum system to mimic poorly understood, isolated phenomena of a far more complex but less-controlled quantum system, while excluding the superimposed secondary structure that would impede a clear understanding⁸. Optical lattices—that is, ultracold neutral atoms trapped in laser-induced periodic potentials^{9,10,11}—are well established systems that simulate an elementary class of many-body lattice model, the conventional s -band Hubbard model^{12,13}. However, a large part of the physics that is relevant in electronic many-body systems is related to the coupling of electrons to magnetic fields via the Lorentz force, and hence remains inaccessible to quantum simulations in conventional optical lattices. Extensive research has been undertaken to establish a similar mechanism for neutral atoms in optical lattices, giving rise to so-called artificial magnetic fields or gauge fields^{14,15} using dynamical techniques—similar to what is sometimes summarized as Floquet engineering for condensed-matter physics¹⁶. This has enabled the single-particle band structures of optical lattices to be endowed with built-in local¹⁷ or even global^{18,19} magnetic flux and the resultant single-particle topological properties; however, this comes at the cost of notable decoherence and markedly reduced lifetimes. An alternative approach towards optical lattice simulators beyond conventional s -band Hubbard physics is the implementation of orbital degrees of freedom by making use of higher Bloch bands^{20,21,22,23,24}. This recent direction has led to interesting new multi-orbital quantum phases, including examples that have local angular momentum. An intriguing, but as-yet unobtained, goal of this approach is to achieve a multi-orbital optical lattice quantum simulator that can, for example, capture bosonic versions of the topological superfluidity of paired electrons²⁵, or of quantum-Hall-related physics²⁶.

Here we take a step in this direction by demonstrating interaction-induced, spontaneous time-reversal symmetry (TRS) breaking and formation of a chiral atomic superfluid in an orbital optical lattice with global angular momentum and topological excitations and edge states. This metastable state exhibits remarkable robustness with a lifetime of hundreds of milliseconds. As an unequivocal signature of the prevalence of global angular momentum, characteristic momentum spectra are observed using time-of-flight spectroscopy. Our experimental observations directly show the spontaneous breaking of TRS in accordance with a mean-field tight-binding model and exact band calculations. The system is expected to exhibit the bosonic counterpart of the quantum anomalous Hall effect^{3,4,5,6,7}; however, not as a result of an engineered band structure, as in the famous Haldane model²⁷. Rather, as shown by theoretical considerations ([Supplementary Information](#)), it is the contact interaction between degenerate p orbitals that leads to a spontaneous breaking of TRS, the formation of global angular momentum, a topologically non-trivial excitation band structure and the existence of topological edge states.

Our experiments use a boron nitride optical lattice that is composed of alternating shallow and deep potential wells—denoted A and B, respectively—arranged on a hexagonal lattice. As indicated in Fig. [1a](#), the lattice potential is formed by three laser beams operating at a wavelength λ of 1,064 nm. The beams propagate within the x – y plane and intersect at an angle of 120°. Each beam comprises two spectral components at frequencies ω_1 and ω_2 , with linear polarizations in the z -direction. Each set of spectral components with the same frequency forms a triangular lattice with adjustable amplitude. By tuning the frequency difference $\omega_1 - \omega_2$, the intensity patterns of both triangular lattices are shifted with respect to each other such that their sum produces a boron nitride lattice geometry with A and B wells. The relative potential offset of the two classes of well, denoted ΔV , can be rapidly tuned. An optical dipole trap provides weak harmonic confinement with regard to the z -direction. For details, see [Methods](#) and [Supplementary information](#).

Fig. 1: Lattice set-up and single-particle band structure.

 **figure1**

a, Lattice potential of the boron nitride optical lattice with two distinct local minima denoted A and B. The grey solid hexagon indicates the unit cell. **b**, Left, a contour plot of the second band of the boron nitride lattice across the second Brillouin zone. Right, the energy dispersion along the trajectory of high-symmetry points highlighted by the red triangle shows a double-well scenario. Two degenerate band minima arise at the K_Δ and K_∇ points. **c**, The first image shows the orbital composition of the second band Bloch function $\langle \{\Phi\}_{\{\{K\}\}}_{\{\Delta\}} \rangle$ associated with the K_Δ point. The shallow wells host s orbitals and the deep well hosts $p_+ = p_x + ip_y$ hybrid orbitals. The colours (green, red, blue) denote local phase values $\langle \nu 2\{\pi\} \rangle / 3, \nu \in \{0,1,2\}$. The region shown corresponds to the unit cell of $\langle \{\Phi\}_{\{\{K\}\}}_{\{\Delta\}} \rangle$, which covers an area of three times the unit cell of the lattice potential. The second (third) panel illustrates the spatial distribution of $\langle |\{\Phi\}_{\{\{K\}\}}_{\{\Delta\}}| \rangle$ when the s orbitals in the shallow wells have lower (higher) energy than the p orbitals in the deep wells. The fourth panel shows the mass current associated with the third panel.

[Full size image](#)

Initially, a Bose–Einstein condensate of ^{87}Rb atoms was loaded into the lowest Bloch band in the centre of the first Brillouin zone, denoted Γ in Fig. 1b. The overall trap depth along the vertical z -axis—including the lattice potential, the dipole trap and gravitation—is 221 nK. As a key feature of our preparation protocol, we applied additional cooling by means of evaporation after the atoms were loaded into the

lattice. The dipole trap depth decreases within 15 ms, such that the overall trap depth along the z -direction is reduced to 41 nK and the energetic atoms can escape. At this stage the atomic wavefunction is composed of s orbitals residing in the deep B wells of the lattice. In a subsequent rapid quench the atoms are excited to the second band (compare with Fig. 1b) while remaining at the Γ point, which constitutes a dynamically unstable energy maximum²⁸. This is accomplished by tuning ΔV in approximately 100 μ s according to the diagram in Fig. 2a, until the local s orbitals in the B wells come to lie between the s and p orbitals in the A wells and hence belong to the second band. This also leads to a further reduction, to 24 nK, of the overall trap depth with respect to the z -direction, and thus an additional boost of evaporative cooling. Typical momentum spectra (Fig. 2c) recorded shortly (0.5 ms) after the quench show that a large number of Bloch states of the second band are populated with no apparent coherence²⁸. Related excitation protocols without additional evaporation have been used previously with bipartite square lattices^{22,23} and with hexagonal lattices^{29,30}. For details, see [Methods](#) and [Supplementary Information](#).

Fig. 2: Formation of second-band condensates.



a, The experimental sequence used to populate the second band. Initially, atoms are loaded into the s orbitals of the deep B wells (left). Subsequently, the relative potential offset of A and B wells is rapidly tuned until the local s orbitals in shallow B wells are centred between the s and the p orbitals in the deep A wells (right). For this setting, the s orbitals in the shallow B wells are predominantly populated and form the second band. **b**, Exact band calculation of the momentum distribution for the Bloch function $\langle \{\Phi\}_{\{K\}} \rangle_{\{\Delta\}}$. h , Planck's constant. **c**, Momentum spectra at various holding times. The top and bottom rows correspond to second-band condensates with dominant condensate fractions at K_Δ and K_∇ , respectively. The middle row shows condensates with nearly equal condensate fractions at K_Δ and K_∇ .

[Full size image](#)

The second band gives rise to a symmetric double-well scenario in quasi-momentum space. It possesses two inequivalent global energy minima located at the corners of the first Brillouin zone—denoted K_Δ and K_∇ in Fig. 1b—which exhibit perfect

degeneracy, protected by TRS. A central observation of this work is that, in a re-condensation process, TRS is spontaneously broken and a condensate forms in either of the two K points with equal probability. This is shown in Fig. 2c, which displays momentum spectra recorded after variable holding times of between 0.5 ms and 755 ms. As time proceeds, sharp Bragg resonances grow at the K_Δ and K_∇ points.

These resonances indicate the build-up of long-range coherence, and hence the formation of condensate fractions at K_Δ and K_∇ . Notably, these condensate fractions—according to the observations—are generally not equally sized, as is shown in Fig. 2c, in which the three rows show examples with either a dominant K_Δ component (top), a dominant K_∇ component (bottom) or both components of similar size (middle).

We next point out that the observation of a dominant condensate fraction in either of the K points constitutes clear evidence of broken TRS. Exact band theory shows that the momentum spectra observed in the top and bottom rows of Fig. 2c are very well reproduced by the calculated momentum spectra of the Bloch functions associated with K_Δ and K_∇ , respectively. For example, the calculated momentum spectrum of the Bloch function at K_Δ in Fig. 2b is plotted for comparison in the top row of Fig. 2c. Hence, the observation of population in a single K point unequivocally indicates the presence of a wavefunction that is well approximated by the Bloch function associated with that K point. Note that these Bloch functions, $\langle \{\Phi\}_{\{K\}} \rangle_{\{\Delta\}}$ and $\langle \{\Phi\}_{\{\{K\}\}} \rangle_{\{\nabla\}}$, inherently break TRS, as stated in Fig. 1c. The first panel schematically illustrates the composition of $\langle \{\Phi\}_{\{\{K\}\}} \rangle_{\{\Delta\}}$ in terms of local s orbitals in the shallow wells and p_x and p_y orbitals in the deep wells, which form $p_+ = p_x + ip_y$ hybrid orbitals (p_- in case of K_∇). The three distinct colours indicate local phases that differ by $2\pi/3$, which results from an inherent vortical phase texture of $\langle \{\Phi\}_{\{\{K\}\}} \rangle_{\{\Delta\}}$. In the second and third panels of Fig. 1c, $|\langle \{\Phi\}_{\{K\}} \rangle_{\{\Delta\}}|$, which is derived from exact band theory, is plotted for two different settings of ΔV , showing that different relative populations at A and B wells can be adjusted. The fourth panel shows the vortical mass current associated with $\langle \{\Phi\}_{\{\{K\}\}} \rangle_{\{\Delta\}}$ for the same choice of ΔV as in the third panel. Note that the vortices residing at each deep well across the entire lattice all share the same sense of rotation—an interesting property that is associated with the threefold rotation symmetry of the hexagonal lattice in connection with the twofold degeneracy of the p orbital manifold in two dimensions.

We define an experimental measure of chirality $\chi = (n_\Delta - n_\nabla)/(n_\Delta + n_\nabla)$ as the imbalance between $\langle \{\Phi\}_{\{\{K\}\}} \rangle_{\{\Delta\}}$ and $\langle \{\Phi\}_{\{\{K\}\}} \rangle_{\{\nabla\}}$ condensate populations, n_Δ and n_∇ , respectively. This quantity is observed to be random in each experimental implementation with nearly zero average over many shots. However, although for short holding times—that is, in

the initial phase of the condensation process—a distribution of χ with a maximum at zero is found, for long times beyond 100 ms this distribution develops pronounced maxima around ± 0.5 . This is shown in Fig. 3: in Fig. 3a, the average of the modulus of the chirality $\langle |\chi| \rangle$ is plotted against the holding time, whereas in Fig. 3b histograms of the distribution of χ are shown for holding times ranging from 35 ms to 505 ms. As is seen in Fig. 3a, $\langle |\chi| \rangle$ is small for short holding times of a few ms, and continuously increases until it reaches a maximum at around 0.4 for a holding time of about 265 ms, where the distribution of χ (compare with Fig. 3b) shows a pronounced bimodal structure. According to these observations, the condensation process develops in two stages: the first stage spontaneously breaks $U(1)$ symmetry, forming a condensate that is approximately described by an equal superposition of Bloch states $\langle \{\Phi\}_{\{K\}} \rangle_{\{\Delta\}}$ and $\langle \{\Phi\}_{\{K\}} \rangle_{\{\nabla\}}$, thus globally preserving TRS and zero net angular momentum. Alternatively, as in the one-dimensional double-well scenario of ref. 31, domains could be formed, such that locally TRS is broken but the net angular momentum remains at zero. However, the narrow width of the observed Bragg peaks—seen in the momentum spectra with equally occupied K points in Fig. 2c—indicate well established coherence over large parts of the lattice, which is not compatible with a fine-grain domain structure. The second condensation stage breaks the global TRS by spontaneously bifurcating to form either of the two states $\langle \{\Phi\}_{\{K\}} \rangle_{\{\Delta\}}$ or $\langle \{\Phi\}_{\{K\}} \rangle_{\{\nabla\}}$, with equal probability.

Fig. 3: Spontaneous breaking of TRS.

 **figure3**

- a**, Evolution of chirality, which is characterized by the mean value of $|\chi|$. The inset specifies the definition of χ . The error bars denote the s.e.m. for 46 experimental runs.
- b**, Stacked histograms of χ for different holding times. **c**, In situ absorption images are recorded of a plane oriented perpendicular to the $x-y$ plane for various holding times

in the lattice. A stream of atoms escapes from the trap along the direction of gravity ($-z$ axis) for holding times between ten and several hundred microseconds.

[Full size image](#)

Theoretical considerations (detailed in the [Supplementary Information](#)) suggest that the second stage of the condensation process is triggered by the ferromagnetic collisional interactions within the manifold of degenerate p orbitals in the deep lattice wells. In the presence of such collisions, the ground state according to mean-field theory is given by a condensate in either of the two K points rather than a superposition of both (see [Supplementary Information](#)). The atoms are self-organized into an order of synchronized vortices centred at each of the deep wells across the entire boron nitride lattice, as illustrated in Fig. 1c. The fraction of atoms populating the p_+ orbitals give rise to a non-zero global angular momentum. To access the ground state, which requires build-up of global orbital angular momentum, angular momentum must be exchanged with the environment. Indeed, a signature of this process is observed in the experiment. As shown in Fig. 3c, during the second condensation phase, past about 10 ms holding time, we observe a stream of atoms leaving the lattice perpendicular to the lattice plane (x - y plane) along the direction of gravity ($-z$ -direction). This supports the interpretation that kinetic energy and angular momentum are transferred out of the lattice plane into the weakly confined z -direction, and finally escape from the lattice. It is of interest to note that, for stronger collisional interactions, under the assumption of quasi-momentum conservation, a condensate at the M points (Fig. 1b) is predicted to have a lower energy (Supplementary Fig. 5). However, a phase-separated mixed state with equal contributions from both K points might nevertheless be energetically more favourable.

The plots in Fig. 2c are obtained with ΔV adjusted during step 1 in Fig. 2a, such that most of the atoms in the second band reside in local s orbitals in the shallow wells and thus do not contribute notable orbital angular momentum. This corresponds to the wavefunction illustrated in the second panel of Fig. 1c. We now discuss how, by means of a slightly modified preparation protocol, a state with large global orbital angular momentum can be experimentally formed, which possesses a wavefunction according to the third panel of Fig. 1c. By adding an additional step (step 2 in Fig. 4a) 205 ms after the preparation protocol of step 1 in Fig. 2a, one may relocate a substantial portion of the atomic population towards the vortical p orbitals in the deep wells. This step consists of adiabatically tuning ΔV (in 1 ms) until the local s orbitals in the shallow wells lie energetically above the p orbitals of the deep wells (see [Methods](#) and [Supplementary Information](#)). The absolute value of the corresponding wavefunction is shown in the third panel of Fig. 1c. In Fig. 4c we observe the resulting faster band relaxation that notably depletes the second band after only 10 ms. This observation indicates that the collision dynamics is now dominated

by atoms in the p orbitals of the deep wells, which provide faster decay due to increased overlap with the s orbitals of the lowest band²³. As a direct signature of dominant population of the p orbitals, their additional nodes lead to destructive interference, thus preventing the occurrence of Bragg resonances within the areas enclosed by red dashed circles in Fig. 4c. This observation follows the exact band calculations in Fig. 4b. Note the contrast with the analogous spectra in Fig. 2b and with the corresponding experimental spectra in the top row of Fig. 2c. A large global orbital angular momentum arises, to which each atom in the p_+ orbitals contributes a portion \hbar . A quantitative analysis of the dependence of angular momentum on ΔV is shown in [Supplementary Fig. 4](#).

Fig. 4: Global angular momentum.



a, Illustration of the extended preparation protocol: after executing step 1 as in Fig. 2a, in step 2, ΔV is adiabatically tuned such that the atomic population in the second band is relocated towards the p orbitals in the deep wells. **b**, Exact band calculations of the momentum distribution for the Bloch function $\langle \{\Phi\}_{\{K\}} \rangle_{\{\Delta\}}$ for dominant population of p_+ orbitals. The red dashed circles highlight the resulting absence of certain higher-order Bragg peaks, in contrast to Fig. 2b. **c**, Momentum spectra for extended preparation protocol at various holding times, analogous to those in Fig. 2c.

[Full size image](#)

Symmetric double-well scenarios in quasi-momentum space that lead to an interaction-induced spontaneous breaking of TRS and the formation of phases with staggered chiral order have been previously reported^{22,31,32}. The long-lived atomic orbital superfluid devised in this work exhibits global angular momentum of the ground state wavefunction, although the Hamiltonian preserves TRS. As a consequence, basic Bogoliubov-de Gennes analysis verifies the emergence of bosonic topological excitations and edge modes ([Supplementary Information](#)). This opens up

the prospect of studying these signatures experimentally. A direct comparison between experiment and theory would be enabled with regards to fundamental concepts that are related to, but have no previous analogue in, condensed-matter electronic and spin materials. Previous calculations have shown that, in a checkerboard square lattice with alternating shallow and deep wells and local non-zero angular momentum order, interaction-induced gaps should open in Bogoliubov quasiparticle spectra, and edge states protected by topological invariants should occur^{33,34}. The proposed Zeeman-like bias is, however, an experimental challenge to implement for orbital degrees of freedom. Here, the boron nitride lattice resolves this challenge by spontaneously breaking TRS globally (driven by intrinsic interaction) with an emerging global angular momentum order. This paves the way to study dynamically controlled quasiparticles as exotic as a possible counterpart of Majorana fermions in a bosonic superfluid. The latter is widely sought-after in electronic topological superconductors, and the [Supplementary Information](#) presents calculations that support this expectation.

Methods

Realization of optical lattice

A two-dimensional hexagonal boron nitride (BN) optical lattice potential is created by three laser beams, propagating in the x - y plane and intersecting at 120° angles. Each laser beam comprises two frequency components ω_1 and ω_2 —which are both linearly polarized along the z direction—with wavelength $\lambda \approx 1,064$ nm and therefore with negative detuning with respect to the relevant atomic transitions of rubidium atoms at 780 nm and 795 nm. The two frequency components are derived from two independent lasers. Experimentally, we first combine the two laser beams at frequencies ω_1 and ω_2 , respectively, before splitting them into three beams. The total electric field for all beams is then written as

$$\begin{aligned} \$\$ \begin{array}{l} \bf{E}(r,t)=E_1\{\bf{e}\}_z\sum_j\cos(\{\bf{k}\}_j\cdot\bf{r}-\omega_1t+\theta_j)+E_2\{\bf{e}\}_z\sum_j\cos(\{\bf{k}\}_j^*\prime\cdot\bf{r}-\omega_2t+\theta_j^*\prime). \end{array} \$\$ \end{aligned}$$

Here, the wave vectors are given by $\{\bf{k}\}_1=\{\bf{k}\}_z\{\rm{L}\}$ ($-\sqrt{3}/2, 1/2$), $\{\bf{k}\}_2=\{\bf{k}\}_z\{\rm{L}\}$ ($\sqrt{3}/2, 1/2$), $\{\bf{k}\}_3=\{\bf{k}\}_z\{\rm{L}\}$ ($0, -1$)), and $\{\bf{k}\}_j^*\prime=\{\omega_2/\omega_1\}\{\bf{k}\}_j$, where $\{\bf{k}\}_z\{\rm{L}\}=\omega_1/c$. $\theta_j=\omega_1L_j/c+\theta_0$ and $\theta_j^*\prime=\omega_2L_j/c+\theta_0^*\prime$, where L_j denotes the optical path length of the j th beam from the splitting point to the centre of

the lattice. The corresponding laser intensity $I(\mathbf{r})$ is proportional to the time averaging of the square of the electric field according to

$$\begin{aligned} & \text{\$\$}\backslash\text{begin}\{\text{array}\}\{\text{ll}\}I(\{\text{bf}\{\mathbf{r}\}\})\backslash\text{propto}\&\&\backslash\text{frac}\{3\}{2}\{\mathbf{E}\}_{\{1\}}^{\{2\}}+ \\ & \{\mathbf{E}\}_{\{1\}}^{\{2\}}\sum_{\{\langle i,j\rangle\}}\cos[\{\{\text{bf}\{k\}\}_{\{i\}}-\{\text{bf}\{k\}\}_{\{j\}}\}]\cdot \\ & \{\text{bf}\{\mathbf{r}\}\}+\{\theta\}_{\{i\}}-\{\theta\}_{\{j\}}]\&+\backslash\text{frac}\{3\}{2}\{\mathbf{E}\}_{\{2\}}^{\{2\}}+ \\ & \{\mathbf{E}\}_{\{2\}}^{\{2\}}\sum_{\{\langle i,j\rangle\}}\cos[\{\{\text{bf}\{k\}\}_{\{i\}}^{\{\prime\}}-\& \\ & \{\text{bf}\{k\}\}_{\{j\}}^{\{\prime\}}\}]\cdot \\ & \{\text{bf}\{\mathbf{r}\}\}+\{\theta\}_{\{i\}}^{\{\prime\}}-\{\theta\}_{\{j\}}^{\{\prime\}}],\text{\$end}\{\text{array}\}\$\$ \end{aligned}$$

where the summation $\langle i,j \rangle$ is limited to $\langle 1,2 \rangle$, $\langle 2,3 \rangle$, $\langle 3,1 \rangle$. The generated optical lattice potential is proportional to the laser intensity and takes the form

$$\begin{aligned} & \text{\$\$}\backslash\text{begin}\{\text{array}\}\{\text{ll}\}\{V\}_{\{\rm BN\}}(\{\text{bf}\{\mathbf{r}\}\})=\&-\{V\}_{\{1\}}\{3+2\sum_{\{\langle i,j\rangle\}}\cos[\{\{\text{bf}\{k\}\}_{\{i\}}-\{\text{bf}\{k\}\}_{\{j\}}\}]\cdot \\ & \{\text{bf}\{\mathbf{r}\}\}+(\{\theta\}_{\{i\}}-\{\theta\}_{\{j\}})]\&-\{V\}_{\{2\}}\{3+2\sum_{\{\langle i,j\rangle\}}\cos[\{\{\text{bf}\{k\}\}_{\{i\}}^{\{\prime\}}-\& \\ & \{\text{bf}\{k\}\}_{\{j\}}^{\{\prime\}}\}]\cdot \\ & \{\text{bf}\{\mathbf{r}\}\}+(\{\theta\}_{\{i\}}^{\{\prime\}}-\{\theta\}_{\{j\}}^{\{\prime\}})],\text{\$end}\{\text{array}\}\$\$ \end{aligned}$$

where $V_{1,2} \geq 0$ for the relevant case of red detuning. Each of the two spectral components creates a triangular lattice potential, which sum up to form the total potential V_{BN} . No interference terms arise because the frequency difference $\Delta\omega = \omega_1 - \omega_2$ is chosen in the range of a few GHz, which exceeds by far all relevant timescales of the atom dynamics. The relative position of the two triangular lattices is determined by the phase differences

$$\begin{aligned} & \text{\$\$}\Delta\{\theta\}_{\{ij\}}=(\{\theta\}_{\{i\}}-\{\theta\}_{\{j\}})-(\{\theta\}_{\{i\}}^{\{\prime\}}-\& \\ & \{\theta\}_{\{j\}}^{\{\prime\}})=\backslash\text{frac}\{\{\omega\}_{\{1\}}-\{\omega\}_{\{2\}}\}\{c\}(\{L\}_{\{i\}}-\& \\ & \{L\}_{\{j\}}).\text{\$\$} \end{aligned}$$

Note that with $\Delta\omega \approx 2\pi \times 3$ GHz, a change of the lengths L_i of the order of 10 μm corresponds to irrelevant changes of $\Delta\theta_{ij}$ of the order of $10^{-4} \times 2\pi$. Hence, $\Delta\theta_{ij}$ can be readily adjusted without the need for interferometric control of the lengths L_i .

Experimentally, we choose convenient values for the lengths L_1 , L_2 and L_3 and lock the frequency difference between the two lasers accordingly to fine-tune the relative position of the two triangular lattices appropriately to generate the desired boron nitride optical lattice. We set $((\{L\}_{\{1\}}-\{L\}_{\{2\}},\{L\}_{\{2\}}-\{L\}_{\{3\}},\{L\}_{\{3\}}-\{L\}_{\{1\}})=(-6.04,3.02,3.02))$ cm and $(\Delta\omega = \{\omega\}_{\{1\}}-\{\omega\}_{\{2\}}=2\{\rm pi\}/3.308)$ GHz, which leads to $(\Delta\theta_{12}, \Delta\theta_{23}, \Delta\theta_{31}) = (-4\{\rm pi\}/3, 2\{\rm pi\}/3, 2\{\rm pi\}/3)$ and hence the boron nitride lattice potential

$$\begin{aligned}
& \text{\$\$} \begin{array}{l} \{V\}_{\rm BN}(\{r\}) = -\{V\}_1 \left(3 + 2 \sum_{i,j} \langle i, j \rangle \cos \left[(\{k_i\} - \{k_j\}) \cdot \{r\} \right] - \frac{2\pi}{3} \right) \\ + \{V\}_2 \left(3 + 2 \sum_{i,j} \langle i, j \rangle \cos \left[(\{k_i\} - \{k_j\}) \cdot \{r\} \right] + \frac{2\pi}{3} \right) \end{array} \text{\$\$}
\end{aligned}$$

The first (second) term describes the triangular lattice potential that gives rise to the A sites (B sites) in the combined boron nitride lattice shown in Fig. 1a. The potential difference between A wells and B wells can be readily adjusted on the microsecond timescale by tuning the ratio V_1/V_2 . To avoid deformations of the lattice potential, the relative frequency difference between the two sets of triangular lattices and the laser intensities are carefully stabilized.

Loading of lattice and detection schemes

A Bose–Einstein condensate of typical 40,000 ^{87}Rb atoms in the state $|F=1, m_F=-1\rangle$ (where F is the quantum number of total angular momentum and m_F = magnetic quantum number) is prepared in an optical dipole trap formed by two crossed laser beams with trapping frequencies of $\omega_x, \omega_y, \omega_z = 2\pi \times 26, 27, 71 \text{ Hz}$. Including the gravitational force (pointing into the $-z$ direction) the trap depth along the $-z$ direction is 34 nK. A bias magnetic field of 1 G is applied along the z axis. Within 120 ms, the lattice beam intensity is ramped up to $V_1 = 7.04 E_R$ and $V_2 = 8.03 E_R$, where $E_R = h^2/2m\lambda^2$. At this stage the overall trap depth along the $-z$ direction is 221 nK. To provide additional evaporative cooling, after 5 ms, the depth of the optical dipole trap is ramped down in 15 ms, such that the overall trap depth along the $-z$ direction is reduced to 41 nK. Excitation into the second band is obtained by swapping the depths of the A and B sites via linearly changing (V_1, V_2) to $(7.81, 7.23) E_R$ rapidly in 0.1 ms. The trap depth along the $-z$ direction is thereby further reduced to 24 nK, which gives rise to further evaporation.

We recorded momentum spectra via time-of-flight spectroscopy or performed band mapping that enabled us to observe the quasi-momentum distribution. These techniques were used to derive the data in Fig. 2c. To obtain the data in Fig. 4c, the experimental protocol was slightly extended. After excitation to the second band and a subsequent holding time of 205 ms, the p orbitals in the A wells are lowered by continuously increasing V_1 to $8.35 E_R$ in 1 ms. Therefore, atoms are transferred from the s orbitals in the shallow B wells to the p orbitals in adjacent deep A wells. Momentum spectra of the atoms in the x – y plane were obtained by switching off all potentials in less than 1 μs and, after a 20-ms-long ballistic expansion, performing absorption imaging. For band mapping, we decreased the intensity of the lattice

exponentially with a time constant of 260 μ s followed by 20 ms of ballistic expansion before performing absorption imaging. For the atom loss data shown in Fig. 3c, we performed in-situ absorption imaging of a plane perpendicular to the x - y plane, after the atoms were excited to the second band and held there for a variable time.

Data availability

All data presented in the figures are available upon request from the corresponding authors.

Code availability

The numerical simulations were performed with MATLAB R2019b. Codes are available upon request from the corresponding authors.

References

1. 1.

Sato, M. & Ando, Y. Topological superconductors: a review. *Rep. Prog. Phys.* **80**, 076501 (2017).

[ADS](#) [MathSciNet](#) [Article](#) [Google Scholar](#)

2. 2.

Wheatley, J. C. Experimental properties of superfluid ^3He . *Rev. Mod. Phys.* **47**, 415–470 (1975).

[ADS](#) [CAS](#) [Article](#) [Google Scholar](#)

3. 3.

Yu, R. et al. Quantized anomalous Hall effect in magnetic topological insulators. *Science* **329**, 61–64 (2010).

[ADS](#) [CAS](#) [Article](#) [Google Scholar](#)

4. 4.

Chang, C.-Z. et al. Experimental observation of the quantum anomalous Hall effect in a magnetic topological insulator. *Science* **340**, 167–170 (2013).

[ADS](#) [CAS](#) [Article](#) [Google Scholar](#)

5. 5.

Liu, C.-X., Zhang, S.-C. & Qi, X.-L. The quantum anomalous hall effect: theory and experiment. *Annu. Rev. Condens. Matter Phys.* **7**, 301–321 (2016).

[ADS](#) [Article](#) [Google Scholar](#)

6. 6.

Deng, Y. et al. Quantum anomalous Hall effect in intrinsic magnetic topological insulator MnBi₂Te₄. *Science* **367**, 895–900 (2020).

[ADS](#) [CAS](#) [Article](#) [Google Scholar](#)

7. 7.

Serlin, M. et al. Intrinsic quantized anomalous Hall effect in a moiré heterostructure. *Science* **367**, 900–903 (2020).

[ADS](#) [CAS](#) [Article](#) [Google Scholar](#)

8. 8.

Feynman, R. P. Simulating physics with computers. *Int. J. Theor. Phys.* **21**, 467–488 (1982).

[MathSciNet](#) [Article](#) [Google Scholar](#)

9. 9.

Verkerk, P. et al. Dynamics and spatial order of cold cesium atoms in a periodic optical potential. *Phys. Rev. Lett.* **68**, 3861–3864 (1992).

[ADS](#) [CAS](#) [Article](#) [Google Scholar](#)

10. 10.

Hemmerich, A. & Hänsch, T. W. Two-dimesional atomic crystal bound by light. *Phys. Rev. Lett.* **70**, 410–413 (1993).

[ADS](#) [CAS](#) [Article](#) [Google Scholar](#)

11. 11.

Grynberg, G. & Robilliard, C. Cold atoms in dissipative optical lattices. *Phys. Rep.* **355**, 335–451 (2001).

[ADS](#) [CAS](#) [Article](#) [Google Scholar](#)

12. 12.

Bloch, I. Ultracold quantum gases in optical lattices. *Nat. Phys.* **1**, 23–30 (2005).

[CAS](#) [Article](#) [Google Scholar](#)

13. 13.

Lewenstein, M. et al. Ultracold atomic gases in optical lattices: mimicking condensed matter physics and beyond. *Adv. Phys.* **56**, 243–379 (2007).

[ADS](#) [Article](#) [Google Scholar](#)

14. 14.

Dalibard, J., Gerbier, F., Juzeliūnas, G. & Öhberg, P. Colloquium: artificial gauge potentials for neutral atoms. *Rev. Mod. Phys.* **83**, 1523–1543 (2011).

[ADS](#) [CAS](#) [Article](#) [Google Scholar](#)

15. 15.

Galitski, V., Juzeliūnas, G. & Spielman, I. B. Artificial gauge fields with ultracold atoms. *Phys. Today* **72**, 38–44 (2019).

[ADS](#) [CAS](#) [Article](#) [Google Scholar](#)

16. 16.

Oka, T. & Kitamura, S. Floquet engineering of quantum materials. *Annu. Rev. Condens. Matter Phys.* **10**, 387–408 (2019).

[ADS](#) [Article](#) [Google Scholar](#)

17. 17.

Jotzu, G. et al. Experimental realization of the topological Haldane model with ultracold fermions. *Nature* **515**, 237–240 (2014).

[ADS](#) [CAS](#) [Article](#) [Google Scholar](#)

18. 18.

Aidelsburger, M. et al. Realization of the Hofstadter Hamiltonian with ultracold atoms in optical lattices. *Phys. Rev. Lett.* **111**, 185301 (2013).

[ADS](#) [CAS](#) [Article](#) [Google Scholar](#)

19. 19.

Miyake, H., Siviloglou, G. A., Kennedy, C. J., Burton, W. C. & Ketterle, W. Realizing the Harper Hamiltonian with laser-assisted tunneling in optical lattices. *Phys. Rev. Lett.* **111**, 185302 (2013).

[ADS](#) [Article](#) [Google Scholar](#)

20. 20.

Liu, W. V. & Wu, C. Atomic matter of nonzero-momentum Bose-Einstein condensation and orbital current order. *Phys. Rev. A* **74**, 013607 (2006).

[ADS](#) [Article](#) [Google Scholar](#)

21. 21.

Lewenstein, M. & Liu, W. V. Orbital dance. *Nat. Phys.* **7**, 101–103 (2011).

[CAS](#) [Article](#) [Google Scholar](#)

22. 22.

Wirth, G., Ölschläger, M. & Hemmerich, A. Evidence for orbital superfluidity in the *P*-band of a bipartite optical square lattice. *Nat. Phys.* **7**, 147–153 (2011).

[CAS](#) [Article](#) [Google Scholar](#)

23. 23.

Kock, T., Hippler, C., Ewerbeck, A. & Hemmerich, A. Orbital optical lattices with bosons. *J. Phys. At. Mol. Opt. Phys.* **49**, 042001 (2016).

[ADS](#) [Article](#) [Google Scholar](#)

24. 24.

Li, X. & Liu, W. V. Physics of higher orbital bands in optical lattices: a review. *Rep. Prog. Phys.* **79**, 116401 (2016).

[ADS](#) [MathSciNet](#) [Article](#) [Google Scholar](#)

25. 25.

Qi, X. L. & Zhang, S. C. Topological insulators and superconductors. *Rev. Mod. Phys.* **83**, 1057 (2011).

[ADS](#) [CAS](#) [Article](#) [Google Scholar](#)

26. 26.

von Klitzing, K. et al. 40 years of the quantum Hall effect. *Nat. Rev. Phys.* **2**, 397–401 (2020).

[Article](#) [Google Scholar](#)

27. 27.

Haldane, F. D. M. Model for a quantum Hall effect without Landau levels: condensed-matter realization of the “parity anomaly”. *Phys. Rev. Lett.* **61**, 2015–2018 (1988).

[ADS](#) [CAS](#) [Article](#) [Google Scholar](#)

28. 28.

Sharma, V., Choudhury, S. & Mueller, E. J. Dynamics of Bose-Einstein recondensation in higher bands. *Phys. Rev. A* **101**, 033609 (2020).

[ADS](#) [CAS](#) [Article](#) [Google Scholar](#)

29. 29.

Weinberg, M., Staarmann, C., Ölschläger, C., Simonet, J. & Sengstock, K. Breaking inversion symmetry in a state-dependent honeycomb lattice: artificial graphene with tunable band gap. *2D Mater.* **3**, 024005 (2016).

[Article](#) [Google Scholar](#)

30. 30.

Jin, S. et al. Evidence of Potts-Nematic superfluidity in a hexagonal sp^2 optical lattice. *Phys. Rev. Lett.* **126**, 035301 (2021).

[ADS](#) [CAS](#) [Article](#) [Google Scholar](#)

31. 31.

Parker, C. V., Ha, L.-C. & Chin, C. Direct observation of effective ferromagnetic domains of cold atoms in a shaken optical lattice. *Nat. Phys.* **9**, 769–774 (2013).

[CAS](#) [Article](#) [Google Scholar](#)

32. 32.

Struck, J. et al. Quantum simulation of frustrated classical magnetism in triangular optical lattices. *Science* **333**, 996–999 (2011).

[ADS](#) [CAS](#) [Article](#) [Google Scholar](#)

33. 33.

Xu, Z.-F., You, L., Hemmerich, A. & Liu, W. V. π -Flux dirac bosons and topological edge excitations in a bosonic chiral p -wave superfluid. *Phys. Rev. Lett.* **117**, 085301 (2016).

[ADS](#) [Article](#) [Google Scholar](#)

34. 34.

Di Liberto, M., Hemmerich, A. & Morais Smith, C. Topological varma superfluid in optical lattices. *Phys. Rev. Lett.* **117**, 163001 (2016).

[ADS](#) [Article](#) [Google Scholar](#)

[Download references](#)

Acknowledgements

This work is supported by the National Key R&D Program of China (grant no. 2018YFA0307200), by the Key-Area Research and Development Program of Guangdong Province (grant no. 2019B030330001), by the NSFC (grant no. U1801661), by the high-level special funds from SUSTech (grant no. G02206401), by a fund from Guangdong province (grant no. 2019ZT08X324 (X.-Q.W., G.-Q.L., J.-

Y.L. and Z.-F.X.)), by AFOSR grant no. FA9550-16-1-0006, by MURI-ARO grant no. W911NF-17-1-0323 through UC Santa Barbara, Shanghai Municipal Science and Technology Major Project (grant no. 2019SHZDZX01) (W.V.L.) and by DFG-He2334/17-1 (A.H.).

Funding

Open access funding provided by Universität Hamburg.

Author information

Author notes

1. These authors contributed equally: Xiao-Qiong Wang, Guang-Quan Luo

Affiliations

1. Department of Physics, Southern University of Science and Technology, Shenzhen, China

Xiao-Qiong Wang, Guang-Quan Luo, Jin-Yu Liu & Zhi-Fang Xu

2. Shenzhen Institute for Quantum Science and Engineering, Southern University of Science and Technology, Shenzhen, China

Xiao-Qiong Wang, Guang-Quan Luo, Jin-Yu Liu, W. Vincent Liu & Zhi-Fang Xu

3. Department of Physics and Astronomy, University of Pittsburgh, Pittsburgh, PA, USA

W. Vincent Liu

4. Wilczek Quantum Center, School of Physics and Astronomy and T. D. Lee Institute, Shanghai Jiao Tong University, Shanghai, China

W. Vincent Liu

5. Shanghai Research Center for Quantum Sciences, Shanghai, China

W. Vincent Liu

6. Institute of Laser Physics, University of Hamburg, Hamburg, Germany

Andreas Hemmerich

Authors

1. Xiao-Qiong Wang
[View author publications](#)

You can also search for this author in [PubMed](#) [Google Scholar](#)

2. Guang-Quan Luo
[View author publications](#)

You can also search for this author in [PubMed](#) [Google Scholar](#)

3. Jin-Yu Liu
[View author publications](#)

You can also search for this author in [PubMed](#) [Google Scholar](#)

4. W. Vincent Liu
[View author publications](#)

You can also search for this author in [PubMed](#) [Google Scholar](#)

5. Andreas Hemmerich
[View author publications](#)

You can also search for this author in [PubMed](#) [Google Scholar](#)

6. Zhi-Fang Xu
[View author publications](#)

You can also search for this author in [PubMed](#) [Google Scholar](#)

Contributions

X.-Q.W. and J.-Y.L. carried out the experiments. G.-Q.L., Z.-F.X. and W.V.L. performed the calculations. Z.-F.X. devised the experiment with input by A.H. The lattice design was contributed by A.H. The manuscript was prepared by Z.-F.X, W.V.L. and A.H. All authors discussed the research.

Corresponding authors

Correspondence to [W. Vincent Liu](#) or [Andreas Hemmerich](#) or [Zhi-Fang Xu](#).

Ethics declarations

Competing interests

The authors declare no competing interests.

Additional information

Peer review information *Nature* thanks the anonymous reviewers for their contribution to the peer review of this work. Peer reviewer reports are available.

Publisher's note Springer Nature remains neutral with regard to jurisdictional claims in published maps and institutional affiliations.

Supplementary information

Supplementary Information

This file contains supplementary text, supplementary equations s1 – s31, supplementary figures s1 – s7 and supplementary references.

Peer Review File

Rights and permissions

Open Access This article is licensed under a Creative Commons Attribution 4.0 International License, which permits use, sharing, adaptation, distribution and reproduction in any medium or format, as long as you give appropriate credit to the original author(s) and the source, provide a link to the Creative Commons license, and indicate if changes were made. The images or other third party material in this article are included in the article's Creative Commons license, unless indicated otherwise in a credit line to the material. If material is not included in the article's Creative Commons license and your intended use is not permitted by statutory regulation or exceeds the permitted use, you will need to obtain permission directly from the copyright holder. To view a copy of this license, visit <http://creativecommons.org/licenses/by/4.0/>.

Reprints and Permissions

About this article



Check for
updates

Cite this article

Wang, XQ., Luo, GQ., Liu, JY. *et al.* Evidence for an atomic chiral superfluid with topological excitations. *Nature* **596**, 227–231 (2021). <https://doi.org/10.1038/s41586-021-03702-0>

[Download citation](#)

- Received: 24 December 2020
- Accepted: 07 June 2021
- Published: 11 August 2021
- Issue Date: 12 August 2021
- DOI: <https://doi.org/10.1038/s41586-021-03702-0>

Comments

By submitting a comment you agree to abide by our [Terms](#) and [Community Guidelines](#). If you find something abusive or that does not comply with our terms or guidelines please flag it as inappropriate.

[Download PDF](#)

Advertisement

This article was downloaded by **calibre** from <https://www.nature.com/articles/s41586-021-03702-0>

- Article
- [Published: 11 August 2021](#)

Actively variable-spectrum optoelectronics with black phosphorus

- [Hyungjin Kim^{1,2}](#),
- [Shiekh Zia Uddin^{1,2}](#),
- [Der-Hsien Lien^{1,2}](#),
- [Matthew Yeh ORCID: orcid.org/0000-0001-8711-6505^{1,2}](#),
- [Nima Sefidmooye Azar³](#),
- [Sivacarendran Balendhran ORCID: orcid.org/0000-0002-4390-3491⁴](#),
- [Taehun Kim^{1,2}](#),
- [Niharika Gupta ORCID: orcid.org/0000-0002-1053-5821^{1,2}](#),
- [Yoonsoo Rho⁵](#),
- [Costas P. Grigoropoulos ORCID: orcid.org/0000-0002-8505-4037⁵](#),
- [Kenneth B. Crozier ORCID: orcid.org/0000-0003-0947-001X^{3,4,6}](#) &
- [Ali Javey ORCID: orcid.org/0000-0001-7214-7931^{1,2}](#)

[Nature](#) volume **596**, pages 232–237 (2021) [Cite this article](#)

- 1850 Accesses
- 39 Altmetric
- [Metrics details](#)

Subjects

- [Materials for optics](#)

- [Nanoscale devices](#)
- [Optical materials and structures](#)

Abstract

Room-temperature optoelectronic devices that operate at short-wavelength and mid-wavelength infrared ranges (one to eight micrometres) can be used for numerous applications^{1,2,3,4,5}. To achieve the range of operating wavelengths needed for a given application, a combination of materials with different bandgaps (for example, superlattices or heterostructures)^{6,7} or variations in the composition of semiconductor alloys during growth^{8,9} are used. However, these materials are complex to fabricate, and the operating range is fixed after fabrication. Although wide-range, active and reversible tunability of the operating wavelengths in optoelectronic devices after fabrication is a highly desirable feature, no such platform has been yet developed. Here we demonstrate high-performance room-temperature infrared optoelectronics with actively variable spectra by presenting black phosphorus as an ideal candidate. Enabled by the highly strain-sensitive nature of its bandgap, which varies from 0.22 to 0.53 electronvolts, we show a continuous and reversible tuning of the operating wavelengths in light-emitting diodes and photodetectors composed of black phosphorus. Furthermore, we leverage this platform to demonstrate multiplexed nondispersive infrared gas sensing, whereby multiple gases (for example, carbon dioxide, methane and water vapour) are detected using a single light source. With its active spectral tunability while also retaining high performance, our work bridges a technological gap, presenting a potential way of meeting different requirements for emission and detection spectra in optoelectronic applications.

Access options

Subscribe to Journal

Get full journal access for 1 year

\$199.00

only \$3.90 per issue

[Subscribe](#)

All prices are NET prices.

VAT will be added later in the checkout.

Tax calculation will be finalised during checkout.

Rent or Buy article

Get time limited or full article access on ReadCube.

from \$8.99

[Rent or Buy](#)

All prices are NET prices.

Additional access options:

- [Log in](#)
- [Access through your institution](#)
- [Learn about institutional subscriptions](#)

Fig. 1: Strain-tunable bandgap in black phosphorus.

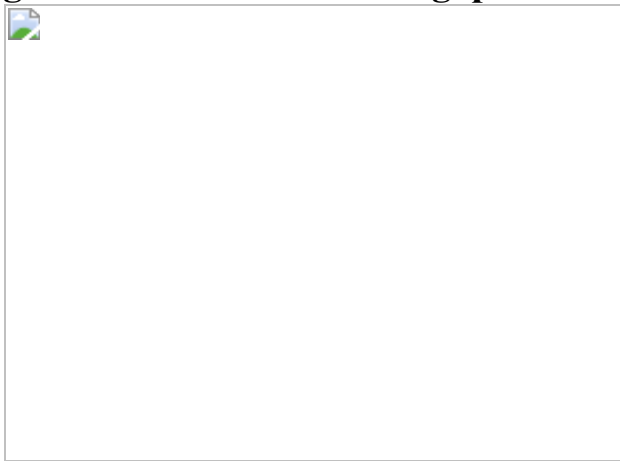


Fig. 2: Strain-induced modification of the bandgap in bP.



Fig. 3: Strain-tunable MWIR LEDs based on a bP–MoS₂ heterostructure.

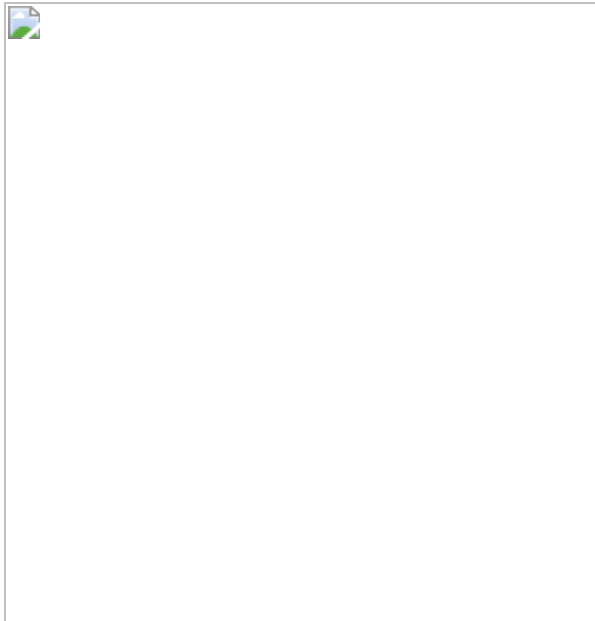
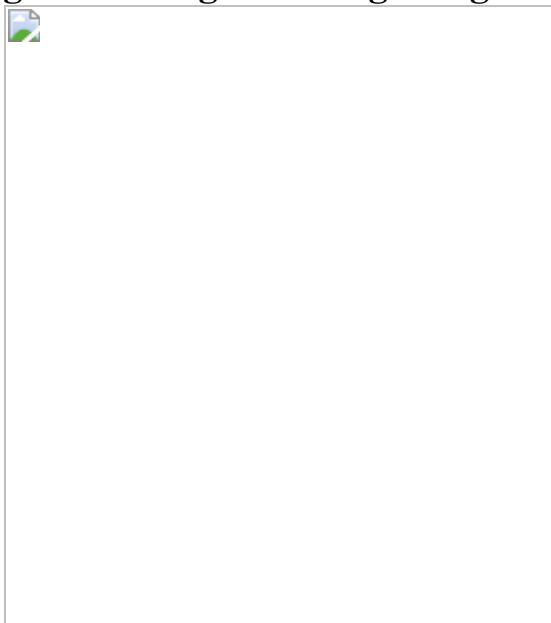


Fig. 4: NDIR gas sensing using strain-tunable LEDs.



Data availability

All data generated or analysed during this study are included in this published article. [Source data](#) are provided with this paper.

References

1. 1.

Kahn, J. M. & Barry, J. R. Wireless infrared communications. *Proc. IEEE* **85**, 265–298 (1997).

[Google Scholar](#)

2. 2.

Vollmer, M. & Mollmann, K.-P. *Infrared Thermal Imaging: Fundamentals, Research and Applications* (2nd edn) (Wiley-VCH, Weinheim, 2018).

3. 3.

Bagavathiappan, S., Lahiri, B. B., Saravanan, T., Philip, J. & Jayakumar, T. Infrared thermography for condition monitoring—a review. *Infrared Phys. Technol.* **60**, 35–55 (2013).

[ADS](#) [Google Scholar](#)

4. 4.

Baker, M. J. et al. Using Fourier transform IR spectroscopy to analyze biological materials. *Nat. Protocols* **9**, 1771–1791 (2014).

[CAS](#) [Google Scholar](#)

5. 5.

Gibson, D. & Macgregor, C. A novel solid state non-dispersive infrared CO₂ gas sensor compatible with wireless and portable deployment. *Sensors (Basel)* **13**, 7079–7103 (2013).

[ADS](#) [CAS](#) [Google Scholar](#)

6. 6.

Haugan, H. J., Szmulowicz, F., Brown, G. J. & Mahalingam, K. Bandgap tuning of InAs/GaSb type-II superlattices for mid-infrared detection. *J. Appl. Phys.* **96**, 2580–2585 (2004).

[ADS](#) [CAS](#) [Google Scholar](#)

7. 7.

Kang, J., Tongay, S., Zhou, J., Li, J. & Wu, J. Band offsets and heterostructures of two-dimensional semiconductors. *Appl. Phys. Lett.* **102**, 012111 (2013).

[ADS](#) [Google Scholar](#)

8. 8.

Wu, J. et al. Universal bandgap bowing in group-III nitride alloys. *Solid State Commun.* **127**, 411–414 (2003).

[ADS](#) [CAS](#) [Google Scholar](#)

9. 9.

Ning, C.-Z., Dou, L. & Yang, P. Bandgap engineering in semiconductor alloy nanomaterials with widely tunable compositions. *Nat. Rev. Mater.* **2**, 17070 (2017).

[ADS](#) [CAS](#) [Google Scholar](#)

10. 10.

Yang, Z. et al. Single-nanowire spectrometers. *Science* **365**, 1017–1020 (2019).

[ADS](#) [CAS](#) [Google Scholar](#)

11. 11.

Kramer, I. J., Levina, L., Debnath, R., Zhitomirsky, D. & Sargent, E. H. Solar cells using quantum funnels. *Nano Lett.* **11**, 3701–3706 (2011).

[ADS](#) [CAS](#) [Google Scholar](#)

12. 12.

Whitney, W. S. et al. Field effect optoelectronic modulation of quantum-confined carriers in black phosphorus. *Nano Lett.* **17**, 78–84 (2017).

[ADS](#) [CAS](#) [Google Scholar](#)

13. 13.

Liu, Y. et al. Gate-tunable giant stark effect in few-layer black phosphorus. *Nano Lett.* **17**, 1970–1977 (2017).

[ADS](#) [CAS](#) [Google Scholar](#)

14. 14.

Yablonovitch, E. & Kane, E. O. Band structure engineering of semiconductor lasers for optical communications. *J. Lightwave Technol.* **6**, 1292–1299 (1988).

[ADS](#) [CAS](#) [Google Scholar](#)

15. 15.

Thompson, S. E. et al. A 90-nm logic technology featuring strained-silicon. *IEEE Trans. Electron Dev.* **51**, 1790–1797 (2004).

[ADS](#) [CAS](#) [Google Scholar](#)

16. 16.

Chen, Y. et al. Strain engineering and epitaxial stabilization of halide perovskites. *Nature* **577**, 209 (2020).

[ADS](#) [CAS](#) [Google Scholar](#)

17. 17.

Lee, C., Wei, X., Kysar, J. W. & Hone, J. Measurement of the elastic properties and intrinsic strength of monolayer graphene. *Science* **321**, 385–388 (2008).

[ADS](#) [CAS](#) [Google Scholar](#)

18. 18.

Bertolazzi, S., Brivio, J. & Kis, A. Stretching and breaking of ultrathin MoS₂. *ACS Nano* **5**, 9703–9709 (2011).

[CAS](#) [Google Scholar](#)

19. 19.

Rodin, A. S., Carvalho, A. & Neto, A. C. Strain-induced gap modification in black phosphorus. *Phys. Rev. Lett.* **112**, 176801 (2014).

[ADS](#) [CAS](#) [Google Scholar](#)

20. 20.

Quereda, J. et al. Strong modulation of optical properties in black phosphorus through strain-engineered rippling. *Nano Lett.* **16**, 2931–2937 (2016).

[ADS](#) [CAS](#) [Google Scholar](#)

21. 21.

Zhang, Z. et al. Strain-modulated bandgap and piezo-resistive effect in black phosphorus field-effect transistors. *Nano Lett.* **17**, 6097–6103

(2017).

[ADS](#) [CAS](#) [Google Scholar](#)

22. 22.

Zhang, G. et al. Infrared fingerprints of few-layer black phosphorus. *Nat. Commun.* **8**, 14071 (2017).

[ADS](#) [CAS](#) [PubMed](#) [PubMed Central](#) [Google Scholar](#)

23. 23.

Çakır, D., Sahin, H. & Peeters, F. M. Tuning of the electronic and optical properties of single-layer black phosphorus by strain. *Phys. Rev. B Condens. Matter Mater. Phys.* **90**, 205421 (2014).

[ADS](#) [Google Scholar](#)

24. 24.

Huang, S. et al. Strain-tunable van der Waals interactions in few-layer black phosphorus. *Nat. Commun.* **10**, 2447 (2019).

[ADS](#) [PubMed](#) [PubMed Central](#) [Google Scholar](#)

25. 25.

Ma, W. et al. Piezoelectricity in multilayer black phosphorus for piezotronics and nanogenerators. *Adv. Mater.* **32**, 1905795 (2020).

[CAS](#) [Google Scholar](#)

26. 26.

Sanchez-Perez, J. R. et al. Direct-bandgap light-emitting germanium in tensilely strained nanomembranes. *Proc. Natl Acad. Sci. USA* **108**, 18893–18898 (2011).

[ADS](#) [CAS](#) [PubMed](#) [PubMed Central](#) [Google Scholar](#)

27. 27.

Takei, K. et al. Quantum confinement effects in nanoscale-thickness InAs membranes. *Nano Lett.* **11**, 5008–5012 (2011).

[ADS](#) [CAS](#) [Google Scholar](#)

28. 28.

Ling, X., Wang, H., Huang, S., Xia, F. & Dresselhaus, M. S. The renaissance of black phosphorus. *Proc. Natl Acad. Sci. USA* **112**, 4523–4530 (2015).

[ADS](#) [CAS](#) [PubMed](#) [PubMed Central](#) [Google Scholar](#)

29. 29.

Ge, S. et al. Dynamical evolution of anisotropic response in black phosphorus under ultrafast photoexcitation. *Nano Lett.* **15**, 4650–4656 (2015).

[ADS](#) [CAS](#) [Google Scholar](#)

30. 30.

Bhaskar, P., Achtstein, A. W., Vermeulen, M. J. W. & Siebbeles, L. D. A. Radiatively dominated charge carrier recombination in black phosphorus. *J. Phys. Chem. C* **120**, 13836–13842 (2016).

[CAS](#) [Google Scholar](#)

31. 31.

Chen, C. et al. Bright mid-infrared photoluminescence from thin-film black phosphorus. *Nano Lett.* **19**, 1488–1493 (2019).

[ADS](#) [CAS](#) [PubMed](#) [PubMed Central](#) [Google Scholar](#)

32. 32.

Du, Y. et al. Auxetic black phosphorus: a 2D material with negative Poisson's ratio. *Nano Lett.* **16**, 6701–6708 (2016).

[ADS](#) [CAS](#) [PubMed](#) [PubMed Central](#) [Google Scholar](#)

33. 33.

Wang, J. et al. Mid-infrared polarized emission from black phosphorus light-emitting diodes. *Nano Lett.* **20**, 3651–3655 (2020).

[ADS](#) [CAS](#) [PubMed](#) [PubMed Central](#) [Google Scholar](#)

34. 34.

Zong, X. et al. Black phosphorus-based van der Waals heterostructures for mid-infrared light-emission applications. *Light Sci. Appl.* **9**, 114 (2020).

[ADS](#) [CAS](#) [PubMed](#) [PubMed Central](#) [Google Scholar](#)

35. 35.

Chang, T.-Y. et al. Black phosphorus mid-infrared light-emitting diodes integrated with silicon photonic waveguides. *Nano Lett.* **20**, 6824–6830 (2020).

[ADS](#) [CAS](#) [PubMed](#) [PubMed Central](#) [Google Scholar](#)

36. 36.

Haug, A. Auger recombination in direct-gap semiconductors: band-structure effects. *J. Phys. C* **16**, 4159 (1983).

[ADS](#) [CAS](#) [Google Scholar](#)

37. 37.

Kurtz, S. R., Biefeld, R. M. & Dawson, L. R. Modification of valence-band symmetry and Auger threshold energy in biaxially compressed InAs_{1-x}Sb_x. *Phys. Rev. B* **51**, 7310 (1995).

[ADS](#) [CAS](#) [Google Scholar](#)

38. 38.

Lee, D.-D. & Lee, D.-S. Environmental gas sensors. *IEEE Sens. J.* **1**, 214–224 (2001).

[ADS](#) [CAS](#) [Google Scholar](#)

39. 39.

Dinh, T.-V., Choi, I.-Y., Son, Y.-S. & Kim, J.-C. A review on non-dispersive infrared gas sensors: improvement of sensor detection limit and interference correction. *Sens. Actuators B* **231**, 529–538 (2016).

[CAS](#) [Google Scholar](#)

40. 40.

Gomes, J., Rodrigues, J. J., Rabêlo, R. A., Kumar, N. & Kozlov, S. IoT-enabled gas sensors: technologies, applications, and opportunities. *J. Sens. Actuator Netw.* **8**, 57 (2019).

[Google Scholar](#)

41. 41.

Deng, Y. et al. Black phosphorus–monolayer MoS₂ van der Waals heterojunction p-n diode. *ACS Nano* **8**, 8292–8299 (2014).

[CAS](#) [Google Scholar](#)

42. 42.

Youngblood, N., Chen, C., Koester, S. J. & Li, M. Waveguide-integrated black phosphorus photodetector with high responsivity and low dark current. *Nat. Photonics* **9**, 247–252 (2015).

[ADS](#) [CAS](#) [Google Scholar](#)

43. 43.

Yuan, H. et al. Polarization-sensitive broadband photodetector using a black phosphorus vertical p–n junction. *Nat. Nanotechnol.* **10**, 707–713 (2015).

[ADS](#) [CAS](#) [Google Scholar](#)

44. 44.

Guo, Q. et al. Black phosphorus mid-infrared photodetectors with high gain. *Nano Lett.* **16**, 4648–4655 (2016).

[ADS](#) [CAS](#) [Google Scholar](#)

45. 45.

Huang, M. et al. Broadband black-phosphorus photodetectors with high responsivity. *Adv. Mater.* **28**, 3481–3485 (2016).

[ADS](#) [CAS](#) [Google Scholar](#)

46. 46.

Chen, X. et al. Widely tunable black phosphorus mid-infrared photodetector. *Nat. Commun.* **8**, 1672 (2017).

[ADS](#) [PubMed](#) [PubMed Central](#) [Google Scholar](#)

47. 47.

Bullock, J. et al. Polarization-resolved black phosphorus/molybdenum disulfide mid-wave infrared photodiodes with high detectivity at room

temperature. *Nat. Photonics* **12**, 601–607 (2018).

[ADS](#) [CAS](#) [Google Scholar](#)

48. 48.

Amani, M., Regan, E., Bullock, J., Ahn, G. H. & Javey, A. Mid-wave infrared photoconductors based on black phosphorus-arsenic alloys. *ACS Nano* **11**, 11724–11731 (2017).

[CAS](#) [Google Scholar](#)

49. 49.

Wu, J., Mao, N., Xie, L., Xu, H. & Zhang, J. Identifying the crystalline orientation of black phosphorus using angle-resolved polarized Raman spectroscopy. *Angew. Chem. Int. Ed.* **54**, 2366–2369 (2015).

[CAS](#) [Google Scholar](#)

50. 50.

Castellanos-Gomez, A. et al. Deterministic transfer of two-dimensional materials by all-dry viscoelastic stamping. *2D Mater.* **1**, 011002 (2014).

[CAS](#) [Google Scholar](#)

51. 51.

Favron, A. et al. Photooxidation and quantum confinement effects in exfoliated black phosphorus. *Nat. Mater.* **14**, 826–832 (2015).

[ADS](#) [CAS](#) [Google Scholar](#)

52. 52.

Foo, E., Jaafar, M., Aziz, A. & Sim, L. C. Properties of spin coated epoxy/silica thin film composites: effect of nano- and micron-size

fillers. *Compos. Part A Appl. Sci. Manuf.* **42**, 1432–1437 (2011).

[Google Scholar](#)

53. 53.

Mei, H., Landis, C. M. & Huang, R. Concomitant wrinkling and buckle-delamination of elastic thin films on compliant substrates. *Mech. Mater.* **43**, 627–642 (2011).

[Google Scholar](#)

54. 54.

Madelung, O. *Semiconductors: Data Handbook* (3rd edn) (Springer, Berlin, 2004).

55. 55.

Kim, H. et al. Synthetic WSe₂ monolayers with high photoluminescence quantum yield. *Sci. Adv.* **5**, eaau4728 (2019).

[ADS](#) [PubMed](#) [PubMed Central](#) [Google Scholar](#)

56. 56.

Gramling, H. M. et al. Spatially precise transfer of patterned monolayer WS₂ and MoS₂ with features larger than 10⁴ μm² directly from multilayer sources. *ACS Appl. Electron. Mater.* **1**, 407–416 (2019).

[CAS](#) [Google Scholar](#)

57. 57.

Nguyen, V. et al. Deterministic assembly of arrays of lithographically defined WS₂ and MoS₂ monolayer features directly from multilayer

sources into van der Waals heterostructures. *J. Micro Nano-Manuf.* **7**, 041006 (2019).

[CAS](#) [Google Scholar](#)

58. 58.

Huang, Y. et al. Interaction of black phosphorus with oxygen and water. *Chem. Mater.* **28**, 8330–8339 (2016).

[CAS](#) [Google Scholar](#)

59. 59.

Qiao, J., Kong, X., Hu, Z. X., Yang, F. & Ji, W. High-mobility transport anisotropy and linear dichroism in few-layer black phosphorus. *Nat. Commun.* **5**, 4475 (2014).

[ADS](#) [CAS](#) [Google Scholar](#)

60. 60.

Desai, S. B. et al. Strain-induced indirect to direct bandgap transition in multilayer WSe₂. *Nano Lett.* **14**, 4592–4597 (2014).

[ADS](#) [CAS](#) [Google Scholar](#)

61. 61.

Matthewson, M. J., Kurkjian, C. R. & Gulati, S. T. Strength measurement of optical fibers by bending. *J. Am. Ceram. Soc.* **69**, 815–821 (1986).

[CAS](#) [Google Scholar](#)

62. 62.

Plechinger, G. et al. Control of biaxial strain in single-layer molybdenite using local thermal expansion of the substrate. *2D Mater.*

2, 015006 (2015).

[Google Scholar](#)

63. 63.

Luo, W., Song, Q., Zhou, G., Tuschel, D. & Xia, G. Study of black phosphorus using angle-resolved polarized Raman spectroscopy with 442 nm excitation. Preprint at <https://arxiv.org/abs/1610.03382> (2016).

64. 64.

Zhang, Z. M., Lefever-Button, G. & Powell, F. R. Infrared refractive index and extinction coefficient of polyimide films. *Int. J. Thermophys.* **19**, 905–916 (1998).

[CAS](#) [Google Scholar](#)

65. 65.

Sherrott, M. C. et al. Anisotropic quantum well electro-optics in few-layer black phosphorus. *Nano Lett.* **19**, 269–276 (2019).

[ADS](#) [CAS](#) [Google Scholar](#)

66. 66.

Beal, A. R. & Hughes, H. P. Kramers-Kronig analysis of the reflectivity spectra of 2H-MoS₂, 2H-MoSe₂ and 2H-MoTe₂. *J. Phys. Chem.* **12**, 881 (1979).

[CAS](#) [Google Scholar](#)

67. 67.

Hori, Y., Ando, Y., Miyamoto, Y. & Sugino, O. Effect of strain on band structure and electron transport in InAs. *Solid-State Electron.* **43**, 1813–1816 (1999).

[ADS](#) [CAS](#) [Google Scholar](#)

68. 68.

Delimitis, A. et al. Strain distribution of thin InN epilayers grown on (0001) GaN templates by molecular beam epitaxy. *Appl. Phys. Lett.* **90**, 061920 (2007).

[ADS](#) [Google Scholar](#)

69. 69.

Orsal, G. et al. Bandgap energy bowing parameter of strained and relaxed InGaN layers. *Opt. Mater. Express* **4**, 1030–1041 (2014).

[ADS](#) [Google Scholar](#)

70. 70.

Varshni, Y. P. Band-to-band radiative recombination in groups IV, VI, and III-V semiconductors (I). *Phys. Status Solidi* **19**, 459 (1967).

[CAS](#) [Google Scholar](#)

71. 71.

Vodopyanov, K. L., Graener, H., Phillips, C. C. & Tate, T. J. Picosecond carrier dynamics and studies of Auger recombination processes in indium arsenide at room temperature. *Phys. Rev. B* **46**, 13194 (1992).

[ADS](#) [CAS](#) [Google Scholar](#)

72. 72.

Rogalski, A. & Józwikowski, K. The intrinsic carrier concentration in $\text{Pb}_{1-x}\text{Sn}_x\text{Te}$, $\text{Pb}_{1-x}\text{Sn}_x\text{Se}$, and $\text{PbS}_{1-x}\text{Se}_x$. *Phys. Status Solidi* **111**, 559 (1989).

[ADS](#) [CAS](#) [Google Scholar](#)

73. 73.

Klann, R., Höfer, T. & Buhleier, R. Fast recombination processes in lead chalcogenide semiconductors studied via transient optical nonlinearities. *J. Appl. Phys.* **77**, 277 (1995).

[ADS](#) [CAS](#) [Google Scholar](#)

74. 74.

Marchetti, S., Martinelli, M. & Simili, R. The Auger recombination coefficient in InAs and GaSb derived from the infrared dynamical plasma reflectivity. *J. Phys. Condens. Matter* **14**, 3653–3656 (2002).

[ADS](#) [CAS](#) [Google Scholar](#)

[Download references](#)

Acknowledgements

We thank H. M. Fahad for help with setting up the gas-sensing instrument. Luminescence studies were funded by the US Department of Energy, Office of Science, Office of Basic Energy Sciences, Materials Sciences and Engineering Division under contract DE-AC02-05-CH11231 (EMAT program KC1201). Photodetector fabrication and testing were funded by the Defense Advanced Research Projects Agency under contract HR0011-16-1-0004. K.B.C. acknowledges funding from the Australian Research Council (grant numbers DP180104141 and FT140100577). H.K. acknowledges support from Samsung Scholarship.

Author information

Affiliations

1. Department of Electrical Engineering and Computer Sciences,
University of California, Berkeley, CA, USA

Hyungjin Kim, Shiekh Zia Uddin, Der-Hsien Lien, Matthew
Yeh, Taehun Kim, Niharika Gupta & Ali Javey

2. Materials Sciences Division, Lawrence Berkeley National Laboratory,
Berkeley, CA, USA

Hyungjin Kim, Shiekh Zia Uddin, Der-Hsien Lien, Matthew
Yeh, Taehun Kim, Niharika Gupta & Ali Javey

3. Department of Electrical and Electronic Engineering, University of
Melbourne, Melbourne, Victoria, Australia

Nima Sefidmooye Azar & Kenneth B. Crozier

4. School of Physics, University of Melbourne, Melbourne, Victoria,
Australia

Sivacarendran Balendhran & Kenneth B. Crozier

5. Department of Mechanical Engineering, University of California,
Berkeley, CA, USA

Yoonsoo Rho & Costas P. Grigoropoulos

6. Australian Research Council (ARC) Centre of Excellence for
Transformative Meta-Optical Systems (TMOS), University of
Melbourne, Melbourne, Victoria, Australia

Kenneth B. Crozier

Authors

1. Hyungjin Kim
[View author publications](#)

You can also search for this author in [PubMed](#) [Google Scholar](#)

2. Shiekh Zia Uddin

[View author publications](#)

You can also search for this author in [PubMed](#) [Google Scholar](#)

3. Der-Hsien Lien

[View author publications](#)

You can also search for this author in [PubMed](#) [Google Scholar](#)

4. Matthew Yeh

[View author publications](#)

You can also search for this author in [PubMed](#) [Google Scholar](#)

5. Nima Sefidmooye Azar

[View author publications](#)

You can also search for this author in [PubMed](#) [Google Scholar](#)

6. Sivacarendran Balendhran

[View author publications](#)

You can also search for this author in [PubMed](#) [Google Scholar](#)

7. Taehun Kim

[View author publications](#)

You can also search for this author in [PubMed](#) [Google Scholar](#)

8. Niharika Gupta

[View author publications](#)

You can also search for this author in [PubMed](#) [Google Scholar](#)

9. Yoonsoo Rho

[View author publications](#)

You can also search for this author in [PubMed](#) [Google Scholar](#)

10. Costas P. Grigoropoulos
[View author publications](#)

You can also search for this author in [PubMed](#) [Google Scholar](#)

11. Kenneth B. Crozier
[View author publications](#)

You can also search for this author in [PubMed](#) [Google Scholar](#)

12. Ali Javey
[View author publications](#)

You can also search for this author in [PubMed](#) [Google Scholar](#)

Contributions

H.K. and A.J. conceived the idea for the project and designed the experiments. H.K., S.Z.U. and D.-H.L. performed optical measurements. H.K., M.Y. and T.K. fabricated devices. S.Z.U., N.S.A., S.B. and K.B.C. performed optical simulations. N.G. helped with gas-sensing experiments. Y.R. and C.P.G. helped with Raman measurements. H.K. wrote the manuscript. All authors discussed the results and commented on the manuscript.

Corresponding author

Correspondence to [Ali Javey](#).

Ethics declarations

Competing interests

The authors declare no competing interests.

Additional information

Peer review information *Nature* thanks Kah Wee Ang, Andres Castellanos-Gomez and the other, anonymous, reviewer(s) for their contribution to the peer review of this work.

Publisher's note Springer Nature remains neutral with regard to jurisdictional claims in published maps and institutional affiliations.

Extended data figures and tables

Extended Data Fig. 1 Strain applied in bP.

a, Photographic image of the two-point bending apparatus used here. An electrical linear actuator that can push/pull one point of the two-point bending apparatus applies a continuous and precise amount of uniaxial tensile strain to bP. **b**, Schematic of the two-point bending apparatus. Strain is calculated as $\varepsilon = t \sin \theta / a$, where ε is the amount of strain; t is the thickness of the substrate; a is the length of the substrate; and θ represents the angle of bending, which is equal to $a/(2R)$ where R is the radius of the curvature⁶⁰. Note that the circular arc approximation is not satisfied when θ is large at strains of 20% or more⁶¹. **c**, Raman spectra of the bP measured in Fig. 1 and Fig. 2. **d**, Schematic showing the atomic vibrations that correspond to Raman modes of $\backslash(\{\{\backslash\text{rm}\{A\}\}\}_{_}\{\{\backslash\text{rm}\{g\}\}\}^{\{1\}}\})$ (out-of-plane), $\backslash(\{\{\backslash\text{rm}\{B\}\}\}_{_}\{\{\backslash\text{rm}\{2g\}\}\})$ (in-plane; zigzag), and $\backslash(\{\{\backslash\text{rm}\{A\}\}\}_{_}\{\{\backslash\text{rm}\{g\}\}\}^{\{2\}}\})$ (in-plane; armchair). **e**, Optical image of the strained bP flake on the PETG substrate.

Extended Data Fig. 2 Detailed optical characterization of strained bP.

a, Photoluminescence (PL) peak wavelength as a function of transfer temperature. We characterized the photoluminescence peak wavelength as a function of biaxial compressive strain before and after the application of tensile strain (1.21%, zigzag). Each measurement was performed for five bP samples with thickness 20–22 nm. Samples were compressively strained by different amounts via different transfer temperatures ($T_{\text{tr}} = 20\text{ }^{\circ}\text{C}$, $50\text{ }^{\circ}\text{C}$, $70\text{ }^{\circ}\text{C}$, $90\text{ }^{\circ}\text{C}$ and $95\text{ }^{\circ}\text{C}$). The photoluminescence peak shift resulting from

tensile strain increased with increasing biaxial compressive strain (as determined by transfer temperature). This is understood to be the result of the following. At high biaxial strain, the larger friction-induced resistance prevents the sliding of the 2D materials⁵⁵. At lower transfer temperatures—that is, with reduced biaxial compressive strain—the bP is thus more likely to slip during bending of the substrate, such that the intended uniaxial tensile strain is not efficiently delivered to the bP. This could be because, at lower values of biaxial strain (that is, lower transfer temperatures), the friction-induced resistance that would prevent sliding of the bP is reduced.

b, Laser power dependence of strain effect. We characterized the laser-induced heating effect on the bandgap shift by measuring photoluminescence peak wavelengths as a function of laser power. As the excitation spot size was similar or slightly smaller than the bP size, this helped to prevent the thermal expansion of the surrounding PETG by laser excitation (this thermal expansion could have elicited unexpected strain or slippage of bP from the PETG⁶²). Regardless of the strain in bP, an excitation power higher than $1,500 \text{ W cm}^{-2}$ always resulted in blueshift of the photoluminescence, attributed to thermal heating by the laser⁶³. Although the photoluminescence peak position recovered after cooling to room temperature without excitation, when the laser intensity was even higher (higher than around 20 kW cm^{-2}), there was visible damage to bP, which did not return to its original photoluminescence peak position. Therefore, we kept the laser incident power for photoluminescence measurements below 600 W cm^{-2} , such that the photoluminescence peak of the exfoliated sample remained constant. This laser incident power is much less than that of the least powerful laser pump (roughly 20 kW cm^{-2}), a value that is known to have a laser thermal effect in bP and MoS₂ transferred on polyimide or PDMS^{62,63}.

c, Bandgap shift under different directions of strain with respect to the crystal orientation of bP. As the direction of tensile strain changed with respect to the crystal orientation of bP, there was no apparent difference in the strain-induced bandgap shift. This observation is consistent with previous results from a similar bending experiment performed on six-layer bP atop a polyethylene terephthalate (PET) substrate²². AC, armchair; ZZ, zigzag. **d**, Absorption at excitation wavelength for bP under zero strain, compressive strain and 1.21% of tensile strain. We found that strain had no notable effects on the absorption

of light by bP at the photoluminescence excitation wavelength. Even though the bP bandgap was being modulated by strain, because our excitation wavelength was far from the absorption edge, the enhancement in photoluminescence cannot be attributed to increased absorption. **e**, Reversibility and repeatability of bandgap tuning in bP using compressive strain (0.6%) and tensile strain (1.2%). The photoluminescence peak from 20 nm bP shifts and recovers throughout ten cycles of bending and relaxation. At much higher strain, the PETG is subject to plastic deformation, exhibiting no return to its original state.

Extended Data Fig. 3 Detailed characterization of variable-spectrum bP LED.

a, Dependence on current density of the electroluminescence peak wavelength, showing the reliability of strain-tunable emission at different injection levels. To prevent degradation at high temperatures and to minimize the effect of localized hot spots on device performance, we used a polyimide film with high thermal conductivity, coupled with a Peltier module, to facilitate heat dissipation and to keep a constant temperature during operation. We also maintained a forward current density of less than 20% of the lowest injection level where thermal failure started to take place. When the current density was high, the devices failed sooner, and visible degradation was observed in the channel region. We therefore kept the current levels within the range shown (around 4 A cm^{-2} to 90 A cm^{-2}) and the device showed stable operations over roughly 8 h (see Extended Data Fig. [5d, e](#)). **b**, Distribution of angular intensity of the strain-tunable bP LED, calculated with finite-difference time domain (FDTD) simulations (FDTD Solutions, Lumerical). Precise computations await further study on changes in the refractive index of bP with strain (compressive and tensile), but here we simply calculated the angular distribution of the bP LED at two different peak wavelengths, using the published refractive indices of bP without strain. **c**, Left, schematic of the device architecture. Right, table showing published^{[28,47,64,65,66](#)} complex refractive indices of the polyimide substrate, bP and MoS₂; these values were used for simulations. We found the angular distributions at two different wavelengths to be close enough that we could assume there was no discrepancy between the power

collections at these two emission wavelengths using an objective lens with a fixed collection angle. **d**, I - V curves of a strain-tunable bP–MoS₂ LED measured at 0.20% of compressive strain and 1.06% of tensile strain.

Extended Data Fig. 4 Temperature-dependent performance of strain-tunable bP LED.

a, Electroluminescence spectra for the bP LED on a polyimide substrate, operating at a constant current density of 20 A cm⁻² and at different temperatures, under compressive strain (0.2%) or tensile strain (1.0%). **b**, **c**, Peak wavelength (**b**) and peak intensity (**c**) of the electroluminescence from the bP LED under different strains and at different temperatures. Note that, to achieve heat dissipation and a uniform temperature control during device operation, dry N₂ gas was consistently purged, and a mechanically flexible heat sink was installed, connected to the cold finger of the cryostat.

Extended Data Fig. 5 Tuning emission wavelengths to detect different gases.

a, Normalized electroluminescence spectra of bP LED with 0.2% compressive strain, 0.3% tensile strain and 1.0% tensile strain, for detecting CO₂, CH₄ and H₂O, respectively. **b**, **c**, Sensor response from the device under 0.2% compressive strain in the presence of CH₄ gas (**b**) and under 0.3% tensile strain in the presence of CO₂ gas (**c**). Our approach showed minimal CH₄ detection at a concentration of 2.5% under 0.2% compressive strain, and at 0.3% tensile strain, it could no longer detect CO₂ gas. **d**, **e**, Stability of the gas-sensing setup for the bP LED measured under 0.2% compressive strain (**d**) and 0.3% tensile strain (**e**). Both measurements were performed at a current density of 20 A cm⁻² with $f_{\text{mod}} = 1$ kHz. Over 8 h of measurement, the device exhibited a maximum drift of 0.90% and 1.22% for 0.2% compressive strain and 0.3% tensile strain, respectively.

Extended Data Fig. 6 Strain-tunable photoconductors based on bP.

a, Schematic of a strain-tunable bP photoconductor. **b**, Schematic of the device architecture, showing the generation of a photocurrent at a bias voltage. **c**, Optical micrograph of the device. D, drain; S, source. **d**, Strain-dependent spectral photoresponse. A/W, amps/watts. **e**, Polarization-dependent responsivity at 4.0 μm and 2.0 μm for the device under 0.4% compressive strain and 1.0% tensile strain, respectively. **f**, I - V curves for the strain-tunable bP photoconductor measured in the dark and under illumination by a 1,000 K black body. **g**, Rise and fall times (between photoresponses of 10% and 90%) under 0.4% compressive and 1.0% tensile strain, using a 1,650-nm laser at roughly 10 mW cm^{-2} . All measurements were conducted at a bias voltage of 100 mV from a device comprising bP of thickness 22 nm.

Extended Data Fig. 7 Detailed characterization of a variable-spectrum bP photoconductor.

a, Spectral noise density under 0.4% compressive and 1.0% tensile strain. The dashed line indicates the $1/f$ curve at low frequency. **b**, Normalized photoresponse of the strain-tunable bP photoconductor measured as a function of modulation frequency. The device was measured at a $V_d = 100$ mV and excited by a 1,650-nm laser, showing a 3-dB frequency of 10 kHz. **c**, Specific detectivity (D^*) as a function of wavelength at room temperature, for the bP device with 0.4% compressive and 1.0% tensile strain and for various commercially available photodetectors.

Extended Data Fig. 8 Setups for measuring photoluminescence and electroluminescence.

a, The IRPL setup. **b**, The infrared electroluminescence (IREL) setup. For both measurements, the emission from bP was collected by a reflective objective and sent to the external port of the FT-IR spectrometer, with $f_{\text{mod}} = 5$ kHz, $\tau_{\text{Lock-in}} = 300$ μs and optical velocity = 0.0633 cm s^{-1} . Ref., reference; Vac. chamber, vacuum chamber. The total interferogram from the HgCdTe (MCT) detector and the modulated interferogram from the voltage preamplifier were used to separate the

photoluminescence/electroluminescence signal from the thermal background.

Extended Data Table 1 Strain-induced bandgap shift of semiconductors in the SWIR/MWIR range

[Full size table](#)

Extended Data Table 2 Parameters used to calculate the theoretical quantum yield from the ABC model

[Full size table](#)

Supplementary information

[Supplementary Video 1](#)

Dynamic emission spectrum tuning of bP-LED. Real-time measurement of emission spectrum from actively variable spectrum bP-LED. When tensile strain is applied by bending, the emission has a peak around 2.7 μm . When tensile strain is released and there is only compressive strain, the emission peak is shifted to 4.1 μm . The time period between the bending and release is 21 s. The spectrum is modulated without drift over 500 times of bending cycles and 6 hours of operation time.

Source data

[Source Data Fig. 1](#)

[Source Data Fig. 2](#)

[Source Data Fig. 3](#)

[Source Data Fig. 4](#)

Rights and permissions

[Reprints and Permissions](#)

About this article



Cite this article

Kim, H., Uddin, S.Z., Lien, DH. *et al.* Actively variable-spectrum optoelectronics with black phosphorus. *Nature* **596**, 232–237 (2021). <https://doi.org/10.1038/s41586-021-03701-1>

Download citation

- Received: 22 January 2021
- Accepted: 07 June 2021
- Published: 11 August 2021
- Issue Date: 12 August 2021
- DOI: <https://doi.org/10.1038/s41586-021-03701-1>

Comments

By submitting a comment you agree to abide by our [Terms](#) and [Community Guidelines](#). If you find something abusive or that does not comply with our terms or guidelines please flag it as inappropriate.

[Access through your institution](#)

[Change institution](#)

[Buy or subscribe](#)

Advertisement

This article was downloaded by **calibre** from <https://www.nature.com/articles/s41586-021-03701-1>

| [Section menu](#) | [Main menu](#) |

- Article
- [Published: 11 August 2021](#)

Structured fabrics with tunable mechanical properties

- [Yifan Wang ORCID: orcid.org/0000-0003-2284-520X^{1,2 na1}](#),
- [Liuchi Li ORCID: orcid.org/0000-0002-1360-4757^{1 na1}](#),
- [Douglas Hofmann³](#),
- [José E. Andrade¹](#) &
- [Chiara Daraio ORCID: orcid.org/0000-0001-5296-4440¹](#)

[Nature](#) volume **596**, pages 238–243 (2021) [Cite this article](#)

- 3654 Accesses
- 305 Altmetric
- [Metrics details](#)

Subjects

- [Mechanical engineering](#)
- [Mechanical properties](#)
- [Soft materials](#)

Abstract

Structured fabrics, such as woven sheets or chain mail armours, derive their properties both from the constitutive materials and their geometry^{1,2}. Their design can target desirable characteristics, such as high impact resistance, thermal regulation, or electrical conductivity^{3,4,5}. Once realized, however,

the fabrics' properties are usually fixed. Here we demonstrate structured fabrics with tunable bending modulus, consisting of three-dimensional particles arranged into layered chain mails. The chain mails conform to complex shapes², but when pressure is exerted at their boundaries, the particles interlock and the chain mails jam. We show that, with small external pressure (about 93 kilopascals), the sheets become more than 25 times stiffer than in their relaxed configuration. This dramatic increase in bending resistance arises because the interlocking particles have high tensile resistance, unlike what is found for loose granular media. We use discrete-element simulations to relate the chain mail's micro-structure to macroscale properties and to interpret experimental measurements. We find that chain mails, consisting of different non-convex granular particles, undergo a jamming phase transition that is described by a characteristic power-law function akin to the behaviour of conventional convex media. Our work provides routes towards lightweight, tunable and adaptive fabrics, with potential applications in wearable exoskeletons, haptic architectures and reconfigurable medical supports.

Access options

Subscribe to Journal

Get full journal access for 1 year

\$199.00

only \$3.90 per issue

[Subscribe](#)

All prices are NET prices.

VAT will be added later in the checkout.

Tax calculation will be finalised during checkout.

Rent or Buy article

Get time limited or full article access on ReadCube.

from \$8.99

[Rent or Buy](#)

All prices are NET prices.

Additional access options:

- [Log in](#)
- [Access through your institution](#)
- [Learn about institutional subscriptions](#)

Fig. 1: The design and prototype of the architected chain mail fabrics.

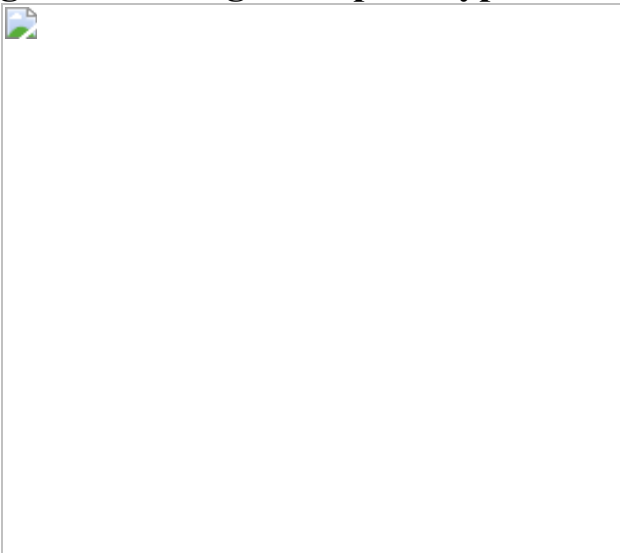


Fig. 2: Bending and tensile tests with variable confining pressure.

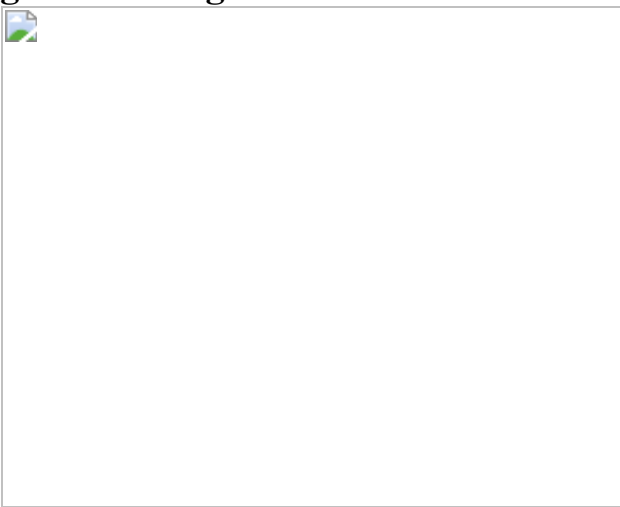
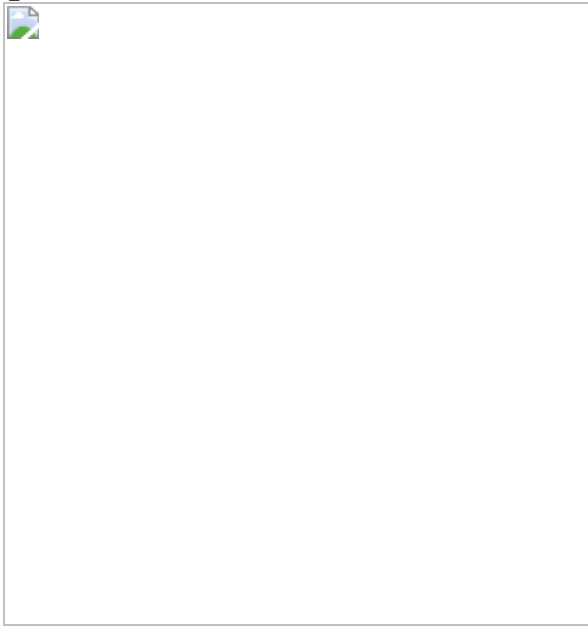


Fig. 3: Micro-structural information obtained from simulations at different confining pressures.



Fig. 4: Shape reconfigurability, tunable impact resistance, and applications.



Data availability

The data that support the findings of this study are available from the corresponding author upon reasonable request and online

(<https://github.com/Daraio-lab/StructuredFabricsTunable-WangY>).

References

1. 1.

Chen, X., Taylor, L. W. & Tsai, L. J. An overview on fabrication of three-dimensional woven fabric preforms for composites. *Text. Res. J.* **81**, 932–944 (2011).

2. 2.

Engel, J. & Liu, C. Creation of a metallic micromachined chain mail fabric. *J. Micromech. Microeng.* **17**, 551–556 (2007).

[ADS](#) [Article](#) [Google Scholar](#)

3. 3.

Tabiei, A. & Nilakantan, G. Ballistic impact of dry woven fabric composites: a review. *Appl. Mech. Rev.* **61**, 010801 (2008).

[ADS](#) [Article](#) [Google Scholar](#)

4. 4.

Cai, L. et al. Warming up human body by nanoporous metallized polyethylene fabric. *Nat. Commun.* **8**, 496 (2017).

[ADS](#) [Article](#) [Google Scholar](#)

5. 5.

Stoppa, M. & Chiolerio, A. Wearable electronics and smart fabrics: a critical review. *Sensors* **14**, 11957–11992 (2014).

[ADS](#) [CAS](#) [Article](#) [Google Scholar](#)

6. 6.

Mondal, S. Phase change materials for smart fabrics—an overview. *Appl. Therm. Eng.* **28**, 1536–1550 (2008).

[CAS](#) [Article](#) [Google Scholar](#)

7. 7.

Gauvreau, B. et al. Color-changing and color-tunable photonic bandgap fiber fabrics. *Opt. Express* **16**, 15677–15693 (2008).

[ADS](#) [CAS](#) [Article](#) [Google Scholar](#)

8. 8.

Cherenack, K., Zysset, C., Kinkeldei, T., Münzenrieder, N. & Tröster, G. Woven electronic fibers with sensing and display functions for smart fabrics. *Adv. Mater.* **22**, 5178–5182 (2010).

[CAS](#) [Article](#) [Google Scholar](#)

9. 9.

Cherenack, K. & van Pieterson, L. Smart fabrics: challenges and opportunities. *J. Appl. Phys.* **112**, 091301 (2012).

[ADS](#) [Article](#) [Google Scholar](#)

10. 10.

Chen, J. et al. Micro-cable structured fabric for simultaneously harvesting solar and mechanical energy. *Nat. Energy* **1**, 16138 (2016).

[ADS](#) [CAS](#) [Article](#) [Google Scholar](#)

11. 11.

Ploszajski, A. R., Jackson, R., Ransley, M. & Miodownik, M. 4D printing of magnetically functionalized chainmail for exoskeletal biomedical applications. *MRS Adv.* **4**, 1361–1366 (2019).

[CAS](#) [Article](#) [Google Scholar](#)

12. 12.

Liu, A. J. & Nagel, S. R. Jamming is not just cool any more. *Nature* **396**, 21 (1998).

[ADS](#) [CAS](#) [Article](#) [Google Scholar](#)

13. 13.

Liu, A. J. & Nagel, S. R. The jamming transition and the marginally jammed solid. *Annu. Rev. Condens. Matter Phys.* **1**, 347–369 (2010).

[ADS](#) [Article](#) [Google Scholar](#)

14. 14.

Bi, D., Zhang, J., Chakraborty, B. & Behringer, R. P. Jamming by shear. *Nature* **480**, 355–358 (2011).

[ADS](#) [CAS](#) [Article](#) [Google Scholar](#)

15. 15.

Jaeger, H. Celebrating *Soft Matter*'s 10th anniversary: toward jamming by design. *Soft Matter* **11**, 12 (2015).

[ADS](#) [CAS](#) [Article](#) [Google Scholar](#)

16. 16.

Narang, Y. S., Vlassak, J. J. & Howe, R. D. Mechanically versatile soft machines through laminar jamming. *Adv. Funct. Mater.* **28**, 1707136 (2018).

[Article](#) [Google Scholar](#)

17. 17.

Brown, E. et al. Universal robotic gripper based on the jamming of granular material. *Proc. Natl Acad. Sci. USA* **107**, 18809–18814 (2010).

[ADS](#) [CAS](#) [Article](#) [Google Scholar](#)

18. 18.

Wang, Y. et al. Architected lattices with adaptive energy absorption. *Extreme Mech. Lett.* **33**, 100557 (2019).

[Article](#) [Google Scholar](#)

19. 19.

Aejmelaeus-Lindstrom, P., Willmann, J., Tibbits, S., Gramazio, F. & Kohler, M. Jammed architectural structures: towards large-scale reversible construction. *Granul. Matter* **18**, 28 (2016).

[Article](#) [Google Scholar](#)

20. 20.

Brown, E., Nasto, A., Athanassiadis, A. G. & Jaeger, H. M. Strain stiffening in random packings of entangled granular chains. *Phys. Rev. Lett.* **108**, 108302 (2012).

[ADS](#) [Article](#) [Google Scholar](#)

21. 21.

Dyskin, A. V., Estrin, Y., Kanel-Belov, A. J. & Pasternak, E. A new concept in design of materials and structures: assemblies of interlocked tetrahedron-shaped elements. *Scr. Mater.* **44**, 2689–2694 (2001).

[CAS](#) [Article](#) [Google Scholar](#)

22. 22.

Dyskin, A. V., Pasternak, E. & Estrin, Y. Mortarless structures based on topological interlocking. *Front. Struct. Civ. Eng.* **6**, 188–197 (2012).

[Google Scholar](#)

23. 23.

Zweben, C., Smith, W. & Wardle, M. Test methods for fiber tensile strength, composite flexural modulus, and properties of fabric-reinforced laminates. In *Composite Materials: Testing and Design (Fifth Conference)* 228–262 (1979).

24. 24.

Manti, M., Cacucciolo, V. & Cianchetti, M. Stiffening in soft robotics: a review of the state of the art. *IEEE Robot. Autom.* **23**, 93–106 (2016).

[Article](#) [Google Scholar](#)

25. 25.

Wang, L. et al. Controllable and reversible tuning of material rigidity for robot applications. *Mater. Today* **21**, 563–576 (2018).

[Google Scholar](#)

26. 26.

Meng, H. & Li, G. A review of stimuli-responsive shape memory polymer composites. *Polymer* **54**, 2199–2221 (2013).

[CAS](#) [Article](#) [Google Scholar](#)

27. 27.

White, T. J. & Broer, D. J. Programmable and adaptive mechanics with liquid crystal polymer networks and elastomers. *Nat. Mater.* **14**, 1087–1098 (2015).

[ADS](#) [CAS](#) [Article](#) [Google Scholar](#)

28. 28.

Jackson, J. A. et al. Field responsive mechanical metamaterials. *Sci. Adv.* **4**, eaau6419 (2018).

[ADS](#) [CAS](#) [Article](#) [Google Scholar](#)

29. 29.

Biggs, J. et al. Electroactive polymers: developments of and perspectives for dielectric elastomers. *Angew. Chem. Int. Ed.* **52**, 9409–9421 (2013).

[CAS](#) [Article](#) [Google Scholar](#)

30. 30.

Kawamoto, R., Andò, E., Viggiani, G. & Andrade, J. E. Level set discrete element method for three-dimensional computations with triaxial case study. *J. Mech. Phys. Solids* **91**, 1–13 (2016).

[ADS](#) [MathSciNet](#) [Article](#) [Google Scholar](#)

31. 31.

Kawamoto, R., Andò, E., Viggiani, G. & Andrade, J. E. All you need is shape: predicting shear banding in sand with LS-DEM. *J. Mech. Phys. Solids* **111**, 375–392 (2018).

[ADS](#) [Article](#) [Google Scholar](#)

32. 32.

Li, L., Marteau, E. & Andrade, J. Capturing the inter-particle force distribution in granular material using LS-DEM. *Granul. Matter* **21**, 43 (2019).

[Article](#) [Google Scholar](#)

33. 33.

Cundall, P. A. & Strack, O. D. L. A discrete numerical model for granular assemblies. *Geotechnique* **29**, 47–65 (1979).

[Article](#) [Google Scholar](#)

34. 34.

Majmudar, T. S. & Behringer, R. P. Contact force measurements and stress-induced anisotropy in granular materials. *Nature* **435**, 1079–1082 (2005).

[ADS](#) [CAS](#) [Article](#) [Google Scholar](#)

35. 35.

Silbert, L. E. et al. Granular flow down an inclined plane: Bagnold scaling and rheology. *Phys. Rev. E* **64**, 051302 (2001).

[ADS](#) [CAS](#) [Article](#) [Google Scholar](#)

36. 36.

Miskin, M. Z. & Jaeger, H. M. Adapting granular materials through artificial evolution. *Nat. Mater.* **12**, 326–331 (2013).

[ADS](#) [CAS](#) [Article](#) [Google Scholar](#)

37. 37.

Pratapa, P. P., Liu, K. & Paulino, H. Geometric mechanics of origami patterns exhibiting Poisson's ratio switch by breaking mountain and

valley assignment. *Phys. Rev. Lett.* **122**, 155501 (2019).

[ADS](#) [MathSciNet](#) [CAS](#) [Article](#) [Google Scholar](#)

[Download references](#)

Acknowledgements

We thank K. Liu for discussions; A. Pate, H. Ramirez and M. Zuleta for printing the aluminum chain mails ; D. Ruffatto for helping with printing early-stage prototypes; and S. Fan for assistance with photographing the 3D-printed sample in Figs. 1d, f and 4a, b. Y.W and C.D. acknowledge support from the Foster and Coco Stanback Space Innovation fund, Facebook and the Army Research Office grant W911NF-17-1-0147. L.L. and J.E.A. acknowledge support from the Army Research Office (MURI grant number W911NF-19-1-0245). This research was carried out at the California Institute of Technology and the Jet Propulsion Laboratory under a contract with the National Aeronautics and Space Administration, and funded through the President's and Director's Fund Program. Computational resources were provided by the High Performance Computing Center at Caltech.

Author information

Author notes

1. These authors contributed equally: Yifan Wang, Liuchi Li

Affiliations

1. Division of Engineering and Applied Science, California Institute of Technology, Pasadena, CA, USA

Yifan Wang, Liuchi Li, José E. Andrade & Chiara Daraio

2. School of Mechanical and Aerospace Engineering, Nanyang Technological University, Singapore, Singapore

Yifan Wang

3. Jet Propulsion Laboratory/ California Institute of Technology,
Pasadena, CA, USA

Douglas Hofmann

Authors

1. Yifan Wang
[View author publications](#)

You can also search for this author in [PubMed](#) [Google Scholar](#)

2. Liuchi Li
[View author publications](#)

You can also search for this author in [PubMed](#) [Google Scholar](#)

3. Douglas Hofmann
[View author publications](#)

You can also search for this author in [PubMed](#) [Google Scholar](#)

4. José E. Andrade
[View author publications](#)

You can also search for this author in [PubMed](#) [Google Scholar](#)

5. Chiara Daraio
[View author publications](#)

You can also search for this author in [PubMed](#) [Google Scholar](#)

Contributions

Y.W. and C.D. designed the sample structure and the experiments. Y.W. fabricated the sample, performed the experiments and analysed experimental data. L.L. and J.E.A. designed the LS-DEM model. L.L.

performed the LS-DEM simulations and analysed numerical results. D.H. printed the metallic chain mail. Y.W., L.L. and C.D. wrote the manuscript. All authors interpreted the results and reviewed the manuscript.

Corresponding author

Correspondence to [Chiara Daraio](#).

Ethics declarations

Competing interests

The authors declare no competing interests.

Additional information

Peer review information *Nature* thanks Laurent Orgeas and the other, anonymous, reviewer(s) for their contribution to the peer review of this work.

Publisher's note Springer Nature remains neutral with regard to jurisdictional claims in published maps and institutional affiliations.

Extended data figures and tables

[Extended Data Fig. 1 Construction of the ‘digital twin’ and the envelope.](#)

a, The actual particle geometry (left) and the corresponding nodes and surface triangulations of the constructed digital twin (right). **b**, The corresponding ‘grids’ of the constructed digital twin with colour indicating the signed shortest distance to the particle surface. **c, d**, The initial configurations of the envelopes (represented by connected spheres) and of the granular assemblies with (**c**) and without (**d**) topological interlocking. The centroids of three adjacent spheres form a triangle with surface area A

and in-ward surface normal n . **e**, The probability distribution of the radii of the constituent membrane spheres of the envelope used for the interlocked fabric sheet (blue, **c**) and non-interlocked assembly (red, **d**). The notation ± 0.025 indicates the lower and upper bound for each value shown on the x axis.

Extended Data Fig. 2 The bending test simulation and illustration of how we categorized each contact into either the ‘compressive’ or ‘tensile’ type.

a, Evolution of total kinetic energy (blue) and total contact number (red) of all constituent particles of a fabric sheet under two confining pressures: 13 kPa (upper panel) and 93 kPa (lower panel). **b**, Evolution of total contact number for the same fabric sheet during the ‘isotropic compression only’ simulation stage for six different applied confining pressures. **c**, Evolution of average deflection of loaded particles during the ‘three-point bending added’ simulation stage for the same six different applied confining pressures. **d**, In each of the subfigures, \mathbf{F} is the total contact force vector and \mathbf{n}_1 and \mathbf{n}_2 are vectors pointing from the contact position to the respective centroid location of each contact particle.

Extended Data Fig. 3 Details of the 3D architected particles and fabrics.

Left column, Probability distribution of the digital twin’s edge lengths for all five additionally considered shapes (coloured in red) in comparison to that of the hollow octahedron (coloured in blue). In the inset, S and N represent the total surface area of the considered particle geometry and the number of nodes of the corresponding digital twin, respectively, while S_0 and N_0 represent those of the hollow octahedron and its digital twin. Right column, the corresponding assembled sheets (one layer) together with a closer look at the associated interlocking pattern.

Extended Data Fig. 4 Details of the classical chain mail fabrics.

The same comparison as in Extended Data Fig. 4 for classical chain mails consisting ring-shaped (**a**) and square-shaped particles (**b**). Left column, probability distribution of the digital twin's edge lengths for two different chainmail shapes (coloured in red) in comparison to that of the hollow octahedron (coloured in blue). Right column, the corresponding assembled chain mail sheets (one layer) together with a closer look at the associated interlocking pattern.

Extended Data Fig. 5 Comparing experimental and numerical results of two-layer fabrics consisting of particles of different shapes and loaded along different directions.

a, Comparison between experimental and simulation results on fabrics consisting of interlocking particles constructed from three orthogonal rings. **b, c**, Bending and tensile moduli along different directions for fabrics consisting of particles constructed from three orthogonal rings (**b**) and cubic frame (**c**). The error bars shown in (a) and (b) represent the standard deviations obtained from five separate experiments and four separate simulations.

Extended Data Table 1 Packing fraction of different fabric sheets under various confining pressures, and fitting parameters used for the power-law relation shown in Fig. 3g

[Full size table](#)

Extended Data Table 2 Average dimensions computed from four separate simulations

[Full size table](#)

Extended Data Table 3 Values of the model parameters used in this study

[Full size table](#)

Extended Data Table 4 The Poisson's ratio obtained during uni-axial tensile tests under different pressures for fabrics with three particle geometries

[Full size table](#)

Supplementary information

Video 1

A LS-DEM simulation showing two fabric layers when a confining pressure $P = 13$ kPa (top) is applied, followed by a three-point bending test (bottom).

Video 2

A LS-DEM simulation showing two fabric layers when a confining pressure $P = 93$ kPa (top) is applied, followed by a three-point bending test (bottom).

Video 3

An experiment captured by high-speed camera (100 times playback) showing a stainless steel bead impacting at 3 m/s onto the fabrics at zero confining pressure.

Video 4

An experiment captured by high-speed camera (100 times playback) showing a stainless steel bead impacting at 3 m/s onto the fabrics at 67 kPa confining pressure.

Rights and permissions

[Reprints and Permissions](#)

About this article



Check for
updates

Cite this article

Wang, Y., Li, L., Hofmann, D. *et al.* Structured fabrics with tunable mechanical properties. *Nature* **596**, 238–243 (2021).
<https://doi.org/10.1038/s41586-021-03698-7>

[Download citation](#)

- Received: 23 August 2020
- Accepted: 07 June 2021
- Published: 11 August 2021
- Issue Date: 12 August 2021
- DOI: <https://doi.org/10.1038/s41586-021-03698-7>

Comments

By submitting a comment you agree to abide by our [Terms](#) and [Community Guidelines](#). If you find something abusive or that does not comply with our terms or guidelines please flag it as inappropriate.

[Access through your institution](#)

[Change institution](#)

[Buy or subscribe](#)

Associated Content

[Chain-mail fabric stiffens under confining pressure](#)

- Laurent Orgéas

News & Views 11 Aug 2021

Advertisement

This article was downloaded by **calibre** from <https://www.nature.com/articles/s41586-021-03698-7>

| [Section menu](#) | [Main menu](#) |

- Article
- [Published: 11 August 2021](#)

Direct imaging of single-molecule electrochemical reactions in solution

- [Jinrun Dong](#) [ORCID: orcid.org/0000-0002-4438-7310](#)^{1 na1},
- [Yuxian Lu](#)^{1 na1},
- [Yang Xu](#)¹,
- [Fanfan Chen](#)¹,
- [Jinmei Yang](#)¹,
- [Yuqiang Chen](#)¹ &
- [Jiandong Feng](#) [ORCID: orcid.org/0000-0002-2143-3986](#)¹

[Nature](#) volume **596**, pages 244–249 (2021) [Cite this article](#)

- 5494 Accesses
- 30 Altmetric
- [Metrics details](#)

Subjects

- [Cell adhesion](#)
- [Chemical physics](#)
- [Electrochemistry](#)
- [Imaging studies](#)
- [Super-resolution microscopy](#)

Abstract

Chemical reactions tend to be conceptualized in terms of individual molecules transforming into products, but are usually observed in experiments that probe the average behaviour of the ensemble. Single-molecule methods move beyond ensemble averages and reveal the statistical distribution of reaction positions, pathways and dynamics^{1,2,3}. This has been shown with optical traps and scanning probe microscopy manipulating and observing individual reactions at defined locations with high spatial resolution^{4,5}, and with modern optical methods using ultrasensitive photodetectors^{3,6,7} that enable high-throughput single-molecule measurements. However, effective probing of single-molecule solution chemistry remains challenging. Here we demonstrate optical imaging of single-molecule electrochemical reactions⁷ in aqueous solution and its use for super-resolution microscopy. The method utilizes a chemiluminescent reaction involving a ruthenium complex electrochemically generated at an electrode⁸, which ensures minimal background signal. This allows us to directly capture single photons of the electrochemiluminescence of individual reactions, and to develop super-resolved electrochemiluminescence microscopy for imaging the adhesion dynamics of live cells with high spatiotemporal resolution. We anticipate that our method will advance the fundamental understanding of electrochemical reactions and prove useful for bioassays and cell-imaging applications.

Access options

Subscribe to Journal

Get full journal access for 1 year

\$199.00

only \$3.90 per issue

[Subscribe](#)

All prices are NET prices.
VAT will be added later in the checkout.
Tax calculation will be finalised during checkout.

Rent or Buy article

Get time limited or full article access on ReadCube.

from \$8.99

[Rent or Buy](#)

All prices are NET prices.

Additional access options:

- [Log in](#)
- [Access through your institution](#)
- [Learn about institutional subscriptions](#)

Fig. 1: Single-molecule ECL imaging setup and observation of stochastic reactions.

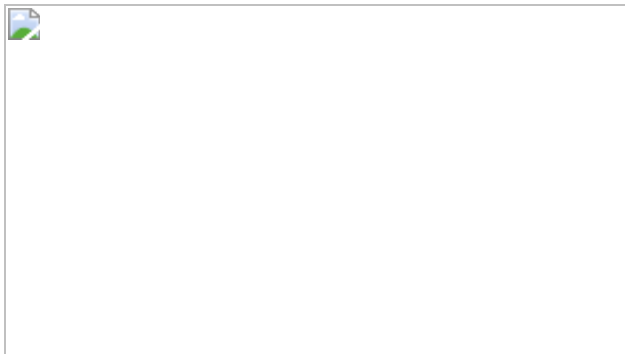


Fig. 2: Observation of single-molecule reactions at different exposure times.

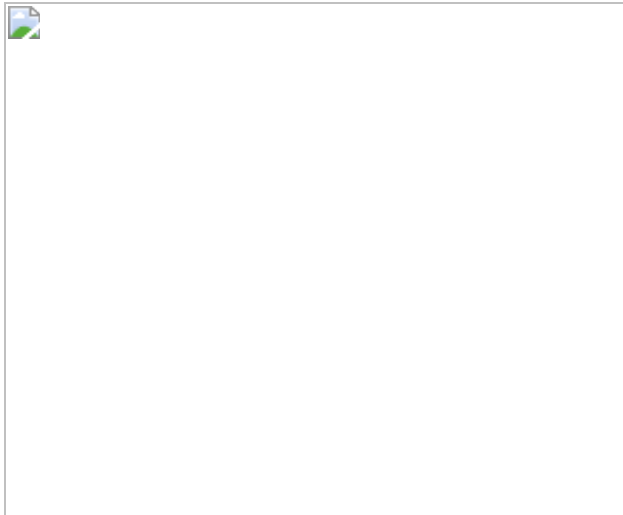


Fig. 3: Kinetic analysis of single-molecule ECL reactions.



Fig. 4: Single-molecule ECL imaging of ITO structures.

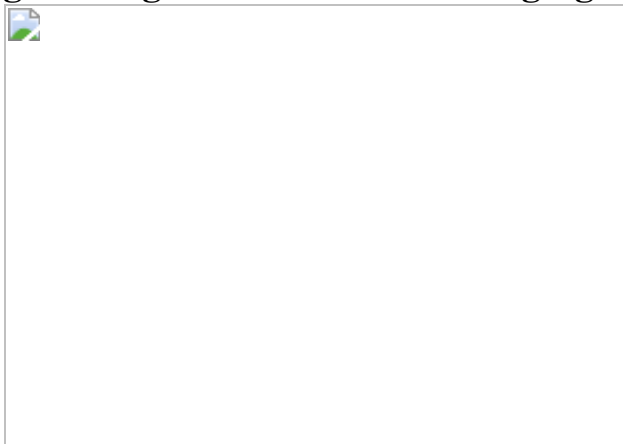


Fig. 5: Single-molecule ECL imaging of live cells.



Data availability

The data that support the findings of this study are included in the paper and its [Supplementary Information](#) and Supplementary Videos and are available from the corresponding author upon reasonable request.

References

1. 1.

Ho, W. Single-molecule chemistry. *J. Chem. Phys.* **117**, 11033–11061 (2002).

[ADS](#) [CAS](#) [Article](#) [Google Scholar](#)

2. 2.

Roeffaers, M. B. J. et al. Spatially resolved observation of crystal-face-dependent catalysis by single turnover counting. *Nature* **439**, 572–575 (2006).

[ADS](#) [CAS](#) [Article](#) [Google Scholar](#)

3. 3.

Sambur, J. B. et al. Sub-particle reaction and photocurrent mapping to optimize catalyst-modified photoanodes. *Nature* **530**, 77–80 (2016).

[ADS](#) [CAS](#) [Article](#) [Google Scholar](#)

4. 4.

Liu, L. R. et al. Building one molecule from a reservoir of two atoms. *Science* **360**, 900–903 (2018).

[ADS](#) [CAS](#) [Article](#) [Google Scholar](#)

5. 5.

de Oteyza, D. G. et al. Direct imaging of covalent bond structure in single-molecule chemical reactions. *Science* **340**, 1434–1437 (2013).

[ADS](#) [Article](#) [Google Scholar](#)

6. 6.

Chen, T. et al. Optical super-resolution imaging of surface reactions. *Chem. Rev.* **117**, 7510–7537 (2017).

[CAS](#) [Article](#) [Google Scholar](#)

7. 7.

Collinson, M. M. & Wightman, R. M. Observation of individual chemical reactions in solution. *Science* **268**, 1883–1885 (1995).

[ADS](#) [CAS](#) [Article](#) [Google Scholar](#)

8. 8.

Bard, A. J. *Electrogenerated Chemiluminescence* (CRC Press, 2004).

9. 9.

Zhang, J., Arbault, S., Sojic, N. & Jiang, D. Electrochemiluminescence imaging for bioanalysis. *Annu. Rev. Anal. Chem.* **12**, 275–295 (2019).

[CAS](#) [Article](#) [Google Scholar](#)

10. 10.

Miao, W. J., Choi, J. P. & Bard, A. J. Electrogenerated chemiluminescence 69: the tris(2,2'-bipyridine)ruthenium(II), $(\text{Ru}(\text{bpy})_3)^{2+}$ /tri-*n*-propylamine (TPrA) system revisited—a new route involving TPrA $^{\cdot+}$ cation radicals. *J. Am. Chem. Soc.* **124**, 14478–14485 (2002).

[CAS](#) [Article](#) [Google Scholar](#)

11. 11.

Sentic, M. et al. Mapping electrogenerated chemiluminescence reactivity in space: mechanistic insight into model systems used in immunoassays. *Chem. Sci.* **5**, 2568–2572 (2014).

[CAS](#) [Article](#) [Google Scholar](#)

12. 12.

Fan, F. R. F. & Bard, A. J. Observing single nanoparticle collisions by electrogenerated chemiluminescence amplification. *Nano Lett.* **8**, 1746–1749 (2008).

[ADS](#) [CAS](#) [Article](#) [Google Scholar](#)

13. 13.

Ma, C. et al. Dynamically imaging collision electrochemistry of single electrochemiluminescence nano-emitters. *Chem. Sci.* **9**, 6167–6175 (2018).

[CAS](#) [Article](#) [Google Scholar](#)

14. 14.

Jin, Z. & Bard, A. J. Atom-by-atom electrodeposition of single isolated cobalt oxide molecules and clusters for studying the oxygen evolution reaction. *Proc. Natl Acad. Sci. USA* **117**, 12651–12656 (2020).

[CAS](#) [Article](#) [Google Scholar](#)

15. 15.

Chen, M. M. et al. Spatiotemporal imaging of electrocatalytic activity on single 2D gold nanoplates via electrogenerated chemiluminescence microscopy. *Chem. Sci.* **10**, 4141–4147 (2019).

[CAS](#) [Article](#) [Google Scholar](#)

16. 16.

Islam, M. Einstein–Smoluchowski diffusion equation: a discussion. *Phys. Scr.* **70**, 120–125 (2004).

[ADS](#) [CAS](#) [Article](#) [Google Scholar](#)

17. 17.

Bard, A. J. & Faulkner, L. R. *Electrochemical Methods: Fundamentals and Applications* (Wiley, 2000).

18. 18.

Cid, C. P., Spada, E. & Sartorelli, M. Effect of the cathodic polarization on structural and morphological properties of FTO and ITO thin films. *Appl. Surf Sci.* **273**, 603–606 (2013).

[ADS](#) [CAS](#) [Article](#) [Google Scholar](#)

19. 19.

Xu, K., Babcock, H. P. & Zhuang, X. Dual-objective STORM reveals three-dimensional filament organization in the actin cytoskeleton. *Nat. Methods* **9**, 185–188 (2012).

[CAS](#) [Article](#) [Google Scholar](#)

20. 20.

Voci, S. et al. Surface-confined electrochemiluminescence microscopy of cell membranes. *J. Am. Chem. Soc.* **140**, 14753–14760 (2018).

[CAS](#) [Article](#) [Google Scholar](#)

21. 21.

Rust, M. J., Bates, M. & Zhuang, X. W. Sub-diffraction-limit imaging by stochastic optical reconstruction microscopy (STORM). *Nat.*

Methods **3**, 793–796 (2006).

[CAS](#) [Article](#) [Google Scholar](#)

22. 22.

Sharonov, A. & Hochstrasser, R. M. Wide-field subdiffraction imaging by accumulated binding of diffusing probes. *Proc. Natl Acad. Sci. USA* **103**, 18911–18916 (2006).

[ADS](#) [CAS](#) [Article](#) [Google Scholar](#)

23. 23.

Chovin, A., Garrigue, P., Vinatier, P. & Sojic, N. Development of an ordered array of optoelectrochemical individually readable sensors with submicrometer dimensions: application to remote electrochemiluminescence imaging. *Anal. Chem.* **76**, 357–364 (2004).

[CAS](#) [Article](#) [Google Scholar](#)

24. 24.

Nieuwenhuizen, R. P. J. et al. Measuring image resolution in optical nanoscopy. *Nat. Methods* **10**, 557–562 (2013).

[CAS](#) [Article](#) [Google Scholar](#)

25. 25.

Deschout, H. et al. Precisely and accurately localizing single emitters in fluorescence microscopy. *Nat. Methods* **11**, 253–266 (2014).

[CAS](#) [Article](#) [Google Scholar](#)

26. 26.

Innocenzi, P., Kozuka, H. & Yoko, T. Fluorescence properties of the Ru(bpy)₃²⁺ complex incorporated in sol–gel-derived silica coating

films. *J. Phys. Chem. B* **101**, 2285–2291 (1997).

[CAS](#) [Article](#) [Google Scholar](#)

27. 27.

Geiger, B., Spatz, J. P. & Bershadsky, A. D. Environmental sensing through focal adhesions. *Nat. Rev. Mol. Cell Biol.* **10**, 21–33 (2009).

[CAS](#) [Article](#) [Google Scholar](#)

28. 28.

Deschout, H. et al. Complementarity of PALM and SOFI for super-resolution live-cell imaging of focal adhesions. *Nat. Commun.* **7**, 13693 (2016).

[ADS](#) [CAS](#) [Article](#) [Google Scholar](#)

29. 29.

Ding, H., Guo, W. & Su, B. Imaging cell-matrix adhesions and collective migration of living cells by electrochemiluminescence microscopy. *Angew. Chem. Int. Ed.* **132**, 457–464 (2020).

[Article](#) [Google Scholar](#)

30. 30.

Valenti, G. et al. Single cell electrochemiluminescence imaging: from the proof-of-concept to disposable device-based analysis. *J. Am. Chem. Soc.* **139**, 16830–16837 (2017).

[CAS](#) [Article](#) [Google Scholar](#)

[Download references](#)

Acknowledgements

This work was funded by the National Natural Science Foundation of China (21974123), the Natural Science Foundation of Zhejiang Province (LR20B050002), the Fundamental Research Funds for the Central Universities (2019XZZX003-01) and the Hundreds Program of Zhejiang University. We thank G. Tang for advice with cell culture, the Micro and Nano Fabrication Centre at Zhejiang University for facility support and W. Wang at the State Key Laboratory of Modern Optical Instrumentation for assistance with FIB.

Author information

Author notes

1. These authors contributed equally: Jinrun Dong, Yuxian Lu

Affiliations

1. Laboratory of Experimental Physical Biology, Department of Chemistry, Zhejiang University, Hangzhou, China

Jinrun Dong, Yuxian Lu, Yang Xu, Fanfan Chen, Jinmei Yang, Yuang Chen & Jiandong Feng

Authors

1. Jinrun Dong

[View author publications](#)

You can also search for this author in [PubMed](#) [Google Scholar](#)

2. Yuxian Lu

[View author publications](#)

You can also search for this author in [PubMed](#) [Google Scholar](#)

3. Yang Xu

[View author publications](#)

You can also search for this author in [PubMed](#) [Google Scholar](#)

4. Fanfan Chen

[View author publications](#)

You can also search for this author in [PubMed](#) [Google Scholar](#)

5. Jinmei Yang

[View author publications](#)

You can also search for this author in [PubMed](#) [Google Scholar](#)

6. Yuang Chen

[View author publications](#)

You can also search for this author in [PubMed](#) [Google Scholar](#)

7. Jiandong Feng

[View author publications](#)

You can also search for this author in [PubMed](#) [Google Scholar](#)

Contributions

J.F. conceived the idea, designed and supervised all experiments, and wrote the manuscript. J.D. prepared the samples, performed the experiments and analysed the data. Y.L. performed super-resolution imaging and image analysis. Y.X. conducted data analysis and sample characterizations. F.C. prepared cell samples and performed labelling. J.Y. and Y.C. carried out experimental characterizations.

Corresponding author

Correspondence to [Jiandong Feng](#).

Ethics declarations

Competing interests

The authors declare no competing interests.

Additional information

Peer review information *Nature* thanks the anonymous reviewers for their contribution to the peer review of this work.

Publisher's note Springer Nature remains neutral with regard to jurisdictional claims in published maps and institutional affiliations.

Supplementary information

Supplementary Information

This file contains the Supplementary Methods, Supplementary Discussions, Supplementary Figs 1-31 and Supplementary References.

Video 1 Observed single-molecule ECL signals under applied voltage

Video data acquired from the EMCCD reveal the single-molecule ECL signals for the result presented in Fig. 1. Limited by the data size, only part of the raw data is shown.

Video 2 Influence of exposure time during the acquisition

With increasing exposure time, the appearance of the single-molecule ECL events changes from isolated to continuous signals (Fig. 2).

Video 3 Concentration dependence of stochastic observations

The video data correspond to results shown in Supplementary Fig. 15, which is also discussed in Fig. 3.

[Video 4 The processing of super-resolved ECL imaging](#)

The video data (for Fig. 4) reveal the processing of the single-molecule localizations of ECL reactions frame by frame. A ROI of Fig. 4 is used in the video for illustration. After localizing individual emitters, a super-resolved ECL image is reconstructed.

[Video 5 Processed video from live cell single-molecule ECL imaging](#)

The video data show the dynamic visualization of cell adhesions at different moments (36 s, 48 s, 60 s, 72 s) for two selected adhesive regions in Fig. 5.

Rights and permissions

[Reprints and Permissions](#)

About this article



Check for
updates

Cite this article

Dong, J., Lu, Y., Xu, Y. *et al.* Direct imaging of single-molecule electrochemical reactions in solution. *Nature* **596**, 244–249 (2021).
<https://doi.org/10.1038/s41586-021-03715-9>

[Download citation](#)

- Received: 17 July 2020
- Accepted: 09 June 2021
- Published: 11 August 2021

- Issue Date: 12 August 2021
- DOI: <https://doi.org/10.1038/s41586-021-03715-9>

Comments

By submitting a comment you agree to abide by our [Terms](#) and [Community Guidelines](#). If you find something abusive or that does not comply with our terms or guidelines please flag it as inappropriate.

[Access through your institution](#)

[Change institution](#)

[Buy or subscribe](#)

Associated Content

[A microscopy technique that images single reaction events in total darkness](#)

- Frédéric Kanoufi
- Neso Sojic

News & Views 11 Aug 2021

Advertisement

This article was downloaded by **calibre** from <https://www.nature.com/articles/s41586-021-03715-9>

- Article
- [Published: 28 June 2021](#)

Photoinduced copper-catalysed asymmetric amidation via ligand cooperativity

- [Caiyou Chen](#) ORCID: [orcid.org/0000-0001-7536-7139¹](https://orcid.org/0000-0001-7536-7139),
- [Jonas C. Peters](#) ORCID: [orcid.org/0000-0002-6610-4414¹](https://orcid.org/0000-0002-6610-4414) &
- [Gregory C. Fu](#) ORCID: [orcid.org/0000-0002-0927-680X¹](https://orcid.org/0000-0002-0927-680X)

[Nature](#) volume 596, pages 250–256 (2021) [Cite this article](#)

- 12k Accesses
- 27 Altmetric
- [Metrics details](#)

Subjects

- [Asymmetric catalysis](#)
- [Asymmetric synthesis](#)
- [Catalytic mechanisms](#)
- [Synthetic chemistry methodology](#)
- [Photocatalysis](#)

Abstract

The substitution of an alkyl electrophile by a nucleophile is a foundational reaction in organic chemistry that enables the efficient and convergent

synthesis of organic molecules. Although there has been substantial recent progress in exploiting transition-metal catalysis to expand the scope of nucleophilic substitution reactions to include carbon nucleophiles^{1,2,3,4}, there has been limited progress in corresponding reactions with nitrogen nucleophiles^{5,6,7,8}. For many substitution reactions, the bond construction itself is not the only challenge, as there is a need to control stereochemistry at the same time. Here we describe a method for the enantioconvergent substitution of unactivated racemic alkyl electrophiles by a ubiquitous nitrogen-containing functional group, an amide. Our method uses a photoinduced catalyst system based on copper, an Earth-abundant metal. This process for asymmetric N-alkylation relies on three distinct ligands—a bisphosphine, a phenoxide and a chiral diamine. The ligands assemble *in situ* to form two distinct catalysts that act cooperatively: a copper/bisphosphine/phenoxide complex that serves as a photocatalyst, and a chiral copper/diamine complex that catalyses enantioselective C–N bond formation. Our study thus expands enantioselective N-substitution by alkyl electrophiles beyond activated electrophiles (those bearing at least one *sp*- or *sp*²-hybridized substituent on the carbon undergoing substitution)^{8,9,10,11,12,13} to include unactivated electrophiles.

Access options

Subscribe to Journal

Get full journal access for 1 year

\$199.00

only \$3.90 per issue

[Subscribe](#)

All prices are NET prices.

VAT will be added later in the checkout.

Tax calculation will be finalised during checkout.

Rent or Buy article

Get time limited or full article access on ReadCube.

from \$8.99

[Rent or Buy](#)

All prices are NET prices.

Additional access options:

- [Log in](#)
- [Access through your institution](#)
- [Learn about institutional subscriptions](#)

Fig. 1: Chiral secondary amides.

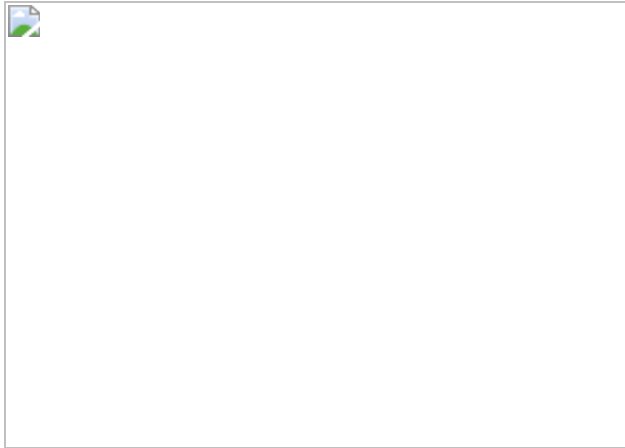


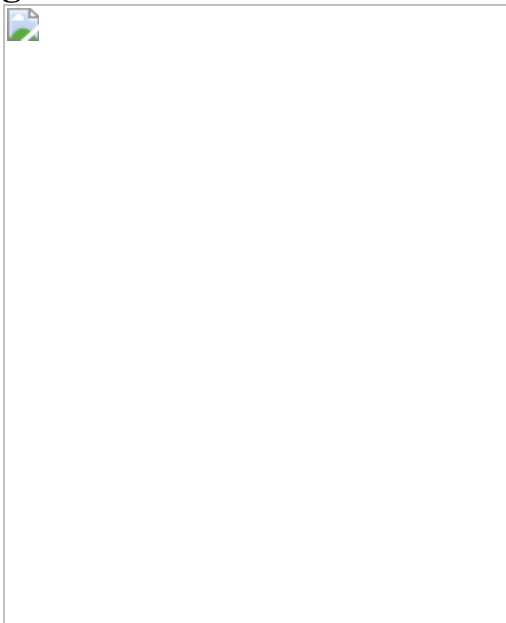
Fig. 2: An array of amides that serve as nucleophilic coupling partners.



Fig. 3: An array of alkyl bromides that serve as electrophilic coupling partners.



Fig. 4: Mechanism.



Data availability

The data that support the findings of this study are available within the paper, its [Supplementary Information](#) (experimental procedures and characterization data) and from the Cambridge Crystallographic Data

Centre (<https://www.ccdc.cam.ac.uk/structures>; crystallographic data are available free of charge under CCDC reference numbers CCDC 2055329–2055338).

References

1. 1.

Fu, G. C. Transition-metal catalysis of nucleophilic substitution reactions: a radical alternative to S_N1 and S_N2 processes. *ACS Cent. Sci.* **3**, 692–700 (2017).

[CAS Article](#) [Google Scholar](#)

2. 2.

Choi, J. & Fu, G. C. Transition metal-catalyzed alkyl–alkyl bond formation: another dimension in cross-coupling chemistry. *Science* **356**, eaaf7230 (2017).

[Article](#) [Google Scholar](#)

3. 3.

Kaga, A. & Chiba, S. Engaging radicals in transition metal-catalyzed cross-coupling with alkyl electrophiles: recent advances. *ACS Catal.* **7**, 4697–4706 (2017).

[CAS Article](#) [Google Scholar](#)

4. 4.

Iwasaki, T. & Kambe, N. Ni-catalyzed C–C couplings using alkyl electrophiles. *Top. Curr. Chem.* **374**, 66 (2016).

[Article](#) [Google Scholar](#)

5. 5.

Bissember, A. C., Lundgren, R. J., Creutz, S. E., Peters, J. C. & Fu, G. C. Transition-metal-catalyzed alkylations of amines with alkyl halides: photoinduced, copper-catalyzed couplings of carbazoles. *Angew. Chem. Int. Ed.* **52**, 5129–5133 (2013).

[CAS Article](#) [Google Scholar](#)

6. 6.

Do, H.-Q., Bachman, S., Bissember, A. C., Peters, J. C. & Fu, G. C. Photoinduced, copper-catalyzed alkylation of amides with unactivated secondary alkyl halides at room temperature. *J. Am. Chem. Soc.* **136**, 2162–2167 (2014).

[CAS Article](#) [Google Scholar](#)

7. 7.

Peacock, D. M., Roos, C. B. & Hartwig, J. F. Palladium-catalyzed cross coupling of secondary and tertiary alkyl bromides with a nitrogen nucleophile. *ACS Cent. Sci.* **2**, 647–652 (2016).

[CAS Article](#) [Google Scholar](#)

8. 8.

Grange, R. L., Clizbe, E. A. & Evans, P. A. Recent developments in asymmetric allylic amination reactions. *Synthesis* **48**, 2911–2968 (2016).

[CAS Article](#) [Google Scholar](#)

9. 9.

Zhang, H. et al. Construction of the N1–C3 linkage stereogenic centers by catalytic asymmetric amination reaction of 3-bromooxindoles with indolines. *Org. Lett.* **16**, 2394–2397 (2014).

[CAS Article](#) [Google Scholar](#)

10. 10.

Kainz, Q. M. et al. Asymmetric copper-catalyzed C–N cross-couplings induced by visible light. *Science* **351**, 681–684 (2016).

[ADS](#) [CAS](#) [Article](#) [Google Scholar](#)

11. 11.

Zhang, X. et al. An enantioconvergent halogenophilic nucleophilic substitution (S_N2X) reaction. *Science* **363**, 400–404 (2019).

[ADS](#) [CAS](#) [Article](#) [Google Scholar](#)

12. 12.

Bartoszewicz, A., Matier, C. D. & Fu, G. C. Enantioconvergent alkylations of amines by alkyl electrophiles: copper-catalyzed nucleophilic substitutions of racemic α -halolactams by indoles. *J. Am. Chem. Soc.* **141**, 14864–14869 (2019).

[CAS](#) [Article](#) [Google Scholar](#)

13. 13.

Wang, Y., Wang, S., Shan, W. & Shao, Z. Direct asymmetric N-propargylation of indoles and carbazoles catalyzed by lithium SPINOL phosphate. *Nat. Commun.* **11**, 226 (2020).

[ADS](#) [CAS](#) [Article](#) [Google Scholar](#)

14. 14.

Greenberg, A., Breneman, C. M. & Liebman, J. F. (eds). *The Amide Linkage: Structural Significance in Chemistry, Biochemistry, and Materials Science* (Wiley, 2000).

15. 15.

Ponra, S., Boudet, B., Phansavath, P. & Ratovelomanana-Vidal, V. Recent developments in transition-metal-catalyzed asymmetric hydrogenation of enamides. *Synthesis* **53**, 193–214 (2021).

[CAS Article](#) [Google Scholar](#)

16. 16.

Wang, J.-W. et al. Catalytic asymmetric reductive hydroalkylation of enamides and enecarbamates to chiral aliphatic amines. *Nat. Commun.* **12**, 1313 (2020).

[ADS Article](#) [Google Scholar](#)

17. 17.

Brown, D. G. & Böstrom, J. Analysis of past and present synthetic methodologies on medicinal chemistry: where have all the new reactions gone? *J. Med. Chem.* **59**, 4443–4458 (2016).

[CAS Article](#) [Google Scholar](#)

18. 18.

Taylor, J. E. & Bull, S. D. in *Comprehensive Organic Synthesis* 2nd edn, vol. 6 (eds Knochel, P. & Molander, G. A.) 427–478 (Elsevier, 2014).

19. 19.

Carey, J. S., Laffan, D., Thomson, C. & Williams, M. T. Analysis of the reactions used for the preparation of drug candidate molecules. *Org. Biomol. Chem.* **4**, 2337–2347 (2006).

[CAS Article](#) [Google Scholar](#)

20. 20.

Matier, C. D., Schwaben, J., Peters, J. C. & Fu, G. C. Copper-catalyzed alkylation of aliphatic amines induced by visible light. *J. Am. Chem. Soc.* **139**, 17707–17710 (2017).

[CAS](#) [Article](#) [Google Scholar](#)

21. 21.

Ahn, J. M., Peters, J. C. & Fu, G. C. Design of a photoredox catalyst that enables the direct synthesis of carbamate-protected primary amines via photoinduced, copper-catalyzed N-alkylation reactions of unactivated secondary halides. *J. Am. Chem. Soc.* **139**, 18101–18106 (2017).

[CAS](#) [Article](#) [Google Scholar](#)

22. 22.

Hossain, A., Bhattacharyya, A. & Reiser, O. Copper's rapid ascent in visible-light photoredox catalysis. *Science* **364**, eaav9713 (2019).

[Article](#) [Google Scholar](#)

23. 23.

Cheng, L.-J. & Mankad, N. P. C–C and C–X coupling reactions of unactivated alkyl electrophiles using copper catalysis. *Chem. Soc. Rev.* **49**, 8036–8064 (2020).

[CAS](#) [Article](#) [Google Scholar](#)

24. 24.

Carreira, E. M. & Yamamoto, H. (eds.) *Comprehensive Chirality* (Academic, 2012).

25. 25.

Reyes, R. L. et al. Asymmetric remote C–H borylation of aliphatic amides and esters with a modular iridium catalyst. *Science* **369**, 970–974 (2020).

[ADS](#) [CAS](#) [Article](#) [Google Scholar](#)

26. 26.

Ordóñez, M., Labastida-Galvan, V. & Lagunas-Rivera, S. Stereoselective synthesis of GABOB, carnitine and statine phosphonates analogues. *Tetrahedron Asymmetry* **21**, 129–147 (2010).

[Article](#) [Google Scholar](#)

27. 27.

Hale, J. J. et al. The discovery of 3-(N-alkyl)aminopropylphosphonic acids as potent S1P receptor agonists. *Bioorg. Med. Chem. Lett.* **14**, 3495–3499 (2004).

[CAS](#) [Article](#) [Google Scholar](#)

28. 28.

Ordóñez, M., Cativiela, C. & Romero-Estudillo, I. An update on the stereoselective synthesis of γ -amino acids. *Tetrahedron Asymmetry* **27**, 999–1055 (2016).

[Article](#) [Google Scholar](#)

29. 29.

Souto, J. A. & Muniz, K. in *Asymmetric Synthesis* vol. 2 (eds Christmann, M. & Bräse, S) 371–375 (Wiley-VCH, 2012).

30. 30.

Antonopoulou, G. et al. Synthesis of 2-oxoamides based on sulfonamide analogs of γ -amino acids and their activity on

phospholipase A₂. *J. Pept. Sci.* **14**, 1111–1120 (2008).

[CAS](#) [Article](#) [Google Scholar](#)

31. 31.

Comprehensive Asymmetric Catalysis vol. I–III (eds. Jacobsen, E. N., Pfaltz, A. & Yamamoto, H.) (Springer, 1999).

32. 32.

Teegardin, K., Day, J. I., Chan, J. & Weaver, J. Advances in photocatalysis: a microreview of visible light mediated ruthenium and iridium catalyzed organic transformations. *Org. Process Res. Dev.* **20**, 1156–1163 (2016).

[CAS](#) [Article](#) [Google Scholar](#)

33. 33.

Creutz, S. E., Lotito, K. J., Fu, G. C. & Peters, J. C. Photoinduced Ullmann C–N coupling: demonstrating the viability of a radical pathway. *Science* **338**, 647–651 (2012).

[ADS](#) [CAS](#) [Article](#) [Google Scholar](#)

34. 34.

Ribelli, T. G., Lorandi, F., Fantin, M. & Matyjaszewski, K. Atom transfer radical polymerization: billion times more active catalysts and new initiation systems. *Macromol. Rapid Commun.* **40**, 1800616 (2019).

[Article](#) [Google Scholar](#)

35. 35.

Lusztyuk, J., Maillard, B., Deycard, S., Lindsay, D. A. & Ingold, K. U. Kinetics for the reaction of a secondary alkyl radical with tri-*n*-

butylgermanium hydride and calibration of a secondary alkyl radical clock reaction. *J. Org. Chem.* **52**, 3509–3514 (1987).

[CAS Article](#) [Google Scholar](#)

36. 36.

Anslyn, E. V. & Dougherty, D. A. in *Modern Physical Organic Chemistry*, 156 (University Science Books, 2006).

[Download references](#)

Acknowledgements

This manuscript is dedicated to the memory of Gregory P. Harlow. Support has been provided by the National Institutes of Health (National Institute of General Medical Sciences, R01–GM109194), the Beckman Institute (support of the Laser Resource Center, as well as the Center for Catalysis and Chemical Synthesis, the EPR facility, and the X-ray crystallography facility), the Gordon and Betty Moore Foundation (support for the Center for Catalysis and Chemical Synthesis), the Dow Next-Generation Educator Fund (grant to Caltech) and Boehringer–Ingelheim Pharmaceuticals. We thank C. Citek, T. M. Donnell, J. Dørfler, P. Garrido Barros, L. M. Henling, P. H. Oyala, F. Schneck, M. Shahgoli, D. VanderVelde and J. R. Winkler for assistance and discussions.

Author information

Affiliations

1. Division of Chemistry and Chemical Engineering, California Institute of Technology, Pasadena, CA, USA

Caiyou Chen, Jonas C. Peters & Gregory C. Fu

Authors

1. Caiyou Chen

[View author publications](#)

You can also search for this author in [PubMed](#) [Google Scholar](#)

2. Jonas C. Peters

[View author publications](#)

You can also search for this author in [PubMed](#) [Google Scholar](#)

3. Gregory C. Fu

[View author publications](#)

You can also search for this author in [PubMed](#) [Google Scholar](#)

Contributions

C.C. performed all experiments. C.C., J.C.P. and G.C.F. wrote the manuscript. All authors contributed to the analysis and the interpretation of the results.

Corresponding authors

Correspondence to [Jonas C. Peters](#) or [Gregory C. Fu](#).

Ethics declarations

Competing interests

The authors declare no competing interests.

Additional information

Peer review information *Nature* thanks the anonymous reviewers for their contribution to the peer review of this work.

Publisher's note Springer Nature remains neutral with regard to jurisdictional claims in published maps and institutional affiliations.

Extended data figures and tables

[Extended Data Fig. 1 Continued scope of alkyl bromides serving as electrophilic coupling partners.](#)

Couplings were generally conducted using 0.5 mmol of the amide, and **N1*** was used as the diamine, unless otherwise noted. All data represent the average of two experiments. The per cent yield represents purified product.

^aElectrophile (1.5 equiv.), Cu(CH₃CN)₄PF₆ (15 mol%), **P** (5 mol%), **N1*** (20 mol%), K₃PO₄ · H₂O (1.5 equiv.; in place of Cs₂CO₃), 10 °C. Ar¹, *p*-(F₃C)C₆H₄.

Supplementary information

[Supplementary Information](#)

This file contains Supplementary Text and Data, Supplementary Tables 1-2, Supplementary Figures 1-31 and NMR Spectra Data - see contents page for details.

Rights and permissions

[Reprints and Permissions](#)

About this article



Check for
updates

Cite this article

Chen, C., Peters, J.C. & Fu, G.C. Photoinduced copper-catalysed asymmetric amidation via ligand cooperativity. *Nature* **596**, 250–256 (2021). <https://doi.org/10.1038/s41586-021-03730-w>

[Download citation](#)

- Received: 21 February 2021
- Accepted: 16 June 2021
- Published: 28 June 2021
- Issue Date: 12 August 2021
- DOI: <https://doi.org/10.1038/s41586-021-03730-w>

Comments

By submitting a comment you agree to abide by our [Terms](#) and [Community Guidelines](#). If you find something abusive or that does not comply with our terms or guidelines please flag it as inappropriate.

[Access through your institution](#)

[Change institution](#)

[Buy or subscribe](#)

Advertisement

This article was downloaded by **calibre** from <https://www.nature.com/articles/s41586-021-03730-w>

- Article
- [Published: 04 August 2021](#)

Connectomes across development reveal principles of brain maturation

- [Daniel Witvliet](#)^{1,2},
- [Ben Mulcahy](#) [ORCID: orcid.org/0000-0002-3336-245X](#)¹ natl,
- [James K. Mitchell](#) [ORCID: orcid.org/0000-0003-3359-6165](#)^{3,4} natl,
- [Yaron Meirovitch](#) [ORCID: orcid.org/0000-0002-1946-8012](#)^{4,5},
- [Daniel R. Berger](#)⁴,
- [Yuelong Wu](#)⁴,
- [Yufang Liu](#)¹,
- [Wan Xian Koh](#)¹,
- [Rajeev Parvathala](#)⁵,
- [Douglas Holmyard](#)¹,
- [Richard L. Schalek](#)⁴,
- [Nir Shavit](#)⁵,
- [Andrew D. Chisholm](#)⁶,
- [Jeff W. Lichtman](#) [ORCID: orcid.org/0000-0002-0208-3212](#)^{4,7},
- [Aravinthan D. T. Samuel](#) [ORCID: orcid.org/0000-0002-1672-8720](#)^{3,4} &
- [Mei Zhen](#) [ORCID: orcid.org/0000-0003-0086-9622](#)^{1,2,8}

[Nature](#) volume **596**, pages 257–261 (2021) [Cite this article](#)

- 6759 Accesses
- 528 Altmetric

- [Metrics details](#)

Subjects

- [Development of the nervous system](#)
- [Developmental biology](#)
- [Neural circuits](#)
- [Neuroscience](#)

Abstract

An animal's nervous system changes as its body grows from birth to adulthood and its behaviours mature^{1,2,3,4,5,6,7,8}. The form and extent of circuit remodelling across the connectome is unknown^{3,9,10,11,12,13,14,15}. Here we used serial-section electron microscopy to reconstruct the full brain of eight isogenic *Caenorhabditis elegans* individuals across postnatal stages to investigate how it changes with age. The overall geometry of the brain is preserved from birth to adulthood, but substantial changes in chemical synaptic connectivity emerge on this consistent scaffold. Comparing connectomes between individuals reveals substantial differences in connectivity that make each brain partly unique. Comparing connectomes across maturation reveals consistent wiring changes between different neurons. These changes alter the strength of existing connections and create new connections. Collective changes in the network alter information processing. During development, the central decision-making circuitry is maintained, whereas sensory and motor pathways substantially remodel. With age, the brain becomes progressively more feedforward and discernibly modular. Thus developmental connectomics reveals principles that underlie brain maturation.

Access options

Subscribe to Journal

Get full journal access for 1 year

\$199.00

only \$3.90 per issue

[Subscribe](#)

All prices are NET prices.

VAT will be added later in the checkout.

Tax calculation will be finalised during checkout.

Rent or Buy article

Get time limited or full article access on ReadCube.

from \$8.99

[Rent or Buy](#)

All prices are NET prices.

Additional access options:

- [Log in](#)
- [Access through your institution](#)
- [Learn about institutional subscriptions](#)

Fig. 1: The developing brain maintains overall geometry with increasing numbers of synapses and connections.

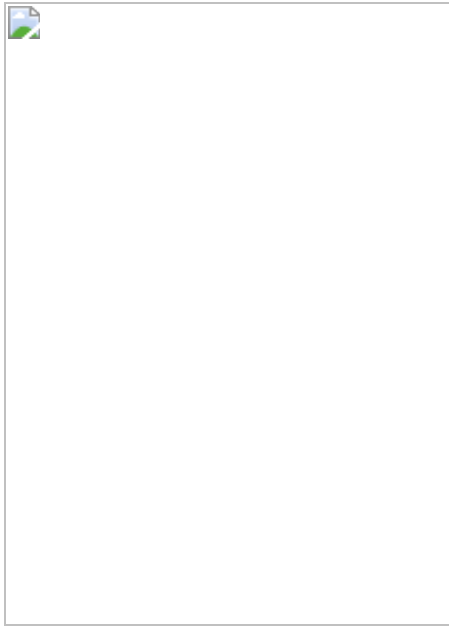


Fig. 2: Connectomes of isogenic individuals include both stereotyped and variable connections.

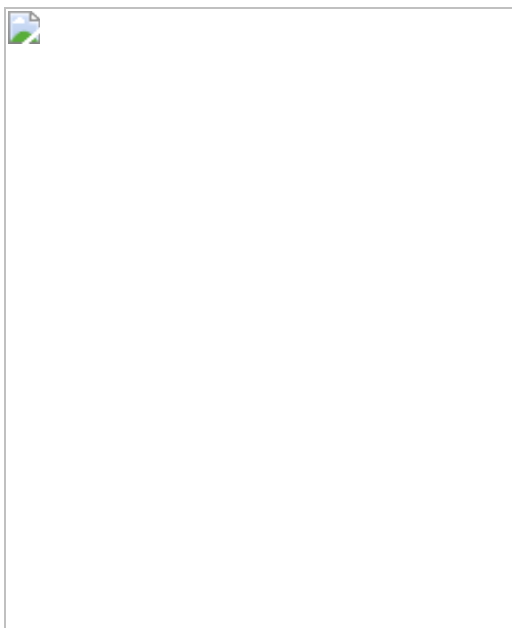


Fig. 3: Developmental increase in feedforward signalling and modularity.

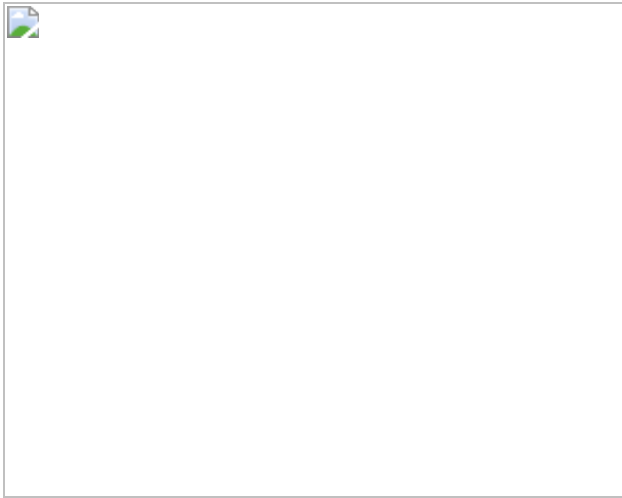
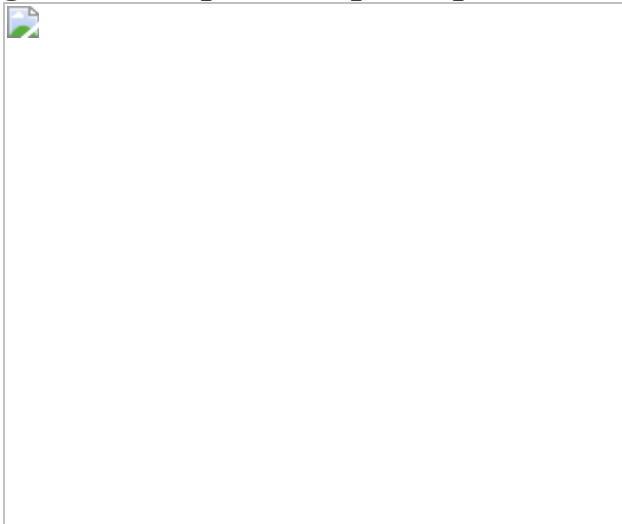


Fig. 4: Developmental principles of brain maturation.



Data availability

All electron microscopy images and volumetric reconstructions are available at <https://bossdb.org/project/witvliet2020>. Connectivity matrices for all datasets are available at <http://www.nemanode.org> and as Supplementary Tables.

Code availability

All scripts and files used to generate all figures are available at <https://github.com/dwitvliet/nature2021>.

References

1. 1.

Bucher, D., Prinz, A. A. & Marder, E. Animal-to-animal variability in motor pattern production in adults and during growth. *J. Neurosci.* **25**, 1611–1619 (2005).

[CAS](#) [Article](#) [Google Scholar](#)

2. 2.

Kämper, G. & Murphey, R. Maturation of an insect nervous system: Constancy in the face of change. *Comp. Biochem. Physiol. A* **109**, 23–32 (1994).

[Article](#) [Google Scholar](#)

3. 3.

Gerhard, S., Andrade, I., Fetter, R. D., Cardona, A. & Schneider-Mizell, C. M. Conserved neural circuit structure across *Drosophila* larval development revealed by comparative connectomics. *eLife* **6**, e29089 (2017).

[Article](#) [Google Scholar](#)

4. 4.

Kagan, J., Herschkowitz, N. & Herschkowitz, E. C. *A Young Mind in a Growing Brain* (Lawrence Erlbaum, 2005).

5. 5.

Pujala, A. & Koyama, M. Chronology-based architecture of descending circuits that underlie the development of locomotor repertoire after birth. *eLife* **8**, e42135 (2019).

[Article](#) [Google Scholar](#)

6. 6.

Hebb, D. O. *The Organization of Behavior: A Neuropsychological Theory* (John Wiley & Sons, 1949).

7. 7.

Hubel, D. H. & Wiesel, T. N. Brain mechanisms of vision. *Sci. Am.* **241**, 150–162 (1979).

[CAS](#) [Article](#) [Google Scholar](#)

8. 8.

Van Horn, M. R. & Ruthazer, E. S. Glial regulation of synapse maturation and stabilization in the developing nervous system. *Curr. Opin. Neurobiol.* **54**, 113–119 (2019).

[Article](#) [Google Scholar](#)

9. 9.

White, J. G., Southgate, E., Thomson, J. N. & Brenner, S. The structure of the nervous system of the nematode *Caenorhabditis elegans*. *Phil. Trans. R. Soc. Lond. B* **314**, 1–340 (1986).

[ADS](#) [CAS](#) [Article](#) [Google Scholar](#)

10. 10.

Scheffer, L. K. et al. A connectome and analysis of the adult *Drosophila* central brain. *eLife* **9**, e57443 (2020).

[CAS](#) [Article](#) [Google Scholar](#)

11. 11.

Karimi, A., Odenthal, J., Drawitsch, F., Boergens, K. M. & Helmstaedter, M. Cell-type specific innervation of cortical pyramidal cells at their apical dendrites. *eLife* **9**, e46876 (2020).

[CAS](#) [Article](#) [Google Scholar](#)

12. 12.

Morgan, J. L. & Lichtman, J. W. An individual interneuron participates in many kinds of inhibition and innervates much of the mouse visual thalamus. *Neuron* **106**, 468–481.e2 (2020).

[CAS](#) [Article](#) [Google Scholar](#)

13. 13.

Randel, N. et al. Inter-individual stereotypy of the *Platynereis* larval visual connectome. *eLife* **4**, e08069 (2015).

[Article](#) [Google Scholar](#)

14. 14.

Kornfeld, J. et al. An anatomical substrate of credit assignment in reinforcement learning. Preprint at <https://doi.org/10.1101/2020.02.18.954354> (2020).

15. 15.

Schneider-Mizell, C. M. et al. Chandelier cell anatomy and function reveal a variably distributed but common signal. preprint. Preprint at <https://doi.org/10.1101/2020.03.31.018952> (2020).

16. 16.

Aicher, C., Jacobs, A. Z. & Clauset, A. Learning latent block structure in weighted networks. *J. Complex Netw.* **3**, 221–248 (2015).

[MathSciNet](#) [Article](#) [Google Scholar](#)

17. 17.

Jin, X., Pokala, N. & Bargmann, C. I. Distinct circuits for the formation and retrieval of an imprinted olfactory memory. *Cell* **164**, 632–643 (2016).

[CAS](#) [Article](#) [Google Scholar](#)

18. 18.

White, J. G., Albertson, D. G. & Anness, M. A. Connectivity changes in a class of motoneurone during the development of a nematode. *Nature* **271**, 764–766 (1978).

[ADS](#) [CAS](#) [Article](#) [Google Scholar](#)

19. 19.

Bargmann, C. I. & Marder, E. From the connectome to brain function. *Nat. Methods* **10**, 483–490 (2013).

[CAS](#) [Article](#) [Google Scholar](#)

20. 20.

Varshney, L. R., Chen, B. L., Paniagua, E., Hall, D. H. & Chklovskii, D. B. Structural properties of the *Caenorhabditis elegans* neuronal network. *PLoS Comput. Biol.* **7**, e1001066 (2011).

[ADS](#) [CAS](#) [Article](#) [Google Scholar](#)

21. 21.

Brenner, S. The genetics of *Caenorhabditis elegans*. *Genetics* **77**, 71–94 (1974).

[CAS](#) [Article](#) [Google Scholar](#)

22. 22.

Mulcahy, B. et al. A pipeline for volume electron microscopy of the *Caenorhabditis elegans* nervous system. *Front. Neural Circuits* **12**, 94 (2018).

[CAS](#) [Article](#) [Google Scholar](#)

23. 23.

Sulston, J. E. & Horvitz, H. R. Post-embryonic cell lineages of the nematode, *Caenorhabditis elegans*. *Dev. Biol.* **56**, 110–156 (1977).

[CAS](#) [Article](#) [Google Scholar](#)

24. 24.

Baena, V., Schalek, R. L., Lichtman, J. W. & Terasaki, M. Serial-section electron microscopy using automated tape-collecting ultramicrotome (ATUM). *Methods Cell Biol.* **152**, 41–67 (2019).

[Article](#) [Google Scholar](#)

25. 25.

Hayworth, K. J. et al. Imaging ATUM ultrathin section libraries with WaferMapper: a multi-scale approach to EM reconstruction of neural circuits. *Front. Neural Circuits* **8**, 68 (2014).

[Article](#) [Google Scholar](#)

26. 26.

Cardona, A. et al. TrakEM2 software for neural circuit reconstruction. *PLoS One* **7**, e38011 (2012).

[ADS](#) [MathSciNet](#) [CAS](#) [Article](#) [Google Scholar](#)

27. 27.

Saalfeld, S., Fetter, R., Cardona, A. & Tomancak, P. Elastic volume reconstruction from series of ultra-thin microscopy sections. *Nat. Methods* **9**, 717–720 (2012).

[CAS](#) [Article](#) [Google Scholar](#)

28. 28.

Saalfeld, S., Cardona, A., Hartenstein, V. & Tomancak, P. CATMAID: collaborative annotation toolkit for massive amounts of image data. *Bioinformatics* **25**, 1984–1986 (2009).

[CAS](#) [Article](#) [Google Scholar](#)

29. 29.

Lim, M. A. et al. Neuroendocrine modulation sustains the *C. elegans* forward motor state. *eLife* **5**, e19887 (2016).

[Article](#) [Google Scholar](#)

30. 30.

Hung, W. L. et al. Attenuation of insulin signalling contributes to FSN-1-mediated regulation of synapse development. *EMBO J.* **32**, 1745–1760 (2013).

[CAS](#) [Article](#) [Google Scholar](#)

31. 31.

Kasthuri, N. et al. Saturated reconstruction of a volume of neocortex. *Cell* **162**, 648–661 (2015).

[CAS](#) [Article](#) [Google Scholar](#)

32. 32.

Meirovitch, Y. et al. A multi-pass approach to large-scale connectomics. Preprint at <https://arxiv.org/abs/1612.02120> (2016).

33. 33.

Matveev, A. et al. A multicore path to connectomics-on-demand. In *Proc. 22nd ACM SIGPLAN Symposium on Principles and Practice of Parallel Programming*, 267–281 (2017).

34. 34.

Meirovitch, Y. et al. Cross-classification clustering: an efficient multi-object tracking technique for 3-d instance segmentation in connectomics. In *Proc. IEEE Conference on Computer Vision and Pattern Recognition*, 8425–8435 (2019).

35. 35.

Blumofe, R. D. et al. Cilk: An efficient multithreaded runtime system. *J. Parallel Distrib. Comput.* **37**, 55–69 (1996).

[Article](#) [Google Scholar](#)

36. 36.

Berger, D. R., Seung, H. S. & Lichtman, J. W. VAST (volume annotation and segmentation tool): efficient manual and semi-automatic labeling of large 3D image stacks. *Front. Neural Circuits* **12**, 88 (2018).

[Article](#) [Google Scholar](#)

37. 37.

Philbrook, A. et al. Neurexin directs partner-specific synaptic connectivity in *C. elegans*. *eLife* **7**, e35692 (2018).

[Article](#) [Google Scholar](#)

38. 38.

Sulston, J., Dew, M. & Brenner, S. Dopaminergic neurons in the nematode *Caenorhabditis elegans*. *J. Comp. Neurol.* **163**, 215–226 (1975).

[CAS](#) [Article](#) [Google Scholar](#)

39. 39.

Duerr, J. S. et al. The *cat-1* gene of *Caenorhabditis elegans* encodes a vesicular monoamine transporter required for specific monoamine-dependent behaviors. *J. Neurosci.* **19**, 72–84 (1999).

[CAS](#) [Article](#) [Google Scholar](#)

40. 40.

Durbin, R. M. *Studies on the Development and Organisation of the Nervous System of Caenorhabditis elegans* (Univ. of Cambridge, 1987).

41. 41.

Cook, S. J. et al. Whole-animal connectomes of both *Caenorhabditis elegans* sexes. *Nature* **571**, 63–71 (2019).

[ADS](#) [CAS](#) [Article](#) [Google Scholar](#)

42. 42.

Faskowitz, J., Yan, X., Zuo, X.-N. & Sporns, O. Weighted stochastic block models of the human connectome across the life span. *Sci. Rep.* **8**, 12997 (2018).

[ADS](#) [Article](#) [Google Scholar](#)

[Download references](#)

Acknowledgements

We thank V. Laskova for help with electron microscopy samples; B. Harris for help with high-pressure freezing; M. Neubauer, D. Kersen, A. Paulino, M. Suriyalaksh, A. Srajer, M. Chang, S. Ihn and J. Ho for help with imaging; A. Cardona, I. Arganda-Carreras and J. Qian for guidance on electron microscopy alignment; S. Cook, C. Rehaluk and M. Wang for synapse annotation in some datasets; J. Ho, C. Morii-Sciolla, I. So, M. and C.-Y. Ho for generating ground truth and proofreading for volumetric reconstruction; A. Matveev, L. Mi and H. Saribekyan for help with analysis algorithms; J. Wang and D. Cao for help with statistics; A. Lin, C. Tabone and V. Venkatachalam for help with data servers; S. Maeng and D. Fong for help with www.nemanode.org; members of our laboratories for comments; G. Si and L. Varshney for critical reading and suggestions; D. Hall, J. Srinivasan and A. Cardona for early advice. J.K.M. was supported by NSF PoLS (NSF 1806818). B.M. was supported by the Mount Sinai Foundation. J.W.L. was supported by the NIMH, Silvio Conte Center (P50 MH094271), the NIH (U24 NS109102-01) and MURI (GG0008784). J.W.L., A.D.T.S. and M.Z. were supported by the HFSP (RGP0051/2014). A.D.T.S. and M.Z. were supported by the NIH (R01-NS082525-01A1). A.D.T.S. was supported by NIH Brain Initiative (1U01NS111697-01) and NSF BRAIN EAGER (IOS-1452593). M.Z. was supported by CIHR (MOP-123250 and Foundation Scheme 154274), the Radcliffe Institute and the Mount Sinai Foundation.

Author information

Author notes

1. These authors contributed equally: Ben Mulcahy, James K. Mitchell

Affiliations

1. Lunenfeld-Tanenbaum Research Institute, Mount Sinai Hospital, Toronto, Ontario, Canada

Daniel Witvliet, Ben Mulcahy, Yufang Liu, Wan Xian Koh, Douglas Holmyard & Mei Zhen

2. Department of Molecular Genetics, University of Toronto, Toronto, Ontario, Canada

Daniel Witvliet & Mei Zhen

3. Department of Physics, Harvard University, Cambridge, MA, USA

James K. Mitchell & Aravinthan D. T. Samuel

4. Center for Brain Science, Harvard University, Cambridge, MA, USA

James K. Mitchell, Yaron Meirovitch, Daniel R. Berger, Yuelong Wu, Richard L. Schalek, Jeff W. Lichtman & Aravinthan D. T. Samuel

5. Computer Science and Artificial Intelligence Laboratory, Massachusetts Institute of Technology, Cambridge, MA, USA

Yaron Meirovitch, Rajeev Parvathala & Nir Shavit

6. Division of Biological Sciences, Section of Cell and Developmental Biology, University of California, San Diego, San Diego, CA, USA

Andrew D. Chisholm

7. Department of Molecular and Cellular Biology, Harvard University, Cambridge, MA, USA

Jeff W. Lichtman

8. Department of Physiology, University of Toronto, Toronto, Ontario, Canada

Mei Zhen

Authors

1. Daniel Witvliet

[View author publications](#)

You can also search for this author in [PubMed](#) [Google Scholar](#)

2. Ben Mulcahy

[View author publications](#)

You can also search for this author in [PubMed](#) [Google Scholar](#)

3. James K. Mitchell

[View author publications](#)

You can also search for this author in [PubMed](#) [Google Scholar](#)

4. Yaron Meirovitch

[View author publications](#)

You can also search for this author in [PubMed](#) [Google Scholar](#)

5. Daniel R. Berger

[View author publications](#)

You can also search for this author in [PubMed](#) [Google Scholar](#)

6. Yuelong Wu

[View author publications](#)

You can also search for this author in [PubMed](#) [Google Scholar](#)

7. Yufang Liu

[View author publications](#)

You can also search for this author in [PubMed](#) [Google Scholar](#)

8. Wan Xian Koh

[View author publications](#)

You can also search for this author in [PubMed](#) [Google Scholar](#)

9. Rajeev Parvathala

[View author publications](#)

You can also search for this author in [PubMed](#) [Google Scholar](#)

10. Douglas Holmyard

[View author publications](#)

You can also search for this author in [PubMed](#) [Google Scholar](#)

11. Richard L. Schalek

[View author publications](#)

You can also search for this author in [PubMed](#) [Google Scholar](#)

12. Nir Shavit

[View author publications](#)

You can also search for this author in [PubMed](#) [Google Scholar](#)

13. Andrew D. Chisholm

[View author publications](#)

You can also search for this author in [PubMed](#) [Google Scholar](#)

14. Jeff W. Lichtman

[View author publications](#)

You can also search for this author in [PubMed](#) [Google Scholar](#)

15. Aravinthan D. T. Samuel

[View author publications](#)

You can also search for this author in [PubMed](#) [Google Scholar](#)

16. Mei Zhen

[View author publications](#)

You can also search for this author in [PubMed](#) [Google Scholar](#)

Contributions

J.W.L., A.D.T.S. and M.Z. conceived the study. Y.M., R.P. and N.S. designed the algorithm for automated volumetric reconstruction (contact Y.M. at yaron.mr@gmail.com). D.R.B. and R.L.S. designed the pipeline for automated electron microscopy acquisition (contact D.R.B. at danielberger@fas.harvard.edu). Y.W. designed software for electron microscopy alignment (contact Y.W. at yuelongwu@fas.harvard.edu). D.W., B.M., J.K.M., D.H., R.L.S. and M.Z. generated and imaged most of the electron micrographs. D.W., B.M. and J.K.M. performed most annotation. D.W. designed and performed most analysis. D.R.B., W.X.K. and Y.L. performed additional experiments and analysis. A.D.C. guided early cell identification and annotation. D.W., J.W.L., A.D.T.S. and M.Z. wrote the manuscript. All authors reviewed the manuscript.

Corresponding authors

Correspondence to [Daniel Witvliet](#) or [Jeff W. Lichtman](#) or [Aravinthan D. T. Samuel](#) or [Mei Zhen](#).

Ethics declarations

Competing interests

The authors declare no competing interests.

Additional information

Peer review information *Nature* thanks the anonymous reviewer(s) for their contribution to the peer review of this work. Peer reviewer reports are available.

Publisher's note Springer Nature remains neutral with regard to jurisdictional claims in published maps and institutional affiliations.

Extended data figures and tables

Extended Data Fig. 1 Electron microscopy reconstruction of cells and synapses in *C. elegans* brains from birth to adulthood.

a, A representative electron microscopy micrograph of the neuropil (from dataset 3). Presynaptic termini of classical chemical synapses are characterized by a pool of clear synaptic vesicles (red arrows) surrounding an active zone (red arrowhead). Presynaptic termini of chemical synapses of modulatory neurons are characterized by mostly DCVs (orange arrows) distant from the active zone (orange arrowhead). Postsynaptic cells are marked by asterisks. The proportion of dense core and clear synaptic vesicles were not quantified. **b**, Neurites grow while maintaining overall brain geometry. Correlation of the relative neurite length of each branch between L1 (dataset 1) and adult (dataset 8). The length of each neurite is normalized against the total neurite length of the neuron. $P = 9.4 \times 10^{-172}$, $r = 0.75$, $n = 947$, Spearman's rank correlation. **c**, Proportion of physical contacts in the brain that harbours at least one chemical synapse at respective developmental time points. **d**, Most connectivity asymmetry at birth is eliminated during L1. Connectivity asymmetry decreases from birth to adulthood, most significantly during L1. Asymmetry is defined as the coefficient of variation (CV) in synapse number between left-right cell pairs. Error bars indicate s.e.m. **e**, Total number of missing connections decreases from birth to adulthood, most significantly during L1. One connection refers to a cell making at least one chemical synapse to another cell. A missing connection is defined as a connection absent in only one dataset and from one side of the brain. **f**, Non-uniform distribution of connections and strengthening of connections across maturation. Distribution of the total number of input and output connections per neuron at birth. **g**, Non-uniform synapse addition to synaptic inputs and outputs of a cell. Top: neurons with higher number of connections at birth (dataset 1) are more likely to receive new synapses at existing input connections by adulthood (averaging datasets 7 and 8). Bottom: no correlation is observed at existing output connections. Each data point represents one cell. Significance is calculated using two-sided Spearman's rank correlation (top: $P = 1.1 \times 10^{-5}$, $n = 166$; bottom: $P = 0.017$, $n = 141$). **h**, Top: neurons with

higher number of connections at birth (dataset 1) are more likely to establish new input connections by adulthood (averaging datasets 7 and 8). Bottom: no correlation is observed at new output connections. Each data point represents one cell. Significance is calculated using two-sided Spearman's rank correlation (top: $P = 1.3 \times 10^{-7}$, $n = 166$; bottom: $P = 0.18$, $n = 141$). **i**, Upper panels: neurons with more input connections at birth are more likely to strengthen these connections during maturation. Left: the number of input connections at birth (dataset 1) is positively correlated with their synapse number increase by adulthood (average of datasets 7 and 8). $P = 1.6 \times 10^{-17}$, $n = 166$ by the Spearman's rank correlation. Right: the number of output connections at birth does not predict the synapse number increase at input connections by adulthood. $P = 0.32$, $n = 120$ by the Spearman's rank correlation. Lower panels: Neither input connection (left) nor output connection (right) at birth predicts the synapse number increase at output connections by adulthood. left: $P = 0.16$, $n = 120$; right: $P = 0.12$, $n = 141$ by the two-sided Spearman's rank correlation. Each point represents one cell. **j**, Upper panels: neurons with higher number of input connections (left) or output connections (right) at birth (dataset 1) are more likely to establish new input connections by adulthood (average of datasets 7 and 8). Left: $P = 5.4 \times 10^{-4}$, $n = 166$; right: $P = 1.7 \times 10^{-4}$, $n = 120$ by the Spearman's rank correlation. Lower panels: Neither the input (left) or output (right) connection number at birth predicts the likelihood to establish new output connections by adulthood. Left: $P = 1.00$, $n = 120$; right: $P = 0.08$, $n = 141$ by the two-sided Spearman's rank correlation. Each data point represents one cell. **k**, Relative number of synapses added to existing connections is correlated between outputs of the same cell compared to connections to and from different cells. Relative number of synapses added represents the fold increase of synapse number from birth (dataset 1) to adulthood (average of datasets 7 and 8). ns (not significant) $P = 0.48$, ** $P = 4.5 \times 10^{-3}$, *** $P = 4.9 \times 10^{-5}$, two-sided Mann–Whitney U test, FDR adjusted using Benjamini–Hochberg correction ($n_{\text{outputs}} = 753$, $n_{\text{inputs}} = 1203$, $n_{\text{other}} = 90709$). Centre line, median; box limits, upper and lower quartiles; whiskers, 1.5x interquartile range; outliers not shown. Top: each data point represents the mean coefficient of variation (CV) in the number of synapses for different sets of connections. The CV of output connections from the

same cell is maintained. The CV of input connections to the same cell increases over time, at the same rate as connections to and from different cells. Error bars indicate s.e.m. Bottom: the difference between the mean CV for output and input connections relative to connections between different cells grows over time. *** $P = 5.3 \times 10^{-7}$, $r = 0.99$, two-sided Spearman's rank correlation.

Extended Data Fig. 2 Closeup of an adult brain connectome.

Wiring diagrams for an adult connectome (dataset 8). Each circle represents a cell. Circle colour denotes cell type. Each line represents a connection with at least one chemical synapse between two cells. Line width indicates synapse number. Straight lines direct information from sensory to muscle layers whereas curved lines direct information in reverse. Cell coordinates are represented as in Fig. 1b, with overlapping cells manually separated.

Extended Data Fig. 3 A physical contact matrix between neurites and muscle fibres in seven volumetrically reconstructed *C. elegans* brains.

Cells are pooled by left-right pairs. The physical contact size is represented by the largest value from the seven datasets. Statistical significance calculated by two-sided Spearman's rank correlation.

Extended Data Fig. 4 Prevalence, location, and synaptic distribution of spine-like protrusions.

a, 3D reconstructions of one neuron class (AIZL and AIZR) across maturation. The overall geometry was maintained, whereas the number of spine-like protrusions (grey arrows) increased over time. **b**, Proportion of postsynaptic spine-like protrusions increases across maturation. *** $P = 6.5 \times 10^{-5}$, two-sided Spearman's rank correlation. **c**, Total number of spine-like protrusions in the brain increases across maturation. *** $P = 5.3 \times 10^{-7}$, two-sided Spearman's rank correlation. **d**, Proportion of synapses with at least one spine-like protrusion postsynaptic partner increases across maturation. *** $P = 1.8 \times 10^{-4}$, two-sided Spearman's rank

correlation. **e**, Distribution of spine-like protrusions by location, with the entry of the neurite into the brain as the most proximal, and the exit or terminal end of the neurite the most distal. **f**, Number of spine-like protrusions that oppose a presynaptic terminal per neuron at birth (average of datasets 1 and 2) and in adulthood (average of datasets 7 and 8). **g**, Proportion of presynaptic inputs onto spine-like protrusions per neuron in adulthood (average of datasets 7 and 8), grouped by their cell type. **h**, Proportion of synapses with spine-like protrusions that comprise stable, variable, and developmentally dynamic connections. Developmentally dynamic connections have the highest proportion. *** (stable-dev. dynamic) $P = 3.7 \times 10^{-34}$, *** (variable-dev. dynamic) $P = 5.1 \times 10^{-25}$, two-tailed Z-test, FDR adjusted using Benjamini–Hochberg correction ($n_{stable} = 10,059$, $n_{variable} = 2,169$, $n_{dev.\ dynamic} = 1,611$).

Extended Data Fig. 5 Connectivity matrix of the *C. elegans* brain throughout maturation.

Connectivity matrix including connections observed in eight *C. elegans* brains. Cells are pooled by left-right pairs. Each connection size represents the largest synapse number in any dataset. Stable, developmentally dynamic, and variable connections are colour-coded (Methods).

Extended Data Fig. 6 A connectome has prevalent variable connections.

a, Composition of stable, developmentally dynamic, and variable connections in each dataset classified by synapse size. **b**, Prevalence of variable connections is not caused by over-annotation of ambiguous synapses. High proportions of both variable and non-variable (stable and developmentally dynamic) connections form at non-variable physical contacts. A physical contact is defined as variable when it is absent from more than one of the seven datasets. **c**, Synapses that constitute non-variable and variable connections, sorted by electron microscopy section numbers that the presynaptic active zone encompasses. All synapses in seven volumetrically segmented datasets are included. Synapses comprising variable connections are marginally smaller than those comprising non-

variable connections, but no threshold can be set to remove exclusively the variable connections. **d**, Proportion of synapses that form a polyadic synapse with synapses of the stable connections. A marginally smaller portion of synapses that comprise variable connections (78%) than those comprising non-variable connections (93%) reside in this configuration. Therefore, variable connections are not fortuitous accidents of synapse annotation. **e**, Synapses comprising non-variable and variable connections sorted by the number of post-synaptic partners. They exhibit similar distributions from monoadic to polyadic. Non-variable connections have marginally more polyadic synapses than variable connections (20% vs 28% for dyadic, and 61% vs 54% for triadic synapses, respectively). No threshold by postsynaptic partner number can be set to filter variable connections. **f**, Proportion of postsynaptic contact area occupied by each postsynaptic partner at each synapse. Synapses comprising variable connections on average occupy less postsynaptic area than synapses comprising non-variable connections, but no threshold can be set to only exclude variable connections. **g**, Any threshold removes both variable and non-variable connections. Total number of non-variable (stable and developmentally dynamic) and variable connections in adulthood (average of datasets 7 and 8) upon thresholding by different synapse numbers. No synapse number provides a filter for specific removal of variable connections: all removes both variable and stable connections. **h**, Thresholding connections by synapse number leaves substantial proportion of variable connections for all cell types. Non-uniform distribution of variable connections remains when connections with low synapse numbers are removed. **i**, Non-uniform distribution of variable and developmentally dynamic connections. Wiring diagrams for variable, stable, and developmentally dynamic connections. Each line represents a connection observed in at least one dataset. Line width indicates the largest number of synapses observed for a connection across datasets. Each circle represents a cell. Cell coordinates are represented as in Fig. 1b. Comparison of the proportion of variable and non-variable connections for each cell type. Non-variable connections include stable and developmentally changing connections. Cell types with significantly higher or lower proportions of variable connections are indicated. Upper panel: * P (modulatory-inter) = 2.2×10^{-2} , * P (modulatory-sensory) = 6.5×10^{-3} , *** P (sensory-motor) = 4.7×10^{-8} , *** P (modulatory-motor) = 5.2×10^{-8} , *** P (inter-

motor) = 1.7×10^{-7} , lower panel: *** P (sensory-muscle) = 6.9×10^{-9} , *** P (modulatory-muscle) = 1.3×10^{-7} , *** P (inter-muscle) = 3.6×10^{-5} , *** P (motor-muscle) = 8.1×10^{-7} . $n = 22\text{--}57$, two-sided Mann–Whitney U test, FDR adjusted using Benjamini–Hochberg correction. Centre line, median; box limits, upper and lower quartiles; whiskers, 1.5x interquartile range; outliers not shown.

Extended Data Fig. 7 Stability of interneuron connections and strengthening of feedforward connections are revealed by assessing connection strength by synapse size.

a, Proportion of developmentally dynamic connections by cell type, when connection strength changes were evaluated by either synapse number (left) or synapse size (middle). Connections between interneurons are the most stable regardless of how synapse weight was evaluated. Right panel: Developmental stability of connections is not correlated with the extend of synapse number increase from birth (average of datasets 1 and 2) to adulthood (average of datasets 7 and 8). **b**, Increase in both feedforward signal flow and modularity across maturation. The number of synapses for stable connections in adults (datasets 7 and 8) relative to birth (datasets 1 and 2). Stable feedforward connections are strengthened more than stable feedback and recurrent connections. ns (not significant) $P = 0.13$, ** P (feedforward-recurrent) = 0.0015, ** P (feedforward-feedback) = 0.0012, two-sided Mann–Whitney U test, FDR adjusted using Benjamini–Hochberg correction ($n_{\text{feedforward}} = 301$, $n_{\text{recurrent}} = 229$, $n_{\text{feedback}} = 107$). Centre line, median; box limits, upper and lower quartiles; whiskers, 1.5x interquartile range; outliers not shown. **c**, Proportions of feedforward, feedback, and recurrent connections for stable and developmentally dynamic connections. ** P (stable-strengthened) = 0.0015, ** P (stable-weakened) = 0.0032, two-tailed Z -test of the proportion of feedforward connections, FDR adjusted using Benjamini–Hochberg correction ($n_{\text{stable}} = 737$, $n_{\text{added}} = 198$, $n_{\text{weakened}} = 18$).

Extended Data Fig. 8 Cell modules across maturation.

a, The log-likelihood score for each WSBM model ([Methods](#)). **b**, Optimal number of modules detected by WSBM using subsets of connections.

Extended Data Fig. 9 Comparison of multiple adult connectomes reveals extensive variability in connectivity.

a, Shared and unique connections for three adult connectomes: dataset 7, dataset 8, and N2U (a) annotated by White et al. 1986 (ref. [40](#)), illustrated in the Venn diagram. Connections of all synapse numbers are included for comparison (Methods). **b**, Re-annotation of N2U increased its variability. Re-annotation of the N2U adult connectome (ref. [41](#)) added 1109 new connections that disproportionately enlarged its pool of unique connections ([Methods](#)). Only 16% contributed to connections shared by three connectomes. This suggests the use of different annotation criteria from the original annotation. **c**, Propensity of forming variable connections correlates with cell type. Comparison between the proportion of adult connectome-defined variable and non-variable connections for each cell type. Adult-defined non-variable connections include the connections that are present in both of our adult datasets as well as the original connectome annotated by White et al. 1986. Cell types with significantly higher or lower proportions of variable connections are denoted; upper panel: *** P (sensory-motor) = 5.1×10^{-5} , *** P (modulatory-motor) = 1.7×10^{-6} , *** P (inter-motor) = 7.5×10^{-5} , lower panel: *** P (sensory-muscle) = 2.6×10^{-6} , *** P (modulatory-muscle) = 9.9×10^{-9} , *** P (inter-muscle) = 4.7×10^{-4} , *** P (motor-muscle) = 2.6×10^{-6} ; two-sided Mann–Whitney U test, FDR adjusted using Benjamini–Hochberg correction. Centre line, median; box limits, upper and lower quartiles; whiskers, 1.5x interquartile range; outliers not shown. **d**, The low variability of connections from motor neurons to muscles cannot be simply explained by saturation of their physical contacts by synapses. Physical contacts are not saturated for connections for any cell type. Motor neurons, which have the lowest proportion of variable connections (Extended Data Fig. [6j](#)), are not restricted by few available potential synaptic partners. Centre line, median; box limits, upper and lower quartiles; whiskers, 1.5x interquartile range; outliers not shown. **e**, Higher variability for certain cell types is not explained by a fixed probability of an erroneous connection by neurons with abundant synapse formation. Top:

the number of synapses for stable output connections by cell types. Modulatory neurons, which exhibit a higher proportion of variable connections than other cell types (Extended Data Fig. 6j), do not exhibit more synapses per stable connection. Centre line, median; box limits, upper and lower quartiles; whiskers, 1.5x interquartile range; outliers not shown. Bottom: The number of variable connections formed by a cell does not correlate with the strength of its stable output connections. Each data point represents one cell. ns (not significant) $P = 0.08$, $r = 0.15$, $n = 139$, two-sided Spearman's rank correlation coefficient. f, Top: the relative number of synapses added to existing stable output connections by cell types. Connections from modulatory neurons, which have a higher proportion of variable connections than other cell types (Extended Data Fig. 6j), do not exhibit higher increase in synapse number than connections from other cell types. Centre line, median; box limits, upper and lower quartiles; whiskers, 1.5x interquartile range; outliers not shown. Bottom: The number of variable connections formed by a cell does not correlate with the number of synapses added to existing stable output connections from birth to adulthood. The relative number of synapses added is quantified as the fold increase of synapse number from birth (dataset 1) to adulthood (averaged of datasets 7 and 8). Each data point represents one cell. ns (not significant) $P = 0.56$, $r = 0.05$, $n = 139$, two-sided Spearman's rank correlation coefficient. For panels d–f, the synapse number for the adult brain (averaged of datasets 7 and 8) is shown.

Extended Data Table 1 Cell types in the nerve ring [Full size table](#)

Supplementary information

Supplementary Information

This file contains extended discussions, supplementary figures s1 – s2 and supplementary references.

Reporting Summary

Supplementary Table 1

Neuron types.

Supplementary Table 2

Synapse number connectivity matrices.

Supplementary Table 3

Synapse size connectivity matrices.

Supplementary Table 4

Physical contact matrices.

Supplementary Table 5

Synapses onto spine-like protrusions.

Supplementary Table 6

Connection classifications.

Supplementary Table 7

Module assignments.

Supplementary Video 1

Fly-through of an adult EM dataset.

Supplementary Video 2

Volumetric reconstruction of an adult dataset.

Supplementary Video 3

Individual neurons across maturation.

Supplementary Video 4

Modules in the adult brain.

Rights and permissions

Reprints and Permissions

About this article



Check for
updates

Cite this article

Witvliet, D., Mulcahy, B., Mitchell, J.K. *et al.* Connectomes across development reveal principles of brain maturation. *Nature* **596**, 257–261 (2021). <https://doi.org/10.1038/s41586-021-03778-8>

Download citation

- Received: 21 May 2020
- Accepted: 29 June 2021
- Published: 04 August 2021
- Issue Date: 12 August 2021
- DOI: <https://doi.org/10.1038/s41586-021-03778-8>

Comments

By submitting a comment you agree to abide by our [Terms](#) and [Community Guidelines](#). If you find something abusive or that does not comply with our terms or guidelines please flag it as inappropriate.

[Access through your institution](#)

[Change institution](#)

[Buy or subscribe](#)

Advertisement

This article was downloaded by **calibre** from <https://www.nature.com/articles/s41586-021-03778-8>

| [Section menu](#) | [Main menu](#) |

- Article
- [Published: 04 August 2021](#)

Microbes exploit death-induced nutrient release by gut epithelial cells

- [Christopher J. Anderson](#) ORCID: [orcid.org/0000-0003-2600-0968^{1,2}](https://orcid.org/0000-0003-2600-0968),
- [Christopher B. Medina](#)³ na1,
- [Brady J. Barron](#) ORCID: [orcid.org/0000-0002-6938-3789³ na1](https://orcid.org/0000-0002-6938-3789),
- [Laura Karvelyte](#)¹,
- [Tania Løve Aaes](#) ORCID: [orcid.org/0000-0001-6813-8629^{1,2}](https://orcid.org/0000-0001-6813-8629),
- [Irina Lambertz](#)^{1,2},
- [Justin S. A. Perry](#) ORCID: [orcid.org/0000-0003-4063-6524⁴](https://orcid.org/0000-0003-4063-6524),
- [Parul Mehrotra](#)^{1,2},
- [Amanda Gonçalves](#)^{1,2},
- [Kelly Lemeire](#)^{1,2},
- [Gillian Blancke](#)^{1,5,6},
- [Vanessa Andries](#)^{1,5,6},
- [Farzaneh Ghazavi](#)^{1,2},
- [Arne Martens](#) ORCID: [orcid.org/0000-0002-9816-2512^{1,2}](https://orcid.org/0000-0002-9816-2512),
- [Geert van Loo](#) ORCID: [orcid.org/0000-0002-8427-4775^{1,2,6}](https://orcid.org/0000-0002-8427-4775),
- [Lars Vereecke](#)^{1,5,6},
- [Peter Vandenabeele](#)^{1,2} &
- [Kodi S. Ravichandran](#) ORCID: [orcid.org/0000-0001-9049-1410^{1,2,3}](https://orcid.org/0000-0001-9049-1410)

[Nature](#) volume **596**, pages 262–267 (2021) [Cite this article](#)

- 5569 Accesses

- 107 Altmetric
- [Metrics details](#)

Subjects

- [Bacteriology](#)
- [Cellular microbiology](#)

Abstract

Regulated cell death is an integral part of life, and has broad effects on organism development and homeostasis¹. Malfunctions within the regulated cell death process, including the clearance of dying cells, can manifest in diverse pathologies throughout various tissues including the gastrointestinal tract². A long appreciated, yet elusively defined relationship exists between cell death and gastrointestinal pathologies with an underlying microbial component^{3,4,5,6}, but the direct effect of dying mammalian cells on bacterial growth is unclear. Here we advance a concept that several Enterobacteriaceae, including patient-derived clinical isolates, have an efficient growth strategy to exploit soluble factors that are released from dying gut epithelial cells. Mammalian nutrients released after caspase-3/7-dependent apoptosis boosts the growth of multiple Enterobacteriaceae and is observed using primary mouse colonic tissue, mouse and human cell lines, several apoptotic triggers, and in conventional as well as germ-free mice *in vivo*. The mammalian cell death nutrients induce a core transcriptional response in pathogenic *Salmonella*, and we identify the pyruvate formate-lyase-encoding *pflB* gene as a key driver of bacterial colonization in three contexts: a foodborne infection model, a TNF- and A20-dependent cell death model, and a chemotherapy-induced mucositis model. These findings introduce a new layer to the complex host–pathogen interaction, in which death-induced nutrient release acts as a source of fuel for intestinal bacteria, with implications for gut inflammation and cytotoxic chemotherapy treatment.

Access options

[Subscribe to Journal](#)

Get full journal access for 1 year

\$199.00

only \$3.90 per issue

[Subscribe](#)

All prices are NET prices.

VAT will be added later in the checkout.

Tax calculation will be finalised during checkout.

Rent or Buy article

Get time limited or full article access on ReadCube.

from \$8.99

[Rent or Buy](#)

All prices are NET prices.

Additional access options:

- [Log in](#)
- [Access through your institution](#)
- [Learn about institutional subscriptions](#)

Fig. 1: Regulated mammalian cell death enhances bacterial growth.

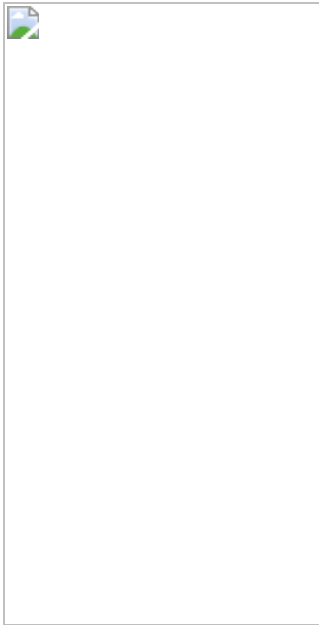


Fig. 2: Mammalian cell death nutrients promote *pflB* expression and growth in *Salmonella*.

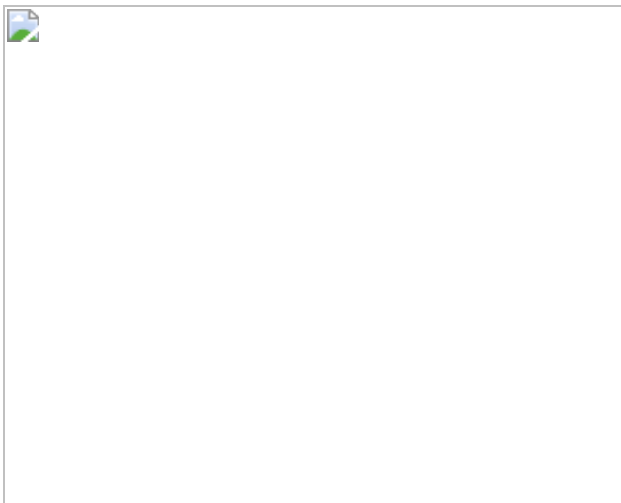


Fig. 3: PflB promotes *Salmonella* fitness during foodborne infection.

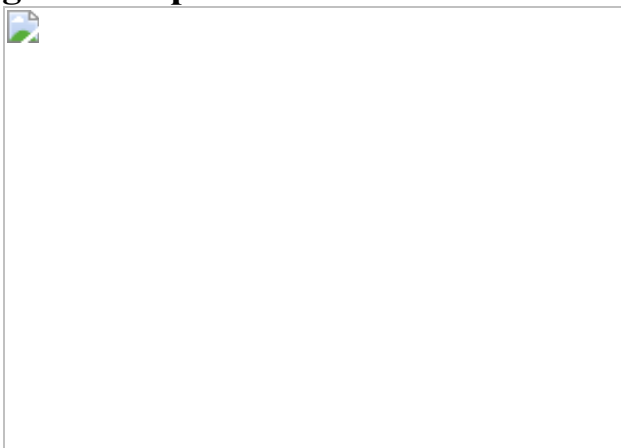
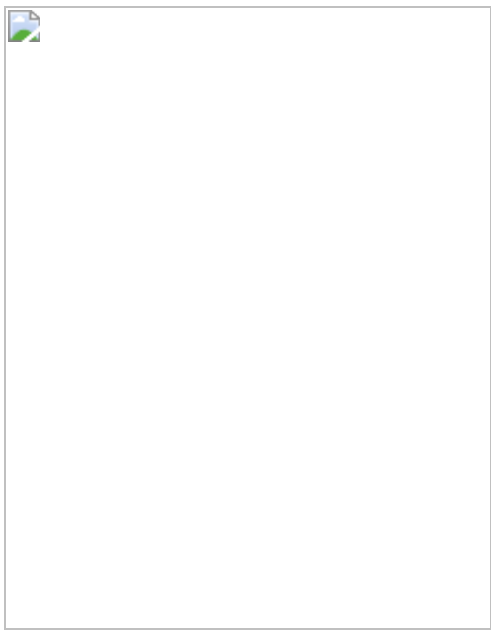


Fig. 4: Intestinal epithelial cell apoptosis fuels *Salmonella* growth in vivo.



Data availability

RNA-seq data have been submitted to the Gene Expression Omnibus (GEO) under accession number [GSE175947](#) and [GSE178167](#). Other data or unique materials generated that support the findings of this study are available from the corresponding author upon request. [Source data](#) are provided with this paper.

References

1. 1.

Boada-Romero, E., Martinez, J., Heckmann, B. L. & Green, D. R. The clearance of dead cells by efferocytosis. *Nat. Rev. Mol. Cell Biol.* **21**, 398–414 (2020).

[CAS](#) [PubMed](#) [PubMed Central](#) [Article](#) [Google Scholar](#)

2. 2.

Doran, A. C., Yurdagul, A. Jr & Tabas, I. Efferocytosis in health and disease. *Nat. Rev. Immunol.* **20**, 254–267 (2020).

[CAS](#) [PubMed](#) [Article](#) [Google Scholar](#)

3. 3.

Bäumler, A. J. & Sperandio, V. Interactions between the microbiota and pathogenic bacteria in the gut. *Nature* **535**, 85–93 (2016).

[ADS](#) [PubMed](#) [PubMed Central](#) [Article](#) [CAS](#) [Google Scholar](#)

4. 4.

Charbonneau, M. R. et al. A microbial perspective of human developmental biology. *Nature* **535**, 48–55 (2016).

[ADS](#) [CAS](#) [PubMed](#) [PubMed Central](#) [Article](#) [Google Scholar](#)

5. 5.

Storek, K. M. & Monack, D. M. Bacterial recognition pathways that lead to inflammasome activation. *Immunol. Rev.* **265**, 112–129 (2015).

[CAS](#) [PubMed](#) [PubMed Central](#) [Article](#) [Google Scholar](#)

6. 6.

Honda, K. & Littman, D. R. The microbiota in adaptive immune homeostasis and disease. *Nature* **535**, 75–84 (2016).

[ADS](#) [CAS](#) [PubMed](#) [Article](#) [Google Scholar](#)

7. 7.

Ke, F. F. S. et al. Embryogenesis and adult life in the absence of intrinsic apoptosis effectors BAX, BAK, and BOK. *Cell* **173**, 1217–1230.e17 (2018).

[CAS](#) [PubMed](#) [Article](#) [Google Scholar](#)

8. 8.

Vince, J. E. & Silke, J. The intersection of cell death and inflammasome activation. *Cell. Mol. Life Sci.* **73**, 2349–2367 (2016).

[CAS](#) [PubMed](#) [Article](#) [Google Scholar](#)

9. 9.

Schwarzer, R., Jiao, H., Wachsmuth, L., Tresch, A. & Pasparakis, M. FADD and caspase-8 regulate gut homeostasis and inflammation by controlling MLKL- and GSDMD-mediated death of intestinal epithelial cells. *Immunity* **52**, 978–993.e6 (2020).

[CAS](#) [PubMed](#) [Article](#) [Google Scholar](#)

10. 10.

Iwamoto, M., Koji, T., Makiyama, K., Kobayashi, N. & Nakane, P. K. Apoptosis of crypt epithelial cells in ulcerative colitis. *J. Pathol.* **180**, 152–159 (1996).

[CAS](#) [PubMed](#) [Article](#) [Google Scholar](#)

11. 11.

Lane, E. R., Zisman, T. L. & Suskind, D. L. The microbiota in inflammatory bowel disease: current and therapeutic insights. *J. Inflamm. Res.* **10**, 63–73 (2017).

[CAS](#) [PubMed](#) [PubMed Central](#) [Article](#) [Google Scholar](#)

12. 12.

Boussios, S., Pentheroudakis, G., Katsanos, K. & Pavlidis, N. Systemic treatment-induced gastrointestinal toxicity: incidence,

clinical presentation and management. *Ann. Gastroenterol.* **25**, 106–118 (2012).

[PubMed](#) [PubMed Central](#) [Google Scholar](#)

13. 13.

Elting, L. S. et al. The burdens of cancer therapy. Clinical and economic outcomes of chemotherapy-induced mucositis. *Cancer* **98**, 1531–1539 (2003).

[PubMed](#) [Article](#) [Google Scholar](#)

14. 14.

Shin, N. R., Whon, T. W. & Bae, J. W. Proteobacteria: microbial signature of dysbiosis in gut microbiota. *Trends Biotechnol.* **33**, 496–503 (2015).

[CAS](#) [PubMed](#) [Article](#) [Google Scholar](#)

15. 15.

Medina, C. B. et al. Metabolites released from apoptotic cells act as tissue messengers. *Nature* **580**, 130–135 (2020).

[ADS](#) [CAS](#) [PubMed](#) [PubMed Central](#) [Article](#) [Google Scholar](#)

16. 16.

Saavedra, P. H. V. et al. Apoptosis of intestinal epithelial cells restricts *Clostridium difficile* infection in a model of pseudomembranous colitis. *Nat. Commun.* **9**, 4846 (2018).

[ADS](#) [PubMed](#) [PubMed Central](#) [Article](#) [CAS](#) [Google Scholar](#)

17. 17.

Christgen, S. et al. Identification of the PANoptosome: a molecular platform triggering pyroptosis, apoptosis, and necroptosis (PANoptosis). *Front. Cell. Infect. Microbiol.* **10**, 237 (2020).

[CAS](#) [PubMed](#) [PubMed Central](#) [Article](#) [Google Scholar](#)

18. 18.

Aaes, T. L. et al. Immunodominant AH1 antigen-deficient necroptotic, but not apoptotic, murine cancer cells induce antitumor protection. *J. Immunol.* **204**, 775–787 (2020).

[CAS](#) [PubMed](#) [Article](#) [Google Scholar](#)

19. 19.

Rasko, D. A. et al. The pangenome structure of *Escherichia coli*: comparative genomic analysis of *E. coli* commensal and pathogenic isolates. *J. Bacteriol.* **190**, 6881–6893 (2008).

[CAS](#) [PubMed](#) [PubMed Central](#) [Article](#) [Google Scholar](#)

20. 20.

Hayden, M. K. et al. Prevention of colonization and infection by *Klebsiella pneumoniae* carbapenemase-producing enterobacteriaceae in long-term acute-care hospitals. *Clin. Infect. Dis.* **60**, 1153–1161 (2015).

[PubMed](#) [Article](#) [Google Scholar](#)

21. 21.

Darfeuille-Michaud, A. et al. Presence of adherent *Escherichia coli* strains in ileal mucosa of patients with Crohn's disease. *Gastroenterology* **115**, 1405–1413 (1998).

[CAS](#) [PubMed](#) [Article](#) [Google Scholar](#)

22. 22.

Cougnoux, A. et al. Bacterial genotoxin colibactin promotes colon tumour growth by inducing a senescence-associated secretory phenotype. *Gut* **63**, 1932–1942 (2014).

[CAS](#) [Article](#) [Google Scholar](#)

23. 23.

Spaulding, C. N. et al. Selective depletion of uropathogenic *E. coli* from the gut by a FimH antagonist. *Nature* **546**, 528–532 (2017).

[ADS](#) [CAS](#) [PubMed](#) [PubMed Central](#) [Article](#) [Google Scholar](#)

24. 24.

Dell, C. L., Neely, M. N. & Olson, E. R. Altered pH and lysine signalling mutants of *cadC*, a gene encoding a membrane-bound transcriptional activator of the *Escherichia coli cadBA* operon. *Mol. Microbiol.* **14**, 7–16 (1994).

[CAS](#) [PubMed](#) [Article](#) [Google Scholar](#)

25. 25.

Knappe, J. & Sawers, G. A radical-chemical route to acetyl-CoA: the anaerobically induced pyruvate formate-lyase system of *Escherichia coli*. *FEMS Microbiol. Lett.* **6**, 383–398 (1990).

[CAS](#) [Google Scholar](#)

26. 26.

Chen, J. et al. Shikonin and its analogs inhibit cancer cell glycolysis by targeting tumor pyruvate kinase-M2. *Oncogene* **30**, 4297–4306 (2011).

[CAS](#) [PubMed](#) [Article](#) [Google Scholar](#)

27. 27.

Chekeni, F. B. et al. Pannexin 1 channels mediate ‘find-me’ signal release and membrane permeability during apoptosis. *Nature* **467**, 863–867 (2010).

[ADS](#) [CAS](#) [PubMed](#) [PubMed Central](#) [Article](#) [Google Scholar](#)

28. 28.

Barthel, M. et al. Pretreatment of mice with streptomycin provides a *Salmonella enterica* serovar Typhimurium colitis model that allows analysis of both pathogen and host. *Infect. Immun.* **71**, 2839–2858 (2003).

[CAS](#) [PubMed](#) [PubMed Central](#) [Article](#) [Google Scholar](#)

29. 29.

Choi, J. & Groisman, E. A. Acidic pH sensing in the bacterial cytoplasm is required for *Salmonella* virulence. *Mol. Microbiol.* **101**, 1024–1038 (2016).

[CAS](#) [PubMed](#) [PubMed Central](#) [Article](#) [Google Scholar](#)

30. 30.

Chen, L. M., Kaniga, K. & Galán, J. E. *Salmonella* spp. are cytotoxic for cultured macrophages. *Mol. Microbiol.* **21**, 1101–1115 (1996).

[CAS](#) [PubMed](#) [Article](#) [Google Scholar](#)

31. 31.

van der Velden, A. W., Lindgren, S. W., Worley, M. J. & Heffron, F. *Salmonella* pathogenicity island 1-independent induction of apoptosis in infected macrophages by *Salmonella enterica* serotype Typhimurium. *Infect. Immun.* **68**, 5702–5709 (2000).

[PubMed](#) [PubMed Central](#) [Article](#) [Google Scholar](#)

32. 32.

Winter, S. E. et al. Gut inflammation provides a respiratory electron acceptor for *Salmonella*. *Nature* **467**, 426–429 (2010).

[ADS](#) [CAS](#) [PubMed](#) [PubMed Central](#) [Article](#) [Google Scholar](#)

33. 33.

Sellin, M. E. et al. Epithelium-intrinsic NAIP/NLRC4 inflammasome drives infected enterocyte expulsion to restrict *Salmonella* replication in the intestinal mucosa. *Cell Host Microbe* **16**, 237–248 (2014).

[CAS](#) [PubMed](#) [Article](#) [Google Scholar](#)

34. 34.

Knodler, L. A. et al. Noncanonical inflammasome activation of caspase-4/caspase-11 mediates epithelial defenses against enteric bacterial pathogens. *Cell Host Microbe* **16**, 249–256 (2014).

[CAS](#) [PubMed](#) [PubMed Central](#) [Article](#) [Google Scholar](#)

35. 35.

Lee, J.-Y. et al. High-fat diet and antibiotics cooperatively impair mitochondrial bioenergetics to trigger dysbiosis that exacerbates pre-inflammatory bowel disease. *Cell Host Microbe* **28**, 273–284.e6 (2020).

[CAS](#) [PubMed](#) [Article](#) [Google Scholar](#)

36. 36.

Goretsky, T. et al. p53 mediates TNF-induced epithelial cell apoptosis in IBD. *Am. J. Pathol.* **181**, 1306–1315 (2012).

[CAS](#) [PubMed](#) [PubMed Central](#) [Article](#) [Google Scholar](#)

37. 37.

Vereecke, L. et al. Enterocyte-specific A20 deficiency sensitizes to tumor necrosis factor-induced toxicity and experimental colitis. *J. Exp. Med.* **207**, 1513–1523 (2010).

[CAS](#) [PubMed](#) [PubMed Central](#) [Article](#) [Google Scholar](#)

38. 38.

Arnold, J. W. et al. Tumor necrosis factor- α mediates the early pathology in *Salmonella* infection of the gastrointestinal tract. *Microb. Pathog.* **14**, 217–227 (1993).

[CAS](#) [PubMed](#) [Article](#) [PubMed Central](#) [Google Scholar](#)

39. 39.

Montassier, E. et al. Chemotherapy-driven dysbiosis in the intestinal microbiome. *Aliment. Pharmacol. Ther.* **42**, 515–528 (2015).

[CAS](#) [PubMed](#) [Article](#) [PubMed Central](#) [Google Scholar](#)

40. 40.

Rigby, R. J. et al. Intestinal bacteria are necessary for doxorubicin-induced intestinal damage but not for doxorubicin-induced apoptosis. *Gut Microbes* **7**, 414–423 (2016).

[CAS](#) [PubMed](#) [PubMed Central](#) [Article](#) [Google Scholar](#)

41. 41.

Lamkanfi, M., Kalai, M., Saelens, X., Declercq, W. & Vandenebeele, P. Caspase-1 activates nuclear factor of the κ -enhancer in B cells independently of its enzymatic activity. *J. Biol. Chem.* **279**, 24785–24793 (2004).

[CAS](#) [PubMed](#) [Article](#) [Google Scholar](#)

42. 42.

Datsenko, K. A. & Wanner, B. L. One-step inactivation of chromosomal genes in *Escherichia coli* K-12 using PCR products. *Proc. Natl Acad. Sci. USA* **97**, 6640–6645 (2000).

[ADS](#) [CAS](#) [PubMed](#) [PubMed Central](#) [Article](#) [Google Scholar](#)

43. 43.

Shivak, D. J. et al. A modular, Tn7-based system for making bioluminescent or fluorescent salmonella and *Escherichia coli* strains. *Appl. Environ. Microbiol.* **82**, 4931–4943 (2016).

[ADS](#) [CAS](#) [PubMed](#) [PubMed Central](#) [Article](#) [Google Scholar](#)

44. 44.

Rivera-Chávez, F. et al. *Salmonella* uses energy taxis to benefit from intestinal inflammation. *PLoS Pathog.* **9**, e1003267 (2013).

[PubMed](#) [PubMed Central](#) [Article](#) [CAS](#) [Google Scholar](#)

45. 45.

Anderson, C. J., Clark, D. E., Adli, M. & Kendall, M. M. Ethanolamine signaling promotes *Salmonella* niche recognition and adaptation during infection. *PLoS Pathog.* **11**, e1005278 (2015).

[PubMed](#) [PubMed Central](#) [Article](#) [CAS](#) [Google Scholar](#)

46. 46.

Rowley, C. A., Anderson, C. J. & Kendall, M. M. Ethanolamine influences human commensal *Escherichia coli* growth, gene expression, and competition with enterohemorrhagic E. Coli O157:H7. *MBio* **9**, e01429-18 (2018).

[PubMed](#) [PubMed Central](#) [Article](#) [Google Scholar](#)

47. 47.

Dondelinger, Y. et al. Serine 25 phosphorylation inhibits RIPK1 kinase-dependent cell death in models of infection and inflammation. *Nat. Commun.* **10**, 1729 (2019).

[ADS](#) [PubMed](#) [PubMed Central](#) [Article](#) [CAS](#) [Google Scholar](#)

48. 48.

Poon, I. K. H. et al. Unexpected link between an antibiotic, pannexin channels and apoptosis. *Nature* **507**, 329–334 (2014).

[ADS](#) [CAS](#) [PubMed](#) [PubMed Central](#) [Article](#) [Google Scholar](#)

49. 49.

Dubois, H. et al. Nlrp3 inflammasome activation and Gasdermin D-driven pyroptosis are immunopathogenic upon gastrointestinal norovirus infection. *PLoS Pathog.* **15**, e1007709 (2019).

[CAS](#) [PubMed](#) [PubMed Central](#) [Article](#) [Google Scholar](#)

[Download references](#)

Acknowledgements

We thank members of the Ravichandran laboratory, M. Kendall and H. Agaisse for numerous discussions and input on this work and for critical reading of the manuscript. We thank H. Remaut for sharing the clinical *E. coli* isolates, A. Wullaert for *Gsdmd* knockout mice, and M. Bertrand for *Ripk1* kinase-dead mice. We thank the Germ-Free and Gnotobiotic Mouse Facility (UGent/UZ Gent/VIB), VIB Protein Core, VIB Flow Cytometry Core, VIB Bioimaging Core, and VIB Nucleomics Core for their contributions. K.S.R. is supported by FWO (Odysseus grant G0F5716N, EOS DECODE 30837538), Special Research Fund UGent (iBOF

BOF20/IBF/037), European Research Council (ERC) under the European Union's Horizon 2020 research and innovation programme (grant agreement no. 835243), grants from NHLBI (P01HL120840), NIGMS (R35GM122542) and the Center for Cell Clearance/University of Virginia School of Medicine; grants to P.V. from the FWO (EOS MODEL-IDI, FWO Grant 30826052, G.0E04.16N, G.0C76.18N, G.0B71.18N, G.0B96.20N), Methusalem (BOF16/MET_V/007), iBOF20/IBF/039 ATLANTIS, Foundation against Cancer (FAF-F/2016/865, F/2020/1505), CRIG and GIGG consortia, and VIB; grants to L.V. from Foundation against cancer (2020-091) and Ghent University (iBOF A21/TT/0612); and grants to G.V.L. from Foundation against Cancer (STK 2014-142 and STK 2018-093) and FWO (G020216N). Additional support was received through the FWO Postdoctoral Fellowship (1225421N to C.J.A., and 1227220N P.M.), NIH T32 Pharmacology Training Grant (T32GM007055 to C.B.M., and B.J.B.), and Ghent University BOF grant (01P02519 to T.L.A.).

Author information

Author notes

1. These authors contributed equally: Christopher B. Medina, Brady J. Barron

Affiliations

1. VIB-UGent Center for Inflammation Research, Ghent, Belgium

Christopher J. Anderson, Laura Karvelyte, Tania Løve Aaes, Irina Lambertz, Parul Mehrotra, Amanda Gonçalves, Kelly Lemeire, Gillian Blancke, Vanessa Andries, Farzaneh Ghazavi, Arne Martens, Geert van Loo, Lars Vereecke, Peter Vandenebeele & Kodi S. Ravichandran

2. Department of Biomedical Molecular Biology, Ghent University, Ghent, Belgium

Christopher J. Anderson, Tania Løve Aaes, Irina Lambertz, Parul Mehrotra, Amanda Gonçalves, Kelly Lemeire, Farzaneh Ghazavi, Arne

Martens, Geert van Loo, Peter Vandenabeele & Kodi S. Ravichandran

3. Center for Cell Clearance, Department of Microbiology, Immunology, and Cancer Biology, University of Virginia, Charlottesville, VA, USA

Christopher B. Medina, Brady J. Barron & Kodi S. Ravichandran

4. Immunology Program, Sloan Kettering Institute, Memorial Sloan Kettering Cancer Center, New York, NY, USA

Justin S. A. Perry

5. Department of Internal Medicine and Pediatrics, Ghent University, Ghent, Belgium

Gillian Blancke, Vanessa Andries & Lars Vereecke

6. Ghent Gut Inflammation Group (GGIG), Ghent University, Ghent, Belgium

Gillian Blancke, Vanessa Andries, Geert van Loo & Lars Vereecke

Authors

1. Christopher J. Anderson

[View author publications](#)

You can also search for this author in [PubMed](#) [Google Scholar](#)

2. Christopher B. Medina

[View author publications](#)

You can also search for this author in [PubMed](#) [Google Scholar](#)

3. Brady J. Barron

[View author publications](#)

You can also search for this author in [PubMed](#) [Google Scholar](#)

4. Laura Karvelyte

[View author publications](#)

You can also search for this author in [PubMed](#) [Google Scholar](#)

5. Tania Løve Aaes

[View author publications](#)

You can also search for this author in [PubMed](#) [Google Scholar](#)

6. Irina Lambertz

[View author publications](#)

You can also search for this author in [PubMed](#) [Google Scholar](#)

7. Justin S. A. Perry

[View author publications](#)

You can also search for this author in [PubMed](#) [Google Scholar](#)

8. Parul Mehrotra

[View author publications](#)

You can also search for this author in [PubMed](#) [Google Scholar](#)

9. Amanda Gonçalves

[View author publications](#)

You can also search for this author in [PubMed](#) [Google Scholar](#)

10. Kelly Lemeire

[View author publications](#)

You can also search for this author in [PubMed](#) [Google Scholar](#)

11. Gillian Blancke

[View author publications](#)

You can also search for this author in [PubMed](#) [Google Scholar](#)

12. Vanessa Andries

[View author publications](#)

You can also search for this author in [PubMed](#) [Google Scholar](#)

13. Farzaneh Ghazavi

[View author publications](#)

You can also search for this author in [PubMed](#) [Google Scholar](#)

14. Arne Martens

[View author publications](#)

You can also search for this author in [PubMed](#) [Google Scholar](#)

15. Geert van Loo

[View author publications](#)

You can also search for this author in [PubMed](#) [Google Scholar](#)

16. Lars Vereecke

[View author publications](#)

You can also search for this author in [PubMed](#) [Google Scholar](#)

17. Peter Vandenabeele

[View author publications](#)

You can also search for this author in [PubMed](#) [Google Scholar](#)

18. Kodi S. Ravichandran

[View author publications](#)

You can also search for this author in [PubMed](#) [Google Scholar](#)

Contributions

C.J.A. and K.S.R. designed all experiments. C.J.A. performed most experiments. C.B.M. and B.J.B. assisted with, and provided conceptual

advice for, multiple experiments. L.K. assisted with multiple experiments. T.L.A. assisted with immunoblotting experiments. I.L., A.G. and K.L. assisted with microscopy image acquisition and analysis. J.S.A.P. assisted with the bioinformatic analysis. P.M. provided conceptual advice for caspase-1/11 mouse experiments. G.B., V.A. and L.V. provided mice, technical assistance and conducted the germ-free mouse experiments. F.G. and P.V. provided mice and conceptual advice for caspase-3/7 mouse experiments. A.M. and G.V.L. provided mice, technical assistance, and conceptual advice for A20-deficient cell lines and mouse experiments.

Corresponding author

Correspondence to [Kodi S. Ravichandran](#).

Ethics declarations

Competing interests

The authors declare no competing interests.

Additional information

Peer review information *Nature* thanks Andreas Baumler and the other, anonymous, reviewer(s) for their contribution to the peer review of this work.

Publisher's note Springer Nature remains neutral with regard to jurisdictional claims in published maps and institutional affiliations.

Extended data figures and tables

[Extended Data Fig. 1 Primary colonocyte death ex vivo.](#)

a, C57BL/6 colonic explant stained with haematoxylin and eosin (H&E) or indicated fluorescent markers. White arrows indicate positive TUNEL

staining. Scale bars, 500 µm (H&E, TUNEL (left)) and 100 µm (TUNEL (right)). **b**, TUNEL-positive cells from C57BL/6 colonic explants quantified using automated slide scanning image analysis from paired samples. Live (DMSO-treated) or staurosporine (2 µM) samples were treated for 8 h ex vivo. $n = 4$ colonocyte explants. CD45⁺ and CD45⁺TUNEL⁺ positive cells from C57BL/6 colonic explants quantified using automated slide scanning image analysis from paired samples. Live (DMSO-treated) or staurosporine (2 µM) samples were treated for 8 h ex vivo. $n = 4$ colonocyte explants. **c**, Activated caspase-3 units (colorimetric assay) of C57BL/6 colonic explants. Live (DMSO-treated) or staurosporine (2 µM) samples were treated for 8 h ex vivo. $n = 3$ independent colonic explants. **d**, Activated caspase-8 units (colorimetric assay) of C57BL/6 colonic explants. Live (DMSO-treated) or staurosporine (2 µM) samples were treated for 8 h ex vivo. $n = 12$ independent colonic explants. **e**, Activated caspase-3 units (colorimetric assay) of C57BL/6 colonic explants. Live (water-treated) or Doxo (20 µg ml⁻¹) samples were treated for 6 h ex vivo. $n = 4$ independent colonic explants. **f**, CFU of *Salmonella* after 9 h of aerobic growth in fresh medium + 20 µg ml⁻¹ Doxo or C57BL/6 colonic explant supernatant following 20 µg ml⁻¹ Doxo treatment ex vivo. $n = 3$. Median is shown **g**, CFU of *Salmonella* and *E. coli* (strain HS) after 9 h of aerobic growth in medium with or without Doxo. $n = 4$. Box plots are as in Fig. 1. Data are mean and s.d. * $P \leq 0.05$, *** $P \leq 0.0005$, two-tailed paired *t*-test (**b–e**), unpaired two-tailed Student's *t*-test (**f**) or two-way ANOVA with Tukey's multiple comparisons test (**g**)

[Source data](#).

Extended Data Fig. 2 Death triggers induce varying degrees of mammalian cell death.

a, Cartoon schematic of in vitro cell line approach. **b**, Schematic of the CT26:FADD system. Doxycycline is used to induce expression of the construct, while addition of B/B induces oligomerization of the FKBP12 domains. Oligomerization leads to caspase activation and subsequent apoptosis. Cell death was measured using flow cytometry 5 h after B/B addition with or without QVD treatment. Membrane integrity was measured

using DNA dye Sytox blue. $n = 5$ per condition. Western blot of the indicated apoptotic caspases (left), necroptotic machinery (right, top), or pyroptotic caspase 1 (right, below). DDR3 cells were used as positive controls for necroptosis. Representative blots from $n = 3$ independent experiments. **c**, CT26 cell death, as measured by flow cytometry. CT26:FADD cell death with or without caspase inhibition via QVD (left, $n = 5$ per condition) 5 h after death induction. CT26 cell death (centre, $n = 4$) 24 h after 600 mJ cm^{-2} UV treatment. CT26 cell death (right, $n = 3$) 24 h after staurosporine treatment. CT26 cell death 24 h after 600 mJ cm^{-2} UV exposure. The DNA dye 7AAD was used to assess membrane integrity. $n = 4$ per condition. CT26 cell death 24 h after $1 \mu\text{M}$ staurosporine treatment. The DNA dye 7-AAD was used to monitor membrane integrity. $n = 3$ per condition. Western blot of the indicated apoptotic caspases (left), pyroptotic caspase 1 (right, top), or necroptotic machinery (right, bottom). DDR3 cells were used as positive controls for necroptosis. Representative blots from $n = 3$ independent experiments. **d**, Bacterial CFU after anaerobic growth in UV irradiated CT26 supernatants ($n = 4$). Data are mean \pm s.e.m. * $P \leq 0.05$, ** $P \leq 0.005$, *** $P \leq 0.0005$, **** $P \leq 0.0001$, two-way ANOVA with Tukey's multiple comparisons test (**b**), one-way ANOVA with Tukey's multiple comparisons test (**c**, left) Student's *t*-test (**c**, centre, right) or multiple two-tailed Student's *t*-tests (**d**)

[Source data](#).

[Extended Data Fig. 3 Mammalian cell death induces time-dependent bacterial outgrowth.](#)

a, CT26:FADD cells were treated overnight with doxycycline to induce construct expression and were then treated with B/B dimerizer, with or without QVD, and supernatants were collected. Periodic *Salmonella* growth measurements were quantified by OD₆₀₀ measurements. $n = 5$ per condition. **b**, *Salmonella* growth. Bacterial growth was assessed via repeated OD₆₀₀ measurements as indicated. **c**, *Salmonella* growth. Bacterial growth was assessed via CFU. Box plots are as in Fig. 1. **d**, CT26 cell death (left), as determined by flow cytometry, following 24-h treatment with 50 μM PAC-1 (apoptosis inducer) and *Salmonella* aerobic growth (right) in

those supernatants. **e**, Bacterial aerobic growth (*Salmonella* (left), *E. coli* strain HS (middle) and *Klebsiella* (right)) in CT26 cell supernatants 24 h after 600 mJ cm⁻² UV irradiation. **f**, Bacterial aerobic growth (*Salmonella* (left), *E. coli* strain HS (middle) and *Klebsiella* (right)) in CT26 cell supernatants 24 h after 1 µM staurosporine treatment. **g**, CT26 cell death (left) and *Salmonella* aerobic growth (right). CT26 cells were pre-treated for 1 h and maintained with 30 µM QVD as indicated. Data are mean ± s.e.m. *P ≤ 0.05, **P ≤ 0.005, ***P ≤ 0.0005, two-way ANOVA with Tukey's multiple comparisons test (**a**, **b**, **d–g**)

[Source data](#).

[**Extended Data Fig. 4 Apoptosis enhances bacterial growth.**](#)

a, Total cell death (left) and membrane integrity (middle) of HCT116 cells 24 h after 600 mJ cm⁻² UV irradiation. Corresponding *Salmonella* aerobic growth (right) in HCT116 supernatants as measured by OD₆₀₀ values. n = 3 per condition. **b**, Total cell death (left) and membrane integrity (middle) of HCT116 cells 24 h after 1 µM staurosporine treatment. Corresponding *Salmonella* aerobic growth (right) in HCT116 supernatants. n = 3 per condition. **c**, Jurkat cell death characterization, as measured by flow cytometry, 4 h after 150 mJ cm⁻² UV irradiation. Representative flow plot (left) and quantification of membrane integrity (middle), n = 3. Corresponding *Salmonella* aerobic CFU (right, n = 6). Box plots are as in Fig. 1. **d**, CT26 cell death after three cycles of freeze–thaw, as measured by flow cytometry. Representative flow plot (left), quantification (middle), and the corresponding *Salmonella* aerobic growth in the supernatants of freeze–thaw conditions (right, n = 4). Data are mean ± s.e.m. *P ≤ 0.05, ***P ≤ 0.0005, two-tailed Student's t-test (**a**, **b**, cell death), two-way ANOVA with Tukey's multiple comparisons test (**a**, **b**, bacterial growth curve), unpaired two-tailed Student's t-test (**c**)

[Source data](#).

[**Extended Data Fig. 5 Mammalian death-driven bacterial growth is protein-independent.**](#)

a, Schematic of supernatant manipulations after induction of apoptosis that ruled out proteins as responsible for enhanced bacterial growth. **b**, Total protein levels in media or CT26 supernatants, with or without FBS, at 24 h after staurosporine treatment following indicated proteinase K or filtration strategies as determined by BCA total protein assay. $n = 4$ per condition. **c**, CFU of *Salmonella*. $n = 3$ per filter size, 9 h of aerobic growth. Median is shown. **d**, CFU of *Salmonella*. $n = 6$ per condition, 9 h of aerobic growth. **e**, CFU of *Salmonella*. $n = 5$ per condition, 9 h of aerobic growth. **f**, CFU of *Salmonella*. $n = 5$ per condition, 9 h of aerobic growth. **g**, CFU of *Salmonella*. $n = 4$ per condition, 9 h of aerobic growth. Box plots as in Fig. 1. Data are mean \pm s.e.m. * $P \leq 0.05$, ** $P \leq 0.005$, *** $P \leq 0.0005$, multiple two-tailed Student's *t*-tests (**c**), one-way ANOVA with multiple comparisons test (**d, e**) or unpaired two-tailed Student's *t*-test (**f, g**)

[Source data](#).

Extended Data Fig. 6 RNA-seq-identified *Salmonella* gene regulation.

a, Schematic for *Salmonella* RNA-seq. Volcano plots of differentially expressed *Salmonella* genes. CT26:FADD (left) or HCT116 (UV) treatment (right). $n = 4$. Table of up and downregulated genes identified in the RNA-seq experiments described in Fig. 2 and the predicted functions and fold changes of the eight *Salmonella* genes conserved between the two independent RNA-seq experiments. Venn diagram of differentially regulated *Salmonella* genes in the two different RNA-seq experiments and the list of eight regulated genes shared between the two datasets. **b**, *Salmonella cadB* expression. $n = 3$ per condition. **c**, CFU of wild-type or $\Delta cadBA$ mutant *Salmonella* (CJA042) after 9 h of aerobic growth. $n = 4$ per condition. **d**, *E. coli* strain HS gene expression. $n = 6$ (stauro) and $n = 3$ (UV). **e**, CFU of wild-type or $\Delta pflB$ mutant *Salmonella* (CJA071) after 9 h of aerobic growth. $n = 4$ per condition., **f**, Formate concentrations in supernatants derived from live (QVD treated), staurosporine-treated, UV-irradiated, or freeze-thaw CT26 cells. $n = 4$ per condition. **g**, CT26 cell death, as measured by flow cytometry. $n = 3$ per condition. **h**, *Salmonella pflB* gene expression. $n = 4$ per condition. Box plots are as in Fig. 1. Data are mean \pm s.e.m. ns, $P > 0.05$. * $P \leq 0.05$, ** $P \leq 0.005$, *** $P \leq 0.0005$,

one-way (**b**, **f**, **h**) or two-way (**c**, **e**) ANOVA with Tukey's multiple comparisons test

[Source data](#).

Extended Data Fig. 7 Pannexin-1 dependent metabolites enhance Enterobacteriaceae growth.

a, Left, percentage annexin V staining and TO-PRO-3 dye uptake. $n = 4$. Right, WT or $\Delta pflB$ (CJA071) *Salmonella* CFU. $n = 11$ per condition. **b**, *Salmonella* CFU after 9 h of anaerobic growth. $n = 4$ per condition. MeMix-6 formulation used: spermidine (3.0 nM); FBP (5 nM); DHAP (0.36 μ M); UDG-glucose (20 nM); GMP (21 nM); IMP (3 3nM). Middle, WT or $pflB$ mutant (CJA071) CFU after 9 h of anaerobic growth Right, *Salmonella pflB* or *cadB* gene expression. $n = 4$ per condition. **c**, CFU after 9 h of anaerobic growth of wild-type with empty vector (LK010), $pflB$ mutant with empty vector (LK037), or complemented $pflB$ mutant (LK049) with or without 0.2% arabinose. $n = 5$. **d**, CFU of the indicated strain of *E. coli* after 7 h of anaerobic growth. $n = 5$. **e**, FBP concentrations. $n = 4$ per condition. Box plots are as in Fig. 1. ns, $P > 0.05$. * $P \leq 0.05$, ** $P \leq 0.005$, *** $P \leq 0.0005$, two-way ANOVA with Sidak's multiple comparisons test (**a**, **b** (right) **c**, **d**), one-way ANOVA with Dunnett's multiple comparisons test compared with medium control (**b** (left)) or one-way ANOVA with Tukey's multiple comparisons test (**e**)

[Source data](#).

Extended Data Fig. 8 *Salmonella* PflB does not affect host morbidity during foodborne infection.

a, *Salmonella* burden of WT (black) or $\Delta cadBA$ (CJA033, green). $n = 7$ mice from 2 cohorts. **b**, *Salmonella* burden of WT (black) or $\Delta pflB$ (CJA057, blue). $n = 6$ SPF mice from 2 cohorts. $n = 9$ germ-free mice from 2 cohorts. * $P \leq 0.05$, ** $P \leq 0.005$ two-tailed Wilcoxon signed rank test with theoretical median of 1 using the calculated competitive index from each mouse. **c**, Body weight (mean \pm s.e.m. is shown). $n = 15$ (WT), $n = 10$ $\Delta SPI-1\Delta SPI-2$, $n = 8$ $\Delta pflB$ mice from 4 cohorts. ns, $P > 0.05$. * $P \leq 0.05$,

*** $P \leq 0.0005$, two-way ANOVA (body weight) or one-way ANOVA (caecal weight, colon length) with Tukey's multiple comparisons test. **d**, Caecal weight. $n = 15$ (WT), $n = 10$ $\Delta\text{SPI-1}\Delta\text{SPI-2}$, $n = 8$ $\Delta p\text{fB}$ mice from 4 cohorts. ns, $P > 0.05$. * $P \leq 0.05$, *** $P \leq 0.0005$, one-way ANOVA with Tukey's multiple comparisons test. **e**, Colon length $n = 15$ (WT), $n = 10$ $\Delta\text{SPI-1}\Delta\text{SPI-2}$, $n = 8$ $\Delta p\text{fB}$ mice from 4 cohorts. ns, $P > 0.05$. * $P \leq 0.05$, *** $P \leq 0.0005$, one-way ANOVA with Tukey's multiple comparisons test. **f**, *Salmonella* burden of WT (black), $\Delta\text{SPI-1}\Delta\text{SPI-2}$ (CJA077, orange) or $\Delta p\text{fB}$ (CJA057, blue). $n = 15$ WT, $n = 8$ $\Delta\text{SPI-1}\Delta\text{SPI-2}$, $n = 8$ $\Delta p\text{fB}$ from 4 cohorts. ns, $P > 0.05$. ** $P \leq 0.005$, Kruskal–Wallis with Dunn's multiple comparisons test. **g**, Competitive index either (black) WT *Salmonella* compared to $\Delta p\text{fB}$ (CJA057) or (orange) $\Delta\text{SPI-1}\Delta\text{SPI-2}$ (CJA077) compared to $\Delta\text{SPI-1}\Delta\text{SPI-2}\Delta p\text{fB}$ (CJA081). $n = 14$ mice from 4 cohorts. ns, $P > 0.05$. * $P \leq 0.05$, two-tailed Mann–Whitney *U*-test. **h**, Cleaved caspase 3 staining in colons. Scale bars, 500 μm (top), 100 μm (zoomed in box). **i**, Percentage body weight of *Casp3^{fl/fl}* control or *Vil-cre^{+/−}*–*Casp3^{fl/fl}* mice after *Salmonella* infection (as in Fig. 3). $n = 11$ female *Casp3^{fl/fl}* control mice, $n = 7$ female *Vil-cre^{+/−}*–*Casp3^{fl/fl}* mice from 3 cohorts. Data are mean \pm s.e.m. **j**, Caecal weight of *Casp3^{fl/fl}* control or *Vil-cre^{+/−}*–*Casp3^{fl/fl}* mice after *Salmonella* infection (as in Fig. 3). $n = 8$ female *Casp3^{fl/fl}* control mice, $n = 7$ female *Vil-cre^{+/−}*–*Casp3^{fl/fl}* mice from 2 cohorts. ns, $P > 0.05$, unpaired two-tailed Student's *t*-test. **k**, Colon length of *Casp3^{fl/fl}* control or *Vil-cre^{+/−}*–*Casp3^{fl/fl}* mice after *Salmonella* infection (as in Fig. 3). $n = 5$ female *Casp3^{fl/fl}* control mice, $n = 5$ female *Vil-cre^{+/−}*–*Casp3^{fl/fl}* mice from 2 cohorts. ns, $P > 0.05$, unpaired two-tailed Student's *t*-test. **l**, *Salmonella* burden in the indicated tissue of *Casp3^{fl/fl}* control or *Vil-cre^{+/−}*–*Casp3^{fl/fl}* mice at day 4 after infection. $n = 11$ female *Casp3^{fl/fl}* control mice, $n = 7$ female *Vil-cre^{+/−}*–*Casp3^{fl/fl}* mice from 3 cohorts. **m**, Competitive index of wild-type *Salmonella* compared to $\Delta p\text{fB}$ (CJA057) in the indicated tissue of *Casp3^{fl/fl}* control or *Vil-cre^{+/−}*–*Casp3^{fl/fl}* mice at day 4 after infection. $n = 8$ female *Casp3^{fl/fl}* control mice, $n = 5$ female *Vil-cre^{+/−}*–*Casp3^{fl/fl}* mice from 2 cohorts. ns, $P > 0.05$. * $P \leq 0.05$, two-tailed Mann–Whitney *U*-test with each tissue analysed separately. Box plots are as in Fig. 1. In **a** and **b**, wild-type and mutant *Salmonella* connected with dotted lines come from the same mouse. The median competitive index is listed below each tissue. ns, $P > 0.05$.

* $P \leq 0.05$, two-tailed Wilcoxon signed rank test with theoretical median of 1 using the calculated competitive index from each mouse

[Source data](#).

Extended Data Fig. 9 Pyroptotic machinery does not impact PflB-dependent fitness.

a, Schematic of the in vitro model system. **b**, Total cell death and membrane integrity of HCT116, as measured by flow cytometry, following 24 h of infection. $n = 4$. **c**, Aerobic growth of gentamicin-resistant *Salmonella* (CJA001) measured by OD₆₀₀. $n = 8$. **d**, Expression of *pflB* and *cadB*. $n = 10$. **e**, *Salmonella* burden of wild-type (black) or $\Delta pflB$ (CJA057, blue) in *Casp1/11* mice. $n = 7$ mice from 2 cohorts. Wild-type and mutant *Salmonella* connected with dotted lines come from the same mouse. The median competitive index is listed below each tissue. Box plots are as in Fig. 1. Data are mean \pm s.e.m. ns, $P > 0.05$. * $P \leq 0.05$, unpaired two-tailed Student's *t*-test (**c**, **d**), two-tailed Wilcoxon signed rank test with theoretical median of 1 using the calculated competitive index from each mouse (**e**)

[Source data](#).

Extended Data Fig. 10 TNF-induced death in A20 deficient cells.

a, Schematic of the in vitro approach. **b**, Immunoblotting for A20 protein in the control HCT116 or A20-knockout HCT116 cells. Blots are representative of $n = 3$ independent experiments. Total cell death and membrane integrity of control or A20-knockout HCT116 cells 24 h after 100 ng ml⁻¹ human TNF stimulation. $n = 3$ per condition. Total cell death of control or A20-knockout HCT116 cells 24 h after 100 ng ml⁻¹ human TNF stimulation with or without QVD. $n = 4$ per condition. Right, western blot of indicated apoptotic caspases. Blots are representative of three independent experiments. **c**, *Salmonella* CFU. $n = 9$ (no TNF), $n = 13$ (+TNF). **d**, *Salmonella pflB* gene expression. *pflB* expression was normalized to 1 in control HCT116 supernatants with and without 100 ng

ml^{-1} human TNF. $n = 7$ per condition. **e**, *Salmonella cadB* gene expression. *cadB* expression was normalized to 1 in control HCT116 supernatants with and without 100 ng ml^{-1} human TNF. $n = 7$ per condition. **f**, CFU of *E. coli* (strain HS) and *Klebsiella*. $n = 7$ per condition per strain. Box plots are as in Fig. 1. Data are mean \pm s.e.m. ns, $P > 0.05$. * $P \leq 0.05$, *** $P \leq 0.0005$, one-way ANOVA with Sidak's multiple comparisons test (**b, d, e**), one-way ANOVA with Tukey's multiple comparisons test (**c**) or unpaired two-tailed Student's *t*-test (**f**)

[Source data](#).

Extended Data Fig. 11 TNF- and A20-dependent cell death enhances Enterobacteriaceae growth.

a, Schematic of in vivo infections. **b**, Activated caspase-3 units. Day 2: $n = 4$ *A20*^{fl/fl} control mice, $n = 6$ *Vil-cre*^{+/−}*A20*^{fl/fl} mice from 2 cohorts. Day 3: $n = 4$ *A20*^{fl/fl} control mice, $n = 4$ *Vil-cre*^{+/−}*A20*^{fl/fl} mice from 2 cohorts. ns, $P > 0.05$. * $P \leq 0.05$, two-way ANOVA with Sidak's multiple comparisons test. **c**, *Salmonella* burden in the ilea. Day 2: $n = 6$ *A20*^{fl/fl} control mice, $n = 7$ *Vil-cre*^{+/−}*A20*^{fl/fl} mice from 2 cohorts. Day 3: $n = 9$ *A20*^{fl/fl} control mice, $n = 4$ *Vil-cre*^{+/−}*A20*^{fl/fl} mice from 2 cohorts. **d**, Competitive index of WT *Salmonella* vs $\Delta p\beta B$ (CJA057) in the ilea. Day 2: $n = 6$ *A20*^{fl/fl} control mice, $n = 7$ *Vil-cre*^{+/−}*A20*^{fl/fl} mice from 2 cohorts. Day 3: $n = 7$ *A20*^{fl/fl} control mice, $n = 4$ *Vil-cre*^{+/−}*A20*^{fl/fl} mice from 2 cohorts. **e**, Percentage body weight. $n = 12$ *A20*^{fl/fl} control mice. $n = 6$ *Vil-cre*^{+/−}*A20*^{fl/fl} mice from 2 cohorts. **f**, Caecal weights. $n = 12$ *A20*^{fl/fl} control mice. $n = 9$ *Vil-cre*^{+/−}*A20*^{fl/fl} mice from 2 cohorts. **g**, *Salmonella* burden. $n = 12$ *A20*^{fl/fl} mice. $n = 6$ *Vil-cre*^{+/−}*A20*^{fl/fl} mice from 2 cohorts. Each tissue was analysed separately. Box plots are as in Fig. 1. Data are mean \pm s.e.m. ns, $P > 0.05$. ** $P \leq 0.005$, *** $P \leq 0.0005$, two-tailed Mann–Whitney *U*-test (**c, d, g**), two-way ANOVA with Sidak's multiple comparisons test (**e**), unpaired two-tailed Student's *t*-test (**f**)

[Source data](#).

Extended Data Fig. 12 Doxorubicin-induced death enhances Enterobacteriaceae growth in vivo.

a, Schematic of in vivo treatment. **b**, Representative images. Colon length (cm) $n = 7$ C57BL/6 and $Casp3^{fl/fl}$ control mice, $n = 12$ C57BL/6 and $Casp3^{fl/fl}$ mice + Doxo, $n = 6$ $Vil-cre^{+/-} Casp3^{fl/fl}$ mice + Doxo from 3 cohorts. Caecal weight (g) $n = 15$ C57BL/6 and $Casp3^{fl/fl}$ control mice, $n = 25$ C57BL/6 and control $Casp3^{fl/fl}$ mice + Doxo, $n = 8$ $Vil-cre^{+/-} Casp3^{fl/fl}$ mice + Doxo from 3 cohorts. Caecal weight (g) $n = 12$ control $Panx1^{+/+}$, $n = 18$ control $Panx1^{+/+}$ + Doxo, $n = 11$ $Panx1^{-/+}$ + Doxo mice from 6 cohorts. **c**, Caecal weight. $n = 6$ C57BL/6, $n = 8$ C57BL/6 mice + Doxo from 2 cohorts. Colon length. $n = 6$ C57BL/6, $n = 8$ C57BL/6 mice + Doxo from 2 cohorts. **d**, CFU of total Enterobacteriaceae. $n = 6$ C57BL/6, $n = 8$ C57BL/6 mice + Doxo from 2 cohorts. **e**, Caecal weight. $n = 4$ C57BL/6, $n = 7$ C57BL/6 mice + Doxo from 2 cohorts. **f**, Colon length. $n = 4$ C57BL/6, $n = 7$ C57BL/6 mice + Doxo from 2 cohorts. **g**, Activated caspase-3 units in the ilea. $n = 4$ C57BL/6, $n = 7$ C57BL/6 mice + Doxo from 2 cohorts. **h**, CFU of endogenous Enterobacteriaceae CFU in the indicated tissues of uninfected C57BL/6 mice with or without Doxo treatment, 2 days after treatment. $n = 4$ female C57BL/6, $n = 7$ female C57BL/6 mice + Doxo from 2 cohorts. The endogenous Enterobacteriaceae was identified as *E. coli* via 16s rRNA sequencing on purified genomic DNA as well as MALDI–TOF (Bruker) analysis on bacterial colonies. Box plots are as in Fig. 1. * $P \leq 0.05$, ** $P \leq 0.005$, *** $P \leq 0.0005$, one-way ANOVA with Tukey's multiple comparisons test (**b**), unpaired two-tailed Student's *t*-test (**c, e–g**), two-tailed Mann–Whitney *U*-test with each tissue analysed separately (**d, h**)

[Source data.](#)

Supplementary information

Supplementary Information

This file contains Supplementary Figs 1–4, which show the uncropped gel data.

Reporting Summary

Supplementary Tables

This file contains Supplementary Tables 1-3, which list the primer sequences, bacterial strains and plasmids used in the study.

Source data

Source Data Fig. 1

Source Data Fig. 2

Source Data Fig. 3

Source Data Fig. 4

Source Data Extended Data Fig. 1

Source Data Extended Data Fig. 2

Source Data Extended Data Fig. 3

Source Data Extended Data Fig. 4

Source Data Extended Data Fig. 5

Source Data Extended Data Fig. 6

Source Data Extended Data Fig. 7

Source Data Extended Data Fig. 8

Source Data Extended Data Fig. 9

[**Source Data Extended Data Fig. 10**](#)

[**Source Data Extended Data Fig. 11**](#)

[**Source Data Extended Data Fig. 12**](#)

Rights and permissions

[Reprints and Permissions](#)

About this article



Check for
updates

Cite this article

Anderson, C.J., Medina, C.B., Barron, B.J. *et al.* Microbes exploit death-induced nutrient release by gut epithelial cells. *Nature* **596**, 262–267 (2021). <https://doi.org/10.1038/s41586-021-03785-9>

[Download citation](#)

- Received: 07 October 2020
- Accepted: 30 June 2021
- Published: 04 August 2021
- Issue Date: 12 August 2021
- DOI: <https://doi.org/10.1038/s41586-021-03785-9>

Comments

By submitting a comment you agree to abide by our [Terms](#) and [Community Guidelines](#). If you find something abusive or that does not comply with our terms or guidelines please flag it as inappropriate.

[Access through your institution](#)

[Change institution](#)

[Buy or subscribe](#)

Advertisement

This article was downloaded by **calibre** from <https://www.nature.com/articles/s41586-021-03785-9>

| [Section menu](#) | [Main menu](#) |

Immunogenicity of Ad26.COV2.S vaccine against SARS-CoV-2 variants in humans
[Download PDF](#)

- Article
- Open Access
- [Published: 09 June 2021](#)

Immunogenicity of Ad26.COV2.S vaccine against SARS-CoV-2 variants in humans

- [Galit Alter](#) [ORCID: orcid.org/0000-0002-7680-9215](#)^{1,2 na1},
- [Jingyou Yu](#)^{1 na1},
- [Jinyan Liu](#)^{1 na1},
- [Abishek Chandrashekhar](#) [ORCID: orcid.org/0000-0001-7821-5552](#)^{1 na1},
- [Erica N. Borducchi](#)^{1 na1},
- [Lisa H. Tostanoski](#) [ORCID: orcid.org/0000-0001-9255-5684](#)^{1 na1},
- [Katherine McMahan](#)^{1 na1},
- [Catherine Jacob-Dolan](#) [ORCID: orcid.org/0000-0001-6641-0342](#)^{1,3 na1},
- [David R. Martinez](#)⁴,
- [Aiquan Chang](#)^{1,3},
- [Tochi Anioke](#)¹,
- [Michelle Lifton](#) [ORCID: orcid.org/0000-0003-0279-2198](#)¹,
- [Joseph Nkolola](#)¹,
- [Kathryn E. Stephenson](#)¹,
- [Caroline Atyeo](#)^{2,3},
- [Sally Shin](#) [ORCID: orcid.org/0000-0002-9306-2264](#)²,
- [Paul Fields](#) [ORCID: orcid.org/0000-0002-9608-6464](#)⁵,
- [Ian Kaplan](#)⁵,
- [Harlan Robins](#)⁵,
- [Fatima Amanat](#) [ORCID: orcid.org/0000-0002-8029-8227](#)⁶,
- [Florian Krammer](#) [ORCID: orcid.org/0000-0003-4121-776X](#)⁶,
- [Ralph S. Baric](#) [ORCID: orcid.org/0000-0001-6827-8701](#)⁴,
- [Mathieu Le Gars](#)⁷,
- [Jerald Sadoff](#)⁷,

- [Anne Marit de Groot⁷](#),
- [Dirk Heerwagh⁸](#),
- [Frank Struyf ORCID: orcid.org/0000-0001-9988-0260⁸](#),
- [Macaya Douoguih⁷](#),
- [Johan van Hoof⁷](#),
- [Hanneke Schuitemaker ORCID: orcid.org/0000-0001-8563-2266⁷](#) &
- [Dan H. Barouch ORCID: orcid.org/0000-0001-5127-4659^{1,2,3}](#)

[Nature](#) volume 596, pages 268–272 (2021) [Cite this article](#)

- 49k Accesses
- 1433 Altmetric
- [Metrics details](#)

Subjects

- [SARS-CoV-2](#)
- [Vaccines](#)

Abstract

The Ad26.COV2.S vaccine^{1,2,3} has demonstrated clinical efficacy against symptomatic COVID-19, including against the B.1.351 variant that is partially resistant to neutralizing antibodies¹. However, the immunogenicity of this vaccine in humans against SARS-CoV-2 variants of concern remains unclear. Here we report humoral and cellular immune responses from 20 Ad26.COV2.S vaccinated individuals from the COV1001 phase I-IIa clinical trial² against the original SARS-CoV-2 strain WA1/2020 as well as against the B.1.1.7, CAL.20C, P.1 and B.1.351 variants of concern. Ad26.COV2.S induced median pseudovirus neutralizing antibody titres that were 5.0-fold and 3.3-fold lower against the B.1.351 and P.1 variants, respectively, as compared with WA1/2020 on day 71 after vaccination. Median binding antibody titres were 2.9-fold and 2.7-fold lower against the B.1.351 and P.1 variants, respectively, as compared with WA1/2020. Antibody-dependent cellular phagocytosis, complement deposition and natural killer cell activation responses were largely preserved against the B.1.351 variant. CD8 and CD4 T cell responses, including central and effector memory responses, were comparable among the WA1/2020, B.1.1.7, B.1.351, P.1 and CAL.20C variants. These data show that neutralizing antibody responses induced by Ad26.COV2.S were reduced against the B.1.351 and P.1 variants, but functional non-neutralizing antibody responses and T cell responses were largely preserved against

SARS-CoV-2 variants. These findings have implications for vaccine protection against SARS-CoV-2 variants of concern.

[Download PDF](#)

Main

SARS-CoV-2 variants that partially escape from neutralizing antibodies to the WA1/2020 strain have emerged, including the B.1.351 variant that was first identified in South Africa^{4,5}. Such variants of concern may reduce the efficacy of current vaccines and natural immunity from SARS-CoV-2 strains that were prevalent at the beginning of the pandemic. The mRNA-1273 and BNT162b2 vaccines have been reported to induce lower neutralizing antibody titres against the B.1.351 variant than against the original WA1/2020 strain^{4,6,7}. Additional SARS-CoV-2 variants include the B.1.1.7 variant that was first identified in the UK⁸, the P.1 and P.2 variants that were first identified in Brazil⁹, and the CAL.20C variant that was first identified in California¹⁰.

Ad26.COV2.S is a replication-incompetent human adenovirus type 26 (Ad26) vector¹¹ that expresses a pre-fusion stabilized SARS-CoV-2 spike protein¹² from the Wuhan 2019 strain, which is identical to the spike protein in the WA1/2020 strain. Ad26.COV2.S demonstrated protective efficacy against SARS-CoV-2 challenges in hamsters and non-human primates^{3,13} and showed safety and immunogenicity in humans^{2,14}. In the phase III ENSEMBLE trial, a single dose of 5×10^{10} viral particles of Ad26.COV2.S resulted in 72%, 68% and 64% protection against moderate to severe COVID-19, and 86%, 88% and 82% protection against severe or critical COVID-19 in the US, Brazil and South Africa, respectively, by day 28 after vaccination¹. In this trial, 69% of sequenced viruses from confirmed COVID-19 cases in Brazil were the P.2 variant, and 95% of sequenced viruses from confirmed COVID-19 cases in South Africa were the B.1.351 variant, which demonstrates that Ad26.COV2.S provided robust protective efficacy against these SARS-CoV-2 variants.

COV1001 is a multicentre, randomized, double-blind, placebo-controlled phase I-IIa trial to evaluate safety, reactogenicity and immunogenicity of Ad26.COV2.S at 5×10^{10} or 1×10^{11} viral particles administered intramuscularly as single-shot or two-shot vaccine schedules, 56 days apart, in healthy adults (NCT04436276)¹⁴. Cohort 1b enrolled 25 adults 18–55 years of age from 29 July 2020 to 7 August 2020 at a single site at Beth Israel Deaconess Medical Center (BIDMC), Boston, Massachusetts, for exploratory immunogenicity studies². The study was approved by the BIDMC Institutional Review Board, and all participants provided written informed consent. Participants were randomly allocated to one of five experimental groups ($n = 5$ per

group): (1) 5×10^{10} viral particles of Ad26.COV2.S on days 1 and 57 (low-dose–low-dose); (2) 5×10^{10} viral particles of Ad26.COV2.S on day 1 and placebo on day 57 as a single-shot vaccine (low-dose–placebo); (3) 1×10^{11} viral particles of Ad26.COV2.S on days 1 and 57 (high-dose–high-dose); (4) 1×10^{11} viral particles of Ad26.COV2.S on day 1 and placebo on day 57 as a single-shot vaccine (high-dose–placebo); or (5) placebo on days 1 and 57 (placebo–placebo).

Antibody responses to variants

Antibody responses were assessed against the SARS-CoV-2 WA1/2020 strain as well as against B.1.351 and other variants of concern. Using a luciferase-based pseudovirus neutralizing antibody (psVNA) assay^{3,15,16}, the median psVNA titres were 169, 142, 102, 80, 60 and 51 against the WA1/2020, D614G, B.1.1.7, CAL.20C, P.1 and B.1.351 strains, respectively, on day 57 (Fig. 1a). The median psVNA titres were 340, 190, 121, 133, 102 and 67, respectively, against these variants on day 71. These data show a 3.3-fold reduction of psVNA titres against P.1 and a 5.0-fold reduction of psVNA titres against B.1.351 as compared with WA1/2020 on day 71. No psVNA titres were observed in placebo recipients. Live virus neutralizing antibody assays¹⁷ showed a greater than 10.6-fold reduction in antibody titres against B.1.351 as than against WA1/2020 on day 71 (Extended Data Fig. 1). This study was not powered to compare responses for the different vaccine doses or regimens.

Fig. 1: Neutralizing and binding antibody responses to SARS-CoV-2 variants.

 **figure1**

a, SARS-CoV-2 psVNA responses against WA1/2020, D614G, B.1.1.7, CAL.20C, P.1 and B.1.351 (**a**), RBD-specific binding antibodies by ELISA against WA1/2020, B.1.1.7, P.1 and B.1.351 (**b**) and RBD-specific and spike (S)-specific binding antibodies by ECLA against WA1/2020, B.1.1.7, P.1 and B.1.351 (Meso Scale Discovery panel 7) (**c**) on days 57 and 71. Red bars reflect median responses. Dotted lines reflect the lower limits of quantification. Filled squares denote placebo–placebo; filled circles denote high dose–placebo; open circles denote high dose–high dose; filled triangles denote low dose–placebo; and open triangles denote low dose–low dose. $n = 25$ independent samples (5 placebo recipients, 20 Ad26.COV2.S vaccine recipients).

[Full size image](#)

On day 57, median receptor binding domain (RBD)-specific binding antibody enzyme-linked immunosorbent assay (ELISA) titres were 1,772, 1,364, 486 and 392 against the WA1/2020, B.1.1.7, P.1 and B.1.351 variants, respectively (Fig. [1b](#)). On day 71, median ELISA titres were 1,962, 1,682, 714 and 683, respectively, against these variants. These data show a 1.2-, 2.7- and 2.9-fold reduction of ELISA titres against B.1.1.7, P.1 and B.1.351 RBD, respectively, as compared with WA1/2020 RBD on day 71. Minimal ELISA titres were observed in recipients that received the placebo.

An electrochemiluminescence assay (ECLA)¹⁸ was also used to evaluate spike- and RBD-specific binding antibody responses to WA1/2020, B.1.1.7, P.1 and B.1.351 (Fig. 1c). Similar to the ELISA titres, median RBD-specific ECLA responses against B.1.1.7, P.1 and B.1.351 were reduced 1.3-, 1.8- and 2.9-fold, and median spike-specific ECLA responses were reduced 1.6-, 1.8- and 2.6-fold, respectively, as compared with WA1/2020 on day 71.

Antibody Fc effector function was assessed on day 71 by systems serology¹⁹, including antibody-dependent cellular phagocytosis (ADCP), antibody-dependent neutrophil phagocytosis (ADNP), antibody-dependent complement deposition (ADCD), and antibody-dependent natural killer cell activation (ADNKA). Spike-specific ADCP, ADNP, ADCD and ADNKA responses against the B.1.351 variant were 1.5-, 2.9-, 1.6- and 1.1-fold reduced, respectively, compared with the WA1/2020 strain with the D614G mutation (Fig. 2a). Comparable IgG, IgM and IgA subclasses and Fc-receptor binding were observed across the variants, with only a slight loss in FcγR2b binding compared to the WA1/2020 strain (Fig. 2b). RBD-specific ADCP, ADNP and ADCD responses were comparable against the WA1/2020, B.1.1.7 and B.1.351 variants (Extended Data Fig. 2). These data show robust spike- and RBD-specific Fc-effector functions against these SARS-CoV-2 variants.

Fig. 2: Systems serology to SARS-CoV-2 variants.

 **figure2**

a, Spike-specific ADCP, ADNP, ADCD and ADNKA responses against WA1/2020 (D614G), B.1.1.7 and B.1.351 on day 71. Red bars reflect median responses. Dotted lines reflect median of placebo recipients. Filled circles denote high dose–placebo; open circles denote high dose–high dose; filled triangles denote low dose–placebo; and open triangles denote low dose–low dose. **b**, Nightingale plots show the median levels of WA1/2020 (D614G), B.1.1.7, B.1.351 spike-specific isotype (IgM, IgA, IgG1, IgG2 and IgG3) (red) and Fc γ R2a, Fc γ R2b and Fc γ R3a (blue) binding. $n = 20$ independent samples from Ad26.COV2.S vaccine recipients.

[Full size image](#)

Cellular immune responses to variants

Spike-specific cellular immune responses were assessed by pooled peptide ELISPOT assays in peripheral blood mononuclear cells on days 57 and 85. IFN γ ELISPOT responses were comparable to WA1/2020, B.1.351, B.1.1.7, P.1 and CAL.20C at both time points, with no evidence of decreased responses against the variants (Fig. 3a). No spike-specific ELISPOT responses were observed in vaccine recipients who received placebo. Spike-specific CD8 $^{+}$ and CD4 $^{+}$ T cell responses were evaluated by multiparameter intracellular cytokine staining (ICS) assays on days 57 and 85 (Extended Data Fig. 3). IFN γ CD8 $^{+}$ and CD4 $^{+}$ T cell responses were comparable to WA1/2020, B.1.351, B.1.1.7, P.1 and CAL.20C variants (Fig. 3b). The median ratios of B.1.351, B.1.1.7 and P.1 to WA1/2020 IFN γ CD8 $^{+}$ T cell responses were 0.98, 0.98 and 0.98, respectively, on day 57, and 0.92, 0.94 and 1.26, respectively, on day 85 (Extended Data Fig. 4). Central memory CD27 $^{+}$ CD45RA $^{-}$ and effector memory CD27 $^{-}$ CD45RA $^{-}$ CD4 $^{+}$ and CD8 $^{+}$ T cell responses were also comparable across these variants (Extended Data Figs. 5, 6). These data show that spike-specific cellular immune responses were not detectably affected by SARS-CoV-2 variants. Polyfunctional analyses showed that CD8 $^{+}$ T cells were primarily IFN γ , TNF and both IFN γ and TNF responses, whereas CD4 $^{+}$ T cells were primarily TNF; IFN γ and TNF; IL-2 and TNF; and IFN γ , IL-2 and TNF responses (Extended Data Fig. 7).

Fig. 3: Cellular immune responses to SARS-CoV-2 variants.

 **figure3**

a, Spike-specific pooled peptide IFN γ ELISPOT responses against WA1/2020, B.1.351, B.1.1.7, P.1 and CAL.20C. $n = 25$ independent samples (5 placebo recipients, 20 Ad26.COV2.S vaccine recipients). PBMC, peripheral blood mononuclear cells. **b**, Spike-specific pooled peptide IFN γ CD4 $^{+}$ and CD8 $^{+}$ T cell responses by ICS assays

against WA1/2020, B.1.351, B.1.1.7, P.1 and CAL.20C. SFC, spot-forming cells. Responses are shown on days 57 and 85. Red bars reflect median responses. Dotted lines reflect lower limits of quantification. Filled squares denote placebo–placebo; filled circles denote high dose–placebo; open circles denote high dose–high dose; filled triangles denote low dose–placebo; and open triangles denote low dose–low dose. $n = 20$ independent samples from Ad26.COV2.S vaccine recipients.

[Full size image](#)

To evaluate the specificity and breadth of individual T cell receptors (TCRs) after vaccination, TCR β sequencing²⁰ was performed to define the repertoires of 8 convalescent individuals and 19 participants receiving the vaccine and 5 receiving placebo on day 63 (Extended Data Table 1). To identify SARS-CoV-2 specific TCRs, the observed TCRs were compared to a TCR dataset that had previously been determined to be SARS-CoV-2-specific and enriched in subjects with natural infection relative to placebos²¹. The breadth (unique rearrangements) and depth (frequency of TCRs) of TCRs specific to either spike or non-spike SARS-CoV-2 proteins were determined, although these analyses may have underestimated total T cell responses. Higher breadth of spike-specific TCRs was observed in vaccine recipients compared with placebos ($P = 0.0014$, Wilcoxon rank-sum test) (Fig. 4a, Extended Data Figs. 8, 9). By contrast, the breadth of non-spike TCRs was comparable in vaccine recipients and controls, as expected because the vaccine did not contain any non-spike immunogens. Substantial breadth of CD8 $^{+}$ and CD4 $^{+}$ T cell responses was also observed (Fig. 4b).

Fig. 4: TCR β repertoire analysis.



a, Spike and non-spike T cell breadth by TCR β sequencing on day 63. *P* values were determined by two-sided Wilcoxon rank-sum tests. Red bars reflect median responses.

b, Breadth of spike-specific CD8 $^{+}$ and CD4 $^{+}$ T cell responses. Filled squares denote placebo–placebo; filled circles denote high dose–placebo; open circles denote high dose–high dose; filled triangles denote low dose–placebo; open triangles denote low dose–low dose; and plus signs denote convalescent samples. In the box-and-whisker plots, the middle line reflects the median, the box reflects the 25th–75th percentiles and the whiskers extend the full range up to 1.5 \times the interquartile range, with outlier points marked individually. $n = 32$ independent samples (8 SARS-CoV-2 convalescent individuals, 5 placebo recipients, 19 Ad26.COV2.S vaccine recipients).

[Full size image](#)

Discussion

SARS-CoV-2 variants have emerged with several mutations in targets of neutralizing antibodies, such as the E484K mutation. Median pseudovirus neutralizing antibody titres induced by Ad26.COV2.S were 5.0-fold lower against the B.1.351 variant and 3.3-fold lower against the P.1 variant as compared with the original WA1/2020 strain, which is a comparable reduction of psVNA titres that has been reported for other vaccines^{4,6,7}. By contrast, functional non-neutralizing antibody responses and CD8⁺ and CD4⁺ T cell responses were largely preserved against SARS-CoV-2 variants of concern.

In the phase III ENSEMBLE trial¹, Ad26.COV2.S was evaluated in the USA, Latin America including Brazil, and South Africa. In South Africa, 95% of sequenced viruses from COVID-19 cases were of the B.1.351 variant, and in Brazil, 69% of sequenced viruses from COVID-19 cases were of the P.2 lineage. Protective efficacy of Ad26.COV2.S against severe or critical disease was similar in all geographic locations by day 28, and protective efficacy against moderate to severe disease was only slightly reduced in South Africa compared with the USA. Although the mechanistic correlates of protection for COVID-19 are not yet known, the robust protective efficacy in these regions despite reduced neutralizing antibodies raises the possibility that functional non-neutralizing antibodies and/or CD8⁺ T cell responses may also contribute to protection. Indeed, TCR β sequencing revealed substantial breadth of T cell responses in individuals vaccinated with Ad26.COV2.S. Alternatively, it is possible that low levels of neutralizing antibodies are sufficient for protection. In a non-human primate model, adoptive transfer of purified IgG was sufficient for protection against SARS-CoV-2 if titres of psVNA exceeded a threshold of approximately 50, but CD8⁺ T cells also contributed to protection if antibody titres were subprotective^{22,23}.

In conclusion, neutralizing antibody responses elicited by Ad26.COV2.S were reduced against the B.1.351 and P.1 variants, but other functional antibody responses and T cell responses were largely preserved against these variants. The relevance of these immune parameters to mechanistic correlates of vaccine efficacy remains to be determined.

Methods

Data reporting

No statistical methods were used to predetermine sample size. The study was randomized, blinded, and placebo controlled. Investigators were blinded to allocation during experiments and outcome assessment.

Pseudovirus-based neutralization assay

The SARS-CoV-2 pseudoviruses expressing a luciferase reporter gene were generated in an approach similar to that described previously^{16,23}. In brief, the packaging plasmid psPAX2 (AIDS Resource and Reagent Program), luciferase reporter plasmid pLenti-CMV Puro-Luc (Addgene), and spike protein expressing pcDNA3.1-SARS CoV-2 SΔCT of variants were co-transfected into HEK293T cells (ATCC, mycoplasma tested) using lipofectamine 2000 (ThermoFisher). Pseudoviruses of SARS-CoV-2 variants were generated by using the WA1/2020 strain (Wuhan/WIV04/2019, GISAID accession ID: EPI_ISL_402124), D614G mutation, B.1.1.7 variant (GISAID accession ID: EPI_ISL_601443), CAL.20C (GISAID accession ID: EPI_ISL_824730), P.1 (GISAID accession ID: EPI_ISL_792683), or B.1.351 variant (GISAID accession ID: EPI_ISL_712096). The supernatants containing the pseudotype viruses were collected 48 h after transfection, and then were purified by centrifugation and filtration with a 0.45-μm filter. To determine the neutralization activity of the plasma or serum samples from participants, HEK293T-hACE2 cells were seeded in 96-well tissue culture plates at a density of 1.75×10^4 cells/well overnight. Three-fold serial dilutions of heat-inactivated serum or plasma samples were prepared and mixed with 50 μl pseudovirus. The mixture was incubated at 37 °C for 1 h before being added to HEK293T-hACE2 cells. Forty-eight hours after infection, cells were lysed in Steady-Glo Luciferase Assay (Promega) according to the manufacturer's instructions. SARS-CoV-2 neutralization titres were defined as the sample dilution at which a 50% reduction in relative light unit (RLU) was observed relative to the average of the virus control wells.

Live virus neutralization assay

Full-length SARS-CoV-2 WA1/2020, B.1.351 and B.1.1.7, viruses were designed to express nanoluciferase (nLuc) and were recovered via reverse genetics¹⁷. One day before the assay, Vero E6 USAMRID cells were plated at 20,000 cells per well in clear-bottom black-walled plates. Cells were inspected to ensure confluence on the day of assay. Serum samples were tested at a starting dilution of 1:20 and were serially diluted threefold up to nine dilution spots. Serially diluted serum samples were mixed in equal volume with diluted virus. Antibody–virus and virus-only mixtures were then incubated at 37 °C with 5% CO₂ for one hour. After incubation, serially diluted sera and virus only controls were added in duplicate to the cells at 75 plaque-forming units at 37 °C with 5% CO₂. Twenty-four hours later, the cells were lysed, and luciferase activity was measured via Nano-Glo Luciferase Assay System (Promega) according to the manufacturer specifications. Luminescence was measured by a Spectramax M3 plate reader (Molecular Devices). Virus neutralization titres were defined as the

sample dilution at which a 50% reduction in RLU was observed relative to the average of the virus control wells.

ELISA

WA1/2020, B.1.1.7 and B.1.351 RBD-specific binding antibodies were assessed by ELISA. In brief, 96-well plates were coated with $2 \mu\text{g ml}^{-1}$ RBD proteins (provided by F. Krammer) in $1\times$ DPBS and incubated at 4°C overnight. After incubation, plates were washed once with wash buffer (0.05% Tween 20 in $1\times$ DPBS) and blocked with 350 μl casein block per well for 2–3 h at room temperature. After incubation, block solution was discarded and plates were blotted dry. Serial dilutions of heat-inactivated serum diluted in casein block were added to wells and plates were incubated for 1 h at room temperature, before three further washes and a 1 h incubation with a 1:4,000 dilution of anti-human IgG HRP (Invitrogen) at room temperature in the dark. Plates were then washed three times, and 100 μl of SeraCare KPL TMB SureBlue Start solution was added to each well; plate development was halted by the addition of 100 μl SeraCare KPL TMB Stop solution per well. The absorbance at 450 nm, with a reference at 650 nm, was recorded using a VersaMax microplate reader. For each sample, ELISA endpoint titre was calculated in Graphpad Prism software, using a four-parameter logistic curve fit to calculate the reciprocal serum dilution that yields a corrected absorbance value (450–650 nm) of 0.2. The \log_{10} -transformed endpoint titres are reported.

ECLA

ECLA plates (MesoScale Discovery SARS-CoV-2 IgG N05CA-1; panel 7) were designed and produced with up to nine antigen spots in each well. The antigens included were WA1/2020, B.1.1.7, P.1 and B.1.351 S and RBD. The plates were blocked with 50 μl of blocker A (1% BSA in MilliQ water) solution for at least 30 min at room temperature shaking at 700 rpm with a digital microplate shaker. During blocking, the serum was diluted 1:5,000. The plates were then washed three times with 150 μl of the MSD kit Wash Buffer, blotted dry, and 50 μl of the diluted samples were added in duplicate to the plates and set to shake at 700 rpm at room temperature for at least 2 h. The plates were again washed three times and 50 μl of SULFO-Tagged anti-Human IgG detection antibody diluted to $1\times$ in Diluent 100 was added to each well and incubated shaking at 700 rpm at room temperature for at least 1 h. Plates were then washed three times and 150 μl of MSD GOLD Read Buffer B was added to each well and the plates were read immediately after on a MESO QuickPlex SQ 120 machine. MSD titres for each sample was reported as RLU, which were calculated as sample RLU minus the blank RLU for each spot for each sample. The limit of detection was defined as 1,000 RLU for each assay.

Systems serology

Both the biophysical and functional quality of polyclonal vaccine induced SARS-CoV-2 antibodies were profiled using systems serology¹⁹. Biophysical profiling was performed using a custom Luminex based assay where individuals bar-coded beads were coated with spike (S) or (RBD) variants by carboxy coupling. The D614G, B.1.1.7 and B.1.351 variants (provided by E. Ollman Saphire and F. Krammer) were profiled. The overall levels of IgG1, IgG2, IgG3, IgA, IgM and Fc γ R2a, Fc γ R2b, Fc γ R3a and Fc γ R3b binding were assessed. Functional profiling included the assessment of ADCP, ADNP, ADCD and ADNKA. In brief, for the ADCP, ADNP and ADCD assays, fluorescent beads (LifeTechnologies) were coupled via carboxy-coupling, and plasma was added, allowing immune complex formation, excess antibodies were washed away, followed by the addition of THP1 monocytes, primary neutrophils, or guinea pig complement, individually, respectively. The level of phagocytosis and complement deposition was assessed by flow cytometry. For ADNKA, ELISA plates were coated with antigen, followed by the addition of plasma. Excess antibodies were washed away following by the addition of primary natural killer cells. Natural killer cells were treated with Golgi Stop (BD) and brefeldin A (Sigma Aldrich) and were stained for the surface markers CD56, CD16 and CD3 and for activity markers CD107a (BD) and MIP-1b (BD). Fluorescence was determined by flow cytometry. Natural killer cells were classified as CD56 $^{+}$ CD16 $^{+}$ CD3 $^{-}$.

ELISPOT assay

ELISPOT plates were coated with mouse anti-human IFN γ monoclonal antibody from MabTech at 1 μ g per well and incubated overnight at 4 °C. Plates were washed with DPBS, and blocked with R10 medium (RPMI with 10% heat-inactivated FBS with 1% of 100× penicillin–streptomycin, 1 M HEPES, 100 mM sodium pyruvate, 200 mM l-glutamine, and 0.1% of 55 mM 2-mercaptoethanol) for 2–4 h at 37 °C. SARS-CoV-2 pooled spike peptides from WA1/2020, B.1.351, B.1.1.7, P.1 and CAL.20C (21st Century Biochemicals) were prepared and plated at a concentration of 2 μ g per well, and 100,000 cells per well were added to the plate. The peptides and cells were incubated for 15–20 h at 37 °C. All steps after this incubation were performed at room temperature. The plates were washed with ELISPOT wash buffer and incubated for 2–4 h with biotinylated mouse anti-human IFN γ monoclonal antibody from MabTech (1 μ g ml $^{-1}$). The plates were washed a second time and incubated for 2–3 h with conjugated Goat anti-biotin AP from Rockland (1.33 μ g ml $^{-1}$). The final wash was followed by the addition of Nitor-blue Tetrazolium Chloride/5-bromo-4-chloro 3' indolylphosphate p-toluidine salt (NBT/BCIP chromagen) substrate solution for 7 min. The chromagen was discarded and the plates were washed with water and dried in a dim place for 24 h. Plates were scanned and counted on a Cellular Technologies Limited Immunospot Analyzer.

ICS assay

Peripheral blood mononuclear cells (10^6 per well) were re-suspended in 100 μ l of R10 medium supplemented with CD49d monoclonal antibody (1 μ g ml $^{-1}$) and CD28 monoclonal antibody (1 μ g ml $^{-1}$). Each sample was assessed with mock (100 μ l of R10 plus 0.5% DMSO; background control), pooled S peptides from WA1/2020, B.1.351, B.1.1.7, P.1 and CAL.20C (21st Century Biochemicals) (2 μ g ml $^{-1}$), or 10 pg ml $^{-1}$ phorbol myristate acetate and 1 μ g ml $^{-1}$ ionomycin (Sigma-Aldrich) (100 μ l; positive control) and incubated at 37 °C for 1 h. After incubation, 0.25 μ l of GolgiStop and 0.25 μ l of GolgiPlug in 50 μ l of R10 was added to each well and incubated at 37 °C for 8 h and then held at 4 °C overnight. The next day, the cells were washed twice with DPBS, stained with aqua live/dead dye for 10 min and then stained with predetermined titres of monoclonal antibodies against CD279 (clone EH12.1, BB700), CD4 (clone L200, BV711), CD27 (clone M-T271, BUV563), CD8 (clone SK1, BUV805), CD45RA (clone 5H9, APC H7) for 30 min. Cells were then washed twice with 2% FBS/DPBS buffer and incubated for 15 min with 200 μ l of BD CytoFix/CytoPerm Fixation/Permeabilization solution. Cells were washed twice with 1× Perm Wash buffer (BD Perm/Wash Buffer 10× in the CytoFix/CytoPerm Fixation/Permeabilization kit diluted with MilliQ water and passed through 0.22- μ m filter) and stained with intracellularly with monoclonal antibodies against Ki67 (clone B56, BB515), IL-21 (clone 3A3-N2.1, PE), CD69 (clone TP1.55.3, ECD), IL-10 (clone JES3-9D7, PE CY7), IL-13 (clone JES10-5A2, BV421), IL-4 (clone MP4-25D2, BV605), TNF (clone Mab11, BV650), IL-17 (clone N49-653, BV750), IFN γ (clone B27; BUV395), IL-2 (clone MQ1-17H12, BUV737), IL-6 (clone MQ2-13A5, APC), CD3 (clone SP34.2, Alexa 700), for 30 min. Cells were washed twice with 1× Perm Wash buffer and fixed with 250 μ l of freshly prepared 1.5% formaldehyde. Fixed cells were transferred to 96-well round bottom plate and analysed by BD FACSymphony system. Data were analysed with FlowJo v.9.9.

T cell receptor variable beta chain sequencing

Immunosequencing of the CDR3 regions of human TCR β chains was performed using the immunoSEQ Assay (Adaptive Biotechnologies). Extracted genomic DNA was amplified in a bias-controlled multiplex PCR, followed by high-throughput sequencing. Sequences were collapsed and filtered to identify and quantitate the absolute abundance of each unique TCR β CDR3 region for further analysis as previously described²⁰. The fraction of T cells was calculated by normalizing TCR β template counts to the total amount of DNA usable for TCR sequencing, where the amount of usable DNA was determined by PCR amplification and sequencing of several reference genes that are expected to be present in all nucleated cells. TCR sequences from repertoires were mapped against a set of TCR sequences that are

known to react to SARS-CoV-2 by matching on V gene, amino acid sequence and J gene. In brief, these sequences were first identified by Multiplex Identification of T-cell Receptor Antigen Specificity (MIRA)²¹. TCRs that react were further screened for enrichment in COVID-19-positive repertoires collected as part of ImmuneCODE compared to COVID-19-negative repertoires to remove TCRs that may be highly public or cross-reactive to common antigens. Individual response could be quantified by the number and/or frequency of SARS-CoV-2 TCRs seen post-vaccine. TCRs were further analysed at the level specific ORF or position within ORF based on the MIRA antigens. The breadth summary metric is calculated as the number of unique annotated rearrangements out of the total number of unique productive rearrangements, while depth summary metric corresponds to the sum frequency of those rearrangements in the repertoire. Sequences of known variants were obtained from GISAID (www.gisaid.org) and aligned to known MIRA antigen locations.

Reporting summary

Further information on research design is available in the [Nature Research Reporting Summary](#) linked to this paper.

Data availability

All data are available in the manuscript and Supplementary information.

References

1. 1.

Sadoff, J. et al. Safety and efficacy of single-dose Ad26.COV2.S vaccine against Covid-19. *N. Engl. J. Med.* <https://doi.org/10.1056/NEJMoa2101544> (2021).

2. 2.

Stephenson, K. E. et al. Immunogenicity of the Ad26.COV2.S Vaccine for COVID-19. *J. Am. Med. Assoc.* **325**, 1535–1544 (2021).

[CAS Article](#) [Google Scholar](#)

3. 3.

Mercado, N. B. et al. Single-shot Ad26 vaccine protects against SARS-CoV-2 in rhesus macaques. *Nature* **586**, 583–588 (2020).

[ADS](#) [CAS](#) [Article](#) [PubMed](#) [PubMed Central](#) [Google Scholar](#)

4. 4.

Wang, P. et al. Antibody resistance of SARS-CoV-2 variants B.1.351 and B.1.1.7. *Nature* **593**, 130–135 (2021).

[ADS](#) [CAS](#) [Article](#) [Google Scholar](#)

5. 5.

Wibmer, C. K. et al. SARS-CoV-2 501Y.V2 escapes neutralization by South African COVID-19 donor plasma. *Nat. Med.* **27**, 622–625 (2021).

[CAS](#) [Article](#) [Google Scholar](#)

6. 6.

Wu, K. et al. Serum neutralizing activity elicited by mRNA-1273 vaccine. *N. Engl. J. Med.* **384**, 1468–1470 (2021).

[Article](#) [Google Scholar](#)

7. 7.

Liu, Y. et al. Neutralizing activity of BNT162b2-elicited serum. *N. Engl. J. Med.* **384**, 466–468 (2021).

[Article](#) [Google Scholar](#)

8. 8.

Davies, N. G. et al. Estimated transmissibility and impact of SARS-CoV-2 lineage B.1.1.7 in England. *Science* **372**, eabg3055 (2021).

[CAS](#) [Article](#) [Google Scholar](#)

9. 9.

Voloch, C. M. et al. Genomic characterization of a novel SARS-CoV-2 lineage from Rio de Janeiro, Brazil. *J. Virol.* <https://doi.org/10.1128/JVI.00119-21> (2021).

10. 10.

Zhang, W. et al. Emergence of a novel SARS-CoV-2 variant in southern California. *J. Am. Med. Assoc.* **325**, 1324–1326 (2021).

[CAS](#) [Article](#) [Google Scholar](#)

11. 11.

Abbink, P. et al. Comparative seroprevalence and immunogenicity of six rare serotype recombinant adenovirus vaccine vectors from subgroups B and D. *J. Virol.* **81**, 4654–4663 (2007).

[CAS](#) [Article](#) [Google Scholar](#)

12. 12.

Bos, R. et al. Ad26 vector-based COVID-19 vaccine encoding a prefusion-stabilized SARS-CoV-2 spike immunogen induces potent humoral and cellular immune responses. *NPJ Vaccines* **5**, 91 (2020).

[CAS](#) [Article](#) [Google Scholar](#)

13. 13.

Tostanoski, L. H. et al. Ad26 vaccine protects against SARS-CoV-2 severe clinical disease in hamsters. *Nat. Med.* **26**, 1694–1700 (2020).

[Article](#) [Google Scholar](#)

14. 14.

Sadoff, J. et al. Interim results of a phase 1–2a trial of Ad26.COV2.S Covid-19 vaccine. *N. Engl. J. Med.* **384**, 1824–1835 (2021).

[CAS](#) [Article](#) [Google Scholar](#)

15. 15.

Chandrashekhar, A. et al. SARS-CoV-2 infection protects against rechallenge in rhesus macaques. *Science* **369**, 812–817 (2020).

[ADS](#) [CAS](#) [Article](#) [Google Scholar](#)

16. 16.

Yu, J. et al. DNA vaccine protection against SARS-CoV-2 in rhesus macaques. *Science* **369**, 806–811 (2020).

[ADS](#) [CAS](#) [Article](#) [Google Scholar](#)

17. 17.

Martinez, D. R. et al. Chimeric spike mRNA vaccines protect against sarbecovirus challenge in mice. Preprint at <https://doi.org/10.1101/2021.03.11.434872> (2021).

18. 18.

Jacob-Dolan, C. et al. Coronavirus-specific antibody cross reactivity in rhesus macaques following SARS-CoV-2 vaccination and infection. *J. Virol.* <https://doi.org/10.1128/JVI.00117-21> (2021).

19. 19.

Chung, A. W. et al. Dissecting polyclonal vaccine-induced humoral immunity against HIV using systems serology. *Cell* **163**, 988–998 (2015).

[CAS](#) [Article](#) [Google Scholar](#)

20. 20.

Robins, H. S. et al. Comprehensive assessment of T-cell receptor beta-chain diversity in $\alpha\beta$ T cells. *Blood* **114**, 4099–4107 (2009).

[CAS](#) [Article](#) [Google Scholar](#)

21. 21.

Snyder, T. M. et al. Magnitude and dynamics of the T-cell response to SARS-CoV-2 infection at both individual and population levels. Preprint at <https://doi.org/10.1101/2020.07.31.20165647> (2020).

22. 22.

McMahan, K. et al. Correlates of protection against SARS-CoV-2 in rhesus macaques. *Nature* **590**, 630–634 (2021).

[ADS](#) [CAS](#) [Article](#) [Google Scholar](#)

23. 23.

Yu, J. et al. Deletion of the SARS-CoV-2 spike cytoplasmic tail increases infectivity in pseudovirus neutralization assays. *J. Virol.* **95**, 11 (2021).

[Article](#) [Google Scholar](#)

[Download references](#)

Acknowledgements

We acknowledge support from Janssen Vaccines & Prevention BV, the Ragon Institute of MGH, MIT, the Massachusetts Consortium on Pathogen Readiness (MassCPR), the Musk Foundation, the National Institutes of Health (CA260476, AI007151, AI152296). D.R.M. is also supported by a Burroughs Wellcome Fund Postdoctoral Enrichment Program Award and a Hanna H. Gray Fellowship from the Howard Hughes Medical Institute. This project has been funded in whole or in part with federal funds from the Office of the Assistant Secretary for Preparedness and Response, Biomedical Advanced Research and Development Authority, under Other Transaction Agreement HHSO100201700018C. We thank MesoScale Discovery for providing the ECLA kits.

Author information

Author notes

1. These authors contributed equally: Galit Alter, Jingyou Yu, Jinyan Liu, Abishek Chandrashekhar, Erica N. Borducchi, Lisa H. Tostanoski, Katherine McMahan, Catherine Jacob-Dolan

Affiliations

1. Center for Virology and Vaccine Research, Beth Israel Deaconess Medical Center, Boston, MA, USA

Galit Alter, Jingyou Yu, Jinyan Liu, Abishek Chandrashekhar, Erica N. Borducchi, Lisa H. Tostanoski, Katherine McMahan, Catherine Jacob-Dolan, Aiquan Chang, Tochi Anioke, Michelle Lifton, Joseph Nkolola, Kathryn E. Stephenson & Dan H. Barouch

2. Ragon Institute of MGH, MIT and Harvard, Cambridge, MA, USA

Galit Alter, Caroline Atyeo, Sally Shin & Dan H. Barouch

3. Harvard Medical School, Boston, MA, USA

Catherine Jacob-Dolan, Aiquan Chang, Caroline Atyeo & Dan H. Barouch

4. University of North Carolina at Chapel Hill, Chapel Hill, NC, USA

David R. Martinez & Ralph S. Baric

5. Adaptive Biotechnologies, Seattle, WA, USA

Paul Fields, Ian Kaplan & Harlan Robins

6. Icahn School of Medicine at Mount Sinai, New York, NY, USA

Fatima Amanat & Florian Krammer

7. Janssen Vaccines & Prevention, Leiden, The Netherlands

Mathieu Le Gars, Jerald Sadoff, Anne Marit de Groot, Macaya Douoguih, Johan van Hoof & Hanneke Schuitemaker

8. Janssen Research & Development, Beerse, Belgium

Dirk Heerwagh & Frank Struyf

Authors

1. Galit Alter

[View author publications](#)

You can also search for this author in [PubMed](#) [Google Scholar](#)

2. Jingyou Yu

[View author publications](#)

You can also search for this author in [PubMed](#) [Google Scholar](#)

3. Jinyan Liu

[View author publications](#)

You can also search for this author in [PubMed](#) [Google Scholar](#)

4. Abishek Chandrashekhar

[View author publications](#)

You can also search for this author in [PubMed](#) [Google Scholar](#)

5. Erica N. Borducchi

[View author publications](#)

You can also search for this author in [PubMed](#) [Google Scholar](#)

6. Lisa H. Tostanoski

[View author publications](#)

You can also search for this author in [PubMed](#) [Google Scholar](#)

7. Katherine McMahan

[View author publications](#)

You can also search for this author in [PubMed](#) [Google Scholar](#)

8. Catherine Jacob-Dolan

[View author publications](#)

You can also search for this author in [PubMed](#) [Google Scholar](#)

9. David R. Martinez

[View author publications](#)

You can also search for this author in [PubMed](#) [Google Scholar](#)

10. Aiquan Chang

[View author publications](#)

You can also search for this author in [PubMed](#) [Google Scholar](#)

11. Tochi Anioke

[View author publications](#)

You can also search for this author in [PubMed](#) [Google Scholar](#)

12. Michelle Lifton

[View author publications](#)

You can also search for this author in [PubMed](#) [Google Scholar](#)

13. Joseph Nkolola

[View author publications](#)

You can also search for this author in [PubMed](#) [Google Scholar](#)

14. Kathryn E. Stephenson

[View author publications](#)

You can also search for this author in [PubMed](#) [Google Scholar](#)

15. Caroline Atyeo

[View author publications](#)

You can also search for this author in [PubMed](#) [Google Scholar](#)

16. Sally Shin

[View author publications](#)

You can also search for this author in [PubMed](#) [Google Scholar](#)

17. Paul Fields

[View author publications](#)

You can also search for this author in [PubMed](#) [Google Scholar](#)

18. Ian Kaplan

[View author publications](#)

You can also search for this author in [PubMed](#) [Google Scholar](#)

19. Harlan Robins

[View author publications](#)

You can also search for this author in [PubMed](#) [Google Scholar](#)

20. Fatima Amanat

[View author publications](#)

You can also search for this author in [PubMed](#) [Google Scholar](#)

21. Florian Krammer

[View author publications](#)

You can also search for this author in [PubMed](#) [Google Scholar](#)

22. Ralph S. Baric

[View author publications](#)

You can also search for this author in [PubMed](#) [Google Scholar](#)

23. Mathieu Le Gars

[View author publications](#)

You can also search for this author in [PubMed](#) [Google Scholar](#)

24. Jerald Sadoff

[View author publications](#)

You can also search for this author in [PubMed](#) [Google Scholar](#)

25. Anne Marit de Groot

[View author publications](#)

You can also search for this author in [PubMed](#) [Google Scholar](#)

26. Dirk Heerwagh

[View author publications](#)

You can also search for this author in [PubMed](#) [Google Scholar](#)

27. Frank Struyf

[View author publications](#)

You can also search for this author in [PubMed](#) [Google Scholar](#)

28. Macaya Douoguih

[View author publications](#)

You can also search for this author in [PubMed](#) [Google Scholar](#)

29. Johan van Hoof

[View author publications](#)

You can also search for this author in [PubMed](#) [Google Scholar](#)

30. Hanneke Schuitemaker

[View author publications](#)

You can also search for this author in [PubMed](#) [Google Scholar](#)

31. Dan H. Barouch

[View author publications](#)

You can also search for this author in [PubMed](#) [Google Scholar](#)

Contributions

J.Y., L.H.T., K.M., C.J.-D., A.C., T.A. and J.N. led the binding and pseudovirus neutralizing antibody assays. D.R.M. and R.S.B. led the live virus neutralization assays. G.A., C.A. and S.S. performed the systems serology. F.A. and F.K. produced the purified proteins. J.L., A.C., E.N.B. and M.L. performed the cellular immune assays. P.F., I.K. and H.R. led the TCR sequencing. K.E.S., M.L.G., J.S., A.M.G., D.H., F.S., M.D., J.V.H. and H.S. led the clinical study. D.H.B. coordinated the study and wrote the paper with all co-authors.

Corresponding author

Correspondence to [Dan H. Barouch](#).

Ethics declarations

Competing interests

D.H.B. is a co-inventor on related vaccine patents. M.L.G., J.S., A.M.G., D.H., F.S., M.D., J.V.H. and H.S. are employees of Janssen Pharmaceuticals and may be co-inventors on related vaccine patents. P.A.F, I.K. and H.R. are employees of Adaptive Biotechnologies. F.K. is a co-inventor on related serologic assay patents, and Mount Sinai has spun out a company, Kantaro, to market serological tests for SARS-CoV-2.

Additional information

Peer review information *Nature* thanks Antonio Bertoletti, Pei-Yong Shi and the other, anonymous, reviewer(s) for their contribution to the peer review of this work.

Publisher's note Springer Nature remains neutral with regard to jurisdictional claims in published maps and institutional affiliations.

Extended data figures and tables

[Extended Data Fig. 1 Live virus neutralizing antibody responses to SARS-CoV-2 variants.](#)

SARS-CoV-2 live virus neutralizing antibody responses against WA1/2020, B.1.1.7 and B.1.351. Red bars reflect median responses. Dotted lines reflect lower limits of quantitation. Filled squares, placebo–placebo; filled circles, high dose–placebo; open circles, high dose–high dose; filled triangles, low dose–placebo; open triangles, low dose–low dose. $n = 25$ independent samples (5 placebo recipients, 20 Ad26.COV2.S vaccine recipients).

Extended Data Fig. 2 RBD-specific functional antibody responses to SARS-CoV-2 variants.

Top, RBD-specific ADCP, ADNP and ADCD against WA1/2020 (D614G), B.1.1.7 and B.1.351. LD, low dose; HD, high dose; PL, placebo on day 71. Filled circles, high dose–placebo; open circles, high dose–high dose; filled triangles, low dose–placebo; open triangles, low dose–low dose. Bottom, RBD-specific isotype (IgG1, IgG3, IgA, IgM) (red) and Fc γ R2a, Fc γ R2b, Fc γ R3a (blue) binding against WA1/2020 (D614G), B.1.1.7, B.1.351 on day 71. $n = 20$ independent samples from Ad26.COV2.S vaccine recipients.

Extended Data Fig. 3 Representative gating for ICS assays.

Sample gating plots are shown.

Extended Data Fig. 4 Ratio of variants versus WA1/2020 CD8 $^{+}$ T cell responses.

Ratio of spike-specific pooled peptide IFN γ CD8 $^{+}$ T cell responses by ICS assays against B.1.351, B.1.1.7 and P.1 versus WA1/2020 on days 57 and 85. Red bars reflect median responses. Filled circles, high dose–placebo; open circles, high dose–high dose; filled triangles, low dose–placebo; open triangles, low dose–low dose. $n = 20$ independent samples from Ad26.COV2.S vaccine recipients.

Extended Data Fig. 5 Central and effector memory CD8 $^{+}$ T cell responses to SARS-CoV-2 variants.

Spike-specific pooled peptide IFN γ central memory CD27 $^{+}$ CD45RA $^{-}$ and effector memory CD27 $^{-}$ CD45RA $^{-}$ CD8 $^{+}$ T cell responses by ICS assays against WA1/2020, B.1.351, B.1.1.7, P.1 and CAL.20C on days 57 and 85. Red bars reflect median responses. Dotted lines reflect lower limits of quantification. Filled circles, high dose–placebo; open circles, high dose–high dose; filled triangles, low dose–placebo; open

triangles, low dose–low dose. $n = 20$ independent samples from Ad26.COV2.S vaccine recipients.

Extended Data Fig. 6 Central and effector memory CD4 $^{\pm}$ T cell responses to SARS-CoV-2 variants.

Spike-specific pooled peptide IFN γ central memory CD27 $^{+}$ CD45RA $^{-}$ and effector memory CD27 $^{-}$ CD45RA $^{-}$ CD4 $^{+}$ T cell responses by ICS assays against WA1/2020, B.1.351, B.1.1.7, P.1 and CAL.20C on days 57 and 85. Red bars reflect median responses. Dotted lines reflect lower limits of quantification. Filled circles, high dose–placebo; open circles, high dose–high dose; filled triangles, low dose–placebo; open triangles, low dose–low dose. $n = 20$ independent samples from Ad26.COV2.S vaccine recipients.

Extended Data Fig. 7 Polyfunctional CD8 $^{\pm}$ and CD4 $^{\pm}$ T cell responses.

WA1/2020 spike-specific pooled peptide monofunctional and multifunctional IFN γ , IL-2 and TNF CD8 $^{+}$ and CD4 $^{+}$ T cell responses by ICS assays on days 57 and 85. Red bars reflect median responses. Dotted lines reflect lower limits of quantification. Filled circles, high dose–placebo; open circles, high dose–high dose; filled triangles, low dose–placebo; open triangles, low dose–low dose. $n = 20$ independent samples from Ad26.COV2.S vaccine recipients.

Extended Data Fig. 8 CD8 $^{+}$ TCR β repertoire analysis.

CD8 $^{+}$ T cell breadth and depth by TCR β sequencing on day 57. Red bars reflect median responses. Filled squares, placebo–placebo; filled circles, high dose–placebo; open circles, high dose–high dose; filled triangles, low dose–placebo; open triangles, low dose–low dose; plus signs, convalescent samples. $n = 32$ independent samples (8 SARS-CoV-2 convalescent individuals, 5 placebo recipients, 19 Ad26.COV2.S vaccine recipients).

Extended Data Fig. 9 CD4 $^{+}$ TCR β repertoire analysis.

CD4 $^{+}$ T cell breadth and depth by TCR β sequencing on day 57. Red bars reflect median responses. Filled squares, placebo–placebo; filled circles, high dose–placebo; open circles, high dose–high dose; filled triangles, low dose–placebo; open triangles, low dose–low dose; plus signs, convalescent samples. $n = 32$ independent samples (8 SARS-CoV-2 convalescent individuals, 5 placebo recipients, 19 Ad26.COV2.S vaccine recipients).

Extended Data Table 1 TCR β repertoire analysis

[Full size table](#)

Supplementary information

Reporting Summary

Rights and permissions

Open Access This article is licensed under a Creative Commons Attribution 4.0 International License, which permits use, sharing, adaptation, distribution and reproduction in any medium or format, as long as you give appropriate credit to the original author(s) and the source, provide a link to the Creative Commons license, and indicate if changes were made. The images or other third party material in this article are included in the article's Creative Commons license, unless indicated otherwise in a credit line to the material. If material is not included in the article's Creative Commons license and your intended use is not permitted by statutory regulation or exceeds the permitted use, you will need to obtain permission directly from the copyright holder. To view a copy of this license, visit <http://creativecommons.org/licenses/by/4.0/>.

Reprints and Permissions

About this article



Check for
updates

Cite this article

Alter, G., Yu, J., Liu, J. *et al.* Immunogenicity of Ad26.COV2.S vaccine against SARS-CoV-2 variants in humans. *Nature* **596**, 268–272 (2021).
<https://doi.org/10.1038/s41586-021-03681-2>

Download citation

- Received: 15 April 2021
- Accepted: 01 June 2021
- Published: 09 June 2021

- Issue Date: 12 August 2021
- DOI: <https://doi.org/10.1038/s41586-021-03681-2>

Comments

By submitting a comment you agree to abide by our [Terms](#) and [Community Guidelines](#). If you find something abusive or that does not comply with our terms or guidelines please flag it as inappropriate.

[Download PDF](#)

Advertisement

This article was downloaded by **calibre** from <https://www.nature.com/articles/s41586-021-03681-2>

| [Section menu](#) | [Main menu](#) |

BNT162b2-elicited neutralization of B.1.617 and other SARS-CoV-2 variants
[Download PDF](#)

- Article
- [Published: 10 June 2021](#)

BNT162b2-elicited neutralization of B.1.617 and other SARS-CoV-2 variants

- [Jianying Liu^{1,2} ✉](#),
- [Yang Liu³ ✉](#),
- [Hongjie Xia](#) [ORCID: orcid.org/0000-0002-2520-7038³](#),
- [Jing Zou³](#),
- [Scott C. Weaver](#) [ORCID: orcid.org/0000-0001-8016-8556^{1,2,4,5,6}](#),
- [Kena A. Swanson](#) [ORCID: orcid.org/0000-0002-3389-8414⁷](#),
- [Hui Cai⁷](#),
- [Mark Cutler⁷](#),
- [David Cooper⁷](#),
- [Alexander Muik](#) [ORCID: orcid.org/0000-0003-4561-2273⁸](#),
- [Kathrin U. Jansen⁷](#),
- [Ugur Sahin⁸](#),
- [Xuping Xie](#) [ORCID: orcid.org/0000-0003-0918-016X³](#),
- [Philip R. Dormitzer](#) [ORCID: orcid.org/0000-0003-0671-6360⁷](#) &
- [Pei-Yong Shi](#) [ORCID: orcid.org/0000-0001-5553-1616^{2,3,4,5,6}](#)

[Nature](#) volume 596, pages 273–275 (2021) [Cite this article](#)

- 69k Accesses
- 4027 Altmetric
- [Metrics details](#)

Subjects

- [RNA vaccines](#)
- [SARS-CoV-2](#)

Abstract

Severe acute respiratory syndrome coronavirus 2 (SARS-CoV-2) is continuing to evolve around the world, generating new variants that are of concern on the basis of their potential for altered transmissibility, pathogenicity, and coverage by vaccines and therapeutic agents^{1,2,3,4,5}. Here we show that serum samples taken from twenty human volunteers, two or four weeks after their second dose of the BNT162b2 vaccine, neutralize engineered SARS-CoV-2 with a USA-WA1/2020 genetic background (a virus strain isolated in January 2020) and spike glycoproteins from the recently identified B.1.617.1, B.1.617.2, B.1.618 (all of which were first identified in India) or B.1.525 (first identified in Nigeria) lineages. Geometric mean plaque reduction neutralization titres against the variant viruses—particularly the B.1.617.1 variant—seemed to be lower than the titre against the USA-WA1/2020 virus, but all sera tested neutralized the variant viruses at titres of at least 1:40. The susceptibility of the variant strains to neutralization elicited by the BNT162b2 vaccine supports mass immunization as a central strategy to end the coronavirus disease 2019 (COVID-19) pandemic globally.

[Download PDF](#)

Main

Since its emergence in late 2019, SARS-CoV-2 has caused more than 174 million infections and more than 3.7 million deaths resulting from COVID-19 worldwide (as of 9 June 2021; <https://coronavirus.jhu.edu/>). Although coronaviruses have a proofreading mechanism to maintain their long genomic RNAs⁶, mutations continuously emerge in circulating viruses. Because the viral spike protein (S) binds to angiotensin-converting enzyme 2 (ACE2), the cellular receptor for virus attachment, and mediates membrane fusion during viral entry, mutations in the spike protein can alter SARS-CoV-2 transmission, tissue tropism, and disease outcome⁷. Indeed, the first prevalent spike mutation, D614G, promotes spike binding to ACE2, leading to enhanced transmission of SARS-CoV-2^{3,8,9,10,11}. Subsequently, another spike mutation, N501Y, emerged convergently in several variants that were first identified in different locations, including the UK (lineage B1.1.7), Brazil (lineage P.1), and South Africa (lineage B.1.351)². The N501Y mutation also increases the affinity of the spike for ACE2 and increases viral transmission^{12,13}. Some mutations in the spike, such as E484K, contribute to evasion of antibody neutralization. The E484K mutation has emerged independently in many variants, such as P.1, B.1.351, B.1.526 (first identified in New York), B.1.525 (first identified in Nigeria), and P3 (first identified in the Philippines)^{1,2,14}. Thus, as the COVID-19 pandemic continues, it is essential to closely

monitor the effects of new mutations or combinations of mutations on viral transmission, pathogenesis, and vaccine and therapeutic efficacies.

BNT162b2, an mRNA vaccine that expresses the full prefusion spike glycoprotein of SARS-CoV-2, is 95% effective against COVID-19¹⁵. The US Food and Drug Administration has authorized BNT162b2 for vaccination of individuals 12 years of age and older under emergency use provisions. Although the sequence of the mRNA in BNT162b2 is based on the original SARS-CoV-2 isolate¹⁶, it has previously been shown that sera from individuals immunized with BNT162b2 retained neutralizing activity against all tested variants, including the B.1.1.7, P.1, B.1.351, B.1.429, B.1.526, and B1.1.7+E484K lineages^{1,2,4,5,17}. Since then, a massive second wave of COVID-19 in India has been associated with the expansion of variant B.1.617.1 to 32 countries, B.1.617.2 to 49 countries, and B.1.618 to 6 countries (as of 31 May 2021; https://cov-lineages.org/lineages/lineage_B.1.618.html). The B.1.617.2 variant has shown evidence of particularly high transmissibility in the UK¹⁸. In addition, variant B.1.525, which was initially detected in Nigeria, has spread to 49 countries. All of these variants are currently circulating in the USA. The World Health Organization has designated the B.1.617 lineage as a variant of concern and B.1.525 as a variant of interest¹⁸. This study analyses BNT162b2-elicited neutralization against these newly identified variants.

To examine the effects of the variants' mutations on neutralization, we used a reverse genetic system to swap the complete spike gene from different variants into an early SARS-CoV-2 isolate¹⁹ (USA-WA1/2020, defined as wild-type) (Extended Data Fig. 1a). We prepared five chimeric viruses with different spike proteins, as follows: (1) B.1.525-spike (with Q52R, A67V, H69/Y70 deletion (Δ 69/70), Y145 deletion (Δ 145), E484K, D614G, Q677H, and F888L from the B.1.525 variant¹⁸); (2) B.1.617.1-spike (with G142D, E154K, L452R, E484Q, D614G, P618R, Q1071H, H1101D, and a synonymous mutation at D111 (nucleotide T21895C) from the B.1.617.1 variant); (3) B.1.617.2-spike (with T19R, G142D, L452R, T478K, D614G, P681R, and D950N from an early B.1.617.2 variant (GISAID (<https://www.gisaid.org/>) accession number EPI_ISL_1663247)); (4) B.1.617.2-v2-spike (with the mutations in B.1.617.2-spike plus an additional E156G substitution and F157–R158 deletion (Δ 157–158) found in currently circulating B.1.617.2 isolates¹⁸); and (5) B.1.618-spike (with H49Y, Y145–H146 deletion (Δ 145–146), E484K, and D614G from the B.1.618 variant²⁰). All mutant viruses yielded infectious titres of more than 10^7 plaque-forming units (PFUs) per millilitre. The B.1.617.1-spike virus formed smaller plaques than other viruses on Vero E6 cells (Extended Data Fig. 1b). All viruses were quantified for their viral RNA genome-to-PFU ratios (a parameter that indicates virus infectivity). None of the variant spikes significantly altered the viral RNA-to-PFU ratio (Extended Data Fig. 1c), suggesting that the viruses had similar specific infectivities. The complete spikes

of all viral stocks were sequenced to ensure that they contained no undesired mutations.

To compare the susceptibility of different variants to neutralization, we performed 50% plaque reduction neutralization (PRNT₅₀) testing using a panel of 20 sera collected from volunteers who were immunized with BNT162b2 in a pivotal clinical trial^{15,21}. The serum specimens were drawn two or four weeks after the second of two immunizations with 30 µg of BNT162b2, which were spaced three weeks apart (Extended Data Fig. 2). Each serum was tested simultaneously for its PRNT₅₀ against the wild-type and mutant viruses (Extended Data Table 1). All the sera neutralized the wild-type and all mutant viruses with titres of 1:40 or higher (Fig. 1). The geometric mean neutralizing titres against the wild-type, B.1.525-spike, B.1.617.1-spike, B.1.617.2-spike, B.1.617.2-v2-spike, and B.1.618-spike viruses were 502, 320, 157, 355, 343, and 331, respectively (Fig. 1). The results indicate that neutralization of all variants, except the B.1.617.1 variant, was only modestly reduced relative to neutralization of the wild-type virus. Although neutralization of B.1.617.1 was reduced more strongly, BNT162b2 immune sera efficiently neutralized the B.1.617.1 virus and all of the other viruses.

Fig. 1: Neutralization of USA-WA1/2020 and variant SARS-CoV-2 viruses by BNT162b2-induced immune sera.

 figure1

The PRNT₅₀ results for USA-WA1/2020 and variant viruses are plotted. Individual PRNT₅₀ values are presented in Extended Data Table 1. Each data point represents the geometric mean PRNT₅₀ against the indicated virus obtained with a serum sample collected two weeks (circles) or four weeks (triangles) after the second dose of vaccine. PRNT₅₀ values were determined in duplicate assays, and the geometric means were calculated ($n = 20$, pooled from two independent experiments). The heights of bars and the numbers over the bars indicate geometric mean titres; error bars show

95% confidence intervals. LOD, limit of detection at 1:40. Statistical significance (two-tailed Wilcoxon matched-pairs signed-rank test) of the difference between geometric mean titres for USA-WA1/2020 and each variant: $P = 0.002$ for B.1.525-spike, $P < 0.0001$ for B.1.617.1-spike, $P = 0.001$ for B.1.617.2-spike, $P = 0.004$ for B.1.617.2-v2-spike, $P = 0.001$ for B.1.618-spike.

[Full size image](#)

In response to the global pandemic of COVID-19, the scientific community has increased surveillance to identify mutations in circulating SARS-CoV-2 strains that might increase infectivity, enhance pathogenicity, or alter coverage by therapeutic agents or vaccines. Such information is essential to guide public policy and the development of countermeasures. As part of ongoing diligence on coverage of variants by the BNT162b2 vaccine, we have engineered variant spike genes into the backbone of the USA-WA1/2020 isolate, and, using the gold standard PRNT₅₀ assay, tested neutralization of the resulting viruses by a panel of BNT162b2-immunized human sera drawn two or four weeks after the second of two doses of BNT162b2 given three weeks apart^{4,5}. Among all tested viruses, those with spike proteins from B.1.351⁴ and B.1.617.1 (this study) exhibited the greatest reduction in neutralization by the sera, with PRNT₅₀ values 0.36 times and 0.31 times, respectively, that of USA-WA1/2020. Similarly, a recent study found that BNT162b2-induced immune sera neutralized a clinical B.1.617.1 isolate with 0.14 times the neutralization titre of the sera against the wild-type virus²². Other studies have found that BNT162b2-induced immune sera have 0.25 to 0.35 times the inhibitory titre against a pseudovirus with a B.1.617.1 spike compared to that against wild-type spike pseudovirus²³, and that BNT162b2-induced immune sera inhibit a pseudovirus with a B.1.618 spike with 0.37 times the serum inhibition titre against a wild-type spike pseudovirus²⁰. Our results showed that among the four tested variants that were first identified in India, B.1.617.1 was the least neutralized, probably owing to the presence of both L452R and E484Q substitutions at the receptor binding site (potentially under positive selection for resistance to neutralization by antibodies)^{1,14,24}. Nevertheless, all variants were still neutralized by all tested sera at titres of at least 40. The reduction in neutralization could be a combined effect of mutation-mediated escape from antibody binding and mutation-altered spike function.

A recent real-world study in participants who had received two doses of BNT162b2 demonstrated an effectiveness of 75% against any documented infection and 100% against documented severe, critical, or fatal disease caused by the variant B.1.351²⁵, which showed a similar reduction in neutralization titres to B.1.617.1. Consistent with the modest reduction in neutralization of the B.1.617.2 variants by BNT162b2-elicited sera reported here, a test-negative case-control study conducted in the UK found that the real-world effectiveness of two doses of BNT162b2 against B.1.617.2 virus was

reduced only modestly to 87.9%, compared with 93.4% effectiveness against B.1.1.7 lineage virus²⁶. Thus, reductions in neutralization such as those observed here have not been demonstrated to result in loss of vaccine efficacy against disease. BNT162b2 elicits not only neutralizing antibodies, but also spike-specific CD4⁺ and CD8⁺ T cells and non-neutralizing antibody-dependent cytotoxicity, which can also serve as immune effectors^{27,28}. Because neutralization titres do not measure all potentially protective vaccine responses, they cannot substitute for studies of vaccine efficacy and the real-world effectiveness of COVID-19 vaccines against variants.

A limitation of the current study is the potential for mutations to alter neutralization by affecting spike function rather than antigenicity, even though the variant viruses exhibited similar infectious titres and specific infectivities to the original USA-WA1/2020 isolate. In addition, we examined the effect of mutations only in the spike glycoproteins. Mutations outside the spike gene could also affect viral replication and host immune response. We also did not examine the durability of neutralization titres against the variant viruses.

New variants will continue to emerge as the pandemic persists. To date, there is no evidence that virus variants have escaped BNT162b2-mediated protection from COVID-19. Therefore, increasing the proportion of the population immunized with current safe and effective authorized vaccines remains a key strategy to minimize the emergence of new variants and end the COVID-19 pandemic.

Methods

Cells

African green monkey kidney epithelial Vero E6 cells (ATCC) were grown in Dulbecco's modified Eagle's medium (DMEM; Gibco/Thermo Fisher) with 10% fetal bovine serum (FBS; HyClone Laboratories) and 1% antibiotic/streptomycin (Gibco). The cell line was authenticated through STR profiling by ATCC and tested negative for mycoplasma.

Construction of SARS-CoV-2 s with variant spikes

All mutations from individual variant spike genes were engineered into an infectious cDNA clone of isolate USA-WA1/2020¹⁹. The spike mutations were introduced using a standard PCR-based mutagenesis method. A detailed protocol for construction of recombinant SARS-CoV-2 has previously been reported²⁹. In brief, the full-length cDNAs of viral genome containing the variant spike mutations were assembled by T4 ligase-mediated in vitro ligation. The resulting genome-length cDNAs were used as

templates to in vitro transcribe full-length viral RNAs. The in vitro transcribed full-length viral RNAs were electroporated into Vero E6 cells. When electroporated cells developed cytopathic effects (due to recombinant virus production and replication) on day 2 after electroporation, the original viral stocks (P0) were collected from the culture medium. The P0 viruses were amplified for another round on Vero E6 cells to produce the P1 stocks of viruses. The infectious titres of P1 viruses were measured by plaque assay on Vero E6 cells as previously described¹⁹. The complete sequences of spike genes from the P1 viruses were verified by Sanger sequencing to ensure that there were no undesired mutations. The P1 viruses were used for subsequent neutralization testing.

Characterization of wild-type and mutant recombinant SARS-CoV-2s

To determine the specific infectivity of each virus, we quantified the P1 stocks for their genomic RNA content and PFUs by quantitative PCR with reverse transcription (RT–qPCR) and plaque assay on Vero E6 cells, respectively. The protocols for RT–qPCR and plaque assay have previously been reported³. Genomic viral RNA-to-PFU ratios (genomes/PFU) were calculated to indicate the specific infectivity of each virus preparation.

BTN162b2 vaccine-immunized human sera

A panel of 20 serum specimens was collected from 15 BTN162b2-immunized participants in a clinical trial^{15,21}. The sera were collected two or four weeks after the second of two doses of 30 µg BNT162b2 mRNA, spaced three weeks apart (Extended Data Fig. 2). Five of the 20 participants provided sera at both two and four weeks after the second dose of vaccine, as detailed in the footnote to Extended Data Table 1.

Plaque-reduction neutralization assay

A PRNT₅₀ assay, which represents the gold standard neutralization assay, was performed to quantify serum-mediated virus suppression. Individual sera were twofold serially diluted in culture medium with a starting dilution of 1:40. The diluted sera were mixed with 100 PFU of wild-type USA-WA1/2020 or variant mutant SARS-CoV-2. After 1 h incubation at 37 °C, the serum and virus mixtures were inoculated onto 6-well plates with a monolayer of Vero E6 cells pre-seeded the previous day. The minimal serum dilution that suppressed more than 50% of viral plaques is defined as PRNT₅₀. A detailed PRNT₅₀ protocol has previously been reported^{21,30}.

Statistical analysis

Statistical analyses were performed by Graphpad Prism 9 for all experiments as detailed in the figure legends. No statistical methods were used to predetermine sample size. The experiments were not randomized and the investigators were not blinded to allocation during experiments and outcome assessment.

Reporting summary

Further information on research design is available in the [Nature Research Reporting Summary](#) linked to this paper.

Data availability

Source data for generating the main figures are available in the online version of the paper. Any other data are available upon request.

References

1. 1.

Chen, R. E. et al. Resistance of SARS-CoV-2 variants to neutralization by monoclonal and serum-derived polyclonal antibodies. *Nat. Med.* **27**, 717–726 (2021).

[CAS](#) [Article](#) [Google Scholar](#)

2. 2.

Xie, X. et al. Neutralization of SARS-CoV-2 spike 69/70 deletion, E484K and N501Y variants by BNT162b2 vaccine-elicited sera. *Nat. Med.* **27**, 620–621 (2021).

[CAS](#) [Article](#) [Google Scholar](#)

3. 3.

Plante, J. A. et al. Spike mutation D614G alters SARS-CoV-2 fitness. *Nature* **592**, 116–121 (2021).

[ADS](#) [CAS](#) [Article](#) [Google Scholar](#)

4. 4.

Liu, Y. et al. Neutralizing activity of BNT162b2-elicited serum. *N. Engl. J. Med.* **384**, 1466–1468 (2021).

[Article](#) [Google Scholar](#)

5. 5.

Liu, Y. et al. BNT162b2-elicited neutralization against new SARS-CoV-2 spike variants. *N. Engl. J. Med.* <https://doi.org/10.1056/NEJMc2106083> (2021).

6. 6.

Smith, E. C., Blanc, H., Surdel, M. C., Vignuzzi, M. & Denison, M. R. Coronaviruses lacking exoribonuclease activity are susceptible to lethal mutagenesis: evidence for proofreading and potential therapeutics. *PLoS Pathog.* **9**, e1003565 (2013).

[CAS](#) [Article](#) [Google Scholar](#)

7. 7.

Zhou, P. et al. A pneumonia outbreak associated with a new coronavirus of probable bat origin. *Nature* **579**, 270–273 (2020).

[ADS](#) [CAS](#) [Article](#) [Google Scholar](#)

8. 8.

Korber, B. et al. Tracking changes in SARS-CoV-2 spike: evidence that D614G increases infectivity of the COVID-19 virus. *Cell* **182**, 812–827.e19 (2020).

[CAS](#) [Article](#) [Google Scholar](#)

9. 9.

Yurkovetskiy, L. et al. Structural and functional analysis of the D614G SARS-CoV-2 spike protein variant. *Cell* **183**, 739–751.e8 (2020).

[CAS](#) [Article](#) [Google Scholar](#)

10. 10.

Hou, Y. J. et al. SARS-CoV-2 D614G variant exhibits efficient replication ex vivo and transmission in vivo. *Science* **370**, 1464–1468 (2020).

[ADS](#) [CAS](#) [PubMed](#) [PubMed Central](#) [Google Scholar](#)

11. 11.

Zhou, B. et al. SARS-CoV-2 spike D614G change enhances replication and transmission. *Nature* **592**, 122–127 (2021).

[ADS](#) [CAS](#) [Article](#) [Google Scholar](#)

12. 12.

Wan, Y., Shang, J., Graham, R., Baric, R. S. & Li, F. Receptor recognition by the novel coronavirus from Wuhan: an analysis based on decade-long structural studies of SARS coronavirus. *J. Virol.* **94**, e00127-20 (2020).

[PubMed](#) [PubMed Central](#) [Google Scholar](#)

13. 13.

Liu, Y. et al. The N501Y spike substitution enhances SARS-CoV-2 transmission. Preprint at <https://doi.org/10.1101/2021.03.08.434499> (2021).

14. 14.

Ku, Z. et al. Molecular determinants and mechanism for antibody cocktail preventing SARS-CoV-2 escape. *Nat. Commun.* **12**, 469 (2021).

[ADS](#) [CAS](#) [Article](#) [Google Scholar](#)

15. 15.

Polack, F. P. et al. Safety and efficacy of the BNT162b2 mRNA Covid-19 vaccine. *N. Engl. J. Med.* **383**, 2603–2615 (2020).

[CAS](#) [Article](#) [Google Scholar](#)

16. 16.

Vogel, A. B. et al. BNT162b vaccines protect rhesus macaques from SARS-CoV-2. *Nature* **592**, 283–289 (2021).

[ADS](#) [CAS](#) [Article](#) [Google Scholar](#)

17. 17.

Zou, J. et al. The effect of SARS-CoV-2 D614G mutation on BNT162b2 vaccine-elicited neutralization. *NPJ Vaccines* **6**, 44 (2021).

[CAS Article](#) [Google Scholar](#)

18. 18.

World Health Organization *Coronavirus Disease (COVID-19): Weekly Epidemiological Update* (11 May 2021)

<https://reliefweb.int/report/world/coronavirus-disease-covid-19-weekly-epidemiological-update-11-may-2021> (OCHA, 2021).

19. 19.

Xie, X. et al. An infectious cDNA clone of SARS-CoV-2. *Cell Host Microbe* **27**, 841–848.e3 (2020).

[CAS Article](#) [Google Scholar](#)

20. 20.

Tada, T. et al. The spike proteins of SARS-CoV-2 B.1.617 and B.1.618 variants identified in India provide partial resistance to vaccine-elicited and therapeutic monoclonal antibodies. Preprint at <https://doi.org/10.1101/2021.05.14.444076> (2021).

21. 21.

Walsh, E. E. et al. Safety and immunogenicity of two RNA-based Covid-19 vaccine candidates. *N. Engl. J. Med.* **383**, 2439–2450 (2020).

[CAS Article](#) [Google Scholar](#)

22. 22.

Edara, V. V. et al. Infection and vaccine-induced neutralizing antibody responses to the SARS-CoV-2 B.1.617.1 variant. Preprint at <https://doi.org/10.1101/2021.05.09.443299> (2021).

23. 23.

Hoffmann, M. et al. SARS-CoV-2 variant B.1.617 is resistant to Bamlanivimab and evades antibodies induced by infection and vaccination. Preprint at <https://doi.org/10.1101/2021.05.04.442663> (2021).

24. 24.

Tchesnokova, V. et al. Acquisition of the L452R mutation in the ACE2-binding interface of Spike protein triggers recent massive expansion of SARS-CoV-2 variants. Preprint at <https://doi.org/10.1101/2021.02.22.432189> (2021).

25. 25.

.Abu-Raddad, L. J., Chemaitelly, H. & Butt, A. A. Effectiveness of the BNT162b2 Covid-19 vaccine against the B.1.1.7 and B.1.351 variants. *N. Engl. J. Med.* <https://doi.org/10.1056/NEJMc2104974> (2021).

26. 26.

Bernal, J. L. et al. Effectiveness of COVID-19 vaccines against the B.1.617.2 variant. Preprint at <https://doi.org/10.1101/2021.05.22.21257658> (2021).

27. 27.

Tauzin, A. et al. A single BNT162b2 mRNA dose elicits antibodies with Fc-mediated effector functions and boost pre-existing humoral and T cell responses. Preprint at <https://doi.org/10.1101/2021.03.18.435972> (2021).

28. 28.

Sahin, U. et al. BNT162b2 vaccine induces neutralizing antibodies and poly-specific T cells in humans. *Nature* <https://doi.org/10.1038/s41586-021-03653-6> (2021).

29. 29.

Xie, X. et al. Engineering SARS-CoV-2 using a reverse genetic system. *Nat. Protocols* **16**, 1761–1784 (2021).

[CAS](#) [Article](#) [Google Scholar](#)

30. 30.

Muruato, A. E. et al. A high-throughput neutralizing antibody assay for COVID-19 diagnosis and vaccine evaluation. *Nat. Commun.* **11**, 4059 (2020).

[ADS](#) [CAS](#) [Article](#) [Google Scholar](#)

[Download references](#)

Acknowledgements

The study was supported by Pfizer and BioNTech. We thank the participants in Pfizer–BioNTech clinical trial C4591001, from whom the post-immunization human sera were obtained. We also thank our colleagues at Pfizer and BioNTech who developed and produced the BNT162b2 vaccine candidate.

Author information

Author notes

1. These authors contributed equally: Jianying Liu, Yang Liu

Affiliations

1. Department of Microbiology and Immunology, University of Texas Medical Branch, Galveston, TX, USA

Jianying Liu & Scott C. Weaver

2. Institute for Human Infections and Immunity, University of Texas Medical Branch, Galveston, TX, USA

Jianying Liu, Scott C. Weaver & Pei-Yong Shi

3. Department of Biochemistry and Molecular Biology, University of Texas Medical Branch, Galveston, TX, USA

Yang Liu, Hongjie Xia, Jing Zou, Xuping Xie & Pei-Yong Shi

4. Institute for Translational Sciences, University of Texas Medical Branch, Galveston, TX, USA

Scott C. Weaver & Pei-Yong Shi

5. Center for Biodefense and Emerging Infectious Diseases, University of Texas Medical Branch, Galveston, TX, USA

Scott C. Weaver & Pei-Yong Shi

6. Sealy Institute for Vaccine Sciences, University of Texas Medical Branch, Galveston, TX, USA

Scott C. Weaver & Pei-Yong Shi

7. Pfizer Vaccine Research and Development, Pearl River, NY, USA

Kena A. Swanson, Hui Cai, Mark Cutler, David Cooper, Kathrin U. Jansen & Philip R. Dormitzer

8. BioNTech, Mainz, Germany

Alexander Muik & Ugur Sahin

Authors

1. Jianying Liu

[View author publications](#)

You can also search for this author in [PubMed](#) [Google Scholar](#)

2. Yang Liu

[View author publications](#)

You can also search for this author in [PubMed](#) [Google Scholar](#)

3. Hongjie Xia

[View author publications](#)

You can also search for this author in [PubMed](#) [Google Scholar](#)

4. Jing Zou

[View author publications](#)

You can also search for this author in [PubMed](#) [Google Scholar](#)

5. Scott C. Weaver

[View author publications](#)

You can also search for this author in [PubMed](#) [Google Scholar](#)

6. Kena A. Swanson

[View author publications](#)

You can also search for this author in [PubMed](#) [Google Scholar](#)

7. Hui Cai

[View author publications](#)

You can also search for this author in [PubMed](#) [Google Scholar](#)

8. Mark Cutler

[View author publications](#)

You can also search for this author in [PubMed](#) [Google Scholar](#)

9. David Cooper

[View author publications](#)

You can also search for this author in [PubMed](#) [Google Scholar](#)

10. Alexander Muik

[View author publications](#)

You can also search for this author in [PubMed](#) [Google Scholar](#)

11. Kathrin U. Jansen

[View author publications](#)

You can also search for this author in [PubMed](#) [Google Scholar](#)

12. Ugur Sahin

[View author publications](#)

You can also search for this author in [PubMed](#) [Google Scholar](#)

13. Xuping Xie

[View author publications](#)

You can also search for this author in [PubMed](#) [Google Scholar](#)

14. Philip R. Dormitzer

[View author publications](#)

You can also search for this author in [PubMed](#) [Google Scholar](#)

15. Pei-Yong Shi

[View author publications](#)

You can also search for this author in [PubMed](#) [Google Scholar](#)

Contributions

Conceptualization: K.U.J., U.S., X.X., K.A.S., A.M., P.R.D., P.-Y.S.; methodology: J.L., Y.L., H.X., J.Z., S.C.W., K.A.S., H.C., A.M., K.U.J., U.S., X.X., P.R.D., P.-Y.S.; investigation: J.L., Y.L., H.X., J.Z., S.C.W., K.A.S., H.C., M.C., D.C., K.U.J., U.S., X.X., P.R.D., P.-Y.S.; data curation: J.L., Y.L., M.C., D.C., X.X., P.-Y.S.; writing, original draft: J.L., Y.L., U.S., X.X., P.R.D., P.-Y.S.; writing, review and editing: S.C.W., K.A.S., A.M., K.U.J., U.S., X.X., P.R.D., P.-Y.S.; supervision: K.U.J., U.S., X.X., P.R.D., P.-Y.S.; funding acquisition: K.U.J., U.S., P.R.D., P.-Y.S.

Corresponding authors

Correspondence to [Ugur Sahin](#) or [Xuping Xie](#) or [Philip R. Dormitzer](#) or [Pei-Yong Shi](#).

Ethics declarations

Competing interests

X.X. and P.-Y.S. have filed a patent on the reverse genetic system of SARS-CoV-2. K.A.S., H.C., M.C., D.C., K.U.J., and P.R.D. are employees of Pfizer and may hold stock options. A.M. and U.S. are employees of BioNTech and may hold stock options. Y.L., H.X., J.Z., X.X. and P.-Y.S. received compensation from Pfizer to perform the project.

Additional information

Peer review information *Nature* thanks the anonymous reviewers for their contribution to the peer review of this work.

Publisher's note Springer Nature remains neutral with regard to jurisdictional claims in published maps and institutional affiliations.

Extended data figures and tables

[Extended Data Fig. 1 Construction and characterization of SARS-CoV-2s with variant spikes.](#)

a, Diagram of engineered variant spike mutations. Mutations from variant spikes were engineered into isolate USA-WA1/2020. Mutations and deletions are indicated in red and by dotted lines, respectively. Nucleotide and amino acid positions are also indicated. Different regions of SARS-CoV-2 genome are indicated: L (leader sequence), ORF (open reading frame), RBD (receptor binding domain), S (spike

glycoprotein), S1 (N-terminal furin cleavage fragment of S), S2 (C-terminal furin cleavage fragment of S), E (envelope protein), M (membrane protein), N (nucleoprotein), and UTR (untranslated region). **b**, Plaque morphologies of recombinant SARS-CoV-2s. Plaque assays were performed on Vero E6 cells in six-well plates. **c**, Comparison of viral genomic RNA-to-PFU ratios ($\log_{10}[\text{RNA}/\text{PFU}]$) of recombinant SARS-CoV-2s. The genomic RNA and PFU of individual virus stocks were measured by RT-qPCR and plaque assay, respectively. The RNA/PFU ratios were calculated to determine specific infectivities. Dots represent individual biological replicates from four aliquots of viruses ($n = 4$, one experiment). Bars and error bars show means with 95% confidence intervals. A non-parametric two-tailed Mann–Whitney test was used to determine the significance of differences between USA-WA1/2020 and variant viruses. P values were adjusted using the Bonferroni correction to account for multiple comparisons. Differences were considered significant if $P < 0.05$; n.s., no statistical difference.

Extended Data Fig. 2 BNT162b2 immunization scheme and serum collection.

Twenty human sera were obtained from 15 trial participants, 2 weeks (circles) or 4 weeks (triangles) after the second dose of BNT162b2 vaccine. Five of the 15 participants provided sera at both 2 and 4 weeks after the second dose of vaccine.

Extended Data Table 1 PRNT₅₀ values of sera from BNT162b2-immunized trial participants against USA-WA1/2020 and variant SARS-CoV-2 viruses
[Full size table](#)

Supplementary information

Reporting Summary

Rights and permissions

[Reprints and Permissions](#)

About this article



Check for
updates

Cite this article

Liu, J., Liu, Y., Xia, H. *et al.* BNT162b2-elicited neutralization of B.1.617 and other SARS-CoV-2 variants. *Nature* **596**, 273–275 (2021). <https://doi.org/10.1038/s41586-021-03693-y>

[Download citation](#)

- Received: 19 May 2021
- Accepted: 04 June 2021
- Published: 10 June 2021
- Issue Date: 12 August 2021
- DOI: <https://doi.org/10.1038/s41586-021-03693-y>

Comments

By submitting a comment you agree to abide by our [Terms](#) and [Community Guidelines](#). If you find something abusive or that does not comply with our terms or guidelines please flag it as inappropriate.

[Download PDF](#)

Advertisement

This article was downloaded by **calibre** from <https://www.nature.com/articles/s41586-021-03693-y>.

Reduced sensitivity of SARS-CoV-2 variant Delta to antibody neutralization

[Download PDF](#)

- Article
- [Published: 08 July 2021](#)

Reduced sensitivity of SARS-CoV-2 variant Delta to antibody neutralization

- [Delphine Planas^{1,2},](#)
- [David Veyer^{3,4},](#)
- [Artem Baidaliuk ORCID: orcid.org/0000-0002-8351-1142⁵,](#)
- [Isabelle Staropoli¹,](#)
- [Florence Guivel-Benhassine¹,](#)
- [Maaran Michael Rajah ORCID: orcid.org/0000-0002-6674-8850^{1,6},](#)
- [Cyril Planchais⁷,](#)
- [Françoise Porrot ORCID: orcid.org/0000-0001-8995-3614¹,](#)
- [Nicolas Robillard⁴,](#)
- [Julien Puech⁴,](#)
- [Matthieu Prot⁵,](#)
- [Floriane Gallais^{8,9},](#)
- [Pierre Gantner^{8,9},](#)
- [Aurélie Velay^{8,9},](#)
- [Julien Le Guen¹⁰,](#)
- [Najiby Kassis-Chikhani¹¹,](#)
- [Dhiaeddine Edriss⁴,](#)
- [Laurent Belec⁴,](#)
- [Aymeric Seve¹²,](#)
- [Laura Courtellemont¹²,](#)
- [Hélène Pétré³,](#)
- [Laurent Hocqueloux ORCID: orcid.org/0000-0002-2264-4822¹²,](#)
- [Samira Fafi-Kremer^{8,9},](#)
- [Thierry Prazuck¹²,](#)
- [Hugo Mouquet⁷,](#)
- [Timothée Bruel ORCID: orcid.org/0000-0002-3952-4261^{1,2 na1},](#)
- [Etienne Simon-Lorière ORCID: orcid.org/0000-0001-8420-7743^{5 na1},](#)

- [Felix A. Rey](#) ORCID: [orcid.org/0000-0002-9953-7988^{13 na1}](https://orcid.org/0000-0002-9953-7988) &
- [Olivier Schwartz](#) ORCID: [orcid.org/0000-0002-0729-1475^{1,2 na1}](https://orcid.org/0000-0002-0729-1475)

[Nature](#) volume **596**, pages 276–280 (2021)[Cite this article](#)

- 289k Accesses
- 5460 Altmetric
- [Metrics details](#)

Subjects

- [Antibodies](#)
- [SARS-CoV-2](#)
- [Vaccines](#)
- [Viral immune evasion](#)

Abstract

The SARS-CoV-2 B.1.617 lineage was identified in October 2020 in India^{1,2,3,4,5}. Since then, it has become dominant in some regions of India and in the UK, and has spread to many other countries⁶. The lineage includes three main subtypes (B1.617.1, B.1.617.2 and B.1.617.3), which contain diverse mutations in the N-terminal domain (NTD) and the receptor-binding domain (RBD) of the SARS-CoV-2 spike protein that may increase the immune evasion potential of these variants. B.1.617.2—also termed the Delta variant—is believed to spread faster than other variants. Here we isolated an infectious strain of the Delta variant from an individual with COVID-19 who had returned to France from India. We examined the sensitivity of this strain to monoclonal antibodies and to antibodies present in sera from individuals who had recovered from COVID-19 (hereafter referred to as convalescent individuals) or who had received a COVID-19 vaccine, and then compared this strain with other strains of SARS-CoV-2. The Delta variant was resistant to neutralization by some anti-NTD and anti-RBD monoclonal antibodies, including bamlanivimab, and these antibodies showed impaired binding to the spike protein. Sera collected from convalescent individuals up to 12 months after the onset of symptoms were fourfold less potent against the Delta variant relative to the Alpha variant (B.1.1.7). Sera from individuals who had received one dose of the Pfizer or the AstraZeneca vaccine had a barely discernible inhibitory effect on the Delta variant. Administration of two doses of the vaccine generated a neutralizing response in 95% of individuals, with titres three- to fivefold lower against the Delta variant than against the Alpha variant. Thus, the

spread of the Delta variant is associated with an escape from antibodies that target non-RBD and RBD epitopes of the spike protein.

[Download PDF](#)

Main

The SARS-CoV-2 Delta variant (B.1.617.2) has been detected in many countries. It has become predominant in the Indian state of Maharashtra and probably other Indian regions⁴, and represented 77% of the sequenced viruses circulating in the UK between 2 June and 9 June 2021⁶. It has been classified as a variant of concern (VOC) and is believed to be 60% more transmissible than the Alpha variant (B.1.1.7). Little is known about the sensitivity of the Delta variant to the humoral immune response. Recent reports have indicated that members of the B.1.617 lineage exhibit a reduced sensitivity to certain monoclonal and polyclonal antibodies compared to the Alpha variant^{1,2,3,4,5,7,8,9}.

Isolation and characterization of the Delta variant

We isolated the Delta variant from a nasopharyngeal swab of a symptomatic individual a few days after his return to France from India. The virus was amplified by two passages on Vero E6 cells. Sequences of the swab and the outgrown virus were identical, and identified the Delta variant (GISAID accession ID: EPI_ISL_2029113) (Extended Data Fig. 1). When compared to the D614G strain (belonging to the basal B.1 lineage), which was used here as a reference, the spike protein contained eight mutations, including four mutations in the NTD (T19R, G142D, Δ156–157 and R158G), two in the RBD (L452R and T478K), one mutation close to the furin-cleavage site (P681R) and one in the S2 region (D950N) (Extended Data Fig. 1). This set of mutations was different from that observed in other members of the B.1.617 lineage and other VOCs (Extended Data Fig. 1). Viral stocks were titrated using S-Fuse reporter cells and Vero cells^{10,11}. The viral titres were similar in the two target cells and reached 10^5 – 10^6 infectious units per ml. Large syncytia expressing the spike protein were observed in cells that were infected with the Delta variant (Extended Data Fig. 2). Future work will help to determine whether Delta is more fusogenic than other variants, as suggested here by the large size of Delta-induced syncytia.

Phylogenetic analysis of the B.1.617 lineage

To contextualize the isolate of the Delta variant reported here, we inferred a global phylogeny by subsampling the diversity of SARS-CoV-2 sequences available on the

GISAID EpiCoV database (Extended Data Fig. 3). The B.1.617 lineage, which is divided into three sublineages according to the PANGO classification¹², derives from the B.1 lineage (D614G). The three sublineages show multiple changes in the spike protein, including the L452R substitution in the RBD, which has already been observed in other variants such as B.1.429, and P681R. This substitution is located in the furin-cleavage site and may enhance the fusogenic activity of the spike protein¹³. The E484Q substitution—which may be functionally similar to the antibody-escape mutation E484K that is found in the Beta and Gamma variants (B.1.351 and P.1, respectively)—is present in the B.1.617.1 and B.1.617.3 subtypes, and is likely to have reverted in the Delta sublineage, as it was present in a sequence (B.1.617) ancestral to the three sublineages¹⁴ (Extended Data Fig. 1). Whether the absence of E484Q, the presence of T478K or other changes in the spike protein or elsewhere may facilitate viral replication and transmissibility remains unknown. Notably, the B.1.617 lineage is not homogeneous, with multiple mutations that are fixed in a sublineage (for example, the spike protein mutations T19R, G142D or D950N) also being detected at lower frequencies in other sublineages. This may reflect founder effects or similar selective pressures acting on these emerging variants.

Mutational changes in the Delta variant

The locations of the spike protein mutations in the Delta variant showed a similar overall distribution to those that appeared in other VOCs. In particular, in addition to D614G, the D950N mutation mapped to the trimer interface (Extended Data Fig. 4a), suggesting that this mutation may contribute to the regulation of spike protein dynamics, as shown for the D614G mutation¹³. As with other VOCs, some mutations in the Delta variant cluster in the NTD (Extended Data Fig. 4b). The 156–157 deletion and G158R mutation in the Delta variant map to the same surface as the 144 and 241–243 deletions in the Alpha and Beta (B.1.351) variants, respectively. The T19R mutation maps to a surface patch that has several mutations in the Alpha variant. These altered residues are found in the NTD ‘supersite’ that is targeted by most anti-NTD neutralizing antibodies¹⁵. In the RBD, mutations appearing in VOCs map to the periphery of the ACE2-binding surface (Extended Data Fig. 4c), suggesting that the virus accumulates mutations there to reduce or avoid recognition by antibodies while maintaining binding to ACE2. For example, the L452R mutation found in the Delta variant impairs neutralization by antibodies¹⁶ and is located at this periphery. The only mutation within the ACE2 patch is at location 501, which increases the affinity of the RBD for ACE2 and is also involved in antibody escape¹³. The T478K mutation in the RBD is unique to the Delta variant and falls within the epitope region of potent neutralizing monoclonal antibodies categorized as ‘Class 1’¹⁷ (Extended Data Fig. 4c). This mutation is close to the E484K mutation that facilitates antibody escape¹³. These observations prompted us to analyse the neutralization potential, against the Delta

variant, of monoclonal antibodies and sera from convalescent individuals who had recovered from COVID-19 and from individuals who had been vaccinated against COVID-19.

Neutralization of Delta by antibodies

We assessed the sensitivity of the Delta variant to a panel of human monoclonal antibodies using the S-Fuse assay. We tested four clinically approved monoclonal antibodies that target the RBD^{18,19} (bamlanivimab (LY-CoV555), etesevimab (LY-CoV016), casirivimab (REGN10933) and imdevimab (REGN10987)), as well as eight anti-RBD (RBD-48, RBD-85, RBD-98 and RBD-109) and anti-NTD (NTD-18, NTD-20, NTD-69 and NTD-71) monoclonal antibodies derived from convalescent individuals (C.P. et al., manuscript in preparation). Neutralizing anti-RBD monoclonal antibodies can be classified into four main categories^{17,20}. RBD-48 and RBD-85 belong to the first category (Class 1) and act by blocking the binding of the ‘up’ conformation of RBD to ACE2¹⁷. The precise epitopes of RBD-98 and RBD-109 are not yet defined but overlap with those of RBD-48 and RBD-85. The anti-NTD antibodies bind to uncharacterized epitopes.

We measured the potency of the four therapeutic antibodies against the Delta variant and included as a comparison D614G (B.1) and the Alpha and Beta variants. The antibodies neutralized D614G with a half-maximal inhibitory concentration (IC_{50}) that ranged from 1.2×10^{-3} to $6.5 \times 10^{-2} \mu\text{g ml}^{-1}$ (Fig. 1). Etesivimab exhibited a 200-fold increase in IC_{50} against the Alpha variant. As previously reported, bamlanivimab and etesivimab did not neutralize the Beta variant²¹. Bamlanivimab lost antiviral activity against the Delta variant, in line with previous results that showed that L452R is an escape mutation for this antibody¹⁶. Etesivimab, casirivimab and imdevimab remained active against the Delta variant (Fig. 1).

Fig. 1: Neutralization of the SARS-CoV-2 variants D614G, Alpha, Beta and Delta by therapeutic monoclonal antibodies.

 figure 1

Neutralization curves of monoclonal antibodies. Dose–response analysis of neutralization of the D614G strain and the Alpha, Beta and Delta variants by four

therapeutic monoclonal antibodies (bamlanivimab, etesivimab, casirivimab and imdevimab). Data are mean \pm s.d. of four independent experiments.

[Source data](#)

[Full size image](#)

The four other anti-RBD monoclonal antibodies neutralized D614G. The IC₅₀ values of RBD-48 and RBD-98 were about 15–100-fold higher for the Alpha variant than for D614G, whereas RBD-85 exhibited increased activity against the Alpha variant. Three monoclonal antibodies inhibited the Delta variant, whereas RBD-85 was inactive (Extended Data Fig. 5).

The four anti-NTD monoclonal antibodies were globally less efficient than anti-RBD monoclonal antibodies. They inhibited D614G with a high IC₅₀ value (1–60 µg ml⁻¹) (Extended Data Fig. 5). Three anti-NTD antibodies lost activity against the Alpha and Delta variants, whereas the fourth (NTD-18) inhibited the two variants to some extent. Thus, the Delta variant escapes neutralization by some antibodies that target the RBD or NTD.

We examined by flow cytometry the binding of each monoclonal antibody to Vero cells infected with the different variants, and used radar plots to show the binding of all antibodies tested (Extended Data Fig. 6). D614G was recognized by the 12 monoclonal antibodies tested. The Alpha and Delta variants were recognized by nine and by seven monoclonal antibodies, respectively. Bamlanivimab no longer bound to the Delta variant. We also analysed the binding of the 12 monoclonal antibodies to the Beta variant, which is more resistant to neutralization. Bamlanivimab and etesivimab lost their binding to the Beta variant, and only five of the antibodies bound to this variant (Extended Data Fig. 6). Thus, the escape of the Delta variant and other variants from neutralization is due to a reduction or loss of binding of the antibodies.

Sensitivity of Delta to convalescent sera

We examined the neutralization ability of sera from convalescent individuals. We first selected samples from 56 donors in a cohort of individuals from the French city of Orléans. All individuals had tested positive for SARS-CoV-2 infection by quantitative PCR with reverse transcription (qRT-PCR) or serology and included critical, severe, mild-to-moderate and asymptomatic cases of COVID-19 (Extended Data Table 1). The individuals were not vaccinated at the time at which samples were taken. We have previously characterized the potency of these sera against D614G, Alpha and Beta isolates¹¹. We analysed samples taken from individuals a median of 188 days after the onset of symptoms (referred to as month-6 samples), and calculated the median half-

maximal effective dilution (ED_{50}) for each combination of serum and virus (Extended Data Fig. 7a). With the Alpha variant, we obtained similar ED_{50} values in this series of experiments to those in our previous analysis¹¹ (Extended Data Fig. 7b). We thus included our published data for D614G and Beta in the comparison. With the Delta variant, neutralization titres were significantly decreased by four- to sixfold when compared to the Alpha and D614G strains, respectively (Extended Data Fig. 7a). This reduction in neutralizing titres was similar against the Delta and Beta variants (Extended Data Fig. 7a).

We asked whether this neutralization profile was maintained for longer periods of time. We analysed sera from 47 individuals from another cohort consisting of healthcare workers from Strasbourg University Hospitals who had a qRT–PCR-confirmed diagnosis of COVID-19 and who experienced mild disease^{22,23}. Twenty-six individuals were unvaccinated, and 21 had received a single dose of vaccine 7–81 days before sampling. The samples were collected at a later time point (month 12), with a median of 330 and 359 days for unvaccinated and vaccinated individuals, respectively²³ (Extended Data Table 1). As observed previously²³, the neutralization activity was globally low at month 12 in unvaccinated individuals (Fig. 2a). There was a fourfold decrease in ED_{50} against the Beta and Delta variants relative to the Alpha variant (Fig. 2a). The 21 individuals within the month-12 cohort who had had a single dose of vaccine included 9 individuals who had received the AstraZeneca vaccine, 9 the Pfizer vaccine and 3 the Moderna vaccine. Sera from these vaccinated participants showed a marked increase in neutralizing antibody titres against the Alpha, Beta and Delta variants, as compared to convalescent individuals who had not been vaccinated (Fig. 2a). Therefore, as shown with other variants^{23,24}, a single dose of vaccine boosts cross-neutralizing antibody responses to the Delta variant.

Fig. 2: Sensitivity of the SARS-CoV-2 variants D614G, Alpha, Beta and Delta to sera from convalescent individuals and vaccinated individuals.

 figure2

Neutralization titres of the sera against the indicated viral isolates are expressed as ED_{50} values. **a**, Neutralizing activity of sera from the Strasbourg cohort of convalescent individuals ($n = 26$; left) and convalescent individuals who had been vaccinated ($n = 21$; right). Samples were collected at month 12 (M12) after the onset

of symptoms. **b**, Neutralizing activity of sera from recipients of the Pfizer vaccine, sampled at week 3 (W3) after vaccination ($n = 16$; left) and week 8 (W8) after vaccination (week 5 after the second dose) ($n = 16$; right). **c**, Neutralizing activity of sera from recipients of the AstraZeneca vaccine, sampled at week 10 (W10) after vaccination ($n = 23$; left) and week 16 (W16) after vaccination (week 4 after the second dose) ($n = 20$; right). The dotted line indicates the limit of detection ($ED_{50} = 30$). Data are mean from two independent experiments. A two-sided Friedman test with Dunn's multiple comparison was performed between each of the viral strains. * $P < 0.05$, ** $P < 0.01$, *** $P < 0.001$, **** $P < 0.0001$. Strasbourg cohort, unvaccinated (M12): D614G versus Beta, $P = 0.0052$; D614G versus Delta, $P = 0.0052$; Alpha versus Beta, $P < 0.0001$; Alpha versus Delta, $P < 0.0001$. Strasbourg cohort, vaccinated (M12): D614G versus Beta, $P < 0.0001$; Alpha versus Beta, $P < 0.0001$; Alpha versus Delta, $P < 0.0001$. Pfizer (W3): D614G versus Beta, $P = 0.0001$; D614G versus Delta, $P = 0.0013$. Pfizer (W8): D614G versus Beta, $P = 0.0002$; Alpha versus Beta, $P < 0.0001$; Alpha versus Delta, $P = 0.0098$. AstraZeneca (W10): D614G versus Beta, $P < 0.0001$; D614G versus Delta, $P < 0.0001$; Alpha versus Beta, $P = 0.0006$; Alpha versus Delta, $P = 0.0056$. AstraZeneca (W16): D614G versus Beta, $P < 0.0001$; D614G versus Delta, $P = 0.0005$, Alpha versus Beta, $P < 0.0001$; Alpha versus Delta, $P < 0.0001$.

[Source data](#)

[Full size image](#)

We then classified the individuals as neutralizers (individuals whose serum contained neutralizing antibodies that were detectable at the first serum dilution of 1/30) and non-neutralizers, for the viral variants and the two cohorts (Extended Data Fig. [7c](#)). Sera from between 76% and 92% of individuals neutralized the four strains at month 6. The fraction of neutralizers was lower in the second cohort at month 12, and this effect was particularly marked for the Beta and Delta variants. Sera from 88% of individuals neutralized the Alpha variant, whereas sera from only 47% of individuals neutralized the Delta variant. After vaccination, sera from 100% of the convalescent individuals neutralized the four strains (Extended Data Fig. [7c](#)).

Thus, the Delta variant exhibits enhanced resistance to neutralization by sera from convalescent individuals who have not been vaccinated, particularly by one year after the infection.

Sensitivity of Delta to sera from vaccinated individuals

We next asked whether vaccine-elicited antibodies neutralized the Delta variant in individuals who had not previously been infected with SARS-CoV-2. We randomly

selected 59 individuals from a cohort of vaccinated individuals in Orléans. The characteristics of these individuals are outlined in Extended Data Table 2. Sixteen individuals received the Pfizer vaccine. They were sampled at week 3 after the first dose and week 8 (corresponding to week 5 after the second dose). Thirteen individuals were also sampled at week 16. Forty-three individuals received the AstraZeneca vaccine. Sera from 23 individuals were sampled after 1 dose (week 10) and from 20 other individuals after 2 doses (week 16, corresponding to week 4 after the second dose). We measured the potency of the sera against D614G and the Alpha, Beta and Delta variants (Fig. 2b,c).

With the Pfizer vaccine, after a single dose (at week 3) the levels of neutralizing antibodies were low against D614G, and almost undetectable against the Alpha, Beta and Delta variants (Fig. 2b). Titres significantly increased after the second dose. We observed a threefold and a sixteenfold reduction in the neutralization titres against the Delta and the Beta variants, respectively, when compared to the Alpha variant (Fig. 2b). Similar differences between strains were observed at a later time point (week 16), although titres were globally slightly lower (Extended Data Fig. 7b).

A similar pattern was observed with the AstraZeneca vaccine. A single dose (week 10) induced low levels of antibodies neutralizing the Delta and Beta variants, when compared to the D614G and Alpha strains (Fig. 2c). Four weeks after the second dose (week 16), neutralizing titres were strongly increased. There was, however, a fivefold and a ninefold reduction in neutralization titres against the Delta and the Beta variants, respectively, relative to the Alpha variant (Fig. 2c).

We then classified the vaccine recipients as neutralizers and non-neutralizers, for the four viral strains (Extended Data Fig. 7d,e). For the Pfizer vaccine, sera from 13% of individuals neutralized the Delta variant after a single dose. Sera from 81 to 100% of individuals neutralized any of the four stains after the second dose, at week 8. This fraction remained stable at week 16, with the exception of the Beta variant, which was neutralized by sera from only 46% of the individuals. Sera from 74% and 61% of individuals that received a single dose of the AstraZeneca vaccine neutralized the D614G and the Alpha strains, respectively. This fraction sharply dropped with the Beta and the Delta variants, which were inhibited by only 4 and 9% of the sera, respectively. Four weeks after the second dose of the AstraZeneca vaccine, sera from 95–100% of individuals neutralized the four strains.

Therefore, a single dose of Pfizer or AstraZeneca either showed low or no efficiency against the Beta and the Delta variants. Both vaccines generated a neutralizing response that efficiently targeted the Delta variant only after the second dose.

Discussion

We studied the cross-reactivity of monoclonal antibodies to pre-existing SARS-CoV-2 strains, sera from convalescent individuals six or twelve months after the onset of COVID-19 symptoms and sera from recent recipients of a COVID-19 vaccine against an infectious Delta isolate. Some monoclonal antibodies, including bamlanivimab, lost their ability to bind to the spike protein and no longer neutralized the Delta variant. We also showed that the Delta variant is less sensitive to sera from naturally immunized individuals. Vaccination of convalescent individuals boosted the humoral immune response to well above the threshold of neutralization. These results strongly suggest that vaccination of previously infected individuals is likely to be protective against a large array of circulating viral strains, including the Delta variant.

In individuals who had not previously been infected with SARS-CoV-2, a single dose of either the Pfizer or the AstraZeneca vaccine induced a barely detectable level of neutralizing antibodies against the Delta variant. About 10% of the sera neutralized this variant. However, a two-dose regimen generated high sero-neutralization levels against the Alpha, Beta and Delta variants in individuals sampled at week 8 to week 16 after vaccination. Levels of neutralizing antibodies are highly predictive of immune protection from symptomatic SARS-CoV-2 infection²⁵. A recent report analysing all sequenced symptomatic cases of COVID-19 in England was used to estimate the effect of vaccination on infection²⁶. Effectiveness was notably lower for the Delta variant than for the Alpha variant after one dose of the AstraZeneca or the Pfizer vaccine. The two-dose effectiveness against the Delta variant was estimated to be 60% and 88% for the AstraZeneca and the Pfizer vaccine, respectively²⁶. Our neutralization experiments indicate that antibodies elicited by the Pfizer and AstraZeneca vaccines are efficacious against the Delta variant, but about three- to fivefold less potent than they are against the Alpha variant. There was no major difference in the levels of antibodies elicited by the Pfizer or the AstraZeneca vaccines.

Potential limitations of our work include the low number of vaccinated individuals analysed and the lack of characterization of cellular immunity, which may be more cross-reactive than the humoral response. Future work with more individuals and longer survey periods will help to characterize the role of humoral responses in the efficacy of vaccines against circulating variants.

Our results demonstrate that the emerging Delta variant partially—but notably—escapes neutralizing monoclonal antibodies and polyclonal antibodies elicited by previous infection with SARS-CoV-2 or by vaccination.

Methods

Data reporting

No statistical methods were used to predetermine sample size. The experiments were not randomized and the investigators were not blinded to allocation during experiments and outcome assessment. Our research complies with all relevant ethical regulations.

Orléans cohort of convalescent and vaccinated individuals

Since 27 August 2020, a prospective, monocentric, longitudinal, interventional cohort clinical study enrolling 170 individuals with SARS-CoV-2 infection (with different disease severities) and 59 healthy control individuals has been ongoing, and aims to describe the persistence of specific and neutralizing antibodies over a 24-month period. This study was approved by the Ile de France IV ethical committee. At enrolment, written informed consent was collected and participants completed a questionnaire that covered sociodemographic characteristics, virological findings (SARS-CoV-2 qRT–PCR results, including date of testing), clinical data (date of symptom onset, type of symptoms, hospitalization) and data related to anti-SARS-CoV-2 vaccination if ever (brand product, date of first and second doses). The serological status of participants was assessed every three months. Those who underwent anti-SARS-CoV-2 vaccination had regular blood sampling after the first dose of vaccine (ClinicalTrials.gov Identifier: NCT04750720). The primary outcome was the presence of antibodies to SARS-CoV-2 spike protein as measured with the S-Flow assay. The secondary outcome was the presence of neutralizing antibodies as measured with the S-Fuse assay. For the present study, we selected 56 convalescent individuals and 59 vaccinated individuals (16 with Pfizer and 43 with AstraZeneca). Study participants did not receive any compensation.

Strasbourg cohort of convalescent individuals

Since April 2020, a prospective, monocentric, longitudinal, interventional cohort clinical study enrolling 308 hospital staff from the Strasbourg University Hospitals who had a qRT–PCR-confirmed diagnosis of SARS-CoV-2 infection has been ongoing (ClinicalTrials.gov Identifier: NCT04441684). At enrolment (from 17 April 2020), written informed consent was collected and participants completed a questionnaire that covered sociodemographic characteristics, virological findings (SARS-CoV-2 qRT–PCR results, including date of testing) and clinical data (date of symptom onset, type of symptoms, hospitalization). This study was approved by the Institutional Review Board of Strasbourg University Hospital. The serological status of the participants has been described at months 3 and 6 after the onset of symptoms^{22,23}. Laboratory identification of SARS-CoV-2 was performed at least 10 days before inclusion by qRT–PCR testing on nasopharyngeal swab specimens according to current guidelines (Institut Pasteur; WHO technical guidance). The assay targets two regions of the viral RNA-dependent RNA polymerase (RdRp) gene with a threshold of detection of 10

copies per reaction. The primary outcome was the presence of antibodies to the SARS-CoV-2 spike protein as measured with the S-Flow assay. The secondary outcome was the presence of neutralizing antibodies as measured with the S-Fuse assay. For the present study, we randomly selected 47 convalescent individuals at month 12 (26 unvaccinated and 21 vaccinated). Study participants did not receive any compensation.

Phylogenetic analysis

All SARS-CoV-2 sequences available on the GISAID EpiCov database as of 21 May 2021 were retrieved. A subset of complete and high-coverage sequences, as indicated in GISAID, assigned to lineages B.1.617.1, B.1.617.2 and B.1.617.3 were randomly subsampled to contain up to five sequences per country and epidemiological week in R with the packages tidyverse and lubridate. Together with a single B.1.617 sequence this subset was included in the global SARS-CoV-2 phylogeny reconstructed with augur and visualized with auspice as implemented in the Nextstrain pipeline (<https://github.com/nextstrain/ncov>; version from 21 May 2021)²⁷. Within Nextstrain, a random subsampling approach capping a maximum number of sequences per global region was used for the contextual non-B.1.617 sequences. Acknowledgement of the contributing and originating laboratories for all sequences used in the analysis is provided in Supplementary Table 1.

Three-dimensional mapping of mutations on B1.617.2 and other variants to the surface of the spike protein

Panels in Extended Data Fig. 4 were prepared with the PyMOL Molecular Graphics System, v.2.1 (Schrödinger). The atomic model used (Protein Data Bank code: 6XR8) has been previously described²⁸.

S-Fuse neutralization assay

U2OS-ACE2 GFP1-10 or GFP 11 cells, also termed S-Fuse cells, become GFP⁺ when they are productively infected by SARS-CoV-2^{10,11}. Cells tested negative for mycoplasma. Cells were mixed (ratio 1:1) and plated at 8×10^3 per well in a μClear 96-well plate (Greiner Bio-One). The indicated SARS-CoV-2 strains were incubated with serially diluted monoclonal antibodies or sera for 15 min at room temperature and added to S-Fuse cells. The sera were heat-inactivated 30 min at 56 °C before use. Eighteen hours later, cells were fixed with 2% paraformaldehyde (PFA), washed and stained with Hoechst (dilution 1:1,000, Invitrogen). Images were acquired with an Opera Phenix high-content confocal microscope (PerkinElmer). The GFP area and the number of nuclei were quantified using Harmony software (PerkinElmer). The percentage of neutralization was calculated using the number of syncytia as value with

the following formula: $100 \times (1 - (\text{value with serum} - \text{value in 'non-infected'}) / (\text{value in 'no serum'} - \text{value in 'non-infected'}}))$. The neutralizing activity of each serum was expressed as the ED₅₀ value. ED₅₀ values (in µg ml⁻¹ for monoclonal antibodies and in dilution values for sera) were calculated with a reconstructed curve using the percentage of the neutralization at the different concentrations.

Clinical history of the patient infected with B.1.617.2

A 54-year-old man was admitted on 27 April 2021 to the emergency department of the Hôpital Européen Georges Pompidou hospital in Paris, France, for an acute respiratory distress syndrome with fever. He had no medical background and came back from a trip to India (West Bengal and a few days spent in Delhi) 10 days before (17 April 2021), where he stayed 15 days for his work. The onset of symptoms (abdominal pain and fever) was approximately 18 April 2021. The nasopharyngeal swab tested positive for SARS-CoV-2 at his date of admission. Lung tomo-densitometry showed a mild (10–25%) COVID-19 pneumonia without pulmonary embolism. He initially received oxygen therapy (2 l min⁻¹), dexamethasone (6 mg per day) and enoxaparin (0.4 ml twice a day). His respiratory state worsened on day 3 (30 April 2021). He was transferred to an intensive care unit, in which he received high-flow oxygen therapy (maximum 12 l min⁻¹). His respiratory condition improved, and he was transferred back to a conventional unit on day 8 (5 May 2021). He was discharged from hospital on day 15 (May 10 2021).

Virus strains

The reference D614G strain (hCoV-19/France/GE1973/2020) was supplied by the National Reference Centre for Respiratory Viruses hosted by the Institut Pasteur and headed by S. van der Werf. This viral strain was supplied through the European Virus Archive – Global (EVAg) platform, a project that has received funding from the European Union's Horizon 2020 research and innovation program under grant agreement no. 653316. The variant strains were isolated from nasal swabs using Vero E6 cells and amplified by one or two passages. B.1.1.7 originated from an individual in Tours (France) who had returned from the UK. B.1.351 (hCoV-19/France/IDF-IPP00078/2021) originated from an individual in Creteil (France). B.1.617.2 was isolated from a nasopharyngeal swab of a hospitalized patient who had returned from India, as described above. The swab was provided and sequenced by the Laboratoire de Virologie of the Hopital Européen Georges Pompidou (Assistance Publique des Hôpitaux de Paris). All individuals provided informed consent for the use of the biological materials. Titration of viral stocks was performed on Vero E6, with a limiting dilution technique allowing a calculation of TCID₅₀, or on S-Fuse cells. Viruses were sequenced directly on nasal swabs, and after one or two passages on Vero cells. Sequences were deposited in the GISAID database immediately after their

generation, with the following IDs: D614G: EPI_ISL_414631; B.1.1.7: EPI_ISL_735391; B.1.1.351: EPI_ISL_964916; B.1.617.2: ID: EPI_ISL_2029113.

Flow cytometry

Vero cells were infected with the indicated viral strains at a multiplicity of infection (MOI) of 0.1. Two days after, cells were detached using PBS-EDTA and transferred into U-bottom 96-well plates (50,000 cells per well). Cells were fixed in 4% PFA for 15–30 min at room temperature. Cells were then incubated for 15–30 min at room temperature with the indicated monoclonal antibodies ($1 \mu\text{g ml}^{-1}$) in PBS, 1% BSA, 0.05% sodium azide and 0.05% saponin. Cells were washed with PBS and stained using anti-IgG AF647 (1:600 dilution) (Thermo Fisher Scientific). Stainings were also performed on control uninfected cells. Data were acquired on an Attune Nxt instrument using Attune Nxt Software v.3.2.1 (Life Technologies) and analysed with FlowJo v.10.7.1 (Becton Dickinson).

Antibodies

The four therapeutic antibodies were provided by CHR Orleans. Human anti-SARS-CoV2 monoclonal antibodies were cloned from S-specific blood memory B cells of individuals who were convalescing from COVID-19 (C.P. et al., manuscript in preparation). Recombinant human IgG1 monoclonal antibodies were produced by co-transfection of Freestyle 293-F suspension cells (Thermo Fisher Scientific) as previously described²⁹, purified by affinity chromatography using protein G sepharose 4 fast flow beads (GE Healthcare) and validated by enzyme-linked immunosorbent assay (ELISA) against the trimeric S, RBD, S2 and NTD proteins (C.P. et al., manuscript in preparation).

Statistical analysis

Flow cytometry data were analysed with FlowJo v.10 software (TriStar). Calculations were performed using Excel 365 (Microsoft). Figures were drawn using GraphPad Prism 9. Statistical analysis was conducted using GraphPad Prism 9. Statistical significance between different groups was calculated using the tests indicated in each figure legend.

Reporting summary

Further information on research design is available in the [Nature Research Reporting Summary](#) linked to this paper.

Data availability

All data supporting the findings of this study are available within the Article or from the corresponding authors upon request. Viral sequences are available upon request and were deposited at GISAID (<https://www.gisaid.org/>) under the following numbers: hCoV-19/France/GE1973/2020 (D614G): EPI_ISL_414631; Alpha (B.1.1.7): EPI_ISL_735391; Beta (B.1.351): EPI_ISL_964916 and Delta (B.1.617.2): EPI_ISL_2029113. [Source data](#) are provided with this paper.

References

1. 1. Yadav, P. D. et al. Neutralization of variant under investigation B.1.617 with sera of BBV152 vaccinees. *Clin. Infect. Dis.* <https://doi.org/10.1093/cid/ciab411> (2021).
2. 2. Ferreira, I. et al. SARS-CoV-2 B.1.617 emergence and sensitivity to vaccine-elicited antibodies. Preprint at <https://doi.org/10.1101/2021.05.08.443253> (2021).
3. 3. Hoffmann, M. et al. SARS-CoV-2 variant B.1.617 is resistant to Bamlanivimab and evades antibodies induced by infection and vaccination. *Cell Rep.* <https://doi.org/10.1016/j.celrep.2021.109415> (2021).
4. 4. Cherian, S. et al. Convergent evolution of SARS-CoV-2 spike mutations, L452R, E484Q and P681R, in the second wave of COVID-19 in Maharashtra, India. Preprint at <https://doi.org/10.1101/2021.04.22.440932> (2021).
5. 5. Edara, V.-V. et al. Infection and vaccine-induced neutralizing-antibody responses to the SARS-CoV-2 B.1.617 variants. *New Eng. J. Med.* <https://doi.org/10.1056/NEJMc2107799> (2021).
6. 6.

Public Health England. Variants: distribution of case data, 11 June 2021. <https://www.gov.uk/government/publications/covid-19-variants-genomically-confirmed-case-numbers/variants-distribution-of-case-data-11-june-2021> (2021).

7. 7.

Tada, T. et al. The spike proteins of SARS-CoV-2 B.1.617 and B.1.618 variants identified in India provide partial resistance to vaccine-elicited and therapeutic monoclonal antibodies. Preprint at <https://doi.org/10.1101/2021.05.14.444076> (2021).

8. 8.

Liu, J. et al. BNT162b2-elicited neutralization of B.1.617 and other SARS-CoV-2 variants. *Nature* <https://doi.org/10.1038/s41586-021-03693-y> (2021).

9. 9.

Wall, E. C. et al. Neutralising antibody activity against SARS-CoV-2 VOCs B.1.617.2 and B.1.351 by BNT162b2 vaccination. *Lancet* **397**, 2331–2333 (2021).

[CAS](#) [Article](#) [Google Scholar](#)

10. 10.

Buchrieser, J. et al. Syncytia formation by SARS-CoV-2-infected cells. *EMBO J.* **39**, e106267 (2020).

[CAS](#) [Article](#) [Google Scholar](#)

11. 11.

Planas, D. et al. Sensitivity of infectious SARS-CoV-2 B.1.1.7 and B.1.351 variants to neutralizing antibodies. *Nat. Med.* **27**, 917–924 (2021).

[CAS](#) [Article](#) [Google Scholar](#)

12. 12.

Rambaut, A. et al. A dynamic nomenclature proposal for SARS-CoV-2 lineages to assist genomic epidemiology. *Nat. Microbiol.* **5**, 1403–1407 (2020).

[CAS](#) [Article](#) [Google Scholar](#)

13. 13.

Plante, J. A. et al. The variant gambit: COVID-19's next move. *Cell Host Microbe* **29**, 508–515 (2021).

[CAS](#) [Article](#) [Google Scholar](#)

14. 14.

Centers for Disease Control and Prevention. SARS-CoV-2 variant classifications and definitions. <https://www.cdc.gov/coronavirus/2019-ncov/cases-updates/variant-surveillance/variant-info.html> (2021).

15. 15.

McCallum, M. et al. N-terminal domain antigenic mapping reveals a site of vulnerability for SARS-CoV-2. *Cell* **184**, 2332–2347 (2021).

[CAS](#) [Article](#) [Google Scholar](#)

16. 16.

Starr, T. N., Greaney, A. J., Dingens, A. S. & Bloom, J. D. Complete map of SARS-CoV-2 RBD mutations that escape the monoclonal antibody LY-CoV555 and its cocktail with LY-CoV016. *Cell Rep. Med.* **2**, 100255 (2021).

[Article](#) [Google Scholar](#)

17. 17.

Barnes, C. O. et al. SARS-CoV-2 neutralizing antibody structures inform therapeutic strategies. *Nature* **588**, 682–687 (2020).

[ADS](#) [CAS](#) [Article](#) [Google Scholar](#)

18. 18.

Taylor, P. C. et al. Neutralizing monoclonal antibodies for treatment of COVID-19. *Nat. Rev. Immunol.* **21**, 382–393 (2021).

[CAS](#) [Article](#) [Google Scholar](#)

19. 19.

Starr, T. N. et al. Prospective mapping of viral mutations that escape antibodies used to treat COVID-19. *Science* **371**, 850–854 (2021).

[ADS](#) [CAS](#) [Article](#) [Google Scholar](#)

20. 20.

Liu, L. et al. Potent neutralizing antibodies against multiple epitopes on SARS-CoV-2 spike. *Nature* **584**, 450–456 (2020).

[CAS](#) [Article](#) [Google Scholar](#)

21. 21.

Wang, P. et al. Antibody resistance of SARS-CoV-2 variants B.1.351 and B.1.1.7. *Nature* **593**, 130–135 (2021).

[ADS](#) [CAS](#) [Article](#) [Google Scholar](#)

22. 22.

Fafi-Kremer, S. et al. Serologic responses to SARS-CoV-2 infection among hospital staff with mild disease in eastern France. *EBioMedicine* **59**, 102915 (2020).

[Article](#) [Google Scholar](#)

23. 23.

Gallais, F. et al. Anti-SARS-CoV-2 antibodies persist for up to 13 months and reduce risk of reinfection. Preprint at <https://doi.org/10.1101/2021.05.07.21256823> (2021).

24. 24.

Krammer, F. et al. Antibody responses in seropositive persons after a single dose of SARS-CoV-2 mRNA vaccine. *N. Engl. J. Med.* **384**, 1372–1374 (2021).

[CAS](#) [Article](#) [Google Scholar](#)

25. 25.

Khoury, D. S. et al. Neutralizing antibody levels are highly predictive of immune protection from symptomatic SARS-CoV-2 infection. *Nat. Med.* (2021).

26. 26.

Bernal, J. L. et al. Effectiveness of COVID-19 vaccines against the B.1.617.2 variant. Preprint at <https://doi.org/10.1101/2021.05.22.21257658> (2021).

27. 27.

Hadfield, J. et al. Nextstrain: real-time tracking of pathogen evolution. *Bioinformatics* **34**, 4121–4123 (2018).

[CAS](#) [Article](#) [Google Scholar](#)

28. 28.

Cai, Y. et al. Distinct conformational states of SARS-CoV-2 spike protein. *Science* **369**, 1586–1592 (2020).

[ADS](#) [CAS](#) [Article](#) [Google Scholar](#)

29. 29.

Lorin, V. & Mouquet, H. Efficient generation of human IgA monoclonal antibodies. *J. Immunol. Methods* **422**, 102–110 (2015).

[CAS](#) [Article](#) [Google Scholar](#)

30. 30.

Tzou, P. L. et al. Coronavirus antiviral research database (CoV-RDB): an online database designed to facilitate comparisons between candidate anti-coronavirus compounds. *Viruses* **12**, 1006 (2020).

[CAS](#) [Article](#) [Google Scholar](#)

[Download references](#)

Acknowledgements

We thank N. Casartelli for critical reading of the manuscript; P. Guardado Calvo for discussion; the individuals who participated in the study; members of the Virus and Immunity Unit for discussions and help; N. Aulner and the UTechS Photonic BioImaging (UPBI) core facility (Institut Pasteur), a member of the France BioImaging network, for image acquisition and analysis; and the DRCI, CIC, Médecine du Travail and Pôle de Biologie teams (CHU de Strasbourg) for the

management of the Strasbourg cohort and serology testing. The Opera system was co-funded by the Institut Pasteur and the Région Île de France (DIM1Health). Work in the O.S. laboratory is funded by the Institut Pasteur, Urgence COVID-19 Fundraising Campaign of Institut Pasteur, Fondation pour la Recherche Médicale (FRM), ANRS, the Vaccine Research Institute (ANR-10-LABX-77), Labex IBEID (ANR-10-LABX-62-IBEID), ANR/FRM Flash Covid PROTEO-SARS-CoV-2 and IDISCOVR. Work in UPBI is funded by grant ANR-10-INSB-04-01 and the Région Île-de-France program DIM1-Health. D.P. is supported by the Vaccine Research Institute. The H.M. laboratory is funded by the Institut Pasteur, the Milieu Intérieur Program (ANR-10-LABX-69-01), INSERM, REACTing, EU (RECOVER) and Fondation de France (00106077) grants. The S.F.K. laboratory is funded by Strasbourg University Hospitals (SeroCoV-HUS; PRI 7782), the Programme Hospitalier de Recherche Clinique (PHRC N 2017–HUS no. 6997), the Agence Nationale de la Recherche (ANR-18-CE17-0028), Laboratoire d’Excellence TRANSPLANTEX (ANR-11-LABX-0070_TRANSPLANTEX) and the Institut National de la Santé et de la Recherche Médicale (UMR_S 1109). The E.S.-L. laboratory is funded by the Institut Pasteur and the French Government’s Investissement d’Avenir programme, Laboratoire d’Excellence ‘Integrative Biology of Emerging Infectious Diseases’ (grant no. ANR-10-LABX-62-IBEID). The funders of this study had no role in study design, data collection, analysis and interpretation, or writing of the Article.

Author information

Author notes

1. These authors contributed equally: Timothée Bruel, Etienne Simon-Lorière, Felix A. Rey, Olivier Schwartz

Affiliations

1. Virus and Immunity Unit, Department of Virology, Institut Pasteur, CNRS UMR 3569, Paris, France

Delphine Planas, Isabelle Staropoli, Florence Guivel-Benhassine, Maaran Michael Rajah, Françoise Porrot, Timothée Bruel & Olivier Schwartz

2. Vaccine Research Institute, Creteil, France

Delphine Planas, Timothée Bruel & Olivier Schwartz

3. INSERM, Functional Genomics of Solid Tumors (FunGeST), Centre de Recherche des Cordeliers, Université de Paris and Sorbonne Université, Paris,

France

David Veyer & Hélène Péré

4. Laboratoire de Virologie, Service de Microbiologie, Hôpital Européen Georges Pompidou, Assistance Publique des Hôpitaux de Paris, Paris, France

David Veyer, Nicolas Robillard, Julien Puech, Dhiaeddine Edriss & Laurent Belec

5. G5 Evolutionary Genomics of RNA Viruses, Department of Virology, Institut Pasteur, Paris, France

Artem Baidaliuk, Matthieu Prot & Etienne Simon-Lorière

6. Université de Paris, Sorbonne Paris Cité, Paris, France

Maaran Michael Rajah

7. Laboratory of Humoral Immunology, Department of Immunology, Institut Pasteur, INSERM U1222, Paris, France

Cyril Planchais & Hugo Mouquet

8. CHU de Strasbourg, Laboratoire de Virologie, Strasbourg, France

Floriane Gallais, Pierre Gantner, Aurélie Velay & Samira Fafi-Kremer

9. Université de Strasbourg, INSERM, IRM UMR_S 1109, Strasbourg, France

Floriane Gallais, Pierre Gantner, Aurélie Velay & Samira Fafi-Kremer

10. Service de Gériatrie, Hôpital Européen Georges Pompidou, Assistance Publique des Hôpitaux de Paris, Paris, France

Julien Le Guen

11. Unité d'Hygiène Hospitalière, Service de Microbiologie, Hôpital Européen Georges Pompidou, Assistance Publique des Hôpitaux de Paris, Paris, France

Najiby Kassis-Chikhani

12. CHR d'Orléans, Service de Maladies Infectieuses, Orléans, France

Aymeric Seve, Laura Courtellemont, Laurent Hocqueloux & Thierry Prazuck

13. Structural Virology Unit, Department of Virology, Institut Pasteur, CNRS UMR 3569, Paris, France

Felix A. Rey

Authors

1. Delphine Planas

[View author publications](#)

You can also search for this author in [PubMed](#) [Google Scholar](#)

2. David Veyer

[View author publications](#)

You can also search for this author in [PubMed](#) [Google Scholar](#)

3. Artem Baidaliuk

[View author publications](#)

You can also search for this author in [PubMed](#) [Google Scholar](#)

4. Isabelle Staropoli

[View author publications](#)

You can also search for this author in [PubMed](#) [Google Scholar](#)

5. Florence Guivel-Benhassine

[View author publications](#)

You can also search for this author in [PubMed](#) [Google Scholar](#)

6. Maaran Michael Rajah

[View author publications](#)

You can also search for this author in [PubMed](#) [Google Scholar](#)

7. Cyril Planchais

[View author publications](#)

You can also search for this author in [PubMed](#) [Google Scholar](#)

8. Françoise Porrot

[View author publications](#)

You can also search for this author in [PubMed](#) [Google Scholar](#)

9. Nicolas Robillard

[View author publications](#)

You can also search for this author in [PubMed](#) [Google Scholar](#)

10. Julien Puech

[View author publications](#)

You can also search for this author in [PubMed](#) [Google Scholar](#)

11. Matthieu Prot

[View author publications](#)

You can also search for this author in [PubMed](#) [Google Scholar](#)

12. Floriane Gallais

[View author publications](#)

You can also search for this author in [PubMed](#) [Google Scholar](#)

13. Pierre Gantner

[View author publications](#)

You can also search for this author in [PubMed](#) [Google Scholar](#)

14. Aurélie Velay

[View author publications](#)

You can also search for this author in [PubMed](#) [Google Scholar](#)

15. Julien Le Guen

[View author publications](#)

You can also search for this author in [PubMed](#) [Google Scholar](#)

16. Najiby Kassis-Chikhani

[View author publications](#)

You can also search for this author in [PubMed](#) [Google Scholar](#)

17. Dhiaeddine Edriss

[View author publications](#)

You can also search for this author in [PubMed](#) [Google Scholar](#)

18. Laurent Belec

[View author publications](#)

You can also search for this author in [PubMed](#) [Google Scholar](#)

19. Aymeric Seve

[View author publications](#)

You can also search for this author in [PubMed](#) [Google Scholar](#)

20. Laura Courtellemont

[View author publications](#)

You can also search for this author in [PubMed](#) [Google Scholar](#)

21. Hélène Péré

[View author publications](#)

You can also search for this author in [PubMed](#) [Google Scholar](#)

22. Laurent Hocqueloux

[View author publications](#)

You can also search for this author in [PubMed](#) [Google Scholar](#)

23. Samira Fafi-Kremer

[View author publications](#)

You can also search for this author in [PubMed](#) [Google Scholar](#)

24. Thierry Prazuck

[View author publications](#)

You can also search for this author in [PubMed](#) [Google Scholar](#)

25. Hugo Mouquet

[View author publications](#)

You can also search for this author in [PubMed](#) [Google Scholar](#)

26. Timothée Bruel

[View author publications](#)

You can also search for this author in [PubMed](#) [Google Scholar](#)

27. Etienne Simon-Lorière

[View author publications](#)

You can also search for this author in [PubMed](#) [Google Scholar](#)

28. Felix A. Rey

[View author publications](#)

You can also search for this author in [PubMed](#) [Google Scholar](#)

29. Olivier Schwartz

[View author publications](#)

You can also search for this author in [PubMed](#) [Google Scholar](#)

Contributions

Experimental strategy design, experiments: D.P., D.V., A.B., I.S., F.G.-B., M.M.R., F.P., T.B., E.S.-L. and F.A.R. Vital materials: D.V., C.P., N.R., J.P., M.P., F.G., P.G., A.V., J.L.G., L.C., N.K.-C., D.E., L.B., A.S., H.P., L.H., S.F.-K., T.P. and H.M.
Manuscript writing: D.P., T.B., E.S.-L., F.A.R. and O.S. Manuscript editing: D.V., M.M.R., H.P., L.H., S.F.K., T.P. and H.M.

Corresponding authors

Correspondence to [Timothée Bruel](#) or [Olivier Schwartz](#).

Ethics declarations

Competing interests

C.P., H.M., O.S, T.B. and F.A.R. have a pending patent application for the anti-RBD monoclonal antibodies described in the present study (PCT/FR2021/070522). F.A.R. is a member of the Board of MELETIOS Therapeutics and of the Scientific Advisory Board of eureKARE. The remaining authors declare no competing interests.

Additional information

Peer review information *Nature* thanks the anonymous reviewers for their contribution to the peer review of this work.

Publisher's note Springer Nature remains neutral with regard to jurisdictional claims in published maps and institutional affiliations.

Extended data figures and tables

Extended Data Fig. 1 Schematic overview of the B.1.617 sublineage and VOCs.

a, b, Schematic overview of the B.1.617 sublineage (**a**) and the VOCs B.1.1.7 (Alpha), P1 (Gamma) and B.1.351 (Beta) (**b**). Consensus sequences with a focus on the spike protein were built with the Sierra tool³⁰. Amino acid modifications in comparison to the ancestral Wuhan-Hu-1 sequence (NC_045512) are indicated.

Extended Data Fig. 2 SARS-CoV-2 variants induce syncytia in S-Fuse cells.

S-Fuse cells were exposed to the indicated SARS-CoV-2 strain (at a MOI of 10^{-3}). The cells become GFP⁺ when they fuse together. After 20 h, infected cells were stained with anti-spike antibodies and Hoechst to visualize nuclei. Syncytia (green), spike protein (red) and nuclei (blue) are shown. Representative images from three independent experiments are shown. Scale bar, 50 μm .

Extended Data Fig. 3 Global phylogeny of SARS-CoV-2 highlighting the B.1.617 lineage.

The maximum likelihood tree was inferred using IQ-Tree, as implemented in the Nextstrain pipeline on a subsampled dataset of 3,794 complete genomes. Branch lengths are scaled according to the number of nucleotide substitutions from the root of the tree. The branches corresponding to key lineages are coloured: B.1.1.7, dark blue; B.1.351, light blue; P.1, beige; B.1.617, pink; B.1.617.1, green; B.1.617.2, red; and B.1.617.3, orange. A black circle indicates the position of the viruses studied here.

Extended Data Fig. 4 Mapping mutations of the Delta variant and other variants of concern to the surface of the spike protein.

a, The spike protein trimer (Protein Data Bank code: 6XR8, corresponding to a closed spike trimer with all three RBDs in the ‘down’ conformation) is shown with its surface coloured according to domains: NTD in dark blue, RBD in green, the remainder of S1 in yellow and S2 in light blue. Interfaces between protomers were left white to help visualize the boundaries of the protomers. The three polypeptide chains in the trimer

were arbitrarily defined as A, B and C. Surface patches corresponding to residues mutated in the Delta variant are coloured in red. The bottom panel has the front protomer (chain A) removed to show the trimer interface (buried regions in the trimer are in white). The mutations in Delta are labelled in the bottom panel. **b**, NTD shown in three orthogonal views. The left panel corresponds roughly to the orientation seen in chain B in **a**, and the middle panel shows a view from the back. The right panel shows a view from the top of the trimer. Mutations found in the main variants of concern are indicated. The mutations found in the Delta variant are in red. **c**, RBD shown in three orthogonal views, coloured according to solvent exposure in the context of the closed spike: green and white indicate exposed and buried surfaces, as in **a**. The ACE2-binding surface is coloured in pink. The left panel shows a view from the top of the trimer, and the middle panel a view from below. The right panels show a view down the ACE2-binding surface, highlighted in pink in the bottom panel. Mutations found in the main variants of concern are indicated. The mutations found in the Delta variant are in red. The ovals indicate the epitope regions of the four main classes of anti-RBD neutralizing antibodies. Note that the mutations on the RBD cluster all around the ACE2 patch. Panels were prepared with the PyMOL Molecular Graphics System, v.2.1 (Schrödinger).

Extended Data Fig. 5 Neutralization of the SARS-CoV-2 variants D614G, Alpha, Beta and Delta by monoclonal antibodies that target the RBD and the NTD domains.

Neutralization curves of monoclonal antibodies. Dose–response analysis of the neutralization by four anti-RBD and four anti-NTD antibodies on the D614G strain (grey) and the Alpha (dark blue), Beta (light blue) and Delta (orange) variants. Data are mean ± s.d. of three independent experiments.

[Source data](#)

Extended Data Fig. 6 Binding of anti-SARS-CoV-2 monoclonal antibodies to Vero cells infected with the SARS-CoV-2 variants D614G, Alpha, Beta and Delta.

Vero cells were infected with the indicated variants at a MOI of 0.1. After 48 h, cells were stained with anti-SARS-CoV-2 monoclonal antibodies ($1 \mu\text{g ml}^{-1}$) and analysed by flow-cytometry. **a**, Gating strategy. **b**, Histograms show the binding of bamlanivimab, imdevimab and RBD-85 to Vero cells infected with the indicated variants. **c**, Radar charts represent for each antibody the logarithm of the mean of fluorescent intensity of the staining, relative to the non-infected condition. Data are representative of three independent experiments.

[Source data](#)

Extended Data Fig. 7 Sensitivity of the SARS-CoV-2 variants D614G, Alpha, Beta and Delta to sera from convalescent individuals and vaccinated individuals.

a, ED₅₀ values for the neutralizing activity of sera from convalescent individuals from the Orléans cohort against the four viral variants. Samples were collected 6 months after the onset of symptoms (M6 POS). The sensitivity of the D614G and Alpha variants to sera from 25 individuals has been described previously¹¹. Fifty-six sera (including the 25 previous sera) were tested against the Beta and Delta variants. Neutralization data obtained in this study and in ref. ¹¹ were compared (middle) and correlated (right). Similar results were obtained, allowing the datasets to be bridged. Data are mean from two independent experiments. The dotted line indicates the limit of detection (ED₅₀ = 30). A two-sided Kruskal–Wallis test with Dunn’s multiple comparison was performed between each of the viral strains. *P < 0.05, **P < 0.01, ***P < 0.001, ****P < 0.0001. D614G versus Beta, P = 0.0153; D614G versus Delta, P = 0.0008; Alpha versus Delta, P = 0.0014. **b**, ED₅₀ values for the neutralizing activity of sera from individuals who received a Pfizer vaccine, sampled at week 16 (corresponding to week 13 after the second dose). Data are mean from two independent experiments. The dotted line indicates the limit of detection (ED₅₀ = 30). A two-sided Kruskal–Wallis test with Dunn’s multiple comparison was performed between each viral strain. *P < 0.05, **P < 0.01, ***P < 0.001, ****P < 0.0001. D614G versus Beta, P < 0.0001; D614G versus Delta, P = 0.0375; Alpha versus Beta, P < 0.0001; Alpha versus Delta, P = 0.0375. **c–e**, Fraction of neutralizers in the cohorts of convalescent or vaccinated individuals. Individuals with an ED₅₀ of neutralization above 30 were categorized as neutralizers and are indicated in blue. Non-neutralizers are in grey. **c**, Analysis of convalescent individuals from the Orléans cohort collected at month 6 (left; related to **a**), and unvaccinated (middle; related to Fig. ^{2a}) or vaccinated (right, related to Fig. ^{2a}) individuals from the Strasbourg cohort collected at month 12. **d**, Sera from recipients of the Pfizer vaccine were sampled at week 3 (left), week 8 (middle) (both related to Fig. ^{2c}) and week 16 (right; related to **b**) after vaccination. **e**, Sera from recipients of the AstraZeneca vaccine were sampled at week 10 (left) and week 16 (right) after vaccination (related to Fig. ^{2c}). The numbers indicate the percentage of neutralizers.

[Source data](#)

Extended Data Table 1 Characteristics of the two cohorts of convalescent individuals

[Full size table](#)

Extended Data Table 2 Characteristics of the cohort of vaccinated individuals

[Full size table](#)

Supplementary information

Supplementary Table 1

Supplementary Table acknowledging the laboratories who contributed to the GISAID sequences used in the Extended Data Fig. 3.

Reporting Summary

Source data

Source Data Fig. 1

Source Data Fig. 2

Source Data Extended Data Fig. 5

Source Data Extended Data Fig. 6

Source Data Extended Data Fig. 7

Rights and permissions

Reprints and Permissions

About this article



Check for
updates

Cite this article

Planas, D., Veyer, D., Baidaliuk, A. *et al.* Reduced sensitivity of SARS-CoV-2 variant Delta to antibody neutralization. *Nature* **596**, 276–280 (2021).
<https://doi.org/10.1038/s41586-021-03777-9>

[Download citation](#)

- Received: 26 May 2021
- Accepted: 29 June 2021
- Published: 08 July 2021
- Issue Date: 12 August 2021
- DOI: <https://doi.org/10.1038/s41586-021-03777-9>

Comments

By submitting a comment you agree to abide by our [Terms](#) and [Community Guidelines](#). If you find something abusive or that does not comply with our terms or guidelines please flag it as inappropriate.

[Download PDF](#)

Advertisement

This article was downloaded by **calibre** from <https://www.nature.com/articles/s41586-021-03777-9>

| [Section menu](#) | [Main menu](#) |

- Article
- [Published: 21 July 2021](#)

SAR1B senses leucine levels to regulate mTORC1 signalling

- [Jie Chen](#) [ORCID: orcid.org/0000-0002-7091-7231](#)^{1,2} nat,
- [Yuhui Ou](#)¹ nat,
- [Rong Luo](#)³,
- [Jie Wang](#)⁴,
- [Dong Wang](#)¹,
- [Jialiang Guan](#)³,
- [Yi Li](#)^{1,2},
- [Peixue Xia](#)²,
- [Peng R. Chen](#) [ORCID: orcid.org/0000-0002-0402-7417](#)^{2,4} &
- [Ying Liu](#) [ORCID: orcid.org/0000-0002-3328-026X](#)^{1,2,5}

[Nature](#) volume 596, pages 281–284 (2021) [Cite this article](#)

- 9555 Accesses
- 36 Altmetric
- [Metrics details](#)

Subjects

- [Cell biology](#)
- [Nutrient signalling](#)

Abstract

The mTOR complex 1 (mTORC1) controls cell growth in response to amino acid levels¹. Here we report SAR1B as a leucine sensor that regulates mTORC1 signalling in response to intracellular levels of leucine. Under conditions of leucine deficiency, SAR1B inhibits mTORC1 by physically targeting its activator GATOR2. In conditions of leucine sufficiency, SAR1B binds to leucine, undergoes a conformational change and dissociates from GATOR2, which results in mTORC1 activation. SAR1B–GATOR2–mTORC1 signalling is conserved in nematodes and has a role in the regulation of lifespan. Bioinformatic analysis reveals that SAR1B deficiency correlates with the development of lung cancer. The silencing of SAR1B and its parologue SAR1A promotes mTORC1-dependent growth of lung tumours in mice. Our results reveal that SAR1B is a conserved leucine sensor that has a potential role in the development of lung cancer.

Access options

Subscribe to Journal

Get full journal access for 1 year

\$199.00

only \$3.90 per issue

[Subscribe](#)

All prices are NET prices.

VAT will be added later in the checkout.

Tax calculation will be finalised during checkout.

Rent or Buy article

Get time limited or full article access on ReadCube.

from \$8.99

[Rent or Buy](#)

All prices are NET prices.

Additional access options:

- [Log in](#)
- [Access through your institution](#)
- [Learn about institutional subscriptions](#)

Fig. 1: SAR1B senses intracellular leucine levels to regulate mTORC1 signalling through GATOR2.

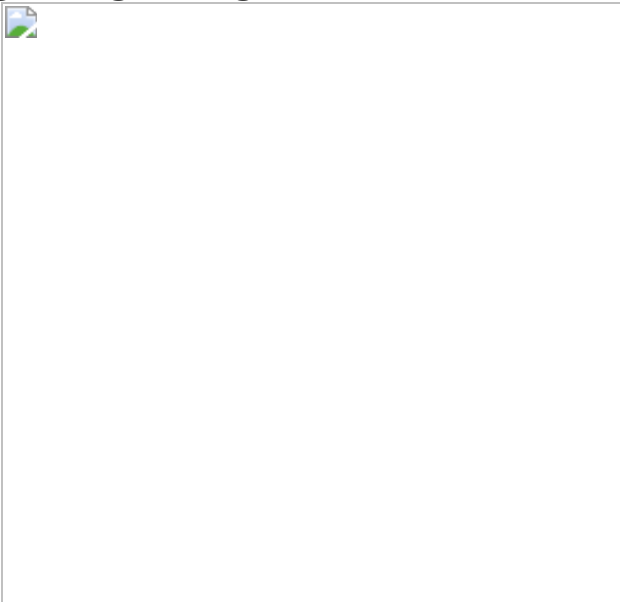


Fig. 2: SAR1B directly binds leucine.

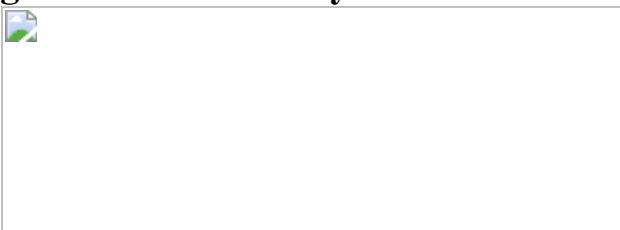


Fig. 3: *sar-1* has a conserved role in *C. elegans*.

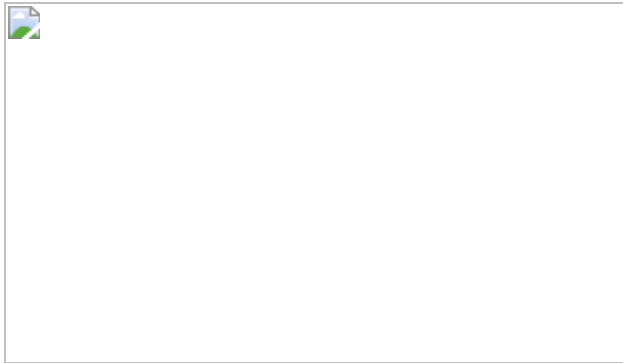
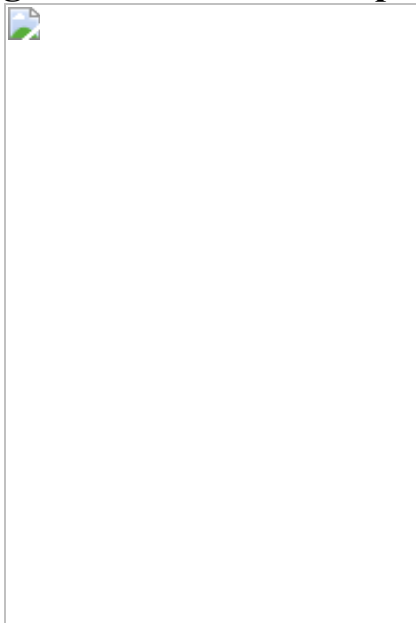


Fig. 4: SAR1B acts as a potential tumour suppressor in lung cancer.



Data availability

All data that support the findings of this study are contained in the Article and its [Supplementary Information](#); any further relevant data are available from corresponding authors upon reasonable request. [Source data](#) are provided with this paper.

References

1. 1.

Dibble, C. C. & Manning, B. D. Signal integration by mTORC1 coordinates nutrient input with biosynthetic output. *Nat. Cell Biol.* **15**,

555–564 (2013).

[CAS](#) [Article](#) [Google Scholar](#)

2. 2.

Wullschleger, S., Loewith, R. & Hall, M. N. TOR signaling in growth and metabolism. *Cell* **124**, 471–484 (2006).

[CAS](#) [Article](#) [Google Scholar](#)

3. 3.

Jewell, J. L., Russell, R. C. & Guan, K. L. Amino acid signalling upstream of mTOR. *Nat. Rev. Mol. Cell Biol.* **14**, 133–139 (2013).

[CAS](#) [Article](#) [Google Scholar](#)

4. 4.

Bar-Peled, L. et al. A Tumor suppressor complex with GAP activity for the Rag GTPases that signal amino acid sufficiency to mTORC1. *Science* **340**, 1100–1106 (2013).

[ADS](#) [CAS](#) [Article](#) [Google Scholar](#)

5. 5.

Chantranupong, L. et al. The CASTOR proteins are arginine sensors for the mTORC1 pathway. *Cell* **165**, 153–164 (2016).

[CAS](#) [Article](#) [Google Scholar](#)

6. 6.

Wolfson, R. L. et al. Sestrin2 is a leucine sensor for the mTORC1 pathway. *Science* **351**, 43–48 (2016).

[ADS](#) [CAS](#) [Article](#) [Google Scholar](#)

7. 7.

Zanetti, G., Pahuja, K. B., Studer, S., Shim, S. & Schekman, R. COPII and the regulation of protein sorting in mammals. *Nat. Cell Biol.* **14**, 20–28 (2012).

[CAS](#) [Article](#) [Google Scholar](#)

8. 8.

Sancak, Y. et al. The Rag GTPases bind raptor and mediate amino acid signaling to mTORC1. *Science* **320**, 1496–1501 (2008).

[ADS](#) [CAS](#) [Article](#) [Google Scholar](#)

9. 9.

Wolfson, R. L. et al. KICSTOR recruits GATOR1 to the lysosome and is necessary for nutrients to regulate mTORC1. *Nature* **543**, 438–442 (2017).

[ADS](#) [CAS](#) [Article](#) [Google Scholar](#)

10. 10.

Lynch, C. J., Fox, H. L., Vary, T. C., Jefferson, L. S. & Kimball, S. R. Regulation of amino acid-sensitive TOR signaling by leucine analogues in adipocytes. *J. Cell. Biochem.* **77**, 234–251 (2000).

[CAS](#) [Article](#) [Google Scholar](#)

11. 11.

Lynch, C. J. Role of leucine in the regulation of mTOR by amino acids: revelations from structure–activity studies. *J. Nutr.* **131**, 861S–865S (2001).

[CAS](#) [Article](#) [Google Scholar](#)

12. 12.

Lapierre, L. R. et al. The TFEB orthologue HLH-30 regulates autophagy and modulates longevity in *Caenorhabditis elegans*. *Nat. Commun.* **4**, 2267 (2013).

[ADS](#) [Article](#) [Google Scholar](#)

13. 13.

Chen, J. et al. Metformin extends *C. elegans* lifespan through lysosomal pathway. *eLife* **6**, e31268 (2017).

[Article](#) [Google Scholar](#)

14. 14.

Vellai, T. et al. Genetics: influence of TOR kinase on lifespan in *C. elegans*. *Nature* **426**, 620 (2003).

[ADS](#) [CAS](#) [Article](#) [Google Scholar](#)

15. 15.

Harrison, D. E. et al. Rapamycin fed late in life extends lifespan in genetically heterogeneous mice. *Nature* **460**, 392–395 (2009).

[ADS](#) [CAS](#) [Article](#) [Google Scholar](#)

16. 16.

Guertin, D. A. & Sabatini, D. M. Defining the role of mTOR in cancer. *Cancer Cell* **12**, 9–22 (2007).

[CAS](#) [Article](#) [Google Scholar](#)

17. 17.

Ding, B., Parmigiani, A., Yang, C. & Budanov, A. V. Sestrin2 facilitates death receptor-induced apoptosis in lung adenocarcinoma cells through regulation of XIAP degradation. *Cell Cycle* **14**, 3231–3241 (2015).

[CAS](#) [Article](#) [Google Scholar](#)

18. 18.

Chen, K. B. et al. Sestrin2 expression is a favorable prognostic factor in patients with non-small cell lung cancer. *Am. J. Transl. Res.* **8**, 1903–1909 (2016).

[CAS](#) [PubMed](#) [PubMed Central](#) [Google Scholar](#)

19. 19.

Buse, M. G. & Reid, S. S. Leucine. a possible regulator of protein turnover in muscle. *J. Clin. Invest.* **56**, 1250–1261 (1975).

[CAS](#) [Article](#) [Google Scholar](#)

20. 20.

Chen, J. et al. KLHL22 activates amino-acid-dependent mTORC1 signalling to promote tumorigenesis and ageing. *Nature* **557**, 585–589 (2018).

[ADS](#) [CAS](#) [Article](#) [Google Scholar](#)

[Download references](#)

Acknowledgements

We thank I. Hanson for reading and editing the manuscript. This work was supported by the National Natural Science Foundation of China (31925012 and 91854205), the National Key Research and Development Program of China (2017YFA0504000973) and an HHMI International Research

Scholar Program (55008739) to Y. Liu. Y. Liu was also supported by Beijing Advanced Innovation Center for Genomics, Peking-Tsinghua Center for Life Sciences, and the Tencent Foundation through the XPLORER PRIZE.

Author information

Author notes

1. These authors contributed equally: Jie Chen, Yuhui Ou

Affiliations

1. State Key Laboratory of Membrane Biology, Institute of Molecular Medicine, College of Future Technology, Peking University, Beijing, China

Jie Chen, Yuhui Ou, Dong Wang, Yi Li & Ying Liu

2. Peking–Tsinghua Center for Life Sciences, Academy for Advanced Interdisciplinary Studies, Peking University, Beijing, China

Jie Chen, Yi Li, Peixue Xia, Peng R. Chen & Ying Liu

3. PKU–Tsinghua–NIBS Graduate Program, Academy for Advanced Interdisciplinary Studies, Peking University, Beijing, China

Rong Luo & Jialiang Guan

4. Synthetic and Functional Biomolecules Center, Beijing National Laboratory for Molecular Sciences, College of Chemistry and Molecular Engineering, Peking University, Beijing, China

Jie Wang & Peng R. Chen

5. Beijing Advanced Innovation Center for Genomics, Beijing, China

Ying Liu

Authors

1. Jie Chen

[View author publications](#)

You can also search for this author in [PubMed](#) [Google Scholar](#)

2. Yuhui Ou

[View author publications](#)

You can also search for this author in [PubMed](#) [Google Scholar](#)

3. Rong Luo

[View author publications](#)

You can also search for this author in [PubMed](#) [Google Scholar](#)

4. Jie Wang

[View author publications](#)

You can also search for this author in [PubMed](#) [Google Scholar](#)

5. Dong Wang

[View author publications](#)

You can also search for this author in [PubMed](#) [Google Scholar](#)

6. Jialiang Guan

[View author publications](#)

You can also search for this author in [PubMed](#) [Google Scholar](#)

7. Yi Li

[View author publications](#)

You can also search for this author in [PubMed](#) [Google Scholar](#)

8. Peixue Xia

[View author publications](#)

You can also search for this author in [PubMed](#) [Google Scholar](#)

9. Peng R. Chen

[View author publications](#)

You can also search for this author in [PubMed](#) [Google Scholar](#)

10. Ying Liu

[View author publications](#)

You can also search for this author in [PubMed](#) [Google Scholar](#)

Contributions

J.C., Y.O. and Y. Liu conceived the studies. J.C. and Y.O. performed most of the experiments and analysed the data with help from R.L. and D.W. Y. Li and P.X. generated worm strains. J.G. and J.C. performed bioinformatic analysis. J.W. and P.R.C. synthesized the leucine probe. J.C., Y.O. and Y. Liu wrote the manuscript.

Corresponding authors

Correspondence to [Jie Chen](#) or [Ying Liu](#).

Ethics declarations

Competing interests

The authors declare no competing interests.

Additional information

Peer review information *Nature* thanks Tibor Vellai and the other, anonymous, reviewer(s) for their contribution to the peer review of this work. Peer reviewer reports are available.

Publisher's note Springer Nature remains neutral with regard to jurisdictional claims in published maps and institutional affiliations.

Extended data figures and tables

Extended Data Fig. 1 SAR1B regulates leucine-dependent mTORC1 signalling.

a, Identification of amino-acid-sensitive GATOR2-interacting proteins by immunoprecipitation and mass spectrometry analysis. **b, c**, Knockdown of SAR1B specifically affects leucine-dependent mTORC1 signalling. AAs, amino acid mixture. **d**, SAR1B is not involved in insulin-dependent mTORC1 signalling. **e, f**, Knockdown of SAR1B suppresses the induction of autophagy under leucine starvation (**e**), which is altered by administration of the mTORC1 inhibitor rapamycin (**f**). Data are mean \pm s.e.m., $n = 3$ biologically independent repeats. *** $P < 0.001$; unpaired, two-tailed Student's *t*-test. **g**, Expression of Flag-tagged SAR1B restores leucine sensitivity in SAR1B-deficient cells. **h**, SAR1B functions upstream of Rag GTPase. Rag^{DN}, dominant-negative Rag GTPase. **i**, SAR1B is required for preventing mTORC1 lysosomal localization under leucine starvation. LAMP2, lysosome marker. **j, k**, SAR1A compensates for the loss of SAR1B in mTORC1 signalling. **l**, mTORC1 activity is not affected in SAR1B-knockout cells. **m, n**, Knockdown of SAR1B upregulates the transcription of SAR1A. Data are mean \pm s.e.m., $n = 3$ biologically independent repeats. ns, no significant difference; ** $P < 0.01$; *** $P < 0.001$; unpaired, two-tailed Student's *t*-test. **o**, Simultaneous silencing of SAR1A and SAR1B persistently activates mTORC1. For gel source data, see Supplementary Fig. 1.

Extended Data Fig. 2 SAR1B regulates mTORC1 in a COPII-and GTPase activity-independent manner.

a–c, Locking SAR1A and SAR1B into GDP- or GTP-loaded states does not affect their roles in regulating mTORC1 activity (**a, b**) or mTORC1 localization (**c**). **d, e**, Knockdown of SAR1B, but not other COPII components, affects the leucine sensitivity of mTORC1. Knockdown

efficiencies were quantified by qPCR. Data are mean \pm s.e.m., $n = 3$ biologically independent repeats. ** $P < 0.01$; *** $P < 0.001$; unpaired, two-tailed Student's t -test. For gel source data, see Supplementary Fig. 1.

Extended Data Fig. 3 SAR1B modulates mTORC1 activity by interacting with GATOR2.

a, b, SAR1B interacts with the GATOR2 subunit SEH1L (**a**) but not the GATOR1 subunit DEPDC5 (**b**) in a leucine-sensitive fashion. MG132 was added to prevent proteasomal degradation of DEPDC5²⁰. **c**, The interaction of SAR1B with GATOR2 is sensitive to leucine starvation, but not to arginine starvation. The asterisks represent the IgG light chain. **d**, SAR1A also interacts with GATOR2 in a leucine-sensitive manner. **e**, Preparation of tag-free SAR1B recombinant proteins. GF, gel-filtration chromatography; Q, anion-exchange chromatography. **f**, SAR1B directly binds MIOS but not other GATOR2 subunits. **g, h**, Depletion of MIOS abolishes the interaction between SAR1B and GATOR2. **i**, SAR1B regulates mTORC1 signalling in a GATOR2-dependent manner.

Extended Data Fig. 4 The binding of SAR1B with GATOR2 is essential for the regulation of mTORC1 signalling.

a, Alignment of SAR1B protein sequences across species by Jalview. Identical residues (*) and similar (:) residues are indicated. **b**, Structure of hamster SAR1B (Protein Data Bank code 1F6B) displayed by PyMOL, with H58, E114 and E122 highlighted. **c**, SAR1B mutants that are incapable of binding GATOR2 are unable to prevent mTORC1 lysosomal localization under leucine deficiency. LAMP2, lysosome marker. mTOR–lysosome colocalization was quantified. Data are mean \pm s.e.m., $n = 3$ biologically independent repeats. ns, no significant difference; *** $P < 0.001$; unpaired, two-tailed Student's t -test. For gel source data, see Supplementary Fig. 1.

Extended Data Fig. 5 Leucine stimulates SAR1B dissociation from GATOR2 and lysosomes in vitro.

a, Isolation of the GATOR2 protein complex from cells by anti-Flag immunoprecipitation. **b, c**, Leucine, but not any other amino acid, stimulates SAR1B dissociation from the GATOR2 protein complex in vitro. The asterisks represent the IgG light chain. **d**, Intracellular distribution of SAR1B in the presence or absence of leucine. **e**, SAR1B associates with lysosomes isolated from leucine-starved cells. The addition of leucine to the lysosomes stimulates SAR1B dissociation in vitro. **f**, SAR1B mutants that are incapable of binding to MIOS cannot associate with lysosomes. Twenty μM of leucine was used in this in vitro assay. **g**, SAR1B disassociates from GATOR2 complex derived from cells that are triple knockout for sestrin 1, sestrin 2 and sestrin 3 upon leucine stimulation in vitro. **h**, SAR1B does not interact with sestrin 2. For gel source data, see Supplementary Fig. 1.

Extended Data Fig. 6 SAR1B undergoes a conformational change and dissociates from GATOR2 upon binding to leucine.

a, b, SAR1B recombinant proteins purified from bacteria do not bind to radiolabelled leucine. Sestrin 2, positive control. Rap2a, negative control. Data are mean \pm s.e.m., $n = 3$ repeated measurements for one biological sample. ns, no significant difference; *** $P < 0.001$; unpaired, two-tailed Student's *t*-test. **c, d**, SAR1B recombinant proteins purified from HEK293T cells bind to radiolabelled leucine in vitro. Data are mean \pm s.e.m., $n = 3$ repeated measurements for one biological sample. ns, no significant difference; *** $P < 0.001$; unpaired, two-tailed Student's *t*-test. **e**, Leucine binding induces a conformational change of SAR1B. Data are mean \pm s.e.m., $n = 3$ biologically independent repeats. **f, g**, SAR1A recombinant proteins purified from HEK293T cells bind to leucine. **h, i**, SAR1B mutants that are incapable of interacting with MIOS bind to leucine with an affinity similar to that of wild-type SAR1B. Data are mean \pm s.e.m., $n = 3$ biologically independent repeats. **j, k**, SAR1B mutants with impaired leucine-binding ability undergo little or no conformational change upon leucine supplementation. Data are mean \pm s.e.m., $n = 3$ biologically independent repeats. **l, m**, SAR1B mutants with impaired leucine-binding ability persistently associate with GATOR2 (**l**) and lysosomes (**m**) even in the presence of 20 μM leucine. **n**, Sestrin 2 directly binds SEH1L but not other subunits of GATOR2. **o**, SAR1B and sestrin 2 sequentially dissociate from GATOR2 in vitro upon stimulation with increasing concentrations of

leucine. The asterisks represent the IgG light chain. **p**, **q**, Treatment of cells with increasing leucine concentrations stimulates a sequential dissociation of SAR1B and sestrin 2 from GATOR2 (**p**) and elicits a two-phase activation of mTORC1 (**q**). For gel source data, see Supplementary Fig. 1.

Extended Data Fig. 7 SAR1B and sestrin 2 detect different structural features of leucine.

a, Leucine analogues with modifications at the amino group, the carboxyl group or the side chain. **b**, **c**, Modifications at the carboxyl group of leucine are tolerated by SAR1B. Sestrin 2 tolerates modifications at the side chain to some extent. Protein complexes were immunopurified from leucine-starved HEK293T cells stably expressing tagged GATOR2. Leucine analogues were directly added to immunoprecipitates in vitro to induce SAR1B or sestrin 2 dissociation. The asterisks represent the IgG light chain. **d**, The workflow for capture of receptor proteins by LeuProbe. LeuProbe has a modified carboxyl group compared to native leucine. **e**, LeuProbe has an ability to stimulate mTORC1 activation similar to that of native leucine. **f**, LeuProbe captures SAR1B, but not sestrin 2. **g**, Interaction of LeuProbe with SAR1B can be competed against by an excess amount of native leucine. For gel source data, see Supplementary Fig. 1.

Extended Data Fig. 8 Different leucine sensing events in myotubes and adipocytes.

a, SAR1B, but not other COPII components, is highly expressed in mouse muscle tissue. Expression, transcripts per million. **b**, Similar to sestrin 2, sestrin 1 partially tolerates modifications at the side chain of leucine. The asterisk represents the IgG light chain. **c**, Differentiation of C2C12 and 3T3-L1 cells into myotubes and adipocytes. **d**, SAR1B and sestrin 1 are expressed in myotubes and interact with GATOR2, whereas sestrin 2 is expressed in adipocytes and interacts with GATOR2. Protein–protein interactions were assayed by anti-WDR24 immunoprecipitation. **e**, Activation of mTORC1 in myotubes and adipocytes in response to leucine analogue treatments. **f**, **g**, The indicated leucine analogues can be transported into cells without being hydrolysed. Columns are data from

n = 1 biological repeat. **h, i**, Leucine starvation induces a sequential binding of sestrin 1 and SAR1B to GATOR2 and a corresponding two-phase mTORC1 inactivation in myotubes. **j, k**, Leucine starvation induces the binding of sestrin 2 to GATOR2 and therefore mTORC1 inhibition in adipocytes. **l, m**, Leucine stimulation induces the dissociation of sestrin 2 from GATOR2 and therefore mTORC1 activation in adipocytes. For gel source data, see Supplementary Fig. 1.

Extended Data Fig. 9 SAR1B has a conserved role in regulating TORC1 signalling in *C. elegans*.

a–c, *sar-1*, but not any other subunit of COPII, is involved in *CeTORC1* signalling. HLH-30 nuclear localization is quantified to represent TORC1 inactivation. Data are mean \pm s.e.m., *n* = 3 biologically independent repeats. ns, no significant difference; ***P* < 0.01; ****P* < 0.001; unpaired, two-tailed Student's *t*-test. **d–g**, Expression of the codon-optimized human SAR1B::GFP restores *CeTORC1* signalling in *sar-1*-deficient *C. elegans*. Data are mean \pm s.e.m., *n* = 3 biologically independent repeats. ****P* < 0.001; unpaired, two-tailed Student's *t*-test. **h–j**, *sar-1* regulates *CeTORC1* in a GATOR2-dependent manner. CeMios, *F39C12.1*; CeShe1L, *npp-18*. Data are mean \pm s.e.m., *n* = 3 biologically independent repeats. ***P* < 0.01; ****P* < 0.001; unpaired, two-tailed Student's *t*-test. **k, l**, *sar-1* and *sesn-1* are not involved in arginine- or isoleucine-dependent TORC1 signalling in *C. elegans*. Data are mean \pm s.e.m., *n* = 3 biologically independent repeats. ****P* < 0.001; unpaired, two-tailed Student's *t*-test. **m**, Tissue distribution of *sar-1* and *sesn-1* in *C. elegans*. **n**, *sar-1* regulates worm lifespan in a GATOR2-dependent manner. *n* = 3 biologically independent repeats. Data are representative one repeat. log-rank test for survival comparisons. **o**, RNAi knockdown efficiency of *let-363*. Data are mean \pm s.e.m., *n* = 3 biologically independent repeats. ****P* < 0.001; unpaired, two-tailed Student's *t*-test. **p, q**, *sar-1* functions upstream of TORC1 to regulate *C. elegans* lifespan. *n* = 3 biologically independent repeats. Data are representative one repeat. log-rank test for survival comparisons. For gel source data, see Supplementary Fig. 1

[Source data](#).

Extended Data Fig. 10 Deficiency of SAR1A and SAR1B correlates with mTORC1 activation in lung cancers and promotes anchorage-independent cell growth.

a, Tables summarizing the number and frequency of SAR1B alterations in human lung squamous cell carcinoma and lung adenocarcinoma datasets. **b**, *SAR1A* mRNA levels are downregulated in cases with (w/) SAR1B deletion compared to those without (w/o) SAR1B deletion. Box plots show the median and quartiles (boxes) and minimum to maximum (whiskers).

*** $P < 0.001$; unpaired, one-tailed Student's *t*-test. **c**, SAR1A transcription cannot be upregulated in human lung cancer cells with SAR1B copy loss, in contrast to wild-type lung fibroblasts. Data are mean \pm s.e.m., $n = 3$ biologically independent repeats. ns, no significant difference;

*** $P < 0.001$; unpaired, two-tailed Student's *t*-test. **d**, mTORC1 is constitutively activated in human lung cancer cells with SAR1B copy loss.

e, Lower expression level of SAR1B correlates with worse prognoses in patients with lung cancer. log–rank test. **f**, **g**, Silencing of SAR1A and SAR1B in human lung fibroblasts leads to constitutive mTORC1 activation even under leucine deprivation. **h**, **i**, SAR1A and SAR1B regulate mTORC1 signalling in a Rag-GTPase-dependent manner in human lung fibroblasts. Rag^{DN}, dominant-negative Rag GTPase. **j**, Deficiency of SAR1A and SAR1B promotes anchorage-independent cell growth in soft agar, and the cell growth is sensitive to treatment with 100 nM rapamycin (rapa.). Colony numbers were counted and indicated as columns. Data are mean \pm s.e.m., $n = 3$ biologically independent repeats. ns, no significant difference; *** $P_{\text{adj}} < 0.001$; one-way analysis of variance (ANOVA) test. **k**,

Silencing of SAR1A and SAR1B increases the sensitivity of human lung fibroblasts to rapamycin. For gel source data, see Supplementary Fig. 1.

Extended Data Fig. 11 Silencing of SAR1A and SAR1B promotes subcutaneous xenograft tumour growth.

Silencing of SAR1A and SAR1B promotes mTORC1-dependent growth of subcutaneous xenograft tumours. Tumour growth was recorded every other day. Tumour weights were obtained on the last day. Data are mean \pm s.e.m., $n = 10$ mice (with an expectation that $n = 9$ mice for HFL1 sgSAR1B plus

shSAR1A), one biological repeat. ns, no significant difference; *** $P_{\text{adj}} < 0.001$; One-way ANOVA test. For gel source data, see Supplementary Fig. 1

[Source data](#).

Extended Data Fig. 12 Deficiency of SAR1A and SAR1B promotes orthotopic xenograft tumour growth in the lung of mice.

a–c, Silencing of SAR1A and SAR1B promotes mTORC1-dependent growth of xenograft tumours in the lungs of mice. Lungs with tumours *in situ* (**a**, **b**) and representative haematoxylin and eosin staining of lung sections (**c**) are shown. Surface tumour lesion areas are calculated as mean \pm s.d.. HFL1: $n = 8$ mice for sgCtrl and shCtrl, sgSAR1B-1 and shSAR1A + rapa., sgSAR1B-2 and shSAR1A – rapa.; $n = 9$ mice for sgSAR1B-1 and shSAR1A – rapa., sgSAR1B-2 and shSAR1A + rapa.; IMR-90, $n = 8$ mice for sgCtrl and shCtrl, sgSAR1B-1 and shSAR1A – rapa., sgSAR1B-2 and shSAR1A – rapa.; $n = 9$ mice for sgSAR1B-1 and shSAR1A + rapa., sgSAR1B-2 and shSAR1A + rapa. One biological repeat. **d**, Immunohistochemical staining shows that silencing of SAR1A and SAR1B activates protein synthesis, inhibits autophagy and promotes cell proliferation in orthotopic lung tumours. **e**, Deficiency of SAR1A and SAR1B hyperactivates mTORC1 in the orthotopic tumours. **f**, Deficiency of sestrins in HLF1 cells stimulates continuous mTORC1 activation. **g–i**, Deficiency of sestrins promotes mTORC1-dependent growth of subcutaneous and lung orthotopic tumours. For subcutaneous tumours, data are mean \pm s.e.m., $n = 10$ mice (with an expectation that $n = 9$ mice for sgCtrl), one biological repeat. ** $P_{\text{adj}} < 0.01$, *** $P_{\text{adj}} < 0.001$; one-way ANOVA test. For orthotopic tumours, surface tumour lesion areas are calculated as mean \pm s.d., $n = 7$ mice for sgCtrl; $n = 9$ mice for sgRNAs against sestrins; $n = 8$ mice for sgRNAs against sestrins + rapa.. For gel source data, see Supplementary Fig. 1

[Source data](#).

Supplementary information

Supplementary Information

This file contains the Supplementary Methods.

Reporting Summary

Supplementary Figure 1

The uncropped western blots and gels.

Peer Review File

Source data

Source Data Fig. 3

Source Data Fig. 4

Source Data Extended Data Fig. 9

Source Data Extended Data Fig. 11

Source Data Extended Data Fig. 12

Rights and permissions

Reprints and Permissions

About this article



Cite this article

Chen, J., Ou, Y., Luo, R. *et al.* SAR1B senses leucine levels to regulate mTORC1 signalling. *Nature* **596**, 281–284 (2021).
<https://doi.org/10.1038/s41586-021-03768-w>

[Download citation](#)

- Received: 14 May 2020
- Accepted: 24 June 2021
- Published: 21 July 2021
- Issue Date: 12 August 2021
- DOI: <https://doi.org/10.1038/s41586-021-03768-w>

Comments

By submitting a comment you agree to abide by our [Terms](#) and [Community Guidelines](#). If you find something abusive or that does not comply with our terms or guidelines please flag it as inappropriate.

[Access through your institution](#)

[Change institution](#)

[Buy or subscribe](#)

Associated Content

How the amino acid leucine activates the key cell-growth regulator mTOR

- Tibor Vellai

News & Views 21 Jul 2021

Advertisement

This article was downloaded by **calibre** from <https://www.nature.com/articles/s41586-021-03768-w>

| [Section menu](#) | [Main menu](#) |

Rewiring of the ubiquitinated proteome determines ageing in *C. elegans*

[Download PDF](#)

- Article
- Open Access
- [Published: 28 July 2021](#)

Rewiring of the ubiquitinated proteome determines ageing in *C. elegans*

- [Seda Koyuncu](#)¹,
- [Rute Loureiro](#)¹,
- [Hyun Ju Lee](#)¹,
- [Prerana Wagle](#)¹,
- [Marcus Krueger](#) ORCID: orcid.org/0000-0002-5846-6941^{1,2} &
- [David Vilchez](#) ORCID: orcid.org/0000-0002-0801-0743^{1,2,3}

[Nature](#) volume 596, pages 285–290 (2021) [Cite this article](#)

- 20k Accesses
- 202 Altmetric
- [Metrics details](#)

Subjects

- [Ageing](#)
- [Proteasome](#)

Abstract

Ageing is driven by a loss of cellular integrity¹. Given the major role of ubiquitin modifications in cell function², here we assess the link between ubiquitination and ageing by quantifying whole-proteome ubiquitin signatures in *Caenorhabditis elegans*. We find a remodelling of the ubiquitinated proteome during ageing, which is ameliorated by longevity paradigms such as dietary restriction and reduced insulin signalling. Notably, ageing causes a global loss of ubiquitination that is triggered by

increased deubiquitinase activity. Because ubiquitination can tag proteins for recognition by the proteasome³, a fundamental question is whether deficits in targeted degradation influence longevity. By integrating data from worms with a defective proteasome, we identify proteasomal targets that accumulate with age owing to decreased ubiquitination and subsequent degradation. Lowering the levels of age-dysregulated proteasome targets prolongs longevity, whereas preventing their degradation shortens lifespan. Among the proteasomal targets, we find the IFB-2 intermediate filament⁴ and the EPS-8 modulator of RAC signalling⁵. While increased levels of IFB-2 promote the loss of intestinal integrity and bacterial colonization, upregulation of EPS-8 hyperactivates RAC in muscle and neurons, and leads to alterations in the actin cytoskeleton and protein kinase JNK. In summary, age-related changes in targeted degradation of structural and regulatory proteins across tissues determine longevity.

[Download PDF](#)

Main

Ageing can be delayed by evolutionary conserved pathways such as dietary restriction and reduced insulin/insulin-like growth factor (IGF-1) signalling¹. The attachment of the small protein ubiquitin to lysine residues of specific targets is a central pathway by which cellular decisions are made², but the effect of ubiquitination in ageing remains unclear. Numerous proteins are ubiquitinated in a dynamic and tightly regulated manner through a sequential mechanism that involves E3 ubiquitin ligases, which are responsible for substrate selection². However, deubiquitinating enzymes (DUBs) can reverse this process⁶.

The ubiquitination cascade also links additional molecules to the internal lysine sites of the primary ubiquitin. Ubiquitin has seven lysine residues, all of which can form polyubiquitin chains. A Lys48-linked polyubiquitin chain is the primary signal for degradation by the proteasome—the main selective proteolytic system in eukaryotic cells^{2,3}. As such, the ubiquitin–proteasome system regulates the levels of several structural and short-lived regulatory proteins. Here we asked whether ageing modifies the ubiquitination and targeted degradation of regulatory proteins that, in turn, could actively influence longevity. To this end, we used an antibody that recognizes di-glycine moieties linked by an isopeptide bond to lysine sites of proteins⁷. These epitopes, which constitute remnants of ubiquitination followed by tryptic digestion, can be engaged in biochemical isolation and mass spectrometry to provide site-specific information and quantification of ubiquitin modifications across the proteome⁷.

Ub-proteome remodelling during ageing

The median lifespan of wild-type *C. elegans* is 19 days⁸. Thus, we compared the ubiquitin (Ub)-modified proteome of worms at the first day of adulthood with young (day 5), mid-age (day 10) and aged adults (day 15). Moreover, we assessed age-matched long-lived genetic models of dietary restriction (*eat-2(ad1116)*) and reduced insulin/IGF-1 signalling (*daf2(e1370)*) (Fig. 1a). With high reproducibility between biological replicates, our assay identified ubiquitination sites for 3,373 peptides that correspond to 1,485 distinct proteins (Extended Data Fig. 1a, Supplementary Table 1). The levels of multiple Ub-peptides changed with age in wild-type and long-lived mutant worms compared with their respective day-1 adults (Fig. 1b, Supplementary Table 1). In wild-type worms, the total number of differentially abundant Ub-peptides increased after day 5. Most of these changes were linked to downregulated ubiquitination levels. By contrast, long-lived mutants had fewer downregulated Ub-peptides during ageing. In fact, *daf2* worms had an increased number of upregulated Ub-peptides with age (Fig. 1c,d). Given that *C. elegans* undergoes a widespread proteome remodelling during ageing^{9,10}, we quantified the total amounts of individual proteins to compare with Ub-peptides (Supplementary Table 2). In many instances, differences in ubiquitination levels could not be simply ascribed to a similar change in the protein amounts (Extended Data Fig. 1b–d, Supplementary Table 3).

Fig. 1: Rewiring of the Ub-proteome with age.



- a**, Scheme of ubiquitin proteomics by di-glycine (diGly) peptide enrichment in wild-type (WT) and long-lived mutant worms. **b**, Heat maps representing \log_2 -transformed fold changes in Ub-peptide levels at different days (D) of adulthood compared with the corresponding day-1 adult strain. For each strain, only Ub-peptides significantly

changed in at least one age are shown. **c**, Number of significantly downregulated and upregulated Ub-peptides compared with the respective day-1 adult strain. **d**, Percentage of downregulated and upregulated Ub-peptides among the total number of significantly changed Ub-peptides per condition. **e**, The \log_2 -transformed fold changes of differentially abundant Ub-peptides and their corresponding total protein levels comparing day-15 and day-5 wild-type worms. **f**, The \log_2 -transformed fold changes of differentially abundant Ub-peptides in day-15 wild-type worms and comparison with age-matched *eat-2* and *daf-2* mutants. In **b–f**, $n = 4$; two-sided *t*-test, false discovery rate (FDR) < 0.05 was considered significant. **g–i**, Immunoblot of Ub-proteins in wild-type (**g**), *eat-2(ad1116)* (**h**) and *daf-2(e1370)* (**i**) worms at different days of adulthood. α -tubulin was used as a loading control. The images are representative of four independent experiments. **j**, Immunoblot of Ub-proteins in wild-type worms treated with $13.7 \mu\text{g ml}^{-1}$ PR-619 (broad-spectrum DUB inhibitor) or vehicle control (dimethyl sulfoxide, DMSO) for 4 h before lysis. Representative of three independent experiments. For gel source data, see Supplementary Fig. [1](#).

[Full size image](#)

Because we detected a higher number of ubiquitination changes after day 5, we directly compared day-5 and day-15 wild-type worms. In aged worms, 350 Ub-peptides were upregulated, whereas 1,813 Ub-peptides were downregulated, which supports the idea that ageing is particularly associated with a loss of ubiquitination (Fig. [1e](#), Supplementary Table [4](#)). Only 123 upregulated and 582 downregulated Ub-peptides correlated with a change in the total protein levels in the same direction. The other differentially abundant Ub-peptides were inversely correlated with protein levels or corresponded to proteins that did not change in abundance with age (Fig. [1e](#), Extended Data Fig. [1e,f](#), Supplementary Table [5](#)). The amounts of Ub-peptides can be influenced by transcription, translation and proteolysis, which are dysregulated during ageing and rescued by longevity paradigms^{[1,3,11,12](#)}. Notably, pro-longevity pathways also prevented age-related changes in ubiquitination (Fig. [1f](#), Extended Data Fig. [1g](#), Supplementary Table [6](#)).

DUBs diminish ubiquitination with age

To further assess age-related changes in ubiquitination, we performed western blot analysis. Wild-type worms exhibited a global decrease in levels of Ub-protein after day 8 of adulthood (Fig. [1g](#), Extended Data Fig. [2a](#)). However, Ub-protein levels remained similar in *eat-2* mutants during ageing, and increased in *daf-2* mutants after day 1 (Fig. [1h,i](#), Extended Data Fig. [2b,c](#)). In contrast to their global downregulated ubiquitination, aged wild-type worms expressed higher or similar levels of ubiquitin-encoding genes (*ubq-1*, *ubq-2* and *ubl-1*) compared with either young wild-type

worms or age-matched long-lived mutants. Similarly, ageing and longevity paradigms did not change the expression of *usp-14*, a gene induced by ubiquitin deficiency¹³ (Extended Data Fig. 2d–g). Moreover, aged wild-type worms did not exhibit decreased total levels or half-life of protein ubiquitin itself (Extended Data Fig. 2h–j).

E3 ligases and DUBs directly modulate ubiquitination levels. In *C. elegans*, there are more than 170 E3 ligases¹⁴ but we only found significant changes in the expression of 12 E3s with age. By contrast, there are 45 DUBs in *C. elegans*⁶, but a higher proportion (14 DUBs) were upregulated in aged wild-type worms (Extended Data Fig. 3a, b, Supplementary Table 7). Dietary restriction rescued the levels of CSN-6, a component of the COP9 signalosome that removes ubiquitin-like proteins from cullin E3 complexes, inhibiting their activity and the subsequent ubiquitination of proteasomal targets¹⁵. In addition to CSN-6, reduced insulin/IGF-1 signalling prevented the upregulation of most of the age-dysregulated DUBs (Extended Data Fig. 3b). Knockdown of distinct age-dysregulated DUBs ameliorated loss of ubiquitination during ageing, including *csn-6* (which encodes the worm orthologue of human COPS6), *H34C03.2* (USP4), *F07A11.4* (USP19), *math-33* (USP7), *usp-5* (USP5), *usp-48* (USP48) and *otub-3* (OTUD6A) (Extended Data Fig. 3c–g). To examine whether increased DUB activity underlies the age-associated decline in ubiquitination, we used the broad-spectrum DUB inhibitor PR-619 (ref. 16). Notably, treatment with the DUB inhibitor in old worms was sufficient to rescue low ubiquitination levels and extend lifespan (Fig. 1j, Extended Data Fig. 3h).

Impaired targeted degradation with age

Given the high number of downregulated Ub-peptides during ageing, a subset of these events could reduce selective degradation by the proteasome. We found that 192 proteins were less ubiquitinated in at least one of their lysine sites during ageing, whereas the total levels of the protein increased (Fig. 2a, Extended Data Fig. 1e). If these proteins are age-dysregulated proteasomal targets, defects in proteasome activity could diminish their degradation in young worms. To decrease proteasome function, we knocked down the *rpn-6* proteasome subunit^{17,18}. Loss of proteasome activity resulted in widespread changes in the proteome of day-5 young adults (Extended Data Fig. 4a, Supplementary Table 8). In addition to potential indirect effects caused by proteasome dysfunction, upregulated proteins could include direct proteasome targets, particularly if they also have increased Ub-peptide levels. We identified 40 proteins that exhibit an increase in both their total and Ub-peptide levels after *rpn-6* RNA interference (RNAi) in young adults. By integrating data from untreated aged worms, we found that 10 proteasome-modulated proteins became more abundant with age, and at least one of their lysine sites was less ubiquitinated (Fig. 2a, Supplementary Table 8). The age-dysregulated proteasome targets were IFB-2, EPS-8, RPL-4, M01G12.9,

C46C2.2, F54D1.6, DDI-1, LEC-1, HSP-43 and USP-5. Notably, ageing or *rpn-6* knockdown did not increase the mRNA levels of most of these targets, including IFB-2 and EPS-8 (Extended Data Fig. 4b,c).

Fig. 2: Age-related deubiquitination impairs targeted degradation of longevity regulators.

 figure2

a, Ten Ub-proteins increase after *rpn-6* RNAi treatment in young wild-type adults (*rpn-6* RNAi/Vector RNAi) and become less ubiquitinated but more abundant with age (day 15/day 5). **b**, Volcano plot of proteins containing Lys48-linked polyUb in day-5 adult wild-type worms ($n = 3$, FDR < 0.05). The $-\log_{10}(P \text{ value})$ of a two-sided *t*-test is plotted against the \log_2 -transformed fold change values from immunoprecipitation (IP) with an antibody against Lys48-linked polyUb compared with a control anti-Flag antibody. Red dots indicate age-dysregulated proteasome targets. **c, d**, Knockdown of either *iβ-2* (**c**) or *eps-8* (**d**) after development extends lifespan ($P < 0.0001$). **e**, Western blot analysis with an antibody against IFB-2 of wild-type worms at different days of adulthood. α-tubulin is the loading control. Representative of four independent experiments. **f**, Western blot analysis with an antibody against EPS-8 of wild-type worms. Representative of three independent experiments. **g**, Western blot analysis with an antibody against IFB-2 of wild-type and IFB-2(K255R/K341R) (Ub-less) mutant worms at day 2 of adulthood. Representative of three independent experiments. **h**, Ubiquitin-less IFB-2 mutant worms have a shorter lifespan than wild-type worms ($P < 0.0001$). **i**, Western blot analysis with an antibody against EPS-8 of worms expressing endogenous wild-type EPS-8::HA or EPS-8(K524R/K583R/K621R)::HA (Ub-less) at day 1 of adulthood. Representative of three independent experiments. **j**, EPS-8 (Ub-less) mutants are short-lived ($P < 0.0001$). In lifespan experiments, P values were determined by two-sided log-rank test; $n = 96$ worms per condition. Lifespan data are representative of at least two independent experiments. Supplementary Table 11 contains replicate data of independent lifespan experiments. For gel source data, see Supplementary Fig. 1.

[Full size image](#)

Several age-dysregulated proteasome targets such as EPS-8 contained Lys48-linked polyUb chains for proteasomal recognition. By contrast, they did not have Lys63-linked polyUb, with the exception of LEC-1 and IFB-2 that contained both Lys63 and Lys48 ubiquitin linkages (Fig. 2b, Extended Data Fig. 4d, Supplementary Table 2). Together, our data indicate that the age-related deubiquitination of distinct proteins reduces their recognition and subsequent degradation by the proteasome.

Proteasome targets determine lifespan

Age-dysregulated proteasome targets such as EPS-8, IFB-2, RPL-4 and F54D1.6 are required for normal development^{19,20,21,22,23}. Whereas these factors endow benefits early in life, we asked whether their age-associated upregulation is detrimental for adult lifespan. We hypothesized that if age-dysregulated proteasome targets are not essential for adult viability, lowering their levels after development could prolong longevity. Both the chaperone *hsp-43* and *usp-5* are essential for cell viability^{24,25} and their knockdown in adult worms shortened lifespan (Extended Data Fig. 4e). By contrast, single knockdown of *iβ-2*, *eps-8*, *rpl-4*, *M01G12.9*, *C46C2.2* or *F54D1.6* during adulthood was sufficient to extend lifespan (Fig. 2c,d, Extended Data Fig. 4e).

Intrigued by the robust effects of IFB-2 and EPS-8 on lifespan, we confirmed by western blot that their protein levels increase with age (Fig. 2e,f, Extended Data Fig. 4f-h). We then asked whether the age-associated deubiquitination that affects proteins such as IFB-2 and EPS-8 is conserved across tissues. Using a worm tissue expression prediction tool²⁶, we classified proteins with ubiquitination changes according to their tissue expression. The bioinformatic analysis indicated that tissues such as the germline, muscle, intestine, epidermis or neurons express several proteins that contain downregulated Ub-peptides with age (Extended Data Fig. 5a, Supplementary Table 10). Similar to lysates from whole worms, the global amounts of Ub-proteins decreased in isolated germlines, intestines and heads during ageing, which indicates that the loss of ubiquitination occurs throughout the organism (Extended Data Fig. 5b). The amounts of the ubiquitously expressed EPS-8 protein²⁰ were increased in different somatic tissues with age (Extended Data Fig. 5c), which correlates with global deubiquitination across tissues. Because the *iβ-2* gene is specifically expressed in intestinal cells⁴, protein levels of IFB-2 were upregulated in the intestine of old worms but were not detectable in other tissues (Extended Data Fig. 5d).

Tissue-specific knockdown of *rpn-6* in the intestine, epidermis, neurons or muscle increased the amounts of EPS-8 in young worms, which indicates that the proteasome modulates EPS-8 in all of these tissues (Extended Data Fig. 5e-h). According to its intestinal-specific expression, only knockdown of *rpn-6* in the intestine upregulated

IFB-2 levels (Extended Data Fig. 5e–h). Together, these experiments support the idea that the ubiquitin–proteasome system acts in a cell-autonomous manner to regulate IFB-2 and EPS-8. Besides intracellular regulation, inter-organ communication also influences organismal ageing. For example, neurons elicit signals that modulate the ageing of distal tissues²⁷. To assess whether inter-organ communication influences global ubiquitination levels, we used *unc-13* mutant worms that are deficient in the release of neurotransmitters²⁸. Whereas blocking neurotransmission did not affect ubiquitination levels in young worms, it exacerbated the age-associated decline in older worms (Extended Data Fig. 5i). Concomitantly, the amounts of EPS-8 and IFB-2 were further upregulated in aged *unc-13* mutants compared with wild-type worms, which suggests that cell non-autonomous mechanisms impinge on organismal ubiquitination levels (Extended Data Fig. 5j, k).

To confirm a direct link between loss of ubiquitination in IFB-2 and EPS-8 with the regulation of longevity, we blocked the ubiquitination of endogenous IFB-2 and EPS-8 by generating lysine (K) to arginine (R) mutants. Among the three ubiquitinated sites identified in IFB-2, Lys255 and Lys341 exhibited a pronounced deubiquitination during ageing (Supplementary Table 1). Notably, the K255R/K341R double mutation increased IFB-2 protein levels in young adult worms and shortened lifespan (Fig. 2g, h, Extended Data Fig. 6a). Thus, upregulation of IFB-2 levels was sufficient to decrease lifespan, as further supported by overexpression experiments (Extended Data Fig. 6b).

Within EPS-8, Lys524, Lys583 and Lys621 showed a robust deubiquitination in aged worms (Extended Data Fig. 1f). Ubiquitin-less mutations did not result in loss of EPS-8 function, as EPS-8(K524R/K583R/K621R) mutants did not exhibit embryonic lethality or developmental arrest (Extended Data Fig. 6c, d). However, EPS-8(K524R/K583R/K621R) worms had upregulated EPS-8 protein levels at young adult stages, resulting in a short-lived phenotype (Fig. 2i, j). Notably, knockdown of *eps-8* after development was sufficient to rescue the short-lived phenotype of EPS-8(K524R/K583R/K621R) mutants (Extended Data Fig. 6e). Thus, the age-related deubiquitination and subsequent impaired degradation of IFB-2 and EPS-8 determine lifespan.

Intestinal alteration by increased IFB-2

Because age-dysregulated proteasome targets have different roles, they could act in a tissue-specific manner. Indeed, RNAi against the intermediate filament *iβ-2* in the intestine alone was sufficient to extend longevity, whereas RNAi in other tissues did not affect lifespan (Fig. 3a, Extended Data Fig. 7a, b). IFB-2 and other interacting intermediate filament proteins form the intermediate filament-rich layer—an evolutionary conserved region in the apical cytoplasm of intestinal cells that is

essential for intestinal morphogenesis and integrity⁴. During adulthood, pathological conditions impair the network of intestinal intermediate filaments such as IFB-2, which loses its typical enrichment in the apical region⁴. Because loss of intestinal integrity is also a characteristic of ageing²⁹, we examined the intracellular distribution of IFB-2. We found that ageing triggers the mislocalization of IFB-2 from the apical part to the rest of the cytoplasm and its accumulation into foci (Extended Data Fig. 7c, d). By filter trap experiments, we confirmed the aggregation of endogenous IFB-2 during ageing, a process accelerated by ubiquitin-less IFB-2 mutations (Fig. 3b, c, Extended Data Fig. 7e).

Fig. 3: Increased IFB-2 levels induce age-related intestinal alterations.



a, Intestinal-specific knockdown (KD) of *iβ-2* extends lifespan. *P* value determined by two-sided log-rank test; *n* = 96 worms per condition. Lifespan data are representative of two independent experiments. Supplementary Table 11 contains replicate data of independent experiments. **b**, Filter trap analysis with an antibody against IFB-2 of wild-type worms at different ages. Representative of eight independent experiments. **c**, Filter trap analysis with an antibody against IFB-2 of wild-type and IFB-2 (Ub-less) mutant worms. Representative of four independent experiments. **d, e**, Filter trap experiments with an antibody against GFP of worms expressing IFC-1::GFP under the *iβ-1* promoter (**d**) or IFP-1::GFP under the *iβ-1* promoter (**e**). Representative of two independent experiments. **f**, Quantification of bacterial colonization. Fluorescence of mCherry-expressing *E. coli* within the intestine relative to day 1 (D1) Vector RNAi. Data are mean ± s.e.m. D1 Vector RNAi, *n* = 56 worms from 3 independent experiments; D1 *iβ-2* RNAi, *n* = 35; D5 Vector RNAi, *n* = 53; D5 *iβ-2* RNAi, *n* = 55; D10 Vector RNAi, *n* = 45; D10 *iβ-2* RNAi, *n* = 39. **g**, Bacterial colonization relative to day-10 adult wild-type worms. Data are mean ± s.e.m. Wild-type, *n* = 50 worms from 3 independent experiments; Ub-less IFB-

2, $n = 47$. In **f** and **g**, P values were determined by two-sided t -test. NS, not significant. In all experiments, RNAi was initiated at day 1 of adulthood.

[Source data](#)

[Full size image](#)

With age, other intestinal intermediate filaments (IFC-1, IFC-2 and IFP-1) and the intestinal filament organizer IFO-1 also lost their apical localization and accumulated into aggregates (Extended Data Fig. [7f–k](#)). Notably, knockdown of *iβ-2* after development ameliorated these age-related changes (Fig. [3d,e](#), Extended Data Fig. [8a–c](#)). Because intestinal alterations trigger bacterial colonization^{[29](#)}, we asked whether IFB-2 influences this deleterious process. Notably, knockdown of *iβ-2* diminished bacterial invasion in the intestine of aged worms, whereas ubiquitin-less IFB-2 mutations exacerbated this phenotype (Fig. [3f,g](#), Extended Data Fig. [8d,e](#)). Thus, increased levels of IFB-2 could underlie the collapse of other intermediate filaments during ageing, leading to loss of intestinal integrity.

Increased EPS-8 levels hyperactivate RAC

Although the levels of EPS-8 increased in distinct tissues with age, it regulated organismal lifespan through its activity within muscle and neurons (Fig. [4a,b](#), Extended Data Fig. [9a,b](#)). EPS-8 promotes the exchange of GDP for GTP on RAC protein, which then becomes active to regulate a wide range of pathways^{[30](#)}. *C. elegans* expresses three *rac*-like genes (*rac-2*, *mig-2* and *ced-10*) required for development^{[31](#)}. Similar to EPS-8, knockdown of either *rac-2* or *mig-2* in muscle and neurons after development extended lifespan (Fig. [4c](#), Extended Data Fig. [9c–f](#)). Moreover, knockdown of *mig-2* prevented the short lifespan induced by the ubiquitin-less EPS-8 variant, which supports the idea that EPS-8 decreases longevity through RAC hyperactivation (Fig. [4c](#)).

Fig. 4: Increased EPS-8 levels shorten lifespan through RAC hyperactivation.

 **figure4**

a, b, Muscle-specific (**a**) and neuronal-specific (**b**) knockdown of *eps-8* after development extends lifespan. **c**, Knockdown of *mig-2* after development extends longevity and rescues the short lifespan induced by ubiquitin-less EPS-8. *P* values in **a–c** were determined by two-sided log-rank test; *n* = 96 worms per condition.

Supplementary Table 11 contains replicate data of independent experiments. **d**, Staining of filamentous actin with phalloidin. *eps-8* RNAi prevents age-associated destabilization of actin filaments. Scale bar, 20 μ m. Representative of two independent experiments. **e**, Knockdown of *mig-2* rescues the disruption of actin filaments in day-3 adult worms induced by ubiquitin-less EPS-8. Scale bar, 20 μ m. Representative of two independent experiments. **f**, Thrashing movements per 30 s (*n* = 45 worms per condition from three independent experiments). Knockdown of *mig-2* suppresses motility deficits induced by ubiquitin-less EPS-8 in young adult worms. Data are mean \pm s.e.m. *P* values in **f** determined by two-sided *t*-test. In all experiments, RNAi was initiated at day 1 of adulthood.

[Source data](#)

[Full size image](#)

RAC induces phosphorylation and subsequent activation of the protein kinase JNK, which regulates transcription factors involved in cell survival and death signalling^{30,32}. In correlation with upregulated EPS-8 levels, we observed increased phosphorylation of JNK during ageing (Extended Data Fig. 9g). By contrast, the knockdown of *eps-8* reduced JNK phosphorylation in aged worms (Extended Data Fig. 9h). The worm JNK

homologue KGB-1 protects against stress during development, but its activity becomes detrimental with the onset of adulthood³³. Knockdown of *kgb-1* during adulthood ameliorated the short-lived phenotype of ubiquitin-less EPS-8 mutants (Extended Data Fig. 9*i*), which indicates that RAC signalling influences longevity through JNK activation.

RAC also promotes the polymerization and remodelling of the actin cytoskeleton³⁴. With age, muscle cells exhibit unorganized actin filaments that impair organismal motility³⁵. Notably, *eps-8* knockdown from adulthood prevented the age-associated destabilization of muscle actin networks and associated myosin filaments, ameliorating deficits in motility (Fig. 4*d*, Extended Data Fig. 10*a,b*). By contrast, knockdown of *eps-8* did not rescue age-associated changes in actin organization within intestinal and epidermal cells (Extended Data Fig. 10*c,d*). Filter trap experiments indicated that actin protein also aggregates during ageing, whereas knockdown of *eps-8* rescued this phenotype (Extended Data Fig. 10*e*). To determine in which tissues the increased EPS-8 levels trigger actin aggregation, we used tissue-specific RNAi. Knockdown of *eps-8* in the muscle or neurons reduced actin aggregation during ageing, whereas knockdown in other tissues did not prevent aggregation (Extended Data Fig. 10*f–i*).

Similar to *eps-8*, lowering the levels of hyperactivated RAC after development prevented the destabilization of muscle actin cytoskeleton during ageing (Extended Data Fig. 10*j,k*). Moreover, knockdown of *mig-2* rescued the accelerated disruption of actin filaments, aggregation of actin and motility deficits induced by ubiquitin-less EPS-8 (Fig. 4*e,f*, Extended Data Fig. 10*l*). Thus, hyperactivation of RAC by increased EPS-8 levels could result in excessive actin remodelling and polymerization, leading to altered actin networks with age.

Discussion

Our study has demonstrated a global deubiquitination across tissues during ageing that impairs targeted proteasomal degradation of lifespan regulators. Besides IFB-2 and EPS-8, we identified other dysregulated proteasome targets such as the cytokine receptor F54D1.6 and the solute carrier C46C2.2 that could have synergistic effects on ageing. Because ubiquitination also tags proteins for degradation through autophagy, our datasets have implications for understanding the link between autophagy and longevity³. Notably, we identified more than 1,000 ubiquitination changes during ageing that do not induce alterations in protein levels. These ubiquitination events could modulate protein activity and localization, and lead to longevity modifiers.

Methods

C. elegans strains and maintenance

C. elegans were grown and maintained at 20 °C on standard Nematode Growth Medium (NGM) seeded with *E. coli* (OP50)³⁶. Wild-type (N2), DA1116 (*eat-2(ad1116)II*), and RW1596 (*myo-3(st386)V; stEx30[myo-3p::GFP::myo-3 + rol-6(su1006)]*) were provided by the *Caenorhabditis* Genetics Center (CGC) (University of Minnesota), that is supported by the NIH Office of Research Infrastructure Programs (P40 OD010440). CF1041 (*daf2(e1370)III*) was provided by C. Kenyonu8). MT7929 (*unc-13(e51)I*) outcrossed four times to wild-type N2 was provided by T. Hoppe. AGD1657 (*unc-119(ed3)III; uthSi13[gly-19p::LifeAct::mRuby::unc-54 3'UTR::cb-unc-119(+)]IV*) and AGD1654 (*unc-119(ed3)III; uthSi10[col-19p::LifeAct::mRuby::unc-54 3'UTR::cb-unc-119(+)]IV*)³⁷ were a gift from A. Dillin. BJ49 (*kcIs6[iβ-2p::iβ-2a::CFP]IV*)³⁸, BJ186 (*kcIs30[iβ-1p::iβ-1::YFP; myo-3p::mCherry::unc-54]III*)³⁹, BJ324 (*kcEx78[iβ-1p::iβ-1::eGFP; unc-119(ed3)+J; unc-119(ed3)III]*), BJ316 (*iβ-2(kc16[iβ-2a/e::YFP]J)X*), and BJ312 (*kcIs40[iβ-1p::iβ-1::eGFP]IV*)⁴⁰ were a gift from R. E. Leube.

To generate the strains DVG197 (N2, *ocbEx162[sur-5p::iβ-2, myo-3p::GFP]*) and DVG198 (N2, *ocbEx163[sur-5p::iβ-2, myo-3p::GFP]*), a DNA plasmid mixture containing 70 ng μl^{-1} of the plasmids *sur5-p::iβ-2* (pDV199) and 20 ng μl^{-1} pPD93_97 (*myo3-p::GFP*) was injected into the gonads of adult N2 hermaphrodite worms by standard methods⁴¹. To construct the *C. elegans* plasmid (pDV199) for overexpression of *iβ-2*, pPD95.77 from the Fire Lab kit was digested with SphI and XmaI to insert 3.6-kb of the *sur-5* promoter. The resultant vector was then digested with KpnI and EcoRI to excise GFP and insert a multi-cloning site. *F10C1.7 (iβ-2)* was PCR-amplified from cDNA to include 5' NheI and 3' NotI restriction sites and then cloned into the aforementioned vector. The construct was sequence verified. The corresponding control DVG9 strain (N2, *ocbEx9[myo3p::GFP]*) was generated by microinjecting N2 worms with 20 ng μl^{-1} pPD93_97 (ref. ⁴²).

For tissue-specific RNAi assays, we used either *rde-1* or *sid-1* mutant worms in which wild-type *rde-1* or *sid-1* expression has been rescued using tissue-specific promoters, respectively. Tissue-specific knockdown was validated in the original publications. In the VP303 strain (*rde-1(ne219)V; kbIs7[nhx-2p::rde-1 + rol-6(su1006)]*), RNAi treatment is only effective in the intestine⁴³. For muscle-specific knockdown, we used the WM118 strain (*rde-1(ne300)V; neIs9[myo-3p::HA::RDE-1 + rol-6(su1006)]*)⁴⁴. For neuronal-specific RNAi, we used the TU3401 strain (*sid-1(pk3321)V; uIs69[pCFJ90(myo-2p::mCherry) + unc-119p::sid-1]*)⁴⁵. For epidermal-specific RNAi experiments, we used the NR222 strain (*rde-1(ne219)V; kzIs9 [(pKK1260) lin-26p::NLS::GFP + (pKK1253) lin-26p::rde-1 + rol-6(su1006)]*)⁴⁶. All the tissue-specific RNAi strains were provided by the CGC.

Ubiquitin-less IFB-2 and EPS-8 mutant worms were generated at SunyBiotech (<http://www.sunybiotech.com>) by CRISPR–Cas9 methodology. The IFB-2(K255R/K341R) mutant strain (VDL07, *iβ-2(syb2876)II*) was generated using the sgRNAs sg1-CCACCAAGTTGATCTTGAGACA and sg2-CCTCCGATTATCGGTGAAGACT. The strain expressing endogenous wild-type EPS-8 tagged with 3xHA (VDL05, *eps-8(syb2901)IV*) was generated by CRISPR–Cas9 using sg1-CCTGTATTCACTATTAAACCCAAT and sg2-CACTATTAAACCCAATTCTCTAGG. The strain expressing endogenous EPS-8(K524R/K583R/K621R::3xHA) (VDL06, *eps-8(syb2901, syb3149)IV*) was generated using sg1-GGAGAGTCGTTGAGGCATGAGG and sg2-AGGAGCTGACTGTTCACAAAGGGG. Because *eps-8* generates several different isoforms, the numbering of ubiquitination sites corresponds to the leading EPS-8 isoform identified in our proteomics data (that is, transcript Y57G11C.24g.1, EPS-8 protein isoform g). The strain expressing endogenous IFB-2 tagged with GFP (VDL08, *iβ-2(syb3973)II*) was also generated at SunyBiotech using sg1-CCAGACGACGGTCGCTTCTCCC and sg2-CCGTTAAGAAATCTCCATCATCT. In all the aforementioned strains, the editing was confirmed by sequencing the *iβ-2* and *eps-8* genes in both directions.

Lifespan assays

Young hermaphrodite adults were randomly picked from maintenance plates and transferred onto plates with OP50 *E. coli*. After 6 h of egg laying, adult worms were removed from the plates. Then, synchronized larvae were raised and fed OP50 *E. coli* at 20 °C until they developed into hermaphrodite adults. Once worms reached adulthood, they were randomly picked and transferred onto plates with HT115 *E. coli* carrying empty vector or RNAi clones for lifespan assays. For the non-integrated lines DVG9, DVG197 and DVG198, GFP-positive worms were selected for lifespan studies. All the lifespan assays of adult worms were conducted at 20 °C. In total, 96 worms were assessed per condition and scored every day or every other day⁴⁷. Sample sizes were determined according to our previous studies and other publications^{8,47}. Lifespan experiments were not blinded.

From the initial worm population, we censored the worms that were lost or burrowed into the medium as well as those that exhibited bagging or ‘protruding vulva’. Supplementary Table 11 indicates the total number of uncensored worms and total number (uncensored + censored) of worms observed in each experiment. GraphPad PRISM 6 software was used to determine median lifespan and generate lifespan graphs. OASIS software (version 1) was used for statistical analysis to determine mean lifespan⁴⁸. *P* values were calculated using the log-rank (Mantel–Cox) method. The *P* values refer to experimental and control worms in a single experiment. In the

main and extended data figures, each graph shows a representative lifespan experiment. See Supplementary Table 11 for statistical analysis and replicate data.

RNAi constructs

For RNAi experiments, hermaphrodite worms were fed *E. coli* (HT115) containing an empty control vector (L4440) or expressing double-stranded RNAi when they reached adulthood. *M01G12.9*, *C46C2.2*, *F54D1.6*, *ddi-1*, *usp-5*, *rac-2*, *csn-6*, *math-33*, *H34C03.2*, *usp-48*, *prp-8*, *cyk-3* and *F07A11.4* RNAi constructs were obtained from the Ahringer RNAi library. *ifb-2*, *eps-8*, *rpn-6.1*, *hsp-43*, *rpl-4*, *lec-1*, *mig-2*, *ced-10*, *kgb-1*, *cyclid-1*, *usp-50*, *csn-5*, *otub-3* and *eif3.F* RNAi constructs were obtained from the Vidal RNAi library. All RNAi constructs were sequence verified. See Supplementary Table 12 for further details about double-stranded RNAi constructs used for knockdown assays.

Synchronization of large populations

To obtain large populations of synchronized hermaphrodite worms for proteomics, western blot, filter trap and quantitative PCR (qPCR), we used the bleaching technique⁴⁹. In brief, young adult worms were collected by transferring random chunks of agar from maintenance plates and let them grow until there were sufficient young hermaphrodites for bleaching. Then, young worms were treated with alkaline hypochlorite solution (3 ml of bleach 4% (Fischer), 1.5 ml 5 N KOH, 5.5 ml dH₂O) for 4 min to destroy adult tissues and obtain eggs. After four washes with M9 buffer, eggs were maintained on M9 buffer without food overnight to allow hatching but prevent further development. Synchronized L1 larvae were randomly collected, raised and fed OP50 *E. coli* at 20 °C until late L4 larvae stage. Then, worms were transferred onto plates with OP50 *E. coli* (alternatively, HT115 *E. coli* for RNAi experiments) covered with 100 µg ml⁻¹ 5-fluoro-2' deoxyuridine (FUdR) to prevent the development of progeny. Every five days, adult worms were transferred onto fresh plates.

Quantitative proteomics of the Ub-modified proteome and analysis

For label-free quantitative proteomics, wild-type, *daf2(e1370)* and *eat-2(ad1116)* hermaphrodite worms were randomly collected with M9 buffer at days 1, 5, 10 and 15 of adulthood. For proteomics analysis of proteasome-less worms, we collected day 5 adult worms treated with either Vector RNAi or *rpn-6* RNAi. To remove bacteria, we washed the worms five times with M9 buffer. Then, worms were resuspended in 10 M urea containing 50 mM triethylammonium bicarbonate (TEAB) and 25 mM *N*-ethylmaleimide. Protein was extracted using a Precellys 24 homogenizer (Bertin Technologies). Samples were centrifuged at 18,000g for 10 min at room temperature and supernatants were collected. Then, we determined protein concentrations with

Pierce BCA protein assay (Thermo Scientific). For each sample, 22 mg of total protein were used as starting material and treated with 5 mM dithiothreitol (DTT) for 30 min at room temperature to reduce disulfide bonds. Carbamidomethylation was performed by incubation with 30 mM chloroacetamide for 30 min at room temperature. The urea concentration was diluted to 2 M with 50 mM ammonium bicarbonate and samples were digested with 220 µg trypsin (1:100 (w/w) enzyme:substrate ratio) for 3 h at room temperature. Then, we further added 220 µg trypsin and digested the samples overnight. After digestion, we added 0.5% formic acid and centrifuged 3,500g for 5 min the samples to remove precipitate. Peptides were desalted with 500-mg tC18 Sep-Pak cartridge (Waters). Then, 200 µg of peptides was separated and cleaned up using C18 Stage Tips (Thermo Fischer) for label-free proteomics of total protein levels. The rest of the material was used for enrichment of Ub-modified peptides. First, peptides were frozen at -80 °C for 3 h and then completely dried by vacuum centrifugation. Dried samples were dissolved in immunoaffinity purification solution (IAP). For enrichment of Ub-modified peptides, we used PTMScan Ubiquitin Remnant Motif (K-ε-GG) Antibody Bead Conjugate (Cell Signaling Technology). This antibody has specificity for diGly tag, which is the remnant of ubiquitin left on proteins after trypsin digestion. For each sample, 40 µl of antibody-bead conjugates were added and incubated for 6 h with gentle rotation at 4 °C. Then, beads were washed three times with ice-cold PBS and ice-cold water. Ub-modified peptides were eluted by incubating twice with 100 µl of 0.15% trifluoroacetic acid. Finally, peptides were desalted using C18 Stage Tips and analysed by label-free quantitative proteomics.

The liquid chromatography tandem mass spectrometry (LC–MS/MS) equipment consisted of an EASY nLC 1000 coupled to the quadrupole based QExactive Plus Orbitrap instrument (Thermo Scientific) via a nano-spray electroionization source. Peptides were separated on an in-house packed 50 cm column (2.7 µm C18 beads, Dr. Maisch) using a binary buffer system: (A) 0.1% formic acid and (B) 0.1% formic acid in 80% acetonitrile. The content of buffer B was raised from 5% to 30% within 65 min and followed by an increase to 50% within 10 min. Then, within 1 min, buffer B fraction was raised to 95% and then followed by washing and column equilibration for 15 min. Eluting peptides were ionized by an applied voltage of 2.2 kV. The capillary temperature was 275 °C and the S-lens RF level was set to 60. MS1 spectra were acquired using a resolution of 70,000 at 200 *m/z*, an automatic gain control target of 3×10^6 and a maximum injection time of 20 ms in a scan range of 300–1,750 Th. The ten most intense peaks were selected for isolation and fragmentation in the higher collisional dissociation cell using a normalized collision energy of 27 at an isolation window of 1.8 Th. Dynamic exclusion was enabled and set to 20 s. The MS/MS scan properties were: 17,500 resolution at 200 *m/z*, an automatic gain control target of 5×10^5 and a maximum injection time of 60 ms. For protein identification and LFQ in ubiquitin-proteomics experiments, we used the LFQ mode and MaxQuant (version 1.5.3.8) default settings⁵⁰. For proteomics data sets of total protein levels in ageing and

proteasome-less worms, we used Spectronaut 11 (Biognosys) with the BGS Factory Settings and MaxQuant (version 1.5.3.8) with default settings, respectively. MS2 spectra were searched against the *C. elegans* Uniprot database, including a list of common contaminants. FDRs on protein and peptide–spectrum match level were estimated by the target-decoy approach to 0.01% (protein FDR) and 0.01% (peptide–spectrum match FDR), respectively. The minimal peptide length was set to 7 amino acids and the match-between runs option was enabled. Carbamidomethylation (C) was considered as a fixed modification, whereas oxidation (M), acetylation (protein N-term) and GlyGly (K) were included as variable modifications. All the downstream analyses of the resulting output were performed with R program (version 4.0.5) and Perseus (version 1.6.2.3). Protein groups flagged as ‘reverse’, ‘potential contaminant’ or ‘only identified by site’ were removed. LFQ values were log₂-transformed and missing values were replaced using an imputation-based approach. Significant differences between the experimental groups were assessed by two-sided Student’s *t*-test for samples. A permutation-based FDR approach was applied to correct for multiple testing. For worm tissue expression prediction, we used the database <http://worm.princeton.edu>²⁶. Sample sizes for proteomics experiments were chosen based on previous studies on ubiquitin proteomics in mammalian cells⁵¹, global proteomics changes during ageing in *C. elegans*^{9,10} and our previous work on proteomics analysis of *C. elegans*⁸. Sample collection was not performed in a blinded manner. Once the samples were processed for proteomics, the mass spectrometry was performed by the CECAD Proteomics Facility in a blinded manner.

Immunoprecipitation of Lys48 and Lys63-linked polyUb and proteomics analysis

Wild-type worms were randomly collected at day 5 of adulthood with M9 buffer and washed five times with M9 to remove bacteria. Then, worms were lysed in protein lysis buffer (50 mM Tris-HCl at pH 6.7, 150 mM NaCl, 1% NP40, 0.25% sodium deoxycholate, 1 mM EDTA, 1 mM NaF, 25 mM *N*-ethylmaleimide, and protease inhibitor cocktail (Roche)) using a Precellys 24 homogenizer. Samples were centrifuged at 18,000g for 10 min at 4 °C and supernatants were collected. We measured protein concentrations and used 2.5 mg of protein as starting material for each sample. The samples were incubated on ice for 3 h with anti-ubiquitin antibody, Lys48-specific, clone Apu2 (Merck, 05-1307, 1:50. RRID: AB_1587578) or anti-ubiquitin antibody, Lys63-specific, clone Apu3 (Merck, 05-1308, 1:50. RRID: AB_1587580). As a co-immunoprecipitation control, the same amount of protein was incubated with anti-Flag antibody (Sigma, F7425, 1:100; RRID: AB_439687) in parallel. Then, samples were incubated with 50 µl of µMACS MicroBeads (Miltenyi Biotec, 130-071-001) for 1 h on the overhead shaker at 4 °C. Subsequently, samples were loaded to pre-cleared µMACS column (Miltenyi Biotec, 130-042-701). Beads

were washed three times with 50 mM Tris (pH 7.5) buffer containing 150 mM NaCl, 5% glycerol and 0.05% Triton and then washed five times with 50 mM Tris (pH 7.5) and 150 mM NaCl. After that, columns were subjected to in-column tryptic digestion containing 7.5 mM ammonium bicarbonate, 2 M urea, 1 mM DTT and 5 ng ml⁻¹ trypsin. Peptides were eluted using two times 50 µl of elution buffer 1 containing 2 M urea, 7.5 mM ambic and 15 mM chloroacetamide and incubated overnight at room temperature with mild shaking. Then, samples were stage-tipped the next day for label-free quantitative proteomics assay.

All samples were analysed on a Q-Exactive Plus (Thermo Scientific) mass spectrometer coupled to an EASY nLC 1200 UPLC (Thermo Scientific). Peptides were loaded with solvent A (0.1% formic acid in water) onto an in-house packed analytical column (50 cm × 75 µm I.D., filled with 2.7 µm Poroshell EC120 C18 (Agilent)). Peptides were chromatographically separated at a constant flow rate of 250 nl min⁻¹ using the 150-min method: 3–5% solvent B (0.1% formic acid in 80% acetonitrile) within 1 min, 5–30% solvent B (0.1% formic acid in 80% acetonitrile) within 65 min, 30–50% solvent B within 13 min and 50–95% solvent B within 1 min, followed by washing and column equilibration. The mass spectrometer was operated in data-dependent acquisition mode. The MS1 survey scan was acquired from 300 to 1,750 *m/z* at a resolution of 70,000. The top 10 most abundant peptides were subjected to higher collisional dissociation fragmentation at a normalized collision energy of 27% and the automatic gain control target was set to 5×10^5 charges. Product ions were detected in the Orbitrap at a resolution of 17,500. All mass spectrometric raw data were processed with MaxQuant (version 1.5.3.8) using default parameters as described above. LFQ was performed using the LFQ mode and MaxQuant default settings. All downstream analyses were carried out on LFQ values with Perseus (version 1.6.2.3). Sample sizes for immunoprecipitation experiments followed by label-free quantitative proteomics were determined according to our previous publications^{52,53}. Sample collection was not performed in a blinded manner.

Once the samples were processed for proteomics, the mass spectrometry was performed by the CECAD Proteomics Facility in a blinded manner.

Cycloheximide and DUB inhibitor treatment

To assess the half-life of protein ubiquitin, we blocked ubiquitin synthesis by cycloheximide treatment⁵⁴. Synchronized adult worms by bleaching technique were randomly transferred onto plates with OP50 bacteria covered with a final concentration of 54.5 µg ml⁻¹ cycloheximide (Sigma-Aldrich) during the indicated times in the corresponding figure. For DUB inhibitor experiments, synchronized adult worms were randomly transferred onto plates with OP50 bacteria covered containing a

final concentration of 13.7 µg ml⁻¹ PR-619¹⁶ (Merck) or vehicle control (DMSO) for 4 h and then collected for western blot analysis.

RNA isolation and quantitative RT–PCR

Total RNA was isolated using RNABee (Tel-Test) from approximately 2,000 adult hermaphrodite worms synchronized by bleaching technique at the ages indicated in the corresponding figures. Sample size was determined according to our previous publications^{8,42}. cDNA was generated using a qScript Flex cDNA synthesis kit (Quantabio). SybrGreen real-time qPCR experiments were performed with a 1:20 dilution of cDNA using the CFC384 Real-Time System (Bio-Rad). Data were analysed with the comparative $2\Delta\Delta C_t$ method using the geometric mean of *cdc-42*, *pmp-3* and *Y45F10D.4* as housekeeping genes⁵⁵. qPCR experiments were not blinded. See Supplementary Table 13 for details about the primers used for quantitative RT–PCR.

Western blot

C. elegans were synchronized by bleaching technique and collected randomly at the indicated ages in the corresponding figures. Then, worms were lysed in protein lysis buffer (50 mM Hepes at pH 7.4, 150 mM NaCl, 1 mM EDTA, 1% Triton X-100, 2 mM sodium orthovanadate, 1 mM PMSF and protease inhibitor cocktail (Roche)) using a Precellys 24 homogenizer. Worm lysates were centrifuged at 8,000g for 5 min at 4 °C and the supernatant was collected. Protein concentrations were determined with Pierce BCA protein assay (Thermo Scientific). Total protein (30 µg) was separated by SDS-PAGE, transferred to polyvinylidene difluoride membranes (Millipore) and subjected to immunoblotting. Western blot analysis was performed with anti-IFB-2 (Developmental Studies Hybridoma Bank, MH33, 1:1,000, RRID: AB_528311), anti-EPS8L2 (Abcam, ab85960, 1:1,000, RRID: AB_1924963), anti-GFP (AMSBIO, 210-PS-1GFP, 1:5,000, RRID: AB_10013682) and anti- α -tubulin (Sigma, T6199, 1:5,000, RRID: AB_477583). For analysis of JNK phosphorylation, we used the antibodies anti-JNK (Cell Signaling, 9252, 1:1,000, RRID: AB_2250373) and anti-phospho-JNK (Thr183/Tyr185) (Cell Signaling, 9251, 1:1,000; RRID: AB_331659) previously validated in *C. elegans*⁵⁶. When indicated in the corresponding figure, we also performed analysis of total IFB-2 levels with antibody MH33 in whole *C. elegans* lysates without the centrifugation step.

For assessing ubiquitinated proteins by western blot, worms were lysed in lysis buffer (50 mM Tris-HCl, pH 7.8, 150 mM NaCl, 0.25% sodium deoxycholate, 1 mM EDTA, 25 mM *N*-ethylmaleimide, 2 mM sodium orthovanadate, 1 mM PMSF and protease inhibitor cocktail (Roche)) using Precellys 24 homogenizer. The cell debris was removed by centrifugation at 10,600g for 10 min at 4 °C and the supernatant was collected. Protein concentrations were determined with standard BCA protein assay (Thermo Scientific). Then, 30 µg of total protein was separated by SDS-PAGE, transferred to nitrocellulose membranes (Millipore) and subjected to immunoblotting. Western blot analysis was performed with anti-ubiquitin (Sigma, 05-944, clone P4D1-A11, 1:1,000, RRID: AB_441944) and α -tubulin (Sigma, T6199, 1:5,000; RRID AB_477583). Sample size was

determined according to our previous publications^{8,53}. Western blot experiments were not blinded.

Isolation of tissues for western blot analysis

Adult hermaphrodite worms synchronized by egg laying technique were collected and washed with M9 buffer. Then, worms were randomly picked and suspended into a droplet of M9 buffer on a glass slide. To cut off the head, two 27-gauge needles were moved in scissors motion. Decapitation was normally followed by the extrusion of at least one germline arm and the intestine. Heads, germlines and intestines were carefully separated using 27-gauge needles. A 20 µl pipette was used for collection of these tissues, which were then transferred to 1.5 ml Eppendorf tubes. Tissues were fast frozen and kept at -80 °C until a total of approximately 1,000 samples of each isolated tissue could be collected and combined to have enough material for western blot analysis. The collected tissues were then lysed in protein lysis buffer and protein concentrations were determined with Pierce BCA as detailed in the previous section for western blot analysis.

Filter trap

Synchronized adult hermaphrodite worms by bleaching technique were randomly collected and washed with M9 buffer and worm pellets were frozen with liquid N2. Frozen worm pellets were thawed on ice and worm lysates were generated in non-denaturing protein lysis buffer (50 mM HEPES (pH 7.4), 150 mM NaCl, 1 mM EDTA, 1% Triton X-100) supplemented with 2 mM sodium orthovanadate, 1 mM PMSF and protease inhibitor cocktail (Roche)) using a Precellys 24 homogenizer. Worm lysates were centrifuged at 8,000g for 5 min at 4 °C to remove debris and the supernatant was collected. Then, 100 µg of total protein was supplemented with 0.5% SDS and loaded onto a cellulose acetate membrane assembled in a slot blot apparatus (Bio-Rad). The membrane was then washed with 0.2% SDS and aggregates were assessed by immunoblotting using anti-IFB-2 (Developmental Studies Hybridoma Bank, MH33, 1:1,000, RRID: AB_528311), anti-GFP (AMSBIO, 210-PS-1GFP, 1:5,000, RRID: AB_10013682), and anti-β-actin (Abcam, ab8226, 1:5,000; RRID

AB_306371). Sample size was determined according to our previous publications^{[42,53](#)}. Filter trap experiments were not blinded.

Motility assay

C. elegans were synchronized on *E. coli* (OP50) bacteria until L4 stage by egg laying technique and then randomly transferred to *E. coli* (HT115) bacteria containing either control empty vector or RNAi for the rest of the experiment. At the day of adulthood indicated in the corresponding figures, *C. elegans* were randomly picked and transferred to a drop of M9 buffer and after 30 s of adaptation the number of body bends was counted for 30 s. A body bend was defined as change in direction of the bend at the mid-body^{[53,57](#)}. Sample size was determined according to our previous publications^{[42,53](#)}. Motility assays were not blinded.

Phalloidin staining

Adult hermaphrodite *C. elegans* were synchronized by egg laying technique and randomly collected at the ages indicated in the corresponding figures, washed with M9 buffer and fixed with ice cold 4% formaldehyde solution for 15 min. Worms were permeabilized with 2% Tween-20 in 1× PBS (pH 7.2) for 30 min at room temperature. Then, worms were treated with β-mercaptoethanol solution (120 mM Tris-HCl (pH 6.8), 5% β-mercaptoethanol, 1% Triton X-100) for 10 min. The worms were washed three times with 0.2% 1× PBS-Tween (pH 7.2) and three times with 1% BSA in 0.2% 1× PBS-Tween (pH 7.2). Worms were stained with rhodamine-phalloidin (Thermo Fischer, R415, 1:100) for 45 min. Three washes using 0.2% 1× PBS-Tween (pH 7.2) were followed before the cover slips were mounted on FluorSave Reagent (Merck, 345789). The sample size for imaging experiments was determined according to previous publications^{[8,42](#)}. Imaging experiments were not blinded.

Bacterial colonization assay

Bacterial colonization or invasion experiments were performed as previously described^{[29](#)}. All HT115 *E. coli* bacteria were cultured under

carbenicillin selection. After overnight growth at 37 °C, bacterial cultures were induced with 1 mM IPTG for 4 h, collected and concentrated 10 times by centrifugation. Concentrated RNAi cultures were mixed at a ratio of 4:1 with concentrated HT115 bacteria expressing mCherry from the pDP151 plasmid. NGM agar plates were seeded with the bacterial mixed culture (4 parts HT115 RNAi, 1 part HT115 expressing mCherry) and allowed to dry for 24 h at room temperature. L4 larvae synchronized by egg laying technique were then randomly transferred onto these plates and analysed by fluorescence microscopy at days 1, 5 and 10 of adulthood. Before the analysis, worms were gently collected from the RNAi or mCherry agar plates, washed three times with M9 buffer, and placed onto OP50 *E. coli* plates to feed for 2 h to remove residual fluorescent bacteria from the intestine. Then, worms were immobilized using 0.1% azide in M9 buffer on 2% agarose pad. Images of worms were acquired with a Zeiss Axio Zoom.V16 fluorescence microscope. For quantification of fluorescence signal, worms were outlined and quantified using ImageJ software (version 1.5|s). Sample size for quantification of fluorescence reporters was determined according to our previous studies and other publications^{8,58}. Bacterial colonization assays were not blinded.

Quantification of hatched eggs and development into adults

Synchronized worms by egg laying technique were raised and fed OP50 *E. coli* at 20 °C until late L4 stage. Then, late L4 larvae were picked in a random manner and singly plated. After 24 h, the adult worm was removed and the number of eggs per plate was measured. The plate was kept for another 24 h, when the number of live progeny, visible as L1 larvae, was scored to assess the percentage of hatched eggs. L1 larvae were cultured for 50 h and the number of adult worms was scored in each plate. Sample size was determined according to previous work from our laboratory⁸. These experiments were not blinded.

Reporting summary

Further information on research design is available in the [Nature Research Reporting Summary](#) linked to this paper.

Data availability

There is no restriction on data availability. Readers can interact with the ubiquitin and global proteomics data using the following Shiny Web apps by downloading the datasets provided in the apps:

<https://vilchezlab.shinyapps.io/shiny-volcanoplot/> and

<https://vilchezlab.shinyapps.io/shiny-heatmap/>. Proteomics data have been deposited in the ProteomeXchange Consortium via the PRIDE partner repository with the dataset identifiers PXD024338 (ubiquitin proteomics of ageing and long-lived worms), PXD025128 (global protein proteomics of ageing and long-lived worms), PXD024094 (ubiquitin proteomics upon *rpn-6* RNAi), PXD024095 (global protein proteomics upon *rpn-6* RNAi), PXD024093 (immunoprecipitation Lys48-linked polyUb) and PXD024045 (immunoprecipitation Lys63-linked polyUb). MS2 spectra in proteomics experiments were searched against the *C. elegans* Uniprot database (<https://www.uniprot.org/proteomes/UP000001940>). For worm tissue expression analysis, we used the database <http://worm.princeton.edu>. [Source data](#) are provided with this paper.

Code availability

Custom code used in this article can be accessed at

<https://github.com/Vilchezlab/UbProteomics2021>.

References

1. 1.

Campisi, J. et al. From discoveries in ageing research to therapeutics for healthy ageing. *Nature* **571**, 183–192 (2019).

[ADS](#) [CAS](#) [PubMed](#) [PubMed Central](#) [Google Scholar](#)

2. 2.

Finley, D. Recognition and processing of ubiquitin-protein conjugates by the proteasome. *Annu. Rev. Biochem.* **78**, 477–513 (2009).

[CAS](#) [PubMed](#) [PubMed Central](#) [Google Scholar](#)

3. 3.

Vilchez, D., Saez, I. & Dillin, A. The role of protein clearance mechanisms in organismal ageing and age-related diseases. *Nat. Commun.* **5**, 5659 (2014).

[ADS](#) [CAS](#) [Google Scholar](#)

4. 4.

Geisler, F. et al. The intestinal intermediate filament network responds to and protects against microbial insults and toxins. *Development* **146**, dev169482(2019).

[Google Scholar](#)

5. 5.

Di Fiore, P. P. & Scita, G. Eps8 in the midst of GTPases. *Int. J. Biochem. Cell Biol.* **34**, 1178–1183 (2002).

[Google Scholar](#)

6. 6.

Papaevgeniou, N. & Chondrogianni, N. The ubiquitin proteasome system in *Caenorhabditis elegans* and its regulation. *Redox Biol.* **2**, 333–347 (2014).

[CAS](#) [PubMed](#) [PubMed Central](#) [Google Scholar](#)

7. 7.

Xu, G., Paige, J. S. & Jaffrey, S. R. Global analysis of lysine ubiquitination by ubiquitin remnant immunoaffinity profiling. *Nat. Biotechnol.* **28**, 868–873 (2010).

[CAS](#) [PubMed](#) [PubMed Central](#) [Google Scholar](#)

8. 8.

Lee, H. J. et al. Prostaglandin signals from adult germ stem cells delay somatic aging of *Caenorhabditis elegans*. *Nat. Metab.* **1**, 790–810 (2019).

[CAS](#) [PubMed](#) [PubMed Central](#) [Google Scholar](#)

9. 9.

Narayan, V. et al. Deep proteome analysis identifies age-related processes in *C. elegans*. *Cell Syst.* **3**, 144–159 (2016).

[CAS](#) [PubMed](#) [PubMed Central](#) [Google Scholar](#)

10. 10.

Walther, D. M. et al. Widespread proteome remodeling and aggregation in aging *C. elegans*. *Cell* **161**, 919–932 (2015).

[CAS](#) [PubMed](#) [PubMed Central](#) [Google Scholar](#)

11. 11.

Gonskikh, Y. & Polacek, N. Alterations of the translation apparatus during aging and stress response. *Mech. Ageing Dev.* **168**, 30–36 (2017).

[CAS](#) [Google Scholar](#)

12. 12.

Stegeman, R. & Weake, V. M. Transcriptional signatures of aging. *J. Mol. Biol.* **429**, 2427–2437 (2017).

[CAS](#) [PubMed](#) [PubMed Central](#) [Google Scholar](#)

13. 13.

Hanna, J., Meides, A., Zhang, D. P. & Finley, D. A ubiquitin stress response induces altered proteasome composition. *Cell* **129**, 747–759 (2007).

[CAS](#) [Google Scholar](#)

14. 14.

Kipreos, E. T. Ubiquitin-mediated pathways in *C. elegans*. *WormBook* <https://doi.org/10.1895/wormbook.1.7.1> (2005).

15. 15.

Clague, M. J., Urbé, S. & Komander, D. Breaking the chains: deubiquitylating enzyme specificity begets function. *Nat. Rev. Mol. Cell Biol.* **20**, 338–352 (2019).

[CAS](#) [Google Scholar](#)

16. 16.

Altun, M. et al. Activity-based chemical proteomics accelerates inhibitor development for deubiquitylating enzymes. *Chem. Biol.* **18**, 1401–1412 (2011).

[CAS](#) [Google Scholar](#)

17. 17.

Vilchez, D. et al. Increased proteasome activity in human embryonic stem cells is regulated by PSMD11. *Nature* **489**, 304–308 (2012).

[ADS](#) [CAS](#) [PubMed](#) [PubMed Central](#) [Google Scholar](#)

18. 18.

Vilchez, D. et al. RPN-6 determines *C. elegans* longevity under proteotoxic stress conditions. *Nature* **489**, 263–268 (2012).

[ADS](#) [CAS](#) [Google Scholar](#)

19. 19.

Croce, A. et al. A novel actin barbed-end-capping activity in EPS-8 regulates apical morphogenesis in intestinal cells of *Caenorhabditis elegans*. *Nat. Cell Biol.* **6**, 1173–1179 (2004).

[CAS](#) [Google Scholar](#)

20. 20.

Ding, M. et al. The cell signaling adaptor protein EPS-8 is essential for *C. elegans* epidermal elongation and interacts with the ankyrin repeat protein VAB-19. *PLoS One* **3**, e3346 (2008).

[ADS](#) [PubMed](#) [PubMed Central](#) [Google Scholar](#)

21. 21.

Fraser, A. G. et al. Functional genomic analysis of *C. elegans* chromosome I by systematic RNA interference. *Nature* **408**, 325–330 (2000).

[ADS](#) [CAS](#) [Google Scholar](#)

22. 22.

Karabinos, A., Schünemann, J. & Weber, K. Most genes encoding cytoplasmic intermediate filament (IF) proteins of the nematode *Caenorhabditis elegans* are required in late embryogenesis. *Eur. J. Cell Biol.* **83**, 457–468 (2004).

[CAS](#) [Google Scholar](#)

23. 23.

Simmer, F. et al. Genome-wide RNAi of *C. elegans* using the hypersensitive *rrf3* strain reveals novel gene functions. *PLoS Biol.* **1**, E12 (2003).

[PubMed](#) [PubMed Central](#) [Google Scholar](#)

24. 24.

Kovács, L. et al. Role of the deubiquitylating enzyme DmUsp5 in coupling ubiquitin equilibrium to development and apoptosis in *Drosophila melanogaster*. *PLoS One* **10**, e0120875 (2015).

[PubMed](#) [PubMed Central](#) [Google Scholar](#)

25. 25.

Rogalla, T. et al. Regulation of Hsp27 oligomerization, chaperone function, and protective activity against oxidative stress/tumor necrosis factor alpha by phosphorylation. *J. Biol. Chem.* **274**, 18947–18956 (1999).

[CAS](#) [Google Scholar](#)

26. 26.

Kaletsky, R. et al. Transcriptome analysis of adult *Caenorhabditis elegans* cells reveals tissue-specific gene and isoform expression. *PLoS Genet.* **14**, e1007559 (2018).

[PubMed](#) [PubMed Central](#) [Google Scholar](#)

27. 27.

Taylor, R. C., Berendzen, K. M. & Dillin, A. Systemic stress signalling: understanding the cell non-autonomous control of

proteostasis. *Nat. Rev. Mol. Cell Biol.* **15**, 211–217 (2014).

[CAS](#) [PubMed](#) [PubMed Central](#) [Google Scholar](#)

28. 28.

Richmond, J. E., Davis, W. S. & Jorgensen, E. M. UNC-13 is required for synaptic vesicle fusion in *C. elegans*. *Nat. Neurosci.* **2**, 959–964 (1999).

[CAS](#) [PubMed](#) [PubMed Central](#) [Google Scholar](#)

29. 29.

Egge, N. et al. Age-onset phosphorylation of a minor actin variant promotes intestinal barrier dysfunction. *Dev. Cell* **51**, 587–601 (2019).

[CAS](#) [PubMed](#) [PubMed Central](#) [Google Scholar](#)

30. 30.

Mack, N. A., Whalley, H. J., Castillo-Lluva, S. & Malliri, A. The diverse roles of Rac signaling in tumorigenesis. *Cell Cycle* **10**, 1571–1581 (2011).

[CAS](#) [PubMed](#) [PubMed Central](#) [Google Scholar](#)

31. 31.

Lundquist, E. A., Reddien, P. W., Hartwieg, E., Horvitz, H. R. & Bargmann, C. I. Three *C. elegans* Rac proteins and several alternative Rac regulators control axon guidance, cell migration and apoptotic cell phagocytosis. *Development* **128**, 4475–4488 (2001).

[CAS](#) [Google Scholar](#)

32. 32.

Davis, R. J. Signal transduction by the JNK group of MAP kinases. *Cell* **103**, 239–252 (2000).

[CAS](#) [Google Scholar](#)

33. 33.

Twumasi-Boateng, K. et al. An age-dependent reversal in the protective capacities of JNK signaling shortens *Caenorhabditis elegans* lifespan. *Aging Cell* **11**, 659–667 (2012).

[CAS](#) [Google Scholar](#)

34. 34.

Scita, G. et al. An effector region in Eps8 is responsible for the activation of the Rac-specific GEF activity of Sos-1 and for the proper localization of the Rac-based actin-polymerizing machine. *J. Cell Biol.* **154**, 1031–1044 (2001).

[CAS](#) [PubMed](#) [PubMed Central](#) [Google Scholar](#)

35. 35.

Baird, N. A. et al. HSF-1-mediated cytoskeletal integrity determines thermotolerance and life span. *Science* **346**, 360–363 (2014).

[ADS](#) [CAS](#) [PubMed](#) [PubMed Central](#) [Google Scholar](#)

36. 36.

Brenner, S. The genetics of *Caenorhabditis elegans*. *Genetics* **77**, 71–94 (1974).

[CAS](#) [PubMed](#) [PubMed Central](#) [Google Scholar](#)

37. 37.

Higuchi-Sanabria, R. et al. Spatial regulation of the actin cytoskeleton by HSF-1 during aging. *Mol. Biol. Cell* **29**, 2522–2527 (2018).

[PubMed](#) [PubMed Central](#) [Google Scholar](#)

38. 38.

Hüsken, K. et al. Maintenance of the intestinal tube in *Caenorhabditis elegans*: the role of the intermediate filament protein IFC-2. *Differentiation* **76**, 881–896 (2008).

[Google Scholar](#)

39. 39.

Carberry, K. et al. The novel intestinal filament organizer IFO-1 contributes to epithelial integrity in concert with ERM-1 and DLG-1. *Development* **139**, 1851–1862 (2012).

[CAS](#) [PubMed](#) [PubMed Central](#) [Google Scholar](#)

40. 40.

Geisler, F. et al. Intestinal intermediate filament polypeptides in *C. elegans*: common and isotype-specific contributions to intestinal ultrastructure and function. *Sci. Rep.* **10**, 3142 (2020).

[ADS](#) [CAS](#) [PubMed](#) [PubMed Central](#) [Google Scholar](#)

41. 41.

Mello, C. C., Kramer, J. M., Stinchcomb, D. & Ambros, V. Efficient gene transfer in *C. elegans*: extrachromosomal maintenance and integration of transforming sequences. *EMBO J.* **10**, 3959–3970 (1991).

[CAS](#) [PubMed](#) [PubMed Central](#) [Google Scholar](#)

42. 42.

Noormohammadi, A. et al. Somatic increase of CCT8 mimics proteostasis of human pluripotent stem cells and extends *C. elegans* lifespan. *Nat. Commun.* **7**, 13649 (2016).

[ADS](#) [CAS](#) [PubMed](#) [PubMed Central](#) [Google Scholar](#)

43. 43.

Espelt, M. V., Estevez, A. Y., Yin, X. & Strange, K. Oscillatory Ca²⁺ signaling in the isolated *Caenorhabditis elegans* intestine: role of the inositol-1,4,5-trisphosphate receptor and phospholipases C beta and gamma. *J. Gen. Physiol.* **126**, 379–392 (2005).

[CAS](#) [PubMed](#) [PubMed Central](#) [Google Scholar](#)

44. 44.

Yigit, E. et al. Analysis of the *C. elegans* Argonaute family reveals that distinct Argonautes act sequentially during RNAi. *Cell* **127**, 747–757 (2006).

[CAS](#) [Google Scholar](#)

45. 45.

Calixto, A., Chelur, D., Topalidou, I., Chen, X. & Chalfie, M. Enhanced neuronal RNAi in *C. elegans* using SID-1. *Nat. Methods* **7**, 554–559 (2010).

[CAS](#) [PubMed](#) [PubMed Central](#) [Google Scholar](#)

46. 46.

Qadota, H. et al. Establishment of a tissue-specific RNAi system in *C. elegans*. *Gene* **400**, 166–173 (2007).

[CAS](#) [PubMed](#) [PubMed Central](#) [Google Scholar](#)

47. 47.

Amrit, F. R., Ratnappan, R., Keith, S. A. & Ghazi, A. The *C. elegans* lifespan assay toolkit. *Methods* **68**, 465–475 (2014).

[CAS](#) [Google Scholar](#)

48. 48.

Yang, J. S. et al. OASIS: online application for the survival analysis of lifespan assays performed in aging research. *PLoS One* **6**, e23525 (2011).

[ADS](#) [CAS](#) [PubMed](#) [PubMed Central](#) [Google Scholar](#)

49. 49.

Porta-de-la-Riva, M., Fontrodona, L., Villanueva, A. & Ceron, J. Basic *Caenorhabditis elegans* methods: synchronization and observation. *J. Vis. Exp.* **64**, e4019 (2012).

[Google Scholar](#)

50. 50.

Cox, J. et al. Accurate proteome-wide label-free quantification by delayed normalization and maximal peptide ratio extraction, termed MaxLFQ. *Mol. Cell. Proteomics* **13**, 2513–2526 (2014).

[CAS](#) [PubMed](#) [PubMed Central](#) [Google Scholar](#)

51. 51.

Kim, W. et al. Systematic and quantitative assessment of the ubiquitin-modified proteome. *Mol. Cell* **44**, 325–340 (2011).

[CAS](#) [PubMed](#) [PubMed Central](#) [Google Scholar](#)

52. 52.

Fatima, A. et al. The ubiquitin-conjugating enzyme UBE2K determines neurogenic potential through histone H3 in human embryonic stem cells. *Commun. Biol.* **3**, 262 (2020).

[CAS](#) [PubMed](#) [PubMed Central](#) [Google Scholar](#)

53. 53.

Koyuncu, S. et al. The ubiquitin ligase UBR5 suppresses proteostasis collapse in pluripotent stem cells from Huntington's disease patients. *Nat. Commun.* **9**, 2886 (2018).

[ADS](#) [PubMed](#) [PubMed Central](#) [Google Scholar](#)

54. 54.

Hanna, J., Leggett, D. S. & Finley, D. Ubiquitin depletion as a key mediator of toxicity by translational inhibitors. *Mol. Cell. Biol.* **23**, 9251–9261 (2003).

[CAS](#) [PubMed](#) [PubMed Central](#) [Google Scholar](#)

55. 55.

Hoogewijs, D., Houthoofd, K., Matthijssens, F., Vandesompele, J. & Vanfleteren, J. R. Selection and validation of a set of reliable reference genes for quantitative *sod* gene expression analysis in *C. elegans*. *BMC Mol. Biol.* **9**, 9 (2008).

[PubMed](#) [PubMed Central](#) [Google Scholar](#)

56. 56.

Oh, S. W. et al. JNK regulates lifespan in *Caenorhabditis elegans* by modulating nuclear translocation of forkhead transcription factor/DAF-16. *Proc. Natl Acad. Sci. USA* **102**, 4494–4499 (2005).

[ADS](#) [CAS](#) [PubMed](#) [PubMed Central](#) [Google Scholar](#)

57. 57.

Brignull, H. R., Moore, F. E., Tang, S. J. & Morimoto, R. I. Polyglutamine proteins at the pathogenic threshold display neuron-specific aggregation in a pan-neuronal *Caenorhabditis elegans* model. *J. Neurosci.* **26**, 7597–7606 (2006).

[CAS](#) [PubMed](#) [PubMed Central](#) [Google Scholar](#)

58. 58.

Zhang, Q. et al. The mitochondrial unfolded protein response is mediated cell-non-autonomously by retromer-dependent Wnt signaling. *Cell* **174**, 870–883 (2018).

[CAS](#) [PubMed](#) [PubMed Central](#) [Google Scholar](#)

[Download references](#)

Acknowledgements

The European Research Council (ERC Starting Grant-677427 StemProteostasis), the Deutsche Forschungsgemeinschaft (DFG) (VI742/4-1 and Germany's Excellence Strategy-CECAD, EXC 2030-390661388) and the Center for Molecular Medicine Cologne (C16) supported this research. We are grateful to the CECAD Proteomics Facility and C. Klein for their advice and contribution to proteomics experiments and analysis. We thank R. E. Leube for providing the *C. elegans* strains expressing intestinal intermediate filaments with fluorescent tags. We also thank P. M. Douglas for providing the HT115 bacteria driving mCherry expression. We thank R. Higuchi-Sanabria for comments on the manuscript.

Funding

Open access funding provided by Universität zu Köln.

Author information

Affiliations

1. Cologne Excellence Cluster for Cellular Stress Responses in Aging-Associated Diseases (CECAD), University of Cologne, Cologne, Germany

Seda Koyuncu, Rute Loureiro, Hyun Ju Lee, Prerana Wagle, Marcus Krueger & David Vilchez

2. Center for Molecular Medicine Cologne (CMMC), University of Cologne, Cologne, Germany

Marcus Krueger & David Vilchez

3. Faculty of Medicine, University Hospital Cologne, Cologne, Germany

David Vilchez

Authors

1. Seda Koyuncu

[View author publications](#)

You can also search for this author in [PubMed](#) [Google Scholar](#)

2. Rute Loureiro

[View author publications](#)

You can also search for this author in [PubMed](#) [Google Scholar](#)

3. Hyun Ju Lee

[View author publications](#)

You can also search for this author in [PubMed](#) [Google Scholar](#)

4. Prerana Wagle

[View author publications](#)

You can also search for this author in [PubMed](#) [Google Scholar](#)

5. Marcus Krueger

[View author publications](#)

You can also search for this author in [PubMed](#) [Google Scholar](#)

6. David Vilchez

[View author publications](#)

You can also search for this author in [PubMed](#) [Google Scholar](#)

Contributions

S.K. and D.V. performed most of the experiments, data analysis and interpretation. R.L. generated the *iβ-2(OE)* strains and helped with other experiments. H.J.L. performed experiments of isolated tissues. P.W. generated the Shiny Web apps and contributed to analysis of proteomics data. M.K. provided critical advice on the project. The manuscript was written by D.V. All authors discussed the results and commented on the manuscript.

Corresponding author

Correspondence to [David Vilchez](#).

Ethics declarations

Competing interests

The authors declare no competing interests.

Additional information

Peer review information *Nature* thanks Andrew Dillin, Donald Kirkpatrick and the other, anonymous, reviewer(s) for their contribution to the peer review of this work. Peer reviewer reports are available.

Publisher's note Springer Nature remains neutral with regard to jurisdictional claims in published maps and institutional affiliations.

Extended data figures and tables

Extended Data Fig. 1 Differences in the levels of Ub-peptides often do not directly correlate with a change in the total amounts of the protein.

a, Principal component analysis indicates high reproducibility in proteomics of Ub-peptides among the four biological replicates for each experimental condition (wild type, *eat-2(ad1116)*, *daf2(e1370)* at day 1, 5, 10 and 15 of adulthood). **b–d**, Heat maps representing \log_2 -transformed fold changes of all the differentially abundant Ub-peptides and their corresponding total protein levels at the indicated day and genetic background ($n = 4$, two-sided *t*-test, FDR < 0.05 was considered significant). In each heat map, only significantly changed Ub-peptides are shown. Supplementary Table 3 contains complete list of all identified Ub-peptides and levels of the respective protein. **e**, Integrated proteomics analysis of \log_2 -transformed fold changes in the levels of Ub-peptides and corresponding proteins comparing day-15 and day-5 wild-type worms ($n = 4$, two-sided *t*-test, FDR < 0.05). **f**, The total protein levels of myosin MYO-2 and paramyosin UNC-15 remain similar during ageing, but they contain multiple downregulated and upregulated Ub-sites. EPS-8 protein becomes more abundant with age, and most of its Ub-sites are significantly downregulated ($n = 4$, two-sided *t*-test, FDR < 0.05 was considered significant). Because EPS-8 has many different isoforms, we show the ubiquitination sites numbered according to the leading isoform identified in our proteomics data (EPS-8 protein isoform g). **g**, Among the 1,813 downregulated ubiquitin modifications in aged wild-type worms (WT d15/WT d5), age-matched *eat-2* (*eat-2* d15/WT d15) and *daf2* mutants (*daf2* d15/WT d15) exhibited increased ubiquitination for 952 and 336 peptides, respectively. Among the 350 upregulated ubiquitin modifications in aged wild-type worms, age-matched *eat-2* and *daf2* worms exhibited decreased ubiquitination for 234 and 251 peptides, respectively.

Extended Data Fig. 2 Loss of ubiquitination in aged wild-type worms is not associated with lower expression or half-life of protein ubiquitin itself.

a, Immunoblot of Ub-proteins in wild-type worms at the indicated days of adulthood. The images are representative of four independent experiments. **b**, Immunoblot of Ub-proteins in *eat-2(ad1116)* mutant worms. Representative of four independent experiments. **c**, Immunoblot of Ub-proteins in *daf2(e1370)* mutant worms. Representative of three independent experiments. **d**, qPCR analysis of ubiquitin (*ubq-1*), ubiquitin-ribosomal fusion (*ubq-2*, *UBL-1*) and ubiquitin-stress response (*usp-14*) genes comparing day-1 and day-15 wild-type adult worms. Graph represents the relative expression to day 1 adult wild-type worms (mean ± s.e.m., $n = 9$). P values: *ubq-1* ($P = 0.0117$), *ubq-2* ($P = 0.0042$), *UBL-1* ($P = 0.0598$), *usp-14* ($P = 0.5326$). **e**, qPCR analysis comparing day-1 and day-15 *eat-2* mutant worms. Graph represents the relative expression to day 1 adult *eat-2* mutant worms (mean ± s.e.m., $n = 9$). P values: *ubq-1* ($P = 0.0668$), *ubq-2* ($P = 0.0144$), *UBL-1* ($P < 0.0001$), *usp-14* ($P = 0.0786$). **f**, qPCR analysis comparing day 1 and day 15 *daf2* mutant worms. Graph represents the relative expression to day 1 adult *daf2* mutant worms (mean ± s.e.m., day 1 ($n = 9$); day 15 ($n = 8$)). P values: *ubq-1* ($P = 0.0057$), *ubq-2* ($P = 0.5710$), *UBL-1* ($P = 0.7593$), *usp-14* ($P = 0.2199$). **g**, qPCR analysis comparing day 15 wild-type worms with age-matched long-lived mutant worms. Graph represents the relative expression to wild-type worms (mean ± s.e.m., wild-type ($n = 9$); *eat-2* ($n = 9$); *daf2* ($n = 8$)). Wild-type worms express higher levels of *ubq-1* gene at day 15 of adulthood (wild-type versus *eat-2*: $P = 0.0341$; wild-type versus *daf2*: $P < 0.0001$). **h**, The log₂-transformed label-free quantification (LFQ) values of protein ubiquitin (UBQ-1 ;UBQ-2) from global proteomics analysis of wild-type, *eat-2(ad1116)* and *daf2(e1370)* worms at the indicated ages ($n = 4$, mean ± s.e.m.). The total amounts of protein ubiquitin itself slightly increase in wild-type worm with age (wild-type d1 versus wild-type d15: $P < 0.0001$). Old wild-type and aged-matched *daf2* mutant worms have similar levels of total protein ubiquitin (wild-type d15 versus *daf2* d15: $P = 0.2669$). Label-free proteomics of total protein levels (Supplementary Table 2) was performed in input samples separated from the same lysates

used for analysis of the Ub-modified proteome before the enrichment with an anti-diGly antibody. In **d–h**, *P* values were determined by two-sided *t*-test. **i**, Western blot of free ubiquitin (Ub) in worms treated with 54.5 µg ml^{−1} cycloheximide (CHX) to block ubiquitin synthesis. Worms were lysed at the indicated time after CHX treatment. The images are representative of three independent experiments. **j**, Quantification of the western blots presented in the previous figure. Graph represents the percentage of free Ub levels relative to time point 0 h of CHX treatment (mean ± s.e.m., *n* = 3 independent experiments). For gel source data, see Supplementary Fig. 1.

Source data

Extended Data Fig. 3 Single knockdown of specific age-dysregulated DUBs ameliorates the global decline in Ub-protein levels of aged wild-type worms.

a, Heat map representing all the differentially abundant E3 ubiquitin ligases in old (day 15) wild-type worms compared with young (day 5) wild-type worms (*n* = 4, two-sided *t*-test, FDR < 0.05 was considered significant). The levels of differentially abundant E3s in old wild-type worms were also compared with age-matched long-lived *eat-2* and *daf-2* mutants. **b**, Heat map representing all the differentially abundant DUBs in old wild-type worms compared with young wild-type worms (*n* = 4, two-sided *t*-test, FDR < 0.05 was considered significant). The levels of differentially abundant DUBs in old wild-type worms were also compared with age-matched long-lived *eat-2* and *daf-2* mutants. **c**, Immunoblot of Ub-proteins and α-tubulin in day 10 wild-type worms upon knockdown of *prp-8*, *eif3.F*, *cyk-3* and *F07A11.4* after development. The images are representative of three independent experiments. **d**, Immunoblot of Ub-proteins in day-10 wild-type worms upon knockdown of *usp-5* and *otub-3* after development. Representative of three independent experiments. **e**, Immunoblot of Ub-proteins in day-10 wild-type worms upon knockdown of *math-33* and *H34C03.2* after development. Representative of four independent experiments. **f**, Immunoblot of Ub-proteins in day-10 wild-type worms upon knockdown of *cyld-1* and *csn-6* after development. Representative of four independent experiments. **g**, Immunoblot of Ub-proteins in day-10 wild-type worms upon knockdown of *usp-50*, *csn-5* and *usp-48* after

development. Representative of four independent experiments. In **c–g**, RNAi was initiated at day 1 of adulthood. **h**, Wild-type worms treated with 13.7 µg ml⁻¹ of the broad-spectrum DUB inhibitor PR-619 at day 9 of adulthood for 24 h ($P = 0.0162$) or from day 9 of adulthood until the end of the experiment ($P < 0.0001$) live longer compared with untreated wild-type worms. P values: two-sided log-rank test, $n = 96$ worms per condition. Supplementary Table 11 contains statistics and replicate data of independent lifespan experiments. For gel source data, see Supplementary Fig. 1.

Extended Data Fig. 4 Ageing does not increase the mRNA levels of age-dysregulated proteasome targets.

a, Heat map representing log₂-transformed fold changes of all the differentially abundant proteins comparing *rpn-6* RNAi-treated wild-type worms with Vector RNAi-treated wild-type worms at day 5 of adulthood ($n = 3$, two-sided *t*-test, FDR < 0.05 was considered significant). Loss of proteasome activity results in widespread changes in the individual protein levels of young adults, including 297 downregulated proteins and 509 upregulated proteins. See Supplementary Table 8 for complete list of all the detected proteins. **b**, The mRNA levels of age-dysregulated proteasome targets do not increase with age. In fact, *iβ-2* ($P = 0.0026$) and *eps-8* ($P = 0.0194$) mRNA levels decrease in aged worms. Graph represents the relative expression to young (day 5) adult worms (mean ± s.e.m., $n = 3$). **c**, Loss of *rpn-6* does not upregulate the mRNA levels of age-dysregulated proteasome targets in young worms (day 5), with the exception of the deubiquitinase *usp-5* ($P = 0.0019$) that could indicate a compensatory mechanism to ameliorate ubiquitin deficits triggered by dysregulated proteasome activity. Graph represents the relative expression to Vector RNAi control (mean ± s.e.m., $n = 3$). RNAi treatment was initiated at day 1 of adulthood. In **b**, **c**, P values were determined by two-sided *t*-test. **d**, Volcano plot of proteins containing Lys63-linked polyUb chains in wild-type worms at day 5 of adulthood ($n = 3$, FDR < 0.05). $-\log_{10}(P \text{ value})$ of a two-sided *t*-test is plotted against the log₂-transformed fold change of LFQ values from immunoprecipitation experiments using an antibody against Lys63-linked polyUb compared with anti-Flag antibody. Red dots indicate age-dysregulated proteasome targets. **e**, Knockdown of either *hsp-43*

($P = 0.0010$) or *usp-5* ($P = 0.0146$) during adulthood shortens lifespan, indicating that these genes are essential for adult viability. Knockdown of either *ddi-1* ($P = 0.8277$) or *lec-1* ($P = 0.7034$) does not significantly affect lifespan. In contrast, single knockdown of *rpl-4* ($P = 0.0283$), *M01G12.9* ($P < 0.0001$), *C46C2.2* ($P = 0.0196$) and *F54D1.6* ($P = 0.0400$) extends lifespan. In each lifespan experiment, RNAi was initiated at day 1 of adulthood. P values were determined by two-sided log-rank test; $n = 96$ worms per condition. Lifespan data are representative of two independent experiments. Supplementary Table 11 contains statistics and replicate data of independent lifespan experiments. **f**, Western blot analysis with an antibody against GFP of integrated transgenic worms expressing *iβ-2p::iβ-2a::CFP*. α -tubulin is the loading control. Representative of two independent experiments. **g**, Western blot with an antibody against GFP of worms expressing endogenous IFB-2 tagged with GFP. Representative of two independent experiments. **h**, Western blot analysis of total IFB-2 levels with an anti-IFB-2 antibody in whole wild-type *C. elegans* extracts without mild centrifugation to collect supernatant. Representative of three independent experiments. For gel source data, see Supplementary Fig. 1.

[Source data](#)

[**Extended Data Fig. 5 The age-associated decline in ubiquitination levels occurs across tissues.**](#)

a, Bioinformatics classification of proteins that exhibit differences in their Ub-peptides in aged wild-type worms (day 15) according to the tissues where these proteins are expressed. **b**, Immunoblot of Ub-proteins in lysates of whole worms or isolated germlines, intestines and heads from wild-type worms at the indicated days of adulthood. Representative of two independent experiments. **c**, Western blot analysis with an antibody against EPS-8 of isolated intestines and heads from wild-type worms at the indicated days. Representative of two independent experiments. **d**, Western blot analysis with an antibody against IFB-2 of isolated intestines and heads from wild-type worms at the indicated days. Representative of two independent experiments. **e**, Western blot with antibodies to EPS-8 and IFB-2 after intestinal-specific knockdown (KD) of *rpn-6*. RNAi rescued in the intestine of RNAi-deficient worms (*rde-1(ne219); nhx-2p::rde-1* strain).

f, Western blot with antibodies to EPS-8 and IFB-2 after neuronal-specific KD of *rpn-6*. RNAi rescued in the neurons of RNAi-deficient worms (*sid-1(pk3321); unc-119p::sid-1* strain). **g**, Western blot with antibodies to EPS-8 and IFB-2 after muscle-specific KD of *rpn-6*. RNAi rescued in the muscle of RNAi-deficient worms (*rde-1(ne300); myo-3p::rde-1* strain). **h**, Western blot with antibodies to EPS-8 and IFB-2 after epidermal-specific KD of *rpn-6*. RNAi rescued in the epidermis of RNAi-deficient worms (*rde-1(ne219); lin-26p::rde-1* strain). In **e–h**, RNAi treatment was initiated at day 1 of adulthood. Worms were analysed at day 5 of adulthood. Representative of two independent experiments. **i**, Immunoblot of Ub-proteins in wild-type and *unc-13(e51)* mutant worms at the indicated days of adulthood. Representative of three independent experiments. **j**, Western blot with an antibody against EPS-8 in wild-type and *unc-13(e51)* mutant worms at day 10 of adulthood. Representative of three independent experiments. **k**, Western blot with an antibody against IFB-2 in wild-type and *unc-13(e51)* mutant worms at day 10 of adulthood. Representative of three independent experiments. For gel source data, see Supplementary Fig. 1.

Extended Data Fig. 6 Increased levels of IFB-2 and EPS-8 shorten adult lifespan.

a, Western blot with an antibody against IFB-2 of whole lysates from wild-type worms and IFB-2 K255R/K341R (Ub-less) mutant worms at day 2 of adulthood. The images are representative of two independent experiments. **b**, Non-integrated transgenic DVG197 and DVG198 strains overexpressing *iβ-2* under *sur-5* promoter exhibit a short lifespan phenotype compared with the control strain ($P < 0.0001$). P values were determined by two-sided log-rank test; $n = 96$ worms per condition. Lifespan data are representative of two independent experiments. **c**, Percentage of hatched eggs (mean \pm s.e.m., $n = 10$ worms scored per condition from 2 independent experiments). EPS-8(K524R/K583R/K621R) (Ub-less) mutants do not exhibit embryonic lethality ($P = 0.7806$). **d**, Percentage of L1 larvae that developed into adults (mean \pm s.e.m., $n = 10$ worms scored per condition from 2 independent experiments). Ubiquitin-less EPS-8 mutants do not exhibit developmental arrest ($P = 0.0507$). In **c, d**, P values were determined by two-sided *t*-test. **e**, Ubiquitin-less EPS-8 mutant worms live shorter than with worms that express wild-type EPS-8 (EPS-8 (WT) +

Vector RNAi versus EPS-8 (Ub-less) + Vector RNAi, $P = 0.0030$).

Knockdown of *eps-8* after development suppresses the deleterious effects on lifespan induced by Ub-less EPS-8 mutations (EPS-8 (WT) + *eps-8* RNAi versus EPS-8 (Ub-less) + *eps-8* RNAi, $P = 0.3394$). P values determined by two-sided log-rank test, $n = 96$ worms per condition. Supplementary Table 11 contains statistics and replicate data of independent lifespan experiments. For gel source data, see Supplementary Fig. 1.

[Source data](#)

Extended Data Fig. 7 Ageing induces mislocalization and aggregation of IFB-2 and other intestinal intermediate filaments.

a, Muscle-specific knockdown of *iβ-2* does not affect lifespan ($P = 0.3755$). **b**, Neuronal-specific knockdown of *iβ-2* does not affect lifespan ($P = 0.6381$). In each lifespan experiment, RNAi was initiated during adulthood, P values determined by two-sided log-rank test, $n = 96$ worms per condition. Supplementary Table 11 contains statistics and replicate data of independent lifespan experiments. **c**, Representative images of transgenic worms expressing IFB-2::CFP under *iβ-2* promoter at different days of adulthood. On the left, IFB-2::CFP is presented in greyscale to show more visibly the IFB-2 aggregates. Merge images present IFB-2::CFP (blue) + DIC (differential interference contrast). Scale bar, 200 μm. Representative of three independent experiments. **d**, Images of worms expressing endogenous IFB-2 tagged with GFP at different days of adulthood. Scale bar, 100 μm. Representative of two independent experiments. **e**, Filter trap analysis with an antibody against GFP of worms expressing endogenous IFB-2 tagged with GFP. Representative of three independent experiments. **f**, Images of worms expressing endogenous IFC-2 tagged with YFP or the integrated transgenes *ifc-1p::IFC-1::GFP* and *iβ-1p::IFP-1::GFP*. Scale bar, 100 μm. Representative of two independent experiments. **g**, Filter trap analysis with an antibody against GFP of *C. elegans* expressing IFC-1::GFP under *ifc-1* promoter. Representative of two independent experiments. **h**, Filter trap with an antibody to GFP of *C. elegans* expressing endogenous intestinal intermediate filament IFC-2 tagged with YFP. Representative of three independent experiments. **i**, Filter

trap with an antibody to GFP of *C. elegans* expressing IFP-1::GFP under *iβ-1* promoter. Representative of two independent experiments. **j**, Images of worms expressing the intestinal filament organizer IFO-1::YFP under *iβ-1* promoter. Scale bar, 100 μm. Representative of three independent experiments. **k**, Filter trap with an antibody to GFP of worms expressing IFO-1::YFP under *iβ-1* promoter. Representative of four independent experiments.

Extended Data Fig. 8 Downregulation of increased IFB-2 levels ameliorates loss of intestinal integrity and bacterial colonization.

a, *iβ-2* RNAi ameliorates age-related changes in the intracellular distribution and aggregation of the intestinal intermediate filaments IFC-1, IFC-2 and IFP-1 as well as the intestinal filament organizer IFO-1. We examined worms expressing endogenous IFC-2 tagged with YFP or the integrated transgenes *iβ-1p::IFC-1::GFP*, *iβ-1p::IFP-1::GFP*, and *iβ-1p::IFO-1::GFP*. *iβ-2* RNAi was initiated during adulthood. Scale bar, 25 μm. Representative of two independent experiments. **b**, Filter trap analysis with an antibody to GFP of *C. elegans* expressing endogenous intestinal intermediate filament IFC-2 tagged with YFP. *iβ-2* RNAi was initiated during adulthood. Representative of four independent experiments. **c**, Filter trap analysis with an antibody to GFP of worms expressing IFO-1::YFP under *iβ-1* promoter. *iβ-2* RNAi was initiated during adulthood. Representative of three independent experiments. **d**, Images of bacterial colonization in the intestine of wild-type *C. elegans* at different days of adulthood. RNAi was initiated during adulthood. Scale bar, 200 μm. Representative of three independent experiments. **e**, Images of bacterial colonization in the intestine of wild-type and IFB-2(K255R/K341R) (Ub-less) mutant worms at day 10 of adulthood. Scale bar, 200 μm. Representative of three independent experiments. Quantifications of bacterial colonization are shown in Fig. 3f,g.

Extended Data Fig. 9 Age-related hyperactivation of RAC by increased EPS-8 levels increases JNK phosphorylation.

a, Intestinal-specific knockdown of *eps-8* after development does not affect lifespan ($P = 0.1486$). **b**, Epidermal-specific knockdown of *eps-8* during adulthood does not affect lifespan ($P = 0.3149$). **c**, Single knockdown of RAC orthologues *mig-2* ($P < 0.0001$) and *rac-2* ($P = 0.0008$) during adulthood extends lifespan in wild-type worms. Knockdown of RAC orthologue *ced-10* does not affect lifespan ($P = 0.3227$). **d**, Intestinal-specific knockdown of either *mig-2* ($P = 0.7340$) or *rac-2* ($P = 0.6021$) during adulthood does not affect lifespan. **e**, Muscle-specific knockdown of either *mig-2* ($P < 0.0001$) or *rac-2* ($P = 0.0003$) during adulthood extends lifespan. **f**, Neuronal-specific knockdown of either *mig-2* ($P < 0.0001$) or *rac-2* ($P < 0.0001$) during adulthood extends lifespan. **g**, Western blot analysis with antibodies to phosphorylated JNK (P-JNK), total JNK and α -tubulin of wild-type worms at different days of adulthood. Representative of three independent experiments. **h**, Western blot analysis with antibodies to P-JNK, total JNK and α -tubulin of wild-type worms at day 10 of adulthood. *eps-8* RNAi was initiated during adulthood. Representative of two independent experiments. **i**, Knockdown of *kgb-1* after development extends longevity (EPS-8 (WT) Vector RNAi versus EPS-8 (WT) *kgb-1* RNAi, $P < 0.0001$) and rescues the short lifespan induced by ubiquitin-less EPS-8 mutant variant (EPS-8 (WT) Vector RNAi versus EPS-8 (Ub-less) Vector RNAi ($P < 0.0001$); EPS-8 (WT) *kgb-1* RNAi versus EPS-8 (Ub-less) *kgb-1* RNAi ($P = 0.8061$)). In each lifespan experiment, RNAi was initiated at day 1 of adulthood. P values were determined by two-sided log-rank test, $n = 96$ worms per condition. Supplementary Table 11 contains statistics and replicate data of independent lifespan experiments. For gel source data, see Supplementary Fig. 1.

Extended Data Fig. 10 Lowering hyperactivated RAC signalling prevents alterations in actin networks induced by increased EPS-8 levels.

a, Myosin heavy chain tagged to GFP indicates destabilization of myosin filaments in muscle cells during ageing, whereas knockdown of *eps-8* during adulthood maintains organization of the myosin network. Scale bar, 20 μ m. Representative of three independent experiments. **b**, Data are mean \pm s.e.m. thrashing movements over a 30-s period on day 1 ($n = 30$ worms per condition, three independent experiments), day 3 ($n = 30$ worms

per condition, three independent experiments) and day 10 ($n = 45$ worms per condition, three independent experiments) of adulthood. Knockdown of *eps-8* after development ameliorates the age-associated decline in motility (day 1 vector RNAi versus day 1 *eps-8* RNAi, $P = 0.2127$; day 3 Vector RNAi versus day 3 *eps-8* RNAi, $P < 0.0001$; day 10 Vector RNAi versus day 10 *eps-8* RNAi, $P < 0.0001$). P values were determined by two-sided *t*-test. **c**, Images of transgenic worms expressing LifeAct::mRuby in the epidermis. Scale bar, 20 μm . Representative of two independent experiments. **d**, Images of transgenic worms expressing LifeAct::mRuby in the intestine. Scale bar, 100 μm . Representative of two independent experiments. **e**, Filter trap analysis with an antibody to β -actin in wild-type worms. Knockdown of *eps-8* during adulthood reduces the amounts of actin aggregates in aged worms. Representative of six independent experiments. **f**, Filter trap analysis with an antibody to β -actin. Muscle-specific knockdown of *eps-8* during adulthood reduces the amounts of actin aggregates in aged worms. Representative of three independent experiments. **g**, Neuronal-specific knockdown of *eps-8* results in decreased actin aggregates during ageing. Representative of three independent experiments. **h**, Epidermal-specific knockdown of *eps-8* does not decrease age-related actin aggregation. Representative of three independent experiments. **i**, Intestinal-specific knockdown of *eps-8* does not decrease age-related actin aggregation. Representative of three independent experiments. **j**, Knockdown of either *mig-2* or *rac-2* during adulthood ameliorates the age-associated destabilization of actin filaments in muscle cells. RNAi treatment was initiated at day 1 of adulthood. Scale bar, 20 μm . Representative of two independent experiments. **k**, Knockdown of either *mig-2* or *rac-2* during adulthood ameliorates the age-associated destabilization of myosin filaments in muscle cells. Scale bar, 20 μm . Representative of two independent experiments. **l**, Filter trap with an antibody to β -actin in worms expressing endogenous wild-type EPS-8 or mutant Ub-less EPS-8 at day 3 of adulthood. Representative of three independent experiments. In all the experiments, RNAi was initiated at day 1 of adulthood.

[Source data](#)

Supplementary information

Supplementary Figure 1

This file contains source data for gel electrophoresis.

Reporting Summary

Supplementary Table 1

Proteomic analysis of Ub-peptides from wild-type, *eat-2* and *daf-2* worms at day 1, 5, 10 and 15 of adulthood (n= 4, two-sided *t*-test, False Discovery Rate (FDR)<0.05 was considered significant).

Supplementary Table 2

Shotgun label-free proteomics of protein levels in wild-type, *eat-2* and *daf-2* worms at day 1, 5, 10 and 15 of adulthood (n= 4, two-sided *t*-test, FDR<0.05 was considered significant). Shotgun proteomics experiments were performed in input samples separated from the lysates used for analysis of the ubiquitin-modified proteome before enrichment with anti-diGly antibodies.

Supplementary Table 3

Integrated proteomics analysis of Ub-modified peptide levels and total protein levels (n= 4, two-sided *t*-test, FDR<0.05 was considered significant).

Supplementary Table 4

Comparison of the Ub-modified proteome of old wild-type worms (day 15) versus young worms (day 5) (n= 4, two-sided *t*-test, FDR<0.05 was considered significant).

Supplementary Table 5

Integrated proteomics analysis of Ub-modified peptide levels and total protein levels in aged wild-type worms (day 15) compared with young worms (day 5) (n= 4, two-sided *t*-test, FDR<0.05 was considered significant).

Supplementary Table 6

Changes in Ub-modified peptides in aged wild-type worms rescued in age-matched long-lived mutant worms (n= 4, two-sided *t*-test, FDR<0.05 was considered significant).

Supplementary Table 7

Differentially abundant E3s and DUBs in old (day 15) wild-type worms compared with young (day 5) wild-type worms (n= 4, two-sided *t*-test, FDR<0.05 was considered significant). The levels of differentially abundant E3s and DUBs in old wild-type worms were also compared with age-matched long-lived *eat-2* and *daf-2* mutants.

Supplementary Table 8

Proteomic analysis of the levels of Ub-peptides and total protein comparing empty vector RNAi with *rpn-6* RNAi-treated wild-type worms at day 5 of adulthood (n= 3, two-sided *t*-test, FDR<0.05 was considered significant). This file also contains integrated analysis with list of Ub-proteins that increased upon *rpn-6* RNAi in young adults (day 5), and also became less ubiquitinated but more abundant during the aging process (aged worms (day 15) versus young worms (day 5)).

Supplementary Table 9

Proteomics data from immunoprecipitation experiments using antibody against proteins containing Lys48 or Lys63-linked ubiquitin chains compared with control FLAG antibody in wild-type worms at day 5 of adulthood (n=3, two-sided *t*-test, FDR<0.05 was considered significant).

Supplementary Table 10

Tissue-specific expression analysis using the bioinformatic tool <http://worm.princeton.edu> of proteins containing downregulated or upregulated Ub-modified peptides in aged wild-type worms.

Supplementary Table 11

Statistics and replicate data of independent lifespan experiments.

Supplementary Table 12

Sequences for RNAi constructs used for knockdown assays.

Supplementary Table 13

List of primers used for qPCR assay.

Peer Review File

Source data

Source Data Fig. 3

Source Data Fig. 4

Source Data Extended Data Fig. 2

Source Data Extended Data Fig. 4

Source Data Extended Data Fig. 6

Source Data Extended Data Fig. 10

Rights and permissions

Open Access This article is licensed under a Creative Commons Attribution 4.0 International License, which permits use, sharing, adaptation, distribution and reproduction in any medium or format, as long as you give appropriate credit to the original author(s) and the source, provide a link to the Creative Commons license, and indicate if changes were made. The images or other third party material in this article are included in the article's Creative Commons license, unless indicated otherwise in a credit line to the material. If material is not included in the article's Creative Commons license and your intended use is not permitted by statutory regulation or exceeds the permitted use, you will need to obtain permission directly from the copyright holder. To view a copy of this license, visit <http://creativecommons.org/licenses/by/4.0/>.

[Reprints and Permissions](#)

About this article



Check for
updates

Cite this article

Koyuncu, S., Loureiro, R., Lee, H.J. *et al.* Rewiring of the ubiquitinated proteome determines ageing in *C. elegans*. *Nature* **596**, 285–290 (2021). <https://doi.org/10.1038/s41586-021-03781-z>

[Download citation](#)

- Received: 19 November 2020
- Accepted: 29 June 2021
- Published: 28 July 2021

- Issue Date: 12 August 2021
- DOI: <https://doi.org/10.1038/s41586-021-03781-z>

Comments

By submitting a comment you agree to abide by our [Terms](#) and [Community Guidelines](#). If you find something abusive or that does not comply with our terms or guidelines please flag it as inappropriate.

[Download PDF](#)

Associated Content

[Protein pile-up plays havoc in ageing nematode worms](#)

- Bart P. Braeckman

News & Views 28 Jul 2021

Advertisement

This article was downloaded by **calibre** from <https://www.nature.com/articles/s41586-021-03781-z>

- Article
- [Published: 28 July 2021](#)

Regulated control of gene therapies by drug-induced splicing

- [Alex Mas Monteys](#) ^{1,2},
- [Amiel A. Hundley](#)¹,
- [Paul T. Ranum](#)¹,
- [Luis Tededor](#)¹,
- [Amy Muehlmann](#)¹,
- [Euyn Lim](#)¹,
- [Dmitriy Lukashev](#)³,
- [Rajeev Sivasankaran](#)³ &
- [Beverly L. Davidson](#) [ORCID: orcid.org/0000-0002-3715-6290](#)^{1,2}

[Nature](#) volume **596**, pages 291–295 (2021) [Cite this article](#)

- 11k Accesses
- 355 Altmetric
- [Metrics details](#)

Subjects

- [Biotechnology](#)
- [Gene therapy](#)
- [Molecular biology](#)

Abstract

So far, gene therapies have relied on complex constructs that cannot be finely controlled^{1,2}. Here we report a universal switch element that enables precise control of gene replacement or gene editing after exposure to a small molecule. The small-molecule inducers are currently in human use, are orally bioavailable when given to animals or humans and can reach both peripheral tissues and the brain. Moreover, the switch system, which we denote X^{on}, does not require the co-expression of any regulatory proteins. Using X^{on}, the translation of the desired elements for controlled gene replacement or gene editing machinery occurs after a single oral dose of the inducer, and the robustness of expression can be controlled by the drug dose, protein stability and redosing. The ability of X^{on} to provide temporal control of protein expression can be adapted for cell-biology applications and animal studies. Additionally, owing to the oral bioavailability and safety of the drugs used, the X^{on} switch system provides an unprecedented opportunity to refine and tailor the application of gene therapies in humans.

Access options

Subscribe to Journal

Get full journal access for 1 year

\$199.00

only \$3.90 per issue

[Subscribe](#)

All prices are NET prices.

VAT will be added later in the checkout.

Tax calculation will be finalised during checkout.

Rent or Buy article

Get time limited or full article access on ReadCube.

from \$8.99

Rent or Buy

All prices are NET prices.

Additional access options:

- [Log in](#)
- [Access through your institution](#)
- [Learn about institutional subscriptions](#)

Fig. 1: Generation and testing of X^{on}.

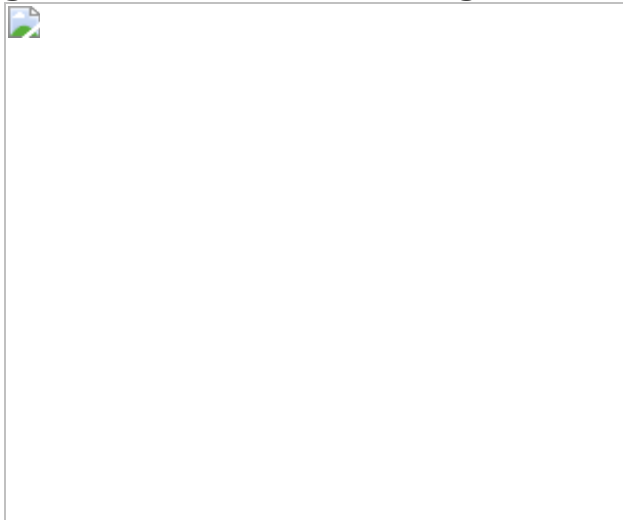


Fig. 2: Activity of X^{on} in liver.

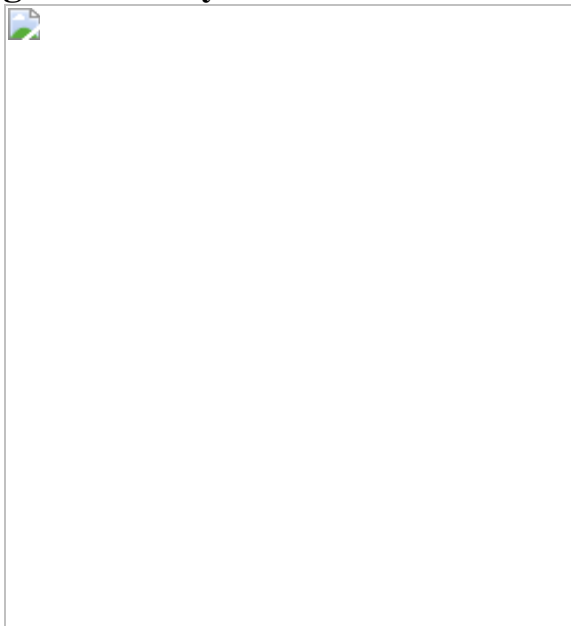


Fig. 3: Drug-induced regulation of Epo.

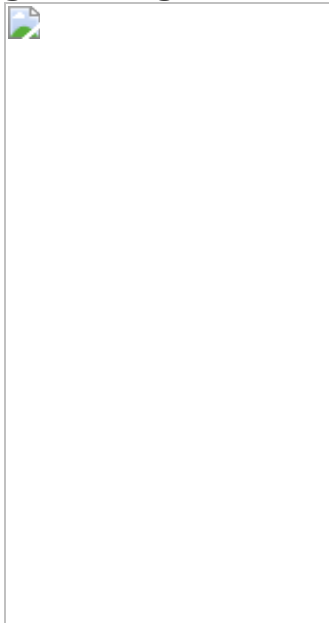
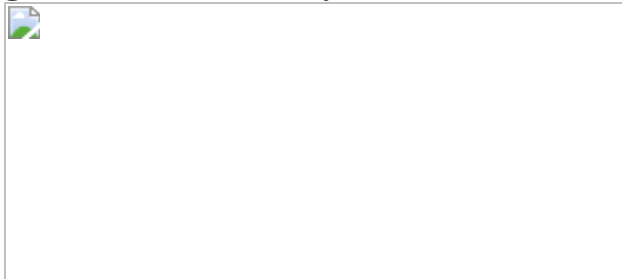


Fig. 4: In vivo activity of X^{on} in the brain.



Data availability

RNA-seq datasets are archived in the NCBI Gene Expression Omnibus under accession number [GSE176527](https://www.ncbi.nlm.nih.gov/geo/query/acc.cgi?acc=GSE176527).

Code availability

The R code to characterize novel LMI070-induced splicing events from RNA-seq data is available at <https://github.com/DavidsonLabCHOP/Xon>.

References

1. 1.

Yen, L. et al. Exogenous control of mammalian gene expression through modulation of RNA self-cleavage. *Nature* **431**, 471–476 (2004).

[ADS](#) [CAS](#) [Article](#) [Google Scholar](#)

2. 2.

Dow, L. E. et al. Inducible *in vivo* genome editing with CRISPR–Cas9. *Nat. Biotechnol.* **33**, 390–394 (2015).

[CAS](#) [Article](#) [Google Scholar](#)

3. 3.

Brown, B. D., Venneri, M. A., Zingale, A., Sergi Sergi, L. & Naldini, L. Endogenous microRNA regulation suppresses transgene expression in hematopoietic lineages and enables stable gene transfer. *Nat. Med.* **12**, 585–591 (2006).

[CAS](#) [Article](#) [Google Scholar](#)

4. 4.

Domenger, C. & Grimm, D. Next-generation AAV vectors—do not judge a virus (only) by its cover. *Hum. Mol. Genet.* **28** (R1), R3–R14 (2019).

[CAS](#) [Article](#) [Google Scholar](#)

5. 5.

Berget, S. M., Moore, C. & Sharp, P. A. Spliced segments at the 5' terminus of adenovirus 2 late mRNA. *Proc. Natl Acad. Sci. USA* **74**, 3171–3175 (1977).

[ADS](#) [CAS](#) [Article](#) [Google Scholar](#)

6. 6.

Cartegni, L. & Krainer, A. R. Disruption of an SF2/ASF-dependent exonic splicing enhancer in *SMN2* causes spinal muscular atrophy in the absence of *SMN1*. *Nat. Genet.* **30**, 377–384 (2002).

[CAS](#) [Article](#) [Google Scholar](#)

7. 7.

Naryshkin, N. A. et al. *SMN2* splicing modifiers improve motor function and longevity in mice with spinal muscular atrophy. *Science* **345**, 688–693 (2014).

[ADS](#) [CAS](#) [Article](#) [Google Scholar](#)

8. 8.

Palacino, J. et al. *SMN2* splice modulators enhance U1-pre-mRNA association and rescue SMA mice. *Nat. Chem. Biol.* **11**, 511–517 (2015).

[CAS](#) [Article](#) [Google Scholar](#)

9. 9.

An Open Label Study OfLMI070 (Branaplam) in Type 1 Spinal Muscular Atrophy (SMA);
<https://clinicaltrials.gov/ct2/show/NCT02268552>

10. 10.

FDA Approves Oral Treatment for Spinal Muscular Atrophy (7 August 2020); <https://www.fda.gov/news-events/press-announcements/fda-approves-oral-treatment-spinal-muscular-atrophy>

11. 11.

Wang, J., Schultz, P. G. & Johnson, K. A. Mechanistic studies of a small-molecule modulator of *SMN2* splicing. *Proc. Natl Acad. Sci. USA* **115**, E4604–E4612 (2018).

[CAS](#) [Article](#) [Google Scholar](#)

12. 12.

Ingolia, N. T., Ghaemmaghami, S., Newman, J. R. & Weissman, J. S. Genome-wide analysis *in vivo* of translation with nucleotide resolution using ribosome profiling. *Science* **324**, 218–223 (2009).

[ADS](#) [CAS](#) [Article](#) [Google Scholar](#)

13. 13.

Eschbach, J. W., Kelly, M. R., Haley, N. R., Abels, R. I. & Adamson, J. W. Treatment of the anemia of progressive renal failure with recombinant human erythropoietin. *N. Engl. J. Med.* **321**, 158–163 (1989).

[CAS](#) [Article](#) [Google Scholar](#)

14. 14.

Chan, K. Y. et al. Engineered AAVs for efficient noninvasive gene delivery to the central and peripheral nervous systems. *Nat. Neurosci.* **20**, 1172–1179 (2017).

[CAS](#) [Article](#) [Google Scholar](#)

15. 15.

Amado, D. A. et al. AAV-mediated progranulin delivery to a mouse model of progranulin deficiency causes T cell-mediated toxicity. *Mol. Ther.* **27**, 465–478 (2019).

[CAS](#) [Article](#) [Google Scholar](#)

16. 16.

Madisen, L. et al. A robust and high-throughput Cre reporting and characterization system for the whole mouse brain. *Nat. Neurosci.* **13**,

133–140 (2010).

[CAS](#) [Article](#) [Google Scholar](#)

17. 17.

Collins, A. L. et al. Mild overexpression of MeCP2 causes a progressive neurological disorder in mice. *Hum. Mol. Genet.* **13**, 2679–2689 (2004).

[CAS](#) [Article](#) [Google Scholar](#)

18. 18.

Van Alstyne, M. et al. Gain of toxic function by long-term AAV9-mediated SMN overexpression in the sensorimotor circuit. *Nat. Neurosci.* **24**, 930–940 (2021).

[Article](#) [Google Scholar](#)

19. 19.

Weber, E. W. et al. Transient rest restores functionality in exhausted CAR-T cells through epigenetic remodeling. *Science* **372**, eaba1786 (2021).

[CAS](#) [Article](#) [Google Scholar](#)

20. 20.

Fu, Y. et al. High-frequency off-target mutagenesis induced by CRISPR–Cas nucleases in human cells. *Nat. Biotechnol.* **31**, 822–826 (2013).

[CAS](#) [Article](#) [Google Scholar](#)

21. 21.

Charlesworth, C. T. et al. Identification of preexisting adaptive immunity to Cas9 proteins in humans. *Nat. Med.* **25**, 249–254 (2019).

[CAS](#) [Article](#) [Google Scholar](#)

22. 22.

Wagner, D. L. et al. High prevalence of *Streptococcus pyogenes* Cas9-reactive T cells within the adult human population. *Nat. Med.* **25**, 242–248 (2019).

[CAS](#) [Article](#) [Google Scholar](#)

23. 23.

Hanlon, K. S. et al. High levels of AAV vector integration into CRISPR-induced DNA breaks. *Nat. Commun.* **10**, 4439 (2019).

[ADS](#) [Article](#) [Google Scholar](#)

24. 24.

Saito, H. et al. Synthetic translational regulation by an L7Ae-kink-turn RNP switch. *Nat. Chem. Biol.* **6**, 71–78 (2010).

[CAS](#) [Article](#) [Google Scholar](#)

25. 25.

Zhong, G. et al. A reversible RNA on-switch that controls gene expression of AAV-delivered therapeutics in vivo. *Nat. Biotechnol.* **38**, 169–175 (2020).

[CAS](#) [Article](#) [Google Scholar](#)

26. 26.

Strobel, B. et al. A small-molecule-responsive riboswitch enables conditional induction of viral vector-mediated gene expression in

mice. *ACS Synth. Biol.* **9**, 1292–1305 (2020).

[CAS](#) [Article](#) [Google Scholar](#)

27. 27.

Brown, B. D. et al. Endogenous microRNA can be broadly exploited to regulate transgene expression according to tissue, lineage and differentiation state. *Nat. Biotechnol.* **25**, 1457–1467 (2007).

[CAS](#) [Article](#) [Google Scholar](#)

28. 28.

Winter, G. E. et al. Phthalimide conjugation as a strategy for in vivo target protein degradation. *Science* **348**, 1376–1381 (2015).

[ADS](#) [CAS](#) [Article](#) [Google Scholar](#)

29. 29.

Buskirk, A. R., Ong, Y. C., Gartner, Z. J. & Liu, D. R. Directed evolution of ligand dependence: small-molecule-activated protein splicing. *Proc. Natl Acad. Sci. USA* **101**, 10505–10510 (2004).

[ADS](#) [CAS](#) [Article](#) [Google Scholar](#)

30. 30.

Roper, J. et al. In vivo genome editing and organoid transplantation models of colorectal cancer and metastasis. *Nat. Biotechnol.* **35**, 569–576 (2017).

[CAS](#) [Article](#) [Google Scholar](#)

31. 31.

O'Connell, K. E. et al. Practical murine hematopathology: a comparative review and implications for research. *Comp. Med.* **65**, 96–

113 (2015).

[PubMed](#) [PubMed Central](#) [Google Scholar](#)

32. 32.

Dobin, A. & Gingeras, T. R. Mapping RNA-seq reads with STAR. *Curr. Protoc. Bioinformatics* **51**, 11.14.1–11.14.19 (2015).

[Article](#) [Google Scholar](#)

33. 33.

Thorvaldsdóttir, H., Robinson, J. T. & Mesirov, J. P. Integrative Genomics Viewer (IGV): high-performance genomics data visualization and exploration. *Brief Bioinform.* **14**, 178–192 (2013).

[Article](#) [Google Scholar](#)

34. 34.

Robinson, J. T. et al. Integrative genomics viewer. *Nat. Biotechnol.* **29**, 24–26 (2011).

[CAS](#) [Article](#) [Google Scholar](#)

35. 35.

Katz, Y. et al. Quantitative visualization of alternative exon expression from RNA-seq data. *Bioinformatics* **31**, 2400–2402 (2015).

[CAS](#) [Article](#) [Google Scholar](#)

36. 36.

Kent, W. J. et al. The human genome browser at UCSC. *Genome Res.* **12**, 996–1006 (2002).

[CAS](#) [Article](#) [Google Scholar](#)

37. 37.

Love, M. I., Huber, W. & Anders, S. Moderated estimation of fold change and dispersion for RNA-seq data with DESeq2. *Genome Biol.* **15**, 550 (2014).

[Article](#) [Google Scholar](#)

38. 38.

Nellore, A. et al. Human splicing diversity and the extent of unannotated splice junctions across human RNA-seq samples on the Sequence Read Archive. *Genome Biol.* **17**, 266 (2016).

[Article](#) [Google Scholar](#)

39. 39.

Kearse, M. G. & Wilusz, J. E. Non-AUG translation: a new start for protein synthesis in eukaryotes. *Genes Dev.* **31**, 1717–1731 (2017).

[CAS](#) [Article](#) [Google Scholar](#)

[Download references](#)

Acknowledgements

We thank E. Lysenko, Z. Hilfinger and J. Weber of the Davidson laboratory, as well as N. Hoque of the Novartis Institute for Biomedical Research for technical assistance. This work was supported in part by the Hereditary Disease Foundation (A.M.M. and P.T.R.), T32 HG009495 (National Institutes of Health) (P.T.R.), NBIR (R.S., D.L., A.M.M. and B.L.D.) and the Children's Hospital of Philadelphia Research Institute.

Author information

Affiliations

1. Raymond G. Perelman Center for Cellular and Molecular Therapeutics, The Children's Hospital of Philadelphia, Philadelphia, PA, USA

Alex Mas Monteys, Amiel A. Hundley, Paul T. Ranum, Luis Tecedor, Amy Muehlmatt, Euyn Lim & Beverly L. Davidson

2. Department of Pathology and Laboratory Medicine, University of Pennsylvania, Philadelphia, PA, USA

Alex Mas Monteys & Beverly L. Davidson

3. Neuroscience Disease Area, Novartis Institutes for BioMedical Research (NIBR), Cambridge, MA, USA

Dmitriy Lukashev & Rajeev Sivasankaran

Authors

1. Alex Mas Monteys

[View author publications](#)

You can also search for this author in [PubMed](#) [Google Scholar](#)

2. Amiel A. Hundley

[View author publications](#)

You can also search for this author in [PubMed](#) [Google Scholar](#)

3. Paul T. Ranum

[View author publications](#)

You can also search for this author in [PubMed](#) [Google Scholar](#)

4. Luis Tecedor

[View author publications](#)

You can also search for this author in [PubMed](#) [Google Scholar](#)

5. Amy Muehlmann

[View author publications](#)

You can also search for this author in [PubMed](#) [Google Scholar](#)

6. Euyn Lim

[View author publications](#)

You can also search for this author in [PubMed](#) [Google Scholar](#)

7. Dmitriy Lukashev

[View author publications](#)

You can also search for this author in [PubMed](#) [Google Scholar](#)

8. Rajeev Sivasankaran

[View author publications](#)

You can also search for this author in [PubMed](#) [Google Scholar](#)

9. Beverly L. Davidson

[View author publications](#)

You can also search for this author in [PubMed](#) [Google Scholar](#)

Contributions

A.M.M. designed the research, performed experiments, analysed data and wrote the manuscript. A.A.H., E.L. and D.L. performed experiments. P.T.R. performed all bioinformatic analyses and wrote the manuscript. L.T. performed all histology analysis and contributed to statistical analyses. A.M. contributed to all *in vivo* studies. R.S. and D.L. assisted with progranulin studies. B.L.D. designed and supervised the research, analysed data and wrote the manuscript.

Corresponding authors

Correspondence to [Alex Mas Monteys](#) or [Beverly L. Davidson](#).

Ethics declarations

Competing interests

B.L.D. serves on the advisory boards and/or has sponsored research from Homology Medicines, Intellia Therapeutics, Spirovant Sciences, Resilience Bio, Patch Bio, Saliogen, Moment Bio, Triplet Biosciences, Panorama Medicines, Roche and NBIR. A.M.M. has sponsored research from NBIR.

Additional information

Peer review information *Nature* thanks Alessandra Biffi, Mikhail Shapiro and the other, anonymous, reviewer(s) for their contribution to the peer review of this work.

Publisher's note Springer Nature remains neutral with regard to jurisdictional claims in published maps and institutional affiliations.

Extended data figures and tables

Extended Data Fig. 1 In vitro assessment of SMN2-on cassettes.

a, Cartoon depicting *SMN2* exon 7 in its native sequence or with splice-site modifications introduced to reduce background levels of exon 7 inclusion (3' acceptor splice site, ind*SMN2*). **b**, Representative RT–PCR reaction showing exon 7 inclusion with the SMN2-on cassettes in the absence of LMI070. The quantification of the exon 7 spliced-in or -out transcripts is depicted as the mean ± s.e.m. of 6 biological replicates. **c**, Exon 7 splicing of the SMN2 and ind*SMN2* cassette in response to LMI070 or RG7800. Representative RT–PCR reaction showing exon 7 inclusion as a function of LMI070 or RG7800 dose. The quantification of the exon 7 spliced-in or spliced-out transcripts are the relative transcript levels presented as the mean ± s.e.m. of 8 biological replicates. **d**, Luciferase activity of the SMN2 and ind*SMN2* cassettes in response to LMI070. The graph shows relative expression of firefly luciferase expressed from the SMN2-on or ind*SMN2*-

on cassettes in cells treated with DMSO or LMI070 (100 nM). The activity of the transfection control *Renilla* luciferase cassette is represented as a line above the bar graph. Data are the mean ± s.e.m. of 8 biological replicates.

Extended Data Fig. 2 Comparison between induced splice junctions in a previous study and in this work.

See ref. ⁸. **a**, Sequence logo of U1 RNA site targeted by LMI070 from 45 spliced-in exons identified by RNA-seq. **b**, To identify splice junctions with the highest induction across both studies we plotted the mean splice junction counts from our study against the mean splice junction counts from the dataset in ref. ⁸ reprocessed using our pipeline. The datasets correlate with Pearson's $r = 0.7$, indicating that induced junctions performed similarly by rank across both datasets. Additionally, the top ranked splice junctions associated with *SF3B3* and *BECNI* were consistent across both datasets. **c**, Sashimi plots depicting novel LMI070-spliced in exons for the *SF3B3* and *BECNI* genes identified in our study and in ref. ⁸ by RNA-seq. Genomic location, position of the LMI070 spliced in exon, and intronic counts observed are indicated.

Extended Data Fig. 3 Candidate minigene cassette responsiveness to LMI070 and splicing response to LMI070 of the SF3B3-X^{on} cassette.

a, Luciferase induction of the minigene cassettes for *SF3B3*, *BECNI*, *C12ORF4* and *PDXDC2*. The fold-change luciferase activity in LMI070-treated samples (depicted as +) is relative to DMSO-treated (depicted as -) cells, with data normalized to *Renilla* luciferase expression. Data are the mean ± s.e.m. of 8 biological replicates. *** $P < 0.0001$ for *SF3B3* versus other candidate exons, *** $P < 0.001$ *C12orf4* versus *PDXDC2*, one-way ANOVA with Bonferroni's post hoc test. **b**, Luciferase activity of the minigene cassettes for *SF3B3*, *BECNI*, *C12ORF4* and *PDXDC2*. Data show expression of firefly luciferase from the minigenes in response to DMSO (-) or LMI070 (+) treatment relative to *Renilla* luciferase activity. Data are mean ± s.e.m. of 8 biological replicates. **c**, Splicing analysis of the *SF3B3-X^{on}* cassette. Representative RT-PCR splicing assay (6 biological

replicates) showing inclusion of the LMI070-induced *SF3B3* exon in response to DMSO or LMI070 treatment. Inclusion of the LMI070 spliced-in exon was detected using primers binding the exons flanking the LMI070-induced exon (left), or using primers binding within the novel exon sequence (right).

Extended Data Fig. 4 Depiction of the frequency that non-AUG start codons are used determined by ribosome profiling.

a, Translation frequency from AUG and non-AUG start codons determined from ribosome profiling³⁹. **b**, Depiction of non-AUG start codons in frame luciferase transcripts expressed under control of the *SF3B3*, *BECN1*, *C12orf4* or *PDXDC2* minigenes.

Extended Data Fig. 5 Analysis of SF3B3-X^{on} expressed from different promoters.

a, Firefly luciferase of the X^{on} cassettes in response to varying doses of LMI070 relative to *Renilla* luciferase (grey line). The data are the mean ± s.e.m. of 8 biological replicates. **b**, Representative RT–PCR for assessment of LMI070-induced pseudo exon expression. Exon inclusion in the X^{on} cassette was detected using primers flanking the pseudo exon. Data are the mean ± s.e.m. of 8 biological replicates. **c**, Representative gels from RT–PCR analysis for assessment of the LMI070-induced pseudo exons expressed from the noted promoters in response to varying doses of LMI070. Pseudo exon inclusion was detected using primers binding within the LMI070-induced pseudo exon and the downstream exon. Splicing was quantified and transcript levels presented as the mean ± s.e.m. of 8 biological replicates.

Extended Data Fig. 6 Assessment of the SF3B3-X^{on} cassette to control translation of eGFP in vitro and in vivo.

a, eGFP expression in HEK293 cells transfected with the SF3B3 minigene cassette (SF3B3-X^{on}-eGFP) and treated 24 h later with DMSO (left) or

LMI070 (right). Bright-field panels are shown below (4 technical replicates). **b**, Representative photomicrograph of heart tissue sections showing eGFP in heart 24 h after treatment with LMI070 at 50 mg kg⁻¹ ($n = 2$ mice). Scale bar, 200 μm. Inset, eGFP expression in cardiomyocytes at a higher magnification. Scale bar, 50 μm. **c**, Extended exposure of the western blot from Fig. 2c (4 mice per group). **d**, PCR assay demonstrates splicing activity in liver, heart and skeletal muscle in response to LMI070 (4 mice per group). **e**, Cartoon depiction of the X^{on} assays designed to quantify the LMI070-induced transcripts and eGFP expression levels from the X^{on} cassette after AAV9-X^{on}-eGFP gene transfer. **f**, Data show average C_t values for eGFP or LMI070-induced expression in heart and skeletal muscle. Fold change of the spliced-in expression cassette is shown relative to basal levels in mice injected with AAV9-X^{on}-eGFP and treated with vehicle (4 mice per group). **g**, Extended exposure of the western blot from Fig. 2h (3 mice per group). **h**, PCR assay demonstrates splicing activity in liver, heart and skeletal muscle after each LMI070 dose (3 mice per group). **i**, Data show average C_t values for eGFP or LMI070-induced expression in heart and skeletal muscle after each dose. Fold change of the spliced expression cassette is shown relative to basal levels in mice injected with AAV9-X^{on}-eGFP and treated with vehicle (3 mice per group).

Extended Data Fig. 7 In vivo activity of X^{on} in brain.

a, Representative photomicrographs (5 mice per group) showing eGFP expression from mice treated intravenously 4 weeks earlier with AAVPHPeB-X^{on}-eGFP, and 24 h after treatment with vehicle or LMI070 at 5 or 50 mg kg⁻¹. Thalamus (Th), hippocampus (Hc), cerebellum (Cb) and facial motor nucleus (VII), cortex (Cx), striatum (Str), substantia nigra (SN), and medial vestibular nucleus (MV) are shown. Scale bar, 100 μm; inset scale bar, 25 μm. In the hippocampus, * and ** denote the polymorphic and CA3 areas, respectively. In the cerebellum, * denotes the deep cerebellar nuclei. **b**, Splicing assays for exon inclusion in the cortex and the hippocampus of mice injected with AAVPHPeB-X^{on}-eGFP (3 mice per group). **c**, RT-qPCR of human progranulin expression. Data are mean ± s.e.m. of 5 mice per group, *** $P < 0.0001$ vehicle versus AAV-treated groups, one-way ANOVA followed by Bonferroni's post-hoc test. **d**,

Splicing assays for exon inclusion in cortex samples of mice injected with AAVPHPeB-X^{on}-PGRN (3 mice per group).

Extended Data Fig. 8 Generation of the miniX^{on} cassette and assessment of miniX^{on} control of SaCas9 for in vivo gene editing in liver.

a, Cartoon depicting the AAV genome size with the SF3B3-X^{on} and SF3B3-miniX^{on} cassettes. **b**, Luciferase induction in HEK293 cells transfected with SF3B3-miniX^{on}-luciferase or SF3B3-X^{on}-luciferase in response to varying doses of LMI070. All samples are normalized to *Renilla* luciferase activity and are relative to DMSO treated cells. Data are the mean ± s.e.m. of 8 biological replicates (***($P < 0.001$) versus SF3B3.X^{on}, two-way ANOVA followed by Bonferroni's post hoc test). **c**, Splicing inclusion assays of the LMI070-induced exon at 100 nM LMI070. Pseudo exon inclusion in the X^{on} cassette was detected using primers flanking the pseudoexon (left) or by priming within the novel exon sequence (right; 4 technical replicates). **d**, Experimental design. Mice were injected with AAV8-miniX^{on}-SaCas9 plus AAV8-sgAi14-eGFP (1×10^{12} viral genomes, 1:1 ratio) and 2 weeks later dosed with vehicle or LMI070 at 50 mg kg⁻¹ to induce SaCas9 expression and editing of the *loxP*-STOP cassette (guides: sgAi14_1: 5'-CTCTAGAGTCGCAGATCCTC-3', sgAi14_2: 5'-ACGAAGTTATTAAGGGTT-3'). One week later, mice were euthanized, and livers processed to assess gene editing by genomic DNA PCR, histology and FACS of isolated hepatocytes. **e**, Representative FACS analysis of hepatocytes obtained from Ai14 mice after LMI070 or vehicle treatment. The gating/sorting strategy (above), and the percentage of tdTomato expressing cells for each condition (below) is shown (4 biological replicates). **f**, Representative photomicrographs of liver sections obtained from AAV injected Ai14 mice 1-week after LMI070 treatment. tdTomato expression (red) is evident in LMI070 treated mice (5 mice per group). Scale bars, 100 μm. **g**, SaCas9 mediated editing of the *loxP*-STOP cassette in Ai14 mice as detected by PCR assay of liver genomic DNA (3 of 5 mice with guides plus LMI, 2 of 4 mice with guides plus vehicle, 1 of 2 untreated mice are shown). A PCR product of 355 bp size corresponding to

the edited Ai14 ROSA Locus was observed in the LMI070-treated mice. **h**, Sanger sequencing of the 355 bp PCR product confirmed targeted deletion of the *loxP*-STOP cassette and DNA repair of the Ai14 reporter locus.

Extended Data Table 1 The genomic locations of candidate LMI070-induced exons and the frequency of events from RNA-seq datasets

[Full size table](#)

Extended Data Table 2 The genomic locations of candidate LMI070-induced exons and the frequency of events from RNA-seq datasets—continued

[Full size table](#)

Extended Data Table 3 Comparison between disclosed hits in a previous study and in this work

[Full size table](#)

Supplementary information

[**Reporting Summary**](#)

Rights and permissions

[Reprints and Permissions](#)

About this article



Check for
updates

Cite this article

Monteys, A.M., Hundley, A.A., Ranum, P.T. *et al.* Regulated control of gene therapies by drug-induced splicing. *Nature* **596**, 291–295 (2021).
<https://doi.org/10.1038/s41586-021-03770-2>

Download citation

- Received: 06 February 2020
- Accepted: 23 June 2021
- Published: 28 July 2021
- Issue Date: 12 August 2021
- DOI: <https://doi.org/10.1038/s41586-021-03770-2>

Comments

By submitting a comment you agree to abide by our [Terms](#) and [Community Guidelines](#). If you find something abusive or that does not comply with our terms or guidelines please flag it as inappropriate.

[Access through your institution](#)

[Change institution](#)

[Buy or subscribe](#)

Advertisement

This article was downloaded by **calibre** from <https://www.nature.com/articles/s41586-021-03770-2>

Structural insights into how Prp5 proofreads the pre-mRNA branch site
[Download PDF](#)

- Article
- Open Access
- [Published: 04 August 2021](#)

Structural insights into how Prp5 proofreads the pre-mRNA branch site

- [Zhenwei Zhang](#) ORCID: [orcid.org/0000-0003-2906-9346](#)¹,
- [Norbert Rigo](#)²,
- [Olexandr Dybkov](#)²,
- [Jean-Baptiste Fourmann](#)²,
- [Cindy L. Will](#)²,
- [Vinay Kumar](#) ORCID: [orcid.org/0000-0001-6642-8876](#)²,
- [Henning Urlaub](#) ORCID: [orcid.org/0000-0003-1837-5233](#)^{3,4},
- [Holger Stark](#) ORCID: [orcid.org/0000-0002-6161-1118](#)¹ &
- [Reinhard Lührmann](#) ORCID: [orcid.org/0000-0003-3253-7518](#)²

Nature volume **596**, pages 296–300 (2021) [Cite this article](#)

- 5806 Accesses
- 22 Altmetric
- [Metrics details](#)

Subjects

- [Cryoelectron microscopy](#)
- [RNA splicing](#)

Abstract

During the splicing of introns from precursor messenger RNAs (pre-mRNAs), the U2 small nuclear ribonucleoprotein (snRNP) must undergo stable integration into the spliceosomal A complex—a poorly understood, multistep process that is facilitated by

the DEAD-box helicase Prp5 (refs. [1,2,3,4](#)). During this process, the U2 small nuclear RNA (snRNA) forms an RNA duplex with the pre-mRNA branch site (the U2–BS helix), which is proofread by Prp5 at this stage through an unclear mechanism^{[5](#)}. Here, by deleting the branch-site adenosine (BS-A) or mutating the branch-site sequence of an actin pre-mRNA, we stall the assembly of spliceosomes in extracts from the yeast *Saccharomyces cerevisiae* directly before the A complex is formed. We then determine the three-dimensional structure of this newly identified assembly intermediate by cryo-electron microscopy. Our structure indicates that the U2–BS helix has formed in this pre-A complex, but is not yet clamped by the HEAT domain of the Hsh155 protein (Hsh155^{HEAT}), which exhibits an open conformation. The structure further reveals a large-scale remodelling/repositioning of the U1 and U2 snRNPs during the formation of the A complex that is required to allow subsequent binding of the U4/U6.U5 tri-snRNP, but that this repositioning is blocked in the pre-A complex by the presence of Prp5. Our data suggest that binding of Hsh155^{HEAT} to the bulged BS-A of the U2–BS helix triggers closure of Hsh155^{HEAT}, which in turn destabilizes Prp5 binding. Thus, Prp5 proofreads the branch site indirectly, hindering spliceosome assembly if branch-site mutations prevent the remodelling of Hsh155^{HEAT}. Our data provide structural insights into how a spliceosomal helicase enhances the fidelity of pre-mRNA splicing.

[Download PDF](#)

Main

To isolate a spliceosome assembly intermediate formed directly before the A complex that still contains Prp5 (Extended Data Fig. [1a](#)), we carried out splicing in *S. cerevisiae* cell extracts with an actin (*Act*) pre-mRNA in which the BS-A is deleted (Extended Data Fig. [1b](#)). With this ΔBS-A substrate, splicing is blocked before catalytic step 1 (Extended Data Fig. [1c](#)), consistent with previous results^{[6](#)}. Spliceosomal complexes formed on ΔBS-A *Act* pre-mRNA lack the U4/U6.U5 tri-snRNP, but contain stoichiometric amounts of U1 and U2 snRNPs (Extended Data Fig. [1d](#)). The proteins Prp5, Msl5 and Mud2 are also abundant, whereas Cus2 is absent (Extended Data Fig. [1e](#) and Supplementary Table [1](#)), indicating that these complexes stall after Prp5 hydrolyses ATP, but before the tri-snRNP has docked. We next carried out single-particle cryo-electron microscopy (cryo-EM) and determined the structure of the ΔBS-A complex at an average resolution of 5.9 Å (ranging from roughly 4.5 Å for U1 to approximately 15 Å for U2) (Extended Data Table [1](#) and Extended Data Fig. [2](#)). Further classification and multibody refinement improved the resolution of the stable U1 snRNP region and adjacent U2 5' region to 4.1 Å and 8.3 Å, respectively (Extended Data Fig. [2](#)). By fitting known X-ray structures of spliceosome components into the EM density map (Extended Data Table [2](#)), together with protein crosslinking coupled with mass spectrometry (CXMS) (Supplementary Table [2](#)), we generated a

three-dimensional (3D) model of the ΔBS-A complex (Fig. 1). This complex consists of two major elongated domains—comprising the U1 and bipartite U2 snRNPs—that are connected by two main bridges (Fig. 1).

Fig. 1: Three dimensional cryo-EM model of the yeast pre-A complex.



a, b, EM density map (**a**) and molecular architecture (**b**) of the *S. cerevisiae* spliceosomal pre-A complex. **a**, Purple, better-resolved U1 density; grey blue and green, better-resolved densities of the 3'- and 5'-regions of U2 snRNP; translucent grey, cryo-EM map of the pre-A complex.

[Full size image](#)

The U2–BS helix is not clamped by Hsh155

Hsh155^{HEAT} adopts a closed conformation after U2 has integrated stably into the spliceosome, clamping the U2–BS helix and binding the bulged BS-A in a pocket formed by Rds3 (PHF5A in humans; see Extended Data Fig. 1f for a summary of yeast and human protein names) and HEAT repeats 15–17 of Hsh155 (refs. 7,8,9,10) (Extended Data Fig. 1g). It is unclear at present what triggers this functionally important structural change. In the ΔBS-A complex, Hsh155^{HEAT} exhibits an open conformation, as in the isolated human 17S U2 (ref. 11) but in notable contrast to its conformation in yeast A complexes (Figs. 1, 2a and Extended Data Fig. 3a) and pre-B, B and B^{act} complexes^{7,8,12,13}. Stem–loop (SL) IIa of U2 snRNA is bound by Hsh155, Cus1 and Prp9 in the ΔBS-A complex, in a similar manner to that seen in the human 17S U2 snRNP and subsequently formed spliceosomal complexes (Extended Data Fig. 3b). An extended helical density element is located directly upstream of SLIIa. This

element is longer than the U2 branchpoint-interacting stem-loop (BSL), which is found in the isolated U2 snRNP and sequesters U2 nucleotides that base pair with the branch site^{11,14} (Extended Data Fig. 3c, d). A modelled, extended U2–BS helix—lacking a bulged BS-A and comprising 13 base pairs—fits well into this density element (Extended Data Fig. 3c), indicating that an extended U2–BS helix has formed. On the basis of CXMS data, the Prp11 zinc finger (Prp11^{ZnF}) could be positioned at the top of the U2–BS helix (Extended Data Fig. 3e, f), akin to its position in A, pre-B, B and B^{act} complexes^{7,8,12,13,15}. In the ΔBS-A complex, the U2–BS helix is located further away from the carboxy (C)-terminal HEAT repeats of Hsh155^{HEAT} compared with its position in the A to B^{act} complexes, and it is not sequestered by Hsh155^{HEAT} (Fig. 2a and Extended Data Fig. 3g). Thus, formation of the U2–BS helix alone does not appear to trigger closure of Hsh155^{HEAT}. As the U2–BS helix has formed, but Hsh155^{HEAT} still exhibits an open conformation and Prp5 is stably bound (see below), we conclude that ΔBS-A complexes are stalled at a pre-A-complex stage, after Prp5-mediated formation of the U2–BS helix, but during/before it carries out its proofreading function.

Fig. 2: The Hsh155 HEAT domain has an open conformation in the pre-A complex.

 **figure2**

a, Conformation of the SF3B1 and Hsh155 HEAT domains and position of the U2–BS helix and U2 snRNA SLI and SLIIa in human 17S U2 snRNP (Protein DataBank (PDB) (<https://www.rcsb.org>) accession number 6Y5Q) and in the *S. cerevisiae* pre-A and A complexes (PDB 6G90). These domains were aligned via Hsh155 heat repeats 19–20, Rse1^{BPA} and U2 SLIIa. Olive green, SLIIa nucleotides; reddish orange, pre-mRNA branch-site nucleotides; purple, BSL nucleotides that later form the U2–BS helix; yellow, BSL nucleotides forming the extended part of the U2–BS helix; dark green, remaining BSL nucleotides; blue, SLI. **b**, Fit of Prp5^{RecA1} into the pre-A EM density. **c**, Location of the Prp5 RecA1 and RecA2 domains in the pre-A complex. **d**, Prp5^{RecA1} contacts U2 snRNA nucleotides that connect the U2–BS helix to U2 SLIIa. The positions of Prp5 amino acids (located outside of the SAT motif) that when mutated suppress branch-site mutations are indicated in black.

[Full size image](#)

Location of Prp5 in the pre-A complex

Prp5 was initially proposed to ‘proofread’ formation of the U2–BS helix by coordinating the rate of U2–BS base pairing with its ATPase activity⁵. However, more recent studies uncovered a correlation between increased Prp5 retention in early spliceosomal complexes and decreased tri-snRNP recruitment, suggesting that the physical presence of Prp5, rather than its ATPase activity, has a key role in its proofreading function¹⁶. In the human 17S U2 snRNP, the Prp5 RecA (Prp5^{RecA}) domains sequester the BSL together with the TAT–SF1 protein and the C-terminal HEAT repeats of SF3B1 (ref. [11](#)), thereby preventing formation of the U2–BS helix. We find here that, in the yeast pre-A complex, Cus2 (human TAT–SF1) has dissociated and the Prp5^{RecA} domains are located between the U2 3'-region and the U2–BS helix (Fig. [2b,c](#) and Extended Data Fig. [4a–d](#)). Compared with their position in 17S U2 snRNP, the Prp5^{RecA} domains in the pre-A complex are located further away from Hsh155^{HEAT}, with RecA1 fitting well into the niche formed by the amino (N)-terminal region of Prp9 (Prp9^{NTR}), with which it interacts, and the U2–BS helix (Fig. [2b,c](#) and Extended Data Fig. [4c–e](#)). Moreover, Prp5^{RecA1} now contacts the U2 snRNA strand that connects SLIIa and the U2–BS helix (Fig. [2d](#)). This is consistent with the crosslinks of Prp5 to this region (nucleotides 45–49) of yeast U2 snRNA observed previously with a Prp5-associated *S. cerevisiae* spliceosomal complex (designated the Prp5-associated intermediate complex, or FIC) formed on a pre-mRNA with a mutated branch site¹⁶. Finally, CXMS indicates that the NTR of Prp5 interacts extensively with Hsh155 HEAT repeats 1–7 in the pre-A complex (Extended Data Fig. [4a,b](#)), consistent with previous biochemical studies¹⁷.

Pre-A formation involves U2 remodelling

Comparison of the structures of the yeast pre-A complex and human 17S U2 snRNP suggests that, in addition to Prp5^{RecA}, there are other changes in the organization of U2 components during pre-A formation. Relative to its position in 17S U2, the U2 3'-region has moved (Extended Data Fig. [4d,e](#)) and its new location in the pre-A complex is stabilized by newly formed contacts between the U2 3'- and 5'-regions (Extended Data Fig. [4d,e](#)). This movement is a prerequisite for formation of the pre-A complex, as it generates the binding pocket for the repositioned Prp5^{RecA1} (Fig. [2b,c](#) and Extended Data Fig. [4](#)). In the pre-A complex, Prp5^{RecA1} establishes new contacts with the shifted 3'-region by interacting with Prp9^{NTR} (Fig. [2b,c](#) and Extended Data Fig. [4](#)), preventing the further movement of the U2 3'-region that is ultimately required to allow the tri-snRNP to dock to the A complex (see below).

Prp40 bridges U1 and U2 snRNP in pre-A complex

The U1 snRNP structure in the pre-A complex (Extended Data Fig. 5a) is highly similar to that observed in the yeast E, A and pre-B complexes^{13,15,18}, indicating that U1 does not undergo substantial remodelling during early spliceosome assembly. As in the aforementioned complexes, base pairing between the 5'-splice site and the U1 snRNA is also stabilized by Yhc1 and Luc7 in the pre-A complex (Extended Data Fig. 5b). Although only three FF domains of Prp40 (domains 4–6) could be located in the yeast E complex¹⁸, CXMS allowed us to map all six of the FF domains of Prp40 in the pre-A complex (Fig. 1 and Extended Data Fig. 5c,d). FF1 and FF6 bind Luc7 and Snp1, respectively, tethering Prp40 to U1, while FF2–FF5 form an extended binding platform that interacts with numerous proteins, including Snu71 and U2 Rse1. The interaction of FF4 with the WD40 β-propeller domain B (BPB) of Rse1 forms a bridge between the U1 and U2 snRNPs (denoted bridge 1) (Extended Data Figs. 5d, 6a,b) that is not observed in yeast A complexes¹⁵. Bridge 1 also contains the C-terminal region of Snu71, as numerous crosslinks between it and the FF2 and FF3 domains of Prp40, as well as with Rse1^{BPB}, are detected (Extended Data Fig. 5d). In the pre-A complex, U1 and U2 are connected by a second bridge comprising intron nucleotides upstream of the branch site (Extended Data Fig. 6a,c). Although the Prp40 WW domain and Msl5–Mud2 could not be localized based solely on the EM density, CXMS indicates that Msl5–Mud2 is likely to be located near the U2–BS in the pre-A complex, and furthermore remains bound to the Prp40 WW domain (Extended Data Fig. 6d and Supplementary Table 2).

Pre-A complex with a U257A branch-site mutation

Mutations in the conserved yeast branch-site sequence upstream of the BS-A that weaken the U2–BS interaction—including a U-to-A mutation at position 257 of *Act* pre-mRNA (two nucleotides upstream of the BS-A) (Extended Data Fig. 1b)—do not completely block splicing but do lead to the accumulation of spliceosomes in which Prp5 is retained but the tri-snRNP has not yet joined^{5,16}. To determine whether this mutation stalls spliceosome assembly at the pre-A stage, we purified the complexes that form on *Act* U257A pre-mRNA and determined their cryo-EM structure (Extended Data Fig. 7). The RNA and protein compositions of the purified U257A and ΔBS-A complexes were identical (Extended Data Fig. 1d,e and Supplementary Table 1), and an overlay of the U257A and ΔBS-A complexes revealed a highly similar, if not identical, structure at the present level of resolution (Extended Data Fig. 7). Indeed, the structural model of the ΔBS-A pre-A complex fits well without further adjustment into the EM density of the U257A complex (Extended Data Fig. 7). Thus, with the U257A mutant, an extended U2–BS helix has also formed, Hsh155^{HEAT} is in an open conformation, and Prp5^{RecA1} is docked to Prp9^{NTR} and situated close to the U2 snRNA, indicating that U257A complexes are also stalled at the same pre-A stage. The highly similar structure of both pre-A complexes indicates that they represent a

physiologically relevant intermediate that—at least in the case of U257A—can also progress along the wild-type spliceosome assembly pathway.

Dynamics of the pre-A to A transition

Comparison of our pre-A complex with the previously published yeast A complex¹⁵ reveals that the transition from the pre-A to the A complex involves large-scale remodelling that requires displacement of Prp5 (Fig. 3, Extended Data Fig. 8 and Supplementary Video 1). First, the U2 3'-region rotates by roughly 55° relative to the U2 5'-region during A-complex formation. In the pre-A complex, this rotational movement is prohibited by the Prp5^{RecA} domains, which bind in a mutually exclusive manner with the new position of Prp9^{NTR}, the long α-helix of Prp21 and the Prp11 β-sandwich, in the subsequently formed A complex. Second, U1 snRNP rotates by roughly 45° during the transition from the pre-A to the A complex, such that Prp39 now interacts with Lea1. A prerequisite for U1 movement is the dissociation of Prp40 from Rse1, and thus the apparent dissolution of U1–U2 bridge 1 (Fig. 3). The repositioning of U1 and the U2 3'-region is essential to generate the binding platform needed to dock the U4/U6.U5 tri-snRNP during formation of the pre-B complex (Fig. 3). Our studies thus provide a structural explanation for why the docking of tri-snRNP is inhibited when Prp5 is retained in yeast prespliceosomes¹⁶.

Fig. 3: Prp5 blocks the repositioning of U1 and U2 snRNPs that is required to form the tri-snRNP-binding site.

 figure3

Molecular organization of U1 and U2 snRNPs in *S. cerevisiae* pre-A, A (PDB 6G90) and pre-B complexes (PDB 5ZWM and PDB 5ZWN). Movements of U1 and U2 snRNPs during the pre-A to A transition are indicated by curved arrows. All structures were aligned as in Fig. 2. For simplicity, the U1 snRNA stem-loops in the poorly resolved region of the U1 snRNP are not shown in the pre-A, A and pre-B complexes.

[Full size image](#)

Mechanism of proofreading by Prp5

The cryo-EM structures presented here provide structural insights into the mechanism by which Prp5 proofreads the U2–BS helix (Fig. 4). The pre-A and 17S U2 structures are consistent with a model in which, after U2 interacts with the E complex, ATP hydrolysis by Prp5 leads to release of Cus2 and unwinding of the BS-L. This allows formation of the U2–BS helix and repositioning of the U2 3'-region and Prp5^{RecA}, generating the pre-A complex (Fig. 4). The new proofreading (or rather, ‘fidelity checkpoint’) position of Prp5^{RecA} in the pre-A complex transiently prevents the further movement of the U2 3'-domain needed to form an A complex that can subsequently bind the tri-snRNP. As deletion of the BS-A hinders the closure of Hsh155^{HEAT}, but does not affect the stability of the U2–BS helix per se, correct binding of the bulged BS-A by Hsh155^{HEAT} and Rds3 is likely to be a major trigger for the conformational change in Hsh155^{HEAT}. Furthermore, in the pre-A complex, the U2–BS helix is probably flexible, enabling it to intermittently move closer to Hsh155^{HEAT}, which ‘probes’ for its presence. Thus, we propose that when a stable U2–BS with a bulged BS-A is formed, movement of the U2–BS into the open Hsh155^{HEAT} leads to insertion of the BS-A into its binding pocket and closure of the HEAT domain (Fig. 4). Previous mutational analyses of Hsh155 indicated that alignment of the U2–BS duplex with conserved, positively charged amino acids in the C-terminal half of Hsh155 is crucial for closure¹⁹, and this alignment could thus help to properly position the bulged BS-A in its binding pocket.

Fig. 4: Model for Prp5-mediated proofreading of the U2–BS helix.



For simplicity, in this depiction of our proposed mechanism of proofreading by Prp5, Rds3 of the BS-A-binding pocket is not shown, and the U1 snRNP has been omitted from the spliceosomal pre-A and A complexes. The closure of Hsh155^{HEAT} and

release of Prp5 may be highly coordinated events that occur simultaneously rather than sequentially. The dashed arrow indicates that some mutations in the branch-site sequence, including U257A, do not completely abolish conversion of the pre-A complex into the A complex.

[Full size image](#)

Closure of Hsh155^{HEAT} would destabilize not only the Prp5^{NTR} that binds to it, but also the Prp5^{RecA} domains (Fig. 4). Although the latter do not interact with Hsh155^{HEAT}, the coordinated movement of Hsh155^{HEAT} and Prp5^{NTR} and the U2 snRNA nucleotides contacted by Prp5^{RecA1} could also lead to the displacement of Prp5^{RecA} and subsequent release of the entire Prp5 protein. Release of Prp5 would then allow rotation of the U2 3'-region and formation of an A complex (Fig. 4). If the U2–BS helix lacks a bulged BS-A, binding of the latter by Hsh155^{HEAT} and Rds3 would be blocked (Fig. 4). This would prevent the closure of Hsh155^{HEAT} and release of Prp5, blocking the progression of spliceosome assembly and potentially targeting the stalled complex for discard (Fig. 4). As branch-site mutations that destabilize the U2–BS duplex also hinder spliceosome assembly and lead to Prp5 retention^{5,16}, the stability of the U2–BS duplex per se may also affect the conformational state of Hsh155^{HEAT} in pre-A complexes. A destabilized U2–BS helix could also potentially prevent proper bulging of the BS-A²⁰, and in this way hinder closure of Hsh155^{HEAT}.

Various mutations in Prp5 can suppress branch-site mutations, including those in the Prp5 DPLD motif (which is important for the interaction of Prp5 with the U2 snRNP²¹) and also mutations in its SAT motif and those in adjacent regions of RecA1 that have no effect on ATPase activity, such as K372E, N399D and G401E^{5,21}. The Prp5^{N399D} mutant, the SAT mutant TAG and the DPLD mutant AAAA have reduced affinity for yeast prespliceosomes and enhance the binding of tri-snRNPs to spliceosomes¹⁶. Our pre-A structures provide insight into how some of these mutations may destabilize Prp5 binding. In pre-A complexes, the Prp5^{NTR} containing the DPLD motif still interacts with Hsh155^{HEAT} (Extended Data Fig. 4b), and thus mutation of this motif is likely to destabilize the Prp5^{NTR}–Hsh155^{HEAT} interaction. In pre-A complexes, amino acids K372, N399 and G401 are located in the Prp5 region that interacts with the single-stranded U2 snRNA between SLIIa and the U2–BS helix (Fig. 2d). Consistent with less-stable Prp5 binding, these mutations introduce a negative charge that would destabilize the RecA1–U2 snRNA interaction. Although the SAT motif is not located at a Prp5–protein interface, some SAT mutations might alter the conformation of RecA1, thereby indirectly destabilizing its interaction with Prp5^{NTR}. Indeed, several SAT mutations alter the equilibrium between the open and closed conformations of the Prp5^{RecA} domains²². Together, our results indicate that Prp5 does not proofread the U2–BS helix directly, but instead proofreads the RNP

conformation of pre-A complexes, and hinders progression of spliceosome assembly if mutations in the branch site alter the formation of a productive, closed conformation of Hsh155^{HEAT}.

Methods

No statistical methods were used to predetermine sample size. The experiments were not randomized, and investigators were not blinded to allocation during experiments and outcome assessment.

Preparation of yeast whole-cell extracts

Yeast whole-cell extracts were prepared from the *Saccharomyces cerevisiae* 3.2.AID/CRL2101 strain (*MATalpha, prp2-1, ade2, his3, lys2-801, ura3*) (a gift from R.-J. Lin)²³. Yeast were grown in a 100-litre fermenter and extracts were prepared as previously described⁷.

Affinity purification of pre-A complexes

Uncapped actin pre-mRNA lacking the branch-site adenosine (Δ BS-A *Act* pre-mRNA) was tagged at its 5'-end with three MS2 aptamers and transcribed in vitro using T7 RNA polymerase from a template prepared with the QuikChange II site-directed mutagenesis kit (Agilent). Yeast Δ BS-A pre-A spliceosomal complexes were assembled for 45 min at 23 °C in a 175 ml splicing reaction containing 40% yeast whole-cell extract and 1.8 nM Δ BS-A *Act* pre-mRNA with prebound MBP-MS2 fusion protein. The splicing reaction was subsequently chilled on ice and cleared by centrifugation for 10 min at 9,000 rpm at 4 °C in a Fibrelite F14-14 \times 50 cy rotor (Thermo Fisher Scientific). It was then loaded onto two columns, each packed with 600 μ l amylose resin (New England BioLabs) that were pre-equilibrated with GK75 buffer (20 mM HEPES-KOH pH 7.9, 1.5 mM MgCl₂, 75 mM KCl, 5% glycerol, 0.01% NP40, 0.5 mM dithiothreitol (DTT) and 0.5 mM phenylmethylsulfonyl fluoride (PMSF)). The matrix with bound complexes was washed with 3 ml GK75 buffer and spliceosomes were eluted with 15 mM maltose in GK75 buffer. For electron microscopy, peak elution fractions containing approximately 40 pmol of spliceosomal complexes were pooled (1 ml total volume), crosslinked with 0.2 mM BS3 (Thermo Fisher) for 1 h on ice, and loaded onto a 17 ml linear 10–30% (v/v) glycerol/0–0.1% glutaraldehyde gradient containing GK75 buffer. Samples were centrifuged for 17 h at 24,400 r.p.m. in a SureSpin 630 rotor (Sorvall) and collected manually from the top in 28 fractions of 555 μ l each. Crosslinking was stopped by adding 50 mM glycine, pH 7.7, and incubating for 2 h on ice. Fractions were analysed by Cherenkov counting in a Tri-Carb 2100TR scintillation counter (Packard). Two peak fractions containing

2.4 pmol of spliceosomal complexes were buffer-exchanged to GK75 with no glycerol, and concentrated to 250 µl in an Amicon Ultra-0.5 centrifugal filter unit Ultracel-50 (Merck), and then used for preparation of cryo-EM grids. Pre-A complexes assembled on the U257A *Act* pre-mRNA were purified as described above, with the following modifications. The template for in vitro transcription of the U257A *Act* pre-mRNA was purchased from Genscript. Pre-A complexes were assembled in a 252 ml splicing reaction containing 1.7 nM pre-mRNA; before preparation of cryo-EM grids, three peak gradient fractions were buffer exchanged to GK75 buffer containing 0.3% glycerol and samples were concentrated to 100 µl.

RNA and protein composition of pre-A complexes

To determine the RNA and protein composition of the pre-A complexes, we purified the complexes essentially as described above, except that we used a 12-ml splicing reaction, we washed spliceosomes bound to an amylose matrix with 10 ml GK150 and 10 ml GK75 buffer, and we did not incubate the eluted complexes with BS3. Furthermore, the complexes were fractionated on a 10–30% glycerol gradient lacking glutaraldehyde by centrifugation in a TH660 rotor (Thermo Fisher Scientific) for 16 h at 21,500 r.p.m. RNA and proteins were separated on NuPAGE 4–12% Bis-Tris gels (Invitrogen) and visualized by staining with SYBR Gold (Invitrogen) and Coomassie, respectively. The entire lanes were cut into 23 slices (680 fmol ΔBS-A pre-A) or 16 slices (170 fmol U257A pre-A) and proteins were in-gel digested with trypsin overnight. Resulting peptides were separated on a C18 column using an UltiMate3000 (Dionex) ultrahigh performance liquid chromatography system, and analysed by electrospray ionization mass spectrometry in a Thermo Scientific Q Exactive HF (ΔBS-A pre-A) or Orbitrap Exploris 480 mass spectrometer (U257A pre-A). Data were acquired using Thermo Exactive Series 2.8 SP1 and Orbitrap Exploris 480 3.0 software. The U257A pre-A complex was measured in duplicate, and a sum of both measurements is shown in Supplementary Table 1. Proteins were identified by searching fragment spectra against the *S. cerevisiae* Genomic Database (SGD; <https://www.yeastgenome.org>) using Mascot v.2.3.02 as a search engine. For immunoblotting, proteins were separated on denaturing 4–12% NuPAGE gels, transferred to Amersham Protran 0.2-µm nitrocellulose membranes (Cytiva), immunostained with an Amersham ECL Western Blotting Detection Kit (Cytiva), and visualized with an Amersham Imager 680 (Cytiva). Antibodies against the yeast Prp5 and Lea1 proteins were provided by S.-C. Cheng.

Protein–protein crosslinking and identification

For CXMS experiments, spliceosomes were assembled in a 400-ml (experiment 1) or 300-ml (experiment 2) splicing reaction containing 40% yeast whole-cell extract from the 3.2.AID/CRL2101 strain. Following MS2 affinity selection, purified spliceosomal

complexes were crosslinked with 250 µM BS3 for 1 h at 8 °C in a total volume of 3 ml. The reaction was split in half and loaded onto two 17-ml 10–30% (v/v) glycerol gradients and centrifuged in a Surespin 630 rotor (Thermo Fisher Scientific) for 16 h at 24,400 r.p.m. The gradients were fractionated by hand from the top into 28 fractions. Three peak fractions from each gradient, containing approximately 15 pmol of pre-A complexes, were pooled and the crosslinked complexes were pelleted by ultracentrifugation in a S100-AT4 rotor (Thermo Fisher Scientific) and analysed as previously described²⁴. After tryptic digestion, peptides were reverse-phase extracted using Sep-Pak Vac tC18 1cc cartridges (Waters) and fractionated by gel filtration on a Superdex Peptide PC3.2/30 column (GE Healthcare). Next, 50 µl fractions corresponding to an elution volume of 1.2–1.8 ml were analysed in triplicate on a Thermo Scientific Q Exactive HF-X (Experiment 1) or Orbitrap Exploris 480 mass spectrometer (Experiment 2) using Thermo Exactive Series 2.9 and Orbitrap Exploris 480 1.1 software, respectively. Protein–protein crosslinks were identified using the pLink 2.3.9 search engine (pfind.ict.ac.cn/software/pLink) and filtered at a false discovery rate (FDR) of 1% or 5% according to the developer’s recommendations^{25,26}.

EM sample preparation and image acquisition

Purified ΔBS-A or U257A pre-A complexes were absorbed for 15 min or 25 min, respectively, to a thin-layer carbon film that was subsequently attached to R3.5/1 Quantifoil grids. Next, 3.8 µl of sample buffer was applied to the grid and excess buffer was removed using an FEI Vitrobot loaded with pre-wetted filter paper, with a blotting force of 7, blotting time of 6.5 s, at 100% humidity and 4 °C. The sample was subsequently vitrified by plunging into liquid ethane. All cryo-EM data of the ΔBS-A pre-A complex and dataset 1 of the U257A pre-A complex were acquired at 300 kV on a FEI Titan Krios electron microscope (Thermo Fisher Scientific), equipped with a Cs corrector. Images were recorded in integration mode at ×120,700 magnification, corresponding to a calibrated pixel size of 1.16 Å at the specimen level, using a Falcon III direct electron detector. Micrographs were recorded via a Thermo Fischer EPU 2.1, using an exposure time of 1.02 s with 40 movie frames and a total dose of 44 e[−] per Å². In total, 87,604 and 9,170 micrographs were recorded for the ΔBS-A pre-A complex and dataset 1 of the U257A pre-A complex, respectively. Dataset 2 of the U257A pre-A complex (18,332 micrographs) was acquired at 300 kV on an FEI Titan Krios electron microscope (Thermo Fisher Scientific), in integration mode at a calibrated pixel size of 1.06 Å at the specimen level, using a Falcon III direct electron detector. Micrographs were recorded via a Thermo Fischer EPU 2.1, using an exposure time of 1.02 s with 40 movie frames and a total dose of 58 e[−] per Å².

Image processing

Frames were dose-weighted, aligned and summed with MotionCor 2.0 (ref. ²⁷). The defocus values and equiphase averaging (EPA) of the micrographs were determined using Gctf²⁸. Micrographs with a defocus range of 1 μm to 4 μm and a resolution of better than 4.3 \AA based on EPA estimation were retained for further processing. For the $\Delta\text{BS-A}$ pre-A complex, 74,230 out of 87,604 summed micrographs were further processed. Initially, approximately 5.4 million particles were automatically picked using Gautomatch (<https://www2.mrc-lmb.cam.ac.uk/research/locally-developed-software/zhang-software/>). They were then extracted with a box size of 440×440 pixels, and binned to 110×110 pixels (pixel size of 4.64 \AA) in RELION 3.0 (http://www2.mrc-lmb.cam.ac.uk/relion/index.php/Main_Page). Several iterations of reference-free two-dimensional (2D) classification were performed in RELION 3.0, and ‘bad classes’ showing fuzzy or uninterpretable features were removed, yielding 3,143,491 ‘good particles’. A subset of 308,419 particles was used to generate an initial 3D map using the ab initio reconstruction function in cryoSPARC²⁹. Using the ab initio model, this subset of particles was further 3D classified into five classes in RELION 3.0. The best class showing clear features of U1 and U2 snRNP was selected, and the more flexible U2 snRNP region of this map was erased using UCSF Chimera v.1.13.1 (ref. ³⁰). The remaining U1 snRNP was low-pass filtered to 35 \AA and used as 3D reference for further 3D classification for the entire dataset. The retained 3,143,491 particles after 2D classification of the entire dataset were split into 3 subsets and each subset was 3D classified into 5 classes. The best classes of each subset were combined, yielding 986,393 particles, which were then centred and re-extracted to 200×200 pixels (pixel size of 2.32 \AA) and further classified into four classes. After 20 iterations of consensus classification (7.5° sampling interval without local search), a mask was placed around the U1 snRNP and the local angular search range was limited to 20° with a finer sampling interval of 3.7°. The best class (with 504,547 particles) was selected, centred and re-extracted with an original pixel size of 1.16 \AA with a box size of 400×400 pixels and refined with a mask around the U1 snRNP, resulting in a map at 4.3 \AA resolution. Next, using the alignment parameters from the aforementioned masked 3D refinement, the 504,547 particles were focus classified with a mask around the high-resolution U1 core, into 4 classes. The best class (containing 226,656 particles) was selected and refined into a map of the entire pre-A complex with an average resolution of 5.9 \AA (ranging from roughly 4.5 \AA at the U1 region to roughly 15 \AA at the U2 region). The U1 and U2 regions were further improved by multibody refinement to 4.1 \AA and 10 \AA respectively. To further improve the U2 region, we re-extracted the 504,547 particles into a smaller box size of 140×140 pixels (pixel size of 2.32 \AA) with the U2 snRNP centred, and 3D classified into 5 classes with a mask around the U2 snRNP. The best class, with 160,894 particles, was selected and multibody refined with masks around the U2 5'- and 3'-regions, resulting in a map at 8.3 \AA resolution for the 5'-region and one at 9.5 \AA resolution for the 3'-region. All the aforementioned resolutions were estimated on the basis of the RELION gold-standard Fourier shell correlation (0.143 criterion).

For the U257A pre-A complex, initially 460,854 and 869,306 particles were extracted from dataset 1 and dataset 2, respectively, and rescaled to 110×110 pixels, to the same pixel size of 4.64 Å, in RELION 3.0 (http://www2.mrc-lmb.cam.ac.uk/relion/index.php/Main_Page). After several iterations of reference-free 2D classification, 697,892 ‘good particles’ from the two datasets were combined and classified into four classes by 3D classification with only the U1 part as the starting model, to avoid model bias. No class resembling the structure of the mature A complex was observed. Three classes had no discernible structural features of U1 or U2 snRNPs. One class (of 240,145 particles) clearly exhibited the structure of a pre-A complex, and was selected, centred and re-extracted with a pixel size of 2.32 Å with a box size of 220×220 pixels. Re-extracted particles were further 3D classified into four classes with a mask around the U1 part, yielding one class that showed clear secondary structures. This class (80,853 particles) was selected and refined into a map of the entire pre-A complex with an average resolution of 10.4 Å. Multibody refinement improved the U1 part to 7.5 Å. To improve the U2 part, we further classified the 80,853 particles with a mask around the U2 part into four classes, and two classes showing clear U2 density were combined, 3D refined and multibody refined, yielding the U2 part of the structure with 13 Å resolution. All of the aforementioned resolutions were estimated on the basis of the RELION gold-standard Fourier shell correlation (0.143 criterion).

ΔBS-A pre-A model building and refinement

Templates for the U1 and U2 proteins and RNA were obtained wherever possible from published structures (Extended Data Table 2). The U1 snRNP components, except Prp40, were initially docked as rigid bodies into the 4.1 Å EM map of the U1 region. In the central part of the U1 snRNP (resolution ranging from 3.7 Å to 4.3 Å), side chains were manually adjusted into the map using Coot v.0.8.9.2 (ref. 31). The entire model of the U1 snRNP, excluding Prp40, was combined and subjected to real-space refinement in PHENIX v.1.13-2998 (ref. 32), with secondary-structure restraints. The solution structure of the Prp40 FF1 domain and the homology model of domains FF2–FF6 predicted by the SWISS-MODEL suite³³ were truncated to polyalanine, docked into the pre-A map as rigid bodies, and were not refined owing to the limited resolution. The model of Hsh155 (H1–H15) was based on human SF3B1 (H1–H15) but with the sequence changed to that of yeast Hsh155. The model of the ΔBS-A U2/BS helix (U2 nucleotides 32–46; *Act1* pre-mRNA nucleotides 254–268) was generated by deleting the BS-A from the model of the wild-type U2–BS helix using Coot. All U2 snRNP components were docked into the U2 map as rigid bodies without further adjustments, except that Prp9 (amino acids 328–362) and Prp21 (amino acids 173–192) were slightly adjusted using Coot to better fit the EM density, and the linker between the U2–BS helix and SLIIa (U2 nucleotides 47–49) was de novo modelled using Coot. All modelled components in the U2 region were modelled as polyalanine.

and were not refined owing to the limited resolution. The structural model for the ΔBS-A pre-A complex was fit into the EM density obtained for complexes formed on the U257A mutant *Act1* pre-mRNA. The video showing the structural dynamics seen during the transition from the pre-A to the A complex was generated using ChimeraX v1.1.

Reporting summary

Further information on research design is available in the [Nature Research Reporting Summary](#) linked to this paper.

Data availability

The coordinate files have been deposited in the Protein Data Bank (<https://www.rcsb.org>) as follows: U1 snRNP region, PDB accession number 7OQC; U2 snRNP region, PDB 7OQB; and composite truncated model of the pre-A complex, PDB 7OQE. The cryo-EM maps have been deposited in the Electron Microscopy Data Bank (<https://www.ebi.ac.uk/pdbe/emdb/>) as follows: U1 snRNP region of the ΔBS-A pre-A complex, EMD accession number 13029, and of the U257A pre-A complex, EMD 13031; U2 snRNP region of the ΔBS-A pre-A complex, EMD 13028, and of the U257A pre-A complex, EMD 13032; and overall reconstruction of the ΔBS-A pre-A complex, EMD 13033, and of the U257A pre-A complex, EMD 13030. We used the *S. cerevisiae* Genome Database (SGD; <https://www.yeastgenome.org>) in this study.

References

1. 1.

Ruby, S. W., Chang, T. H. & Abelson, J. Four yeast spliceosomal proteins (PRP5, PRP9, PRP11, and PRP21) interact to promote U2 snRNP binding to pre-mRNA. *Genes Dev.* **7**, 1909–1925 (1993).

[CAS](#) [PubMed](#) [Article](#) [PubMed Central](#) [Google Scholar](#)

2. 2.

Abu Dayyeh, B. K., Quan, T. K., Castro, M. & Ruby, S. W. Probing interactions between the U2 small nuclear ribonucleoprotein and the DEAD-box protein, Prp5. *J. Biol. Chem.* **277**, 20221–20233 (2002).

[PubMed](#) [Article](#) [CAS](#) [PubMed Central](#) [Google Scholar](#)

3. 3.

Perriman, R., Barta, I., Voeltz, G. K., Abelson, J. & Ares, M. Jr. ATP requirement for Prp5p function is determined by Cus2p and the structure of U2 small nuclear RNA. *Proc. Natl Acad. Sci. USA* **100**, 13857–13862 (2003).

[ADS](#) [CAS](#) [PubMed](#) [PubMed Central](#) [Article](#) [Google Scholar](#)

4. 4.

Xu, Y. Z. et al. Prp5 bridges U1 and U2 snRNPs and enables stable U2 snRNP association with intron RNA. *EMBO J.* **23**, 376–385 (2004).

[PubMed](#) [PubMed Central](#) [Article](#) [CAS](#) [Google Scholar](#)

5. 5.

Xu, Y. Z. & Query, C. C. Competition between the ATPase Prp5 and branch region-U2 snRNA pairing modulates the fidelity of spliceosome assembly. *Mol. Cell* **28**, 838–849 (2007).

[CAS](#) [PubMed](#) [PubMed Central](#) [Article](#) [Google Scholar](#)

6. 6.

Smith, D. J., Konarska, M. M. & Query, C. C. Insights into branch nucleophile positioning and activation from an orthogonal pre-mRNA splicing system in yeast. *Mol. Cell* **34**, 333–343 (2009).

[CAS](#) [PubMed](#) [PubMed Central](#) [Article](#) [Google Scholar](#)

7. 7.

Rauhut, R. et al. Molecular architecture of the *Saccharomyces cerevisiae* activated spliceosome. *Science* **353**, 1399–1405 (2016).

[ADS](#) [CAS](#) [PubMed](#) [Article](#) [PubMed Central](#) [Google Scholar](#)

8. 8.

Yan, C., Wan, R., Bai, R., Huang, G. & Shi, Y. Structure of a yeast activated spliceosome at 3.5 Å resolution. *Science* **353**, 904–911 (2016).

[ADS](#) [CAS](#) [PubMed](#) [Article](#) [PubMed Central](#) [Google Scholar](#)

9. 9.

Haselbach, D. et al. Structure and conformational dynamics of the human spliceosomal B^{act} complex. *Cell* **172**, 454–464.e11 (2018).

[CAS](#) [PubMed](#) [Article](#) [PubMed Central](#) [Google Scholar](#)

10. 10.

Zhang, X. et al. Structure of the human activated spliceosome in three conformational states. *Cell Res.* **28**, 307–322 (2018).

[ADS](#) [CAS](#) [PubMed](#) [PubMed Central](#) [Article](#) [Google Scholar](#)

11. 11.

Zhang, Z. et al. Molecular architecture of the human 17S U2 snRNP. *Nature* **583**, 310–313 (2020).

[ADS](#) [CAS](#) [PubMed](#) [Article](#) [PubMed Central](#) [Google Scholar](#)

12. 12.

Plaschka, C., Lin, P. C. & Nagai, K. Structure of a pre-catalytic spliceosome. *Nature* **546**, 617–621 (2017).

[ADS](#) [CAS](#) [PubMed](#) [PubMed Central](#) [Article](#) [Google Scholar](#)

13. 13.

Bai, R., Wan, R., Yan, C., Lei, J. & Shi, Y. Structures of the fully assembled *Saccharomyces cerevisiae* spliceosome before activation. *Science* **360**, 1423–1429 (2018).

[ADS](#) [CAS](#) [PubMed](#) [Article](#) [PubMed Central](#) [Google Scholar](#)

14. 14.

Perriman, R. & Ares, M. Jr. Invariant U2 snRNA nucleotides form a stem loop to recognize the intron early in splicing. *Mol. Cell* **38**, 416–427 (2010).

[CAS](#) [PubMed](#) [PubMed Central](#) [Article](#) [Google Scholar](#)

15. 15.

Plaschka, C., Lin, P. C., Charenton, C. & Nagai, K. Prespliceosome structure provides insights into spliceosome assembly and regulation. *Nature* **559**, 419–422 (2018).

[ADS](#) [CAS](#) [PubMed](#) [PubMed Central](#) [Article](#) [Google Scholar](#)

16. 16.

Liang, W. W. & Cheng, S. C. A novel mechanism for Prp5 function in prespliceosome formation and proofreading the branch site sequence. *Genes Dev.* **29**, 81–93 (2015).

[PubMed](#) [PubMed Central](#) [Article](#) [CAS](#) [Google Scholar](#)

17. 17.

Tang, Q. et al. SF3B1/Hsh155 HEAT motif mutations affect interaction with the spliceosomal ATPase Prp5, resulting in altered branch site selectivity in pre-mRNA splicing. *Genes Dev.* **30**, 2710–2723 (2016).

[CAS](#) [PubMed](#) [PubMed Central](#) [Article](#) [Google Scholar](#)

18. 18.

Li, X. et al. A unified mechanism for intron and exon definition and back-splicing. *Nature* **573**, 375–380 (2019).

[ADS](#) [CAS](#) [PubMed](#) [PubMed Central](#) [Article](#) [Google Scholar](#)

19. 19.

Carrocci, T. J., Paulson, J. C. & Hoskins, A. A. Functional analysis of Hsh155/SF3b1 interactions with the U2 snRNA/branch site duplex. *RNA* **24**, 1028–1040 (2018).

[CAS](#) [PubMed](#) [PubMed Central](#) [Article](#) [Google Scholar](#)

20. 20.

Kennedy, S. D., Bauer, W. J., Wang, W. & Kielkopf, C. L. Dynamic stacking of an expected branch point adenosine in duplexes containing pseudouridine-modified or unmodified U2 snRNA sites. *Biochem. Biophys. Res. Commun.* **511**, 416–421 (2019).

[CAS](#) [PubMed](#) [PubMed Central](#) [Article](#) [Google Scholar](#)

21. 21.

Shao, W., Kim, H. S., Cao, Y., Xu, Y. Z. & Query, C. C. A U1-U2 snRNP interaction network during intron definition. *Mol. Cell. Biol.* **32**, 470–478 (2012).

[CAS](#) [PubMed](#) [PubMed Central](#) [Article](#) [Google Scholar](#)

22. 22.

Beier, D. H. et al. Dynamics of the DEAD-box ATPase Prp5 RecA-like domains provide a conformational switch during spliceosome assembly. *Nucleic Acids Res.* **47**, 10842–10851 (2019).

[CAS](#) [PubMed](#) [PubMed Central](#) [Article](#) [Google Scholar](#)

23. 23.

Yean, S. L. & Lin, R. J. U4 small nuclear RNA dissociates from a yeast spliceosome and does not participate in the subsequent splicing reaction. *Mol. Cell. Biol.* **11**, 5571–5577 (1991).

[CAS](#) [PubMed](#) [PubMed Central](#) [Article](#) [Google Scholar](#)

24. 24.

Bertram, K. et al. Cryo-EM structure of a human spliceosome activated for step 2 of splicing. *Nature* **542**, 318–323 (2017).

[ADS](#) [CAS](#) [PubMed](#) [Article](#) [PubMed Central](#) [Google Scholar](#)

25. 25.

Yang, B. et al. Identification of cross-linked peptides from complex samples. *Nat. Methods* **9**, 904–906 (2012).

[CAS](#) [PubMed](#) [Article](#) [PubMed Central](#) [Google Scholar](#)

26. 26.

Chen, Z. L. et al. A high-speed search engine pLink 2 with systematic evaluation for proteome-scale identification of cross-linked peptides. *Nat. Commun.* **10**, 3404 (2019).

[ADS](#) [PubMed](#) [PubMed Central](#) [Article](#) [CAS](#) [Google Scholar](#)

27. 27.

Zheng, S. Q. et al. MotionCor2: anisotropic correction of beam-induced motion for improved cryo-electron microscopy. *Nat. Methods* **14**, 331–332 (2017).

[CAS](#) [PubMed](#) [PubMed Central](#) [Article](#) [Google Scholar](#)

28. 28.

Zhang, K. Gctf: real-time CTF determination and correction. *J. Struct. Biol.* **193**, 1–12 (2016).

[ADS](#) [CAS](#) [PubMed](#) [PubMed Central](#) [Article](#) [Google Scholar](#)

29. 29.

Punjani, A., Rubinstein, J. L., Fleet, D. J. & Brubaker, M. A. cryoSPARC: algorithms for rapid unsupervised cryo-EM structure determination. *Nat. Methods* **14**, 290–296 (2017).

[CAS](#) [PubMed](#) [PubMed Central](#) [Article](#) [Google Scholar](#)

30. 30.

Pettersen, E. F. et al. UCSF Chimera—a visualization system for exploratory research and analysis. *J. Comput. Chem.* **25**, 1605–1612 (2004).

[CAS](#) [Article](#) [Google Scholar](#)

31. 31.

Emsley, P. & Cowtan, K. Coot: model-building tools for molecular graphics. *Acta Crystallogr. D* **60**, 2126–2132 (2004).

[PubMed](#) [Article](#) [CAS](#) [PubMed Central](#) [Google Scholar](#)

32. 32.

Adams, P. D. et al. PHENIX: a comprehensive Python-based system for macromolecular structure solution. *Acta Crystallogr. D* **66**, 213–221 (2010).

[CAS](#) [PubMed](#) [PubMed Central](#) [Article](#) [Google Scholar](#)

33. 33.

Guex, N. & Peitsch, M. C. SWISS-MODEL and the Swiss-PdbViewer: an environment for comparative protein modeling. *Electrophoresis* **18**, 2714–2723 (1997).

[CAS](#) [PubMed](#) [Article](#) [PubMed Central](#) [Google Scholar](#)

34. 34.

Kastner, B., Will, C. L., Stark, H. & Lührmann, R. Structural insights into nuclear pre-mRNA splicing in higher eukaryotes. *Cold Spring Harb. Perspect. Biol.* **11**, a032417 (2019).

[CAS](#) [PubMed](#) [Article](#) [PubMed Central](#) [Google Scholar](#)

35. 35.

Wilkinson, M. E., Charenton, C. & Nagai, K. RNA splicing by the spliceosome. *Annu. Rev. Biochem.* **89**, 359–388 (2020).

[CAS](#) [PubMed](#) [Article](#) [PubMed Central](#) [Google Scholar](#)

36. 36.

Semlow, D. R. & Staley, J. P. Staying on message: ensuring fidelity in pre-mRNA splicing. *Trends Biochem. Sci.* **37**, 263–273 (2012).

[CAS](#) [PubMed](#) [PubMed Central](#) [Article](#) [Google Scholar](#)

37. 37.

Cordin, O. & Beggs, J. D. RNA helicases in splicing. *RNA Biol.* **10**, 83–95 (2013).

[CAS](#) [PubMed](#) [PubMed Central](#) [Article](#) [Google Scholar](#)

38. 38.

Kistler, A. L. & Guthrie, C. Deletion of MUD2, the yeast homolog of U2AF65, can bypass the requirement for sub2, an essential spliceosomal ATPase. *Genes Dev.* **15**, 42–49 (2001).

[CAS](#) [PubMed](#) [PubMed Central](#) [Article](#) [Google Scholar](#)

39. 39.

Zhang, M. & Green, M. R. Identification and characterization of yUAP/Sub2p, a yeast homolog of the essential human pre-mRNA splicing factor hUAP56. *Genes Dev.* **15**, 30–35 (2001).

[PubMed](#) [PubMed Central](#) [Article](#) [Google Scholar](#)

40. 40.

O'Day, C. L., Dalbadie-McFarland, G. & Abelson, J. The *Saccharomyces cerevisiae* Prp5 protein has RNA-dependent ATPase activity with specificity for U2 small nuclear RNA. *J. Biol. Chem.* **271**, 33261–33267 (1996).

[PubMed](#) [Article](#) [PubMed Central](#) [Google Scholar](#)

41. 41.

Wang, Q., Zhang, L., Lynn, B. & Rymond, B. C. A. A BBP-Mud2p heterodimer mediates branchpoint recognition and influences splicing substrate abundance in budding yeast. *Nucleic Acids Res.* **36**, 2787–2798 (2008).

[CAS](#) [PubMed](#) [PubMed Central](#) [Article](#) [Google Scholar](#)

42. 42.

Jacewicz, A., Chico, L., Smith, P., Schwer, B. & Shuman, S. Structural basis for recognition of intron branchpoint RNA by yeast Msl5 and selective effects of interfacial mutations on splicing of yeast pre-mRNAs. *RNA* **21**, 401–414 (2015).

[CAS](#) [PubMed](#) [PubMed Central](#) [Article](#) [Google Scholar](#)

43. 43.

Cretu, C. et al. Structural basis of splicing modulation by antitumor macrolide compounds. *Mol. Cell* **70**, 265–273.e8 (2018).

[CAS](#) [PubMed](#) [Article](#) [PubMed Central](#) [Google Scholar](#)

44. 44.

Lin, P. C. & Xu, R. M. Structure and assembly of the SF3a splicing factor complex of U2 snRNP. *EMBO J.* **31**, 1579–1590 (2012).

[CAS](#) [PubMed](#) [PubMed Central](#) [Article](#) [Google Scholar](#)

45. 45.

Afonine, P. V. et al. Real-space refinement in PHENIX for cryo-EM and crystallography. *Acta Crystallogr. D* **74**, 531–544 (2018).

[CAS](#) [Article](#) [Google Scholar](#)

46. 46.

Ester, C. & Uetz, P. The FF domains of yeast U1 snRNP protein Prp40 mediate interactions with Luc7 and Snu71. *BMC Biochem.* **9**, 29 (2008).

[PubMed](#) [PubMed Central](#) [Article](#) [CAS](#) [Google Scholar](#)

47. 47.

Caspary, F. & Séraphin, B. The yeast U2A'/U2B complex is required for pre-spliceosome formation. *EMBO J.* **17**, 6348–6358 (1998).

[CAS](#) [PubMed](#) [PubMed Central](#) [Article](#) [Google Scholar](#)

[Download references](#)

Acknowledgements

We thank T. Schulz for yeast fermentation; M. Raabe and U. Pleßmann for excellent technical assistance; B. Kastner for helpful discussions and comments on the manuscript; and thank S.-C. Cheng for providing antibodies against *S. cerevisiae* Prp5 and Lea1. This work was supported by the Max Planck Society and the Deutsche Forschungsgemeinschaft (SFB 860 grants to H.U. and H.S.).

Funding

Open access funding provided by Max Planck Society.

Author information

Affiliations

1. Department of Structural Dynamics, MPI for Biophysical Chemistry, Göttingen, Germany

Zhenwei Zhang & Holger Stark

2. Cellular Biochemistry, MPI for Biophysical Chemistry, Göttingen, Germany

Norbert Rigo, Olexandr Dybkov, Jean-Baptiste Fourmann, Cindy L. Will, Vinay Kumar & Reinhard Lührmann

3. Bioanalytical Mass Spectrometry, MPI for Biophysical Chemistry, Göttingen, Germany

Henning Urlaub

4. Bioanalytics Group, Institute for Clinical Chemistry, University Medical Center Göttingen, Göttingen, Germany

Henning Urlaub

Authors

1. Zhenwei Zhang

[View author publications](#)

You can also search for this author in [PubMed](#) [Google Scholar](#)

2. Norbert Rigo

[View author publications](#)

You can also search for this author in [PubMed](#) [Google Scholar](#)

3. Olexandr Dybkov

[View author publications](#)

You can also search for this author in [PubMed](#) [Google Scholar](#)

4. Jean-Baptiste Fourmann
[View author publications](#)

You can also search for this author in [PubMed](#) [Google Scholar](#)

5. Cindy L. Will
[View author publications](#)

You can also search for this author in [PubMed](#) [Google Scholar](#)

6. Vinay Kumar
[View author publications](#)

You can also search for this author in [PubMed](#) [Google Scholar](#)

7. Henning Urlaub
[View author publications](#)

You can also search for this author in [PubMed](#) [Google Scholar](#)

8. Holger Stark
[View author publications](#)

You can also search for this author in [PubMed](#) [Google Scholar](#)

9. Reinhard Lührmann
[View author publications](#)

You can also search for this author in [PubMed](#) [Google Scholar](#)

Contributions

N.R., J.-B.F. and V.K. developed the purification strategy and characterized the pre-A complexes. O.D. and H.U. analysed protein–protein crosslinking data. Z.Z. prepared grids, collected EM data, processed and refined EM data, and built the model. Z.Z. analysed the structure, with input from H.S. and R.L. All authors were involved in data interpretation. The manuscript

was written by R.L., Z.Z. and C.L.W., with input from all authors. R.L. and H.S. supervised the project.

Corresponding authors

Correspondence to [Holger Stark](#) or [Reinhard Lührmann](#).

Ethics declarations

Competing interests

The authors declare no competing interests.

Additional information

Peer review information *Nature* thanks Aaron Hoskins, Navtej Toor and the other, anonymous, reviewer(s) for their contribution to the peer review of this work.

Publisher's note Springer Nature remains neutral with regard to jurisdictional claims in published maps and institutional affiliations.

Extended data figures and tables

[Extended Data Fig. 1 Biochemical characterization of *S. cerevisiae* pre-A spliceosomal complexes.](#)

a, Early assembly of the *S. cerevisiae* spliceosome. Whereas Prp5 and Tat-SF1 (Cus2 in yeast) are stable components of the human 17S U2 snRNP, they appear to be less-stably associated with the yeast U2 snRNP. The spliceosome undergoes numerous structural and compositional rearrangements during its assembly and catalysis of pre-mRNA splicing^{[34,35](#)}. Conserved DEXH/D-box RNA helicases are important driving forces for these rearrangements, and also ensure the proper recognition of the branch site (BS) and the 5'- and 3'-splice sites (ss) via proofreading

mechanisms^{36,37}. Initially an E complex is formed in an ATP-independent manner. In the yeast E complex (also denoted the commitment complex), the 5'-ss is bound by U1 snRNP, and the BS and 3'-end of the intron are bound by a heterodimer of Msl5 and Mud2. RNP rearrangements that lead to the stable association of U2 snRNP and enable the formation of a U2–BS helix—in which an adenosine is bulged, specifying it as the nucleophile for catalytic step 1 of splicing—require the ATP-dependent action of the DEAD-box RNA helicases Sub2 (refs. ^{38,39}; UAP56 in humans) and Prp5 (refs. ^{1,2,3,4,40}). U2 nucleotides that base pair with the BS are initially sequestered in a stem-loop structure denoted the BSL^{11,14}. Sub2 may free the BS region by displacing Msl5 (refs. ^{41,42}), while Prp5 has been proposed to displace U2 snRNP proteins, including Cus2 (TAT–SF1 in humans), from the BSL^{11,14}. This frees U2 nucleotides to base pair with the BS, and leads to the formation of the A complex with stably bound U2 snRNP. **b**, Structure of the BSL and U2–BS helices formed on an *Act* pre-mRNA wild-type (WT) BS (UACUA(**A**)C, where the BS-A is in bold), ΔBS-A (UACUAC) or U257A (UACAA(**A**)C) branch site. Note that the exact conformation of the U257A U2–BS helix is not clear. The U2–BS helix is highlighted in purple, and the extended U2–BS helix, in which the number and nature of base-pairing interactions varies depending on the pre-mRNA intron sequence, is highlighted in yellow. **c**, Deletion of the BS adenosine from the *Act* pre-mRNA stalls splicing before the first catalytic step. Splicing was performed in two independent experiments in yeast extract for 30 min at 23 °C with wild-type (lane 1) or ΔBS-A (lane 2) *Act* pre-mRNA containing MS2 aptamers for affinity purification. *Position of the loading well. **Band artefact not related to pre-mRNA splicing. For gel source data, see Supplementary Fig. 1. **d**, RNA (left gels) and protein (right gels) composition of purified yeast pre-A complexes formed on ΔBS-A and U257A *Act* pre-mRNA. RNA and protein were analysed on NuPAGE gels and visualized by staining with SYBR Gold or Coomassie, respectively, in two independent experiments. Note that fewer picomoles of the U257A pre-A complex were loaded onto the gel and, as a consequence, proteins of lower molecular weight are poorly or not at all visible. **e**, Prp5 is present in both U257A and ΔBS-A pre-A complexes. Proteins from affinity-purified U257A or ΔBS-A pre-A complexes (as indicated above each lane) were analysed by western blotting in two independent experiments with antibodies against *S. cerevisiae* Prp5 or Lea1 (used to ensure equal loading).

f, Proteins localized in the *S. cerevisiae* pre-A complex and their human homologues (shown in parentheses). Only U1–70K, U1–A and U1–C have been identified as stable components of human U1 snRNPs. Human homologues of Snu56 and Prp42 have not been identified. **g**, Residues forming the BS-A-binding pocket. The bulged BS-A is bound in a pocket composed of residues R744, N747, V783 and Y826 of Hsh155 and residue Y36 of Rds3 (refs. [7,8,43](#)). The BS-A ribose and 5'-phosphate are also located near Hsh155 residues K740 and K818, respectively. Most of these residues are evolutionarily highly conserved. A Hsh155 K818A mutation is lethal, as are mutations in residues of Hsh155 that contact the backbone of nucleotides directly adjacent to the bulged BS-A¹⁹. However, many of the Hsh155 residues forming the BS-A binding pocket are nonessential. That is, single alanine substitutions at K740, R744, N747 and V783 do not affect yeast viability, but they do affect recognition of the branch site¹⁹. Substitutions with bulkier amino acids decrease the use of nonconsensus branch sites, whereas substitutions with smaller amino acids increase usage¹⁹.

Extended Data Fig. 2 Cryo-EM and image processing for the ABS-A pre-A complex.

a, Computation sorting scheme. All major image-processing steps are depicted. For a more detailed explanation, see the Methods section on ‘Image processing’. **b**, Typical cryo-EM micrograph (out of a total of 74,230) of the *S. cerevisiae* pre-A complex recorded at $\times 120,700$ magnification with a Titan Krios microscope using a Falcon III direct electron detector operating in integration mode at a calibrated pixel size of 1.16 Å. **c**, Representative cryo-EM 2D class averages of the yeast pre-A complex reveal considerable flexibility between the U1 snRNP and the U2 snRNP. **d**, Left, local-resolution estimations of the cryo-EM reconstruction of the U1 snRNP. Right, plot showing the distribution of orientations for the particles contributing to the U1 reconstruction. **e**, Left, local-resolution estimations of the cryo-EM reconstructions of the U2 5'- and 3'-regions. Right, plot showing the distribution of orientations for the particles contributing to the reconstructions of the U2 5'- and 3'-regions. **f**, A Fourier shell correlation (FSC), calculated using the ‘post-processing’ routine in

RELION, indicates a global resolution of 5.9 Å for the entire yeast pre-A complex and of 4.1 Å, 8.3 Å and 9.5 Å for the multibody-refined U1, U2 5'- and U2 3'-regions, respectively. The resolution was limited to 5.9 Å on average, owing to the movement of the U1 and U2 snRNPs relative to each other. Signal subtraction combined with local refinement improved the more stable U1 snRNP part to 4.1 Å resolution, whereas the bipartite U2 snRNP exhibited considerable internal flexibility and was refined only to 9 Å resolution. As the U2 5'-region—which is composed of the SF3b proteins, U2 SLIIa/b and the U2–BS helix—is attached to the more stable U1 snRNP and is therefore less flexible, further local classification and refinement improved the resolution of the U2 5'-region to 8.3 Å. The U2 3'-region—which comprises the U2 Sm core, U2 SLII, and Lea1 and U2-B'' bound to U2 SLIV, plus the adjacent SF3a core (that is, regions of Prp9, Prp11 and Prp21 whose crystal structure has been determined previously⁴⁴)—does not contact the U1 snRNP and therefore exhibits the greatest flexibility relative to the rest of the complex. **g**, Map versus model FSC curves for the U1, U2, U2 5'- and U2 3'-regions, using PHENIX mtriage⁴⁵.

Extended Data Fig. 3 Open conformation of Hsh155^{HEAT} and spatial organization of the U2–BS helix and U2 SLIIa/b in the pre-A complex.

a, Left, fit of Hsh155^{HEAT} and Rds3 to the pre-A EM density; and right, fit of SF3B1, PHF5A and the N-terminal helix of Prp5 to the human 17S U2 density (PDB accession code 6Y5Q). Previous biochemical studies showed that the N-terminal region (NTR) of yeast Prp5 binds to HEAT repeats (HRs) 1–6 and HR 9–12 of Hsh155 (ref. ¹⁷), and in the human 17S U2 snRNP cryo-EM structure, binding to SF3B1 HR 9–12 involves a long α-helix of the human Prp5^{NTR} (ref. ¹¹). EM density that would accommodate an analogous α-helix of the yeast Prp5^{NTR} is not apparent in the pre-A complex. However, CXMS indicates that the Prp5^{NTR} still interacts extensively with Hsh155, albeit solely with HR 1–7 (see Extended Data Fig. ^{4b}). Base pairing of U2 snRNA with the pre-mRNA branch site (BS) is stabilized by the major scaffolding protein SF3B1 (Hsh155 in *S. cerevisiae*) of the SF3b heteromeric complex, whose HEAT domain undergoes a conformational change during early spliceosome assembly. Hsh155^{HEAT}

and SF3B1^{HEAT} exhibit an open conformation in the pre-A complex and the 17S U2 snRNP, respectively. The closed conformations of the HEAT domains of human SF3B1 and of yeast Hsh155 observed in the A to B^{act} spliceosomal complexes are very similar. Likewise, the open conformation, which we observe here for the first time for Hsh155, also appears to be highly similar in human U2 snRNP and the *S. cerevisiae* pre-A complex. **b**, Similar spatial organization of U2 snRNA SLIIa, Prp9^{ZnF} (SF3A3 in humans) and Cus1 (SF3B2 in humans) in the human 17S U2 snRNP (PDB 6Y5Q) and *S. cerevisiae* pre-A, A (PDB 6G90) and B (PDB 5NRL) complexes. Aligned via U2 SLIIa and HR 19–20 of SF3B1/Hsh155. In the pre-A complex, SLIIb can be localized downstream of SLIIa and is bound by RRM2 of Hsh49. **c**, Fit of a modelled 13-base-pair extended U2–BS helix, lacking a bulged A, to EM density adjacent to SLIIa in the pre-A complex. **d**, Overlay of EM density accommodating the U2–BS helix in the yeast pre-A complex (grey) and EM density accommodating the BSL in human 17S U2 (green) (PDB 6Y5Q). Aligned via U2 SLIIa and HR 19–20 of SF3B1/Hsh155. The sequences of the *S. cerevisiae* and human U2 BSLs are highly conserved¹⁴, allowing a meaningful comparison with the fit of the yeast U2–BS helix. Although the BSL in yeast and human is predicted to form a 9-base-pair stem¹⁴, in the human 17S U2 snRNP, the base of the BSL stem is contacted by a short helix of SF3A3 (designated the separator helix), which ensures that the stem is only 8 base pairs in length¹¹. **e**, Fit in the pre-A EM density of the Prp11^{ZnF} at the top of the U2–BS helix. **f**, Protein crosslinks supporting the positioning of the Prp11^{ZnF} in the pre-A complex. Numbers (colour coded to match protein colours) indicate the positions of crosslinked lysine residues, which are connected by black lines. The Prp11^{ZnF} appears to act independently of the other SF3a proteins and to dock to the end of the extended U2–BS helix concomitantly with, or soon after, its formation. As the Prp11^{ZnF} has thus far been observed at this position solely after formation of the U2–BS helix, its location in the pre-A complex is consistent with the conclusion that a U2–BS helix has formed. It is likely that the Prp11^{ZnF} and the Prp9 separator helix may cooperate in keeping additional intron nucleotides from interacting with the U2 snRNA, and at the same time in stabilizing the end of the U2–BS helix. During clamping of the U2–BS helix by Hsh155^{HEAT}, Prp11^{ZnF} moves together with the U2–BS helix and remains associated with the end of the helix in

the A, pre-B, B and B^{act} complexes. **g**, Side view showing that the U2–BS helix is located further away from the C-terminal HRs of Hsh155^{HEAT} in the pre-A complex compared with its position in the *S. cerevisiae* A complex and the position of the BSL in human 17S U2 snRNP. Aligned via Hsh155 HR 19–20, Rse1^{BPA} and U2 SLIIa. Olive green, SLIIa nucleotides; red orange, pre-mRNA BS nucleotides; purple, BSL nucleotides that later form the U2–BS helix; yellow, BSL nucleotides forming the extended part of the U2–BS helix; dark green, the remaining BSL nucleotides; blue, SLI.

Movement away from Hsh155^{HEAT} would be needed to free the SLI-containing 5'-end of U2 snRNA to undergo the rotational movements necessary to generate an extended U2–BS helix. During the transition from the pre-A to the A complex, the U2–BS helix moves back towards the Hsh155 C-terminal HRs such that the corresponding region of the U2 snRNA that contacts the C-terminal HRs in 17S U2 is located in a similar position in the A complex.

Extended Data Fig. 4 Repositioning of the Prp5 RecA domains and the U2 3'-region during formation of the pre-A complex.

a, Domain organization of the *S. cerevisiae* (y) and human (h) DEAD-box helicase Prp5, with the amino-acid boundaries of each domain indicated below. **b**, Protein crosslinks support the positions of the Prp5 NTR and RecA domains in the pre-A complex. Numbers (colour coded to match protein colours) indicate the positions of crosslinked lysine residues, which are connected by black lines. The proposed path of Prp5 amino acids located more N-terminally of the RecA domains is indicated by a dashed line. That the Prp5 NTR and RecA1 domains, but not RecA2 (and presumably also its C-terminal region), interact with other pre-A components is consistent with previous studies showing that, after destabilization of the U2 BSL, Prp5^{NTR} and Prp5^{RecA1} are sufficient for the subsequent ATP-independent function of Prp5 during A-complex formation¹⁴. **c**, Two different views of the fit of the Prp5 RecA1 and RecA2 domains in an open conformation into the pre-A EM density (low-pass filtered to 10 Å). A closed conformation of the Prp5^{RecA} domain does not fit well to the EM density (not shown). The open conformation of Prp5 found in the pre-A complex indicates that, after ATP hydrolysis, the RecA

domains are able to transit spontaneously from the closed conformation back to the open conformation while probably remaining bound to U2. **d, e**, The positions of the Prp5^{RecA} domains and the U2 3'-region plus SF3a proteins, relative to SF3b, are different in the human 17S U2 snRNP and the yeast pre-A complex. Aligned via U2 SLIIa and HR 19–20 of SF3B1/Hsh155. A cryo-EM structure of an isolated *S. cerevisiae* U2 snRNP is currently lacking. However, the high conservation of the sequence of yeast U2 proteins and their human homologues, and the similar structures of their conserved domains, suggests that the molecular architecture of the isolated U2 snRNP is similar in *S. cerevisiae* and humans. Thus, a comparison of the structures of the human 17S U2 snRNP and yeast pre-A complex reveals structural remodelling that the U2 snRNP most likely undergoes during formation of the pre-A complex. An alignment of the U2 5'-region in both complexes suggests that the U2 3'-region is repositioned after U2 stably interacts during formation of the pre-A complex. Specifically, the U2 3'-domain (that is, the 3'-region minus the SF3a core) and the Prp9^{NTR} rotate towards the Prp5^{RecA} domains, whereas the Prp11 β-sandwich and Hsh49^{RRM2} move towards Prp9^{ZnF}. The shifted position of the U2 3'-region is stabilized by different molecular bridges formed between the U2 3'- and 5'-regions. In the pre-A complex, the bridge formed by U2-B'' RRM2, Prp9 (human SF3A3) and Rse1^{BPC} (human SF3B3) in the 17S U2 snRNP (denoted bridge B) is disrupted, which allows the 3'-region to move further away from the Rse1^{BPC}. This then allows Hsh49^{RRM2} to dock on top of the Prp9^{ZnF}, and by binding to Prp9 on one side and the Prp11 β-sandwich domain on the other, a new bridge involving Hsh49^{RRM2} is formed. Moreover, in the isolated human 17S U2 snRNP, U2 SLIIb forms a second bridge (denoted bridge A) between the U2 3'- and 5'-regions that is not stabilized and is only poorly resolved. By contrast, in the pre-A complex, Hsh49^{RRM2} now binds to the loop of SLIIb and thereby stabilizes the position of SLIIb.

Extended Data Fig. 5 Molecular architecture of the U1 snRNP in the pre-A complex.

a, Two different views of the spatial organization of the yeast U1 snRNP, with the density shown on the left and the molecular model on the right. **b**,

The U1–5' ss helix is stabilized in the pre-A complex by Luc-7 and Yhc1, in the same manner as in the yeast E and A complexes. Top, fit of the U1–5' ss helix plus Luc7 and Yhc1 to the pre-A EM density. Bottom, the U1–5' ss helix and adjacent proteins. **c**, Fit of the Prp40 FF1–6 domains in the pre-A EM density. Top, domain organization of the *S. cerevisiae* Prp40 protein; below, amino-acid boundaries of each domain. WW, domain containing two conserved tryptophans that are spaced 20–22 amino acids apart; FF, domain containing two conserved phenylalanines at its N and C termini. **d**, Protein crosslinks between Prp40, Prp5^{NTR} and other pre-A-complex proteins. Numbers (colour coded to match protein colours) indicate the positions of crosslinked lysine residues, which are connected by black lines. Prp40, Snu71 and Luc7 form a stable trimer⁴⁶ that in the cryo-EM structure of the yeast E complex¹⁸ bridges the U1 snRNP to the branch site, and we show here that they also help to bridge U1 snRNP to U2 during the early stages of prespliceosome formation. In humans and in *Schizosaccharomyces pombe*, Prp5 facilitates formation of the A complex by bridging the U1 and U2 snRNPs⁴, with the Prp5 N-terminal RS domain interacting with proteins of the SF3b complex²¹. Although *S. cerevisiae* Prp5 lacks an N-terminal RS domain, CXMS data indicate that its N terminus also interacts with Snu71 and Rse1^{BPB}. Therefore, the bridge formed by Rse1 and the Prp40–Luc7–Snu71 trimer in the *S. cerevisiae* pre-A complex probably serves as an anchoring point for Prp5's N terminus.

Extended Data Fig. 6 Molecular bridges connecting the U1 and U2 snRNPs in the pre-A complex.

a, Fit of the molecular model of the entire pre-A complex into the EM density (low-pass filtered). The two main bridges that connect the U1 and U2 snRNPs are indicated by arrows. The boxes indicate the regions expanded in **b**, **c**. **b**, Close-up of bridge 1 formed mainly by the interaction of Prp40 with Rse1. Bridge 1 is disrupted during the transition from the pre-A to the A complex (see Fig. 3 and Supplementary Video 1). Deletion analyses of Prp40 showed that although FF domains 3–6 are dispensable for yeast viability, they convey a considerable growth disadvantage when absent⁴⁶. There is also evolutionary conservation of the presence of four or more of the FF domains in Prp40 from various organisms⁴⁶, suggesting that

FF3 and FF4 have important roles during spliceosome assembly and/or splicing. Our crosslinking data indicate that Snu71 also extensively contacts Rse1^{BPB} and FF2 of Prp40 (see Extended Data Fig. 5d). It is conceivable that, in the absence of Prp40 FF3–FF4, Snu71 still interacts with Rse1^{BPB}, the latter being a protein–protein interaction domain that interacts with different proteins in the subsequently formed B and B^{act} spliceosomal complexes. **c**, Close up of bridge 2 that is formed by intron nucleotides between the U2–BS helix and the 5'-ss. By analogy to the situation in later spliceosomal complexes¹², these intron nucleotides are likely to be chaperoned by Hsh49^{RRM1} and Prp11^{ZnF}. Intron nucleotides of the *Act* pre-mRNA (but not of other pre-mRNAs such as *Ubc4*) form a hairpin that can be localized adjacent to the U1 snRNP already in the E complex¹⁸. The resolution is not sufficient to determine the exact intron nucleotides comprising this stem. Note that the intron hairpin is not part of bridge 2. **d**, A lower threshold reveals EM density below the U2–BS helix, adjacent to the open Hsh155^{HEAT} domain, that probably corresponds to the Mud2–Msl5 dimer. The EM map is low-pass filtered to 30 Å resolution. Protein crosslinks supporting the localization of Msl5–Mud2 adjacent to the U2–BS helix are shown. Numbers (colour coded to match protein colours) indicate the positions of crosslinked lysine residues, which are connected by black lines. Msl5–Mud2 could not be precisely modelled into the EM density, presumably because of their structural flexibility. However, on the basis of CXMS data, we tentatively position Msl5–Mud2 into weak density directly downstream of the branch site, close to the U2–BS helix, with Mud2 being bound to the 3'-end of the intron. Formation of the U2–BS helix requires that Msl5 hands the branch site over to the U2 snRNA, and thus Msl5 should already be displaced from the branch site in the pre-A complex. Therefore, retention of Msl5–Mud2 close to the U2–BS helix would be consistent with the binding of Mud2 to the intron downstream of the branch site.

[Extended Data Fig. 7 Cryo-EM and image-processing of the U257A pre-A complex.](#)

a, Computation sorting scheme, with all major image-processing steps depicted. For a more detailed explanation, see the Methods section on

‘Image processing’. **b**, Typical cryo-EM micrograph (out of a total of 27,502) of the *S. cerevisiae* U257A pre-A complex recorded at $\times 120,700$ magnification with a Titan Krios microscope using a Falcon III direct electron detector operating in integration mode at a calibrated pixel size of 1.16 Å. **c**, Representative cryo-EM 2D class averages of the yeast U257A pre-A complex. **d**, FSC calculated using the ‘Post-processing’ routine in RELION indicates a global resolution of 10.4 Å for the entire yeast U257A pre-A complex, and resolutions of 7.5 Å and 13 Å for the multibody-refined U1 and U2 regions, respectively. The global resolution was lower than that of the ΔBS-A pre-A complex, mainly because of the lower number of particles analysed. **e**, Overlay of the EM densities of the ΔBS-A (purple) and U257A (grey) pre-A complexes. **f**, Fit of the 3D model of the ΔBS-A pre-A complex into the EM density of the U257A pre-A complex. Note that, for both complexes, density encompassing Prp5 is first observed at a lower threshold. An extended U2–BS helix has also formed in complexes formed on the U257A mutant. However, the precise conformation of the helix cannot be discerned. The Hsh155^{HEAT} domain is in an open conformation and Prp5 is still bound at the same position, and the same U1–U2 bridges are also observed, indicating that the U257A complexes are also stalled at the same pre-A stage. **g**, Fit of the extended U2–BS helix from the ΔBS-A pre-A complex into the U257A pre-A EM density. **h**, Fit of the Prp5^{RecA} domains and U2–BS helix from the ΔBS-A pre-A model into the EM density of the U257A pre-A complex. **i**, Fit of the Prp40 FF domains and Rse1^{BPB} (which comprise bridge 1) from the ΔBS-A pre-A model into the EM density of the U257A pre-A complex.

Extended Data Fig. 8 Movement of U1 and U2 snRNPs during the transition from the pre-A to the A complex.

a, Close-up of the rotation of the U2 3'-region after the release of Prp5. The 3'-region rotates around the indicated axis by roughly 55°. To better show the movement of the 3'-region, the SmD2 protein is in yellow. For simplicity, only the 3'-region of U2 plus U2 SLII and the U2–BS helix are shown in the pre-A complex and the yeast A complex (PDB 6G90). The pre-A and A complexes are aligned via U2 SLIIa and HR 19–20 of Hsh155. **b**, Close-up of the movement of the U1 snRNP and 3'-region of U2. A top view is shown, with the black dot indicating the pivot point of the U2 3'-

region, which rotates by roughly 55° in the plane of the paper. For simplicity, only the region of U1 snRNP that contains Prp39 is shown. The U1 snRNP rotates around the indicated axis by roughly 45°. In the pre-A complex, Prp39 and Lea1 are separated by roughly 130 Å, but the movements of U1 and U2 bring them into close proximity in the A complex. Even though Lea1 is not essential in *S. cerevisiae*, its depletion prevents formation of the A complex, and adding back Lea1 restores A-complex assembly⁴⁷. The Prp39–Lea1 interaction is a structural marker for the formation of a mature A complex, and as such its absence in the pre-A complex is a clear indication that our complex has stalled at an earlier assembly stage. This interaction is also maintained in the pre-B complex¹³ and is therefore also a structural marker for the conformation that allows joining of the tri-snRNP.

Extended Data Table 1 Cryo-EM data collection, refinement and validation statistics

[Full size table](#)

Extended Data Table 2 Summary of modelled proteins and RNA in the yeast pre-A structure

[Full size table](#)

Supplementary information

[Supplementary Figure 1](#)

PDF showing uncropped images of the gels and western blot shown in this study..

[Reporting Summary](#)

[Supplementary Table 1](#)

Excel table showing the protein composition of purified *S. cerevisiae* pre-A complexes. Proteins were identified by nano LC-ESI MS using MASCOT as a search engine. Only proteins with a ratio of total peptide spectrum

matches (PSMs) to the protein size (expressed in kDa) of at least 1 are shown.

Supplementary Table 2

Excel table showing protein-protein crosslinks identified in *S. cerevisiae* ΔBS-A pre-A complexes. Crosslinks identified by pLink2.3.9 at FDR 1 and 5% are shown. The number of CSMs (crosslinked peptide spectrum matches) are indicated for each crosslinked peptide. "Inter-protein" and "Intra-protein" indicate inter-protein and intra-protein crosslinks, respectively. "Residue 1" and "Residue 2" are the crosslinked residue pairs in Protein 1 and Protein 2, respectively. The data were obtained from two independent crosslinking experiments.

Supplementary Video 1

Mp4 file showing RNP rearrangements during the transformation of the *S. cerevisiae* pre-A complex into an A complex.

Rights and permissions

Open Access This article is licensed under a Creative Commons Attribution 4.0 International License, which permits use, sharing, adaptation, distribution and reproduction in any medium or format, as long as you give appropriate credit to the original author(s) and the source, provide a link to the Creative Commons license, and indicate if changes were made. The images or other third party material in this article are included in the article's Creative Commons license, unless indicated otherwise in a credit line to the material. If material is not included in the article's Creative Commons license and your intended use is not permitted by statutory regulation or exceeds the permitted use, you will need to obtain permission directly from the copyright holder. To view a copy of this license, visit <http://creativecommons.org/licenses/by/4.0/>.

Reprints and Permissions

About this article



Cite this article

Zhang, Z., Rigo, N., Dybkov, O. *et al.* Structural insights into how Prp5 proofreads the pre-mRNA branch site. *Nature* **596**, 296–300 (2021).
<https://doi.org/10.1038/s41586-021-03789-5>

Download citation

- Received: 10 December 2020
- Accepted: 30 June 2021
- Published: 04 August 2021
- Issue Date: 12 August 2021
- DOI: <https://doi.org/10.1038/s41586-021-03789-5>

Comments

By submitting a comment you agree to abide by our [Terms](#) and [Community Guidelines](#). If you find something abusive or that does not comply with our terms or guidelines please flag it as inappropriate.

Download PDF

Advertisement

| [Section menu](#) | [Main menu](#) |

- Article
- [Published: 28 July 2021](#)

Structural basis of ketamine action on human NMDA receptors

- [Youyi Zhang ORCID: orcid.org/0000-0001-7558-6454^{1,2} na1](#),
- [Fei Ye ORCID: orcid.org/0000-0003-4119-3219³ na1](#),
- [Tongtong Zhang ORCID: orcid.org/0000-0002-2414-8048^{1,2} na1](#),
- [Shiyun Lv ORCID: orcid.org/0000-0001-8779-9430^{1,2}](#),
- [Liping Zhou^{2,4}](#),
- [Daohai Du ORCID: orcid.org/0000-0002-6623-7778⁴](#),
- [He Lin⁵](#),
- [Fei Guo⁴](#),
- [Cheng Luo ORCID: orcid.org/0000-0003-3864-8382^{2,4} &](#)
- [Shujia Zhu ORCID: orcid.org/0000-0001-8358-2859^{1,2,6}](#)

[Nature](#) volume 596, pages 301–305 (2021) [Cite this article](#)

- 5235 Accesses
- 86 Altmetric
- [Metrics details](#)

Subjects

- [Cryoelectron microscopy](#)
- [Ion channels in the nervous system](#)

Abstract

Ketamine is a non-competitive channel blocker of *N*-methyl-d-aspartate (NMDA) receptors¹. A single sub-anaesthetic dose of ketamine produces rapid (within hours) and long-lasting antidepressant effects in patients who are resistant to other antidepressants^{2,3}. Ketamine is a racemic mixture of *S*- and *R*-ketamine enantiomers, with *S*-ketamine isomer being the more active antidepressant⁴. Here we describe the cryo-electron microscope structures of human GluN1–GluN2A and GluN1–GluN2B NMDA receptors in complex with *S*-ketamine, glycine and glutamate. Both electron density maps uncovered the binding pocket for *S*-ketamine in the central vestibule between the channel gate and selectivity filter. Molecular dynamics simulation showed that *S*-ketamine moves between two distinct locations within the binding pocket. Two amino acids—leucine 642 on GluN2A (homologous to leucine 643 on GluN2B) and asparagine 616 on GluN1—were identified as key residues that form hydrophobic and hydrogen-bond interactions with ketamine, and mutations at these residues reduced the potency of ketamine in blocking NMDA receptor channel activity. These findings show structurally how ketamine binds to and acts on human NMDA receptors, and pave the way for the future development of ketamine-based antidepressants.

Access options

Subscribe to Journal

Get full journal access for 1 year

\$199.00

only \$3.90 per issue

[Subscribe](#)

All prices are NET prices.

VAT will be added later in the checkout.

Tax calculation will be finalised during checkout.

Rent or Buy article

Get time limited or full article access on ReadCube.

from \$8.99

[Rent or Buy](#)

All prices are NET prices.

Additional access options:

- [Log in](#)
- [Access through your institution](#)
- [Learn about institutional subscriptions](#)

Fig. 1: S-ketamine-bound cryo-EM structures of human GluN1–GluN2A and GluN1–GluN2B NMDA receptors.

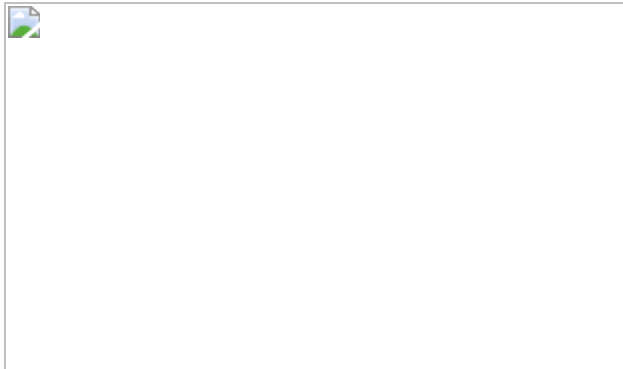
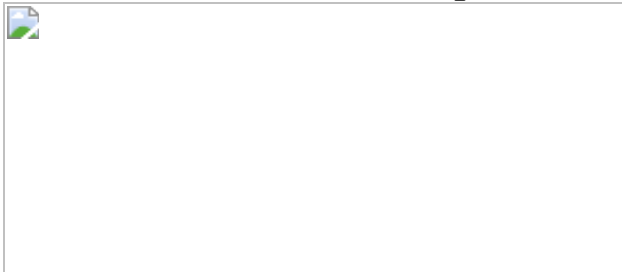


Fig. 2: MD simulation of the S-ketamine-bound TMD of the GluN1–GluN2A receptor.



Fig. 3: Mechanism by which ketamine inhibits GluN1–GluN2A and GluN1–GluN2B NMDA receptors.



Data availability

The cryo-EM maps and structure coordinates for GluN1–GluN2A and GluN1–GluN2B receptors have been deposited in the Electron Microscopy Data Bank under accession numbers [EMD-31308](#) and [EMD-31309](#), and in the Protein Data Bank under accession numbers [7EU7](#) and [7EU8](#), respectively. The structures of *S*-ketamine and *R*-ketamine are accessible from the PubChem database (<https://pubchem.ncbi.nlm.nih.gov/>) under compound CIDs 182137 and 644025, respectively. The human missense mutation c.1925T>G (L642R) in *GRIN2A* was retrieved from the ClinVar database (<https://www.ncbi.nlm.nih.gov/clinvar/>) under variation ID 985631. Additional data that support the findings of this study are available from the corresponding author upon request.

References

1. 1.

Autry, A. E. et al. NMDA receptor blockade at rest triggers rapid behavioural antidepressant responses. *Nature* **475**, 91–95 (2011).

[CAS](#) [PubMed](#) [PubMed Central](#) [Article](#) [Google Scholar](#)

2. 2.

Berman, R. M. et al. Antidepressant effects of ketamine in depressed patients. *Biol. Psychiatry* **47**, 351–354 (2000).

[CAS](#) [PubMed](#) [Article](#) [PubMed Central](#) [Google Scholar](#)

3. 3.

Fava, M. et al. Double-blind, placebo-controlled, dose-ranging trial of intravenous ketamine as adjunctive therapy in treatment-resistant depression (TRD). *Mol. Psychiatry* **25**, 1592–1603 (2020).

[CAS](#) [PubMed](#) [Article](#) [PubMed Central](#) [Google Scholar](#)

4. 4.

Jelen, L. A., Young, A. H. & Stone, J. M. Ketamine: a tale of two enantiomers. *J. Psychopharmacol.* **35**, 109–123 (2021).

[CAS](#) [PubMed](#) [Article](#) [PubMed Central](#) [Google Scholar](#)

5. 5.

Malhi, G. S. & Mann, J. J. Depression. *Lancet* **392**, 2299–2312 (2018).

[PubMed](#) [Article](#) [PubMed Central](#) [Google Scholar](#)

6. 6.

Trivedi, M. H. et al. Medication augmentation after the failure of SSRIs for depression. *N. Engl. J. Med.* **354**, 1243–1252 (2006).

[CAS](#) [PubMed](#) [Article](#) [PubMed Central](#) [Google Scholar](#)

7. 7.

Turner, E. H. Esketamine for treatment-resistant depression: seven concerns about efficacy and FDA approval. *Lancet Psychiatry* **6**, 977–979 (2019).

[PubMed](#) [Article](#) [PubMed Central](#) [Google Scholar](#)

8. 8.

Wilkinson, S. T. et al. The effect of a single dose of intravenous ketamine on suicidal ideation: a systematic review and individual participant data meta-analysis. *Am. J. Psychiatry* **175**, 150–158 (2018).

[PubMed](#) [Article](#) [PubMed Central](#) [Google Scholar](#)

9. 9.

Yang, Y. et al. Ketamine blocks bursting in the lateral habenula to rapidly relieve depression. *Nature* **554**, 317–322 (2018).

[ADS](#) [CAS](#) [PubMed](#) [Article](#) [PubMed Central](#) [Google Scholar](#)

10. 10.

Duman, R. S., Aghajanian, G. K., Sanacora, G. & Krystal, J. H. Synaptic plasticity and depression: new insights from stress and rapid-acting antidepressants. *Nat. Med.* **22**, 238–249 (2016).

[CAS](#) [PubMed](#) [PubMed Central](#) [Article](#) [Google Scholar](#)

11. 11.

Moda-Sava, R. N. et al. Sustained rescue of prefrontal circuit dysfunction by antidepressant-induced spine formation. *Science* **364**, eaat8078 (2019).

[CAS](#) [PubMed](#) [PubMed Central](#) [Google Scholar](#)

12. 12.

Paoletti, P., Bellone, C. & Zhou, Q. NMDA receptor subunit diversity: impact on receptor properties, synaptic plasticity and disease. *Nat. Rev. Neurosci.* **14**, 383–400 (2013).

[CAS](#) [PubMed](#) [Article](#) [PubMed Central](#) [Google Scholar](#)

13. 13.

Karakas, E. & Furukawa, H. Crystal structure of a heterotetrameric NMDA receptor ion channel. *Science* **344**, 992–997 (2014).

[ADS](#) [CAS](#) [PubMed](#) [PubMed Central](#) [Article](#) [Google Scholar](#)

14. 14.

Zhu, S. et al. Mechanism of NMDA receptor inhibition and activation. *Cell* **165**, 704–714 (2016).

[CAS](#) [PubMed](#) [PubMed Central](#) [Article](#) [Google Scholar](#)

15. 15.

Jalali-Yazdi, F., Chowdhury, S., Yoshioka, C. & Gouaux, E. Mechanisms for zinc and proton inhibition of the GluN1/GluN2A NMDA receptor. *Cell* **175**, 1520–1532.e15 (2018).

[CAS](#) [PubMed](#) [PubMed Central](#) [Article](#) [Google Scholar](#)

16. 16.

Chou, T. H., Tajima, N., Romero-Hernandez, A. & Furukawa, H. Structural basis of functional transitions in mammalian NMDA receptors. *Cell* **182**, 357–371.e13 (2020).

[CAS](#) [PubMed](#) [PubMed Central](#) [Article](#) [Google Scholar](#)

17. 17.

Ebert, B., Mikkelsen, S., Thorkildsen, C. & Borgbjerg, F. M. Norketamine, the main metabolite of ketamine, is a non-competitive NMDA receptor antagonist in the rat cortex and spinal cord. *Eur. J. Pharmacol.* **333**, 99–104 (1997).

[CAS](#) [PubMed](#) [Article](#) [PubMed Central](#) [Google Scholar](#)

18. 18.

Erreger, K., Dravid, S. M., Banke, T. G., Wyllie, D. J. & Traynelis, S. F. Subunit-specific gating controls rat NR1/NR2A and NR1/NR2B NMDA channel kinetics and synaptic signalling profiles. *J. Physiol.* **563**, 345–358 (2005).

[CAS](#) [PubMed](#) [PubMed Central](#) [Article](#) [Google Scholar](#)

19. 19.

Burnashev, N. et al. Control by asparagine residues of calcium permeability and magnesium blockade in the NMDA receptor. *Science* **257**, 1415–1419 (1992).

[ADS](#) [CAS](#) [PubMed](#) [Article](#) [PubMed Central](#) [Google Scholar](#)

20. 20.

Song, X. et al. Mechanism of NMDA receptor channel block by MK-801 and memantine. *Nature* **556**, 515–519 (2018).

[ADS](#) [CAS](#) [PubMed](#) [PubMed Central](#) [Article](#) [Google Scholar](#)

21. 21.

Durham, R. J. et al. Conformational spread and dynamics in allosteric of NMDA receptors. *Proc. Natl Acad. Sci. USA* **117**, 3839–3847 (2020).

[CAS](#) [PubMed](#) [PubMed Central](#) [Article](#) [Google Scholar](#)

22. 22.

Iacobucci, G. J. et al. Cross-subunit interactions that stabilize open states mediate gating in NMDA receptors. *Proc. Natl Acad. Sci. USA* **118**, e2007511118 (2021).

[CAS](#) [PubMed](#) [Article](#) [PubMed Central](#) [Google Scholar](#)

23. 23.

Kashiwagi, K. et al. Channel blockers acting at *N*-methyl-d-aspartate receptors: differential effects of mutations in the vestibule and ion channel pore. *Mol. Pharmacol.* **61**, 533–545 (2002).

[CAS](#) [PubMed](#) [Article](#) [PubMed Central](#) [Google Scholar](#)

24. 24.

Chang, L. et al. Comparison of antidepressant and side effects in mice after intranasal administration of (*R,S*)-ketamine, (*R*)-ketamine, and (*S*)-ketamine. *Pharmacol. Biochem. Behav.* **181**, 53–59 (2019).

[CAS](#) [PubMed](#) [Article](#) [PubMed Central](#) [Google Scholar](#)

25. 25.

Lü, W., Du, J., Goehring, A. & Gouaux, E. Cryo-EM structures of the triheteromeric NMDA receptor and its allosteric modulation. *Science* **355**, eaal3729 (2017).

[PubMed](#) [PubMed Central](#) [Article](#) [CAS](#) [Google Scholar](#)

26. 26.

Zanos, P. et al. NMDAR inhibition-independent antidepressant actions of ketamine metabolites. *Nature* **533**, 481–486 (2016).

[ADS](#) [CAS](#) [PubMed](#) [PubMed Central](#) [Article](#) [Google Scholar](#)

27. 27.

Lumsden, E. W. et al. Antidepressant-relevant concentrations of the ketamine metabolite (*2R,6R*)-hydroxynorketamine do not block NMDA receptor function. *Proc. Natl Acad. Sci. USA* **116**, 5160–5169 (2019).

[CAS](#) [PubMed](#) [PubMed Central](#) [Article](#) [Google Scholar](#)

28. 28.

Lee, C. H. et al. NMDA receptor structures reveal subunit arrangement and pore architecture. *Nature* **511**, 191–197 (2014).

[ADS](#) [CAS](#) [PubMed](#) [PubMed Central](#) [Article](#) [Google Scholar](#)

29. 29.

Zhang, J. B. et al. Structural basis of the proton sensitivity of human GluN1-GluN2A NMDA receptors. *Cell Rep.* **25**, 3582–3590.e4 (2018).

[CAS](#) [PubMed](#) [Article](#) [PubMed Central](#) [Google Scholar](#)

30. 30.

Zheng, S. Q. et al. MotionCor2: anisotropic correction of beam-induced motion for improved cryo-electron microscopy. *Nat. Methods* **14**, 331–332 (2017).

[CAS](#) [PubMed](#) [PubMed Central](#) [Article](#) [Google Scholar](#)

31. 31.

Zhang, K. Gctf: real-time CTF determination and correction. *J. Struct. Biol.* **193**, 1–12 (2016).

[ADS](#) [CAS](#) [PubMed](#) [PubMed Central](#) [Article](#) [Google Scholar](#)

32. 32.

Zivanov, J., Nakane, T. & Scheres, S. H. W. Estimation of high-order aberrations and anisotropic magnification from cryo-EM data sets in RELION-3.1. *IUCrJ* **7**, 253–267 (2020).

[CAS](#) [PubMed](#) [PubMed Central](#) [Article](#) [Google Scholar](#)

33. 33.

Pettersen, E. F. et al. UCSF Chimera—a visualization system for exploratory research and analysis. *J. Comput. Chem.* **25**, 1605–1612 (2004).

[CAS](#) [Article](#) [Google Scholar](#)

34. 34.

Adams, P. D. et al. PHENIX: a comprehensive Python-based system for macromolecular structure solution. *Acta Crystallogr. D* **66**, 213–221 (2010).

[CAS](#) [Article](#) [Google Scholar](#)

35. 35.

Morris, G. M. et al. AutoDock4 and AutoDockTools4: automated docking with selective receptor flexibility. *J. Comput. Chem.* **30**, 2785–2791 (2009).

[CAS](#) [PubMed](#) [PubMed Central](#) [Article](#) [Google Scholar](#)

36. 36.

Webb, B. & Sali, A. Comparative protein structure modeling using MODELLER. *Curr. Protoc. Bioinformatics* **54**, 5.6.1–5.6.37 (2016).

[Article](#) [Google Scholar](#)

37. 37.

Schrodinger, LLC *Maestro, Version 9.0* (2009).

38. 38.

Vanommeslaeghe, K. & MacKerell, A. D., Jr. Automation of the CHARMM General Force Field (CGenFF) I: bond perception and atom typing. *J. Chem. Inf. Model.* **52**, 3144–3154 (2012).

[CAS](#) [PubMed](#) [PubMed Central](#) [Article](#) [Google Scholar](#)

39. 39.

Jo, S., Kim, T., Iyer, V. G. & Im, W. CHARMM-GUI: a web-based graphical user interface for CHARMM. *J. Comput. Chem.* **29**, 1859–1865 (2008).

[CAS](#) [PubMed](#) [Article](#) [PubMed Central](#) [Google Scholar](#)

40. 40.

Kumari, R., Kumar, R., Open Source Drug Discovery Consortium & Lynn, A. g_mmpbsa—a GROMACS tool for high-throughput MM-PBSA calculations. *J. Chem. Inf. Model.* **54**, 1951–1962 (2014).

[CAS](#) [PubMed](#) [Article](#) [PubMed Central](#) [Google Scholar](#)

41. 41.

Chen, S. et al. Activation and desensitization mechanism of AMPA receptor-TARP complex by cryo-EM. *Cell* **170**, 1234–1246.e14

(2017).

[CAS](#) [PubMed](#) [PubMed Central](#) [Article](#) [Google Scholar](#)

42. 42.

Meyerson, J. R. et al. Structural basis of kainate subtype glutamate receptor desensitization. *Nature* **537**, 567–571 (2016).

[ADS](#) [CAS](#) [PubMed](#) [PubMed Central](#) [Article](#) [Google Scholar](#)

[Download references](#)

Acknowledgements

We thank B. Zhu, X. Li, C. Liu, F. Meng and Z. Guo for their assistance with cryo-EM data collection; H. Wang, J. Zhang and Y. Gu for assistance with experiments; Y. Sun for advice on human NMDA receptor variants; and M. Poo and E. Xu for proofreading. Financial support is gratefully acknowledged from the National Natural Science Foundation of China (31771115), the National Key R&D Program of China (2017YFA0505700), the Strategic Priority Research Program of the Chinese Academy of Sciences (XDB32020000), the Shanghai Municipal Science and Technology Major Project (2018SHZDZX05) and the Thousand Young Talents Program to S.Z.; and the National Natural Science Foundation of China (81625022, 91853205, 81821005) and the Shanghai Municipal Health Commission in China (18431907100 and 19XD1404700) to C.L.

Author information

Author notes

1. These authors contributed equally: Youyi Zhang, Fei Ye, Tongtong Zhang

Affiliations

1. Institute of Neuroscience, State Key Laboratory of Neuroscience, CAS
Center for Excellence in Brain Science and Intelligence Technology,
Chinese Academy of Sciences, Shanghai, China

Youyi Zhang, Tongtong Zhang, Shiyun Lv & Shujia Zhu

2. University of Chinese Academy of Sciences, Beijing, China

Youyi Zhang, Tongtong Zhang, Shiyun Lv, Liping Zhou, Cheng
Luo & Shujia Zhu

3. College of Life Sciences and Medicine, Zhejiang Sci-Tech University,
Hangzhou, China

Fei Ye

4. Drug Discovery and Design Center, the Center for Chemical Biology,
State Key Laboratory of Drug Research, Shanghai Institute of Material
Medica, Chinese Academy of Sciences, Shanghai, China

Liping Zhou, Daohai Du, Fei Guo & Cheng Luo

5. Criminal Investigation Technology Department, The Third Research
Institute of Ministry of Public Security, Shanghai, China

He Lin

6. Shanghai Center for Brain Science and Brain-Inspired Intelligence
Technology, Shanghai, China

Shujia Zhu

Authors

1. Youyi Zhang
[View author publications](#)

You can also search for this author in [PubMed](#) [Google Scholar](#)

2. Fei Ye

[View author publications](#)

You can also search for this author in [PubMed](#) [Google Scholar](#)

3. Tongtong Zhang

[View author publications](#)

You can also search for this author in [PubMed](#) [Google Scholar](#)

4. Shiyun Lv

[View author publications](#)

You can also search for this author in [PubMed](#) [Google Scholar](#)

5. Liping Zhou

[View author publications](#)

You can also search for this author in [PubMed](#) [Google Scholar](#)

6. Daohai Du

[View author publications](#)

You can also search for this author in [PubMed](#) [Google Scholar](#)

7. He Lin

[View author publications](#)

You can also search for this author in [PubMed](#) [Google Scholar](#)

8. Fei Guo

[View author publications](#)

You can also search for this author in [PubMed](#) [Google Scholar](#)

9. Cheng Luo

[View author publications](#)

You can also search for this author in [PubMed](#) [Google Scholar](#)

10. Shujia Zhu

[View author publications](#)

You can also search for this author in [PubMed](#) [Google Scholar](#)

Contributions

Y.Z. and T.Z. purified and froze the protein, collected and analysed the cryo-EM data, built the atomic model and conducted electrophysiology on GluN1–GluN2A and GluN1–GluN2B receptors, respectively; F.Y., L.Z., and C.L. carried out the docking and MD simulation; D.D. assisted with binding assays; S.L. and F.G. participated in the data analysis; H.L. provided ketamine compounds; Y.Z., F.Y., T.Z. and S.Z. wrote the manuscript with inputs from all the authors. S.Z. conceived the project and supervised the research.

Corresponding authors

Correspondence to [Cheng Luo](#) or [Shujia Zhu](#).

Ethics declarations

Competing interests

The authors declare no competing interests.

Additional information

Peer review information *Nature* thanks the anonymous reviewers for their contribution to the peer review of this work. Peer reviewer reports are available.

Publisher's note Springer Nature remains neutral with regard to jurisdictional claims in published maps and institutional affiliations.

Extended data figures and tables

Extended Data Fig. 1 Expression profile and functional validation of human GluN1–GluN2A and GluN1–GluN2B NMDA receptors.

a, Schematic representation of human GluN1_{EM} (grey), GluN2A_{EM} (green) and GluN2B_{EM} (blue) CTD-truncated constructs. **b**, Representative fluorescence SEC and Coomassie blue gel staining of the purified GluN1–GluN2A_{EM} (left) and GluN1–GluN2B_{EM} receptors (right). Experiments were performed three times independently with similar results. **c, d**, Representative recording traces (left) and the fitted DRCs (right; mean ± s.d.) for (*R,S*)-ketamine inhibition on wild-type GluN1–GluN2A and GluN1–GluN2A_{EM} (**c**), and wild-type GluN1–GluN2B and GluN1–GluN2B_{EM} (**d**) receptors activated with 100 μM coagonists. Ketamine IC₅₀ values, Hill slopes and numbers are listed in Extended Data Table 3.

Extended Data Fig. 2 Overview of cryo-EM image processing and 3D reconstruction of GluN1–GluN2A and GluN1–GluN2B NMDA receptors.

a, Flowchart of the image processing and 3D reconstruction of human GluN1–GluN2A receptors in complex with *S*-ketamine, glycine and glutamate. Typical single particles are circled in red from raw micrographs. The 2D class average images show characteristic 2D views in various orientations. The 3D classes with similar conformations were selected and combined through several rounds of 3D classification for final refinement. **b**, Fourier shell correlation (FSC) curve for the resolution estimation. **c**, Side view of the cryo-EM density map of GluN1–GluN2A receptor coloured by local resolution estimated by Relion 3.1. **d**, Pipelines for single-particle analysis and reconstruction of human GluN1–GluN2B receptor in complex with *S*-ketamine, glycine and glutamate. Same workflow as in **a**. **e**, FSC curve for the resolution estimation. **f**, Side view of the cryo-EM density map of GluN1–GluN2B receptor coloured by local resolution estimated by Relion 3.1.

Extended Data Fig. 3 Representative local densities in GluN1–GluN2A cryo-EM map with fitted atomic model.

a, b, Zoomed-in views of the GluN1-LBD cleft with EM density for glycine (**a**), and the GluN2A-LBD cleft with glutamate (**b**). Key binding residues are shown as sticks. **c, d**, Local densities in extracellular domains of the GluN1 (**a**) and GluN2A (**b**) subunits. EM densities are shown as light grey mesh, while the side chains and N-glycosylation sites of residues are represented as sticks.

Extended Data Fig. 4 Functional validation of the ketamine-binding pocket of NMDA receptors.

a, Representative I – V curves for Mg^{2+} blockage of wild-type GluN1–GluN2A receptors or receptors incorporating a substitution (A, N or V) at GluN2A-L642, recorded in the presence of 100 μM $MgCl_2$. **b, c**, Plot of 3 μM ketamine inhibition level for wild-type (open circle) and mutant (filled circles) amino acid volume (I, V, A or G) at position GluN2B-L643 or GluN2D-L667, shown with a linear regression. R^2 values equal to 0.72 for GluN1–GluN2B and 0.95 for GluN1–GluN2D receptors. **d, e**, (*R,S*)-Ketamine DRCs for the GluN1–GluN2A and GluN1–GluN2B wild-type or mutant receptors incorporating a substitution (A, L or T) at GluN1-V644. All IC_{50} values, Hill slopes and numbers of oocytes are listed in Extended Data Table 3. **f**, Schematic representation of the *S*-ketamine binding site on GluN1–GluN2B receptors analysed by Ligplot⁺.

Extended Data Fig. 5 Molecular basis of *S*- and *R*-ketamine-induced inhibition of GluN1–GluN2A receptors.

a, Chemical structures of left-handed *S*-ketamine and right-handed *R*-ketamine. **b**, r.m.s.d. trajectories for each chain (excluding M1–M2 loops) and *R*-ketamine were calculated on $C\alpha$ atoms based on the initial structure within the whole simulation time of 500 ns. **c**, Left, *R*-ketamine poses obtained in MD simulation along the whole simulation time. Right, schematic diagram of *R*-ketamine and TMD interactions at 500 ns snapshot extracted from MD simulation. Residues involved in the hydrophobic

interactions are shown as starbursts. **d**, Inhibition by 2 μM *S*-ketamine of NMDA receptor activity induced by saturating agonists in wild-type GluN1–GluN2A (0.606 ± 0.018 , $n = 9$ oocytes), GluN1(N616A)–GluN2A (0.020 ± 0.004 , $n = 3$), GluN1(N616Q)–GluN2A (0.027 ± 0.006 , $n = 3$), GluN1–GluN2A(L642A) (0.041 ± 0.012 , $n = 3$), GluN1–GluN2A(L642V) (0.152 ± 0.007 , $n = 3$), GluN1–GluN2A(L642N) (0.020 ± 0.001 , $n = 3$), GluN1(V644A)–GluN2A (0.333 ± 0.038 , $n = 3$), GluN1(V644L)–GluN2A (0.455 ± 0.012 , $n = 3$), GluN1(V644T)–GluN2A (0.602 ± 0.020 , $n = 3$), GluN1(T648V)–GluN2A (0.621 ± 0.015 , $n = 3$), GluN1–GluN2A(T646V) (0.532 ± 0.024 , $n = 4$) and GluN1–GluN2A(N615A) (0.597 ± 0.008 , $n = 3$) receptors. **e**, Inhibition by 2 μM *R*-ketamine of wild-type GluN1–GluN2A (0.404 ± 0.017 , $n = 9$), GluN1(N616A)–GluN2A (0.008 ± 0.001 , $n = 3$), GluN1(N616Q)–GluN2A (0.049 ± 0.008 , $n = 3$), GluN1–GluN2A(L642A) (0.014 ± 0.001 , $n = 3$), GluN1–GluN2A(L642V) (0.065 ± 0.009 , $n = 3$), GluN1–GluN2A(L642N) (0.019 ± 0.001 , $n = 3$), GluN1(T648V)–GluN2A (0.330 ± 0.021 , $n = 3$), GluN1–GluN2A(T646V) (0.423 ± 0.021 , $n = 4$) and GluN1–GluN2A(N615A) (0.344 ± 0.01 , $n = 3$) receptors. **f**, Superposition of the 500 ns snapshots extracted from MD simulation of *S*-ketamine (pink) and *R*-ketamine (cyan) systems, respectively. **g**, Inhibition by 2 μM *R*- and *S*-ketamine of GluN1–GluN2A(N614A) (0.138 ± 0.009 , 0.509 ± 0.014 , $n = 3$) and GluN1–GluN2A(N614Q) (0.140 ± 0.006 , 0.633 ± 0.014 , $n = 3$) receptors. In **d**, **e**, **g**, all data shown are mean \pm s.e.m.; P values are determined by one-way ANOVA with Dunnett's multiple comparison test (** $P < 0.0001$). Each data point represents the result of one oocyte. **h**, *R*-ketamine (left) and *S*-ketamine (right) DRCs (mean \pm s.d.) for wild-type GluN1–GluN2A (IC_{50} : $2.39 \pm 0.45 \mu\text{M}$, $n = 4$ oocytes; $0.60 \pm 0.03 \mu\text{M}$, $n = 3$), GluN1–GluN2A(N614A) ($13.66 \pm 2.49 \mu\text{M}$, $n = 4$; $1.22 \pm 0.44 \mu\text{M}$, $n = 4$) and GluN1–GluN2A(N614Q) ($39.94 \pm 6.72 \mu\text{M}$, $n = 4$; $1.41 \pm 0.38 \mu\text{M}$, $n = 4$) receptors.

Extended Data Fig. 6 Sequence alignment and structural comparison of TMD in ionotropic GluRs.

a, Sequence alignment of TM2–TM3 segments in human GluN1, GluN2A, GluN2B, GluN2C, GluN2D, GluA2 and GluK2, *Xenopus* GluN1, GluN2B and rat GluA2 subunits. The critical residues involved in ketamine binding are highlighted in yellow, and their homologous sites in ionotropic GluRs

are marked in rectangles. **b**, Superposition of the TM2 and TM3 segments between the *S*-ketamine (in brick red)-bound GluN1–GluN2B_{EM} receptor and the MK-801 (in red)-bound GluN1–GluN2B(ΔNTD) receptor (PDB code: 5UN1)²⁰. **c**, MK-801-bound TMD of the triheteromeric GluN1–GluN2A–GluN2B NMDA receptor, viewed parallel to the membrane (PDB code: 5UOW)²⁵. MK-801 binding residues were analysed by LigPlot⁺ (right). **d**, **e**, Superposition of the TM2 and TM3 segments between the *S*-ketamine bound GluN1–GluN2A_{EM} receptor and GluA2 AMPA receptor (PDB code: 5VOT)⁴¹ (**d**) or the GluK2 kainate receptor (PDB code: 5KUF)⁴² (**e**). All superpositions are based on the α-carbon atoms of the conserved SYTANL region.

Extended Data Table 1 Cryo-EM data collection, refinement and validation statistics

[Full size table](#)

Extended Data Table 2 Per-residue decomposition of relative binding energy for residues within 10 Å of *S*-ketamine

[Full size table](#)

Extended Data Table 3 Summary of potency of (*R,S*)-ketamine on human GluN1–GluN2A and GluN1–GluN2B receptors

[Full size table](#)

Extended Data Table 4 Per-residue decomposition of relative binding energy for residues within 10 Å of *R*-ketamine

[Full size table](#)

Supplementary information

[Supplementary Figure 1](#)

Uncropped gels presented in the Extended Data Fig. 1.

[Reporting Summary](#)

[Peer Review File](#)

Video 1

Motions of GluN1-GluN2A TMD in complex with S-ketamine (brick-red) and R-ketamine (blue) during the 500 ns MD simulation. The TMD of GluN1 and GluN2A subunits are shown in grey and green, respectively.

Rights and permissions

Reprints and Permissions

About this article



Check for
updates

Cite this article

Zhang, Y., Ye, F., Zhang, T. *et al.* Structural basis of ketamine action on human NMDA receptors. *Nature* **596**, 301–305 (2021).
<https://doi.org/10.1038/s41586-021-03769-9>

Download citation

- Received: 05 March 2021
- Accepted: 24 June 2021
- Published: 28 July 2021
- Issue Date: 12 August 2021
- DOI: <https://doi.org/10.1038/s41586-021-03769-9>

Comments

By submitting a comment you agree to abide by our [Terms](#) and [Community Guidelines](#). If you find something abusive or that does not comply with our terms or guidelines please flag it as inappropriate.

[Access through your institution](#)

[Change institution](#)

[Buy or subscribe](#)

Advertisement

This article was downloaded by **calibre** from <https://www.nature.com/articles/s41586-021-03769-9>

| [Section menu](#) | [Main menu](#) |

- Matters Arising
- [Published: 11 August 2021](#)

Phantom epistasis between unlinked loci

- [Gibran Hemani](#) [ORCID: orcid.org/0000-0003-0920-1055](#)^{1,2 na2},
- [Joseph E. Powell](#)^{3,4 na2},
- [Huanwei Wang](#) [ORCID: orcid.org/0000-0002-6137-3391](#)⁵,
- [Konstantin Shakhbazov](#),
- [Harm-Jan Westra](#)^{6 na1},
- [Tonu Esko](#)^{7,8,9},
- [Anjali K. Henders](#)⁵,
- [Allan F. McRae](#)⁵,
- [Nicholas G. Martin](#) [ORCID: orcid.org/0000-0003-4069-8020](#)¹⁰,
- [Andres Metspalu](#) [ORCID: orcid.org/0000-0002-3718-796X](#)⁷,
- [Lude Franke](#) [ORCID: orcid.org/0000-0002-5159-8802](#)⁶,
- [Grant W. Montgomery](#) [ORCID: orcid.org/0000-0002-4140-8139](#)⁵,
- [Michael E. Goddard](#)¹¹,
- [Greg Gibson](#) [ORCID: orcid.org/0000-0002-5352-5877](#)¹²,
- [Jian Yang](#) [ORCID: orcid.org/0000-0003-2001-2474](#)^{5,13,14 na2} &
- [Peter M. Visscher](#) [ORCID: orcid.org/0000-0002-2143-8760](#)^{5 na2}

[Nature](#) volume **596**, pages E1–E3 (2021) [Cite this article](#)

- 1762 Accesses
- 50 Altmetric
- [Metrics details](#)

Subjects

- [Epistasis](#)
- [Gene expression](#)
- [Genetic interaction](#)
- [Hardware and infrastructure](#)

The [Original Article](#) was published on 26 February 2014

arising from G. Hemani et al. *Nature* <https://doi.org/10.1038/nature13005> (2014)

Access options

Subscribe to Journal

Get full journal access for 1 year

\$199.00

only \$3.90 per issue

[Subscribe](#)

All prices are NET prices.

VAT will be added later in the checkout.

Tax calculation will be finalised during checkout.

Rent or Buy article

Get time limited or full article access on ReadCube.

from \$8.99

[Rent or Buy](#)

All prices are NET prices.

Additional access options:

- [Log in](#)
- [Access through your institution](#)
- [Learn about institutional subscriptions](#)

Data availability

The gene expression data used to generate the original H2014 paper is available at the Gene Expression Omnibus (GEO) under accession code [GSE53195](#). The ALSPAC genotype data can be accessed via <http://www.bristol.ac.uk/alspac/>. This study makes use of data from dbGaP (accessions phs000428.v1.p1) and EGA (accessions EGAS00001000108 and EGAS00001000090) (see Supplementary Information for a full list of acknowledgements to these datasets).

Code availability

Code is available at: <https://github.com/explodecomputer/eqtl-2d>.

References

1. 1.

Hemani, G. et al. Detection and replication of epistasis influencing transcription in humans. *Nature* **508**, 249–253 (2014).

[ADS](#) [CAS](#) [Article](#) [Google Scholar](#)

2. 2.

Wood, A. R. et al. Another explanation for apparent epistasis. *Nature* **514**, E3–E5 (2014).

[CAS](#) [Article](#) [Google Scholar](#)

3. 3.

Hemani, G. et al. Another explanation for apparent epistasis. *Nature* **514**, E5 (2014).

[CAS](#) [Article](#) [Google Scholar](#)

4. 4.

Hemani, G., Theocharidis, A., Wei, W. & Haley, C. EpiGPU: exhaustive pairwise epistasis scans parallelized on consumer level graphics cards. *Bioinformatics* **27**, 1462–1465 (2011).

[CAS](#) [Article](#) [Google Scholar](#)

5. 5.

Cockerham, C. C. An extension of the concept of partitioning hereditary variance for analysis of covariances among relatives when epistasis is present. *Genetics* **39**, 859–882 (1954).

[CAS](#) [Article](#) [Google Scholar](#)

6. 6.

Cordell, H. J. Epistasis: what it means, what it doesn't mean, and statistical methods to detect it in humans. *Hum. Mol. Genet.* **11**, 2463–2468 (2002).

[CAS](#) [Article](#) [Google Scholar](#)

7. 7.

Wei, W.-H., Hemani, G. & Haley, C. S. Detecting epistasis in human complex traits. *Nat. Rev. Genet.* **15**, 722–733 (2014).

[CAS](#) [Article](#) [Google Scholar](#)

8. 8.

Chang, C. C. et al. Second-generation PLINK: rising to the challenge of larger and richer datasets. *Gigascience* **4**, 7 (2015).

[Article](#) [Google Scholar](#)

9. 9.

de los Campos, G., Sorensen, D. A. & Toro, M. A. imperfect linkage disequilibrium generates phantom epistasis (& perils of big data). *G3 (Bethesda)* **9**, 1429–1436 (2019).

10. 10.

Yang, J. et al. Genomic inflation factors under polygenic inheritance. *Eur. J. Hum. Genet.* **19**, 807–812 (2011).

[Article](#) [Google Scholar](#)

11. 11.

Hemani, G. et al. Inference of the genetic architecture underlying BMI and height with the use of 20,240 sibling pairs. *Am. J. Hum. Genet.* **93**, 865–875 (2013).

[CAS](#) [Article](#) [Google Scholar](#)

12. 12.

Gaunt, T. R. & Davey Smith, G. eNOS and coronary artery disease: publication bias and the eclipse of hypothesis-driven meta-analysis in genetic association studies. *Gene* **556**, 257–258 (2015).

[CAS](#) [Article](#) [Google Scholar](#)

[Download references](#)

Acknowledgements

G.H. was funded by the Wellcome Trust and Royal Society (208806/Z/17/Z). J.E.P. is supported by National Health and Medical Research Council Fellowship (APP1175781). J.Y. and P.M.V. are supported by the Australian Research Council (DP160101343, DP160101056, FT180100186 and FL180100072) and the Australian National Health and Medical Research Council (1078037, 1078901, 1113400 and 1107258). J.Y. is supported by the Westlake Education Foundation. We are extremely grateful to all the families who took part in the ALSPAC study, the midwives for their help in recruiting them, and the whole ALSPAC team, which includes interviewers, computer and laboratory technicians, clerical workers, research scientists, volunteers, managers, receptionists and nurses.

Author information

Author notes

1. Unaffiliated
2. These authors contributed equally: Gibran Hemani, Joseph E. Powell, Jian Yang, Peter M. Visscher

Affiliations

1. MRC Integrative Epidemiology Unit, University of Bristol, Oakfield House, Oakfield Grove, Bristol, UK

Gibran Hemani

2. Population Health Sciences, University of Bristol, Bristol, UK

Gibran Hemani

3. UNSW Cellular Genomics Futures Institute, School of Medical Sciences, University of New South Wales, Sydney, New South Wales, Australia

Joseph E. Powell

4. Garvan-Weizmann Centre for Cellular Genomics, Garvan Institute of Medical Research, Sydney, New South Wales, Australia

Joseph E. Powell

5. Institute for Molecular Bioscience, University of Queensland, Brisbane, Queensland, Australia

Huanwei Wang, Anjali K. Henders, Allan F. McRae, Grant W. Montgomery, Jian Yang & Peter M. Visscher

6. Department of Genetics, University Medical Center Groningen, University of Groningen, Groningen, The Netherlands

Harm-Jan Westra & Lude Franke

7. Estonian Genome Center, University of Tartu, Tartu, Estonia

Tonu Esko & Andres Metspalu

8. Medical and Population Genetics, Broad Institute, Cambridge, MA, USA

Tonu Esko

9. Divisions of Endocrinology, Children's Hospital, Boston, MA, USA

Tonu Esko

10. Queensland Institute of Medical Research, Brisbane, Queensland, Australia

Nicholas G. Martin

11. Faculty of Veterinary and Agricultural Science, University of Melbourne, Melbourne, Victoria, Australia

Michael E. Goddard

12. School of Biology and Centre for Integrative Genomics, Georgia Institute of Technology, Atlanta, GA, USA

Greg Gibson

13. School of Life Sciences, Westlake University, Hangzhou, Zhejiang, China

Jian Yang

14. Westlake Laboratory of Life Sciences and Biomedicine, Hangzhou, Zhejiang, China

Jian Yang

Authors

1. Gibran Hemani

[View author publications](#)

You can also search for this author in [PubMed](#) [Google Scholar](#)

2. Joseph E. Powell

[View author publications](#)

You can also search for this author in [PubMed](#) [Google Scholar](#)

3. Huanwei Wang

[View author publications](#)

You can also search for this author in [PubMed](#) [Google Scholar](#)

4. Konstantin Shakhbazov

[View author publications](#)

You can also search for this author in [PubMed](#) [Google Scholar](#)

5. Harm-Jan Westra

[View author publications](#)

You can also search for this author in [PubMed](#) [Google Scholar](#)

6. Tonu Esko

[View author publications](#)

You can also search for this author in [PubMed](#) [Google Scholar](#)

7. Anjali K. Henders

[View author publications](#)

You can also search for this author in [PubMed](#) [Google Scholar](#)

8. Allan F. McRae

[View author publications](#)

You can also search for this author in [PubMed](#) [Google Scholar](#)

9. Nicholas G. Martin

[View author publications](#)

You can also search for this author in [PubMed](#) [Google Scholar](#)

10. Andres Metspalu

[View author publications](#)

You can also search for this author in [PubMed](#) [Google Scholar](#)

11. Lude Franke

[View author publications](#)

You can also search for this author in [PubMed](#) [Google Scholar](#)

12. Grant W. Montgomery

[View author publications](#)

You can also search for this author in [PubMed](#) [Google Scholar](#)

13. Michael E. Goddard

[View author publications](#)

You can also search for this author in [PubMed](#) [Google Scholar](#)

14. Greg Gibson

[View author publications](#)

You can also search for this author in [PubMed](#) [Google Scholar](#)

15. Jian Yang

[View author publications](#)

You can also search for this author in [PubMed](#) [Google Scholar](#)

16. Peter M. Visscher

[View author publications](#)

You can also search for this author in [PubMed](#) [Google Scholar](#)

Contributions

G.H., J.E.P., J.Y. and P.M.V. conceived the analyses. M.E.G. and P.M.V. developed the theory. G.H., J.E.P. and H.W. conducted the analyses. G.H., J.E.P., P.M.V., J.Y. and G.G. wrote the paper. All authors provided critical feedback on the interpretation of the results

Corresponding author

Correspondence to [Gibran Hemani](#).

Ethics declarations

Competing interests

The authors declare no competing interests.

Additional information

Publisher's note Springer Nature remains neutral with regard to jurisdictional claims in published maps and institutional affiliations.

Supplementary information

Supplementary Information

This file contains Supplementary Methods, Supplementary Notes 1-6, Supplementary Figures 1-9, and Supplementary References.

Reporting Summary

Rights and permissions

Reprints and Permissions

About this article



Check for
updates

Cite this article

Hemani, G., Powell, J.E., Wang, H. *et al.* Phantom epistasis between unlinked loci. *Nature* **596**, E1–E3 (2021). <https://doi.org/10.1038/s41586-021-03765-z>

Download citation

- Received: 03 June 2016
- Accepted: 23 June 2021
- Published: 11 August 2021

- Issue Date: 12 August 2021
- DOI: <https://doi.org/10.1038/s41586-021-03765-z>

Comments

By submitting a comment you agree to abide by our [Terms](#) and [Community Guidelines](#). If you find something abusive or that does not comply with our terms or guidelines please flag it as inappropriate.

[Access through your institution](#)

[Change institution](#)

[Buy or subscribe](#)

Advertisement

This article was downloaded by **calibre** from <https://www.nature.com/articles/s41586-021-03765-z>

| [Section menu](#) | [Main menu](#) |

Amendments & Corrections

- **[Retraction Note: Detection and replication of epistasis influencing transcription in humans](#)** [11 August 2021]

Retraction •

Retraction Note: Detection and replication of epistasis influencing transcription in humans

[Download PDF](#)

- Retraction Note
- [Published: 11 August 2021](#)

Retraction Note: Detection and replication of epistasis influencing transcription in humans

- [Gibran Hemani](#) ORCID: orcid.org/0000-0003-0920-1055^{1,2},
- [Konstantin Shakhbazov](#)^{1,2},
- [Harm-Jan Westra](#)³,
- [Tonu Esko](#)^{4,5,6},
- [Anjali K. Henders](#)⁷,
- [Allan F. McRae](#)^{1,2},
- [Jian Yang](#)¹,
- [Greg Gibson](#)⁸,
- [Nicholas G. Martin](#)⁷,
- [Andres Metspalu](#)⁴,
- [Lude Franke](#)³,
- [Grant W. Montgomery](#)^{7 na1},
- [Peter M. Visscher](#)^{1,2 na1} &
- [Joseph E. Powell](#)^{1,2 na1}

[Nature](#) volume 596, page 306 (2021) [Cite this article](#)

- 2729 Accesses
- 59 Altmetric

- [Metrics details](#)

The [Original Article](#) was published on 26 February 2014

[Download PDF](#)

Retraction to: *Nature* <https://doi.org/10.1038/nature13005> Published online
26 February 2014

In this Letter, we reported the detection and replication of epistatic interactions between common single nucleotide polymorphisms (SNPs) that influence gene expression in peripheral blood, including both *cis–cis* and *cis–trans* interactions. We applied a statistical method widely used to detect epistasis. Wood et al.¹ replicated these findings statistically in an additional whole-genome sequencing dataset but found that a large fraction of these epistatic effects could be explained by tagging sequence variants that were not genotyped in our study. They suggested that the interactions arose owing to haplotypes that tag single additive variants. In our response², we argued that such a mechanism could not explain *cis–trans* interactions. We have since undertaken further analyses to try to understand the mechanism that gives rise to *cis–trans* associations³.

We find that in the presence of imperfectly tagged *cis*-expression quantitative trait loci with large additive effects, the *F*-test statistic used to detect interactions can result in an inflated false positive rate. As a result, we voice concern over whether our reported epistatic associations arose owing to biological mechanisms or from inflated test statistics caused by imperfectly tagged additive effects. All authors agree with the revised scientific interpretation of the original findings but opinions on whether to voluntarily retract the paper are mixed. Authors Gibran Hemani, Konstantin Shakhbazov, Harm-Jan Westra, Tonu Esko, Anjali K. Henders, Allan F. McRae, Jian Yang, Nicholas G. Martin, Andres Metspalu, Lude Franke, Grant W. Montgomery, Peter M. Visscher and Joseph E. Powell agree with the Retraction. Greg Gibson disagrees with the Retraction.

References

1. 1.

Wood, A. et al. Another explanation for apparent epistasis. *Nature* **514**, E3–E5 (2014).

[CAS Article](#) [Google Scholar](#)

2. 2.

Hemani, G. et al. Hemani *et al.* reply. *Nature* **514**, E5–E6 (2014).

[CAS Article](#) [Google Scholar](#)

3. 3.

Hemani, G. et al. Phantom epistasis between unlinked loci. *Nature* <https://doi.org/10.1038/s41586-021-3765-z> (2021).

[Download references](#)

Author information

Author notes

1. These authors contributed equally: Grant W. Montgomery, Peter M. Visscher, Joseph E. Powell

Affiliations

1. Queensland Brain Institute, University of Queensland, Brisbane, Queensland, Australia

Gibran Hemani, Konstantin Shakhbazov, Allan F. McRae, Jian Yang, Peter M. Visscher & Joseph E. Powell

2. University of Queensland Diamantina Institute, University of Queensland, Princess Alexandra Hospital, Brisbane, Queensland, Australia

Gibran Hemani, Konstantin Shakhbazov, Allan F. McRae, Peter M. Visscher & Joseph E. Powell
3. Department of Genetics, University Medical Center Groningen, University of Groningen, Hanzeplein 1, Groningen, The Netherlands

Harm-Jan Westra & Lude Franke
4. Estonian Genome Center, University of Tartu, Tartu, Estonia

Tonu Esko & Andres Metspalu
5. Medical and Population Genetics, Broad Institute, Cambridge, MA, USA

Tonu Esko
6. Divisions of Endocrinology, Children's Hospital, Boston, MA, USA

Tonu Esko
7. Queensland Institute of Medical Research, Brisbane, Queensland, Australia

Anjali K. Henders, Nicholas G. Martin & Grant W. Montgomery
8. School of Biology and Centre for Integrative Genomics, Georgia Institute of Technology, Atlanta, GA, USA

Greg Gibson

Authors

1. Gibran Hemani
[View author publications](#)

You can also search for this author in [PubMed](#) [Google Scholar](#)

2. Konstantin Shakhbazov
[View author publications](#)

You can also search for this author in [PubMed](#) [Google Scholar](#)

3. Harm-Jan Westra
[View author publications](#)

You can also search for this author in [PubMed](#) [Google Scholar](#)

4. Tonu Esko
[View author publications](#)

You can also search for this author in [PubMed](#) [Google Scholar](#)

5. Anjali K. Henders
[View author publications](#)

You can also search for this author in [PubMed](#) [Google Scholar](#)

6. Allan F. McRae
[View author publications](#)

You can also search for this author in [PubMed](#) [Google Scholar](#)

7. Jian Yang
[View author publications](#)

You can also search for this author in [PubMed](#) [Google Scholar](#)

8. Greg Gibson
[View author publications](#)

You can also search for this author in [PubMed](#) [Google Scholar](#)

9. Nicholas G. Martin
[View author publications](#)

You can also search for this author in [PubMed](#) [Google Scholar](#)

10. Andres Metspalu

[View author publications](#)

You can also search for this author in [PubMed](#) [Google Scholar](#)

11. Lude Franke

[View author publications](#)

You can also search for this author in [PubMed](#) [Google Scholar](#)

12. Grant W. Montgomery

[View author publications](#)

You can also search for this author in [PubMed](#) [Google Scholar](#)

13. Peter M. Visscher

[View author publications](#)

You can also search for this author in [PubMed](#) [Google Scholar](#)

14. Joseph E. Powell

[View author publications](#)

You can also search for this author in [PubMed](#) [Google Scholar](#)

Corresponding author

Correspondence to [Gibran Hemani](#).

Rights and permissions

[Reprints and Permissions](#)

About this article



Check for
updates

Cite this article

Hemani, G., Shakhbazov, K., Westra, HJ. *et al.* Retraction Note: Detection and replication of epistasis influencing transcription in humans. *Nature* **596**, 306 (2021). <https://doi.org/10.1038/s41586-021-03766-y>

[Download citation](#)

- Published: 11 August 2021
- Issue Date: 12 August 2021
- DOI: <https://doi.org/10.1038/s41586-021-03766-y>

Comments

By submitting a comment you agree to abide by our [Terms](#) and [Community Guidelines](#). If you find something abusive or that does not comply with our terms or guidelines please flag it as inappropriate.

[Download PDF](#)

Advertisement

This article was downloaded by **calibre** from <https://www.nature.com/articles/s41586-021-03766-y>.